

NASA SP-150

C.1

LOAN COPY: R1
AFWL (WL)
KIRTLAND AFB

0063348



TECH LIBRARY KAFB, NM

The Zodiacal Light and the Interplanetary Medium

A symposium held at
EAST-WEST CENTER
UNIVERSITY OF HAWAII
Honolulu, Hawaii

JANUARY 30—FEBRUARY 2, 1967



NATIONAL AERONAUTICS AND SPACE ADMINISTRATION





0063348

**The Zodiacal Light
and the Interplanetary Medium**



Zodiacal light photograph from Haleakala (P. HUTCHISON, University of Hawaii, January 1967)

The Zodiacal Light and the Interplanetary Medium

Edited by

J. L. WEINBERG

University of Hawaii



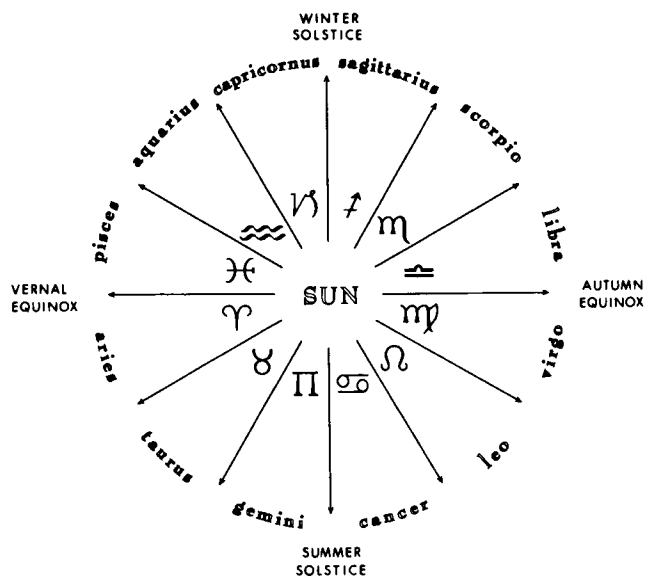
Scientific and Technical Information Division

OFFICE OF TECHNOLOGY UTILIZATION

NATIONAL AERONAUTICS AND SPACE ADMINISTRATION

1967

Washington, D.C.



For Sale by the Superintendent of Documents.
 U.S. Government Printing Office, Washington, D.C. 20402
 Price \$3.00 paper cover
 Library of Congress Catalog Card Number 67-61595

Foreword

This is a meeting I did not attend. The place and date would not have helped to convince my colleagues at the University that this was serious science. Yet the meeting was serious, full and well organized indeed. It is gratifying that the audience will be greatly widened by making this impressive collection of research papers available in book form.

Like most subjects in astronomy, the study of the zodiacal light has progressed from geometry and qualitative explanation to physics and quantitative theory. About 20 years ago the venture to connect the zodiacal light and the corona made the first crude models possible, in which the dust particles had nontrivial sizes and phase functions. Even 10 years ago photoelectric observations from acceptable observing sites were available for less than 100 nights in total. Data on spectrum and polarization were scarce.

Progress has since been made on all fronts. Observational data have greatly increased in quality and quantity. Far more refined models have been fitted to them. These subjects by themselves would have fully justified this meeting. Yet, the onset of a second, more significant advance is also seen. Space vehicles now permit study of these dust grains *in situ*. Direct results of these studies are still scanty and have a bias for the regions close to the earth. But space vehicles have revealed a great deal of information about solar wind, that is, about the medium of gas, radiation, and magnetic fields in which the dust particles describe their orbits.

This knowledge has provided a far more realistic basis for theories of physics and dynamics of the dust, than we had a few years ago. It is therefore entirely fitting that several papers on origin and evolution of the zodiacal dust cloud conclude this book.

H. C. VAN DE HULST
*University Observatory
Leiden, the Netherlands*

Page intentionally left blank

Preface

Discussions during the Twelfth General Assembly of the International Astronomical Union in Hamburg (1964) led to a conference on the Zodiacal Light and the Interplanetary Medium in Honolulu from January 30 through February 3, 1967. Two of the Commissions in the Union have a direct interest in the subject: Commission 21 (Light of the Night Sky) because the zodiacal light is a major photometric component of the light of the night sky; Commission 22 (Meteors and Meteorites) because the zodiacal light is an indicator of the nature of the interplanetary matter. The members and officers of both Commissions participated in the planning and in the program. The meeting was cosponsored by the International Astronomical Union and the American Institute of Aeronautics and Astronautics.

Financial support was provided by the University of Hawaii, the National Aeronautics and Space Administration, and the American Institute of Aeronautics and Astronautics. The sessions were held at the East-West Center of the University of Hawaii. Fifty-six papers were presented during the 4 days of meetings. On the day following the meetings the participants inspected the University's Zodiacal Light Observatory at Mount Haleakala on the Island of Maui. The local arrangements were carried out by the staff of the Zodiacal Light Observatory; J. L. Weinberg, the Director, was assisted by H. M. Mann, R. W. Owen, P. B. Hutchison, and Mrs. C. Hensley (with the aid of G. Kanahele and S. H. Yeaton of the East-West Center Conference Program).

Seventy-four individuals participated from 10 countries: Canada, England, France, India, Israel, Japan, Scotland, Spain, U.S.A., and West Germany. In preparing the proceedings of the symposium for publication, the editor was given general editorial assistance by M. Dubin, G. A. Newkirk, and F. E. Roach.

Because the arrangement of the papers in this volume is different from the order in which they were actually presented, the program outline is given below:

JANUARY 30. OBSERVATIONS

MORNING	<i>Chairman:</i> F. E. Roach Invited speakers: J. L. Weinberg, F. C. Gillett, D. E. Blackwell
AFTERNOON	<i>Chairman:</i> D. E. Blackwell Contributed papers

JANUARY 31. OBSERVATIONS

MORNING	<i>Chairman:</i> J. L. Weinberg Invited speakers: A. W. Peterson, N. B. Divari (presented by Weinberg), R. S. Powell
AFTERNOON	<i>Chairman:</i> M. Huruata Contributed papers

FEBRUARY 1. THE INTERPLANETARY MEDIUM

MORNING *Chairman:* I. B. Strong
 Invited speakers: M. Dubin, J. M. Greenberg, L. Biermann
AFTERNOON *Chairman:* M. Dryer
 Contributed papers
EVENING (The Astronomical Origin and Evolution of the Medium)
 Chairman: F. L. Whipple
 Contributed papers

FEBRUARY 2. THE ASTRONOMICAL ORIGIN
AND EVOLUTION OF THE MEDIUM

MORNING *Chairman:* J. M. Greenberg
 Invited speakers: S. F. Singer, P. M. Millman, F. L. Whipple

F. E. ROACH, *President (1964–1967)*
Commission 21
International Astronomical Union

Contents

I		
PHOTOMETRIC OBSERVATIONS		PAGE
1	A Program of Ground-Based Studies of the Zodiacal Light <i>J. L. Weinberg and H. M. Mann</i>	3
2	Measurement of the Brightness and Polarization of Zodiacal Light From Balloons and Satellites <i>F. C. Gillett</i>	9
3	Toward a Unification of Eclipse and Zodiacal-Light Data <i>D. E. Blackwell and M. F. Ingham</i>	17
4	Multicolor Photometry of the Zodiacal Light <i>Alan W. Peterson</i>	23
5	Reduction of Photometric Measurements of Zodiacal Light for the Influence of Twilight Radiation <i>N. B. Divari</i>	33
6	Rocket Observations of the Brightness of the Zodiacal Light <i>Hiroyoshi Tanabe and Masaaki Huruata</i>	37
7	Observations of the Photometric Axis of the Zodiacal Light <i>Keiji Saito and Masaaki Huruata</i>	41
8	Observations of the Zodiacal Light by Means of Telemetry From Balloons <i>Victor H. Regener and Edwin L. Vande Noord</i>	45
9	Zodiacal-Light Observations From a Sounding Rocket <i>R. D. Wolstencroft and L. J. Rose</i>	49
10	A Five-Color Photometry and Polarimetry of the Zodiacal Light: A Preliminary Report <i>R. D. Wolstencroft and J. C. Brandt</i>	57
11	Photometry of Zodiacal Light and Atmospheric Continuum by H-M Method and Barbier Correlations, and Tenerife Results About the Shape of the Zodiacal Cloud <i>René Dumont</i>	63
12	Recent Polarization Measurements Over the Sky at Tenerife Island <i>Francisco Sanchez Martinez</i>	71
13	Problems of Spectrophotometry of the Zodiacal Light <i>J. F. James</i>	75
14	Noneclipse Observations of the F-Corona <i>M. J. Koomen and R. Tousey</i>	79
15	Some Remarks Concerning the Zodiacal Light <i>C. Hoffmeister[†]</i>	87
16	Infrared Observations of Thermal Radiation From Interplanetary Dust at the Eclipse of November 12, 1966 (ABSTRACT) <i>Alan W. Peterson and Robert M. MacQueen</i>	89
17	Visual Observations of Lunar-Libration-Center Clouds <i>William H. Allen, Walter J. Krumm, and Robert J. Randle</i>	91
18	Lunar-Libration-Cloud Photography <i>J. Wesley Simpson</i>	97
19	Particles of Unknown Origin Photographed at Rocket Altitudes <i>R. Tousey and M. J. Koomen</i>	109

	PAGE
20 Possibility of Continuous Measurement by Optical Radar of the Influx on Earth of Extraterrestrial Dust	<i>Giorgio Fiocco</i> 115

II

PARTICLE COLLECTION AND IMPACT

21 The Characteristics of Interplanetary Dust (ABSTRACT)	
<i>Maurice Dubin and C. L. Hemenway</i>	121
22 Satellite Measurements of Particles Causing Zodiacal Light	
<i>Jose M. Alvarez</i>	123
23 Study of Particles Collected by the 1965 Luster Rocket	
<i>N. N. Greenman, C. B. Gilpin, S. K. Asunmaa, and R. G. Ingersoll</i>	131
24 Preliminary Micrometeorite Results From Gemini IX and XII	
<i>C. L. Hemenway, D. S. Hallgren, and J. F. Kerridge</i>	147
25 Preliminary Results of a Micrometeoroid Collection Experiment in the Gemini Program	
<i>Uri Shafir and Akiva Yaniv</i>	155
26 Evidence of Dust Concentration in the Mesosphere	
<i>O. E. Berg and L. Secretan</i>	161
27 Pegasus Results and Their Interpretation in Relation to Current Mete- oroid Models (ABSTRACT)	
<i>James B. Dozier and Robert J. Naumann</i>	165
28 Particle Collection From the Luster Rocket	
<i>Robert A. Skrivaneck</i>	167
29 Preliminary Results of Investigations of Solid Interplanetary Matter in the Vicinity of the Moon	
<i>T. N. Nazarova, A. K. Rybakov, and G. D. Komissarov</i>	171
30 Elemental Abundances in the Interplanetary Dust	
<i>Paul W. Hodge and Frances W. Wright</i>	173

III

METEOR OBSERVATIONS

31 Space Density of Radio Meteors	<i>Richard B. Southworth</i> 179
32 The Orbits of Meteor Bodies and the Origin of the Hard Component of the Interplanetary Medium	<i>B. L. Kashcheyev and V. N. Lebedinets</i> 189
33 Orbital Distributions of Meteors of Limiting Magnitude +6 Observed From the Southern Hemisphere	<i>Carl S. Nilsson</i> 201

IV

SCATTERING PROPERTIES

34 Small Particles in Space	<i>J. Mayo Greenberg</i> 215
35 Analysis of All Available Zodiacal-Light Observations	
<i>R. S. Powell, P. E. Woodson III, M. A. Alexander, R. R. Circle, A. G. Konheim, D. C. Vogel, and T. W. McElfresh</i>	225
36 Some Models of the Zodiacal Cloud	
<i>L. H. Aller, G. Duffner, M. Dworetzky, D. Gudehus, S. Kilston, D. Leckrone, J. Montgomery, J. Oliver, and E. Zimmerman</i>	243
37 Phase Function of the Zodiacal Cloud	<i>Richard B. Southworth</i> 257

	PAGE
38 On Optical Models Approximating Observations of the Zodiacal Light Outside the Ecliptic <i>R. H. Giese and C. v. Dziembowski</i>	271

V

DYNAMICS

39 Theoretical Considerations of Small Particles in Interplanetary Space <i>L. Biermann</i>	279
40 Dynamics of Submicron Particles ($a < 10^{-5}$ cm) in Interplanetary Space <i>Thomas Schmidt and Hans Elsässer</i>	287
41 Electrostatic Potential of a Cosmic Dust Particle <i>John W. Rhee</i>	291
42 The Thermal Emission of the Zodiacal Cloud (ABSTRACT) <i>C. Kaiser and G. Newkirk, Jr.</i>	299
43 Dynamics of Interplanetary Dust Particles Near the Sun <i>Michael J. S. Belton</i>	301
44 The Cloud of Interplanetary Boulders <i>Martin Harwit</i>	307
45 Collisional Model of Meteoroids <i>J. S. Dohnanyi</i>	315
46 Light Scattered by the Earth's Dust Cloud <i>N. B. Divari</i>	321
47 The Possibility of Dust Concentration Near the Earth <i>Thomas Schmidt</i>	333
48 The Zodiacal Light and Earth-Orbiting Dust <i>S. J. Peale</i>	337
49 The Meteoroid Environment Near the Ecliptic Plane <i>John K. Wall</i>	343

VI

SOLAR WIND

50 Interplanetary Electron Concentration and Variability Measurements With Pioneer VI and VII <i>H. T. Howard and R. L. Koehler</i>	361
51 Satellite Observations of the General Characteristics and Filamentary Structure of the Solar Wind <i>I. B. Strong, J. R. Asbridge, S. J. Bame, and A. Hundhausen</i>	365
52 Solar Wind Induced Torque on the Sun (ABSTRACT) <i>Jerry L. Modisette</i>	373
53 The Interplanetary Solar Wind Ion and Electron Characteristics (ABSTRACT) <i>John H. Wolfe, Richard W. Silva, and D. D. McKibbin</i>	375

VII

ORIGIN AND EVOLUTION

54 Nature and Origin of Zodiacal Dust <i>S. Fred Singer and Lothar W. Bandermann</i>	379
55 Observational Evidence of the Meteoritic Complex <i>Peter M. Millman</i>	399
56 On Maintaining the Meteoritic Complex <i>Fred L. Whipple</i>	409
List of Participants	427
Author Index	429

I

PHOTOMETRIC OBSERVATIONS

Page intentionally left blank

1. A Program of Ground-Based Studies of the Zodiacal Light*

J. L. WEINBERG AND H. M. MANN
Haleakala Observatory
Kula, Maui, Hawaii

RATHER THAN OPEN THE SYMPOSIUM on a negative note by emphasizing the discordance of zodiacal light results, we will outline some recent results from the Haleakala program and current studies in several critical areas.

THE HALEAKALA PROGRAM

Measurements of the zodiacal light were begun at the Haleakala Observatory in 1961 with a single-color photoelectric polarimeter (5300Å; Weinberg, 1964). Since March 1965, when the program was adapted to a multicolor study in the visible and near-infrared regions, we have

obtained observations on 275 nights. We expect to continue certain aspects of both the routine and special observing programs through solar maximum. From these observations we hope to obtain information on both short- and long-term fluctuations in the nightglow and to provide a ground-based backup for the numerous balloon, rocket, and satellite experiments now planned or in operation.

The multiplier phototube now in regular use is a red-sensitive EMR S-20 (table 1) which will cover the range from approximately 3500Å to 9000Å without using prismatic light injection. Tests are being conducted with an S-1 multiplier phototube as a prelude to our construction of a near-infrared photoelectric polarimeter.

Wavelength discrimination is provided by sequential observation with narrow-band inter-

*This research was supported by the National Aeronautics and Space Administration under grant NsG-676 and in part by the Atmospheric Sciences Section, National Science Foundation, under grant GA-326.

TABLE 1. — Multiplier Phototube Calibration Data (EMR Model 541E-01-14)

Test date	Luminous sensitivity, $\mu\text{Å}/\text{lumen}$	Quantum efficiency, percent, at—					Dark current at 10^6 gain at 20° C
		4100Å	4600Å	5600Å	6300Å	8000Å	
6-30-65	231	24	6.5	1.7	4×10^{-9} A after 1 hr
7-16-65	226	24	6.5	1.7	9×10^{-9} A—20 min
9-23-65	236	27	7.0	1.4	9×10^{-9} A—20 min
11-12-65	237	27	7.0	1.4	2.2×10^{-9} A—1 hr
12-10-65	237	27.2	21.8	10.4	6.9
^a 8- 8-66	22.2	18.4	10.0	6.4	7.8×10^{-10} A—overnight
10-12-66	237	27.1	21.6	11.9	7.3	1.7	1.6×10^{-9} A—overnight

^a Relative calibration based on earlier data.

ference filters. In practice the characteristics of such filters (table 2) will vary with temperature and over the filter surface, and it is necessary to measure the characteristics in an optical configuration similar to that in which the filters are to be used. For the very narrow filters one must beware of shifts with time of the band position. Additional details of the instrument and

TABLE 2.—*Characteristics of Interference Filters*

[These filters (except those at 3500Å and 5300Å) are characterized by excellent off-band rejection (transmission less than 0.005 percent).]

Central wavelength		Half-transmission bandwidth, Å (^a)	Maximum transmission, percent
$1/\lambda, \mu^{-1}$	$\lambda, \text{Å}$		
2.86	3500	40	61
2.50	^b 4000	10	
2.30	4355	12	38.5
2.10	4760	11	56.3
1.97	5080	30	64.0
1.89	5300	62	78.2
1.83	5450	20	57.5
1.79	5577I	23	55.2
	IB	12.2	54.1
	II	10.8	56.7
	IIB	7.1	39.8
	III	5.7	41.4
1.74	5752	24.0	42.1
1.64	6080	17.0	65.1
1.59	6300I	31.7	56.3
	IA	22.9	53.6
	II	10.0	41.0
	IIA	9.2	44.8
	III	4.6	36.3
1.55	6437	12.4	55.3
1.48	6745	21.0	57.6
1.41	7100	23.5	59.9
1.22	8200	51.5	57.8
1.15	8700	53	53
1.08	9250	58	64
1.05	^b 9550	80	
0.939	^b 10650	100	

^a Center of filter.

^b On order. (Also on order are additional filters at 5577Å and 6300Å.)

programs will be described in a Haleakala Observatory report now in preparation.

RECENT RESULTS

Nonzodiacal Light Sources of Polarization in Nightglow

The nightglow can be specified by the total or observed brightness (B_{obs}), the brightness of the polarized component (B_{pol}), the orientation of the plane polarization (χ), and the total degree of polarization (p_{tot}).¹ These quantities are related ² by

$$p_{tot} = \frac{\sum_j B_{pol,j}}{\sum_j B_{obs,j}} \neq \sum_j p_j \quad (1)$$

$$\text{or} \quad p_{tot} = \frac{(I_{\perp} - I_{\parallel})_{ZL} + \sum_i (I_{\perp} - I_{\parallel})_i}{(I_{\perp} + I_{\parallel})_{ZL} + \sum_i (I_{\perp} + I_{\parallel})_i} \quad (2)$$

where I_{\perp} and I_{\parallel} are orthogonal components of brightness having their electric vectors perpendicular and parallel, respectively, to the plane through the source, the Earth, and the observed point; ZL and i refer to the zodiacal light and other brightness components, respectively, and $j = ZL + i$. In studies of the nightglow continuum it is usually assumed that all or most of the polarization arises from zodiacal light. Accordingly, $\sum_i (I_{\perp} - I_{\parallel})_i = 0$, and the problem is reduced

to separating the components in the denominator of equation (2).

Recent studies at Haleakala indicate that there are, however, nonzodiacal light sources of appreciable polarization (both astronomical and atmospheric) in the nightglow. Of particular interest is the polarization associated with the 6300Å and, especially, with the 5577Å airglow line emissions. The airglow polarization monotonically increases to a value of several percent near the horizon. In contrast to the strong azimuth dependence of the astronomical sources of polarization, the airglow polarization is relatively uniform in both orientation and degree.

¹ The ellipticity is small and is ignored in this treatment.

² This relationship is given incorrectly in previous publications Weinberg, 1963, 1964).

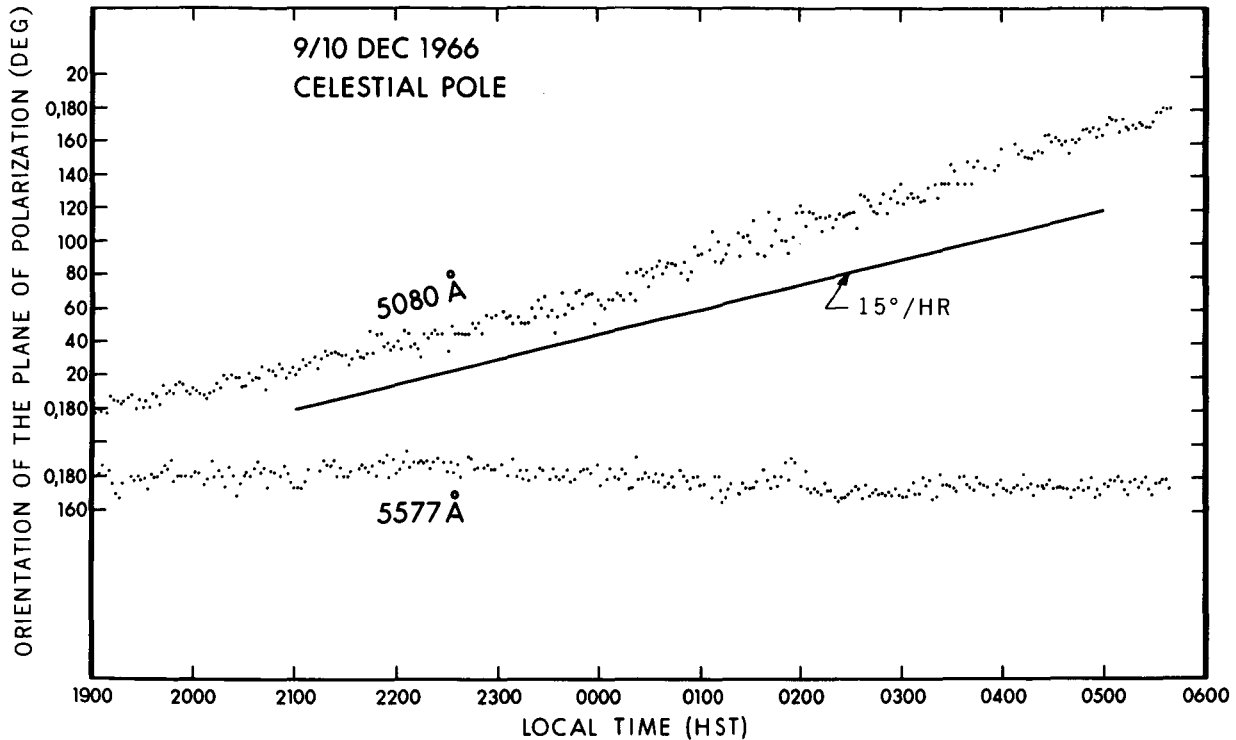


FIGURE 1.—Orientation of plane of polarization in two colors at celestial pole on December 9/10, 1966.

Figure 1 gives an indication of the origin of this polarization. The diurnal variation of the plane of polarization at 5080\AA is primarily associated with the zodiacal light and with the changing position of the sun with respect to the observer and the celestial pole (see, also, Weinberg, 1965). Clearly, the polarization at 5577\AA is not solar oriented. Preliminary calculations (Coulson and Weinberg, unpublished report) suggest that the 5577\AA polarization may be explained by tropospheric scattering of an unpolarized radiation incident on the scattering atmosphere from the E- and/or F-regions.

Although the degree of polarization is small, the airglow lines are "bright," and the intensity of the polarized component is comparable to that of the zodiacal light. Broad-band detection does not, therefore, permit the assumption that $\sum_i (I_{\perp} - I_{\parallel})_i = 0$ in equation (2). In the following section we discuss methods of separating the terms in the denominator of equation (2). There is every indication that the discordance of

results arises from difficulties engendered by different measuring techniques rather than from real changes in the zodiacal light.

Separation of Zodiacal Light From Starlight and Airglow

Starlight

We define starlight as the sum total of brightness from integrated starlight, galactic light, and other sources not having their origin in the atmosphere or in interplanetary space. An empirical technique for deriving the starlight is illustrated in figure 2 where we have plotted the observed brightness at 5300\AA for part of an almucantar including the peak zodiacal light and regions of both high (I) and low (II) galactic latitude. These regions are bounded by points a, b, c, and d, whose galactic coordinates (b^l , l^l) are shown at the top of figure 2. The smooth curve drawn in region I is used as a background for region II above which the differential starlight (the cross-hatched area) is measured. This differential starlight is corrected for atmospheric extinction and scattering and is then added to

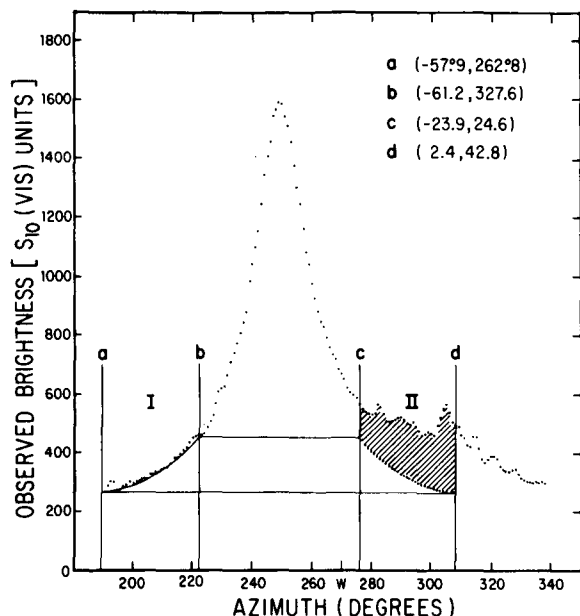


FIGURE 2.—Observed brightness (in 10th mag. vis. stars deg^{-2}) at an elevation of 8° on January 11/12, 1966, for 5300\AA .

the integrated starlight, $J(V)$, corresponding to the b^1 , l^1 of the background or mirror points via a cubic interpolation in tables based on star counts in the selected areas (Roach and Megill, 1961). This sum is termed “starlight.”

For best results the almucantar scan should be approximately centered on the peak zodiacal light. The central value of azimuth, from which the mirror regions are reckoned, is chosen to approximately bisect the brightness distribution near its peak value. The choice of boundaries is governed by the range of azimuth over which the total brightness is measured, by the position of the plane of the galaxy with respect to the peak zodiacal light, and by how close the mirror points are in ecliptic latitude and elongation. To satisfy these requirements and to assure that differential atmospheric scattering will be minimized, the ecliptic must be within $\pm 5^\circ$ of the vertical.

Inherent in the technique are the assumptions that (1) the zodiacal light is approximately symmetric about its axis, (2) the airglow continuum is constant over the range of azimuth included in the measurement, and (3) the starlight is constant. The reproducibility of results obtained on different nights indicates that these assumptions are valid. This technique applied to satellite

observations made perpendicular to the ecliptic appears to be especially well suited for giving the nonzodiacal-light component over a range of perhaps $\pm 40^\circ$ of galactic latitude.

We observe small-scale structure which is not found in the smoothed star-count results, and while existing star-count results cannot be used as a base for separating components of the nightglow at low galactic latitudes, the use of the tabular values does not introduce a significant error at high latitudes where the starlight is relatively faint. This technique is being used to derive a map of the starlight at low galactic latitudes.

Airglow

By careful selection of filters the airglow line emission can be avoided. The principal culprit in making an accurate separation of nightglow components is the airglow continuum. We know neither its nature nor its origin, and it is quite possible that it is not there (at some wavelengths).

The airglow line radiations are not enhanced in the zodiacal light; that is, we observe no enhancement when we scan across the bright regions of zodiacal light with narrow airglow filters (e.g., 5577III and 6300III in table 2). Similarly, we observe no enhancement through suitably blocked continuum filters when we scan across regions of enhanced airglow line emission.

In a study in progress at Haleakala we compare observations of the continuum with observations of the 5577\AA and 6300\AA airglow line emissions at the celestial pole. Figure 3 shows the brightness observed through eight filters at the celestial pole on December 16/17, 1966. The small variation seen through the continuum filters is typical even when the line emission varies by a factor of two or greater. Our preliminary results do not confirm the degree of covariance between 5577\AA line and continuum emission found by other investigators. Analysis of other observations is required before we can assess the effect of line- and continuum-filter characteristics on the inferred degree of covariance. The 5577\AA line emission has its principal maximum at 90 km and a secondary maximum in the F-region which coincides with the maximum of the 6300\AA line emission. Under “normal” conditions the 5577\AA

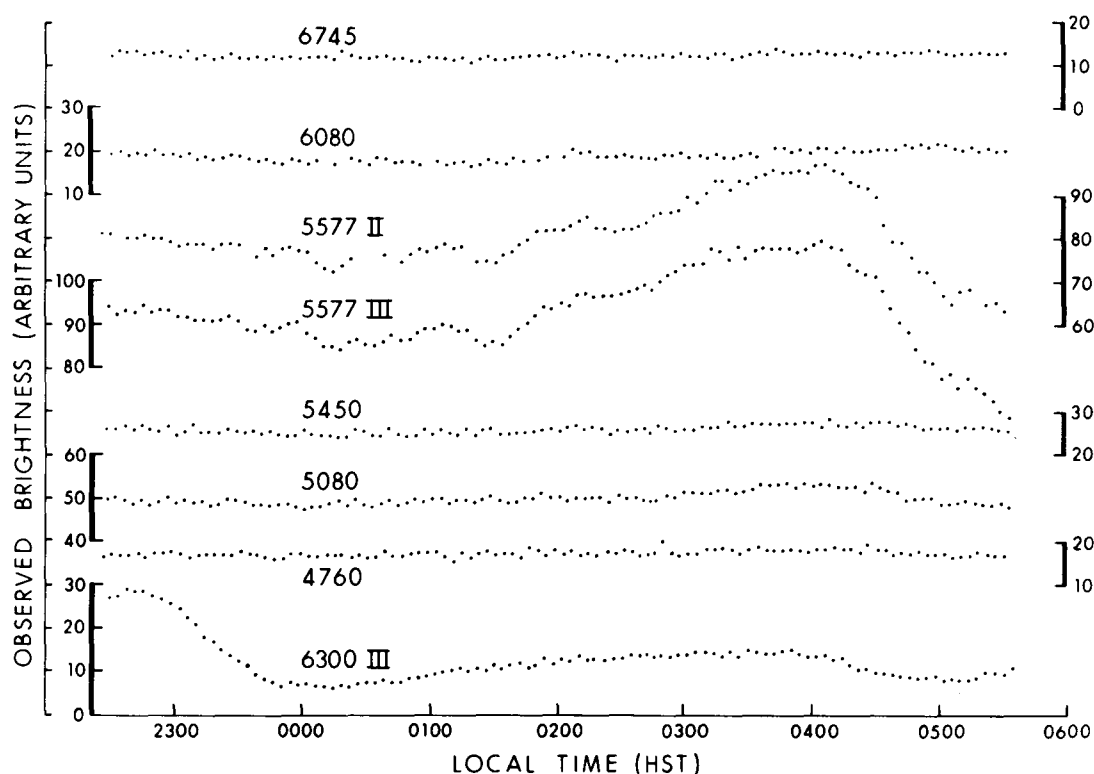


FIGURE 3.—Observed brightness at celestial pole on December 16/17, 1966. The same brightness scale is used for all colors except 5577II which has been reduced by a factor of 1.546.

and 6300\AA line emissions do not covary. When the 6300\AA line emission is enhanced (factor-of-ten enhancements are not uncommon at Haleakala), it covaries with the F-region portion of the 5577\AA line emission and further complicates the study of line and continuum covariance.

Since the zodiacal light extends over the entire sky, observations at some distance from the ecliptic cannot be used effectively for the purpose of estimating the background. Pending the results of additional studies of nightglow covariance groups, we find that the most successful means of separating components involves subtraction of the starlight by some technique and an examination of the nature of the remainder (zodiacal light plus airglow) with time and over the sky.

Comet 1965f and the Zodiacal Cloud

Numerous observations before and after perihelion of Comet 1965f make it possible to examine effects resulting from the newly injected cometary material. We have found no large-scale

changes in the zodiacal light in a 2-week period including perihelion. Additional data are being analyzed in this manner as part of our continuing study of short- and long-term fluctuations in the nightglow.

Multicolor observations were taken of the nightglow over a 9° by 20° section of the sky containing Comet 1965f during several nights following perihelion. The principal Stokes parameters have been derived at 5300\AA both along and normal to the axis throughout the tail of the Comet for one night's observation. Along the axis of the tail the polarization decreases to a neutral point several degrees from the nucleus after which it is negative (electric vector parallel to the scattering plane) throughout the remainder of the tail. This result, as in the case of zodiacal light, requires the presence of dielectric particles. The use of additional observations suggests that it may be possible to delineate a rather small family of allowable solutions for the size distribution of the particles.

Lunar Libration Clouds

In a cooperative program with the Haleakala satellite tracking station of the Smithsonian Astrophysical Observatory (SAO), we have initiated a program of observations of the libration regions in the Earth-Moon system. Based on predictions received from SAO, Cambridge, we have searched for clouds L_4 and L_5 on six different occasions. No visual enhancement was evident on any of the 6 nights. Photoelectric observations by us and photographic observations by the SAO in and around the predicted regions are still being analyzed. In the event that the existence or characteristics of these clouds may be dependent on lunar phase, we plan to observe in and around the predicted regions as often as possible.

CONCLUDING REMARKS

The observer is charged with the responsibility of providing new observations to further limit the allowable size and spatial distributions of the zodiacal dust. Existing observations can be interpreted in many ways and allow us to say little about the mass or density distributions of the zodiacal dust although we can differentiate

between certain dielectric and metallic component models.

Studies now underway at Haleakala should provide information on short- and long-term changes in the position of the symmetry axis of the zodiacal light in total and polarized light and on characteristics of the gegenschein and of the polarized component at large distances from the sun in the plane of the ecliptic. We hope to provide very soon the distribution of brightness and polarization in the ecliptic at eight or more colors in the visible spectrum in the range of 30° to 120° elongation.

By observing over long periods of time and by extending line and continuum covariance studies to many wavelengths in the visible and near infrared, it should be possible to infer something of the nature and origin of the airglow continuum. This, in turn, will enable us to derive the wavelength dependence of the principal Stokes parameters of the zodiacal light over the sky.

ACKNOWLEDGMENTS

The authors wish to thank Roger Owen and Marcia Weinberg for their able assistance.

REFERENCES

- ROACH, F. E., and L. R. MEGILL, 1961, *Astrophys. J.*, **133**, 228.
WEINBERG, J. L., 1963, *Nature*, **198**, 842.
—, 1964, *Ann. d'Astrophys.*, **27**, 718.
—, 1965, *Planet. Sp. Sci.*, **13**, 1311.

2. Measurement of the Brightness and Polarization of Zodiacal Light From Balloons and Satellites

F. C. GILLET

*University of California, San Diego
La Jolla, California*

SATELLITE OBSERVATIONS

THE ADVANTAGES of observing the night sky from above the airglow layer have been well known for some time. Such observations accomplish spatial separation of the airglow from the zodiacal light and interstellar light by confining the airglow emission to a narrow band around the Earth. Also, there are no atmospheric corrections, especially no secondary scattering corrections, and observations can be made at all lunar phases and essentially continuously over long periods of time if the observing platform is an orbiting satellite.

The first observations of this type have recently been made by Dr. E. P. Ney with a zodiacal-light monitor aboard the OSO 2 satellite.

Experiment

The OSO 2 satellite consists of two main components: the sail, which is held approximately perpendicular to the satellite-Sun line and which contains the pointed experiments and solar cells; and the wheel, which is rotated at approximately 25 rpm around an axis along the sail. The spin axis is maintained to within $\pm 4^\circ$ of the plane perpendicular to the satellite-Sun line by automatic pitching but is free to assume any orientation in this plane.

The zodiacal-light monitor consisted of four sky photometers, each with a 10° -diameter field of view, mounted on the wheel with one photometer looking out along the spin axis in the sail direction and the other three photometers looking out

along the spin axis in the antisail direction. Each photometer is equipped with a fixed polaroid sheet, which is rotated with respect to the sky by the spinning wheel. Two telescopes (one in each direction) have a spectral response corresponding to the average of blue and visual magnitudes. The spectral response of one of the remaining telescopes corresponds approximately to the blue system while the other corresponds approximately to the visual system. A fifth photometer is covered by a standard radioactive glow.

In summary, the zodiacal-light monitor observed the brightness and polarization of the night sky above the airglow layer in the three

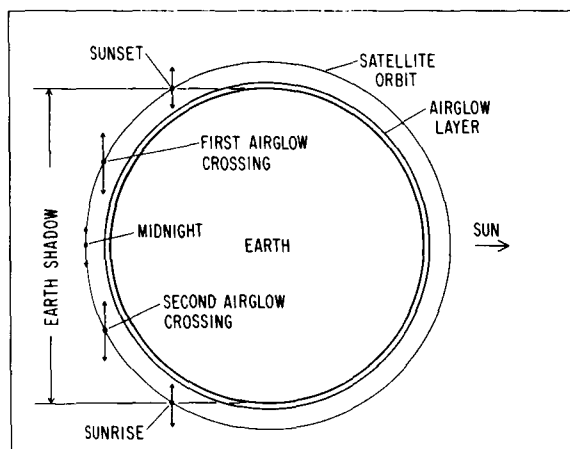


FIGURE 1.—Geometry of satellite observations at various times during a single night with spin axis in the orbit plane.

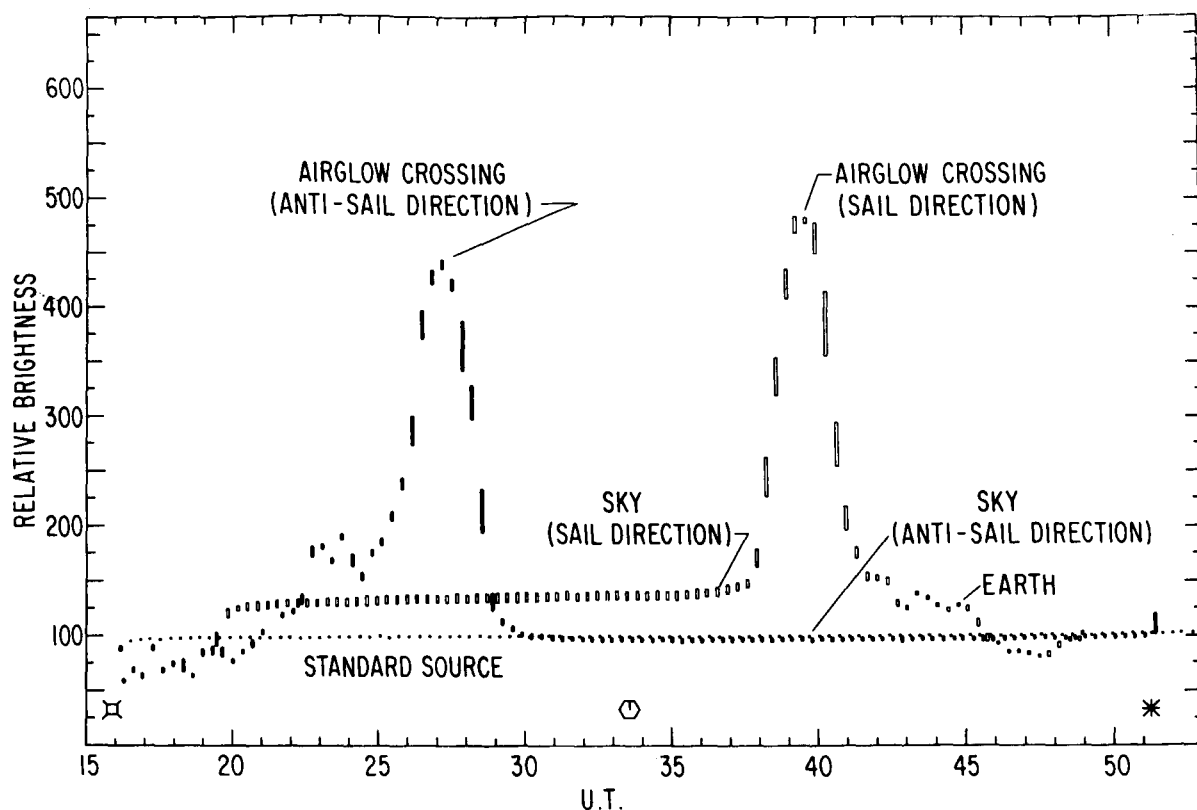


FIGURE 2. — Observed surface brightness versus universal time for sample orbit with spin axis in orbit plane. Symbols from left to right, along the abscissa, indicate sunset, midnight, and sunrise.

spectral regions at elongations between 86° and 94° and unspecified ecliptic inclination.

The satellite was launched into a nearly circular orbit of altitude about 600 km in February 1965 and the zodiacal-light experiment operated satisfactorily until the satellite was turned off in October 1965.

Observations

General Form

Figure 1 shows how the observations are affected by the orbital motion of the satellite when the spin axis is in the orbit plane, and figure 2 shows the observed brightness versus time for one such orbit. Data from three of the telescopes are plotted in figure 2, one in each direction and the standard source telescope. Each box represents 16 data points; the top and bottom indicate the maximum and minimum values for the brightness in that set of points. In this example, the telescopes are turned on at sunset with

the antisail telescopes looking at the Earth and the sail telescope looking at the sky. Some time before midnight the antisail telescopes look at the airglow layer in profile (airglow crossing); and, at midnight, both sets of telescopes are looking at the sky. Between midnight and sunrise there is a second airglow crossing, this time for the sail telescope; and, at sunrise, the sail telescope is looking at the ground and the anti-sail telescopes are looking at the sky. The airglow crossings appear broad because of the 10° field of view of the telescopes.

Time Variations of Sky Brightness

Variations Within a Single Orbit. If the zodiacal light is caused by sunlight scattered off dust particles near the Earth, there should be change in the observed zodiacal-light brightness during the course of the night due to the changes in illumination of the dust along the line of sight. From figure 1 it is seen that the minimum altitude

of sun-illuminated dust at midnight is about 0.5 Earth radii, whereas at sunset or sunrise the minimum altitude is about 0.1 Earth radii. If dust is distributed around the Earth as suggested by Whipple (1961), then a calculation shows that the scattered light from such a dust cloud should be twice as bright at sunset or sunrise as at midnight. Figure 2 shows that the measured sky brightness is constant from midnight to sunrise. The upper limit of the increase toward sunrise is $1S_{10}(V)$, so that the brightness of the dust cloud around the Earth, if it is distributed as suggested by Whipple, is less than $2S_{10}(V)$ at sunrise. Ingham (1962) has calculated that, under similar illumination conditions for his model of zodiacal dust and Whipple's model of dust around the Earth, the contribution due to the dust cloud is about $2S_{10}(V)$; therefore, the observations presented here are not inconsistent with Ingham's calculation.

Variations Over Several Orbits. Except for orbits when the spin axis was pitched to keep it perpendicular to the satellite-Sun line, the sky brightness was remarkably constant from orbit to orbit. On this time scale (several hours) it is expected that changes due to the passage of plasma clouds would be observable.

The observing period was during the minimum of solar activity, so there were a very limited number of events associated with plasma clouds. Table 1 shows events during this period.

An upper limit to the change in sky brightness associated with any of these events is $7S_{10}(V)$. This corresponds to an upper limit of 50 electrons/cc in a plasma cloud with a diameter of $\frac{1}{2}$ AU.

TABLE 1.—Events Associated With Plasma Clouds During Minimum Solar Activity for Several Orbits

Event	Number of events	Dates
Class 3 flare.....	1	June 9, 1965.
Class 2 flare.....	29
CR flare.....	2	Feb. 5 and May 6, 1965.
Proton event.....	1	Mar. 16, 1965.
Imp electron.....	3	Feb. 5, May 25, and June 13, 1965.
Forbush decrease.....	6

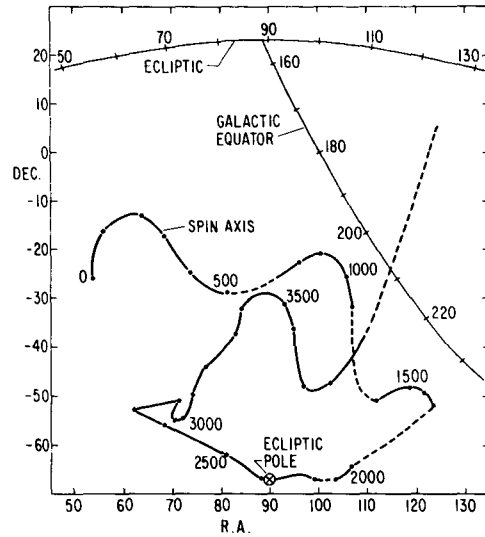


FIGURE 3.—Direction of spin axis as a function of orbit number.

Variations Over Long Time Periods. The changes of sky brightness over time intervals of the order of weeks are due to motions of the field of view on the celestial sphere. Figure 3 shows the direction of spin axis in right ascension and declination as a function of orbit number. Dotted lines indicate regions where the direction is not yet accurately known.

Figure 4 shows the measured visual brightness versus orbit number and the measured standard source brightness versus orbit number. Figure 3 shows that the telescopes observed nearly the same region of the sky on two occasions; orbits near 700 and again near orbits 3400 to 3500. A comparison of the measured sky brightnesses shows that, if the sky brightness were the same during the two observations, then the gain of the photometer must have decreased between orbits 700 and 3450. The same percentage change is shown by the standard-source photometer and also by the other telescopes looking in this direction, so it is assumed that this change is in fact a change in gain for the sky photometers and can be determined as a function of time by the variation in the measured brightness of the standard source.

The absolute calibration of the photometers was accomplished by observing the deflection due to bright stars in the field of view. Alpha Lyrae

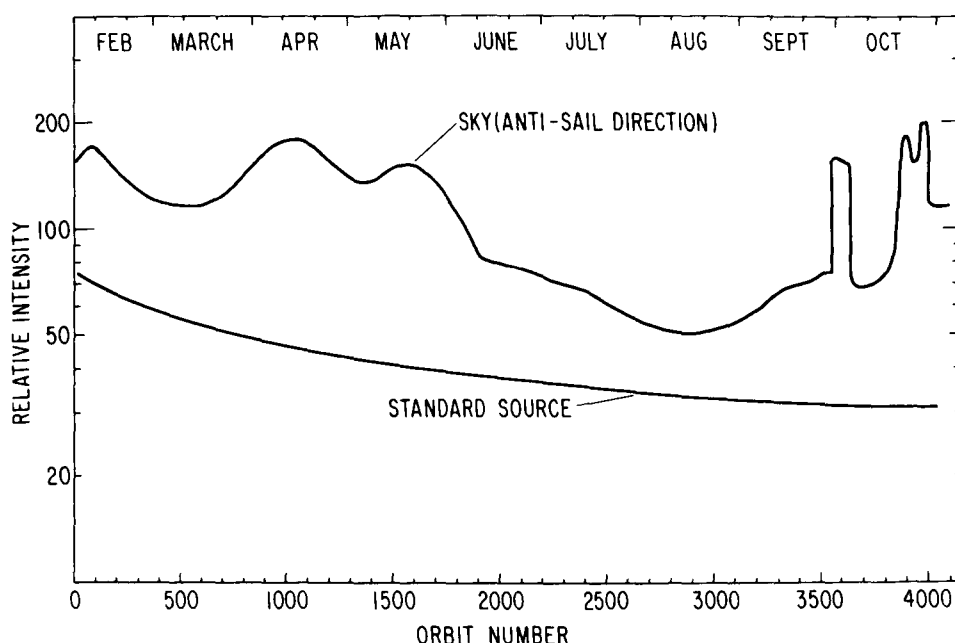


FIGURE 4. — Measured sky brightness versus orbit number and measured standard source brightness versus orbit number.

was pitched in at orbit 3560 and remained in the field of view for about a week, and later on Alpha Aquilae was also pitched into the field.

The separation of the total sky brightness into zodiacal and interstellar components can presently only be done for regions well removed from the Milky Way because of the lack of reliable measurements of integrated starlight near the galactic equator. The only region with galactic latitude greater than 30° is that region near the point of minimum sky brightness near orbit 3000. At this point the total sky brightness is $B_T = 54S_{10}(B)$. From Megill and Roach (1961) the integrated starlight at this point is $26S_{10}(B)$ so that if there are no diffuse sources of interstellar light, $B_{ZL} = 28S_{10}(B)$ for $\epsilon = 90^\circ$ and ecliptic inclination of about 70° . The possible error is estimated to be $\pm 7S_{10}(B)$. The polarized intensity ($B_{||} - B_{\perp}$) at this point is $P_T = 12S_{10}(B) \pm 4$.

BALLOON OBSERVATIONS

Over the past several years we have been studying the night sky from above 100 000 feet by means of cameras and photometers attached to balloons. Observations are made from above all but about 1 percent of the Earth's atmosphere

and the units are designed to operate without orientation systems.

Experiment

The cameras are rotated beneath the balloon and the film is drawn across the focal plane at such a rate that the image of a distant source remains fixed on the film. The resulting exposure is a continuous panoramic picture of a strip of sky near the horizontal. The photometers have a 5° field of view and a rotating polaroid sheet which yields an additional modulation whenever a polarized field is observed. The photometers are rotated beneath the balloon in the same fashion as the cameras, so the output record is an azimuth scan at fixed elevation angle.

Analysis

Photometers

If the position of the balloon is known, and also the times when known stars are in the field of view, then the elevation angle of the field of view can be determined by using the equations of celestial navigation. The azimuth, elongation, ecliptic inclination, etc., of the field of view at any given time can then be determined with

respect to positions of observed stars or other features.

The photometers are calibrated during each flight by means of star deflections. A correction for the fact that the spectral response is not exactly the same as Johnson's B is made by assuming $M = B - k(B - V)$ and finding the value of k which gives the most consistent calibration from all the observed stars.

No extinction corrections are necessary because all measurements are made at the same elevation angle and no secondary scattering corrections are needed because the extinction is generally less than 10 percent.

In order to find the zodiacal-light brightness it is necessary to make several assumptions:

- (1) Only the zodiacal light is polarized: $P_T = P_{ZL}$
- (2) Airglow brightness depends only on the elevation angle
- (3) Diffuse component of interstellar light is constant for galactic latitude greater than 30°
- (4) Integrated starlight for galactic latitude greater than 30° is given by Megill and Roach (1961).

These assumptions are not sufficient to determine the separation unless the airglow brightness and the diffuse interstellar component are known by some other means. The method adopted here is to find values for $B_{ZL}(\epsilon, i) - B_{ZL}(npe)$ where (npe) means $(90^\circ \leq \epsilon \leq 115^\circ, 70^\circ \leq i)$ and assume that $B_{ZL}(npe) = B_{ZL}(90, 90)$. Then $B_{ZL}(90, 90)$ is to be determined from model calculations so it is consistent with the observations of

$$B_{ZL}(\epsilon, i) - B_{ZL}(90, 90)$$

The point where the sky brightness is a minimum is generally in the region $90^\circ \leq \epsilon \leq 115^\circ$ and $i \geq 70^\circ$ so that

$$\begin{aligned} B_{ZL}(\epsilon, i) - B_{ZL}(npe) \\ = B_T(\epsilon, i) - B_T(\min) \\ - \Delta B_{\text{integrated starlight}} \end{aligned}$$

where (ϵ, i) and (\min) are both at the same elevation angle.

Cameras

Analysis of the camera data is the same as that for photometers except for three points:

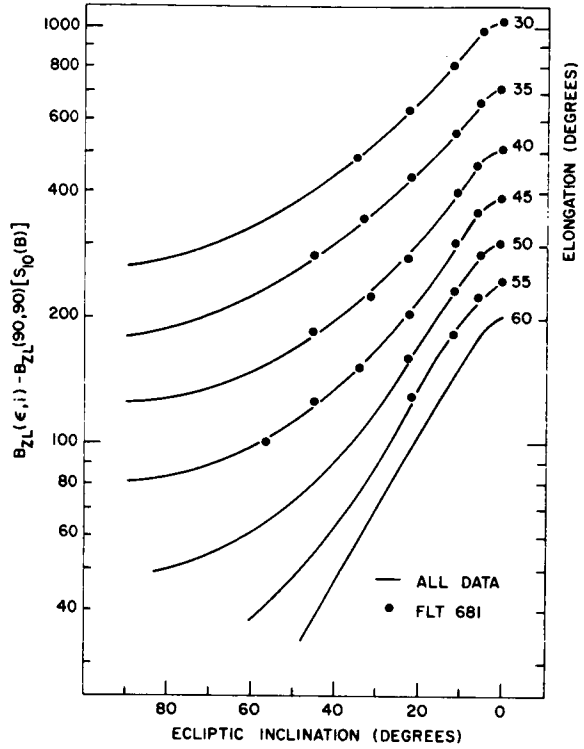


FIGURE 5. $-B_{ZL}(\epsilon, i) - B_{ZL}(90, 90)$ as a function of ecliptic inclination for various values of ϵ .

- (1) Absolute calibration is done by using Milky Way clouds whose brightnesses have been determined by the photometers
- (2) Analysis is carried out for a set of elevation angles
- (3) Extinction must be taken into account

The extinction is evaluated by comparing the zodiacal-light brightness as deduced at two different times and assuming that the brightness depends only on ϵ and not on elevation angle.

Results

Figure 5 shows the results for

$$B_{ZL}(\epsilon, i) - B_{ZL}(90, 90)$$

as a function of ecliptic inclination for various values of ϵ , and figure 6 shows the results for the polarized brightness of the zodiacal light as a function of elongation for various values of i .

Model Calculations

The object of the model calculations is to attempt to find a simple model for the distribution

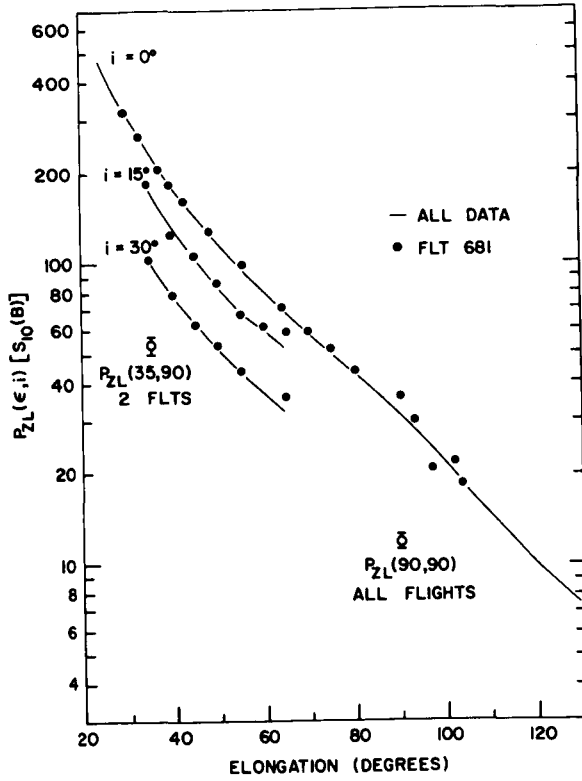


FIGURE 6. — $P_{ZL}(\epsilon, i)$ as a function of elongation for various values of i .

of zodiacal dust which is consistent with the observed data presented in figures 5, 6, and 7 and, in so doing, find the value of $B_{ZL}(90, 90)$. The assumptions made for these calculations are:

- (1) In the plane of the ecliptic $n \propto \left(\frac{1}{r}\right)^m$
- (2) The size distribution of the dust particles is independent of r
- (3) The distribution of particles away from the ecliptic is given by either

$$n(r, d) = n(R, d) \left(\frac{r}{R}\right)^{-m} \quad \text{for model I}$$

or

$$n(r, d) = n\left(R, \left(\frac{R}{r}\right) d\right) \left(\frac{r}{R}\right)^{-m} \quad \text{for model II}$$

The observed value of $B(\epsilon, 0)$ with $B_{ZL}(90, 90)$, initially assumed equal to zero, determines $\sigma(\theta)$, for an assumed value of m , where $\sigma(\theta)$ is the average scattering function for the particles. These values of $\sigma(\theta)$ along with the observed

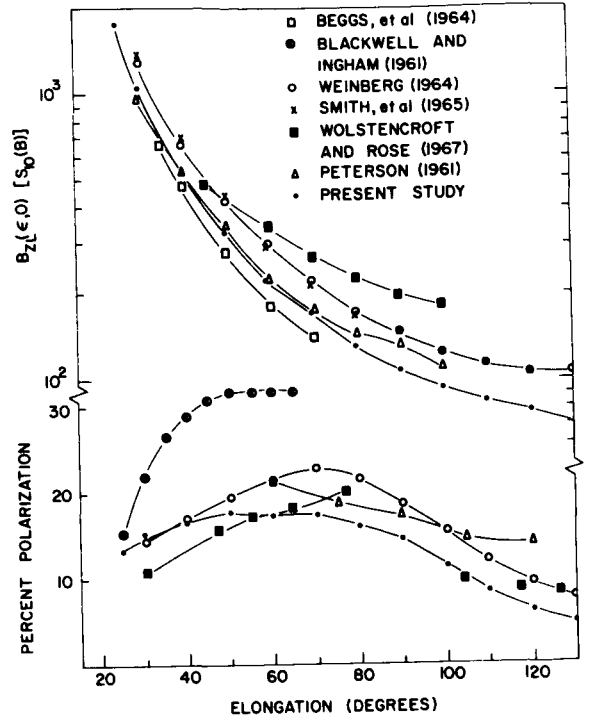


FIGURE 7. — $B_{ZL}(\epsilon, 0)$ and $P(\epsilon, 0)$ versus elongation and comparison with other recent observations.

value of $B(\epsilon, i)$ at some fixed ϵ , and either model I or model II, determines the value of $n(R, d)$. Then, by using $\sigma(\theta)$ and $n(R, d)$, $B_{ZL}(90, 90)$ can be found. An iteration technique then arrives at consistent values for $\sigma(\theta)$, $n(R, d)$, and $B_{ZL}(90, 90)$, given an initial value of m and either model I or model II.

There are two effective checks on such models. One is that the model must predict the correct value for $P_{ZL}(90, 90)$, and the second is that it should reproduce $\frac{B_F(\epsilon, 0)}{B_F(\epsilon, 90)}$ for the F-corona between $1^\circ \leq \epsilon \leq 10^\circ$. Only one model meets these requirements and that is model II with $m = 1/2$. For this model $B_{ZL}(90, 90) = 27S_{10}(B)$ and the distribution of dust away from the ecliptic is very like that of the observed asteroids.

Figure 7 shows $B_{ZL}(\epsilon, 0)$ and the percent polarization of the zodiacal light, P , using this value for $B_{ZL}(90, 90)$, and comparison with other recent investigations. Table 2 shows a comparison of recently deduced values for $B_{ZL}(90, 90)$, and table 3 shows a comparison of measured polarized brightness at 90° elongation.

TABLE 2.—Recently Deduced Values of $B_{ZL}(90,90)$

Author	$B_{ZL}(90,90)$ for $S_{10}(B)$
Weinberg (1964).....	104
Smith et al. (1965).....	62
Beggs et al. (1964).....	77
Wolstencroft and Rose (1967).....	92
Ney (OSO 2 satellite)*.....	28
Present study.....	27

*Unpublished report.

TABLE 3.—Comparison of Measured Polarized Brightnesses at 90° Elongation

Author	$P_{ZL}(90,0)$ for $S_{10}(B)$	$P_{ZL}(90,90)$ for $S_{10}(B)$
Weinberg (1964).....	52	21
Beggs et al. (1964).....		46
Wolstencroft and Rose (1967).....		34
Ney (OSO 2 satellite)*.....		12
Present study.....	31.5	11.5

*Unpublished report.

REFERENCES

- BEGGS, D. W., D. E. BLACKWELL, D. W. DEWHIRST, and R. D. WOLSTENCROFT, 1964, *Mon. Not. Roy. Astron. Soc.*, **127**, 319.
- BLACKWELL, D. E., and M. F. INGHAM, 1961, *Mon. Not. Roy. Astron. Soc.*, **122**, 113.
- INGHAM, M. F., 1962, *Space Science Reviews*, **1**, 576.
- MEGILL, L. R., and F. E. ROACH, 1961, *NBS Technical Note*, No. 106.
- PETERSON, A. W., 1961, *Astrophys. J.*, **133**, 668.
- SMITH, L. L., F. E. ROACH, and R. W. OWEN, 1965, *Planetary Space Sci.*, **13**, 207.
- WEINBERG, J. L., 1964, *Ann. d'Astrophys.*, **27**, 718.
- WHIPPLE, F. L., 1961, *Nature*, **189**, 127.
- WOLSTENCROFT, R. D., and L. J. ROSE, 1967, *Astrophys. J.*, **147**, 271.

Page intentionally left blank

3. Toward a Unification of Eclipse and Zodiacal-Light Data

D. E. BLACKWELL AND M. F. INGHAM
Oxford University
Oxford, England

AT LEAST TWO OPTICAL PHENOMENA show the presence of dust in interplanetary space: the zodiacal light together with the F-component of the solar corona, and the infrared excess of the inner solar corona. The zodiacal light yields information about the distribution of dust in the region beyond $R = 0.5$ AU ($108 R_{\odot}$) corresponding to an elongation $\epsilon = 30^\circ$, the F-component of the corona yields information about the dust in regions that are close to the Sun, $R > 4R_{\odot}$, and also in regions that are far from the Sun, $R \approx 0.5$ AU. A great deal of effort has been devoted in recent years to explaining the zodiacal light in terms of dust densities and dust-scattering functions, but the interpretation of the F-component of the solar corona has been almost wholly neglected. As a consequence, we know practically nothing about the dust density in the region $R < 0.5$ AU and most workers have assumed that it is permissible to extrapolate to 0.01 AU (or $2R_{\odot}$) a dust-density curve determined in the region $0.5 \text{ AU} < R < 1.0 \text{ AU}$.

We wish in this paper to consider the kind of observations that are needed to give the dust density in the region $4R_{\odot} < R < 108R_{\odot}$. Even at this stage it is clear that the observations must be very subtle indeed because if we could remove all the dust in this region there would be very little effect on the F-component of the solar corona. We also emphasize the importance of unifying data concerning the zodiacal light and solar corona, as was first done by van de Hulst (1947) in 1946, rather than treating each region separately. Although this treatment does not result in a simplification of the problem of interpretation, indeed rather the reverse, we suggest

that it gives a more realistic assessment of the situation than hitherto. We begin by surveying briefly the relevant observational data for corona and zodiacal light, then we outline the method of interpretation, and finally we consider what new observations are needed to advance the subject.

AVAILABLE OBSERVATIONAL DATA

Ideally, we should like to know at least the brightness and polarization of the light scattered by the dust cloud over the range of elongation $1^\circ < \epsilon < 180^\circ$, for a range of wavelengths between the infrared and extreme ultraviolet regions. In practice, many factors conspire to prevent us from obtaining these data with reasonable accuracy even for the visible spectrum, and particularly for the solar corona.

Data for the Solar Corona

Intensity of the F-Component

In the corona the F (dust) component is much brighter than the K (electron) component for $\epsilon > 1^\circ$ and a reasonably accurate separation of these two components can be made from measurements of the polarization of the corona. If K and F are the intensities of the K- and F-components, and p_K and p_F their polarizations, we have

$$p_{K+F} = k p_K + (1 - k) p_F$$

where

$$k = K / (K + F)$$

Hence

$$F / (K + F) = 1 - k = \frac{p_K - p_{K+F}}{p_K - p_F}$$

and assuming

$$p_F = 0$$

$$F/K + F = 1 - \frac{p_{K+F}}{p_F}$$

As $p_F \ll p_K$, this assumption has a negligible effect on the accuracy of the separation. At greater elongations, i.e., for $\epsilon > 2^\circ$ the separation of $K+F$, and therefore F , from the sky background becomes more difficult, but a satisfactory separation and measurement of F can be made out to a distance of about $40R_\odot$.

In spite of the many expeditions that have been made to observe solar eclipses, knowledge of the variation of F over a reasonably large range of wavelengths, which involves measurements of $K+F$ and p_{K+F} , is very slight. Among the more serious studies is that of Ney et al. (1961) who made measurements at 4750\AA and 8300\AA and found a slight difference in both p_{K+F} and F . Other measurements (Blackwell et al., 1967) confirm that there is a slight reddening of the inner corona at shorter wavelengths ($\lambda < 8.0\mu$). One measurement at 1.9μ made by Blackwell (1952) at the total solar eclipse of February 1952 showed a large excess of radiation at this wavelength; this measurement is summarized by the ratio

$$\frac{I(\lambda_2, r_2)/I(\lambda_1, r_2)}{I(\lambda_2, r_1)/I(\lambda_1, r_1)} = 2.17$$

Polarization of the F-Component

The measurement of p_F in the coronal region ($\epsilon < 5^\circ$) is extremely difficult. We use as a basis of measurement the equation

$$p_F = \frac{p_{K+F} - kp_K}{1 - k}$$

In order to make use of this equation, we must measure k independently by a method which does not depend upon polarization. In the investigation of Blackwell and Petford (1966a, b), k is measured at 6563\AA by observing the depth of a prominent Fraunhofer line in the spectrum of the solar corona. The measurement is difficult in the inner region because $p_F \sim 0$, and in the outer region because an accurate separation of $K+F$ and sky background is required.

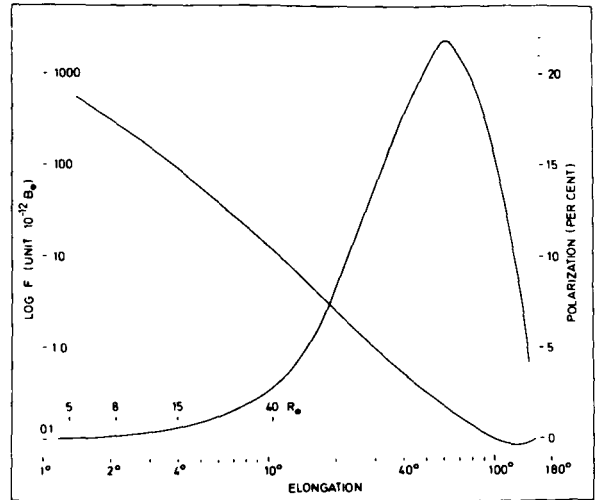


FIGURE 1.—Measurements of $F(\epsilon)$ and $p_F(\epsilon)$. At the left-hand side, the upper curve refers to $F(\epsilon)$ and the lower to $p_F(\epsilon)$.

In figure 1, we give on the left-hand side the variation of F and p_F with elongation for the coronal region following the model of Blackwell and Petford (1966b).

Data for the Zodiacal Light

As the zodiacal light has already been fully treated by Weinberg and Mann in paper number 1, we confine ourselves to the remark that we believe that Weinberg's measurements of brightness and polarization are the most accurate available, and it is pleasing to see that they have been confirmed by the results obtained from rocket studies by Wolstencroft and Rose (1967). It is clearly important to obtain more confirmatory data from rockets.

There is now evidence from both optical data (Beggs et al., 1964) and from direct measurement that the scattering of sunlight by free electrons in interplanetary space does not contribute significantly to the zodiacal light. Following the notation already used for the solar corona, we may therefore say that the measurements referred to give directly the values of F and p_F for this range of elongation. In figure 1 we summarize all the measurements of F and p_F so far derived, adopting the Weinberg measurements for the zodiacal-light region.

BRIEF SURVEY OF THE INTERPRETATION OF $F(\epsilon)$ AND $p_F(\epsilon)$

In the interpretation of $F(\epsilon)$ and $p_F(\epsilon)$ it is inappropriate to consider the observational aspect entirely divorced from theoretical interpretation. We therefore outline briefly the interpretation of the data so far discussed and return later to suggestions for further development of the observational side.

Most attempts to interpret the data have been confined to the zodiacal-light region and consist of a comparison between the predictions of the Mie theory for a particular distribution of particle size and an adopted complex refractive index for the particles. It is also necessary to assume a spatial distribution of the form $n(r) = K \left(\frac{R}{r}\right)^\alpha$, and the further assumption is made that the average complex refractive index is independent of distance from the Sun. With these assumptions, a reasonable agreement between prediction and observation can be obtained.

This method can also be used for the interpretation of the coronal F data, but a better physical picture of this inner region can be obtained if we follow van de Hulst (1947) and Allen (1946) and divide the F-component into a diffraction component (F_d) and a reflection component (F_r). For a particular particle size, the scattering function becomes

$$\pi I(\theta) = \pi I_d(\theta) + \pi I_r(\theta) = J_1^2 \frac{(x \sin \theta)}{\sin^2 \theta} + \gamma/4$$

where

$$x = \frac{2\pi a}{\lambda}$$

The reflection part of the scattering function is thus assumed to be isotropic with an albedo of γ , but certainly in this region, and probably also in the zodiacal-light region, this assumption is of sufficient accuracy. The corresponding reflection component (F_r) is strongly polarized because it originates in large-angle scatter, and the particles responsible for it are close to the Sun. The diffraction part of the scattering function, on the other hand, shows a strong forward scatter. The corresponding diffraction component is weakly

polarized and the particles responsible for it are far from the Sun. Most of the F-component at small elongations is due to F_d ; for example, at $R/R_\odot = 5$, F_d comprises 99.2 percent and F_r only 0.8 percent of F (Blackwell and Ingham, 1967). It is therefore clear that in order to determine the density near the Sun we must separate F_r from F .

The technique of analysis has been developed by Ingham (1961) and by Blackwell and Ingham (1967), and in the latter paper the analysis of $F(\epsilon)$ and $p_F(\epsilon)$ has been carried through to completion.

Briefly, the method is as follows:

If

$$F = F_r + F_d$$

$$p_F = \frac{F_r}{F} \times p_{F_r} + \frac{F_d}{F} \times p_{F_d}$$

Putting $p_{F_d} = 0$ we have

$$p_F = p_{F_r} \times \frac{F_r}{F}$$

and

$$F_r = F \times \frac{p_F}{p_{F_r}} \quad (1)$$

with

$$F_d = F - F_r \quad (2)$$

The quantity p_{F_r} can be calculated with sufficient accuracy from an initial model and by making an assumption about the polarization of light reflected from a particle. As we have measured p_F , equation (1) can be used to calculate $F_r(\epsilon)$ and equation (2) to calculate $F_d(\epsilon)$, from F and p_F . We refer to these as "observed" functions $F_r(\epsilon)$ and $F_d(\epsilon)$. Assuming now that we know the particle-size distribution, then for any arbitrary model of dust distribution we can calculate $F_r(\epsilon)$ and $F_d(\epsilon)$. A comparison between these "calculated" and "observed" functions F_r and F_d will show the ability of the assumed model to account for the observations. Further, we can take advantage of the fact that F_d depends upon only the number density of particles, while

F_r depends also upon their albedo, to derive values of particle density and albedo.

Blackwell and Ingham have made such a calculation by using the particle-size distribution given by measurements using space vehicles (Blackwell and Ingham, 1967), with the result shown in figure 2. The discontinuities result from the division of interplanetary space into zones that has been made for the sake of convenience. This distribution differs from the previously assumed distributions in that the density *decreases* toward the Sun instead of *increasing*. Indeed, the form of this distribution shows very clearly that an increase of F toward the Sun does not necessarily imply an increase of density of dust toward the Sun, for in the corona F (which is almost entirely F_d) originates far from the Sun. The value of γ is 0.16.

Fortunately, we have a check on the curve, for the new model should account for the infrared excess of the inner corona. This excess originates entirely in thermal radiation from particles that are very close to the Sun, and is therefore a measure of the density there. A simple calculation which assumes that each radiates as a blackbody shows that the density in this region is quite insufficient. We overcome this difficulty by noting that we have made the implicit assumption that the albedo is constant — independent of distance from the Sun. Such an assumption is unrealistic because it is equivalent to assuming that the composition of the dust cloud is independent of distance from the Sun,

whereas at least some change may be expected from the differential evaporation of particles. In figure 3 we show the density distribution for another model in which the albedo decreases toward the Sun to a value of 2.7×10^{-3} at $4R_\odot$. Evidently a high concentration of particles of this albedo (corresponding to that of carbon black) could exist near the Sun, even practically in the photosphere, but while they still yield only a small value for F_r their presence is shown by the infrared excess of the corona. Even the density near the Sun given in figure 3 is still not sufficient to account for the observed infrared excess. However, the density near the Sun is very sensitive to the measured value of p_F . The original measurements of p_F were not entirely satisfactory and a small increase in the value at $5R_\odot$, from 0.05 percent to 0.10 percent for example, would result in an increase in density here that would amply account for the observed infrared excess.

A calculation such as this depends upon knowledge of the particle-size distribution. The only data available for the appropriate size range are those obtained from space vehicles in the neighborhood of the Earth, which are summarized by, for example, Alexander et al. (1963). However, the validity of these data has been questioned by Nilsson (1966) and this criticism has been reinforced by the investigation of Shapiro et al. (1966) and of Colombo, Lautman, and Shapiro (1966), and of Colombo, Shapiro, and Lautman (1966), who, among others, can

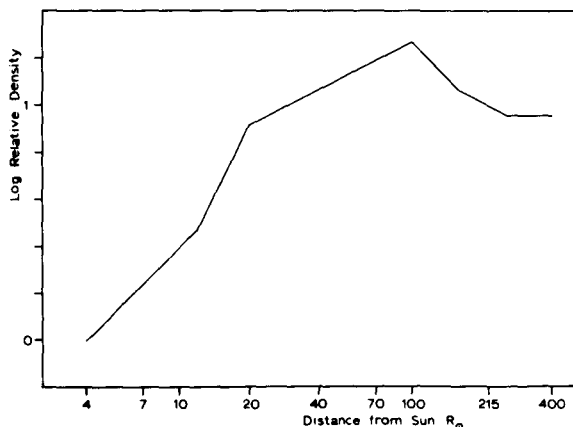


FIGURE 2.—Number density of particles, assuming constant albedo (γ).

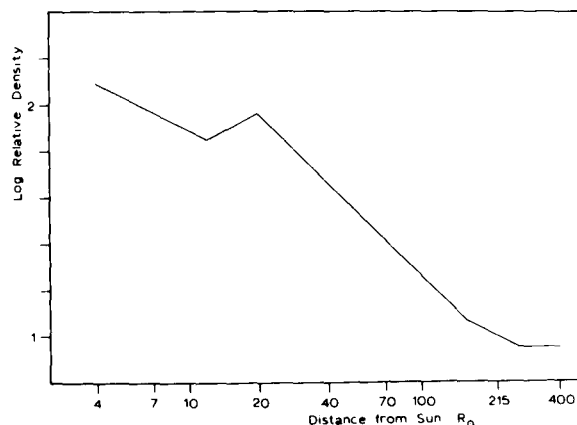


FIGURE 3.—Number density of particles, assuming an albedo which decreases toward the Sun to the value $\gamma = 2.7 \times 10^{-3}$.

find no theoretical explanation for the existence of an enhancement of dust density in the immediate neighborhood of the Earth. In principle, the size distribution can be obtained from optical measurements of the kind that we have been describing, made over a range of wavelengths, and it seems at present that this is the only feasible method.

CONCLUSIONS

It seems that at present our only source of knowledge of dust within $100R_{\odot}$ of the Sun is from measurements of F and p_F , and of the infrared excess. Both measurements, particularly of p_F , are very difficult, and, as existing determinations are likely to be in error, we urge that more effort be devoted to these rather difficult studies of the solar corona.

The interpretation that we have put on the existing measurements shows the importance of including the variation of the properties of the dust cloud with distance from the Sun. In our view, this hitherto neglected factor is probably

of greater importance than the details of large-angle scattering by particles.

Difficulties of interpretation still remain. One of the most important is in the calculation of the infrared excess. For the very small particles involved this calculation should properly be done by using the Mie theory, but for this we need to know the electrical resistivity of the radiating material (which is probably carbon) at high temperatures; these data do not exist. Further, our division of the scattering function into a diffraction component and a reflection component is in itself an approximation to the Mie theory; we use it partly because it is simpler and partly because we lack precise knowledge of the complex refractive index of the dust particles. The approximation is a good one for particles that are large compared with the wavelength of light, and for such particles Fraunhofer diffraction theory is accurate and $p_{Fd} = 0$. However, our smallest particles have a size that is of the order of this wavelength; for these the approximation is less good and the accurate Mie theory ought to be used.

REFERENCES

- ALEXANDER, W. M., C. W. MCCracken, L. SECRETAN, and O. E. BERG, 1963, NASA Technical Note, No. 1669.
 ALLEN, C. W., 1946, *Mon. Not. Roy. Astron. Soc.*, **106**, 137.
 BEGGS, D. W., D. E. BLACKWELL, D. W. DEWHIRST, and R. D. WOLSTENCROFT, 1964, *Mon. Not. Roy. Astron. Soc.*, **127**, 329.
 BLACKWELL, D. E., 1952, *Mon. Not. Roy. Astron. Soc.*, **112**, 652.
 BLACKWELL, D. E., M. F. INGHAM, and A. D. PETFORD, 1967, *Mon. Not. Roy. Astron. Soc.*, **136**, 313.
 BLACKWELL, D. E., and A. D. PETFORD, 1966a, *Mon. Not. Roy. Astron. Soc.*, **131**, 383.
 BLACKWELL, D. E., and A. D. PETFORD, 1966b, *Mon. Not. Roy. Astron. Soc.*, **131**, 399.
 BLACKWELL, D. E., D. W. DEWHIRST, and M. F. INGHAM, 1967, *Advances in Astronomy*, Ed. Z. Kopal, Academic Press.
 COLOMBO, G., D. A. LAUTMAN, I. I. SHAPIRO, 1966, *J. Geophys. Res.* **71**, 5705.
 COLOMBO, G., I. I. SHAPIRO, D. A. LAUTMAN, 1966, *J. Geophys. Res.* **71**, 5719.
 INGHAM, M. F., 1961, *Mon. Not. Roy. Astron. Soc.*, **122**, 157.
 NEY, E. P., W. F. HUCH, P. J. KELLOGG, W. E. STEIN, and F. GILLET, 1961, *Astrophys. J.*, **133**, 616.
 NILSSON, C., 1966, *Science*, **153**, 1242.
 SHAPIRO, I. I., D. A. LAUTMAN, G. COLOMBO, 1966, *J. Geophys. Res.*, **71**, 5695.
 VAN DE HULST, H. C., 1947, *Astrophys. J.*, **105**, 471.
 WEINBERG, J. L., 1964, *Ann. d'Astrophys.*, **27**, 718.
 WOLSTENCROFT, R. D., and L. J. ROSE, 1967, *Astrophys. J.*, **147**, 271.

Page intentionally left blank

4. Multicolor Photometry of the Zodiacal Light

ALAN W. PETERSON
University of Missouri
Columbia, Missouri

Photometric observations of the zodiacal light yielding estimates of the spectral-energy distribution are reviewed from the literature. Color-index measurements based upon two-color photometry are, in general, uncertain by ± 0.1 to ± 0.2 magnitude and suggest that the zodiacal light is about the same color as sunlight. The role of the zodiacal-light color in determining models of the interplanetary-dust distribution is discussed. It is suggested that a zodiacal light having very nearly the same spectral energy distribution as the Sun is possible even with many sub-micron particles in the dust cloud.

Results from a 12-color photometry program performed at McDonald Observatory during 1962 and 1963 are presented. Absolute calibration and extinction measurements were obtained from nightly star readings. In the wavelength range from 3600Å to 7650Å the measured spectral energy distribution of the zodiacal light was fitted to a law of the form $A\lambda^n$. A mean value of the exponent $n = 0.065 \pm 0.049$ (pe) was obtained. The value $n=0$ corresponds to a spectral type G1(V) star. In the range of elongation from 50° to 60°, n attains a maximum value of 0.085 and decreases toward larger and smaller elongations. The corresponding color index for a star with the above spectral-energy distribution is $B-V = 0.61 \pm 0.02$ (pe) or very nearly identical to sunlight.

A search for a correlation between the measured zodiacal-light brightness and the measured extinction coefficient shows that no appreciable correlation exists.

IN THIS PAPER the various studies which have resulted in estimates of the spectral energy distribution of the zodiacal light are reviewed. These studies include visual, spectroscopic, two-color, and multicolor photometry. A brief discussion of the importance of utilizing the spectral energy distribution in fitting theoretical models of the zodiacal light to the observations will follow. Finally, results of a 12-color photometry program are presented for the first time.

ZODIACAL-LIGHT COLOR MEASUREMENTS

Visual Work

Visual estimates of the zodiacal-light color have appeared at various times and range from greenish to crimson (Mitra, 1952). However, Roach and Jamnick (1958) have correctly pointed

out that even the brightest portions of the zodiacal-light cone are about 100 times too faint for color perception to be possible with the normal human eye. Thus, we may disregard all visual estimates of the zodiacal-light color.

Spectrographic Work

Spectrographic study of the zodiacal light was initiated by Fath (1909). He obtained a low-dispersion spectrogram of the zodiacal light which had a continuous, solar-type spectrum containing the blended H and K lines as well as the G-band near 4300Å. Later, Slipher (1933), in an extensive study of the night sky spectrum, obtained spectra of the zodiacal light and gegenschein. The zodiacal-light spectrum contained airglow emissions and traces of the first negative

nitrogen-band systems typical of the aurora and twilight. The nitrogen bands were not definitely present in the gegenschein nor was it possible to say the continuum was that of sunlight.

Hoffmeister (1939) obtained several zodiacal light, gegenschein, and night sky spectra. He concluded that both the zodiacal light and gegenschein resulted from a superposition of sunlight and night sky spectra such that the airglow emission lines were relatively weaker than in the night sky alone. He also noted the twilight flash enhancement of the N_2^+ line at 3914Å.

More recently the very high-resolution zodiacal-light spectrum of Blackwell and Ingham (1961) revealed many individual absorption lines which are directly identifiable with the solar spectrum. Measurements of the relative depths of these lines yielded an estimate of the interplanetary electron density.

In addition to studying airglow enhancements, several Soviet investigators have used fast, low-dispersion spectrographs to obtain the spectral-energy distribution of the zodiacal light and gegenschein. Karyagina (1961) observed the zodiacal light at elongations between 40° and 50° and over the wavelength range from 4100Å to 6600Å. Her results showed a slight excess of blue light. No estimate of the color index was made.

Pariiskii and Gindilis have performed a long series of observations of the gegenschein which are summarized by Gindilis (1962). They find the undisturbed gegenschein has a spectrum relative to sunlight varying as $\lambda^{-1.74}$ which corresponds to a color index $B - V = 0.17$ or similar to a class A5 star. However, other photometric results have shown the gegenschein to be the same color or redder than sunlight.

We conclude that straight spectrographic determinations of the spectral-energy distribution of the zodiacal light are of great value but more work should be done in this area. Many reduction problems such as the wavelength dependences of the background continuum and the normal problems of low-luminosity photographic photometry must be overcome.

Color-Index Measurements

Several programs have yielded two-color esti-

mates of the zodiacal-light color index. As with other techniques for estimating the zodiacal-light color, these measurements also give rather discordant results.

About the earliest measurement of the zodiacal-light color index was made by Elvey and Rudnik (1937). They found the color index on Becker's scale as C.I. = -0.12 or equivalent to a star of spectral class G1. This value was the mean of data from 4 nights of observations. Since then other measurements have yielded color indices both redder and bluer than sunlight. Also, the color index has been found to increase (Behr and Siedentopf, 1953), to decrease (Divari and Asaad, 1960), and to remain constant with elongation (Peterson, 1961). If, indeed, an elongation dependence of the zodiacal-light color index exists, it is very small. However, if such a dependence is found, it would yield information on the dust-particle sizes.

A representative sample of color-index measurements converted to the UBV system is given in table 1.

TABLE 1.—Color-Index Measurements of Zodiacal Light

Investigators	λ_1 , Å	λ_2 , Å	$B - V$
Elvey and Rudnik (1937).....			0.60
Behr and Siedentopf (1953)...	4440	5430	0.75
Divari and Asaad (1960).....	4140	5410	0.46
Peterson (1961).....	4355	5425	0.60 ± 0.12
Divari and Krylova (1963).....	4060	5530	0.47 ± 0.03
Divari, Krylova, and Moroz (1964).....	4700	5200	0.74 ± 0.03

These color indices all appear uncertain by the order of ± 0.1 magnitude, and in turn correspond to a variation of stellar spectral class of from F5 to G8. The lack of better agreement between results can be attributed to some or all of the following:

- (1) Approximate or incorrect estimates of the background starlight and airglow contributions
- (2) Approximate corrections for atmospheric extinction and scattering
- (3) Inaccurate calibrations

- (4) Nonstandard color systems requiring conversion to the UVB system

Hopefully these uncertainties can be reduced.

Spectral Photometry

When photometric measures are made at wavelengths which do not correspond to the wavelengths of a standard magnitude system, it is best to compare the absolute brightnesses directly with the spectral-energy distribution of the Sun. This comparison eliminates the uncertainties of conversion to a standard magnitude system.

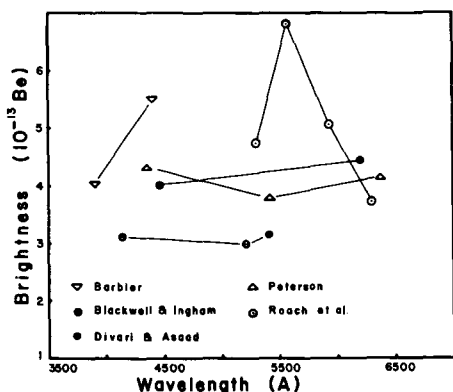


FIGURE 1.—Multicolor-brightness measurements of zodiacal light at $E=40^\circ$.

Figure 1 is a graph showing several multicolor measurements at $E=40^\circ$ converted to units of the mean brightness of the solar disk. Considerable scatter is noted in the results.

RELEVANCE OF COLOR MEASUREMENTS IN THE ZODIACAL-LIGHT PROBLEM

Early attempts to delineate the spectral-energy distribution of the zodiacal light sought merely to answer the question, "Is the zodiacal light caused by reflection from gas molecules or meteoric particles?" Fath's spectrum in 1909 answered this question in favor of dust reflection.

Later Ramanathan (1932) reported airglow enhancements in the brighter zodiacal light. Many investigators then sought to answer the question, "Are the airglow emission lines enhanced in the zodiacal light?" This question has now been answered in the negative except for a possible post-twilight enhancement of some as yet unidentified red and near-infrared emissions (Wolstencroft et al., 1966).

The large electron component suggested by Behr and Siedentopf (1953) would tend to provide neutral scattering and hence a colorless zodiacal light.

Currently we would like to answer the question, "What is the exact zodiacal-light spectral-energy distribution?" Then, with this information one could deduce a more exact set of parameters describing the zodiacal-dust distribution.

Presently, all models of the zodiacal-dust distribution have been derived by fitting a theoretical model to the angular distribution of the zodiacal light measured at one wavelength. However, polarization measurements suggest the presence of many small particles in the zodiacal cloud. Since the angular spread of the diffraction pattern of such particles is large and dependent on wavelength, we should expect color effects to be present, at least in the inner zodiacal light, if such small particles are present. As will be shown, however, a zodiacal light with little inherent color may possibly be deduced by proper choice of the parameters in the calculations.

Some unpublished exploratory calculations have been made along these lines and are presented for illustrative purposes only. Consider the usual integral representing the scattering by the zodiacal cloud. We use the approximate diffraction scattering function of Allen (1946) and assume exponential distributions of dust-particle sizes and particle concentration. We have the column brightness integral

$$j_\lambda(E) = \frac{G}{\sin^{q+1} E} \left(\frac{\lambda}{2\pi} \right)^{3-p} \int_E^{\pi/2} d\theta \int_{x_1}^{x_2} dx \frac{x^{4-p} \sin^q \theta}{2 + x^3 \sin^3 \theta}$$

where $j_\lambda(E)$ is the brightness of the zodiacal light at elongation E and wavelength λ ; G is a constant containing the Sun's surface brightness and other constants. The dust sizes are represented by the parameter $x = 2\pi a/\lambda$ where a is the particle radius. Allen's scattering function then takes the form $I(x, \theta) = \frac{\text{const} \times x^2}{2 + x^3 \sin^3 \theta}$. The dust is assumed to be distributed with radius and solar distance as $n(a, r) = C(a/a_1)^{-p}(D/r)^q$, where a_1 is the minimum particle size and D the astronomical unit. Linear-distance variables have been converted into angle variables.

Numerous practice calculations have been made with the above integral by using various combinations of parameters. An interesting result which did appear is that, to obtain a neutral F-corona and a neutral zodiacal light, one *must* include dust-particle sizes in the 0.1- to 0.2-micron range, and that the radius distribution with $p=3$ in all cases gives the most neutral scattering at

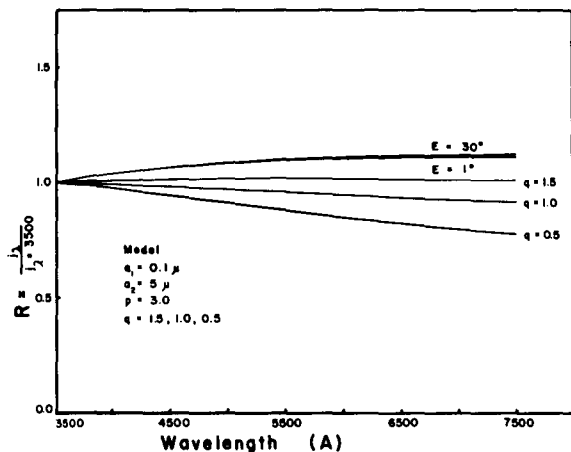


FIGURE 2.—The approximately neutral scattering at two elongation angles of an interplanetary dust model containing very small particles.

all elongations. Figure 2 gives results for $E=30^\circ$ and for $E=1^\circ$ both normalized at $\lambda=3500\text{\AA}$. The bottom three curves are for $E=1^\circ$ and, in ascending order, $q=0.5$, 1.0 , and 1.5 . The two curves for $E=30^\circ$ all very nearly coincide with $q=1.5$ uppermost. In this example, the corona is completely neutral and the zodiacal light slightly red, i.e., varying as $\lambda^{0.15}$. Thus it appears that very small dust particles cannot be ruled out as constituents of the zodiacal dust on the basis of the bluing of the light they scatter. However, they must be distributed with $p \leq 3$ which is not the value usually chosen. A model similar to this appears to be a good starting point for further, more refined calculations.

12-COLOR PHOTOMETRY OF THE ZODIACAL LIGHT

In 1961 a zodiacal-light photometry program was initiated under corporate sponsorship at General Dynamics in Fort Worth, Texas. The observations were performed from Flat Top Mountain on the grounds of McDonald Observatory, Fort Davis, Texas (elevation, 6800 feet).

The main purpose of this program was to investigate the spectral-energy distribution of the zodiacal light over as wide a wavelength range as practicable with phototubes having S-10 response. It was decided to determine the extinction coefficient nightly for each spectral range by using the zodiacal-light photometer itself. In addition, the extinction star readings were used for absolute calibration. Thus, only stars with accurately known V -magnitudes were used for extinction measurements.

During fall observations of the morning zodiacal light, calibration stars were observed during the entire night to determine the extinction coefficient and the calibration-scale factor as accurately as possible. Occasionally some star data were taken after astronomical dawn before the zenith sky had brightened significantly.

Each complete night's observing yielded between 150 and 250 individual star readings from which the extinction coefficients and scale factors were determined at four wavelengths.

There was a stringent selection of observing nights. Those which had detectable clouds in the recording area were avoided. Some otherwise clear nights which had much visible dust near the horizons were also rejected. In all, an average of only 2 nights per lunation yielded sufficiently good data to be completely analyzed.

The Photometer

The dual-channel photometer utilized two equatorially mounted 24-inch-diameter searchlight mirrors. A filter board in front of each S-10 cathode photomultiplier tube carried two colored-glass filters, which were interchanged by a rack gear drive. The signals were amplified with General Radio dc amplifiers and then deflected the beams of a dual-beam oscilloscope. The oscilloscope traces along with 25 illuminated fiducial markers were photographed on a film drum attached to the polar axis of the photometer. Displacing the camera lens between each sweep across the sky, along a line of constant declination, produced a map of the sky brightness in two colors displayed on a rectangular grid of equatorial coordinates. The maps covered a 45° -wide strip of declination with 15 scans from horizon to horizon. Normally only four-color photometry was done on each night. In all, 12 filters

TABLE 2.—Effective Wavelengths of Filters

Filter	λ , Å	Filter	λ , Å
1	3600	7	5475
2	4150	8	6185
3	4390	9	6470
4	4600	10	6740
5	5020	11	6950
6	5265	12	7650

were used and covered the wavelength range from 3600Å to 7650Å. Table 2 shows the effective wavelength of the various filter-photomultiplier combinations. These values were determined in the laboratory with a standardized projection bulb source and a quartz monochromator. The filter band passes at half transmission were between 200Å and 400Å.

Reduction of Star Data

Determination of the extinction coefficient followed the usual procedure. A plot of $-2.5 \log d$, where d is the star reading minus a nearby background reading, versus air mass was made for each star observed through each filter. The slope of the regression line fitted through the data points yielded the extinction coefficient for that star.

The extinction coefficient for spectral class G1 was read from a regression line through the extinction coefficients of the various stars plotted against spectral class of the star. This value was then used for correction of the zodiacal-light data.

In addition, each star reading was corrected to the zenith by use of its own extinction coefficient. The resulting values, averaged for each star and corrected to the reading the star would have if its magnitude were $V=5.00$, were plotted against spectral class and again the value at class G1 was determined. The conversion factor to change scale reading, in terms of voltage, to number of 10-magnitude stars per square degree

($S_{10}(\text{vis})$ units) followed from $K_{\lambda}(*) = \frac{100}{\bar{\Omega}d(G1)}$

where $K_{\lambda}(*)$ is the conversion factor. The value 100 appears because one star of $V=5.00$ equals 100 stars of $V=10.00$. The equivalent angular

field of view of the photometer was 1.06 square degree, and $\bar{d}(G1)$ is the mean deflection of a star of $V=5.00$ and spectral class G1 viewed through the given filter.

The Background Correction

The method of correcting for airglow and the scattered light from the troposphere marks a departure from the usual procedures. We have made no attempt to separate these components of the radiation field. Our procedure is as follows:

(1) Assume both the airglow and the scattered light are independent of azimuth

(2) Opposite the brightest region of the zodiacal light, read the total sky signal along a line of constant declination for many elevation angles

The data at each point is the sum

$$j_{\lambda}(\theta) = (ZL + G + A)e^{-k_{\lambda}m} + S$$

where $j_{\lambda}(\theta)$ sky signal at wavelength λ and elevation angle θ

ZL zodiacal-light brightness at that point

G galactic light, i.e., star background

A airglow emission

$e^{-k_{\lambda}m}$ extinction-reduction factor

S scattered light from all sources

(3) Correct these data for extinction and convert to $S_{10}(\text{vis})$ units, i.e.,

$$j_{\lambda}(\theta) e^{k_{\lambda}m} K_{\lambda}(*) = ZL + G + A + S e^{k_{\lambda}m}$$

(4) From this subtract the galactic light (G) using the charts of Roach and Megill (1961). Also remove the residual zodiacal light using the charts of Elvey and Roach (1937) with an empirical zero-point correction

(5) The resulting quantity $A + S e^{k_{\lambda}m}$ is the composite background correction which, when subtracted from the zodiacal-light data, corrects for airglow and scattered-light contributions simultaneously

The Zodiacal-Light Data

In all, 51 two-color maps were analyzed for zodiacal light along the ecliptic and on the $\pm 1^{\circ}$ and $\pm 2^{\circ}$ circles ecliptic of latitude. Data were read where these circles were intersected by

the circle of declination traversed by the photometer. The elevation angle of each data point was calculated by using the time of the observation. The extinction correction was applied and the result converted to an extra-atmospheric brightness by the conversion factor K_{λ}^* . The galactic light and the composite background correction were removed and the resulting brightness was interpreted as the zodiacal light.

When these data were plotted on a log-log scale of brightness versus elongation angle, the usual straight-line relationship, with little scatter, was found for the brighter zodiacal light ($E < 60^\circ$) despite the fact that some of the data were taken at 2° ecliptic latitude. A best straight line was fitted to the inner zodiacal light and values were interpolated for every 5° of elongation. Beyond 60° elongation, the zodiacal-light distribution does not assume another straight-line slope as previously found (Divari and Asaad, 1960; Peterson, 1961) but curves smoothly. Average values were interpolated every 5° of elongation out to $E = 110^\circ$.

The Spectral-Energy Distribution

At each 5° of elongation the zodiacal-light spectrum was formed by averaging all zodiacal-light brightnesses for each filter. A spectrum of the form

$$B = A\lambda^n$$

was fitted by least squares through the 12-point spectral-energy distribution for the data from $30^\circ < E < 110^\circ$.

Figure 3 shows the resulting values of the spectral exponent n and the probable error of the determination. A value $n = 0$ corresponds to a star of spectral class G1. It is seen that the color of the zodiacal light is very nearly identical to that of the Sun. There is, however, a suggestion of a maximum value for the reddening exponent near $E = 60^\circ$. The exponent decreases both to larger and smaller elongations. We believe the apparent discontinuity in n for $E > 65^\circ$ may be related to combining data taken at different elevation angles. However, we also point out that this apparent maximum reddening occurs at the same elongation as the maximum in polarization and also at the point where the

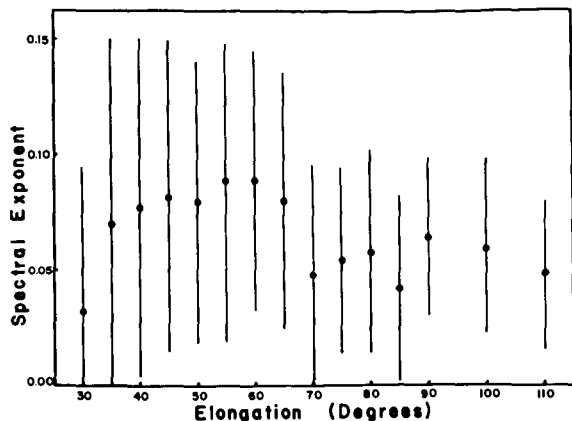


FIGURE 3.—Plot of spectral exponent n versus elongation angle for 12-color spectrum.

logarithmic brightness distribution departs from a straight-line relationship.

Because of the rather large uncertainty in the spectral exponent, we believe that a straight average of the exponents is sufficient to specify the spectral-energy distribution of the zodiacal light. The final average is

$$n = 0.065 \pm 0.049(\text{pe})$$

This represents the mean reddening of the zodiacal light with respect to a star of spectral class G1. Taking the color index of such a star as $B - V = 0.60$, the mean color index of the zodiacal light is

$$B - V = 0.61 \pm 0.02 (\text{pe})$$

Thus we conclude that the color index of the zodiacal light is the same as that of the Sun for which

$$B - V = 0.62 \quad (\text{Allen, 1963})$$

In addition, our probable error for the color index represents an increase in precision by a factor of about five over our previous measurement (Peterson, 1961).

The Angular Distribution of the Zodiacal Light

Because the zodiacal-light results show it to be essentially colorless with respect to sunlight, we have averaged all our spectral-brightness meas-

TABLE 3.—*Brightness Gradients, $E < 60^\circ$*

Investigators	λ , Å	Gradient
Roach et al. (1954).....	5300	-2.22
Regener (1955).....	4500	-2.02
Divari and Asaad (1960).....	4140	-2.4
	5410	-2.1
Blackwell and Ingham (1961).....	6200	-2.4
Peterson (1961).....	4355	-2.22
	5425	-2.19
	6380	-2.19
Divari and Krylova (1963).....	4060	-2.9
Divari, Krylova, and Moroz (1964).....	4600	-2.7
	5200	-2.5
Robley (1962).....	4630	-2.33
	5280	-2.24
	6165	-2.30
Weinberg (1964).....	5300	-2.04
Present work.....	3600 to 7650	-2.04

urements as a function of elongation. On a log-log plot, the brightness gradient between $E = 30^\circ$ and 60° has a value -2.04 . Table 3 shows a comparison of the gradients obtained by several investigators with the present value.

In figure 4 is a comparison of our final averaged zodiacal-light brightnesses with those of Weinberg (1964). The agreement is seen to be good. The average deviation is 2.8 percent for $30^\circ < E < 110^\circ$.

Correlation of Brightness With Extinction Coefficient

A correlation we wished to investigate in this program is whether the final brightness of the zodiacal light depends upon the nightly extinction coefficient. If no correlation is found we may conclude that our correction procedure is valid. Furthermore, possible correlation of zodiacal-light brightness and extinction may be the source of some reported variations in zodiacal-light brightness.

For every five degrees of elongation we have taken, for each filter, the average brightness for all maps and calculated the relative brightness of each mapping with respect to this average. Likewise we have taken Hardie's (1962) tabulated extinction coefficient for best nights at McDonald Observatory and, by using these values as the average, found relative nightly extinction

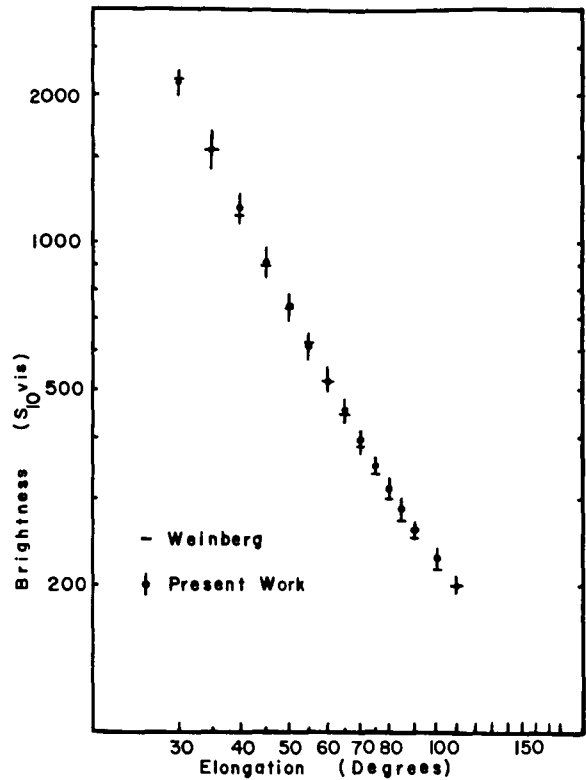


FIGURE 4.—Zodiacal-light-brightness distribution for $30^\circ < E < 110^\circ$ compared with Weinberg's values.

coefficients using our measured values. All spectral-brightness values are now plotted on the same set of axes giving relative brightness versus relative extinction coefficient. Figures 5, 6, and 7 give the results for elongations of 30° ,

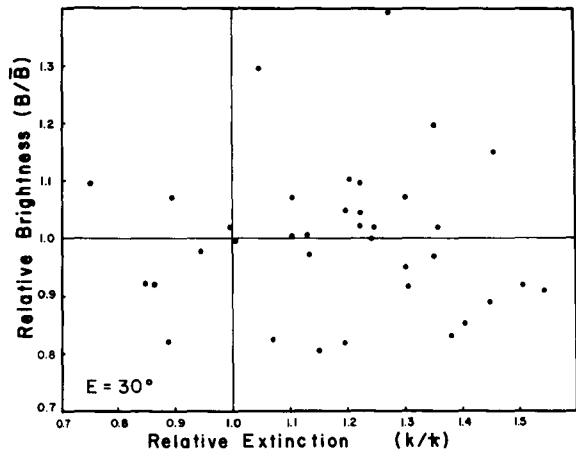


FIGURE 5.—Relative zodiacal-light brightness versus relative extinction coefficient for all data obtained at $E = 30^\circ$.

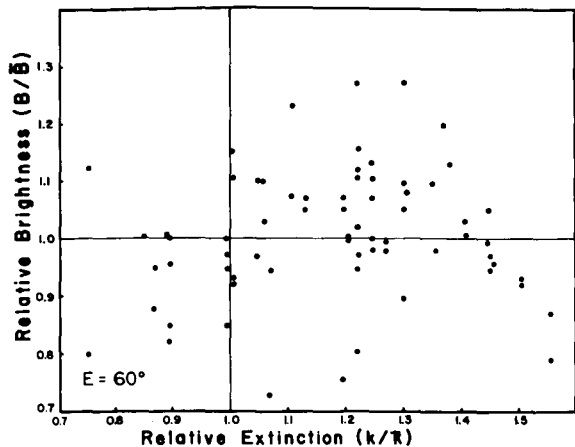


FIGURE 6.—Relative zodiacal-light brightness versus relative extinction coefficient for all data obtained at $E = 60^\circ$.

60° , and 75° , respectively. As can be seen, no apparent correlation exists. Hence, we conclude that our correction procedure is adequate and that no further corrections are necessary.

CONCLUSIONS

The experimental data presented here show the color of the zodiacal light to be very nearly identical to that of sunlight. There is a suggestion of an excess of red light around $E = 60^\circ$ near where the polarization reaches a maximum and where the intensity distribution begins to deviate from an exponential distribution.

Some exploratory calculations tend to show that there would be no contradiction between inclusion of particles with radii in the range from 0.1μ to 0.2μ and the neutral color of both the zodiacal light and the F-corona, if the radius distribution is chosen properly.

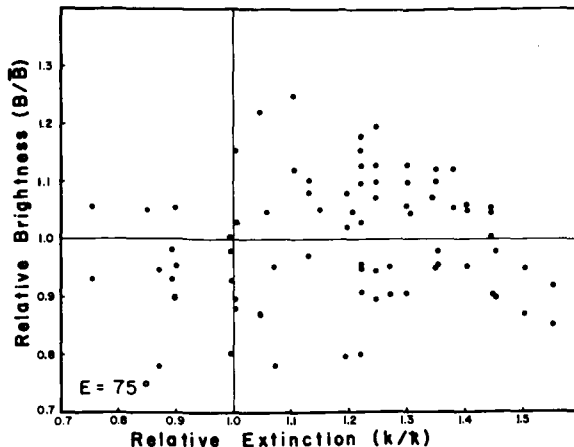


FIGURE 7.—Relative zodiacal-light brightness versus relative extinction coefficient for all data obtained at $E = 75^\circ$.

Because the data were corrected with extinction coefficients determined nightly, and no correlation was found between the final zodiacal-light brightness and the extinction coefficient, we conclude that our analysis procedure is valid. Also the final brightness and angular distribution agree well with Weinberg's data which were obtained with a more elaborate analysis procedure.

ACKNOWLEDGMENTS

The author expresses his appreciation to Dr. W. W. Morgan, former director of McDonald Observatory, for allowing the use of the Flat Top Mountain site for the observations; to Dr. J. C. Redmond, Chief of Applied Research at General Dynamics, Fort Worth, for permission to retain the data discussed here and to complete its analysis; and to Curtis Cannon, Faye Maxfield, and Melba Heiser who performed most of the routine data analysis at General Dynamics/Fort Worth.

REFERENCES

- ALLEN, C. W., 1946, *Mon. Not. Roy. Astron. Soc.*, **106**, 137.
- , 1963, *Astrophysical Quantities* (2d ed., London: Athlone Press).
- BARBIER, D., 1955, *Mém. Soc. Roy. Sci. Liège*, **15**, 55.
- BEHR, A., and H. SIEDENTOPF, 1953, *Zeits. f. Astrophys.*, **32**, 19.
- BLACKWELL, D. E., and M. F. INGHAM, 1961, *Mon. Not. Roy. Astron. Soc.*, **122**, 113.
- DIVARI, N. B., and A. S. ASAAD, 1960, *Soviet Astron.—AJ*, **3**, 832.
- DIVARI, N. B., and S. N. KRYLOVA, 1963, *Soviet Astron.—AJ*, **7**, 391.
- DIVARI, N. B., S. N. KRYLOVA, and V. I. MOROZ, 1964, *Geomag. and Aeron.*, **4**, 684.
- ELVEY, C. T., and F. E. ROACH, 1937, *Astrophys. J.*, **85**, 213.
- ELVEY, C. T., and P. RUDNIK, 1937, *Astrophys. J.*, **86**, 342.
- FATH, E. A., 1909, *Bull. Lick. Obs.*, **5**, 141.
- GINDILIS, L. M., 1962, *Soviet Astron.—AJ*, **6**, 67.
- HARDIE, R. H., 1962, IN *Astronomical Techniques* (W. A. Hiltner, ed.) (Chicago: Univ. of Chicago Press), 185.

- HOFFMEISTER, C., 1940, *Zeits. f. Astrophys.*, **19**, 116.
KARYAGINA, Z. V., 1961, *Soviet Astron. — AJ*, **4**, 828.
MITRA, S. K., 1952, *The Upper Atmosphere* (2d ed., Calcutta: The Asiatic Society).
PETERSON, A. W., 1961, *Astrophys. J.*, **133**, 668.
RAMANATHAN, K. R., 1932, *Nature*, **129**, 280.
REGENER, V. H., 1955, *Astrophys. J.*, **122**, 520.
ROACH, F. E., and P. JAMNICK, 1958, *Sky and Telescope*, **17**, 164.
ROACH, F. E., and L. R. MEGILL, 1961, *Astrophys. J.*, **133**, 228.
ROACH, F. E., H. B. PETTIT, E. TANDBERG-HANSEN, and D. N. DAVIS, 1954, *Astrophys. J.*, **119**, 253.
ROBLEY, R., 1962, *Ann. Geophys.*, **18**, 341.
SLIPHER, V. M., 1933, *J. Roy. Astron. Soc. Canada*, **27**, 365.
WEINBERG, J. L., 1964, *Ann. Astrophys.*, **27**, 718.
WOLSTENCROFT, R. D., J. C. BRANDT, and L. J. ROSE, 1966, *Planetary Space Sci.*, **14**, 445.

Page intentionally left blank

5. Reduction of Photometric Measurements of Zodiacal Light for the Influence of Twilight Radiation*

N. B. DIVARI
Odessa Polytechnic Institute
Odessa, U.S.S.R.

THE ELIMINATION of the various components of the radiation emitted by the night sky from the observed brightness is of great importance in the analysis of photometric measurements of the zodiacal light. However, no one has yet taken into account the component due to the twilight radiation from the sky, although at some positions of the Sun below the horizon, this component can exceed all the other components of the radiation observed.

With the twilight radiation taken into account, the observed brightness of the sky I_0 can be written as

$$I_0 = I_{ZL} p^{\sec z} + S(z, g, i) + \bar{A}(z) + L(b) p^{\sec z} + R(b, z, p) + B(g, A, z) \quad (1)$$

where I_{ZL} is the true brightness of the zodiacal light (outside the Earth's atmosphere), $S(z, g, i)$ the zodiacal light scattered by the troposphere, $\bar{A}(z)$ the atmospheric component of the radiation emitted by the night sky, $L(b)$ the stellar component, $R(b, z, p)$ the stellar component scattered by the troposphere, p the coefficient of transparency, and $B(g, A, z)$ the twilight component of the radiation, i.e., the brightness of the sky representing the sum of the brightnesses of the primary and secondary twilights. The primary twilight is governed by the scattering of solar radiation by the dust and gases of the Earth's atmosphere, while the secondary twilight is governed by the scattering of the primary twilight component by the troposphere. Usually, the component $A(z)$ is determined in one way

or another from the observations, $L(b)$ is calculated on the basis of a star count, while the function $R(b, z, p)$ has been tabulated by Fesenkov (1947). In order to calculate the component S representing the zodiacal radiation scattered by the troposphere, let us, following Fesenkov (1963a), combine the first and second terms of the right-hand side of equation (1)

$$(I_{ZL})_0 = I_{ZL} p^{\sec z} + S = \frac{I_{ZL} p^{\sec z}}{K} \quad (2)$$

where

$$K = \left(1 + \frac{S}{I_{ZL} p^{\sec z}} \right)^{-1}$$

and $(I_{ZL})_0$ is the observed brightness of the zodiacal light. Then, the true brightness of the zodiacal light I_{ZL} outside the Earth's atmosphere can be obtained from the observed brightness of the zodiacal light $(I_{ZL})_0$ by means of the equation

$$I_{ZL} = (I_{ZL})_0 K p^{-\sec z} \quad (3)$$

The values of the coefficient K have been calculated by Fesenkov (1963a and b) for positions of the Sun below the horizon of 16° to 24° on the basis of average models of zodiacal light and the Earth's atmosphere. However, in order to use the coefficient K in practice for the processing of photometric observations, we must subtract from the observed brightness I_0 not only the

*The information contained in this paper was published in *Soviet Astronomy*—AJ, vol. 10, no. 3, Nov.–Dec., 1966.

TABLE 1. — *The Twilight Component B*

A , deg	$\lambda = 0.37\mu$. $p = 0.59$					$\lambda = 0.50\mu$. $p = 0.85$					$\lambda = 0.58\mu$. $p = 0.89$					$\lambda = 0.70\mu$. $p = 0.95$				
	0°	20°	40°	60°	90°	0°	20°	40°	60°	90°	0°	20°	40°	60°	90°	0°	20°	40°	60°	90°
$\mu = 16^\circ$																				
0	133					164					153					169				
20	160	157	151	144	138	201	197	191	183	174	189	186	179	172	163	218	213	204	194	180
40	238	228	204	178	154	321	308	277	242	211	314	299	266	231	199	388	367	320	270	223
60	394	360	289	223	174	728	658	510	387	301	756	676	519	385	293	1100	957	698	485	340
70	521	450	322	227	166	1430	1200	814	548	392	1550	1300	863	567	392	2520	2060	1280	772	482
80	585	433	236	137	92	4550	3260	1620	849	537	5360	3850	1910	984	610	11200	7820	3570	1610	863
$\mu = 18^\circ$																				
0	20					29					31					31				
20	25	24	23	22	21	36	35	34	33	31	40	39	37	36	34	41	40	38	36	33
40	38	36	32	28	23	59	56	50	44	38	66	63	56	48	41	74	70	61	51	41
60	69	62	49	36	27	143	128	97	72	53	166	147	112	82	61	218	190	136	93	63
70	104	87	58	38	26	304	251	163	103	69	359	299	193	123	82	536	431	263	152	91
80	144	103	50	26	16	1130	779	363	167	96	1380	977	460	220	127	2690	1850	809	334	161
$\mu = 22^\circ$																				
0	2					2					3					2				
20	2	2	2	2	2	3	3	3	2	2	3	3	3	3	3	3	3	3	2	2
40	3	3	3	2	2	5	4	4	3	3	6	5	5	4	3	5	5	4	4	3
60	6	6	4	3	2	12	11	8	6	4	15	13	10	7	5	17	15	10	7	4
70	11	9	6	3	2	29	23	14	8	5	34	28	18	11	7	46	36	21	11	6
80	16	11	5	2	1	115	80	35	14	7	143	101	45	20	10	250	172	71	26	11
$\mu = 26^\circ$																				
0	0.2					0.3					0.3					0.2				
20	0.3	0.3	0.3	0.2	0.2	0.3	0.3	0.3	0.3	0.3	0.4	0.4	0.3	0.3	0.3	0.3	0.3	0.3	0.3	0.2
40	0.5	0.4	0.4	0.3	0.2	0.6	0.5	0.5	0.4	0.3	0.7	0.7	0.6	0.5	0.4	0.6	0.6	0.5	0.4	0.3
60	1.0	0.9	0.7	0.4	0.3	1.6	1.4	1.0	0.7	0.5	1.9	1.4	1.2	0.8	0.6	2.1	1.8	1.2	0.8	0.5
70	1.8	1.5	0.9	0.5	0.3	4.1	3.3	2.0	1.1	0.6	4.7	3.9	2.3	1.3	0.8	5.9	4.7	2.7	1.3	0.7
80	2.6	1.9	0.9	0.4	0.2	16.5	11.7	5.1	1.9	0.9	20.1	14.4	6.4	2.5	1.2	33.1	23.1	9.5	1.9	1.1

components $\bar{A}(z)$, $L(b)p^{\sec z}$, and $R(b, z, p)$, but also the twilight component $B(g, A, z)$.

In order to estimate the magnitude of this component, we have calculated it for the average model of the atmosphere taking into account the light scattered by gas and dust. The twilight component $B=B(g, A, z)$ has been calculated by us as the sum of four components:

$$B = B_M + B_{\Pi} + B_{2M} + B_{2\Pi} \quad (4)$$

where B_M and B_{Π} are the brightnesses of the primary twilight, i.e., the brightnesses governed by the scattering of direct sunlight by the atmospheric gases and dust, respectively, and B_{2M} and $B_{2\Pi}$ are the brightnesses of the light from the primary twilight scattered by the troposphere. The calculations were performed on the digital computer "Ural-2" for the average atmospheric model of Kallman-Bijl et al. (1961) with a total ozone content of 0.300 cm and have been described in detail by Divari and Plotnikova (1965). The altitude dependence of the dust concentration was taken from Divari (1964a) in which it was determined on the basis of photometric observations of the twilight sky.

The results of the calculation of the brightness B of the twilight sky for various values of the zenith distance z and azimuth A measured from the Sun's vertical are given in table 1. These brightnesses are expressed in units of stars of 10^m (photovisual) spectral class G2 per square degree; they correspond to monochromatic radiation with wavelengths of 0.37, 0.50, 0.58, and 0.70μ and a coefficient of atmospheric transparency $p=0.59, 0.85, 0.89$, and 0.95 , respectively. By interpolation between the data of table 1, we can easily obtain the brightness B at other points of the celestial sphere and, by means of graphical interpolation on a semi-logarithmic scale, the brightness for various positions of the Sun below the horizon.

In order to compare the magnitude of the twilight component B with the correction S for the tropospheric scattering of zodiacal light, we have shown in table 2 the corrections B and S for $z=70^\circ$, $\lambda=0.50\mu$ ($p=0.85$), and five values of the solar dip angle for the case when the ecliptic is at right angles to the horizon ($i=90^\circ$).

The brightness has been expressed in units of the number of 10^m (photovisual) stars of class G2 per square degree.

TABLE 2. — Corrections for B and S for $z=70^\circ$, $\lambda=0.50\mu$ ($p=0.85$)

g , deg		$A=0^\circ$	$A=10^\circ$	$A=20^\circ$	$A=40^\circ$	$A=60^\circ$	$A=80^\circ$
16	B	1430	1350	1200	814	548	468
	S	26	24	21	15	11	10
18	B	304	289	251	163	103	79
	S	22	21	19	12	10	8
20	B	89	80	72	48	26	21
	S	19	18	16	10	8	7
24	B	11	10	9	6	3	2
	S	15	14	13	9	7	5
28	S	2	2	1.5	1	0.5	0.3
	S	12	12	10	7	5	4

It can be seen from table 2 that for solar dip angles of 16° to 20° , the correction B for twilight radiation is significantly higher than the correction for the tropospheric scattering of zodiacal light ($B > S$). On the other hand, for dips greater than 24° , $B < S$. These results show that for dips of 16° to 20° twilight produces a significant perturbation of the zodiacal light. The twilight component has an appreciable effect in observations along the almucantar $z=70^\circ$ and, especially, $z=80^\circ$. Because of this, the brightness of the zodiacal light at small elongations obtained from photometric observations without correction for twilight can be overestimated. For example, let us consider the variation of brightness along the ecliptic making use of the average value of the brightness outside the Earth's atmosphere obtained from Divari (1964b) on the basis of the results of many workers. Let us assume that the ecliptic is at right angles to the horizon. Then the elongation ϵ , the Sun's dip angle g , and the zenith distance z of the point being observed are connected by the relation $\epsilon=90^\circ-z+g$. If, for simplicity, we correct for the tropospheric scattering of zodiacal light by increasing the coefficient of transparency by 0.02, then the observed brightness of the zodiacal light ($I_{zL,0}$)

is given in terms of the brightness outside the atmosphere I_{ZL} by the equation

$$(I_{ZL})_0 = I_{ZL}(p + 0.02^{\sec z})$$

The twilight component B and the observed brightness of the zodiacal light $(I_{ZL})_0$ are compared in table 3 for three values of the Sun's dip angle. The coefficient of transparency of the Earth's atmosphere has been taken as $p = 0.85$.

TABLE 3.—Comparison of B and $(I_{ZL})_0$ for Three Values of g

z	80°	70°	60°	50°	40°
$(p + 0.02)^{\sec z}$	0.448	0.666	0.757	0.805	0.834
$g = 20^\circ$					
ϵ	30°	40°	50°	60°	70°
$(I_{ZL})_0$	860	648	456	325	261
B	320	89	39	27	15
$g = 18^\circ$					
ϵ	28°	38°	48°	58°	68°
$(I_{ZL})_0$	999	746	503	354	267
B	1130	304	143	101	59
$g = 16^\circ$					
ϵ	26°	36°	46°	56°	66°
$(I_{ZL})_0$	1230	846	553	378	284
B	4550	1430	728	520	311

The approximate estimates given in table 3 show that for a solar dip angle of $g = 20^\circ$, the brightness of twilight has a significant influence

on the observed brightness of the zodiacal light and it must be taken into account at least for low elongations. For $g = 18^\circ$ and $g = 16^\circ$ the brightness of the twilight sky at small elongations considerably exceeds that of the zodiacal light and therefore there is no point in observing the zodiacal light at such dip angles. Because of this, we cannot consider the values of the brightness of the zodiacal light obtained by some observers at elongations less than 30° to be correct, since these observations were carried out with the Sun dipping less than 20° below the horizon, while the influence of twilight on the results was not taken into account. (For example, in Chacaltaya, Blackwell made observations for $\epsilon \geq 20^\circ$ (Ingham, 1961) and Peterson (1961) for $\epsilon \geq 25^\circ$.) It is necessary to point out that if the ecliptic is inclined to the horizon, the importance of twilight will be even greater at these values of the Sun's dip angle.

When making corrections for the twilight component, we should keep in mind that the brightness of the twilight sky is not constant from day to day, but can be variable depending on the concentration of dust in the Earth's atmosphere and variations in the coefficient of transparency. For example, the data given by Divari and Trofimova (1963) show that the absolute values of the brightness of the twilight sky can change by up to a factor of 10 in the course of several days. Therefore, for the determination of the twilight component it is possible to recommend that observations of twilight be made away from the zodiacal-light cone. Using these observations, we can use the preceding tables to obtain the twilight component in the region occupied by the zodiacal-light cone at the times at which observations of the zodiacal light are made.

REFERENCES

- DIVARI, N. B., and L. S. TROFIMOVA, 1963, *Geomagn. i. aëronomiya*, **3**, 657.
 DIVARI, N. B., 1964a, *Uspekhi fiz. nauk*, **84**, 75. [Soviet Physics-Uspekhi, vol. **7**, p. 681.]
 —, 1964b, *Geomagn. i. aëronomiya*, **4**, 886.
 DIVARI, N. B., and L. I. PLOTNIKOVA, 1965, *Astron. zh.*, **42**, 1090. [Soviet Astron.—AJ, Vol. **9**, p. 840.]
 FESENKOV, V. G., 1947, *Meteoric Matter in Interplanetary Space* (Izd. AN SSSR, Moscow). In Russian.
 —, 1963a, *Astron. zh.*, **40**, 31. [Soviet Astron.—AJ, Vol. **7**, p. 23.]
 —, 1963b, *Astron. zh.*, **40**, 882. [Soviet Astron.—AJ, Vol. **7**, p. 670.]
 INGHAM, M. F., 1961, *Monthly Notices Roy. Astron. Soc.*, **122**, 157.
 KALLMAN-BIJL, H., R. L. F. BOYD, H. LAGOW, S. M. POLOSKOV, and W. PRIESTER, 1961, *CIRA* (COSPAR International Reference Atmosphere, Amsterdam: North Holland Publ. Company).
 PETERSON, A. W., 1961, *Astrophys. J.*, **133**, 668.

6. Rocket Observations of the Brightness of the Zodiacal Light

HIROYOSHI TANABE AND MASAOKI HURUHATA
*Tokyo Astronomical Observatory
Tokyo, Japan*

The brightness of the zodiacal light was measured at three wavelengths, 4300Å, 5300Å, and 6000Å, from a rocket on the evening of July 26, 1965. Launched from the Kagoshima Space Center, the rocket reached a maximum altitude of 328 km. Measurements were made from 41° to 15° from the Sun along the ecliptic, thus providing coverage of the observational gap between the inner zodiacal light and the outer corona observed from the ground and from aircraft, respectively, at the time of solar eclipse.

The results are in fairly good accord with ground observations, but show a slightly steeper gradient of the brightness with elongation than those of ground observations, and indicate a slightly higher value for the brightness of the outer corona at 6000Å than Blackwell's.

A SERIES OF ZODIACAL LIGHT OBSERVATIONS made by using balloons and sounding rockets is being planned and conducted by the Tokyo Astronomical Observatory. This paper reports on results of our first rocket experiment, which was made on July 26, 1965, at the Kagoshima Space Center (long. 131°05' E., lat. 31°15' N.). Photoelectric photometry of the zodiacal light was carried out at three wavelengths: 4300Å, 5300Å, and 6000Å. The reason these wavelengths were selected was to be able to compare the rocket observations with previous ground observations, almost all of which have been made near these wavelengths. The ground observations could thus be extended to the observational gap between the outer corona and the inner zodiacal light.

INSTRUMENT

The photometer (fig. 1) consists of a pair of parallel telescopes, each with its own separate optical system and photomultiplier detector. The effective field of view of each telescope is 3°. By means of rotating telescopes, the photom-

eter scans in a plane parallel to the rocket axis from 42° (upward from a normal to the axis) to -22° (downward) after the opening of the nose cone of the rocket. It was intended to scan a wide area of the sky by this movement of the telescope together with the spin motion of the rocket. After one scanning motion, the telescope is fixed at -22°.

In front of each photomultiplier a pair of interference filters is installed, 4300Å and 5300Å for one photomultiplier, 5300Å and 6000Å for the other, such that the two filters in each unit are interchanged every 0.7 second. The transmission curves of these filters are shown in figure 2.

Standard light surfaces and shutters are also provided for intermittent checks of the sensitivities during the flight.

The output signals from the photomultipliers are led through amplifiers to the telemeter transmitter. The electric power for the photomultipliers, amplifiers, and micromotors which drive the filters and telescope is supplied by dry batteries.



FIGURE 1.—Photoelectric photometer used for present observations.

FLIGHT AND ATTITUDE OF THE ROCKET

The rocket [K-9M-12] was launched at 21^h01^m (JST) on July 26, 1965. The nose cone of the rocket was opened at the height of about 70 km, and the maximum height reached was 328 km.

After the opening of the nose cone, the rocket had a precessional motion with a period of 79.7 seconds and a spin motion with 0.55 second. These characteristics of the motion were obtained from the data of the geomagnetic aspect-meter loaded on the same rocket.

By using the data of the geomagnetic aspect-meter and also by identifying the brightness increases at the horizon, the direction and angular radius of the precessional motion could be found. The instantaneous attitude of the rocket and the direction of the telescopes could then be determined. Figure 3 shows the loci of scannings on the celestial sphere made during one precession (270 to 340 seconds after launching) near the maximum height of the trajectory.

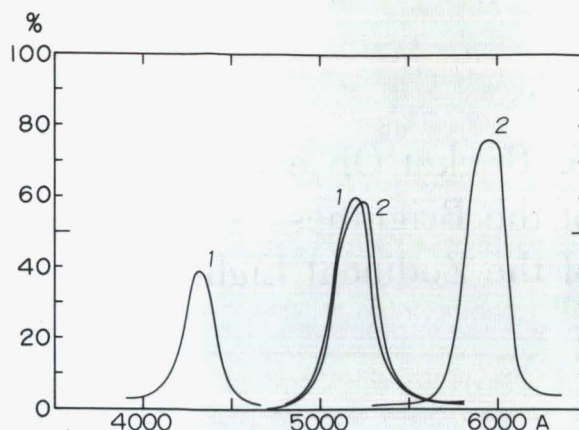


FIGURE 2.—Transmission curves of interference filters. (1 and 2 indicate pairs of filters used in the two telescopes.)

At the highest point of the trajectory, the depression angle of the horizon was 18.0° and the Sun was 4.8° below this horizon. From this analysis it was found that the measurements were made between 15° and 41° from the Sun along the ecliptic.

REDUCTION OF OBSERVATIONS AND RESULTS

Recordings near the maximum height of the rocket, between 328 and 255 km, were used for the present study.

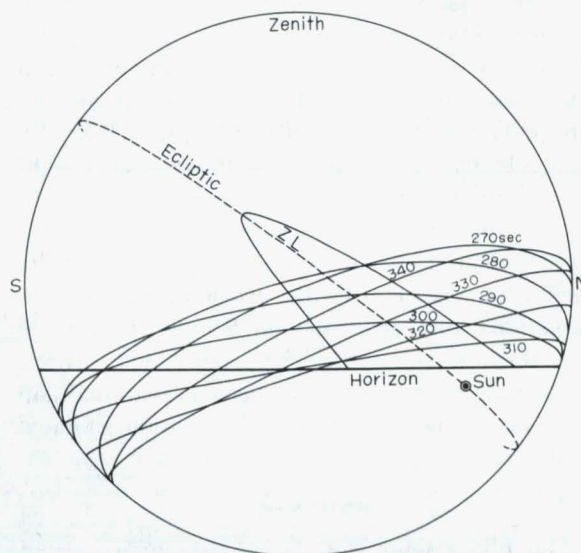


FIGURE 3.—Loci of instantaneous scannings made during one precession near maximum height of trajectory. Western hemisphere of celestial sphere. Times are seconds after launch.

Before the launching several bright stars were observed at various zenith distances with the same photometer, and the conversion factors from the readings to the number of G0 10th magnitude stars per square degree, $S_{10}(\text{vis})$, were determined.

The observations do not require corrections for atmospheric extinction or atmospheric scattered light. The star background component was not subtracted from the measurements because the galactic latitude of the observed region was rather high (about 50°) and the background component was considered to be negligible compared with the bright zodiacal light.

Since the observations were made from heights above 255 km, these data are practically free of contamination by the airglow continuum except those obtained at small elongations, corresponding to the largest depression angle looking from the rocket. To check this airglow contamination at the smaller elongations, the integrated airglow as seen by the photometer as a function of depression angle was examined, taking the height of maximum continuum emission as about 105 km and the upper boundary as 140 km from rocket observations (Packer, 1961). The calculation showed that the measurements at elongations less than 18° are contaminated by the airglow continuum. Assuming a uniform emission layer and a zenith brightness of about $50S_{10}(\text{vis})$ (Roach and Smith, 1964) at 5300\AA , the airglow brightness integrated along the line of sight was estimated to be less than $2000S_{10}(\text{vis})$ at elongation 15° . Considering the brightnesses of the airglow continuum at 4300\AA and 6000\AA to be comparable to that at 5300\AA , the amounts of contamination are less than the probable errors of the measurements, and so were neglected.

The possibility of contamination by the 6300\AA airglow line through the 6000\AA filter was considered. The correction for this contamination, however, is very difficult since the brightness of the 6300\AA line in twilight at various elevations of the Sun is not well known. No correction was attempted on the assumption that the filter transmission and photomultiplier sensitivity were both sufficiently small at 6300\AA to render the contamination negligible.

The telescope was designed carefully by using several diaphragms to eliminate instrumental scattered light, but a small amount might be included in the results, especially in the measurements near the bright horizon.

Results for each wavelength are shown in figures 4, 5, and 6. The values given are averages

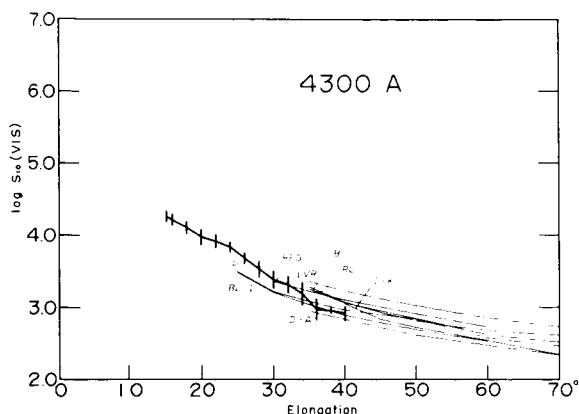


FIGURE 4.— $4300\text{-}\text{\AA}$ brightness along ecliptic. Vertical short lines indicate probable errors. Abbreviations are referred to Weinberg (1964).

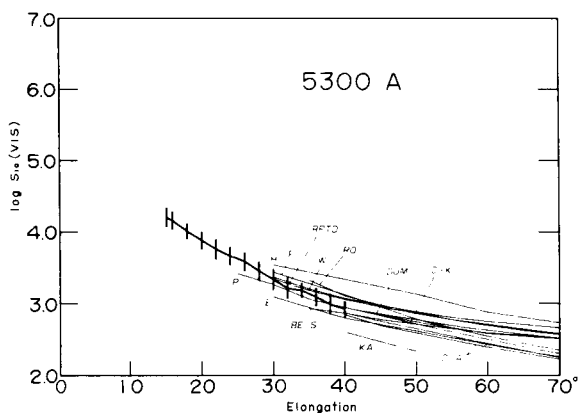


FIGURE 5.— $5300\text{-}\text{\AA}$ brightness along ecliptic. Vertical short lines indicate probable errors. Abbreviations are referred to Weinberg (1964).

of the measurements made in two precessions near the maximum height of the trajectory.

Present results agree, in general, with the previous ground observations summarized by Weinberg (1964), but our results show slightly steeper slopes with the elongation than previous results, and indicate a slightly higher value of the brightness of the outer corona at 6000\AA than Blackwell (1955) reported.

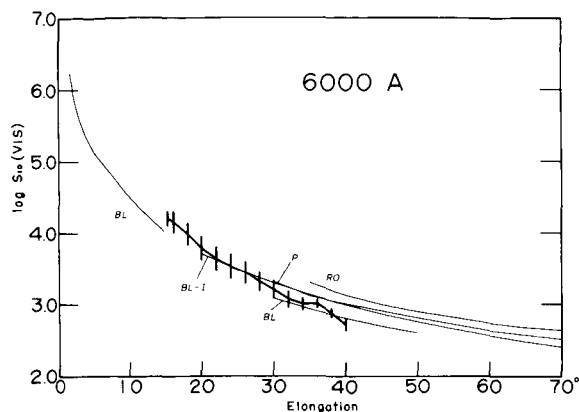


FIGURE 6.—6000Å brightness along ecliptic. Vertical short lines indicate probable errors. Abbreviations are referred to Weinberg (1964).

Figure 7 shows the color indices at various elongations obtained from the ratios of the brightness at 4300Å and 5400Å; the latter value was estimated by interpolation between 5300Å

and 6000Å. The color indices at elongations greater than 34° are less reliable, because the deflections of the original record in this part are small. The color indices of the Sun and Capella (see Allen, 1955), and the values of previous observations (Behr and Siedentopf, 1953; and Blackwell and Ingham, 1961) are also plotted in figure 7.

The color indices obtained from the present data have considerable error so that we may conclude only that the color of the zodiacal light in the elongation between 15° and 40° is almost the same as that of the Sun.

ACKNOWLEDGMENTS

The operation of this rocket was performed by the staff of the Institute of Space and Aeronautical Sciences, University of Tokyo, under the leadership of Prof. D. Mori, to whom the writers are much indebted. They are also indebted to Messrs. T. Nakamura and K. Saito of Tokyo Astronomical Observatory for assistance throughout this experiment.

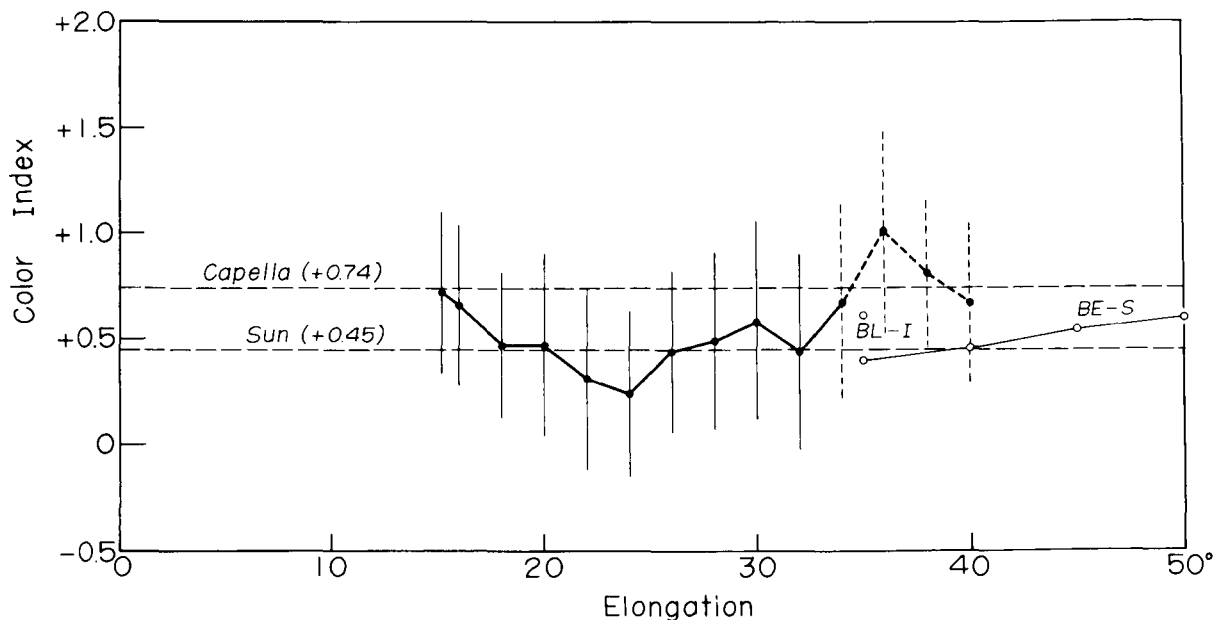


FIGURE 7.—Color indices along ecliptic. Vertical short lines indicate probable errors.

REFERENCES

- ALLEN, C. W., 1955, *Astrophysical Quantities* (London: Athlone Press).
- BEHR, A., and H. SIEDENTOPF, 1953, *Zeits. f. Astrophys.*, **32**, 19.
- BLACKWELL, D. E., 1955, *Mon. Not. Roy. Astron. Soc.*, **115**, 289.
- BLACKWELL, D. E., and M. F. INGHAM, 1961, *Mon. Not. Roy. Astron. Soc.*, **122**, 113.
- PACKER, D. M., 1961, *Ann. de Geophys.*, **17**, 67.
- ROACH, F. E., and L. L. SMITH, 1964, NBS Technical Note, No. 214.
- WEINBERG, J. L., 1964, Summary Report on Zodiacal Light, July 1964, Hawaii Institute of Geophysics, Report HIG-64-11, 18 pp.

7. Observations of the Photometric Axis of the Zodiacal Light

KEIJI SAITO AND MASAOKI HURUHATA
Tokyo Astronomical Observatory
Tokyo, Japan

Photoelectric observations of the photometric axis of the zodiacal light were made at Manuae Island in the South Pacific around the date of the total solar eclipse on May 30, 1965, when the ecliptic was perpendicular to the horizon. The result was compared with the previous instrumental observations and also with visual observations. The concentration of zodiacal-light particles near and inside the Earth's orbit seems not to be on the invariable plane, but rather inclined to the orbital plane of Venus and Mars as was pointed out by Hoffmeister (1941). Another possibility referred to is that the concentration tends to the equatorial plane of the Sun. No effect by the particles in the Earth-Moon system can be found.

THE PLANE OF CONCENTRATION of zodiacal-light particles in interplanetary space seems to be one of the important studies in the investigation of the origin and nature of the particles. Since the 1950's some instrumental measurements have been made by both photographic and photoelectric photometry at sites where the ecliptic was almost perpendicular to the horizon at the time of observation. Such observations include those by Divari and Asaad (1960) in 1957 and by Blackwell and Ingham (1961) in 1958.

Blackwell and Ingham's results of observation coincide fairly well with the inclination of the invariable plane and they suggested the concentration of the particles on the invariable plane.

The same kind of observation in 1964 was made by Huruahata (1965) at the Haleakala Observatory during his stay there. The observations were made in February and March for the evening zodiacal light, and the result was not in agreement with the invariable plane.

OBSERVATIONS IN 1965

The same instrument used at Haleakala was used on Manuae Island (159° W., 19.4° S.) in the South Pacific during the total solar eclipse on May 30, 1965. Observations were made on the

mornings of May 28 and 29 when the ecliptic was also perpendicular to the horizon.

The instrument was a photoelectric photometer which made almucantar sweeps automatically at a rate of 3° per second. The amplified photocurrent was recorded on an electromagnetic oscillograph with a galvanometer whose time constant was $\frac{1}{25}$ second. The azimuth of the photometer was marked on the recording paper by electric contacts with another galvanometer.

The effective field of view was 0.88 square degree. An interference filter which has a broad halfwidth of 330Å was used. The central wavelength was 4950Å and the transmission at the bright airglow line at 5577Å was negligible.

The measured intensities were contaminated by star background, and the correction for that was made by using the mean integrated starlight as a function of galactic latitude given by Megill and Roach (1961).

RESULTS OF OBSERVATIONS

Results of the observations are shown in figure 1 by solid triangles. The previous results in the figure are those indicated in the Introduction. The open circles are from the photographic observations from an aircraft made by Blackwell in 1955 (see Blackwell, 1956). Observations in

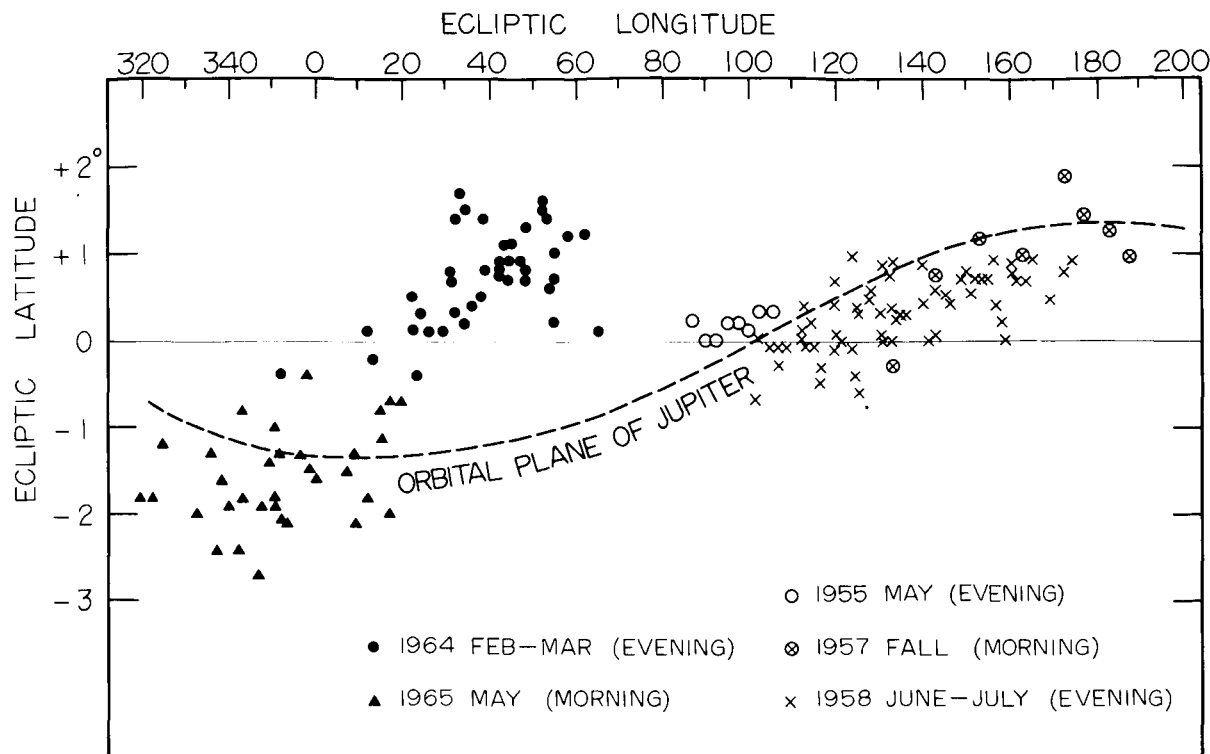


FIGURE 1.—Observed positions of photometric axis of zodiacal light.

1957 by Divari and Komarnitskaya (1966) have been taken from a small-scale diagram and some error of reading from it would be involved in this reproduced figure.

DISCUSSION

We may first point out the big difference in the ecliptic latitude of the photometric axis between our observations in February and March 1964 and May 1965, for evening and morning zodiacal light, respectively. In figure 2 are shown the locations of the Earth at the times of observation and the directions for which the measurements were made. The relative positions for these 2 years with respect to the invariable plane are almost the same, so that the ecliptic latitudes of the photometric axis seen from these two positions of the Earth should be identical if the zodiacal-light particles are concentrated on the invariable plane. The observed results are apparently not in favor of the concentration on the invariable plane.

Based on several hundred visual observations made in the 1930's, Hoffmeister (1941) made an

extensive study of this problem. He and his colleagues made many observations at low geographic latitudes in both hemispheres, and for observations at higher latitudes careful corrections were applied to eliminate the effect of atmospheric extinction to the photometric axis.

The recent instrumental observations were compared with Hoffmeister's results, and fairly good agreement between the two could be recognized. Hoffmeister's conclusion was that the zodiacal-light particles in and around the Earth's orbit are affected by inner planets, while those far out from the Earth's orbit are related to the orbit of Jupiter.

A slight difference between the Hoffmeister result and recent instrumental observations is that his inclinations at the smaller elongations from the Sun are generally somewhat larger than in the remote parts, while the recent observations show the smaller inclination at the smaller elongations.

Another possibility is, as we have pointed out in a previous paper (Huruhata, 1965), the tendency to concentrate to the Sun's equatorial plane

whose ascending node is very close to that of the orbital plane of Venus.

The present observations were made in the direction in which the Sun's equatorial plane lies on the southern side of the ecliptic, and the result of this observation is in fairly good accordance with a concentration on the Sun's

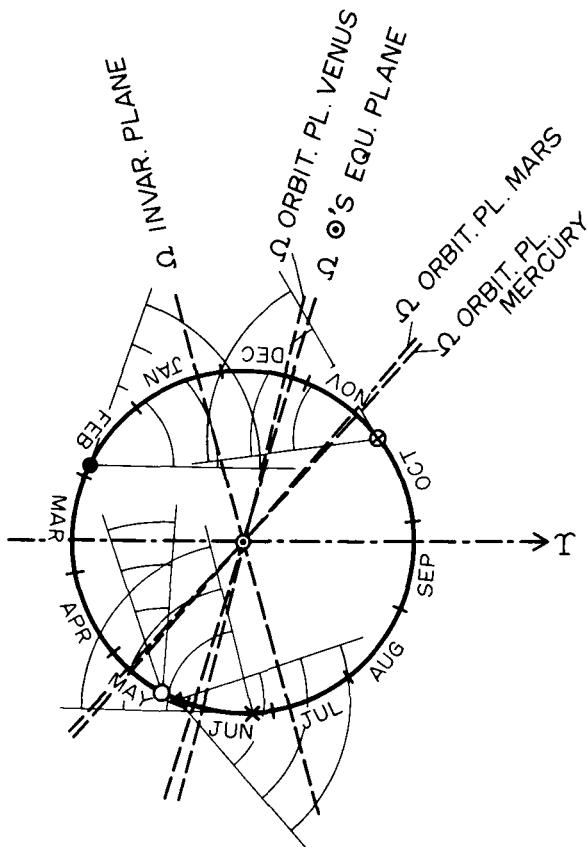


FIGURE 2.—Positions of Earth at times of observation and directions to which observations are made. The marks of position correspond to those in figure 1. Three arcs with centers at observing positions represent distances of 1.0, 0.75, and 0.5 AU from Earth.

equatorial plane. In figure 2, the groups of three arcs with centers at the observing positions of the Earth represent distances of 1.0, 0.75, and 0.5 AU, respectively, from the Earth. If we assume the distance of the particles which are most effective in producing the observed photometric axis of zodiacal light to be around 0.75 AU from the Earth, the observed ecliptic latitudes of the axis can be roughly explained. However, the representation is qualitative rather than quantitative, because the ecliptic latitudes obtained from the above procedure give larger departures from the ecliptic than the observed latitudes. This may be understood if we consider that the plane of concentration of particles is not exactly on the Sun's equatorial plane, but is somewhat inclined to the Sun's equatorial plane.

Divari and Komarnitskaya (1966) point out that the photometric axis may have a dependence on the ecliptic latitude of the Moon, but we cannot recognize that tendency in these observed results.

Recently it has been suggested (Divari, 1965) that the particles very near the Earth may contribute to the brightness of zodiacal light. So far as the photometric axis is concerned, we cannot find any evidence of such possibility.

CONCLUDING REMARKS

In conclusion, we would like to urge that more accurate observations, both for evening and morning zodiacal light, be carried out at various equatorial sites where the observing conditions are good, not only in all seasons to get more information on the axis, but also over a period of some years to find out if there are any long-period changes of the axis.

REFERENCES

- BLACKWELL, D. E., 1956, *Mon. Not. Roy. Astron. Soc.*, **116**, 365.
- BLACKWELL, D. E., and M. F. INGHAM, 1961, *Mon. Not. Roy. Astron. Soc.*, **122**, 133.
- DIVARI, N. B., and A. S. ASAAD, 1960, *Soviet Astron.—AJ*, **3**, 832.
- DIVARI, N. B., 1965, *Soviet Astron.—AJ*, **9**, 493.
- DIVARI, N. B., and N. I. KOMARNITSKAYA, 1966, *Soviet Astron.—AJ*, **9**, 632.
- HOFFMEISTER, C., 1941, *Astr. Nachr.*, **271**, 49.
- HURUHATA, M., 1965, *Planetary Space Sci.*, **13**, 237.
- MEGILL, L. R., and F. E. ROACH, 1961, NBS Technical Note, No. 106.

Page intentionally left blank

8. Observations of the Zodiacal Light by Means of Telemetry From Balloons

VICTOR H. REGENER AND EDWIN L. VANDE NOORD
*University of New Mexico
Albuquerque, New Mexico*

A lightweight balloon-borne telescope equipped with telemetry for zodiacal-light intensity and polarization readings in three colors was flown from Albuquerque, New Mexico, during the International Quiet Sun Years. Two flights have now been completely evaluated. Absolute extraterrestrial intensity and color readings are obtained by using fixed stars as calibration sources. The results show that the exponent of the power law $I = Ce^K$ is $K = -3.03 \pm 0.14$ in the blue ($\lambda_{\text{eff}} = 4350\text{\AA}$) and $K = -3.01 \pm 0.09$ in the visible ($\lambda_{\text{eff}} = 5500\text{\AA}$) regions of the spectrum, where I is the intensity of the zodiacal light on the ecliptic between elongation angles from the Sun of $25^\circ < \epsilon < 35^\circ$. The color index of the zodiacal light in that region was found to be $B-V = 0.60 \pm 0.04$ ($B-V = 0.62$ for the Sun). The average degree of polarization of the zodiacal light over the same region was found to be 0.16 ± 0.02 in the visual and 0.17 ± 0.02 in the blue.

INSTRUMENTATION

THE PAYLOAD OF THE BALLOONS consists of two packages, each weighing 6 pounds. The upper package consists of a refracting telescope of 4-inch aperture and 35-inch focal length, with a two-channel photoelectric photometer and telemetry unit mounted behind the focal plane. One channel provides the brightness and polarization of the zodiacal light in two or three colors by rotating both a color-filter wheel and a polaroid filter in front of the photomultiplier tube. The field of view is 1.80° in diameter. In the other channel, a second photomultiplier tube responds to the traversal of star images over field stops consisting of three narrow slits oriented to provide information on azimuth and elevation, as well as on rate of rotation of the package. An FM-FM telemetry system with two subcarriers permits continuous analog information to be recorded at the ground station for each channel on a two-channel stripchart recorder.

Hanging 10 feet below the telescope is a second package which contains the telemetry

transmitter and a pressure sensor. The train of two packages is suspended from a low-friction thrust bearing and is carried into the stratosphere by four expansible rubber balloons. The telescope is allowed to rotate freely, and it makes almucantar sweeps of the night sky at a constant average elevation angle of 5° . Typical rotation rates obtained during a flight are 20° per second, or slower. Telescope pitching is minimized during the data readout time by reducing the ascent rate, at an altitude of approximately 55 000 feet, from 900 to 350 feet per minute. This reduction is accomplished by arranging for one of the four rubber balloons to burst at that height.

The color wheel contains the green or visual (V) and blue (B) broad-band filters of the U, B, and V color system (Johnson and Morgan, 1951) and an ultraviolet (U') filter. The effective wavelengths of the U', B, and V instrumental system are 4000\AA , 4350\AA , and 5500\AA , respectively, and include the responses of the photomultiplier tube (S-4) and other optical elements. The half-widths at half maximum are on the order of 500\AA .

A neutral-density filter and an opaque sector for dark-current measurements are also included in the filter wheel. The rotation rates of the color wheel and polaroid filter are such that four cycles of polarization modulation are obtained for each color. The sampling period for each color lasts 0.12 second.

EVALUATION OF RECORDINGS

The first step in the data analysis is a determination of the azimuth and elevation history of the flights. This determination is made by identifying stars with a visual magnitude of 5.5 or brighter, which are resolved in the star channel. Each traversal of a star image over the system of three slits provides the direction of rotation, the rotation rate, and information on the elevation angle of the telescope. The ecliptic plane is close in azimuth to that of the peak intensity of the zodiacal-light scan and provides an initial starting azimuth for purposes of decoding the star signals. This information, along with the amplitude of the star deflections, is evaluated by means of a computer program.

The corresponding star deflections in the zodiacal-light channel serve to calibrate the instrument for the various colors in absolute extraterrestrial units. Only those stars with visual or blue magnitude brighter than 4.2 were used for this purpose. The star magnitudes are obtained from the Arizona-Tonantzintla catalog (Iriarte et al., 1965). Although 90 percent of the atmosphere, or more, is usually below the instrument, a theoretical correction factor for atmospheric extinction and absorption is applied to each observation. This correction reduces the deflections to their values outside the atmosphere. The correction factor includes Rayleigh and aerosol scattering, ozone absorption, instrumental response, and the effective blackbody temperature of the stars used. For the flights of November 30 and December 5, 1965, intensities were obtained in each flight for at least 12 different stars. For the present investigation only the visual and blue colors are reduced.

After expressing all observational intensities in absolute units, the individual components of the night sky are separated. The minimum de-

flection for a 360° scan in azimuth is obtained for each color. The correction for extinction is applied and the resulting extraterrestrial values are converted to absolute intensities. The zodiacal light and integrated starlight at the minimum are then removed. The values for zodiacal light are from Roach et al. (1954) and the integrated starlight values from the charts of Roach and Megill (1961). The remaining background light is due to airglow and scattered light and is assumed independent of azimuth. It is subtracted, along with the integrated starlight at the point, from the total extraterrestrial intensities to obtain the intensity of the zodiacal light.

RESULTS

In table 1 the average intensities along the ecliptic are given for the blue and visual colors. The intensities are expressed in $S_{10}(\text{blue})$ and $S_{10}(\text{vis})$ units, respectively. (S_{10} means stars of the 10th magnitude per square degree.) The uncertainty in the intensity values is ± 5 percent. If the zodiacal-light intensities along the ecliptic are expressed as a power law of the form $I \sim \epsilon^K$, where ϵ is the elongation, the following values for K are obtained: blue, -3.03 ± 0.14 ; visual, -3.01 ± 0.09 . These values are definitely higher than those quoted previously; for a recent review, see Divari (1965). The recent rocket results presented in paper No. 6 by Tanabe and Huruata also seem to show a high exponent at small elongation angles.

The B-V color index of the zodiacal light along the ecliptic is also given in table 1. The average

TABLE 1.—*Brightness and Color Index of Zodiacal Light Along Ecliptic. Flights of November 30 and December 5, 1965*

Wavelength	Elongation angle					
	25°	27°	29°	31°	33°	35°
4350 Å (B).....	1550	1240	1010	760	655	580
5500 Å (V).....	2690	2170	1660	1390	1140	990
B-V.....	.60	.61	.54	.66	.60	.58

B-V equals 0.60 ± 0.04 , where B-V is 0.62 for the Sun (Allen, 1963), and we conclude that over this region of elongation the color of the zodiacal light is that of the Sun to within the errors given.

The average degree of polarization of the zodiacal light on the ecliptic in the region from

$\epsilon = 25^\circ$ to $\epsilon = 35^\circ$ is found to be 0.16 ± 0.02 in the visual, and 0.17 ± 0.02 in the blue.

ACKNOWLEDGMENT

This work was supported by the Atmospheric Sciences Section, National Science Foundation. Grants GP-2714 and GA-330.

REFERENCES

- ALLEN, C. W., 1963, *Astrophysical Quantities* (2d ed., London: Athlone Press), 162.
DIVARI, N. B., 1964, *Usp. Fiz. Nauk*, **84**, 75, translation in 1965, *Soviet Physics Uspekhi*, **7**, 681.
IRIARTE, B., H. L. JOHNSON, R. I. MITCHELL, and W. K. WISNIEWSKI, 1965, *Sky and Tel.*, **30**, 21.
JOHNSON, H. L., and W. W. MORGAN, 1951, *Astrophys. J.*, **114**, 522.
ROACH, F. E., and L. R. MEGILL, 1961, *Astrophys. J.*, **133**, 228.
ROACH, F. E., H. B. PETTIT, E. TANDBERG-HANSEN, and D. N. DAVIS, 1954, *Astrophys. J.*, **119**, 253.

Page intentionally left blank

9. Zodiacal-Light Observations From a Sounding Rocket*

R. D. WOLSTENCROFT
*Royal Observatory
Edinburgh, Scotland*

AND
L. J. ROSE
*Kitt Peak National Observatory
Tucson, Arizona*

IN THIS CONTRIBUTION we report measurements of the surface brightness, color index, and state of polarization of the zodiacal light made from an Aerobee 150 sounding rocket. The rocket was launched from the White Sands Missile Range on September 15, 1964, at 0235 m.s.t. and reached a peak altitude of 200 km. The observations described herein were obtained during the 245-second period that the rocket was above an altitude of 130 km.

Four polarimeters and one photometer, responding to five different colors, were flown aboard the rocket. Three of the polarimeters produced no useful data. The two instruments which gave satisfactory data were a photometer containing a standard B-filter and a field of 2.7 square degrees and a polarimeter containing an interference filter with an equivalent width of 180\AA centered on 7030\AA and a field of 17.1 square degrees. We refer to these two instruments as the B-photometer and the R-polarimeter. The effective wavelengths of the polarimeter and of the R magnitude system of Johnson and Mitchell (1962) are practically identical.

The polarimeter comprised a quartz retardation plate, with quarter-wave retardance at 6940\AA , which was rotated in front of an HN 32 Polaroid placed close to the focal plane of the

6-cm-diameter objective; a Fabry lens was used to image the light onto the photocathode of an EMI 9558 photomultiplier tube. In the general case where the incident radiation was a combination of natural light and linearly and circularly polarized light, the modulation of the output voltage from the photomultiplier contained terms at frequencies of twice and four times the quarter-wave-plate rotation frequency, ω . The amplitudes of the 2ω and 4ω components were proportional to the degree of ellipticity and the degree of linear polarization of the incident light, respectively.

An attitude-control system was programmed to scan the instruments along five great-circle paths of typical length 180° at scanning rates of about 4° per second. The actual attitude of the photometers during the flight was derived to an accuracy of about 10° by using aspect information provided by three orthogonally mounted magnetometers, and to an accuracy of 1° by using the time, amplitude, and width of star deflections recorded by the B-photometer. The amplitudes of the star deflections recorded by the two instruments were used to calibrate the surface brightness in units of the equivalent number of B (or R) = 10.0 stars per square degree. We refer to these units as n_B and n_R .

The method of correcting the observations for background sky radiation is summarized as follows—

*Contribution No. 238 from the Kitt Peak National Observatory.

Surface brightness of the zodiacal light, $n(ZL)$:

$$n(ZL) = n(O) - n(IS) - n(NG)$$

where O , IS , and NG refer to the total night-sky radiation, the integrated starlight, and the night-glow, respectively.

Surface brightness of nightglow, $n(NG)$: Observations of three regions of sky obtained twice at substantially different altitudes of the rocket were used to show that the contribution from NG above 130 km was negligible, viz.,

$$n_B(NG) = 10 \pm 20, n_R(NG) = 0 \pm 15$$

Surface brightness of integrated starlight, $n(IS)$: The brightness $n_{PG}(IS)$ in the international photographic magnitude system tabulated by Roach and Megill (1961) was used with the following color coefficients:

$$n_B(IS) = 0.903 n_{PG}(IS)$$

$$n_R(IS) = 4.21 n_B(IS)$$

Degree of polarization: The integrated starlight was assumed to be negligibly polarized so that the degree of polarization of the zodiacal light (in the R magnitude system) is

$$p_R(ZL) = \frac{p_R(O)n_R(O)}{n_R(ZL)}$$

OBSERVATIONAL RESULTS

The pattern of scans executed by the photometers is shown in figure 1. Since the observations were made over a wide range of ecliptic latitude and longitude, some of the results are presented in the coordinate system (ϵ, i) where ϵ is the elongation from the Sun and i , the angle at the Sun between the ecliptic and the great circle joining the Sun and the point, is termed the ecliptic inclination and has the same sign as β , the ecliptic latitude.

In figure 2 the surface brightness in the B magnitude system is shown for part of the fifth scan which was made close to the ecliptic at $i = -5^\circ$. Because of the proximity of the Milky Way, the values are uncertain in the range

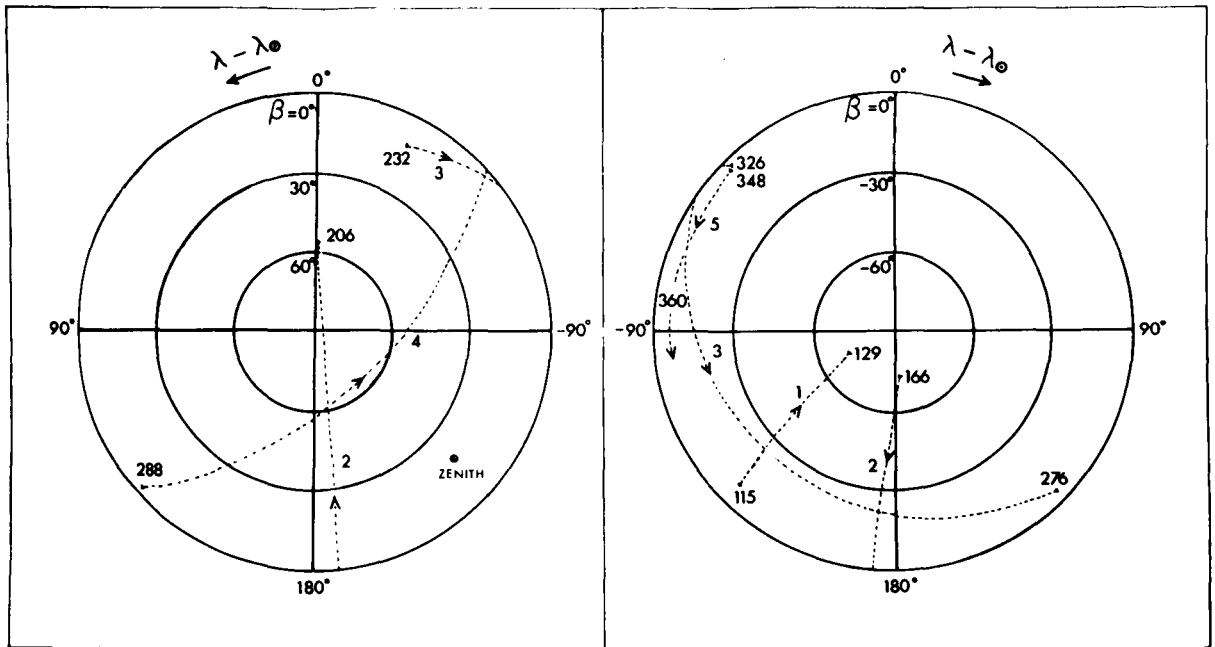


FIGURE 1.—Pattern of photometer scans in ecliptic coordinates. Left- and right-hand figures represent northern and southern ecliptic hemispheres, respectively. Time in seconds after launch is written at the beginning and end of each scan.

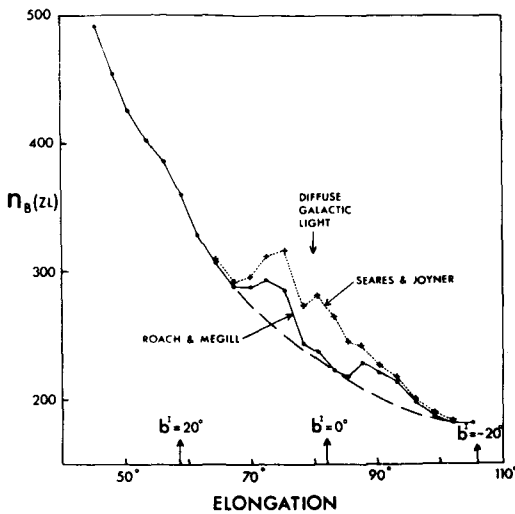


FIGURE 2. — Surface brightness in the B magnitude system for part of the fifth scan.

$70^\circ \leq \epsilon \leq 95^\circ$: interpolated values are indicated by a dashed line in figure 2. Our values are compared with those obtained by Smith, Roach, and Owen (1965) in the V magnitude system in table 1; their values were converted to units of brightness in the B-system by assuming identical colors for the Sun and the zodiacal light. It is difficult to make an exact comparison with the values of Smith et al. (1965) because the precise position of the axis of symmetry of the zodiacal light at the time of our observations is unknown; the values at $\beta = 0^\circ$ and 5° are given in table 1 to illustrate this uncertainty. At $\epsilon = 45^\circ$ the two determinations show approximate agreement. However, as ϵ increases, our values become greater and at $\epsilon = 80^\circ$ they are about 25 percent greater. There are two possible interpretations of this difference. One is that there are systematic errors in one or both investigations; the other is that the zodiacal light and Sun do not have identical colors everywhere. The ratio of the brightness in R and B (the color ratio, $T(ZL)$) is shown in the table and indicates that the zodiacal light becomes bluer with increasing elongation. The errors in T arising from the uncertainty in the correction for galactic radiation are also given; the total errors are greater. The dependence of the color ratio on elongation for all the flight data is illustrated in figure 3. The total standard error in T varies from about 0.3 for the observa-

tions at $b' > 30^\circ$ to about twice that for the low-latitude points. However, the error, which arises principally from the absolute calibration errors of the two photometers, is mostly systematic so that the entire curve may be moved either up or down by ΔT . We conclude that the zodiacal light at $\epsilon > \sim 100^\circ$ is bluer than at $\epsilon < 70^\circ$. The elongation at which the colors of the zodiacal light and Sun become identical is rather uncertain, but is very probably at $\epsilon < 70^\circ$.

TABLE 1. — Surface Brightness of Zodiacal Light Close to Ecliptic

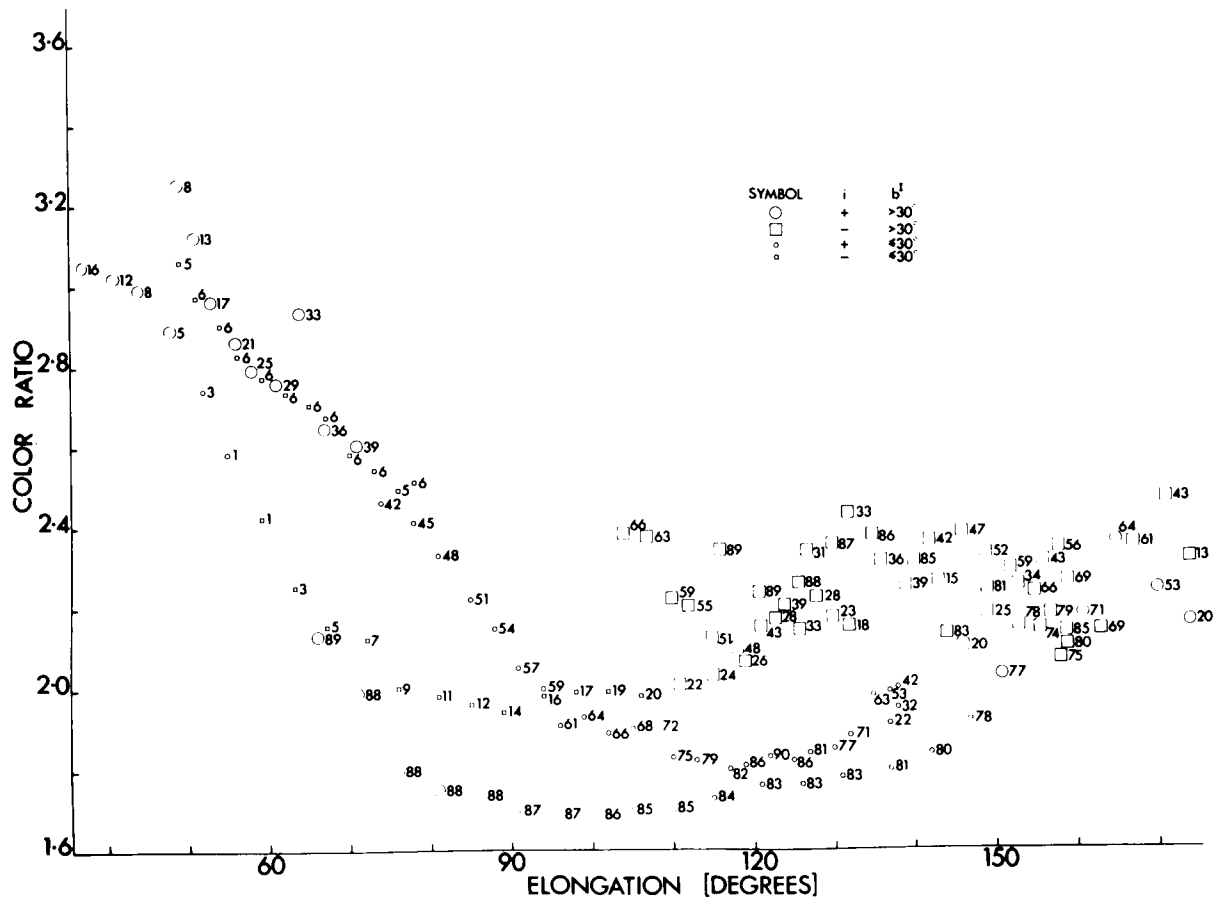
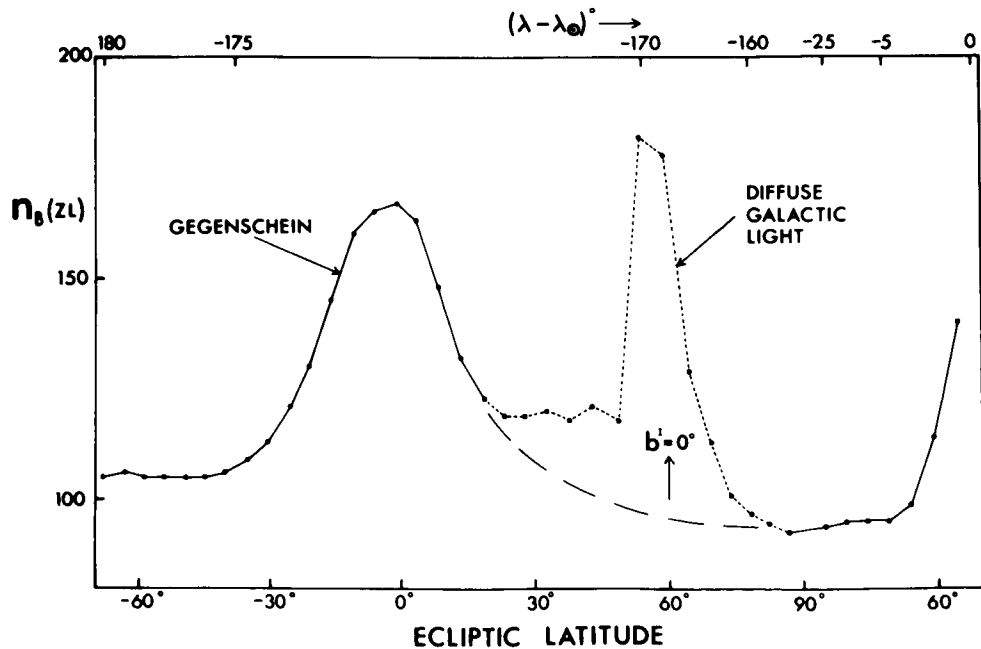
ϵ , deg	Present work			Smith, Roach, and Owen ^(a)	
	$n_R(ZL)$	$n_B(ZL)$	$T(ZL)$ (^b)	$n_B(ZL)$ $\beta = 0^\circ$	$n_B(ZL)$ $\beta = 5^\circ$
45	496 ± 0	534	415
50	1304 ± 0	436 ± 0	2.99 ± 0.00	421	345
55	1120 39	386 10	2.91 0.18	339	285
60	939 29	340 12	2.77 0.18	283	240
65	786 22	295 10	2.71 0.17	240	209
70	688 28	264 10	2.62 0.20	209	189
75	591 33	234 10	2.54 0.25	181	169
80	513 ± 32	203 ± 10	2.54 ± 0.28	164	155

^a Deduced from $n_V(ZL)$ assuming $B - V = 0.62 =$ Solar color index.

^b For Sun, $T(ZL) = \frac{n_R(ZL)}{n_B(ZL)} = 2.89$.

The difference in color between the two regions near the ecliptic poles with $80^\circ \leq i \leq 90^\circ$ and $-80^\circ \geq i \geq -90^\circ$ appears to be real; for example, at $\epsilon = 120^\circ$, $T = 2.3$ in the southern region and 1.8 in the northern region. This excess blueness near the north ecliptic pole may be related to the observed difference in the brightness of these two regions, as discussed subsequently.

Our measurements of the surface brightness at the north ecliptic pole are compared with previous results in table 2. Our best value expressed in the V-system is 143 ± 20 . The surface brightness along the second rocket scan, which passed within 3° of the north ecliptic pole and

FIGURE 3.—Dependence of color ratio $T(ZL)$ on elongation.FIGURE 4.—Surface brightness, $n_b(ZL)$ along second rocket scan which crosses ecliptic at $\lambda - \lambda_{\odot} = -174^\circ$.

20° of the south ecliptic pole, is illustrated in figure 4. This figure shows two interesting features. First, the extrapolated brightness at the south pole exceeds that at the north pole by about 15 percent. Although the north ecliptic pole is at $b' \approx 30^\circ$, the probable error of the integrated starlight correction $\approx \pm 2$ is too small to produce this effect. Second, the symmetry axis of the gegenschein brightness profile lies 3° south of the ecliptic. Similar results were obtained from the R-measurements. The detailed interpretation of these observations is presented in Wolstencroft (1967), where it is pointed out that the observations were made at a time when the Earth was close to its maximum distance above (i.e., north of) the invariable plane of the solar system. If the plane of symmetry of the zodiacal cloud near and beyond the Earth's orbit coincides with the invariable plane, then these observations have a simple interpretation.

TABLE 2. —Surface Brightness of Zodiacal Light at North Ecliptic Pole

Investigator	Year	Brightness			Approximate magnitude system of observation
		B	V	R	
Elvey and Roach	1937	41	^a 73	B
Weinberg ^b	1963	^a 104	186	^a 302	V
Beggs et al. ^c	1964	^a 99	177	^a 288	V
Smith et al. ^c	1965	^a 62	110	^a 179	V
Dumont.....	1965	^a 39	70	^a 114	V
Wolstencroft and Rose.....	1967	92	^a 163	B
Wolstencroft and Rose.....	1967	^a 123	200	R
Average.....		73	129	217	

^a Deduced by assuming solar color index.

^b Taken from table 7 of Weinberg (1963).

^c Calculated by assuming $p(ZL) = 22$ percent at pole.

As a measure of the concentration of the zodiacal light toward its plane of symmetry, Smith, Roach, and Owen (1965) have used the quantity $P(\epsilon)$ shown in figure 5; $P(\epsilon)$ is the ratio of the brightness at elongation ϵ in the ecliptic to that normal to the ecliptic ($i = 90^\circ$). The ratio

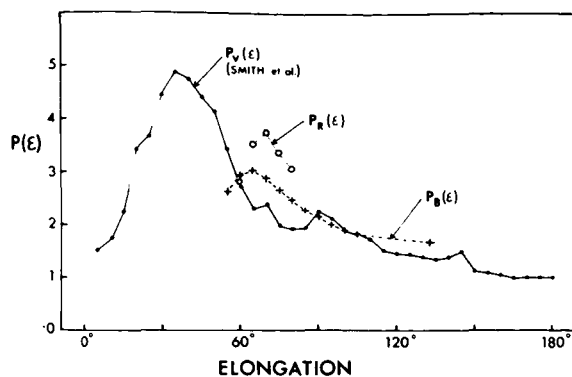


FIGURE 5. —Ratio $P(\epsilon)$ of brightness at elongation ϵ in ecliptic to that normal to ecliptic ($i = 90^\circ$).

in the B- and R-systems obtained by us is shown together with the ratio in V found by Smith et al. (1965). The B- and V-curves show approximate numerical agreement but differ in one important respect: the B-observations do not show the dip between $\epsilon = 50^\circ$ and 90° that is present in V. Smith et al. attribute this dip to the presence of a photometric perturbation of the zodiacal light centered at $\beta = 55^\circ$, $\lambda - \lambda_\odot = 45^\circ$ which leads to some irregularity in the brightness curve normal to the ecliptic. We conclude that this feature was either less extensive or absent at the time of our observations.

Our measurements of the linear polarization of the zodiacal light in the R magnitude system are summarized in figure 6. The number beside each point is the ecliptic inclination, i . The standard error of any point depends on the surface brightness and degree of polarization but is typically about 1 percent polarization. The maximum degree of polarization of 20 percent occurs at about $\epsilon = 75^\circ$. The most important feature of figure 6 is the crossover from positive to negative polarization which occurs at $\epsilon = 165^\circ$. In the case of negative polarization, the polarization plane is parallel to the plane of scattering.

The brightness and polarization measurements have been compared with a number of model calculations for the zodiacal light in the ecliptic carried out by Little, O'Mara, and Aller (1965), Giese (1961, 1963), and Giese and Siedentopf (1962). None of the pure models of Fe, SiO₂, or H₂O show agreement with observation: Fe produces no negative polarization and no gegenschein; SiO₂ produces a polarization maxi-

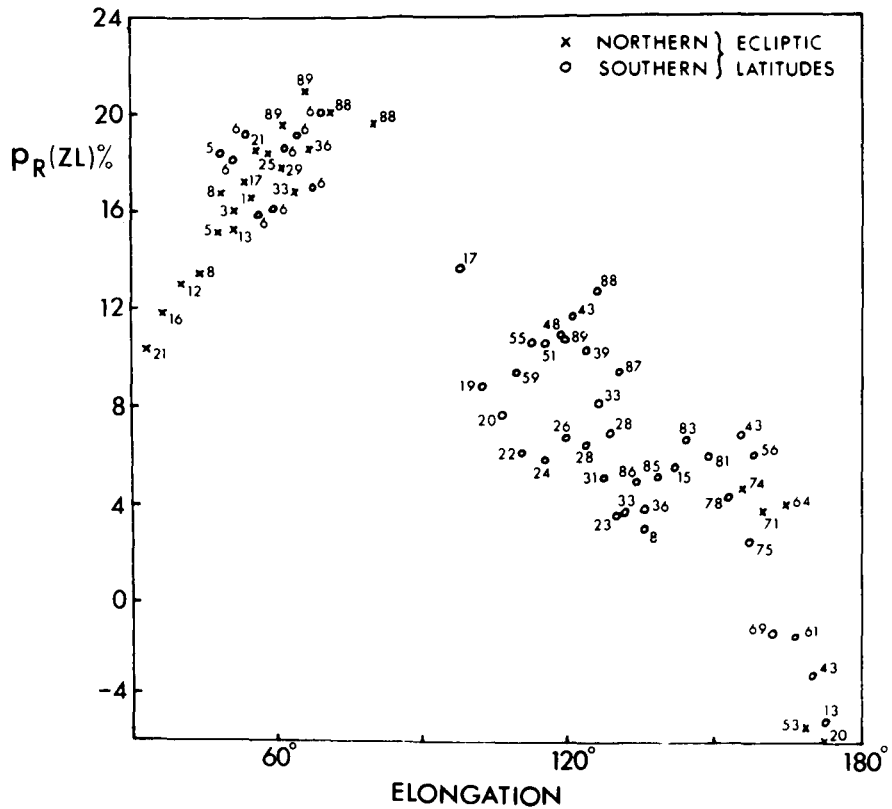


FIGURE 6. — Degree of polarization of zodiacal light at 7000\AA as a function of elongation.

mum at $\epsilon = 155^\circ$: H_2O produces negligible gegenschein. Three models containing combinations of these materials were found to give approximate agreement with observation; they are described in table 3. It is possible to show that ice particles smaller than 100μ are unlikely to exist within 7 AU of the Sun because the time scale for evaporation is very short (Wolstencroft

and Rose, 1967). Thus, model B which comprises a mixture of 85 percent iron particles and 15 percent silicon dioxide particles is the most acceptable of these models. However, it is still imperfect as may be seen from figure 7. Although the agreement is remarkably good at elongations greater than about 100° , this is not so in the region from 35° to 75° elongation.

TABLE 3. — Models of Zodiacal Cloud

Model	$\alpha = \frac{2\pi a}{\lambda}$	Fe	SiO_2	H_2O	Geocentric contribution	Reference
A	$1 \leq \alpha \leq 26$	None	3% olivine; a^{-3} , r^0 or r^{-1}	97%; a^{-4} , r^0 or r^{-1}	None	Little et al. (1965)
B	$4 \leq \alpha \leq 40$	85%; a^{-3+} , r^0	15%; a^{-3} , r^0	None	None	Giese (1961)
C	$1 \leq \alpha \leq 24$	23%; a^{-4} , $r^{-1/2}$	None	77%; a^{-4} , $r^{-1/2}$?% SiO_2 ; a^{-3}	Giese (1963)

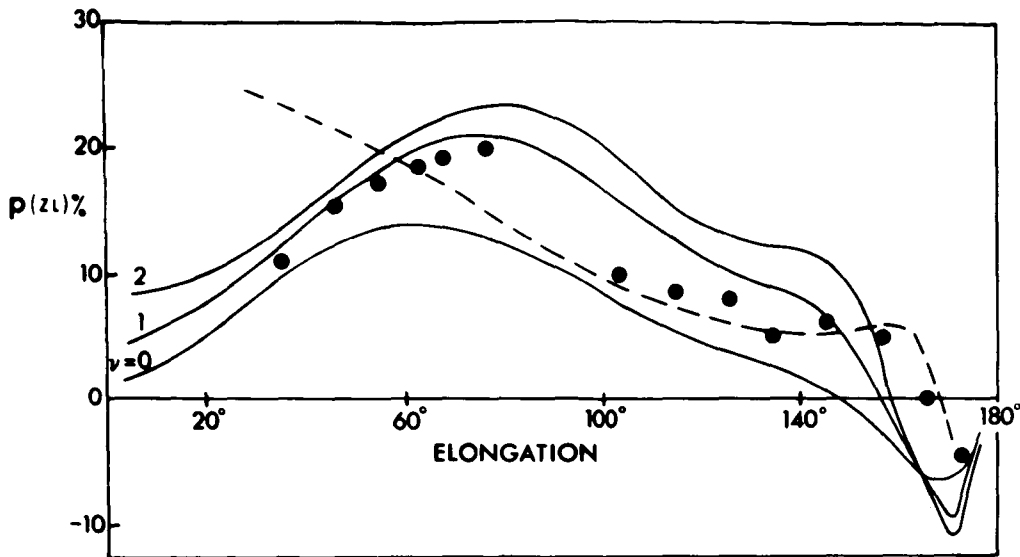


FIGURE 7.—Comparison of observed dependence of degree of polarization on elongation with that calculated by Little et al. (1965) (model A) and by Giese and Siedentopf (1962) (model B). Observed curve is indicated by dots, model A by solid lines, and model B by dashed lines.

Nevertheless, since the polarization at $\epsilon > 120^\circ$ is determined almost entirely by the SiO_2 particles and at $\epsilon < 70^\circ$ by the Fe particles, a model containing a greater proportion of smaller iron particles should perhaps be considered. For particles with $2\pi a/\lambda = 1$, i.e., $a = 0.1\mu$, the polarization of the iron component would be greatest at a scattering angle of 90° so that a polarization maximum at $\epsilon = 75^\circ$ could possibly be produced.

The degree of ellipticity, e , which is the ratio of the Stokes parameters V and I , was measured with the R-polarimeter and the results are shown in figure 8. Both the degree of ellipticity and its modulus are plotted. The height of each rectangle is the average value of e obtained from the number of observations shown in the rectangle. The mean value over the sky is $\bar{e} = -0.9$ percent and the total range of values is from -5.5 to 4.5 percent. The average probable error of a single determination is about 1 percent polarization. Appreciable circular polarization was found in only one region of the sky, at $40^\circ \leq \epsilon \leq 65^\circ$, where e was systematically negative with a mean value of -2.9 percent. It seems likely that this observed circular polarization should be attributed to the zodiacal light since the zodiacal light is the principal contributor to the night-

sky brightness in this region of the sky. To interpret this observation we must answer the question: Can the light scattered by a cloud of particles be partially elliptically polarized if the incident light is unpolarized? The short answer is yes, in principle. According to Perrin (1942) and van de Hulst (1957), a cloud of odd particles (all shapes and sizes) not randomly oriented can produce any combination of linear and circular birefringence and dichroism. However, in prac-

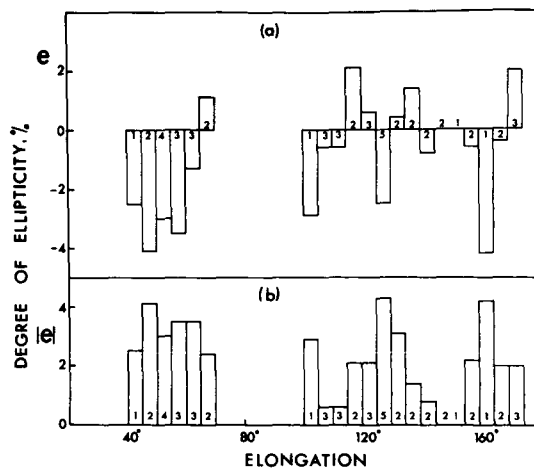


FIGURE 8.—Dependence of degree of ellipticity and its modulus on elongation (at 7000\AA).

tice, the magnitude of the ellipticity should be very small (Velluz, Legrand, and Grosjean, 1965) for most likely inorganic materials except crystalline quartz. Spherical particles can produce no effects of either circular birefringence or dichroism. If we are correct in attributing the observed ellipticity to the zodiacal light, then we must conclude that some of the interplanetary dust particles are asymmetric in either shape or composition. Van de Hulst (1957) has discussed some simplifications of the scattering matrix of a cloud of particles that follow when certain

assumptions about the orientation and distribution of the particles are made. One simple model, discussed by van de Hulst, which may be successful in describing the scattering of sunlight by the interplanetary dust cloud is a cloud of randomly oriented asymmetric particles that are optically active. In this connection it should be noted that crystalline SiO_2 is optically active but the fused variety is not.

A more detailed description of the present investigation is presented in Wolstencroft and Rose (1967).

REFERENCES

- BEGGS, D. W., D. E. BLACKWELL, D. W. DEWHIRST, and R. D. WOLSTENCROFT, 1964, *Mon. Not. Roy. Astron. Soc.*, **128**, 419.
- DUMONT, R., 1965, *Ann. d'Astrophys.*, **28**, 265.
- ELVEY, C. T., and F. E. ROACH, 1937, *Astrophys. J.*, **85**, 213.
- GIESE, R. H., 1961, *Zeits. f. Astrophys.*, **51**, 119.
- , 1963, *Space Science Reviews*, **1**, 589.
- GIESE, R. H., and H. SIEDENTOPF, 1962, *Zeits. f. Astrophys.*, **54**, 200.
- JOHNSON, H. L., and R. I. MITCHELL, 1962, *Commun. Lunar and Planetary Lab.*, Univ. of Arizona, **1**, 73.
- LITTLE, S. J., B. J. O'MARA, and L. H. ALLER, 1965, *Astron. J.*, **70**, 346.
- PERRIN, F., 1942, *J. Chemical Phys.*, **10**, 415.
- ROACH, F. E., and L. R. MEGILL, 1961, *Astrophys. J.*, **133**, 228.
- SEARES, F. H., and M. C. JOYNER, 1928, *Astrophys. J.*, **67**, 24.
- SMITH, L. L., F. E. ROACH, and R. W. OWEN, 1965, *Planetary Space Sci.*, **13**, 207.
- VAN DE HULST, H. C., 1957, *Light Scattering by Small Particles* (New York: John Wiley & Sons, Inc.), ch. 5.
- VELLIZ, L., M. LEGRAND, and M. GROSJEAN, 1965, *Optical Circular Dichroism* (New York: Academic Press; Berlin: Verlag Chemie).
- WEINBERG, J. L., 1963, Ph.D. thesis, Univ. of Colorado.
- WOLSTENCROFT, R. D., 1967, *Planetary Space Sci.*, **15**, 1081.
- WOLSTENCROFT, R. D., and L. J. ROSE, 1967, *Astrophys. J.*, **147**, 271.

10. A Five-Color Photometry and Polarimetry of the Zodiacal Light: A Preliminary Report*

R. D. WOLSTENCROFT
Columbia University
New York, New York

AND

J. C. BRANDT
Goddard Institute for Space Studies, NASA
New York, New York

Simultaneous observations in five colors of the brightness and state of polarization of the night-sky radiation were secured from Mount Chacaltaya, Bolivia, during July and August 1964. The spectral range was from 3650Å to 9515Å. The results of a preliminary analysis of part of these data are presented: a description of the wavelength dependence of the zodiacal-light brightness and polarization, possible complicating emissions from the atmosphere, and some remarks concerning circular polarization of the radiation scattered by dust.

IN ORDER TO DEDUCE the spatial distribution and physical characteristics of the dust particles in interplanetary space solely from the observed properties of the zodiacal light, it is necessary to compare these properties with those calculated for a very large number of models of the interplanetary dust cloud. The properties of the zodiacal light that have been most thoroughly studied, both from the observational and theoretical standpoint, are the distributions along the ecliptic of the surface brightness and the degree of polarization. For realistic models composed of mixtures of particles of different parameters, the total number of possible models is immense.

At present, the difficulty of this problem of determining a "unique" model of the dust cloud is increased by the marked uncertainty in the observed properties of the zodiacal light. Fortunately, we have reason to expect that the precision of the observations will improve in the

future as observations from above the Earth's atmosphere increase and that this will help to reduce the number of models showing partial agreement with observation. Another approach that promises to reduce the number of contending models is that in which the widest categories of observation other than those mentioned above are also employed. One particularly hopeful line of investigation is that of the wavelength dependence of the surface brightness, state of polarization of the zodiacal light, and other quantities derivable from the Stokes parameters. In the present paper, we report observations of this type carried out at five wavelengths in the range from 0.36μ to 0.95μ .

THE POLARIMETERS

The distribution over the sky of the Stokes parameters (I_0 , Q_0 , and U_0) of the night-sky radiation was obtained by using an almucantar instrument (shown in fig. 1), which consists of a brace of five parallel polarimeters (numbered 1 to 5). The effective wavelengths of the observations made with the five polarimeters are listed in table 1.

*Research reported in this paper was supported by National Aeronautics and Space Administration under Grant NGR 33-008-053. This paper is contribution No. 301 from the Kitt Peak National Observatory.

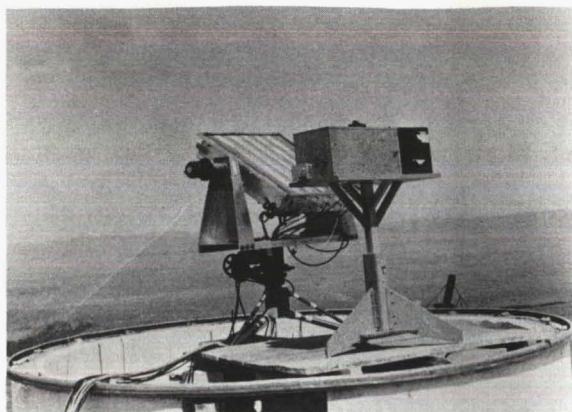


FIGURE 1.—Almucentar instrument.

With minor exceptions, the optical arrangement of each polarimeter was identical. The layout of polarimeter 1 was as follows: A retardation plate, with quarter-wave retardance close to the effective wavelength of the polarimeter of 3650 Å (determined principally by an interference filter of 116 Å equivalent width), was rotated at 15 rps in front of an HNP'B polaroid placed close to the focal plane of the $f/4$ objective (fused quartz) of 10-cm diameter. The light from an area of sky of 5.13° diameter isolated by the field stop in the focal plane was imaged by a Fabry lens of fused quartz onto the photocathode of an EMI 6256S photomultiplier. The interference filter was placed between the Fabry lens and the photocathode. The important features of the five relevant polarimeters are summarized in table 1.

The relation between the Stokes parameters (I_o , Q_o , U_o , and V_o) of the night-sky radiation and

the time dependence of the output voltage, $E(t)$, from the photomultiplier is (see Sekera, 1956):

$$E(t) = K \left[I_o + \left(\frac{1-\eta}{2} \right) Q_o + \left(\frac{1+\eta}{2} \right) (Q_o^2 + U_o^2)^{1/2} \cos(4\omega t - 2\chi) + V_o \sin 2\omega t \right] \quad (1)$$

where $\omega = 15$ rps.

The retardance of the rotating quarter-wave plate, $90^\circ + \eta^\circ$ was in all cases close to 90° so that $\sin \eta \approx \eta$. The Stokes parameters appearing in equation (1) are defined with respect to the instrumental system; K is a brightness-calibration constant and χ is the angle between the polarization plane of the incident light and the transmission axis of the polaroid.

Other useful quantities can be calculated from the Stokes parameters such as the degree of linear polarization and the orientation of the observed plane of polarization; these are, respectively,

$$p_o = \frac{(Q_o^2 + U_o^2)^{1/2}}{I_o} \quad (2)$$

and

$$\chi_o = \frac{1}{2} \arctan (U_o/Q_o) \quad (3)$$

A useful description of the Stokes parameters and related quantities has been given by van de Hulst (1957).

TABLE 1.—Characteristics of Individual Polarimeters

Polarimeter	Effective wavelength, λ_{eff} , Å	$1/\lambda_{\text{eff}}$	Whole half-width of interference filter, Å	Angular diameter of field, deg	Type of photomultiplier	Type of polaroid
1	3650	2.740	116	5.13	EMI 6256S	HNP'B
2	4510	2.217	166	5.05	EMI 9502B	HN22
3	5303	1.885	128	5.14	EMI 9502B	HN32
4	7073	1.414	316	5.20	EMI 9558B	HN22
5	9515	1.051	404	[5.13]	RCA 7102	HR

THE OBSERVATIONS

The observations were made from a subsidiary peak of Mount Chacaltaya, Bolivia, at an altitude of 17 630 feet on 7 nights during July and August 1964; the advantages of this site for zodiacal-light photometry are described by Blackwell and Ingham (1961).

In this paper we describe the results obtained from a preliminary analysis of the data acquired on one scan taken on August 2, 1964, with the azimuth scanner which carried polarimeters 1 to 5; the altitude of the scan was 10° . The scan was completed in 2 minutes. At the time of the observations, the solar zenith distance was $118^\circ 57'$ and the inclination of the ecliptic to the horizon was $85^\circ 3'$.

REDUCTION OF OBSERVATIONS

Night-Sky Radiation

A brief description is given below of the method used to convert the amplified photomultiplier signals from the polarimeter into the Stokes parameters of the incident light.

Phase-sensitive detection of the signal provided five quantities: the mean dc level and the amplitude and phase of the components in the signal voltage that varied at frequencies of 2ω and 4ω . These five quantities could be related to the Stokes parameters of the observed radiation expressed in arbitrary units apart from a polarization-calibration constant k ; k was determined by making observations of a diffuse-source radiating light of known Q/I and U/I , which comprised a diffuse-light source incorporating a tilting-plate calibrator.

In order to express the data from photometers 1 to 5 in units of the standard magnitude systems U , B , V , R , and I , respectively, of Johnson and Mitchell (1962), the values of the deflection, D , of bright identified stars of known magnitude and color were used to solve for the optical depth, τ , and calibration constants, b and c , appearing in calibration equations of the following form:

$$\begin{aligned} 0.4U &= -0.434 \tau_1 m(z) + c_1 - 0.4b_1(U - B) - \log_{10} D_1 \\ 0.4B &= -0.434 \tau_2 m(z) + c_2 - 0.4b_2(U - B) - \log_{10} D_2 \end{aligned} \quad (4)$$

The subscripts 1 and 2 refer to the data obtained with photometers 1 and 2, respectively; $m(z)$ is

the air mass at zenith distance z . From the values of D at some point in the sky measured by photometers 1 and 2, equations (4) were used to derive U and B for the night-sky radiation. Values for I_0 , Q_0 , and U_0 could then be found from U , B , and k in units of the equivalent number of stars of magnitude U (or B) = 10.0 per square degree. Note that the procedure described leads to two separate reductions for the B-, V-, and R-photometers, a fact which provides a useful check on the quality of the results.

The Zodiacal Light

In figures 2 to 5, observational results are presented in their "observed" form, i.e., without any attempt to separate the various contaminants from the desired zodiacal light. However, in figures 6 and 7 we present intensities of the zodiacal light alone, and we describe here the procedure used in the separation.

The integrated starlight was computed for reasonable assumptions concerning the color of this radiation from the tables of Roach and Megill (1961), but only for galactic latitudes $b' \geq 30^\circ$; hence, the Milky Way is still visible in the scan as a region rising above the relatively small integrated starlight correction which is applicable to the region of the zodiacal light.

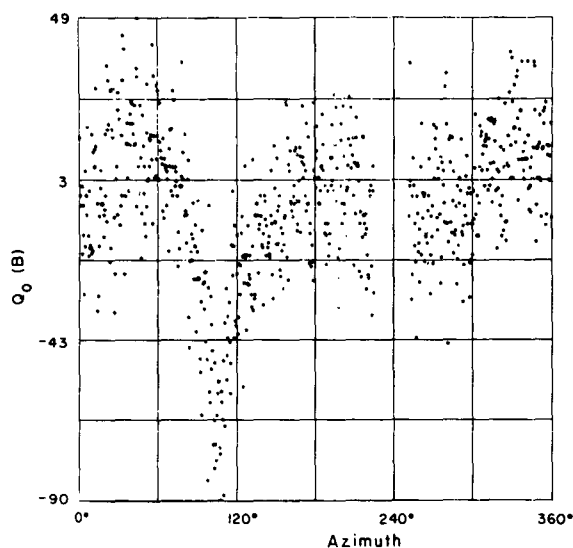


FIGURE 2.—Sample of unsmoothed Q_0 , given here for B-observations.

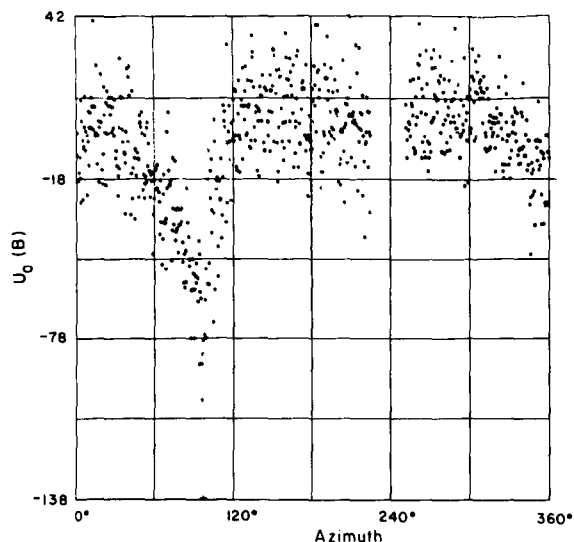


FIGURE 3.—Sample of unsmoothed U_0 , given here for B-observations.

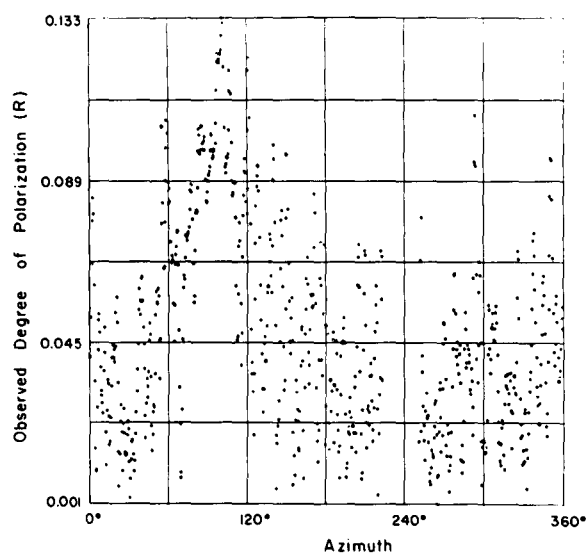


FIGURE 4.—Sample of smoothed, observed degree of polarization (p_0) for R-photometer (determined from smoothed values of I_0 , Q_0 , and U_0) clearly showing the peak in p_0 at position of zodiacal light.

The mean estimate of the light scattered in the atmosphere was based on the calculations of Ashburn (1954), Fesenkov (1964), and Wolstencroft and van Breda (1967).

The airglow was removed by utilizing the rocket observations of Wolstencroft and Rose (1967) and in paper No. 9. The intersections of the

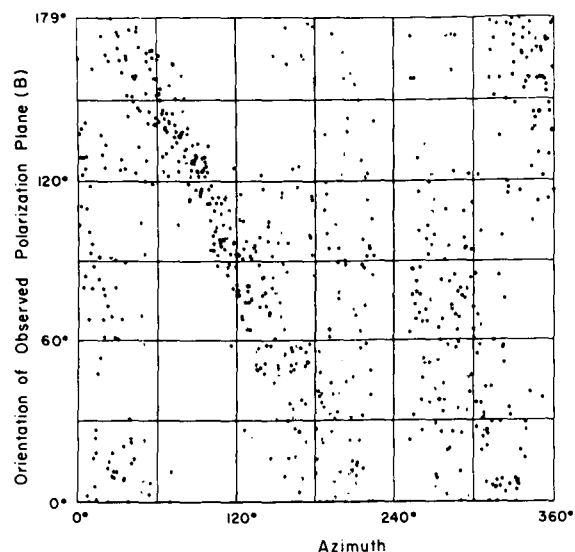


FIGURE 5.—Change (unsmoothed) of orientation of observed plane of polarization, χ_0 , with azimuth for B-photometer; the linear variation expected for plane of polarization of zodiacal light is clearly shown between 60° and 120° azimuth.

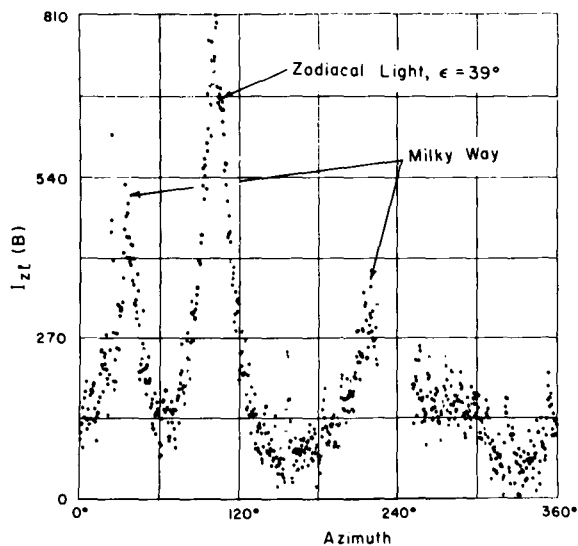


FIGURE 6.—Observed brightness (S_{10}) of zodiacal light in B. Data are unsmoothed. The rest position of photometer is at azimuth 240° (measured west from south) and suppression of data near starting and stopping points results in the gap visible at this position in figs. 2 to 7. Range of azimuth covered is 335°.

Chacaltaya observations and the rocket scans allowed a determination of the airglow correction at typically 6 or 7 points in B and R . Since the

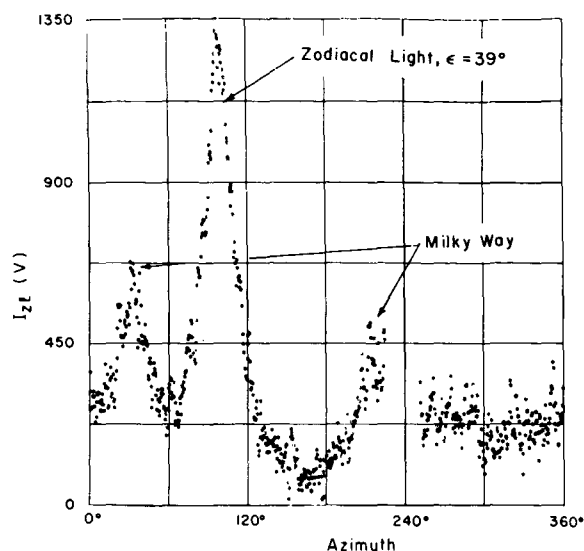


FIGURE 7. — Observed, unsmoothed brightness (S_{10}) of zodiacal light in V .

rocket observations were made in B and R , only those regions where the rocket observations showed the color of the zodiacal light to be approximately the same as that of the Sun could be used to determine the airglow correction in U , V , and I : typically there were 2 or 3 such points on each scan. The airglow correction was reasonably constant and a mean correction was applied to the scans.

The total contribution of the contaminants in figures 6 and 7 amount to 63 percent and 32 percent, respectively, of the maximum brightness of the zodiacal light. The use of observations from above the atmosphere has doubtless increased the accuracy of these corrections.

OBSERVATIONAL RESULTS

Anomalous Twilight Brightness

Removal of radiation of atmospheric origin can be a serious problem at small solar elongations. Usually, such emissions arise by fluorescence, but the enhanced radiation found in the spectral ranges from 6800\AA to 7400\AA and from 9100\AA to $10\,000\text{\AA}$ exhibits a somewhat different character (Wolstencroft, Brandt, and Rose, 1966). The most likely candidates for the two wavelength regions are emission from the (8, 3) and (8, 4) bands of OH.

The post-twilight enhancement found is about a factor of 6 or greater and the elimination of this radiation is clearly necessary to zodiacal-light studies at these wavelengths for small solar elongations; spectral identification and a judicious choice of filter may allow its removal. The atmospheric origin is probably photochemical (since fluorescence of solar radiation in the Meinel bands is thought to be negligible) as noted by Chamberlain (1961); his remarks were made in connection with the report by Sholokhova and Frish (1955) of twilight emission near 1μ .

Possible Circular Polarization

A rough inspection of the data indicates that some sky areas have a degree of ellipticity V/I for the combined radiation of about 0.02 which, at present, is strictly only an upper limit; taking account of the dilution could raise this figure to about 0.04. If this value stands up through the detailed analysis, it will require explanation in terms of scattering from specific types of optically asymmetric dust particles (van de Hulst, 1957). (See the discussion in paper No. 9 by Wolstencroft and Rose.)

Brightness and Polarization of the Zodiacal Light

The surface brightness of the zodiacal light (with contaminants removed as described previously) in B and V is shown in figures 6 and 7; figures 2 to 5 show selected values of Q_o , U_o , p_o , and χ_o for the B - and R -photometers. We note again that the observations refer to an almucantar scan taken at an altitude of 10° .

The results for the zodiacal light at $\epsilon = 39^\circ$ and $\beta = 0^\circ$ are summarized in table 2; the uncertainties in the degree of polarization result primarily from lack of knowledge concerning the degree of polarization of the scattered light. For comparison, Smith, Roach, and Owen (1965) find $S_{10}(V) = 1265$, and Weinberg (1964) gives $p(5300\text{\AA}) = 16.9\%$ for the same ecliptic position; the agreement is entirely satisfactory.

The color inferred from these brightness observations is close to the value currently accepted for the Sun (see table 3). If a blackbody extrapolation is assumed at the solar temperature, we would expect little conspicuous zodiacal light relative to the background in U and I at $\epsilon = 39^\circ$;

TABLE 2.—*Zodiacal light at $\epsilon = 39^\circ$, $\beta = 0^\circ$*

Color	Surface brightness, S_{10}	Degree of polarization, p , percent
B.....	770	21.9 ± 2.8
V.....	1320	18.3 ± 1.8
R.....	2110	20.5 ± 1.3

this is observed. The observations made at smaller solar elongations show an identifiable contribution from the zodiacal light at these wavelengths.

TABLE 3.—*Comparison of Color Inferred for Sun and Zodiacal Light*

Color	Zodiacal light at $\epsilon = 39^\circ$	Sun
B-V.....	0.59	0.62
V-R.....	0.50	0.53

ACKNOWLEDGMENT

This work was begun while both authors were staff members of the Space Division, Kitt Peak National Observatory. We are indebted to Dr. J. W. Chamberlain for his support of this expedition and related projects.

REFERENCES

- ASHBURN, E. V., 1954, *J. Atmospheric and Terrest. Phys.*, **5**, 83.
 BLACKWELL, D. E., and M. F. INGHAM, 1961, *Mon. Not. Roy. Astron. Soc.*, **122**, 113.
 CHAMBERLAIN, J. W., 1961, *Physics of the Aurora and Airglow* (New York: Academic Press), 377.
 FESENKOV, V. G., 1964, *Soviet Astron.—AJ*, **7**, 670.
 JOHNSON, H. L., and R. I. MITCHELL, 1962, *Commun. Lunar and Planetary Lab.*, Univ. of Arizona, **1**, 73.
 ROACH, F. E., and L. R. MEGILL, 1961, *Astrophys. J.*, **133**, 228.
 SEKERA, Z., 1956, in *Advances in Geophysics*, Vol. 3 (H. E. Landsberg, ed.), New York: Academic Press, 43.
 SHOLOKHOVA, YE. E., and M. S. FRISH, 1955, *Doklady Akad. Nauk SSSR*, **105**, 1218.
 SMITH, L. L., F. E. ROACH, and R. W. OWEN, 1965, *Planetary Space Sci.*, **13**, 207.
 VAN DE HULST, H. C., 1957, *Light Scattering by Small Particles* (New York: John Wiley & Sons, Inc.), ch. 5.
 WEINBERG, J. L., 1964, *Ann. d'Astrophys.*, **27**, 718.
 WOLSTENCROFT, R. D., and L. J. ROSE, 1967, *Astrophys. J.*, **147**, 271.
 WOLSTENCROFT, R. D., and I. G. VAN BREDÁ, 1967, *Astrophys. J.*, **147**, 255.
 WOLSTENCROFT, R. D., J. C. BRANDT, and L. J. ROSE, 1966, *Planetary Space Sci.*, **14**, 445.

11. Photometry of Zodiacal Light and Atmospheric Continuum by H-M Method and Barbier Correlations, and Tenerife Results About the Shape of the Zodiacal Cloud

RENE DUMONT
*Observatoire de Bordeaux
33-Floirac, France*

OBSERVATIONS OF ZODIACAL LIGHT, gegenschein, and airglow continuum made on Tenerife Island since January 1964 are discussed along with reduction of the data which was done by a previously described method (Dumont, 1965a). Separation of airglow, interplanetary, and stellar components of the night sky is obtained according to "Hauteurs Multiples" or "H-M" observations. This method involves choosing any fixed direction among the stars and recording its total brightness in the course of its diurnal motion by using the largest possible variation of zenith distance (generally from the zenithal region to 10° elevation), as in Bouguer's method.

From these brightness values can be computed:

(a) The extraterrestrial brightness, L , at the observed point M . (Zodiacal light + stars, but stars which can be seen in the telescope are excluded from its field—0.02 square degree—and lower a great deal the integrated starlight correction, which is obtained from Megill and Roach, 1961.)

(b) The true airglow continuum brightness, Λ , without any effect of obliquity or atmospheric scattering.

METHOD

A wavelength near 5000Å was chosen for the interference filter (halfwidth, 240Å), giving, in terrestrial light, only continuum. Other wavelengths can still be used.

In order to simplify the present explanation, absorption and scattering in the ozone layer and in the low atmosphere are disregarded. If the airglow layer were uniform and constant, the deflection would be

$$I = L + \Lambda \sec \theta$$

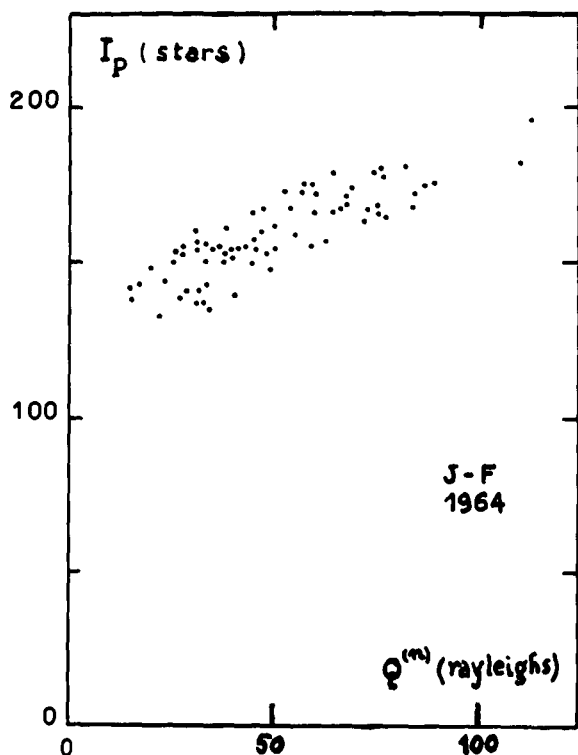
where θ is the obliquity of the incident beam through the emitting layer (θ is a known function of the zenith distance, z). A graphical solution of the sequence of observations would be

$$\begin{aligned} x &= \cos \theta \\ y &= I \cos \theta \end{aligned}$$

Indeed, $y = Lx + \Lambda$.

A survey of the pole (where extraterrestrial light is unknown but unchanging in one night) often shows rather quick and large variations. A correlation between the polar value of the deflection, I_p , and the polar value of the green-line brightness, $Q^{(n)}$, was found by Barbier (1956) (for $\lambda = 5260\text{Å}$, but at 5000Å, the same correlation exists and was shown by both our Haute Provence and our Tenerife results). That correlation suffers a rather large dispersion (fig. 1), but using it is unquestionably better than assuming an unvariable amount of airglow component.

Going on with our ozoneless and scatteringless scheme, let $Q^{(n)} = Q \cos \theta$ be the true brightness

FIGURE 1.—Correlation between I_p and $Q^{(n)}$.

of [OI]5577, and Q be the observed brightness (with a filter of 15\AA halfwidth, which, of course, admits some continuum, which must be subtracted). We may write, for the pole:

$$I_p(Q^{(n)}) = L_p + \sec \theta_p \Lambda(Q^{(n)})$$

where I_p is the 5000\AA polar deflection, and Λ is the (unknown) true brightness of airglow continuum when the true polar brightness of 5577\AA is $Q^{(n)}$; L_p is the (unknown) value of extraterrestrial light at the pole. A similar equation may be written for each observation of the point M which we follow during the night

$$I(Q^{(n)}) = L + \sec \theta \Lambda(Q^{(n)})$$

and a graphical solution would be

$$\begin{aligned} x &= \cos \theta \\ y &= I \cos \theta - I_p(Q^{(n)}) \cos \theta_p \end{aligned}$$

with

$$y = Lx - L_p x_p$$

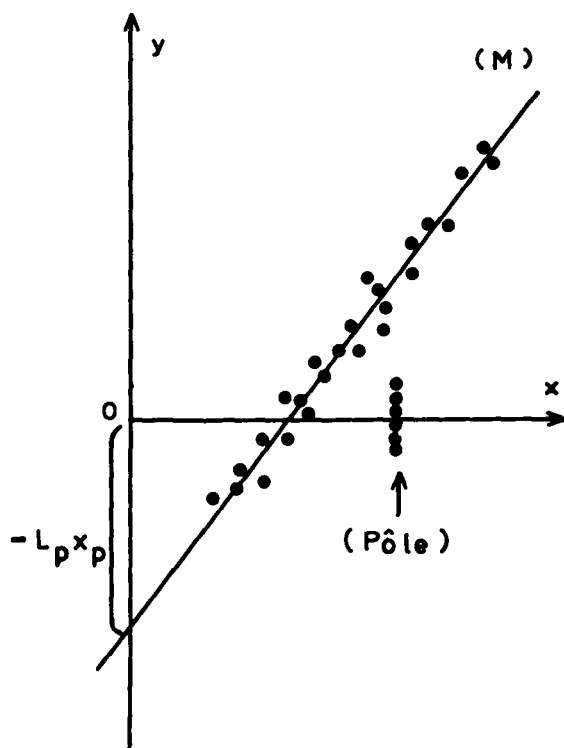


FIGURE 2.—Technique used to derive the extraterrestrial brightnesses (H-M method).

(See fig. 2.) The extraterrestrial brightness, L , of the point, M , and that of the pole, L_p , will therefore be known. From the latter, it is easy to obtain

$$\Lambda(Q^{(n)}) = \cos \theta_p [I_p(Q^{(n)}) - L_p]$$

i.e., to obtain the true brightness of airglow continuum corresponding to the different values of green-line brightness.

Of course, the ozone layer and low atmosphere bring in other terms and make the formulae more complex, but without altering the principles. The effect of these terms (described in detail in Dumont, 1965b) consists mainly of adding to L a "scattered extraterrestrial term," L_p (a function of z , which can be computed), which is the brightness scattered by the particles in the line of sight, lighted by the extraterrestrial vault ($ZL + \text{stars}$), and introducing a similar term Λ_p to account for the light scattered along the beam, lighted by the airglow continuum vault.

Those terms are rather easy to compute and are practically functions of z only. (The influence of other theoretical parameters, like sidereal time,

is very weak.) As for atmospheric extinction, it is assumed that Rayleigh and ozone are, in high-altitude observatories, the only two significant terms concerning the sky background. Aerosols are neglected (except, of course, when observing Bouguer's stars for the absolute calibration) not only because of their moderate amount at high altitude but because their forward-shaped diffraction pattern indicates that the light lost by the incident beam will be almost exactly canceled by the light retrieved along the same beam, lighted by the neighboring celestial zones. A direct proof of the latter assumption can be found in the fact that polar deflection is quite uncorrelated with atmospheric extinction (also see paper No. 4 by Peterson). If fluctuations in the amount of aerosols would control background extinction, as it does for stellar extinction, polar brightnesses would obviously reflect that phenomenon, and they do not.

It should be emphasized that such a method allows separation of extraterrestrial light from airglow in any point of the sky, with no other main hypothesis but a constant value of extraterrestrial light at M during the night. It does not need any other postulate, such as: "Far from ecliptic, zodiacal light may be neglected" . . . or "it does not depend upon ecliptic longitude." Nor does it require any theoretical assumption about the amount of polarization, previous to measuring it, to obtain the separation of brightness components.

The importance of airglow variations must also be stressed. Sometimes they are weak enough to get fair results through a reduction in which a uniform layer is assumed. But often that is not true, since we have rather quick and large changes of the polar deflections at 5000Å and 5577Å. Figure 3, which is an example of that correlation, shows that the 5000Å and 5577Å brightnesses are not rigorously correlated but also that polar total 5000Å deflection has been, in the course of a single night (and it is not unusual), 177 and then 233. (The corresponding values found for Λ were 31 and 62, all in 10th visual G2V stars per square degree.)

Figure 4 shows the results of H-M observations for a point in the ecliptic and another at 45° ecliptic latitude, both 90° from the Sun in ecliptic longitude. At the left, the results reduced by

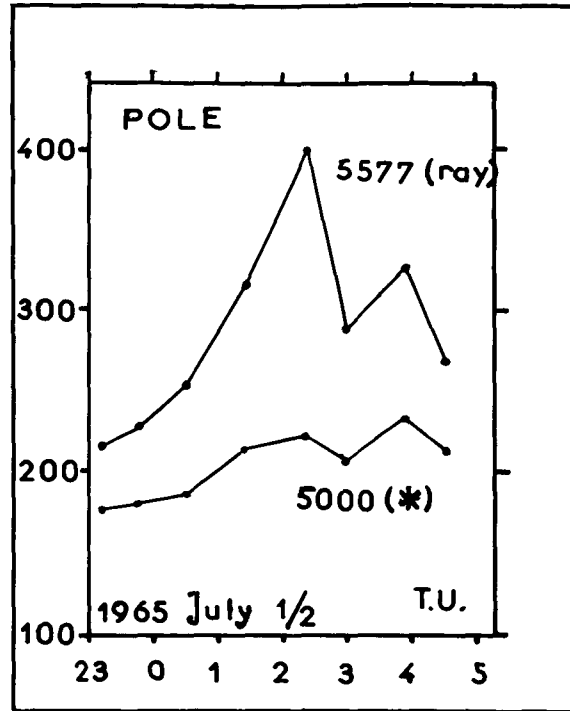


FIGURE 3.—Example of polar deflections at 5000Å and 5577Å.

the present method: Dots, near two straight lines which cross near the Oy axis (giving $-L_p x_p = -55$, thence $L_p = 127$ and $L_{zp} = 105$) are satisfying. At the right of figure 4 are the same observations, reduced with the assumption of a uniform layer. The accuracy of these results is much lower.

Some numerical results, summarized in figure 5, show the mean brightnesses on a quarter of the sky without reference to the weak shifts of zodiacal cones or band from ecliptic symmetry. Zodiacal light in high-latitude regions is still fairly bright (70 at the ecliptic pole), but it depends somewhat upon the longitude. It may be claimed that the H-M method is as accurate far from the ecliptic as well as within the bright cones.

Airglow green continuum is found to follow the green line according to the mean empirical formula:

$$\Lambda = 3.6\sqrt{Q^{(n)}}$$

where Λ is in the usual starlight unit and $Q^{(n)}$ is in rayleighs. This formula gives 15 stars for 20

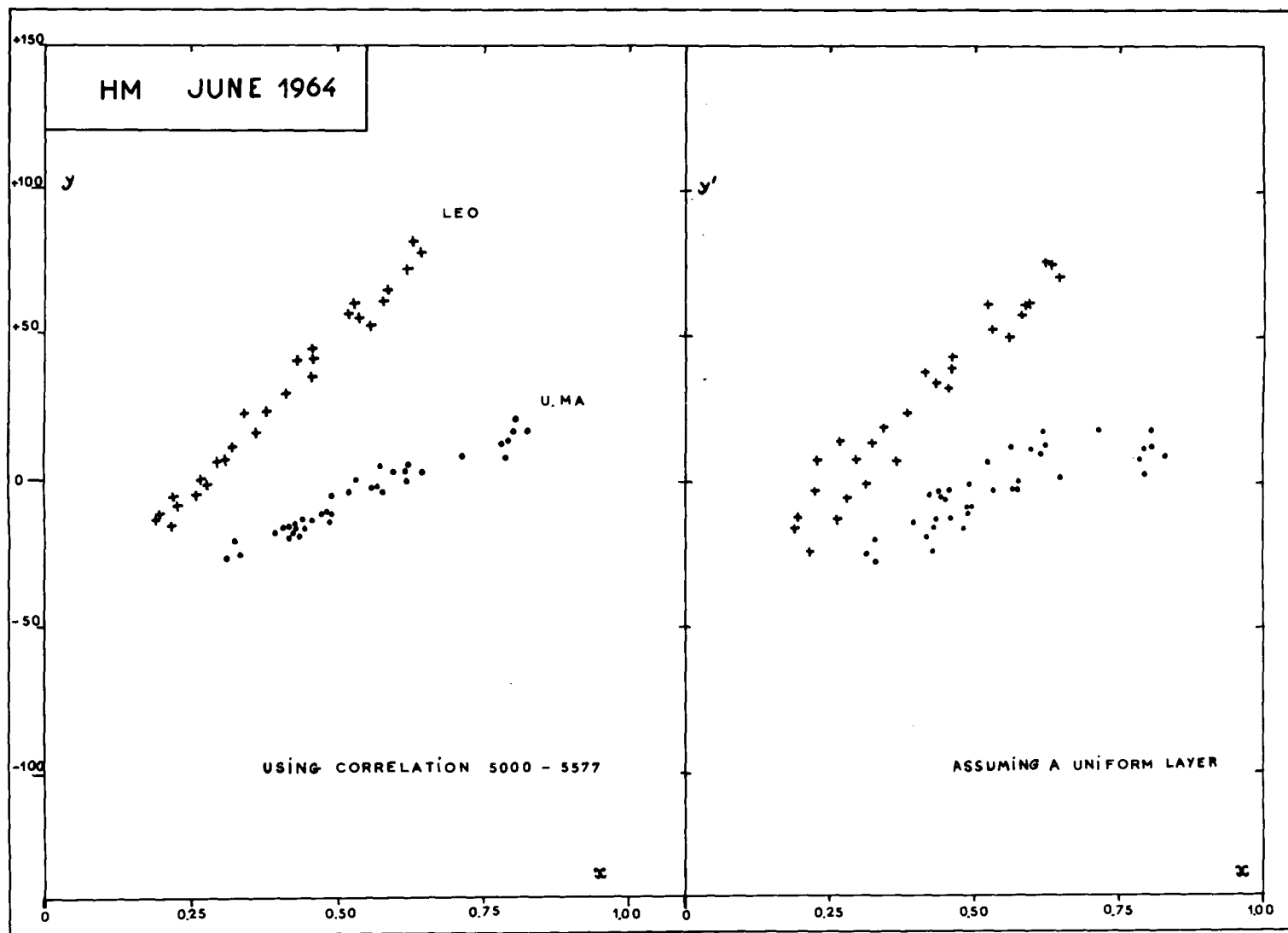


FIGURE 4.—Comparison of reductions of observations for a point in the ecliptic and a point at 45° ecliptic latitude both 90° from Sun made by H-M method. On left: using Barbier's correlation; on right: assuming a Van Rhijn layer.

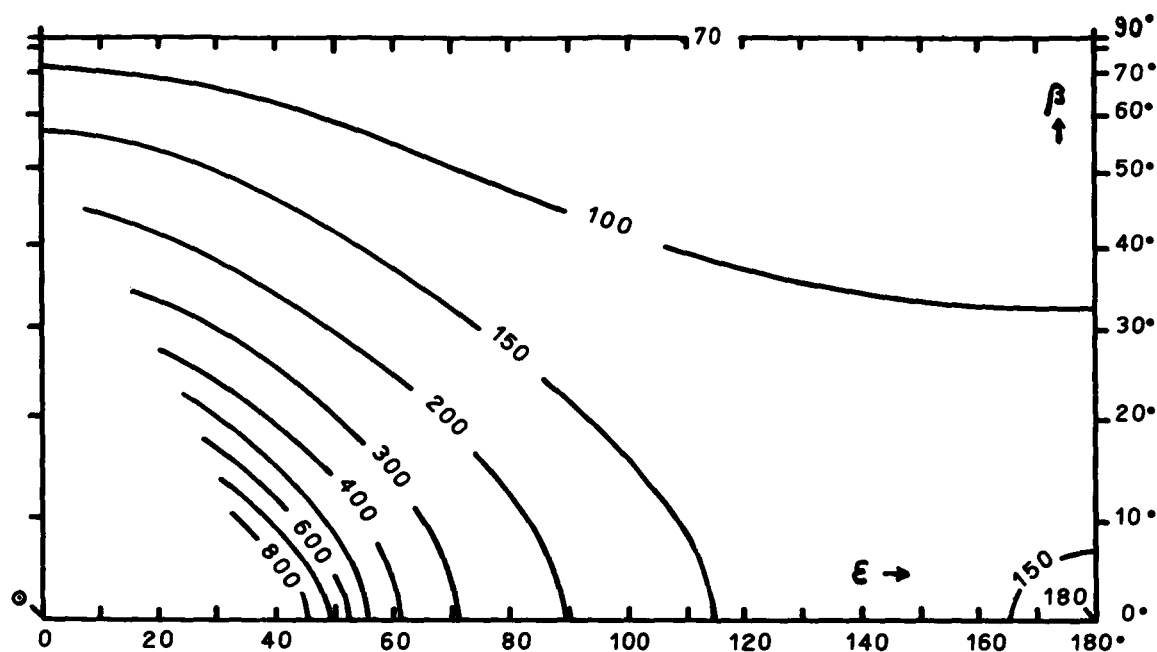


FIGURE 5.—Summary of mean zodiacal brightness for a quarter of sky.

rayleighs and 72 stars for 400 rayleighs (the former values were obtained on Tenerife Island in 1964, the latter in Haute Provence in 1962 and on Tenerife in 1966). The value $Q^{(n)}=400$ will surely be surpassed during the next solar maximum. In the course of the preceding lunation on Tenerife (December 1966), we noticed on some nights a very complicated distribution of $Q^{(n)}$ over the sky, like green-line clouds, with rather sharp edges and quick evolution. They distorted the rough zodiacal isophotes a great deal, especially when they occurred in front of the cones because of the simultaneous increase of green airglow continuum.

Our formula gives values of Λ which are in fair agreement with those of Weinberg (1963). The nonproportionality between Λ and $Q^{(n)}$ (the square root may be written $\Lambda = \alpha Q^{(n)} + \beta$ if variations are not too large) is also apparent in the recent work of Tanabe (1964, 1965), where the existence of an airglow continuum layer “independent of the 5577 Å line” with a mean zenithal brightness of 30 stars (at 5300 Å) is pointed out. If, for values of $Q^{(n)}$ between 100 and 400 rayleighs, we should replace the square-root mean curve by a straight line, 30 would just be its ordinate β (for $Q^{(n)}=0$).

The purpose of the observations made since 1964 on Tenerife Island ($\varphi = 28^\circ$, $h = 2350$ meters) was to use this accurate method of subtracting the airglow component for studying the shape of zodiacal light and gegenschein isophotes and to obtain information about the shape of the zodiacal cloud.

RESULTS AND DISCUSSION

Isophotes of the Gegenschein: How Their Behavior Differs From That of the Far Zodiacal Band

The axis of the far zodiacal band (more than 90° from the Sun) is generally found to deviate 2° or 3° from the ecliptic, northward in winter observations and southward in autumn. The center of the counter glow does not seem to follow that trend, and so far, we have always found it within 1° of the antisolar point. Moreover we do not find any permanent westward or eastward shift. An example of the true isophotes obtained in winter in the antisolar region can be seen in figure 6. Only 15° right or left from the antisun, the zodiacal band lies 2.5° northward from ecliptic line, but the center of the gegenschein patch nevertheless coincides with the antisun. This statement is only true for the final isophotes which refer to the true zodiacal brightness.

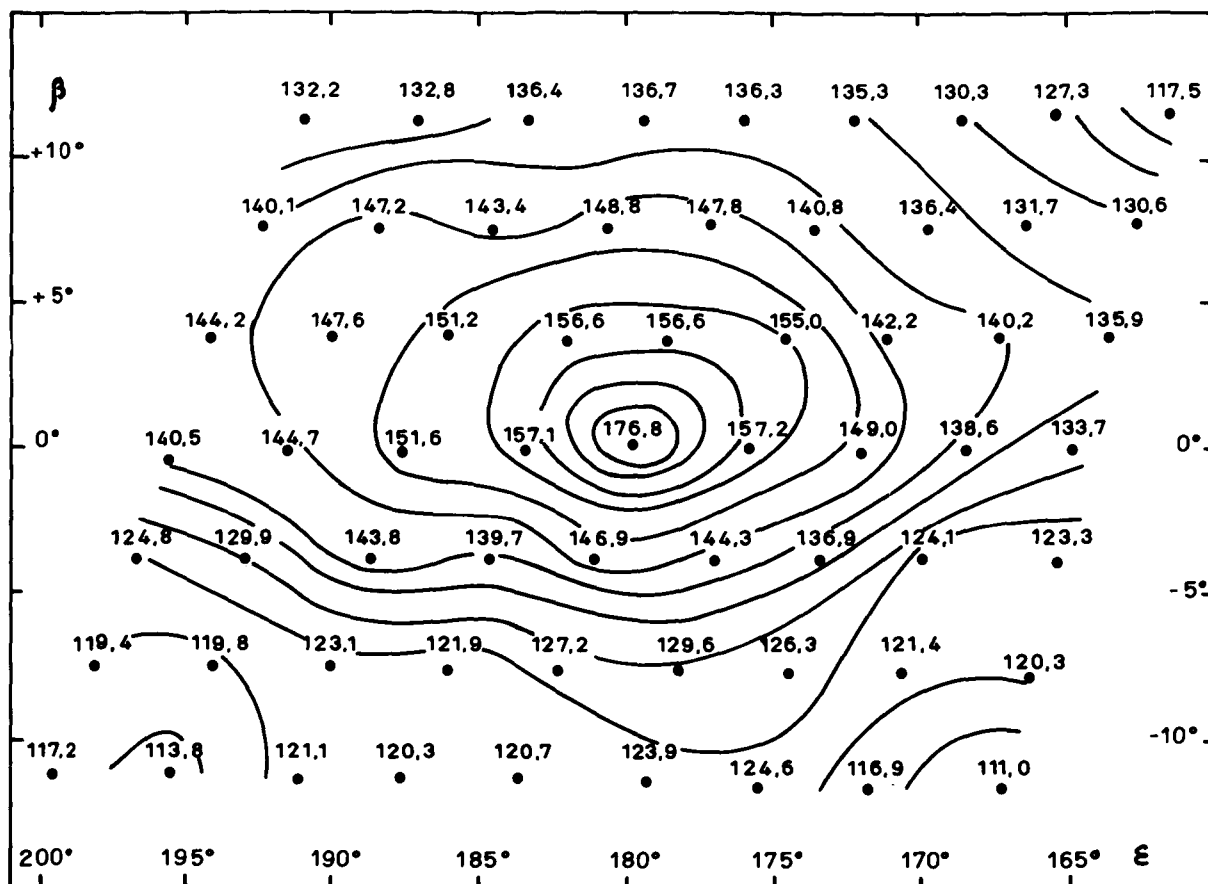


FIGURE 6.—Example of true isophotes obtained in winter in antisolar region.

Especially when the green line varies rapidly, rough 5000Å isotopes, before reduction, do not show the same symmetry. Formerly Dumont (1963) gave the example of a night where $Q^{(n)}$ suffered a continuous and important decrease between the first and the last points of the gegenschein “squaring” (a regular pattern of observed points, successively aimed). Rough isophotes, uniform-layer isophotes, and our H-M isophotes were strikingly dissimilar.

Axis of Zodiacal Cloud, From Observations 90° Away From the Sun, When Earth Crosses Solar Equatorial Plane

Former and various observers of the zodiacal cones or band rarely found them lying along the ecliptic. The plainest and oldest model for the dust cloud is obviously that of a large scattering cloud, symmetrical with respect to the solar equatorial plane. Twice a year, when the Earth crosses that plane, we have an especially good

opportunity for testing this model, because the axis of the cone observed 90° eastward or westward from the Sun would appear nearly 7° above or below the ecliptic line. It would be a rather large phenomenon, easy to be noticed and measured. Suitable epochs are the beginning of June and December, and the corresponding regions are Leo and Aquarius. Such research has already been done on Tenerife in June 1964, June 1966, and December 1966.

The provisional results do not sustain such a simplified model. When the telescope follows a circle perpendicular to the ecliptic and to the direction of the Sun, a slight maximum of brightness is generally found close to the ecliptic, but similar values of the true zodiacal brightness refer to pairs of points—the middle of which are shifted 1° to 3° from the ecliptic (in the very direction corresponding to the solar equatorial hypothesis). This result seems valuable both for

June and December and for Leo and Aquarius. It cannot therefore be imputed to any residual effect of zenith distance coming from airglow or atmospheric extinction. The most reasonable interpretation appears to be a mixture of a great solar cloud, flattened along its equatorial plane, or along the invariable plane of the solar system, and a small circumterrestrial dust ring, mainly bright near the ecliptic plane. According to its isophotes, the gegenschein would probably belong to the terrestrial cloud.

How H-M Observations May Bring Information Concerning Dust Surrounding Earth

We are led to the problem of geocentric concentration of scattering matter. It must be noticed that the existence of terrestrial umbra and penumbra cones provides for the satellite observer, as well as for the ground observer, an interesting means of investigation. Indeed, when during the night we point to an unvariable direction among the stars, our line of sight finally enters the penumbra and then the umbra. The lengths of the penumbra and umbra parts of the beam depend upon the solar longitude and upon the coordinates of the observed point, but even with those parameters remaining fixed, both

lengths still vary a great deal in the course of the night.

From the space-vehicle observations (described by Gillett in paper No. 2) of two unvariable points of the ecliptic (90° from the Sun), it was concluded that there was a very small brightness from the dust which lies very near the Earth.

Our ground observations lead to the same conclusion. In the Tenerife method, the fundamental (and only) hypothesis of a constant extraterrestrial light assumes, in fact, that circumterrestrial zones (a few Earth radii from the ground) bring a weak contribution of the total light scattered along the whole beam. Since H-M results are close to the expected ones (i.e., dots of any point M come along a straight line, and the lines of several points $M, M', M'' \dots$ converge near the Oy axis), the brightness scattered by the dust surrounding the Earth cannot be a significant component of the zodiacal light.

Nevertheless, the slight departures which we notice between H-M theory and experimental diagrams appear to be somewhat systematic. They may soon be able to bring information about the circumterrestrial component of the zodiacal light and perhaps about the dust-density variation as a function of the geocentric distance.

REFERENCES

- BARBIER, D., 1956, *The Airglow and the Aurorae* (E. B. Armstrong and A. Dalgarno, eds.), 38-59 (London: Pergamon Press).
 DUMONT, R., 1963, *Comp. Rend.*, **257**, 2242.
 —, 1965a, *Ann. d'Astrophys.*, **28**, 265.
 —, 1965b, *ibid.*, 275.
 MEGILL, L. R., and F. E. ROACH, 1961, NBS Technical Note, No. 106.
 TANABE, H., 1964, *Pub. Astron. Soc. Japan*, **16**, 340.
 —, 1965, *Pub. Astron. Soc. Japan*, **17**, 339.
 WEINBERG, J. L., 1963, *Photoelectric Polarimetry of the Zodiacal Light at $\lambda 5300$* , Ph. D. dissertation, University of Colorado, 73.

Page intentionally left blank

12. Recent Polarization Measurements Over the Sky at Tenerife Island

FRANCISCO SANCHEZ MARTINEZ
Observatorio del Teide,
Universidad de la Laguna,
Islas Canarias, España

BETWEEN JANUARY 1964 AND JULY 1965, one of the programs of the Teide Observatory ($\varphi = 28^\circ$, $h = 2350$ meters) has been devoted to investigating the amount of polarization of the night sky near 5000\AA , using our 12-inch Cassegrain photoelectric telescope. A Lallemand Cs-Sb photomultiplier was lit through a Fabry lens and a field of 0.02 square degree. A polaroid (which showed a good Malus law with another polaroid provisionally stuck on the diaphragm) rotated near the focus with a period of minutes. The stars visible through the instrument (visual magnitude less than 12.5) were excluded from the field.

The true polarization of the zodiacal light, P_z , has been computed from the observed polarization, p , after taking account of the remaining starlight component ($m_v > 12.5$) and of the airglow continuum, according to its correlation found by Barbier with the green line (see Dumont, 1965a). Approximately 400 points were observed over the whole sky, in the zodiacal band and cones as well as far from them. A summary of our results follows.

The main (perhaps only) parameter upon which P_z depends is the angular distance ω from the Sun. Near $\omega = 60^\circ$, P_z seems to be maximum (0.18) and near $\omega = 90^\circ$, we find $P_z = 0.13$; beyond $\omega = 90^\circ$, P_z decreases and reaches zero beyond $\omega = 160^\circ$. The average curve we obtain and the curve given by Weinberg (1963) are very much alike, although Weinberg's curve was concerned only with ecliptical points. Between solar elongations of 60° and 150° , our values are uniformly lower than those of Weinberg by only 0.04 . There is, however, a great discrepancy with Elsässer's

(1958) and with Blackwell and Ingham's (1961) curves.

Figure 1 shows our mean curve of P_z compared with several others, restricted to ecliptic regions, that is, with $\epsilon = \lambda - \lambda_\odot$ as abscissae ($\beta = 0$). But our curve is also valuable far from the ecliptic with the parameter ω taking the place of the elongation, ϵ .

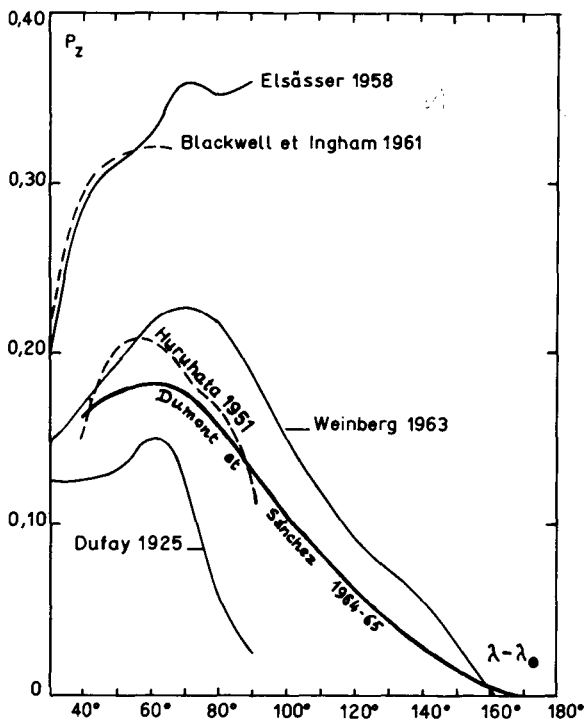


FIGURE 1.—Mean curves published for the true zodiacal polarization versus solar elongation. All curves are valuable near the ecliptic; the curve Dumont et Sanchez is also valuable on the whole sky, replacing the abscissae $\lambda - \lambda_\odot$ by ω (angular distance to the Sun).

Indeed, as suggested by Dumont (1965b) and confirmed by Dumont and Sanchez (1966), for the same angular distance ω from the Sun, we find almost the same amount of polarization, P_z , whether aiming near the ecliptic or far from it. It is even possible to have a very slight excess of polarization (0.01 or 0.02) at high ecliptic latitudes. For the ecliptic pole we find a mean zodiacal brightness of 70 (10th visual G2V stars per square degree) and a mean true zodiacal polarization of 0.15. This value disagrees greatly with that of Fesenkov (1966), who finds a mean true zodiacal polarization of 0.02 and a zodiacal brightness only 1/20 of the total night-sky brightness at the same point. On the other hand, there is a noteworthy agreement with the results of a satellite recording of zodiacal-light polarization, given in paper No. 9 by Wolstencroft and Rose.

Two remarks should be made about the accuracy to be expected from ground polarization measurements.

AIRGLOW CORRECTION

Airglow continuum is a large source of errors when going from the observed value of night-sky polarization, p , to the true amount of zodiacal-light polarization, P_z . Airglow, a practically unpolarized additional component, is dangerous not only because of its variations, but also because even if it did not vary, the adopted value of its brightness would obviously be of great influence upon the final amounts of P_z . We believe that a fair calculation of P_z from ground observations of p is possible, but that it demands a very careful previous separation of the airglow brightness. As for the variations of the latter, it could be noticed that, when reducing the same polarimetric measurements by means of (a) our usual 5000Å to 5577Å method and (b) a similar method which assumes a uniform airglow layer, the results were undoubtedly and systematically more accurate with the first method (i.e., the dispersion of dots from the mean curve, given in fig. 1, increases from (a) to (b)). (See paper No. 11 by Dumont.)

STARLIGHT-BACKGROUND CORRECTION

The best way to compute the starlight-background correction is to use the integrated starlight

over the sky given by Megill and Roach (1961). However, it is well known that the irregularities in apparent distribution of stars involve, for any direction, and especially near the Milky Way, a rather large uncertainty. Therefore, using a nonautomatic telescope and searching areas without stars visible through it, is a way to improve the accuracy of photometric and polarimetric measurements of the zodiacal light.

With an automatic photometer which records all the stars, the starlight term E can be computed from a table of total integrated starlight (table 2 of Megill and Roach, 1961), while a manual and visual instrument which excludes all stars brighter than a given limit, m_0 , leads to a starlight term which can be found by subtracting from the total integrated starlight (table 2 of Megill and Roach, 1961) the amount of starlight according to apparent visual magnitudes $< m_0$ (first columns of table 5 of Megill and Roach, 1961):

$$E_{m_0} = J(v) - \sum_{5.54}^{m_0} J_m(v)$$

For instance, in the case of polarimetry at the ecliptical pole ($l' = 64^\circ$ and $b' = 30^\circ$), table 2 of Megill and Roach (1961) gives $E = J(v) = 64$ visual units with a small photometer (assuming that stars brighter than 5^m will give individual spikes), while for the 12-inch telescope in Tenerife (visual limit $m_0 = 12.5$) we have

$$E_{12.5} = J(v) - \sum_{5.54}^{12.19} J_m(v) = 64 - 47 = 17 \text{ visual units}$$

If it is reasonable to assume that those starlight counts are known with 25-percent uncertainty, observing the ecliptic pole at a medium zenith distance and through a medium airglow intensity involves the following inaccuracies of stellar origin on the final polarization amount:

$\sim \pm 0.04$ with a photometer recording all stars
 ± 0.01 with a telescope excluding until twelfth-magnitude stars

The advantages of middle- or large-sized non-automatic telescopes, with small fields, on classical photometers were also pointed out by

Swings and by Robley. These advantages concern, of course, both photometry and polarimetry. It should be noted that satellite devices, while

avoiding airglow and atmospheric scattering, are not going to improve the situation with respect to the starlight correction.

REFERENCES

- BLACKWELL, D. E., and M. F. INGHAM, 1961, *Mon. Not. Roy. Astron. Soc.*, **122**, 113-127.
DUFAY, J., 1925, *Compt. Rend.*, **181**, 399.
DUMONT, R., 1965a, *Ann. d'Astrophys.*, **28**, 265.
——. 1965b, *ibid.*, 309.
DUMONT, R., and F. SANCHEZ MARTINEZ, 1966, *Ann. d'Astrophys.*, **29**, 113.
ELSÄSSER, H., 1958, *Die Sterne*, **9-10**, 166-169.
FESENKOV, V. G., 1966, *Sov. Astron. — AJ*, **10**, 474.
HURUHATA, M., 1951, *Publ. Astron. Soc. Japan*, **2**, 156-171.
MEGILL, L. R., and F. E. ROACH, 1961, NBS Technical Note, No. 106.
WEINBERG, J. L., 1963, *Photoelectric Polarimetry of the Zodiacal Light at $\lambda 5300$* , Ph. D. dissertation, University of Colorado, 109.

Page intentionally left blank

13. Problems of Spectrophotometry of the Zodiacal Light

J. F. JAMES
University of Manchester
Manchester, England

A survey is given of methods which have been used and are being used for the spectrophotometry of the zodiacal light and similar faint extended sources.

THE SPECTRUM OF THE ZODIACAL LIGHT is an extreme example of a class of phenomena which has always presented great observational difficulties—the continuum with absorption lines. Only if the very greatest care is taken can photometry and line-profile measurement be attempted, and the observer must often be content to measure the equivalent widths of the absorption lines, since these are not affected by the usual instrumental shortcomings. Thus it is not surprising that such a feeble source as the zodiacal light has received comparatively little attention in the past, and it is even less surprising that those attempts at spectrophotometry that have been made have yielded no reliable quantitative measurements of line shapes or wavelengths.

The reasons for attempting such a difficult technical problem are fairly self-evident and are dwelt on only briefly here. First, a measurement of equivalent widths will yield information about the ratio of K- and F-components in the zodiacal light, and second, a measurement of the wavelengths of the Fraunhofer lines will tell if the zodiacal cloud is co-rotating or contra-rotating (or both, or neither). An accurate measurement of a line profile is both least feasible and probably least useful: it might be expected to tell something about the radial-density distribution, but a unique radius-density relation is not to be expected from such a line profile alone. There are too many other unknowns. At the moment we should be well content to have an accurate

knowledge of either of the first two quantities mentioned. The problem is such that even this has so far eluded us.

Early spectra of the nightglow, including the zodiacal light, were obtained by Slipher (1933) and by Hoffmeister (1940). Hoffmeister used photography at a rather low resolution (11\AA at 3500\AA to 66\AA at 5500\AA). No Fraunhofer lines are apparent, and the airglow line at 5577\AA appears to be the only identifiable feature.

The first deliberate search for the Fraunhofer lines at large elongation was that of Blackwell and Ingham (1961) who employed at Chacaltaya a plane-grating spectrograph at about 2\AA resolution, with high-aperture Schmidt optics in the camera. A 30-hour exposure, spread over several nights, yielded one spectrum. A step wedge was used for calibration. The Fraunhofer lines were readily identified, as were the night airglow-emission components, and estimates of some equivalent widths were made. However, wavelength calibration was not undertaken.

The presence of the Fraunhofer lines immediately suggested another observational possibility—that of a detailed study of one of these lines, to measure, if possible, its wavelength and its equivalent width. In order to do this, it was necessary to resort to one of the more sophisticated techniques of spectrophotometry, and photography, which possesses the sole virtue of large spatial information capacity, was abandoned in favor of the inherently more sensitive technique of photoelectric photometry. The Man-

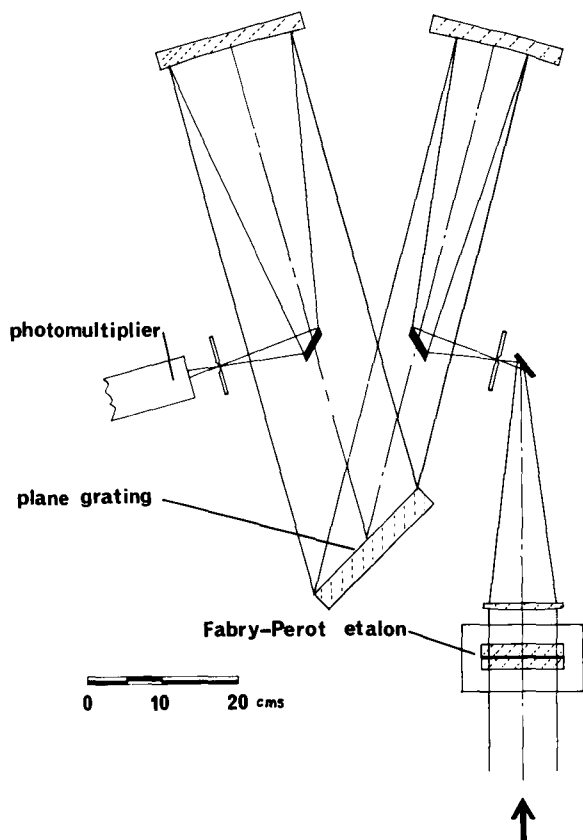


FIGURE 1.—Zodiacal-light interference spectrometer used at Chacaltaya in 1962.

chester/Wisconsin Chacaltaya expedition of 1962¹ used a large Fabry-Pérot etalon (see fig. 1) in series with a large plane-grating spectrometer and studies the $H\beta$ line at a resolution of 1.2\AA . This line was chosen because, first, it is at the weakest part of the airglow emission, and second, it is near the peak of photomultiplier sensitivity. It was chosen from the lines in the vicinity of 5000\AA since it is a "clean" line with only one major satellite and is relatively far removed from neighboring Fraunhofer lines. Its width (1.6\AA) and its depth were suitable for the detection of the shift of about 0.5\AA that was to be expected if the zodiacal light were rotating at about Keplerian velocity. The results of this study were unexpected and are treated with some reserve by the authors (Ring et al., 1964). It

¹ D. Clarke (Manchester); M. Daehler (Wisconsin); J. F. James (Manchester); J. Ring (Manchester) as expedition members. J. E. Mack (Wisconsin) was project director.

became clear, however, that even the advance in sensitivity represented by a Fabry-Pérot spectrometer and a photoelectric detector was only marginally adequate, and even more exotic techniques are being developed for the next attempt.

The difficulties of spectrophotometry resolve themselves into two parts: (1) the geometrical factors which set a limit to the luminous efficiency of the spectrometer, and (2) the physical factors which limit the sensitivity of the radiation detectors.

In recent years there have been considerable improvements in both of these factors, and it is probably true to say that neither the diffraction grating nor the photographic emulsion will play a significant part in future attempts to obtain a zodiacal-light spectrum.

Jacquinet (1954) pointed out that there is, for most spectrometric devices, a geometrical relation between the light grasp (or "speed") and the resolving power (defined as $R = \lambda/\Delta\lambda$) of a spectrometer. The light grasp is defined, for any optical instrument as the product: $L = (\text{Area of aperture stop}) \times (\text{Solid angle subtended by the field stop at the aperture})$ ². The units are $\text{cm}^2\text{-steradians}$.

There are relatively simple formulae for the product of L and R for various classes of spectrometric instrument.

For a prism spectrometer:

$$LR = hb \frac{\lambda}{50} \frac{\partial \mu}{\partial \lambda}$$

where h = Ridge length of prism

b = Base length of prism

For a grating spectrometer:

$$LR = \frac{A}{100} (\sin i + \sin r)$$

where A = Area of grating

For a Fabry-Pérot etalon or a Michelson interference spectrometer:

² In a photographic instrument, the field stop is the size of one grain of the emulsion.

TABLE 1.—Typical LR Products for Various Instruments

Instrument	LR product	L at 1\AA resolution (theoretical)	L (practical)
Prism.....	0.2	$4 \cdot 10^{-5}$	4×10^{-5}
Grating.....	4.0	$8 \cdot 10^{-4}$	8×10^{-4}
Etalon.....	400	$8 \cdot 10^{-2}$	4×10^{-2}
Michelson.....	1600	$3 \cdot 10^{-1}$	1.2×10^{-1}

$$LR = 2\pi A$$

where A = Effective area of beam splitter

Typical values of the LR product for various instruments are given in table 1.

The Michelson spectrometer (fig. 2) has not, until very recently, been considered for exploration of the visible region because of the mechanical difficulty of maintaining the alignment over large ranges of path difference. The problem has now been overcome in several different ways (e.g., Connes and Connes, 1966; Sternberg and James, 1964) and the instrument can now be included with confidence in the list.

Finally we may mention the Iridometer. This new concept of a spectrometer is described by

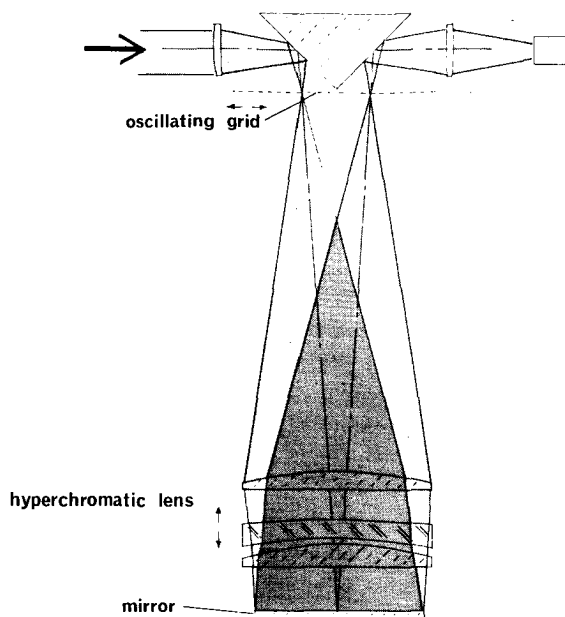


FIGURE 3.—Iridometer (focal isolation spectrometer).

James and Sternberg (unpublished report), and a prototype is now under construction. Theoretically it looks promising, since there is no limit to the luminous efficiency, which is not, in this instance, dependent on the resolving power. The practical snags have yet to be overcome. The principle of operation will be apparent in figure 3.

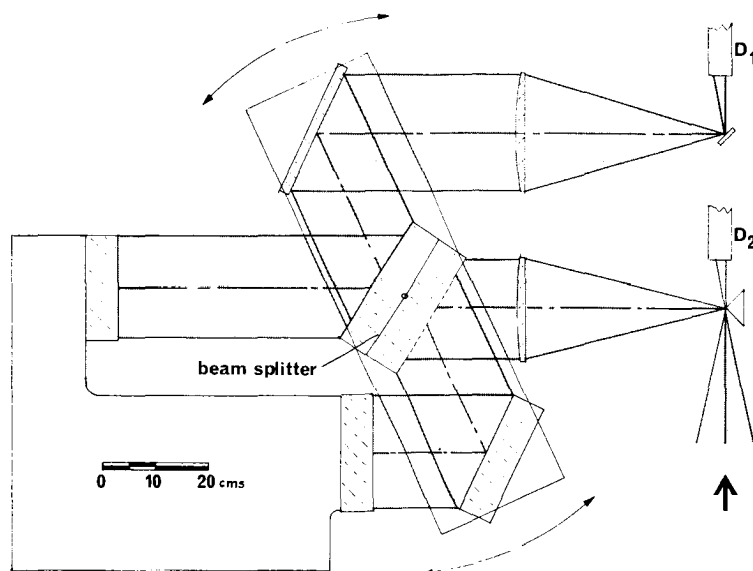


FIGURE 2.—Michelson multiplex interference spectrometer.

A lens and a mirror produce an image of a grid at magnification of -1 , which is superimposed on the grid itself. If the lens is given the largest possible chromatic aberration, there will be good imaging only over a very small range of wavelengths. By oscillating the grid in its own plane in a direction perpendicular to the lines, this small wavelength range will produce an alternating component of the total intensity while the defocused wavelengths will contribute only a steady background. By using a phase-sensitive detector, the intensity of the modulated light can be determined. Present indications are that a resolution of 1\AA is feasible with a luminosity considerably in excess of that of a Michelson spectrometer. It is considered, with an 8-inch-aperture Michelson spectrometer now being designed, as joint favorite for the zodiacal-light problem.

In the matter of detector efficiency, the photomultiplier is supreme in the visible region, although it is chiefly used in the photocurrent-

measurement mode and few people seem to have appreciated its advantage as a photon counter. Recent experiments by the author have shown that a photon-arrival rate at the photocathode of 1 per second can be detected unambiguously in less than 3 minutes, while 1000 photons/sec can be photometered to 1-percent accuracy in about 12 seconds.

The zodiacal light yields about 2.10^4 photons/cm²/sterad/sec/ 1\AA bandwidth at 40° elongation, and if this is multiplied by the luminous efficiency of a large Michelson spectrometer it yields 2400 photons/sec. Thus the problem is now coming within the observer's grasp.

Future observations will probably be made on other Fraunhofer lines than $H\beta$. Although $H\beta$ is a very convenient line to study (calibration sources can be carried to the expedition site), it was found, during the Chacaltaya expedition, to be present, in emission, in parts of the night sky.

REFERENCES

- BLACKWELL, D. E., and M. F. INGHAM, 1961, *Mon. Not. Roy. Astron. Soc.*, **122**, 129.
 CONNES, P., and J. CONNES, 1966, *J. Opt. Soc. Am.*, **56**, 896.
 HOFFMEISTER, C., 1940, *Zeits. f. Astrophys.*, **19**, 116.
 JACQUINOT, P., 1954, *J. Opt. Soc. Am.*, **44**, 761.
 RING, J., D. CLARKE, J. F. JAMES, M. DAEHLER, and J. E. MACK, 1964, *Nature*, **202**, 167.
 SLIPHER, V. M., 1933, *J. Roy. Astron. Soc. Canada*, **27**, 365.
 STERNBERG, R. S., and J. F. JAMES, 1964, *J. Sci. Instr.*, **41**, 225.

14. Noneclipse Observations of the F-Corona*

M. J. KOOMEN AND R. TOUSEY
Naval Research Laboratory
Washington, D.C.

The solar corona from $R=3$ to $R_s=11$ was recorded photographically with rocket-borne coronagraphs on June 28, 1963, and April 28, 1966. Coronal brightnesses were two or more times greater than the model derived from measurements during total solar eclipses. The tentative conclusion was that measurements of the F-corona during a solar eclipse do not record all the zodiacal light and that some of the zodiacal cloud may lie between Earth and Moon where it is shadowed. The rocket-coronagraph experiment was repeated on November 12, 1966. The time selected placed the Moon in the field of view, so as to eclipse the K-corona and the part of the F-corona beyond itself, and also to cast a shadow into the F-corona between itself and the Earth. This time the coronal brightness was lower than previously and in approximate agreement with the model corona. Inspection of the Moon's image suggested that little zodiacal material lay between the Moon and Earth. Since all coronagraphs had identical optical systems and were prepared, cleaned, and calibrated in the same way, it is tentatively concluded that the variable F-coronal brightness is real and may result from variable quantities of scattering material between Earth and Moon.

THIS PAPER REPORTS BRIEFLY on three attempts to photograph the Sun's white-light corona from rockets during noneclipse conditions. The aim was to develop a method of photographing the inner zodiacal light and the K-corona without depending on a solar eclipse and to relate the results to chromospheric and limb features recorded by other means. We therefore chose to record the corona out to approximately 10 solar radii, covering the region where both the inner zodiacal light and the outer K-corona are present. The low coronal brightness at these elongations makes it necessary to have a black sky characteristic of rocket altitudes, and a Lyot coronagraph that is externally occulted to keep instrumental stray light to a very low level. Our coronagraph was small, designed for launching in a biaxial solar-pointing control mounted on an Aerobee 150 rocket. The occulting disk was

placed between 20 and 30 inches in front of the objective lens on a spar which was extended from the instrument after launch. In principle, the optical arrangement was similar to a visual solar aureole photometer designed and described by Evans (1948). Coronal coverage was from 3 to approximately 10 solar radii.

It would have been desirable to record the corona closer to the Sun's limb, but $3R_\odot$ seems to represent a practical minimum for a small instrument with an occulting disk no more than 30 inches from the objective. Attempts to increase the inward coverage produced a rapid increase in stray light and an increasingly severe alinement problem for an occulting disk on an extendible spar.

The instrument was first flown successfully on June 28, 1963, with an external occulter whose edge was serrated (Purcell and Koomen, 1962) in order to minimize diffraction of direct sunlight into the objective aperture.

Figure 1 shows an improved instrument flown

*Work carried out under contract with National Aeronautics and Space Administration.

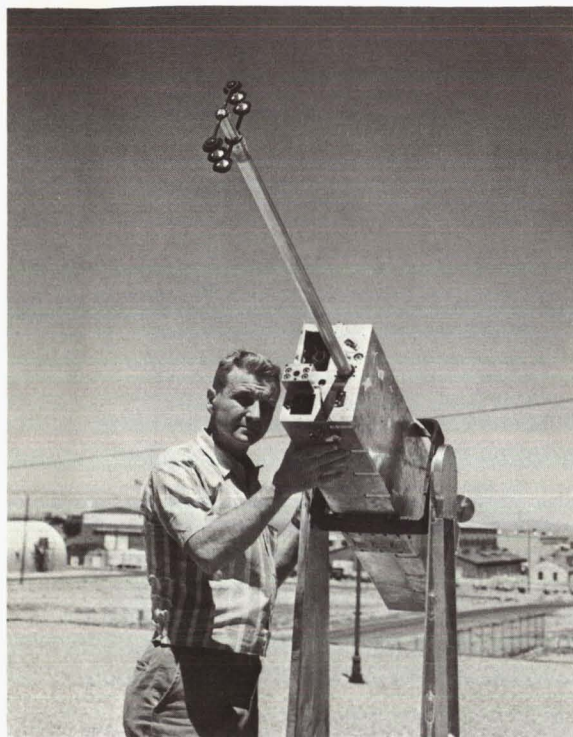


FIGURE 1.—Double coronagraph with external occulting disks in flight position. Objective apertures are closed.

twice in 1966. This instrument has two coronagraphs side by side, with the occulter for each mounted on a common spar. Each occulter consists of three disks in tandem with diameters adjusted to minimize diffraction of direct sunlight into the objective aperture. This type of occulter has been used by Newkirk and Bohlin (1964) with balloon-borne coronagraphs; unlike the saw-toothed occulter, it remains effective even though many particles accumulate on the edges of the disks. Each aperture is shown closed as in its prelaunch condition to preserve the cleanliness required in coronagraph optics. The remainder of the instrument package contains an extreme ultraviolet spectroheliograph, which records chromospheric and limb features in wavelengths between 150\AA and 650\AA .

A flight to 180-km altitude occurred on April 28, 1966, with results shown in figure 2. This is a composite picture made by taking a print from each coronagraph, cutting off the part containing the image of the occulter support, and joining the remaining sections. Obvious artifacts caused

by specks of dirt settling on the field lens have been removed from the figure. There are many coronal streamers, extending to 10 solar radii, and the underlying F-corona is clearly registered on the original negative. The right half of the picture was taken with a concentric polarizer¹ that everywhere transmitted the tangential electric vector and enhanced slightly the contrast of the streamers.

It is characteristic of an externally occulted system that the image is vignetted from the edge of the field inward. For our instrument the vignetting function very nearly compensated for the inward radial increase of coronal brightness, and this accounts for the uniform appearance of the picture. The two instruments had somewhat different vignetting functions, and this, combined with high-contrast printing, accounts for the imperfect match in the two halves of the composite.

The center of the photograph contains an image of the solar disk in the He II emission line at 304\AA , obtained with the extreme ultraviolet spectroheliograph on the same flight and reproduced on the correct scale and properly oriented with respect to the coronal streamers. White dots mark the position of strong limb prominences.

Both the June 1963 and the April 1966 flights gave coronal brightnesses which were higher than the models published by van de Hulst (1953), or by Allen (1963). The June 1963 results were high by a factor of 2 and the 1966 results by a factor of approximately 4.

Stray light, always a possible source of error, was not present, at least in the form usually exhibited in the laboratory. We have considerable confidence that the data are correct: The streamers were obviously real, because they remained fixed in space for 50 separate photographs while the camera focal plane rotated as a result of rocket precession and because they were registered identically in both coronagraphs. The film calibration, densitometry, and so forth, were carried out with great care and we estimate that the absolute brightness was deduced correctly within 25 percent.

¹ Manufactured by Polacoat, Inc., Blue Ash, Ohio.

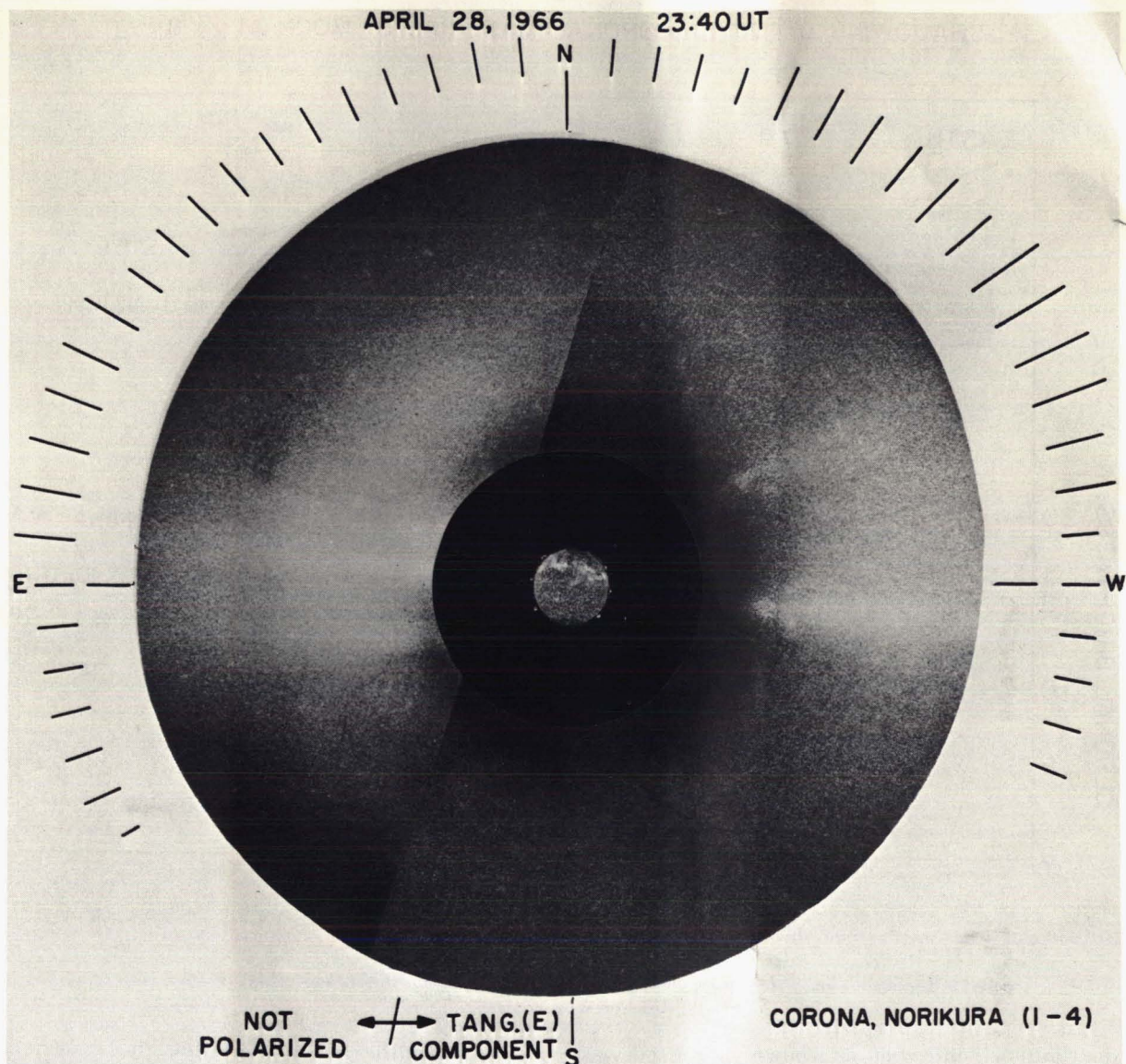


FIGURE 2.—F-corona and streamers photographed on April 28, 1966, with coronagraph of figure 1.

A possible explanation for the enhancement in coronal brightness is to ascribe it to small-particle material lying between the Moon and the Earth. Such material is partly shaded for observers in the eclipse shadow who must look nearly lengthwise into the shadow cone, and its effect is not included in the brightness of the coronal models derived from eclipse measurements.

A test for cislunar scattering material was suggested by J. D. Purcell of the Naval Research

Laboratory (NRL); this test was to launch a coronagraph when the Moon passes nearly in front of the Sun, say at 1° or 2° elongation. The situation shown in figure 3 then occurs. Assume that the zodiacal material lying between the Moon and Earth, by virtue of strong forward scattering, adds a brightness contribution F_E to the brightness of the corona, and that the corona and Moon are observed from the point indicated, with the Moon at 2° elongation from the Sun. Then the corona and Moon will have a brightness

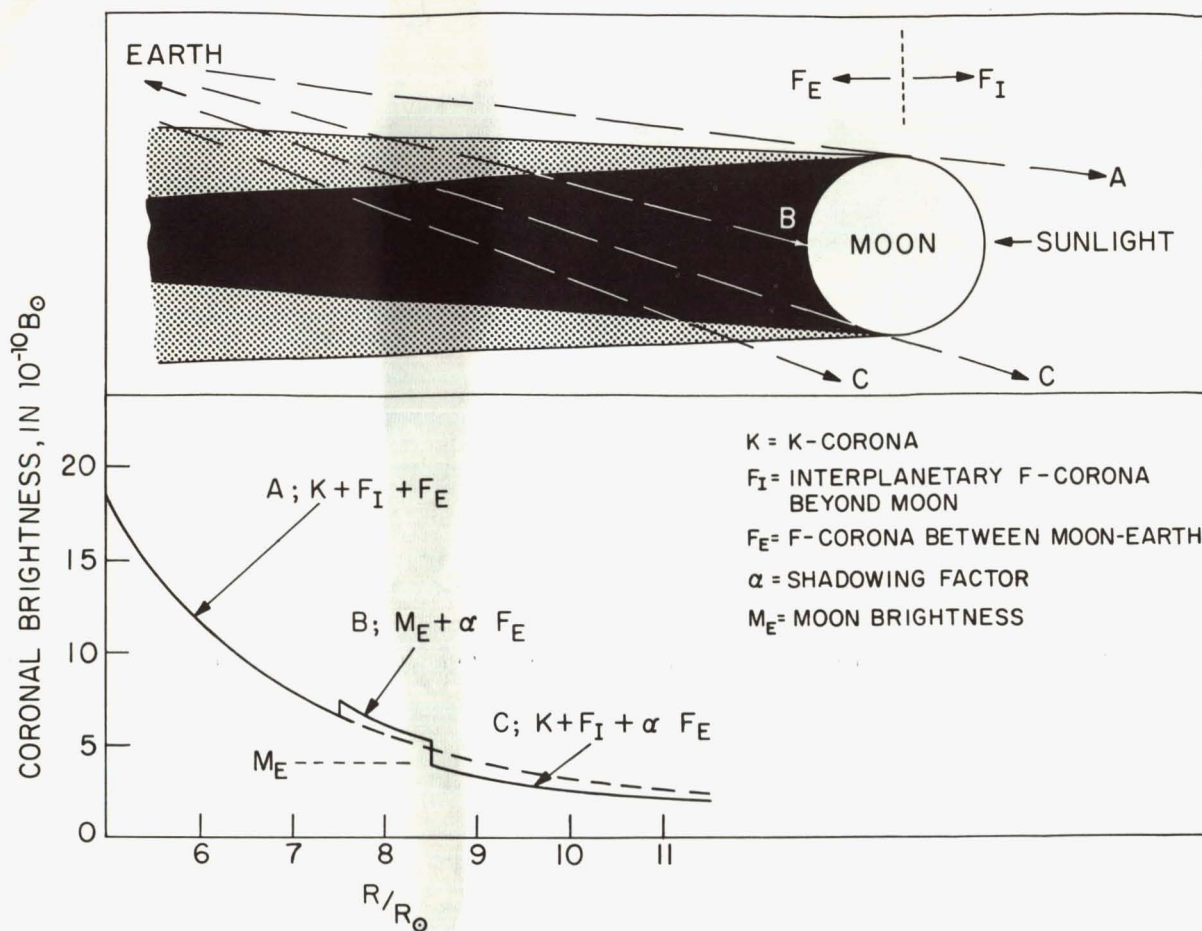
SHADOWING OF OUTER CORONAL MATERIAL BY MOON AT $\epsilon = 8 R/R_{\odot}$ 

FIGURE 3.—Shadowing of interplanetary material between Moon and Earth and effect on apparent brightness of corona.

distribution somewhat as shown in the curve. By observing the corona outward from the Sun, the normal brightness of the K- and F-corona including the contribution F_E is recorded. When the line of sight reaches the Moon the corona is eclipsed except for F_E , and we see the Moon's surface illuminated by the Earth, to a brightness M_E , the normal earthshine, but overlaid with an anomalous brightness distribution decreasing across its face, caused by the progressively greater shadowing of F_E as the line of sight goes across. Finally when the line of sight crosses the far edge of the Moon there should be a slight shadow tail, again caused by looking through the cone of shadowed material. Figure 3 was

plotted with the assumption that the material between the Earth and Moon makes a contribution equal to all the material lying beyond. This may seem excessive, but a relatively low density of small particles between the Moon and the Earth will be sufficient to produce a measurable brightness because of strong forward scattering. For example, a 10μ particle scatters 10^5 more at 2° than at 90° . The shadow method therefore should be a sensitive indicator of the presence of small particles and has the further advantage of being relatively independent of photographic calibration procedures.

An opportunity to carry out the shadow experiment came on November 12, 1966, when there

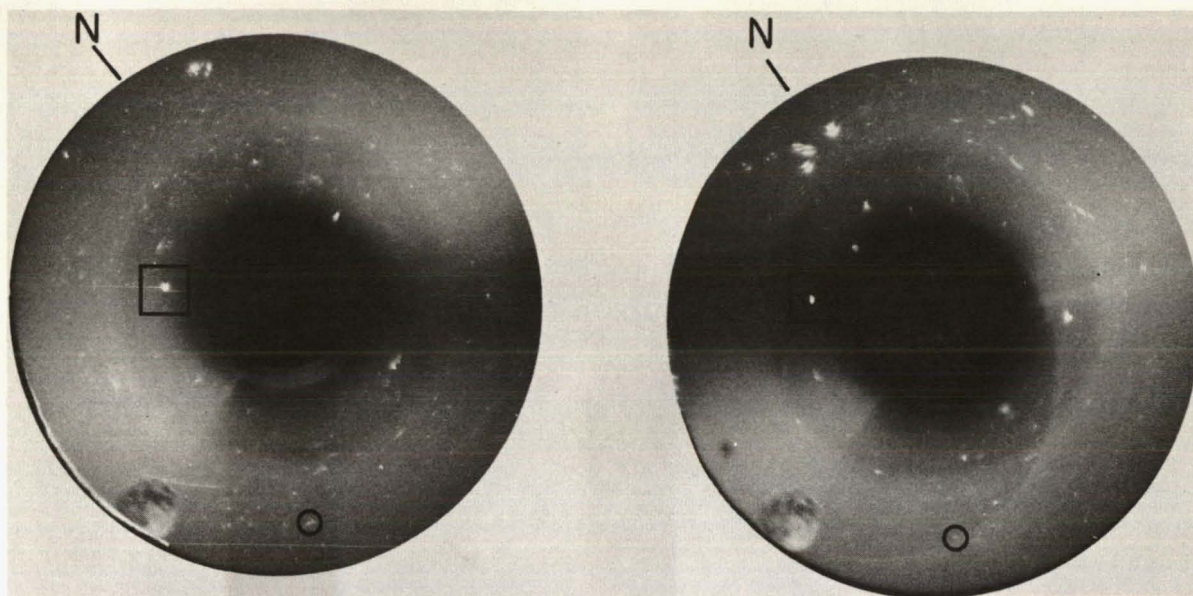


FIGURE 4.—Simultaneous 3-second exposures in coronagraph of figure 1 on November 12, 1966. Positions of Venus and 24 Libra are marked with squares and circles, respectively.

was a total eclipse in South America; at this time the conditions just described could be observed from the rocket launch site at the White Sands Missile Range, New Mexico. The launch time chosen was a compromise. The shadow effect is greatest when the Moon is close to the Sun, say at an elongation of 1° , which is a practical minimum for our coronagraph. However, since our instrument field had a radius of 2.25° , it seemed of interest to have the Moon's elongation large in an attempt to detect a vestige of the new Moon crescent, which cannot be seen by observers on the Earth at elongations less than 8° because of the brightness of the twilight sky. Prints of simultaneous 3-second exposures taken in each of the two coronagraphs are shown in figure 4. The radial shadows on the right and left sides of the pictures are out-of-focus images of the occulter support. Solar north is to the upper left. The streamers and the fanlike distribution in the corona are conspicuous features; they are the same in both instruments and remain fixed in space while the focal plane rotates through some 60° during a series of 60 exposures of varying duration. The Moon is at the lower edge of the field at an elongation of 2° ; we had planned for somewhat less, so that the shadow

tail, if any, could be observed, but the uncertainties connected with the operation resulted in the Moon's location as shown. Since, at this position, vignetting is a minimum, the Moon could here be measured most accurately for any brightness anomaly across its surface; none was detected, however.

The noticeable ring pattern is stray light of about the same contrast as the streamers. This is a typical manifestation of stray light when it occurs; the cause is not exactly known but evidently resulted from slight instrument contamination and misalignment which occurred during the launch. Previous to launch the stray light was below the fog level of the film, with the instrument correctly aligned and clean.

The bright specks are small particles, originating in the instrument interior, which settled on the field lens during the high-vibration phase of the launch. These specks have appeared to a greater or lesser extent in all three launches to date, even though all surfaces and cracks were cleaned carefully before launch. The number of specks was particularly large in this latest launch and has been tentatively traced to a black coating, improperly applied. There are, however, two specks which are images of celestial objects

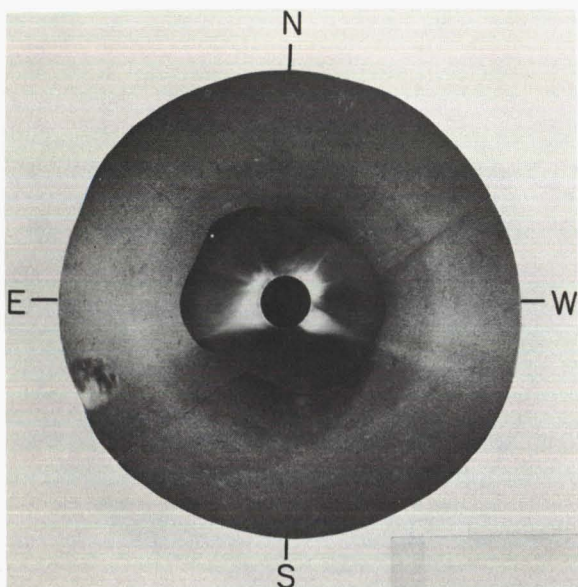


FIGURE 5.—Composite of November 12, 1966, rocket coronagraph exposures and eclipse photograph of inner corona taken by Newkirk. Outer corona by Naval Research Laboratory.

in the field. Venus is directly to the left of center and the 4.7-magnitude star 24 Libra is visible in the lower half as a faint streak among permanent specks.

In figure 5 the best halves of the two pictures with the artifact spots removed have been combined on the proper scale with the remarkable eclipse photograph taken in Bolivia on the same date by Gordon Newkirk of the High Altitude Observatory. The correspondence between the rocket and eclipse photographs is close, one complementing the other. On the originals it is clear that all features in the coronagraph record are extensions of features, sometimes very faint, appearing in the eclipse photograph.

The photometry of Newkirk's eclipse photograph is not yet complete, but the November 12, 1966, rocket results gave an essentially normal brightness for the corona. Figure 6 is an isophote map of figure 5, uncorrected for stray light, and shows that the true contrast of the conspicuous features is actually very low.

Figure 7 shows the polar and equatorial values of figure 6 plotted together with results of the previous flights. The solid lines are plotted from

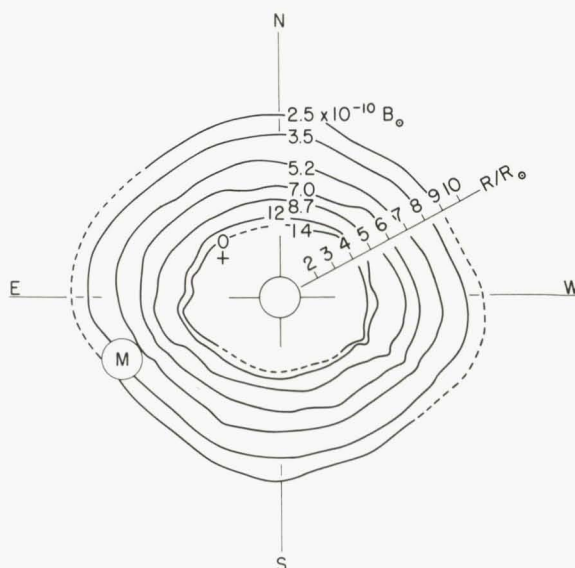


FIGURE 6.—Isophote map derived from coronagraph exposures of figure 5.

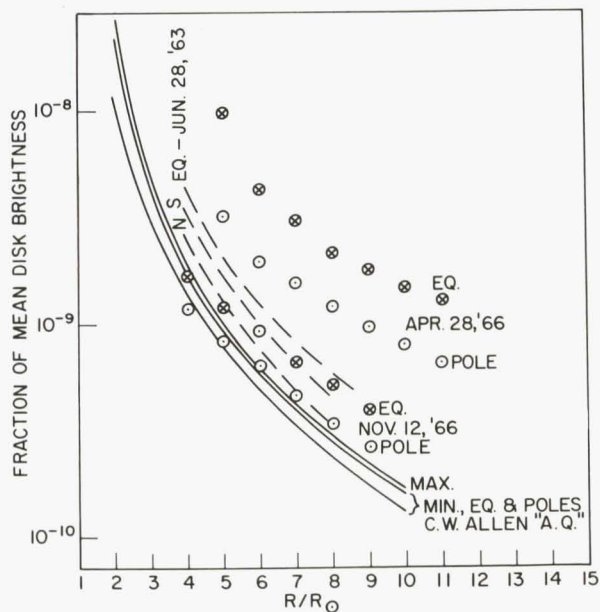


FIGURE 7.—Results of three noneclipse coronal brightness measurements compared with model corona (Allen, 1963).

Allen's "Astrophysical Quantities" (1963). The upper sets of circles are for equator and pole on April 28, 1966; the dashed lines are our 1963 data, and the lower sets of circles are our latest

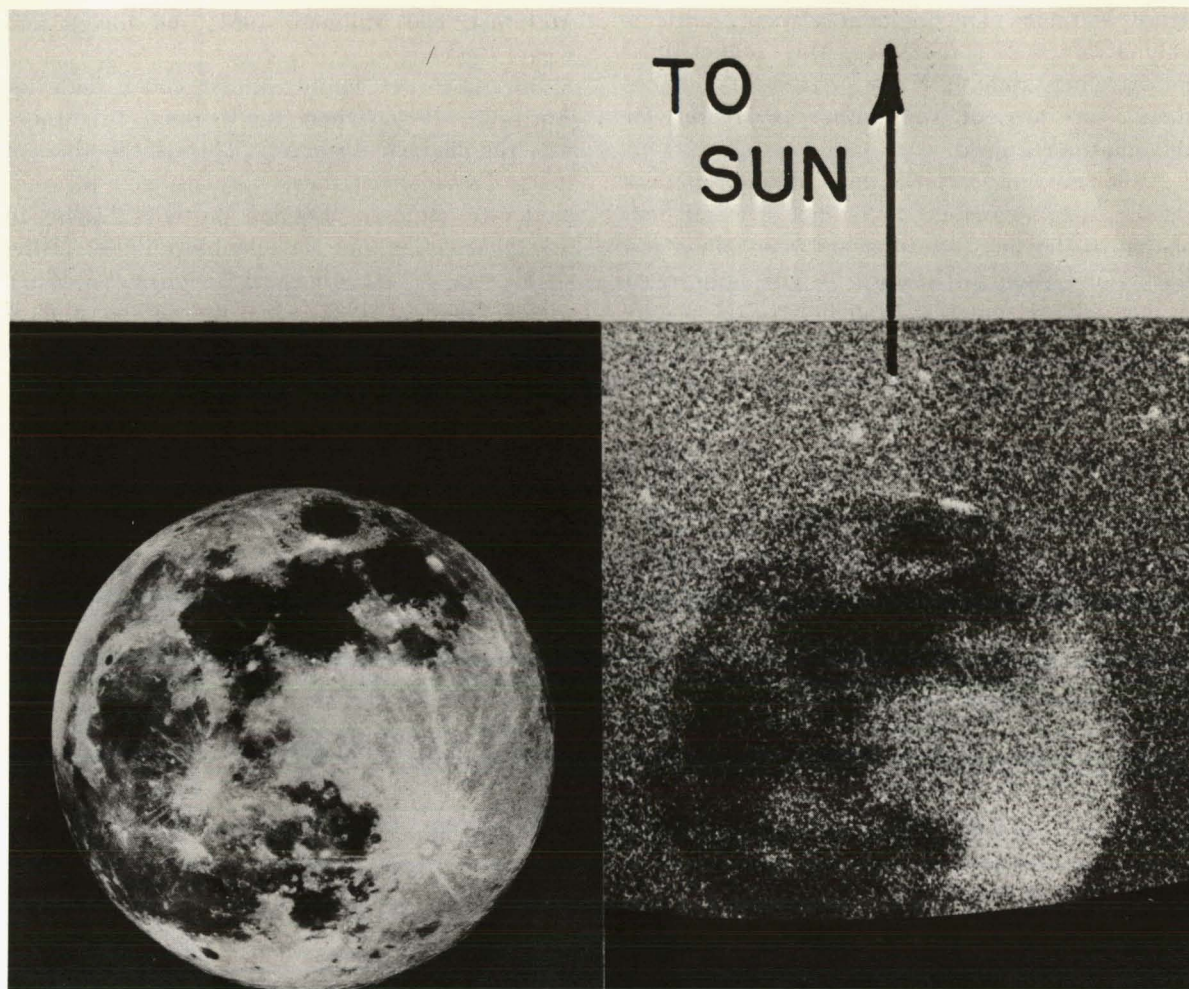


FIGURE 8.—Earth-lit Moon (right) at 2° elongation, 8 radii from the Sun, enlarged from 2-second coronagraph exposure showing, glint on sunward limb. To left is photo of full Moon illuminated at nearly the same phase angle as Earth-lit Moon.

data from November 12, 1966. Taking into account the trace of stray light at the outer position of the field, we have for November 12, 1966, an intensity distribution approximately the same as Allen's model.

Thus our latest results do not confirm the enhanced brightness of the two previous flights, and we have no need to assume that there is a particle population between Moon and Earth.² The result is also consistent with the image of

² A reflight on May 9, 1967, when the Moon was at an elongation of $5R_\odot$ showed no shadow, very few particles, and a corona of the same approximate brightness as on November 12, 1966.

the Earth-lit Moon, which shows no brightness anomaly across its face; the brightness ratios for selected light and dark areas are the same as those published for the full Moon.

Figure 8 shows an enlargement of the Moon image upon which our result is based. To the left is a photograph of the full Moon. In spite of the relatively poor resolution in our Moon image, it can be seen that the brightness distribution is qualitatively similar to that of the full Moon illuminated at nearly the same phase angle.

The bright area on the sunward edge of the Moon is a grazing reflection from a region near

Mare Marginis. The incident glancing angle is only $1.75^\circ \pm 0.25^\circ$; therefore, this region must be extremely smooth. If the surface tilts of more than 2° are present, some other explanation for this glint is required.

Although our coronal and Moon-brightness results for November 12, 1966, are self-consistent in showing little dust between Moon and Earth, and should therefore be given the most weight, we are reluctant to disbelieve the results of our two earlier flights. These results were obtained with optical systems and calibration procedures identical to the latter instrument and appeared uncontaminated with stray light. Therefore, our data suggest the possibility of a variable amount of zodiacal material between Earth and Moon.

One source of such variability may be the lunar libration regions. The L_4 and L_5 points, if they contained much material, would exhibit strong brightness enhancement by forward scattering when they passed between Sun and Earth. However, in none of our flights were these points closer to the Sun than 2 hours in right ascension.

A second possibility is that the Earth was passing through a meteor orbit belt or an influx of small particles at the time of launch. The launch month of June 1963 had an abnormally high value of radar meteor counts, both in the northern and southern hemispheres. (See

McIntosh and Millman, 1964; and Ellyett and Keay, 1964.)

We have not found similar radar data for April 28, 1966, when the coronal brightness was the highest observed. This is the time of the β Taurids, but these normally give a rather moderate number of small particles (27/hr) in the radar range and a negligible number in the visible range ("Handbook of Geophysics," 1961).

November 12, 1966, when the lowest value of coronal brightness was recorded, was during the time of the Northern Taurids. These may not increase the brightness because they normally produce only a small number of particles in both the radar range (14/hr) and the visible range (5/hr). (See "Handbook of Geophysics," 1961.) It may also be significant that on this date no particles were collected by Hemenway et al. on the Gemini XI spacecraft (see paper No. 24).

Whether or not the differences between coronal brightness recorded in the three flights are real, or are caused by some, as yet undetected photometric difficulty, can only be settled by further flights. Another solar experiment containing coronagraphs is planned for launch when the Moon is at 1° elongation from the Sun. This experiment will give a somewhat more sensitive test for cislunar particles than the photograph of November 12, 1966, when the elongation was 2° . As before, the test is relatively insensitive to absolute brightness calibration.

REFERENCES

- ALLEN, C. W., 1963. *Astrophysical Quantities* (2d ed., London: Athlone Press), 176.
 ELLYETT, C. D., and C. S. L. KEAY, 1964. *Science*, **146**, 1458.
 EVANS, J. W., 1948. *J. Opt. Soc. Am.*, **38**, 1083.
Handbook of Geophysics, 1961. U.S. Air Force, Geophysics Research Directorate (New York: The Macmillan Co.), 11.
 MCINTOSH, B. A., and P. M. MILLMAN, 1964. *Science*, **146**, 1457.
 NEWKIRK, G., and D. BOHLIN, 1964. *Applied Optics*, **3**, 543.
 PURCELL, J. D., and M. J. KOOMEN, 1962. *Sky and Telescope*, **24**, 197.
 VAN DE HULST, H. C., 1953. *The Sun* (G. P. Kuiper, ed.) (Chicago: Univ. of Chicago Press), 262.

15. Some Remarks Concerning the Zodiacal Light

C. HOFFMEISTER†
Sternwarte Sonneberg
Thüringen, East Germany

THE STUDY OF PUBLICATIONS SINCE ABOUT 1950 shows that my contributions to the topological problems of the zodiacal light have been vastly disregarded or misinterpreted. The reason may be that the decisive paper was published in the German periodical, *Astronomische Nachrichten*, during World War II. It is incorrect, when Behr and Siedentopf (1953) pretend, that I have tried to coordinate the inner parts of the zodiacal light to the plane of the orbit of Jupiter. The same statement is applicable to the contribution by Schoenberg (1952) in *Landolt-Börnstein*. Haerendel (1965) gives for the ascending node of the plane of symmetry the longitude 120° , which is certainly wrong. His figure 4 shows a value near 90° for the gegenschein, which is correct. The important new contributions by Beggs et al. (1964) are less concerned with topological problems, and the contribution of Elsässer (1954) deals with the innermost parts and the solar corona.

My results are derived from my own and others' observations at low latitudes (Hoffmeister, 1932). I estimated the points of maximal brightness on lines connecting two stars north and south of the ecliptic. Only when the angle between the ecliptic and the vertical did not exceed 15° were the observations used without correction for atmospheric extinction. For larger angles up to 35° corrections were applied, but 63 percent of the total of 4220 observations belong to the undisturbed group. The relation to the orbital plane of Jupiter—or the Laplace invariable plane, which in this case is practically the same—is only valid for the parts of the zodiacal-light matter beyond the orbit of Mars, optically that means the gegenschein region. The least-square solution gave $\Omega = 101.0^\circ$ and $i = 1.31^\circ$. For the inner parts of the zodiacal-light matter,

the nodal lengths are distinctly smaller; the values from my observations are between 33° and 74° ; those obtained from the old observations by Jones are between 44° and 71° . The inclinations are generally somewhat larger than in the remote parts, on the average:

Elongation from the Sun, deg	i by Hoffmeister, deg	i by Jones, deg
25 to 60	2.03	2.76
65 to 120	1.57	1.38

There seems to be no doubt that the distribution of the matter is determined by the orbits of the inner planets from Mercury to Mars. Taking the average inclinations for two adequate groups of planets one gets: Mercury—Venus—Earth, 3.46° ; Venus—Earth—Mars, 1.75° .

In my publication of 1940 the geocentric sine curves for points in different eastern and western elongations from the Sun are shown, from which the heliocentric elements were computed. The observations by Behr and Siedentopf (1953) are in good agreement with these results, so also are the slight northerly deviations from the ecliptic observed by Regener (1955) for the morning zodiacal light in November and the observations by Divari and Krylova (1963).

A second comment refers to the communication by K. Kordylewski (1966) on "A Lunar-Orbit Component in the Zodiacal Band." I can only make the statement that during the 3 years of observations in low latitudes I never observed any irregularities of the kind described in that communication.

A "mottled structure" of the zodiacal band could not have escaped my attention since I

was always on the watch for airglow phenomena, primarily because for my eyes the zodiacal band is by no means a difficult object and most observations were performed under the best possible conditions.

Of course, there occur superimpositions with the phenomena of increased airglow, but these are always of short duration, as the airglow stripes generally are drifting with the air currents at an apparent velocity of 0.5° to 1° a minute. This does not exclude the fact that there are also persistent stripes, remaining unchanged for an hour or so. On the other hand, the possibility of changes in the distribution of interplanetary matter cannot be denied; the general decrease of the phenomena of increased airglow

in frequency and intensity since the extremely high maxima of solar activity in 1947 and 1957 might be taken as an example. But may I nevertheless recall the fact that abnormal aspects of the zodiacal light are reported from the very beginning of the observations. There are the "pulsations" (Cassini, Jones, and Sedlacek), the fast moving waves (Bousfield), the temporary invisibility (Humboldt), the Moon zodiacal light, and the strange "parallaxes" observed by Schmid. In a lecture held at a conference in 1957 I treated the visual observation of the zodiacal light as a psycho-physiological problem (Hoffmeister, 1941, 1942, and 1958), and I think I have given at least some suggestions for understanding those unusual aspects.

REFERENCES

- BEGGS, D. W., D. E. BLACKWELL, D. W. DEWHIRST, and R. D. WOLSTENCROFT, 1964, *Mon. Not. Roy. Astron. Soc.*, **127**, 319.
- BEHR, A., and H. SIEDENTOPF, 1953, *Zeits. f. Astrophys.*, **32**, 19.
- DIVARI, N. B., and S. N. KRYLOVA, 1963, *Soviet Astron.—AJ*, **7**, 391.
- ELSÄSSER, H., 1954, *Zeits. f. Astrophys.*, **33**, 274.
- HAERENDEL, G., 1965, in *Landolt-Börnstein*, Vol. I (H. H. Voight, ed.) (Springer-Verlag, Berlin-Heidelberg-New York).
- HOFFMEISTER, C., 1932, *Veröff. Univ.-Sternw. Berlin-Babelsberg*, X, H. 1, 141 pp.
- , 1940, *Astr. Nachr.*, **271**, 49.
- , 1941, *Astr. Nachr.*, **271**, 204.
- , 1942, *Astr. Nachr.*, **272**, 131.
- , 1958, *Die Sterne*, **34**, 174.
- KORDYLEWSKI, K., 1966, *IAU Circ.* 1985.
- REGENER, V. H., 1955, *Astrophys. J.*, **122**, 520.
- SCHOENBERG, E., 1952, in *Landolt-Börnstein* (H. H. Voight, ed.) (Springer-Verlag, Berlin-Heidelberg-New York).

16. Infrared Observations of Thermal Radiation From Interplanetary Dust at the Eclipse of November 12, 1966 (Abstract)

ALAN W. PETERSON
University of Missouri
Columbia, Missouri

AND
ROBERT M. MACQUEEN
Johns Hopkins University
Baltimore, Maryland

Two successful independent eclipse experiments yielded positive results on the predicted (Peterson, 1963) existence of a thermal-radiation peak at the edge of the dust-free zone surrounding the Sun. Peterson's observations were made through light cirrus clouds at Huachacalla, Bolivia. A scan completely across the corona at 2.23μ was obtained during totality and one across the outer corona at 3.5μ immediately after totality. Preliminary results are presented elsewhere (Peterson, 1967).

MacQueen's observations were made with clear skies from Pulacayo, Bolivia. Scans to within $2R_{\odot}$ of the Sun's center were obtained along and perpendicular to the ecliptic. These data along with data from subsequent successful balloon measurements are presented elsewhere (MacQueen, 1967).

Both eclipse experiments revealed a distinct peak in infrared coronal brightness at $4.0R_{\odot}$ and a smaller peak at $3.5R_{\odot}$. These measurements show conclusively that the zodiacal-dust cloud extends to within $4R_{\odot}$ of the Sun. Preliminary absolute-intensity values for the $4R_{\odot}$ peak are as follows:

2.2μ	2.0×10^{-7}	$w\text{-cm}^{-2}\text{-}\mu^{-1}\text{-ster}^{-1}$	A.W.P.
2.2μ	5.5×10^{-8}	$w\text{-cm}^{-2}\text{-}\mu^{-1}\text{-ster}^{-1}$	R.M.M.
3.5μ	2.4×10^{-7}	$w\text{-cm}^{-2}\text{-}\mu^{-1}\text{-ster}^{-1}$	A.W.P.

REFERENCES

- MACQUEEN, R. M., 1968 (to be published in *Astrophys. J.*).
PETERSON, A. W., 1963, *Astrophys. J.*, **138**, 1216.
——, 1967, *Astrophys. J.*, **148**, L37.

Page intentionally left blank

17. Visual Observations of Lunar-Libration-Center Clouds

WILLIAM H. ALLEN AND WALTER J. KRUMM
Mission Analysis Division, NASA
Moffett Field, California

AND
ROBERT J. RANDLE
Ames Research Center
Moffett Field, California

KORDYLEWSKI OF THE CRACOW OBSERVATORY has reported (Kordylewski, 1961) observations of faintly luminous clouds at the triangular libration centers of the Earth-Moon systems—two clouds several degrees apart at the trailing libration center, L_5 , and a single larger cloud at the leading libration center, L_4 . An attempt to observe these clouds was made in March 1966 from the NASA Ames Research Center Convair 990 aircraft flying at 40 000 feet, hundreds of miles away from artificial lights. A typical flight pattern is shown in figure 1.

OBSERVATIONS

The visual observations were made by a group from NASA which included both experienced observers with a good knowledge of the night sky and younger men with good vision but naive with respect to the sky. The size of the observing group varied from four to eight, with at least one experienced observer aboard each flight. Before the series of flights, the inexperienced observers were shown, in the Foothills College planetarium, the constellations to be observed. At the beginning of each flight, they were again instructed on the constellations to be observed, then left on their own to find the nebulosities if any. The observers were instructed to use peripheral vision in the search. After his observing period, each observer plotted his observations on a star chart. The observers were adapted to the dark by wearing red goggles for a half hour or more before observing.

The positions of the libration centers were computed by considering them purely as Lagrangian points. The Moon, L_4 , and L_5 are assumed to form an equilateral triangle which expands and contracts as the Moon's distance from the Earth changes.

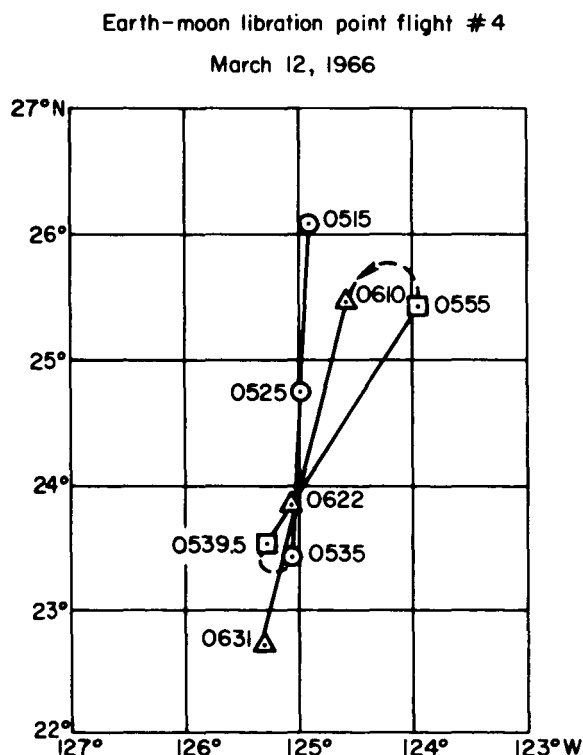


FIGURE 1.—Typical flight pattern of Ames Research Center Convair 990 aircraft.

The search for the L_4 cloud was made between moonset and morning twilight the nights of February 28 and March 1, 1966, and March 1 and 2, 1966. On the first flight, a nebulosity was seen by both inexperienced and experienced observers in an area roughly 5° north of the predicted position. On the second flight, a nebulosity was seen in approximately the same relationship to the predicted position. Nothing was seen in the starfield where the nebulosity had been reported the previous night. The gegenschein was seen by most observers on the first flight but was reported by only one on the second. The observations of the L_4 cloud are summarized in figure 2.

The search for the L_5 cloud was made on the nights of March 9 and 10, 1966, and March 11 and 12, 1966, between evening twilight and moonrise. On the first flight, a nebulosity about 5°

south of the predicted position was reported by most observers. On the second flight a nebulosity was reported, but by fewer observers, in the same relationship to the predicted position. Nothing was seen in the starfield where the nebulosity had been reported the previous night. The L_5 observations are summarized in figure 3.

The gegenschein was seen very clearly by all observers on the first night and seen less clearly, by fewer observers, on the second night. The size of the gegenschein as plotted by the observers correlated directly with their visual thresholds as measured later. Those with high thresholds plotted a small gegenschein, those with low thresholds plotted a large gegenschein.

Two observers from Lockheed Missiles & Space Company made observations independently of the NASA group on all flights (Simpson, 1967). The Lockheed observations

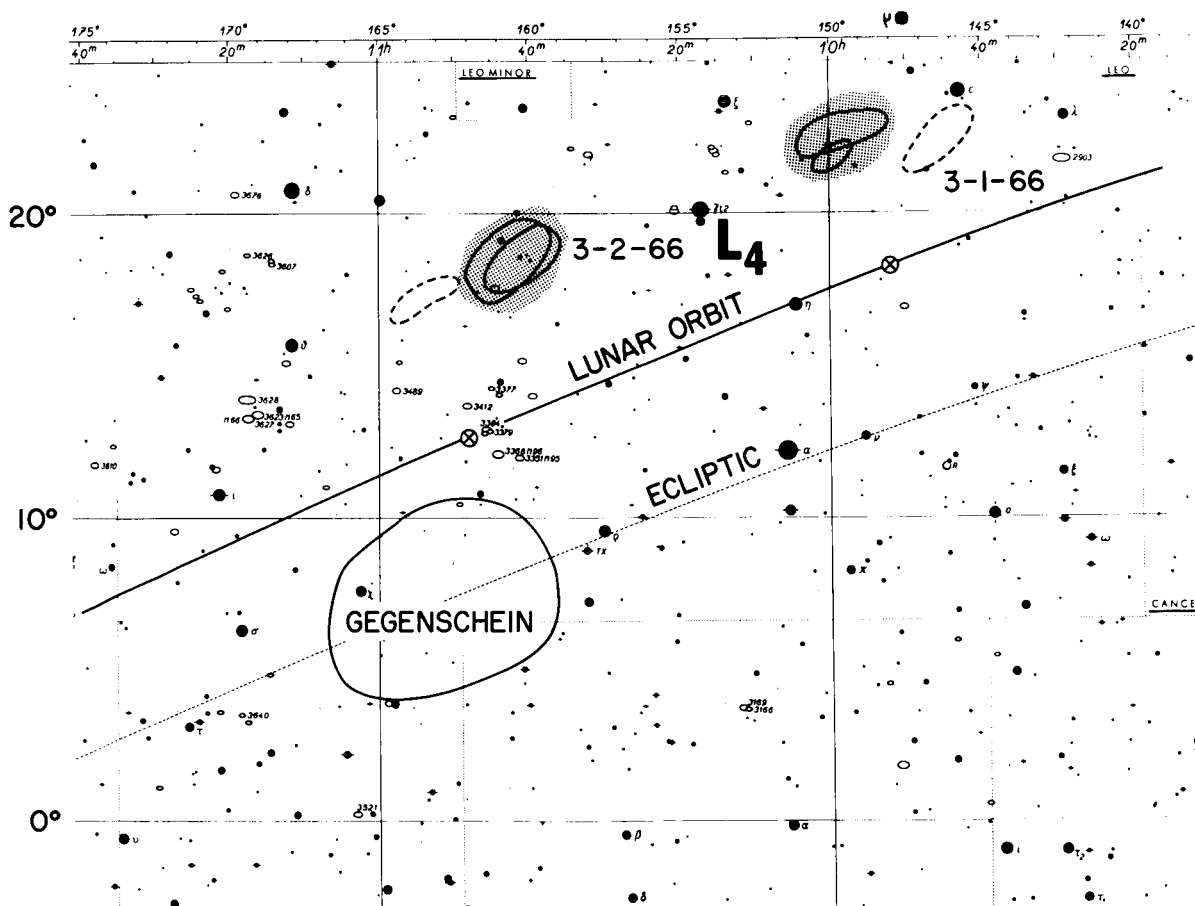
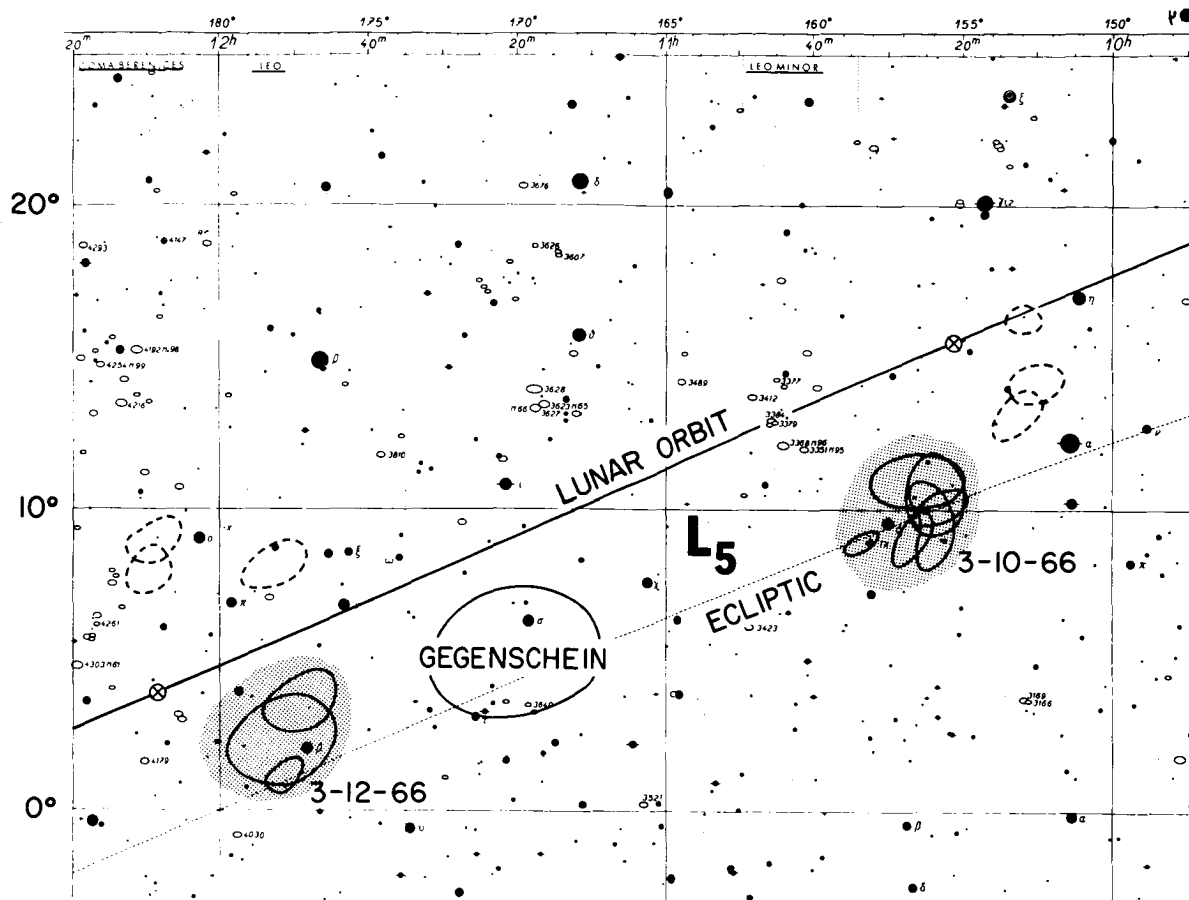


FIGURE 2.—Summary of observations of L_4 cloud.

FIGURE 3.—Summary of observations of L_5 cloud.

confirm the location of the luminosities as reported in this paper.

A second series of observations from the Convair 990 were made by one observer during the period May 20 to 29, 1966, during flights over South America. Only L_4 was surveyed since observation of L_5 was incompatible with scheduled flight times. Observations were made only during the new Moon phase when the clouds would have been visible only through forward scattering. The L_4 cloud was not sighted on any flight although the gegenschein was clearly visible on all flights.

VISUAL MEASUREMENTS

Four of the observers, two experienced and two inexperienced, were given a battery of vision tests. The results are shown in table 1. All observers have normal eyes for their age. Their

foveal thresholds are well above the luminances of the gegenschein; therefore, all the nebulosity observations and gegenschein observations were made scotopically.

Of main interest for the task of sensing dim-light phenomena are the first scores, absolute-brightness discrimination. These scores were obtained using the Douglas visual parameter tester, a device recently procured by NASA for use in orbital vision testing.

The absolute-brightness test is given by placing a variable spot of light on the viewing screen without background illumination of any kind. The spot is about the same diameter as a penny and is viewed from a distance of 28 inches. The brightness of the spot varied continuously from well below threshold to well above threshold. The subject was required only to press a button when the spot disappeared from sight and when

TABLE 1. — *Results of Vision Tests Given to Four Observers*

Apparatus	Test	Observer			
		1	2	3	4
Douglas visual parameter tester.....	Absolute brightness threshold, foot-lamberts—				
	Mean.....	64×10^{-6}	150×10^{-6}	220×10^{-6}	60×10^{-6}
	Range.....	0.00019 to ^a	0.00052 to 0.000075	0.00072 to 0.000068	0.00012 to ^a
	Standard deviation.	58×10^{-6}	90×10^{-6}	120×10^{-6}	20×10^{-6}
Landolt "C" ring chart.....	Acuity.....	20/12.5	20/20	20/25	20/20
Bausch and Lomb orthorater (values are Snellen equivalents).	Acuity—				
	Far (both eyes)...	20/17	20/20	20/20	20/20
	Far (right).....	20/17	20/20	20/25	20/25
	Far (left).....	20/17	20/22	20/25	20/20
	Near (both eyes)...	20/17	20/22	20/20	20/18
	Near (right).....	20/17	20/20	20/29	20/17
	Near (left).....	20/17	20/25	20/22	20/20

^a Beyond range of photometer.

it reappeared from a below-threshold value. When the subject pressed the button the brightness of the spot continued to increase (or decrease) for a time interval randomly selected from six possible intervals, that is, 0, 1, . . . , or 5 seconds. This is accomplished electronically and serves the purpose of preventing the subject from lapsing into a response "set" which would be possible with a constant delay in stimulus reversal. The psychophysical technique is that of a modified "method of limits" in which the stimulus is allowed to approach threshold from two directions.

The brightness values (in foot-lamberts) listed in the table are means based on 20 trials for each subject. Ten of these were thresholds taken for descending values of the stimulus and 10 were for ascending values. The range of values for each subject is also listed. While the range values are more stable figures than the means, they indicate, with the standard deviations, the relative reliability of the data.

There are some inadequacies in this particular brightness test that would contribute to the large

spread of scores, both within subjects and between subjects. One of these was the lack of a fixation point for the eyes when the stimulus spot disappeared.

Since the visual parameter tester is a newly conceived device, the extent of its contribution to the measured variability is not yet known.

The standard deviation for the absolute-brightness data may be used to make tentative probability statements regarding the chances of perceiving a penny-sized spot at a 28-inch viewing distance for given brightness levels (the spot would subtend a visual angle of about 60' of arc). One interpretation of the standard deviation is that about 68 percent of the data points will fall within one sigma (standard deviation) above and below the mean. Taking the mean as the point at which 50 percent of the points fall above and 50 percent below (assuming a symmetrical normal distribution, which may not be strictly true here) the probability of a given brightness value appearing as a threshold can be computed. For instance, for subject 4, whose standard deviation is 20×10^{-6} and whose mean

is 60×10^{-6} foot-lamberts, one sigma below the mean is 40×10^{-6} ft-L. This value will be subject 1's threshold 16 percent of the time. That is, 16 times out of 100 trials, this subject can detect a brightness value this low. For his mean, there is a 50-50 chance of its being the threshold value. Intermediate values may be found from the tabulated function for the normal-probability distribution.

In extrapolating from the visual-sensing qualities of these four observers to values of brightness for the libration clouds, these probabilities would have to be applied to any one observation. An absolute figure cannot be given because the human sensory system displays the characteristics of a probabilistic processor of information.

The acuity data are not strictly pertinent to the visual task of the four observers. They are shown merely to indicate the general level of excellence of their eyes, at least for that variable. The vision tests indicate that all the observers tested were capable of detecting luminance at gegenschein levels ($\sim 60 \times 10^{-6}$ ft-L).

DISCUSSION

To raise the luminance of isotropically scattered light at 1.1 AU to gegenschein levels would

require a local concentration of particles by a factor of 100 (Ingham, 1962). Since the observed luminosities were in the gegenschein range, it can be assumed that if the nebulosities are libration center clouds, the concentration factor must be near 100.

Because the observers used only scotopic vision with luminances near threshold, the reported boundaries of the luminosities have little validity. However, the reporting of different sizes of luminosities by observers with different absolute thresholds indicate that the luminosities were not sharply bounded.

CONCLUSIONS

In summary:

- (1) Luminosities were observed near the predicted L_4 and L_5 positions.
- (2) The observed luminosities maintained the same positions relative to the predicted positions on successive nights.
- (3) A local particle concentration by a factor of 100 would be needed to produce the observed luminosities by isotropic scattering.
- (4) The physical mechanism producing the observed luminosities is not sharply bounded.

REFERENCES

- INGHAM, M. F., 1962, *Space Science Reviews*, **1**, 576.
KORDYLEWSKI, K., 1961, *Acta Astronomica*, **11**, 165.
SIMPSON, J. W., 1967, *Physics Today*, **20**, 39.

Page intentionally left blank

18. Lunar-Libration-Cloud Photography

J. WESLEY SIMPSON

*Lockheed Missiles and Space Company
Sunnyvale, California*

THIS PAPER presents a brief description of the work done during the last 5 years in the study of the lunar libration clouds at the Locksley Observatory. Our interest started with Kordylewski's announcement (1961a, b) and the receipt in 1961 of a letter from Kordylewski by one of our colleagues at Lockheed, describing his work. We started out several months later in our search for clouds located at the Lagrangian points in the Earth-Moon system. During the balance of 1961, and all of 1962 and 1963, our efforts met with failure. We tried various types of ephemerides, including an ephemeris by Kordylewski and an ephemeris taken from an existing lunar program at Lockheed.

It became apparent in the fall of 1963 that we, along with other observers, were failing to take into account some constraint or constraints which prevented our success. Working in reverse, the writer, assisted by Ray G. Miller, established a series of parametric constraints which severely limited both the number of observing windows and the duration of each window. The first time we were able to apply these constraints was on the night of January 3-4, 1964, when we saw the L/5 libration cloud for the first time. An experienced astronomer with no knowledge of our work joined us at the Locksley Observatory that evening. After a period of using the telescope, we went outside where he was given a detailed star chart and a region some 20° by 20° in area was pointed out. He was asked if he could find anything in this region which was not on the chart. After searching the area twice, he stated that there was nothing in the area except a very small cloud which should blow away soon. When he was asked to show where it was located, he pin-

pointed the exact area in which we had plotted the L/5 cloud. The next night was cloudy but the nights of January 5-6 and 6-7 were clear and we again observed the L/5 cloud, plotted its position, and filled out data sheets. Thus we obtained positive observations on 3 of 4 nights. *It was most interesting to us to see the clouds move among the stars at a daily rate closely approximating that of the Moon.* During the next several years we continued to observe, plot, and record both the L/4 and L/5 libration clouds on clear nights.

On February 13, 1966, we took our first photographs of a libration cloud. While preliminary analysis convinced us that we had been successful in obtaining a photograph, a complete analysis had to wait until we completed a study program with NASA Ames Research Center (ARC). ARC announced a series of five flights to be made in their Convair 990 laboratory to observe and attempt to photograph the libration clouds. The first three flights were scheduled for February 28-March 1, March 1-2, and March 2-3, 1966. These flights were intended for observation of the L/4 clouds. Observations of the L/5 clouds were scheduled for the nights of March 9-10 and 11-12, 1966. All flights were made at an altitude of 40 000 feet several hundred miles off the coast of Lower California, far from the lights of any city. The first flight was canceled shortly after takeoff as a result of equipment trouble. On the March 1-2 and 2-3 flights we saw the L/4 clouds. The L/5 clouds were seen on both March 9-10 and 11-12. A composite of our observations is shown in figure 1. On the first night, we saw L/4 in the center of the sickle in Leo. The second night revealed that the cloud had moved to a new

LUNAR LIBRATION - CLOUD VISUAL OBSERVATIONS

By J. W. Simpson and R. G. Miller

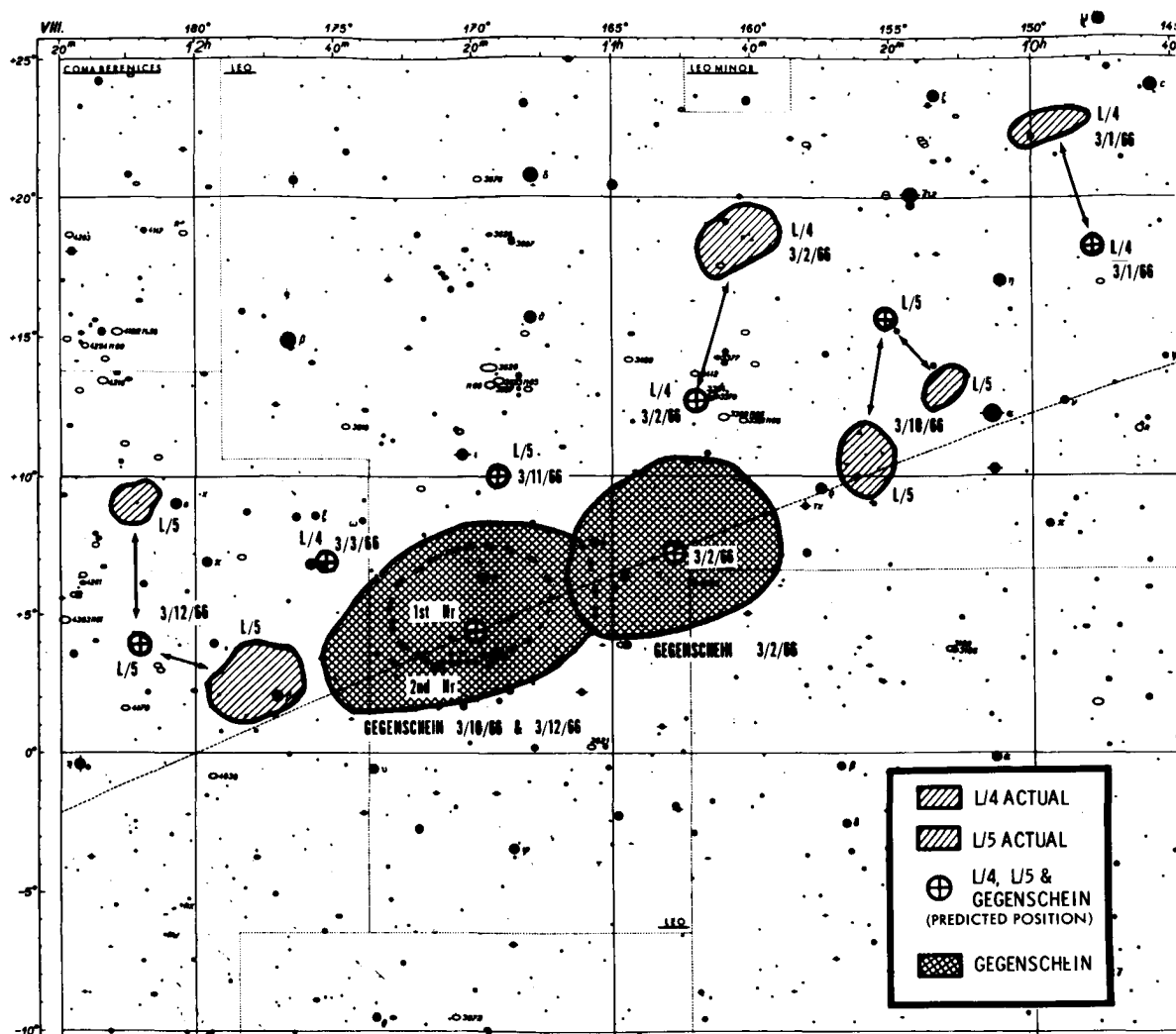


FIGURE 1.—Composite chart of libration-cloud and gegenschein observations made on Convair 990 flights in early March 1966. Note departure of actual positions from predicted positions.

position and the center of the sickle of Leo contained nothing but stars. We also plotted the position of the gegenschein. The L/5 area contained two clouds, as seen frequently in the past. Figure 1 shows the predicted and observed positions along with the estimated size and shape of the clouds at the time of observation. These observations were also confirmed by Allan Gillespie, a guest observer from Stanford University. We have no explanation at this time for the shapes of the clouds or their positions. We have made a

number of observations which show the same behavior, and these are presently under study.

Figure 2 is a typical example of a photograph taken from the Convair 990 aircraft. More than 50 photographs were taken during the flights and, regardless of exposure length, they all exhibited the same pitch, yaw, and roll effect of the airplane. The longer exposures showed darker images and in some cases extensive motion effects. Even if these negatives had contained an image of libration material, it would have been indistinguish-

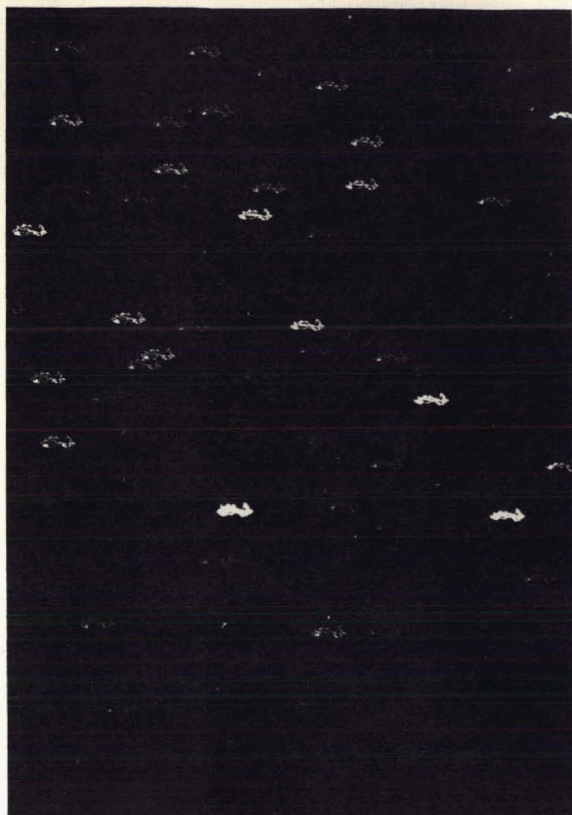


FIGURE 2. — Typical negative made during attempted libration-cloud photography from Convair 990 flights. Camera mounted on a very heavy mount. Note excessive motion during 90-second exposure. Longer exposures increased motion shown. Shortest exposure for a successful libration-cloud photograph taken from Earth is 4 minutes using film working at a speed of ASA 4000. A 2-minute exposure of the gegenschein made from Gemini V showed excessive spacecraft motion.

able, as the aircraft motion would have retraced the image a number of times. Thus, in making either densitometer traces of the negatives or photometer scans of the region, definite contour lines could not be established because of multiple-image retracing. Figure 3 is a plot from a photograph made with a ground-based equatorially mounted, synchronous motor-driven telescope. Contour lines of the clouds were determined with considerable accuracy. A photograph of the gegenschein taken from Gemini V shows the same motion effects as those of the airplane, but they are even more accentuated. Thus we believe that until a truly stabilized platform is built, such as that proposed for the Apollo Applications Pro-

gram Astronomical Telescope Mount, ground-based photography is the only acceptable means for gathering this type of data. The aircraft is most satisfactory for fast exposures, such as those used for eclipses, but it does not lend itself well to libration photography.

VISUAL OBSERVATIONS AND RESULTS

The two L/5 libration clouds photographed were independently located and observed by the author and L. L. Schmid in compliance with parametric constraints devised to facilitate the location of the "clouds." The author plotted the location of the two "clouds" among stars visible to at least 6.5 magnitude. Both the position and contour (shape) of the "clouds" were plotted as accurately as possible and were checked and confirmed by L. L. Schmid.

The pertinent facts of this night's observation were recorded on Locksley Observatory record forms, which are used during libration-cloud observing periods. These data sheets include the time (UT), predicted position, observing conditions, "cloud" data, type of equipment used, and much other statistical data relevant to subsequent data reduction.¹ A photographic reproduction of the appropriate Skalnate Pleso star chart is used and shows both the predicted position and the actual observed positions (fig. 3). The presence of faint stars enables the observers to plot the positions and contour shapes quite accurately. Normally, visual observations precede the placement of the telescope, electronic gear, photographic equipment, and the subsequent test run. This is to allow displacement of the visually observed "cloud" from the center of the field to be photographed and, thereby, eliminate vignetting effects. During the visual-observation period on February 13, 1966, the L/5B² "cloud" was seen first. Even though it was smaller than the L/5A "cloud," the adjacent sky density presented a contrast with the "cloud" which attracted both observers' attention.

The following conclusions can be drawn from the visual observations made on this and past observation dates:

¹ The gegenschein on this date was outside the camera's field of view and was located more than 40° from the L/5 area.

² The smaller of the two "clouds" is designated "L/5B."

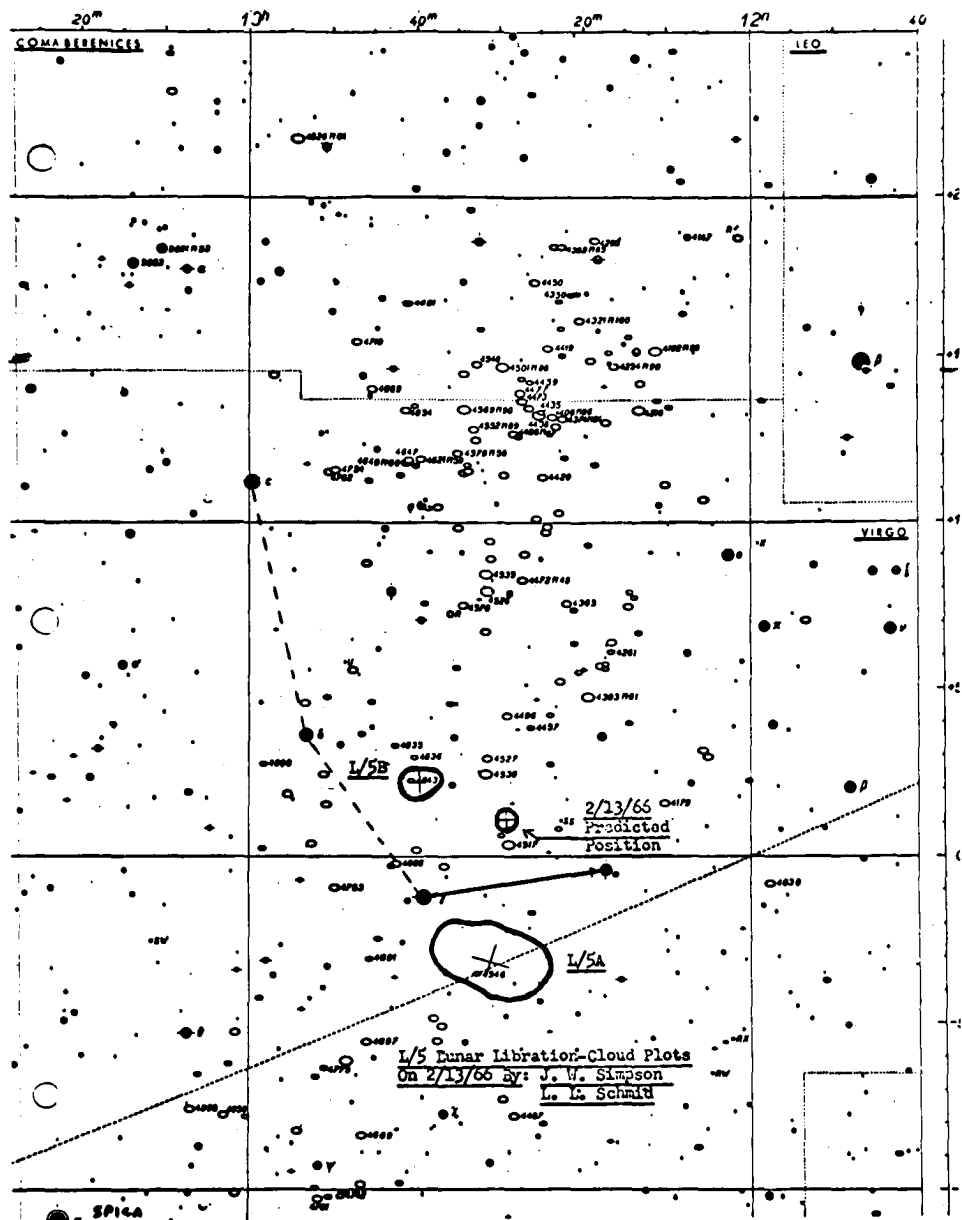


FIGURE 3. — Libration-cloud visual plot made prior to photography on February 13, 1966.

(1) Accurate plotted positions and contours can be made by experienced observers when work is performed in conformance with parametric constraints and a detailed star chart is used for plotting.

(2) Thoroughness in preparation for observation, completion of all record forms, and allowing adequate time for the observer's eyes to adjust to the maximum night-vision capability are of great importance.

(3) The plots made on February 13, 1966, confirm previous observations which have revealed the presence of more than one "cloud" in the L/5 libration-point area. Kordylewski has obtained the same results.

LIBRATION-CLOUD PHOTOGRAPHY

Photographic attempts to record the faint and elusive libration clouds were performed in accordance with procedures established at

the Locksley Observatory. The processing technique, methods of negative examination, and analysis are of sufficient interest to justify their description in the following sections.

Photographic Processing

The films were developed immediately after returning from the Locksley Observatory to minimize possible degradation in the faint latent image of the libration cloud. Processing was performed under rigid time and temperature conditions. A specially devised technique of chemical film speed enhancement was used in the development. The ASA rating of Eastman Plus-X panchromatic film was boosted from 125 to a value in excess of 4000. Whereas grain size normally increases as the film speed is increased, a reversal of this effect is obtained through the Locksley Observatory chemical hypersensitization. As will be seen subsequently in this report, the grain size was very small and the distribution was uniform. These factors were exceedingly important in the success of the photographic results. Evaluation of resolution gave an approximate value of 400 lines per millimeter, as compared with a normal value of approximately 110 lines per millimeter.

Negative Examination and Preliminary Analysis

The negatives were submitted to two Lockheed Missiles and Space Company (LMSC) laboratories for microscopic examination. The first negative examined was one that had been exposed for 8 minutes and was considered to have the best possibility of showing a lunar-libration-cloud image. The negative was examined under a 10-power magnifier and a 120-power microscope and showed fine grain structure, without silver-grain clumping. This area is definitely a difference in silver density and not caused by chemical stain or emulsion defect.

Another laboratory examined the same negative and a second negative exposed for 5 minutes on February 13, 1966. Control negatives taken on March 16, 1966, were also analyzed. The six control negatives were taken of the area in which the libration clouds were observed on February 13, 1966. On the 2 nights when control negatives were taken (March 14 and 16), the exposures and region photographed were the same as for

those taken on February 13, 1966. The control negatives were subjected to the same processing as those exposed on February 13. These negatives were examined under 800 \times magnification with a Bausch and Lomb metallograph research model. Microphotographs taken at 800 \times show grain distribution to be even, with very little silver-grain clumping. The largest size grain was of the order of 0.0007 inch, while the smallest was of the order of 0.000004 inch. The average grain size appeared to be of the order of 0.00015 inch. Each of the three negatives was examined thoroughly by a photomicrography specialist.

Visual Projection Analysis of 8-Minute-Exposure Negative

Examination by visual projection was performed by four independent teams of specialists. In each case, team members individually and collectively agreed that they could trace the outlines of the lunar-libration clouds. The larger cloud, L/5A, covered a greater area and the progression of density changes was gradual. The smaller cloud, L/5B, exhibited a smaller, fainter, but definable area. Adjacent density contours exhibited a sharper degree of contrast, when compared with the L/5A cloud.

Examination of the projected image of the 8-minute-exposure negative with a 35-mm projector, using a 100-watt projection lamp, revealed no detail.

The negative was then placed in another 35-mm projector and the images were projected on a beaded screen. A faint pattern was barely discernible; some of the contour lines were lost in the beading on the screen. When projected on a smooth white surface, the images and contours were visible enough that a trace of the pattern was made from the projected image. When the projector illumination was reduced from 500 to 300 watts, some of the detail was lost. All team members were able to see the libration-cloud outlines. A member of each team made a trace or sketch. At the Physical Sciences Branch of the Lockheed Palo Alto Research Laboratory, one team member could see the silver-image density changes and some contour markings on the negative with the unaided eye.

It should be pointed out that in every case, where positive visual projection results were

achieved, the viewers possessed highly trained eyesight. According to D. E. Buttrey of the Palo Alto Research Laboratory:

Visual recognition of these projected images is a function of the "trained eye" and not that of visual acuity. In other words, a person having normal eyesight, by standard optical tests, would not necessarily see the images, unless his eyes had been conditioned by sustained photo interpretation of faint objects. This would also include minute changes in coloration and shading, or the recognition of faint minute detail not normally visible to the untrained eye.

The team performed an additional test by moving the projector slightly. In each case, the star images and the cloud outline moved together on the screen. Moving the screen did not affect either the star images or cloud outline (fig. 4).

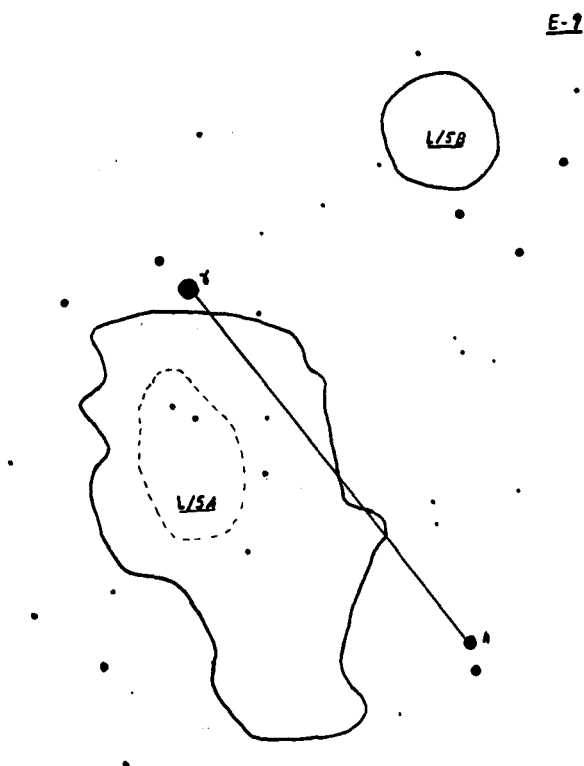


FIGURE 4. — Libration cloud L/5 traced from projected image of 8-minute ground-based exposure.

PHOTOGRAPHIC REPRODUCTION

When initial photographic reproduction was performed, it was quickly ascertained, due to the faint nature of the libration-cloud images, that black-and-white contrast prints blocked out the fine detail. The best results were obtained by printing to a "gray tone." One of the 8 by 10

semimatte prints produced faint outlines of the L/5A cloud, which was not reproducible for publication.

The negatives were then turned over to printing technicians who performed the enlarging phase of the analysis. The first effort was an enlargement of the entire 35-mm negative to a print size measuring nearly 50 inches in length (an enlargement of approximately 35 times). The print was exposed and developed for "gray tone." The star images were round, indicating precision tracking throughout the 8-minute exposure. Contour lines for the L/5A cloud were discernible to the trained eye. The last enlargement phase consisted of making both 8 by 10 and 11 by 14 Kodalith positive transparencies. Density-gradient contour lines are discernible to the trained eye on at least one of the 11 by 14 transparencies.

Photographic Results

An analysis of the negatives taken on February 13, 1966, and control negatives of the same star-field areas, on subsequent dates, shows:

- (1) All negatives, upon completion of development and drying, were free from scratches or emulsion defects.
- (2) All negatives contain definite and measurable silver-image density variations within the area in which the libration clouds were visually sighted and plotted.
- (3) Stars were identified to at least magnitude 9.4, using AAVSO charts for the variable star R Virginis (123307).
- (4) The gegenschein was more than 40° removed from the center of the field and was not recorded on any of the negatives.

DENSITOMETRY

The final confirmation that we had obtained lunar-libration-cloud photographs came as the result of extended analysis of densitometer traces made of the various negatives. This work was performed in the Physical Sciences Section of the Lockheed Palo Alto Research Laboratory. Two groups of negatives were examined in detail. The first group consisted of three negatives taken on February 13, 1966, which were believed to contain libration-cloud images. The second group consisted of six control negatives taken

on March 14 and 16 of the same region at a time when it was known that the libration clouds were not present. In this latter group, all the negatives were taken of the previously photographed region. The exposure and development techniques employed were as nearly identical as possible. All six control negatives, when scanned with the densitometer, produced the same result—no libration clouds present.

In the case of the 8-minute exposure, the presence of real data is discernible to the practiced eye. One has only to hold a mosaic of successive runs or traces through the libration area and look along the traces to see where the excursions appear. Establishing a mean density value for each segment of a given trace permits the analyst to establish density data points for each segment on all traces. The average analysis covered 1 cm^2 of the negative of emulsion surface in the libration-cloud area. The scanning of this 1 cm^2 required 14 consecutive traces or runs. Each trace is displayed in a span covering $19\frac{1}{2}$ incremental segments of approximately 13 mm. In all, more than 276 incremental-segment "mean-value" data points were established for the negatives on which libration-cloud phenomena were believed to exist. From this abundance of data points, the analyst had a choice of either drawing in density plateaus and joining plateaus of equal value, or simply evaluating and drawing in contour gradient lines of equal density. Both methods were employed with the same basic result.

The main exhibit for the densitometry consists of a composite of 14 runs on the 8-minute-exposure negative, with median values determined for each 10 mm increment of scan time for each trace. These median values were evaluated, density-gradient spread limits established, and the resulting contour pattern drawn (fig. 5). A similar pattern was drawn for the 5-minute-exposure negative. Traces were run through the negatives at 45° and 90° angles to the original trace. Additional traces were made by using different slit widths, slit lengths, and scan speeds. These traces revealed the same basic contour configurations, when reduced to a common base value. A photographic reduction was made and super-

imposed over the visual plots. The close agreement is clearly shown in figure 6.

Upon completion of the densitometry analysis, the final summation of the results are best expressed by D. E. Buttrey:

The establishment of the pattern of the libration clouds has been determined from a spatial matrix of densitometer tracings run through the data film. The orientation of the patterns was determined with reference to observable stars in the Gamma and Eta Virginis area. The differential density variations above developed fog background, attributed to the libration clouds, were of the order of 0.012 to 0.028. A density difference of 0.02 corresponds to a change in transmission of the blackened emulsion of approximately 2 percent, which change is known to be about the threshold of the sensitivity of the human eye to variations. And indeed, trained eyes were able to detect the existence of the patterns on the data film before the densitometer tracings yielded tangible evidence of the libration-cloud patterns. The fact that the data film showed the stars to be "point light sources" for an exposure time of 8 minutes is indicative of the accuracy with which the Earth's axial rotation was precisely accounted for. No motion of the "cloud pattern," with respect to the two stars (Gamma and Eta Virginis) was observed either visually or photographically covering an observation period in excess of 1 hour.

The following conclusions were derived from the densitometer analysis:

(1) For the 8-minute-exposure negative, the lowest incremental density spread was 0.111. The highest excursion gave an incremental spread of 0.134 for a mean difference of 0.023. Partial-spread trace values were of the order of 0.138 or a difference of 0.027. These values, while not much above the theoretical 0.02 value given for the density-change resolution of the naked eye, were nevertheless quite appreciable to all of the analysts.

(2) An evaluation of the visual acuity of the three analysts who made traces from the projected image of the original negative established that the 0.02 value is probably for the top portion of those having average untrained eyes. All three of the individuals who made the traces from the projected images exhibited a consistent density-gradient-excursion-recognition value ranging from 0.010 to 0.014. In each case, the analyst has had years of experience in recognizing minute changes in detail, shades of coloration or density, and identification of faint-image objects. All the team members, including those who did not make trace patterns from

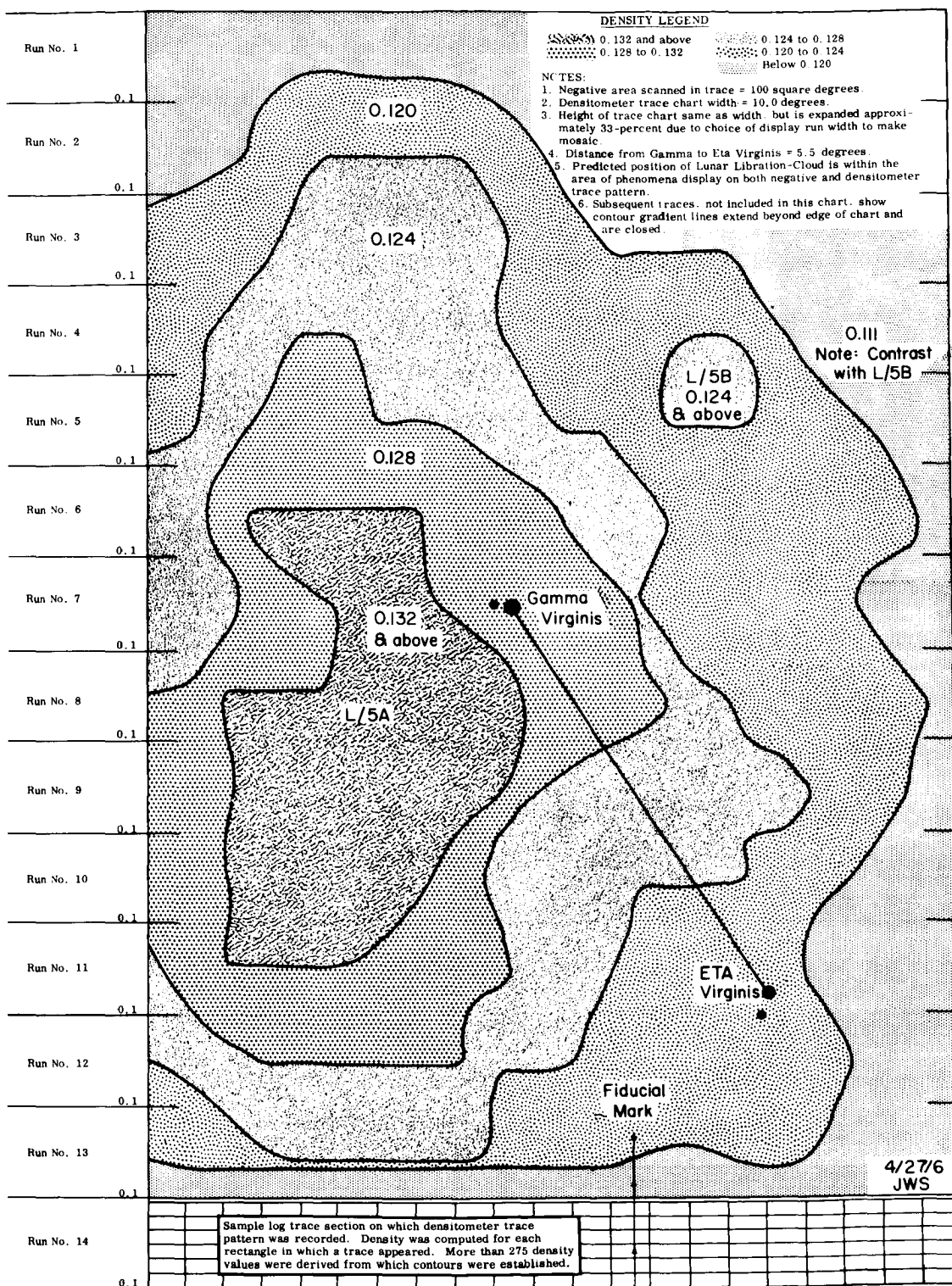


FIGURE 5. — Density-gradient contour plots of L/5A and L/5B libration clouds taken from densitometer traces of 8-minute ground-based exposure. This is a preliminary trace and subsequent traces on this and other negatives showed contours to be closed.

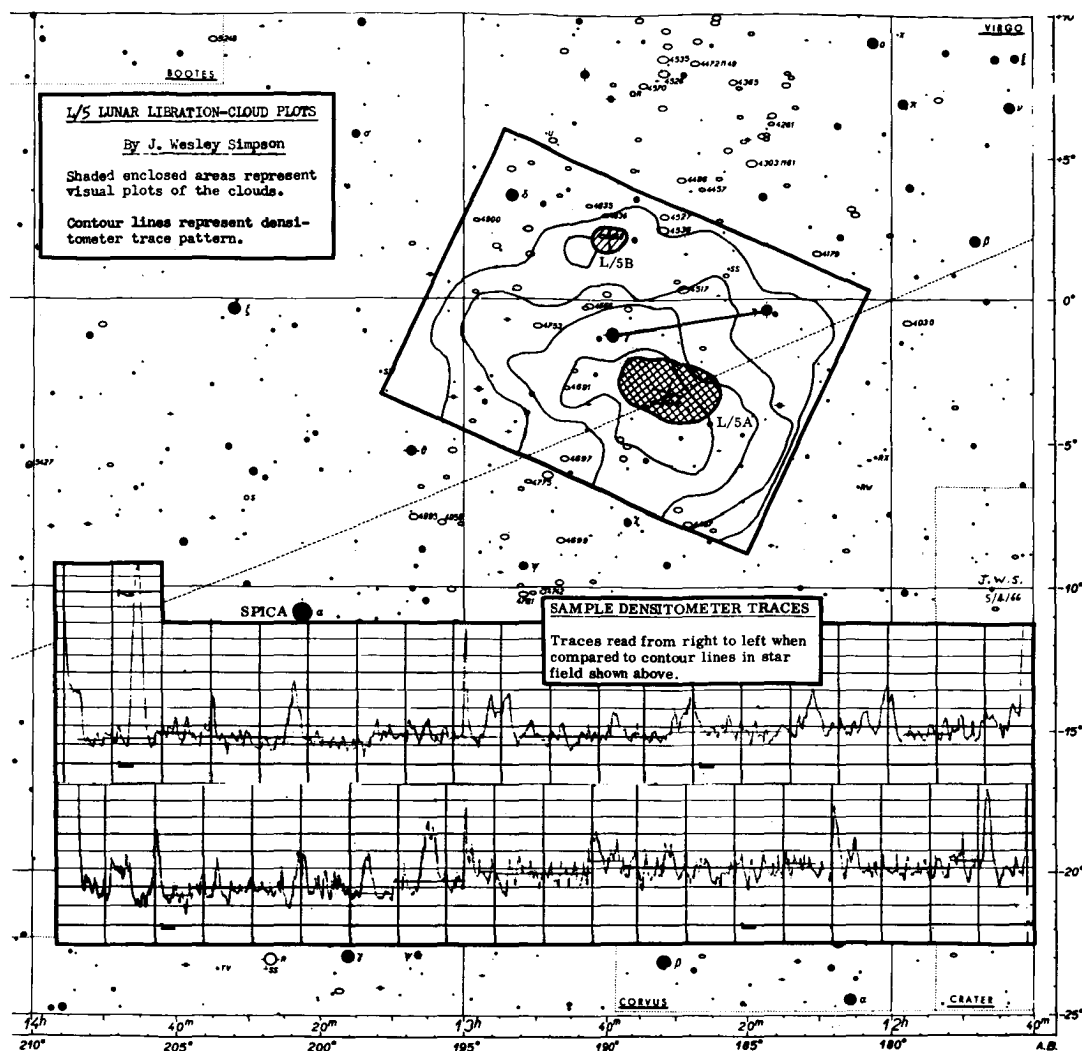


FIGURE 6.—Overlay of visual plot and densitometer trace. Densitometer trace reduced to same scale as visual plot made on star chart.

projected images, saw the libration-cloud pattern on the smooth white screen. These team members also exhibited a density-change-recognition value ranging from 0.010 to 0.015.

(3) Densitometry covered an area of 10° by 10° , or 100 square degrees, as limited by the Cu-Be 1 cm² cutout strip placed on top of the slide. Subsequent runs, using a cutout of 1 by 1.5 cm, showed that the contour-gradient density lines, which are not closed in the prime exhibit, extend beyond the original 1-cm² area scanned and that the contours are closed. Time prevents making a complete mosaic. The purpose of this analysis is only to establish the fact that a

libration-cloud photograph has been obtained. A final report, including additional data, will contain a more detailed analysis.

(4) Densitometry of the negatives showed the presence of real data within the photographic emulsion. *These data are discernible above the values established for sky and development fog.*

(5) When placed within established density-gradient-contour-value limits and established in increments of 0.004 steps, sensitometric data produced definite and observable contour lines.

(6) Identical analysis of contour negatives, taken of the same star field on subsequent dates and subjected to identical processing,

showed a complete absence of readable data associated with the libration-cloud density phenomena.

(7) Regardless of the scan rate or scan angle, the libration-cloud negatives show the presence of real contoured density-gradient data.

(8) In the 100-square-degree area of emulsion scanned by densitometry, several nebulae and nearly 40 stars, including SS Virginis, were positively identified.

LIBRATION-CLOUD CONTOURS

While contours were lightly penciled in for various runs on the negatives, the contour for the 8-minute exposure gave the most clearly definitive contour-gradient lines. Figure 5 shows the density-gradient contour-plot diagram of our choice. While this does not demonstrate a closed pattern, subsequent runs do show that the contour lines, open on the left-hand edge, are closed lines with the density falling off to normal sky brightness.

More than 276 separate density averages were used in establishing the contour lines shown in the prime exhibit. To avoid cluttering the picture, these are not shown as dots in the pattern. For each of the successive 14 runs, covering some 100 square degrees in the sky, straight-line plateaus were drawn and the end points joined to form a contour pattern. This contour agreed closely with that of the method used, from which the diagram resulted. Lines were drawn through points of equal density, but there were a few cases where a lower density value was included within a higher density contour. This number was of no great significance and both the author and R. G. Miller agreed on the choice of the contour lines. While the points through which lines of equal density were drawn were the choice of the analyst, the picture is considered typical.

Density-gradient contour lines were drawn for every 0.004 value, as shown in the legend in the prime exhibit. This value seems to fall out of the density values presented among the total density excursions derived. This value is well within the limits of the densitometer sensitivity and represents approximately one-third of the average density excursion derived

from the traces by analysts from projected image (0.012).

It is interesting to note that the surrounding density of the L/5B cloud represents an excursion of only 0.004 yet this smaller of the two clouds was first to be seen visually by the two observers on February 13, 1966. It is probably due to the low adjacent density to the right of the cloud that this could stand out so clearly. The density of the L/5B cloud is 0.124 and slightly above. Less than a degree of arc to the right, the density is 0.120 and then falls to 0.111. The L/5A cloud, within the 0.124 density contour, is approximately 10 times as large as the L/5B cloud of equal density. However, the change through the adjacent density in steps of 0.004 is so gradual that it was not seen at once.

It is believed that the libration-cloud area may well be a large diffuse area with "density depressions" found within higher density gradient contours.

RELATIONSHIP OF CONTOURS, PATTERN CENTER, AND SIZE TO VISUAL PLOTS AGAINST STAR FIELD

Visual observations showed two distinct libration clouds and no discernible intervening libration-cloud material, but the densitometer traces showed that both "clouds" were encompassed in a vast nebulous area of measurable silver-image density. While the most dense area within L/5A (0.132) is irregular in shape, two centers were chosen. One center was based on rounding out of the contour and the other by disregarding the "necked-in" area adjacent to Gamma Virginis. The difference in the two positions amounted to approximately $\frac{1}{2}^\circ$. The two centers were labeled L/5A-C-1 and L/5A-C-2 for centers 1 and 2, respectively. Center L/5A-C-1 was only $1\frac{1}{4}^\circ$ from the center of the visually plotted center of L/5A. Center L/5A-C-2 was only 0.8° from the center of the visual plot of L/5A.

In the case of L/5B, the densitometer-pattern center was displaced from the center of the visually plotted center by approximately $\frac{1}{3}^\circ$. The visually plotted area differed from the densitometer trace area by less than 0.1° . It is the opinion of the LMSC Lunar Libration-Cloud Research Team that the visual plots and densitometer-trace contours agree very closely.

Figure 6 shows the blocked-in area, which was subjected to densitometry analysis. To prevent confusion from an excess of data on the star plot, only the densitometer-trace pattern areas are shown. The star chart presents dimensions in the approximate ratio of 1:3.7 in the area of interest to the densitometer trace.

The final trace for the 8-minute exposure indicates a cloud length of approximately 40 000 miles. More definitive figures as to length, width, and area are being determined. Actually, the visually observed and plotted center positions are even closer to the L/5A and L/5B densitometer-trace pattern centers than stated when the vertical scale is reduced by one-third. This vertical elongation is due to the choice of run widths used in making up the densitometer-trace mosaic. It is interesting to note that the visual plots were made some 5 weeks prior to the start of the densitometry analysis. The finally accepted mosaic was made approximately 2 months after the visual observations. The position accuracy of the visual observation centers is less than 1° from the measured photographic centers.

CONCLUSIONS

Based on the evaluation by four teams, from the Lockheed Missiles and Space Company, visual, photographic, and densitometry analyses have established the presence of lunar-libration clouds.

The opinion of all the analysts involved in this series of tests is that three negatives contain silver-image density phenomena within their respective emulsions. These negatives, which are identified by star-field location, date, and time, are photographic confirmations of the visually observed L/5 lunar-libration clouds plotted on February 13, 1966.

As to the visual confirmation of the libration clouds, more than a dozen observers have seen them on various dates during the past 3 years we have been observing and plotting them. In paper No. 17 by Allen et al., it is reported that both trained and untrained observers saw the L/4 and L/5 areas on four dates in March 1966 from the Convair 990 aircraft at an altitude of 40 000 feet. He refers to them as "nebulous patches" near the predicted libration points.

REFERENCE

- KORDYLEWSKI, K., 1961, International Astronomical Union (IAU) Circular No. 1760, May 23, 1961.

Page intentionally left blank

19. Particles of Unknown Origin Photographed at Rocket Altitudes*

R. TOUSEY AND M. J. KOOMEN
Naval Research Laboratory
Washington, D.C.

Photographs of the solar corona from $R = 3.5$ to $R_s = 11$, made from Aerobee 150 rockets with externally occulted Lyot coronagraphs, show tracks of particles in the altitude range from 120 to 204 km. By its nature the experiment selects only those particles traveling with approximately the instantaneous velocity of the rocket, since all others cross the field too fast to expose a perceptible trail.

On the flight of June 28, 1963, more than 35 particles were recorded, at distances ranging at least to 500 meters. Their diameters lay in the range from 10μ to 30μ . On April 28, 1966, two coronagraphs were flown side by side, making identical and simultaneous exposures. Many more particles were recorded than on the first flight. The separation between the objective lenses of the two coronagraphs makes it possible to triangulate and obtain ranges and particle trajectories with much greater precision than on the first flight. The experiment was repeated on November 12, 1966, and this time many fewer particles were recorded. Analysis of the photographs for all flights indicates that many particles were far away. Since the Sun's altitude was about 30° at the time of flight, the many particles recorded on the ascent lay in a cone ahead of and above the rocket. Because of the characteristics of their tracks, it is proposed that many of the particles are of natural origin, rather than ejected from the rocket. A large population of such particles would contribute significantly to the brightness of the corona, as photographed from the rocket.

THE ROCKET CORONAGRAPH (see paper no. 14 by Koomen and Tousey) has an extraordinary ability to detect small particles in space owing to the fact that the scattering angle to the Sun within its field of view is 0.75° to 2.5° , where Mie forward scattering approaches maximum intensity. The consequences of this characteristic were not appreciated until the first flight on June 28, 1963, when it was found that many photographs of the solar corona were of no value because they were covered with a large number of bright particle trails. The particles recorded and the optical characteristics of the coronagraph for particle detection are described by Tousey et al. (1967). In this

flight a single coronagraph was carried to an altitude of 204 km. Distances to particles were determined by measurement of the out-of-focus widths of the photographed particle trails. In effect, this involved triangulating by using the 1-inch diameter of the coronagraph objective as a base line. The farthest particle recorded was at instrument infinity and was no less than 500 meters away.

From the photographic densities of the tracks, the distances to the particles, and Mie scattering theory assuming spheres of index 1.33 (Penndorf, 1962), the particle diameters were determined to lie in the range from 10μ to 30μ ; smaller particles would have been too faint to record, and larger particles, presumably, were of low abundance. Almost all the particles were moving outward from the

*Work carried out under contract with the National Aeronautics and Space Administration.

instrument to the Sun with velocities ranging from close to zero relative to the rocket to as high as 10 meters per second. Velocities transverse to the solar vector were low, between 0.1 and 1.5 meters per second, except for some faster particles whose velocities could not be determined because they crossed the field of view completely during an exposure.

The experiment was repeated on April 28 and November 12, 1966. Each of the flights carried a parallel pair of coronagraphs. Since the objectives were spaced 6 inches apart, particle distances could be measured from stereo pairs of photographs with some six times greater precision than with a single instrument. Distance measurements on November 12, 1966, were especially precise because there were two infinity reference objects on each photograph, Venus and 24 Libra. Particles were observed as on the first flight, but on April 28, 1966, they were far more numerous, and on November 12, 1966, they were very few, except for one great puff.

CHARACTERISTICS OF TRACKS

The distances and velocities of the particles observed on all three flights have been determined for all particles that could be measured. Analysis of the data is not yet complete and a more precise set of measurements is being made. In the following paragraphs some observations and conclusions from the data at hand are presented.

Because the particles were traveling with velocities close to the rocket velocity and because most of them were moving away from the rocket, it is natural to conclude that the particles originated from the rocket. Nevertheless, the possibility that some of them did not come from the rocket is not ruled out. The principal argument supporting this other point of view is that it is difficult to explain why some particles and groups of particles traveled as they did, if they came from the rocket. The fact that all recorded particles were moving with nearly the same velocity as the rocket cannot by itself be taken as proof that they came from the rocket, because small particles moving at even moderate speeds relative to the rocket would cross the field of view too rapidly to expose a detectable trail. The

coronagraph is indeed very selective, recording trails of small particles only if their relative velocity transverse to the solar vector is less than a few meters per second.

Along the solar vector much greater velocity components are permissible. Recorded speeds ranged as high as 50 meters per second, but 90 percent were between 10 meters per second and zero. However, almost all the particles were found to be moving away from the rocket, out of the conical field of view of the instrument toward the Sun. Since in much of the altitude range covered air drag is negligible, this may seem to be conclusive evidence that the particles were streaming out of the rocket, probably propelled by some residual gas pressure. However, the possibility has not been eliminated that some natural source of particles was present and that its characteristics were such that the particles traveled in the general direction to the Sun.

Across the field of view and below peak altitude, particle velocities in the vertical direction were usually less than the rocket velocity on both ascent and descent, as though they were held back by air drag. But this occurred at altitudes where the mean free path was 100 meters or more, and here the effect of air drag should be negligible. Furthermore, on November 12, 1966, particles were observed with vertical-velocity components greater than that of the rocket, thus overtaking it. On the other hand, below 120-km altitude where the mean free path is 3 meters, air drag becomes strong and rocket velocities exceed 1 km/sec; small particles, regardless of their origin, could not keep up with the rocket, hence none was recorded.

In all the flights, particles were observed at the trajectory peak, which ranged from 175 km to 204 km. Because the sun was at approximately 30° elevation, the observed particles were always located above the rocket. Their velocities across the field of view were generally random, and their distances ranged from very close to 500 meters or more. Particle behavior near peak was the same on all flights; figure 1, from the original flight, is the best example. Particles crisscrossed the narrow field of view at positions out to several hundred feet away from and above the

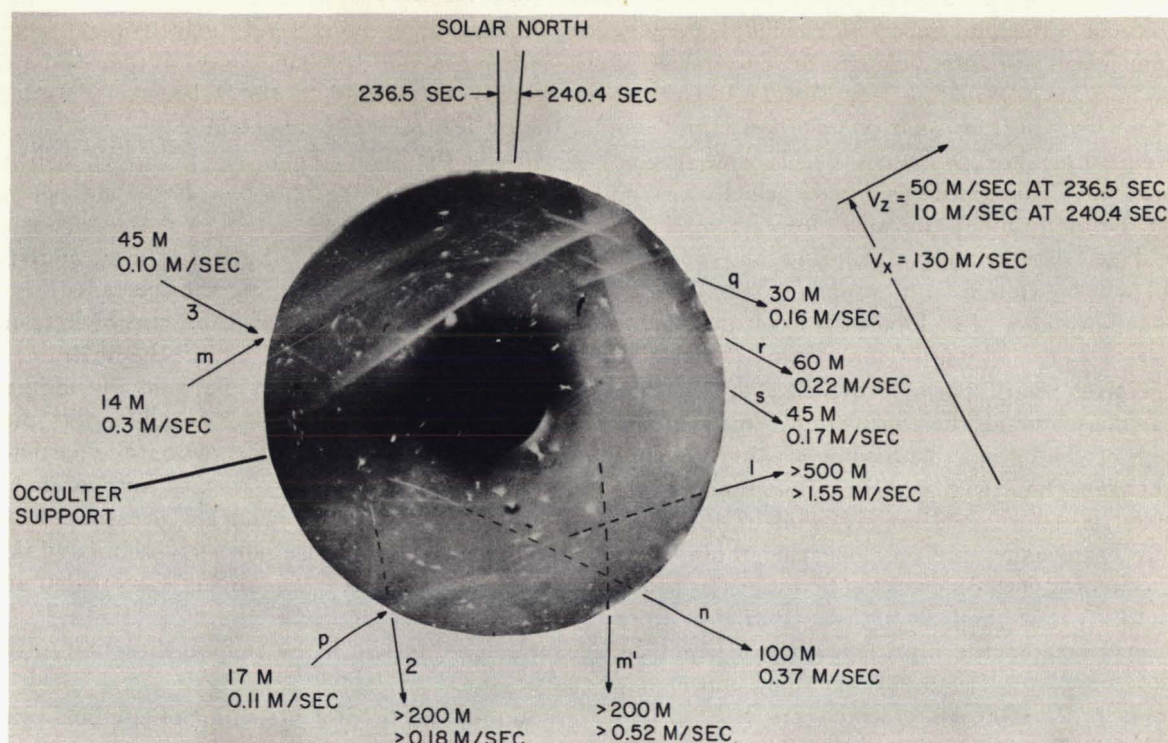


FIGURE 1.—Particle trails recorded with a rocket coronagraph on June 28, 1963, during a 3.8-second exposure just before reaching peak altitude at 204.4 km. Spots are from material loosened during launch and deposited on the field lens.

rocket. This behavior does not seem to be compatible with the theory that these particles came from the rocket.

On each flight, one or more clouds of a puff-like nature have appeared and contain many particles all traveling in roughly one direction. These occurrences were at random times, apparently unrelated to events associated with the rocket such as the release of despin weights or shutter operation. If puffs were produced by outgassing of the rocket, they would be less likely to occur on descent than ascent, but this was not found to be the case. Figure 2 shows the great cloud encountered on April 28, 1966. Four successive stereo pairs are reproduced. The commencement of the cloud nearly completely fogged the first exposure, although its duration was only 4 seconds. In the following exposures, the particles became fewer and fewer. As can be seen by reference to the velocity vectors shown in the figure, the rocket was approaching the peak altitude of 175 km. When photographed, the particles were above the rocket. Transverse

to the solar vector, they were moving parallel and opposite to the resultant velocity of the rocket. Along the solar vector they were moving toward the Sun. It is difficult to find a point on the rocket from which these particles could have originated; this point would have to lie above and to the north in order to propel particles across the field in this fashion. But the coronagraph was in the ogive of the rocket; the nose tip itself was only a foot or two higher than the occulter, and the rocket skin extended no more than 8 inches to the north. The conclusion is that the rocket encountered a moving cloud of particles from some source other than the rocket.

We propose that this cloud, as well as other clouds and isolated particles photographed on all three flights, is of natural origin; yet we do not exclude a contribution originating from the rocket.

We suggest that they are micrometeoritic material originating from occasional micrometeorites that approach the Earth at glancing

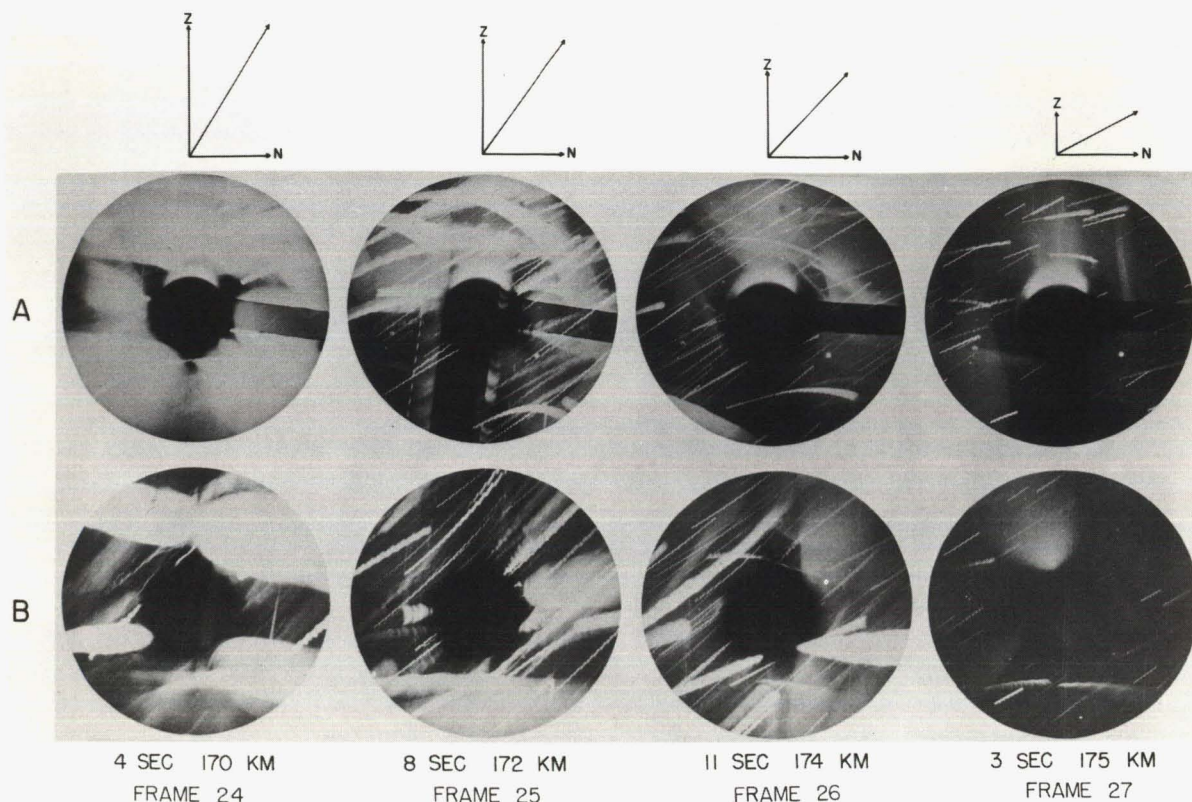


FIGURE 2. — A sequence of stereo pairs of photographs of Sun's corona from $R=3.5$ to $R_{\odot}=9$ made with rocket-borne coronagraphs on April 28, 1966. These photographs show the trails of the cloud of particles suddenly encountered just before peak altitude at 175 km. Some were so close that their trails cover a large part of the field, others were far away. The periodic jaggedness of the trails was caused by jitter of the biaxial pointing control. Above are shown the vertical component of the rocket velocity and the 20-m/sec north component. In instrument A, the sharp-edged shadow on the right was produced by a polarizing strip.

angles, break up, and project upward a spray that ascends before falling back to Earth. We believe they form one tiny part of the 1000 tons of material in the tens-of-micron-diameter range that reaches the Earth every day.

It may be of significance that the coronal brightness values from the three flights correlate with the number of particles observed. The highest brightness and greatest number of particles were observed on April 28, 1966. Next in order were the values for June 28, 1963. The lowest brightness was on November 12, 1966, and then we recorded only one great puff of particles, and a few scattered particles before and after; perhaps coincidentally, Hemenway et al. in paper no. 24 reports collecting almost no

particles on Gemini XII, which was in orbit on November 12, 1966, contrary to results from earlier flights.

Incoming dust would be expected to contribute measurably to the brightness of the solar corona in the range of small elongations covered by the rocket coronagraphs. Because of Mie forward scattering, the enhancement produced by a small amount of dust would be great. However, not all this enhancement would be detected in coronal measurements made during total eclipses of the Sun, because some or perhaps all the incoming dust would lie in the umbra and penumbra. With rocket coronagraphs, however, there would be no shadowing and this enhancement would be observed and recorded. On the other hand, the

effect of the incoming dust on the intensity of the zodiacal light, as ordinarily measured from the Earth's surface at night, would be negligible

because the elongation angles at which the zodiacal light is seen are so great that intensification by forward scattering does not occur.

REFERENCES

- PENNDORF, R., 1962, *J. Opt. Soc. Am.*, **52**, 402.
TOUSEY, R., M. J. KOOMEN, R. E. MCCULLOUGH, and R. T. SEAL, Jr., 1967 (G. S. Hawkins, ed.), NASA SP-135, 333.

Page intentionally left blank

20. Possibility of Continuous Measurement by Optical Radar of the Influx on Earth of Extraterrestrial Dust*

GIORGIO FIOCCO

*Massachusetts Institute of Technology
Cambridge, Massachusetts*

WORK BY A FEW GROUPS has shown the feasibility of utilizing a pulsed optical radar to detect the presence of particulate matter in the Earth's atmosphere. The technique utilizes a pulsed ruby laser as a source of radiation. The intensity and delay of the received echoes is related to the physical characteristics of atmospheric constituents and to their distribution with altitude.

Our work has developed as follows: Early experiments carried out during the summer of 1963 showed anomalous returns that were tentatively interpreted as being due to the presence of stratifications in the region from 60 to 90 kilometers and to the fragmentation of incoming micrometeorites in the region from 110 to 140 kilometers (Fiocco and Smullin, 1963; Fiocco and Colombo, 1964). It was found that the echoes from the higher level were associated with the presence of sporadic-E irregularities (Fiocco, 1965). If our interpretation of the data is correct, it would be possible to ascribe both the optical echoes and the ionization irregularities to the influx on Earth of extraterrestrial fragile particles of the order of 10^5 tons per day. While this value is admittedly very high, in much of the subsequent work, however, no additional evidence for these E-region echoes has been found, indicating that these echoes, if real, were related to a period

of high influx. There is some evidence for unusual meteoric activity and increased accretion of magnetic spherules in the summer of 1963. We have additional results obtained in 1964 and 1965 which indicate occasional echoes from stratifications at heights of 60 to 90 kilometers. Some of these results, obtained at high latitudes, were associated with noctilucent-cloud displays (Fiocco and Grams, 1966).

The stratospheric aerosol layer in the 15-to-25-kilometer region was monitored with some continuity during 1964 and 1965. These observations were carried out when the layer was perturbed because of the Mount Agung volcanic eruption and showed a negative correlation between the fluctuations of ozone and the fluctuation of dust (Fiocco and Grams, 1964; Grams and Fiocco, 1967).

An important aspect of the interpretation of optical radar data is the separation of those contributions due to molecules from those due to dust. Since it is difficult to provide absolute calibrations of useful accuracy, we have so far only measured the relative intensity of echoes as a function of range and have assumed that (a) in some range of heights the contributions due to molecules prevail and (b) the molecular distribution with height follows a standard behavior; thus, the presence of an excess of scatterers at specific heights can be inferred.

In general, however, one would like to be able to separate instrumentally the contributions of the Rayleigh scatterers from those of the larger

*This work is supported by the National Aeronautics and Space Administration under Grants NGR-22-009-(114) and NGR-22-009-(131).

particles by taking advantage of their different scattering characteristics. This should be possible by transmitting several wavelengths and by the use of the two polarizations and bistatic geometries. (Spectral analyses of laser scattered echoes leading to a determination of the aerosol content of air have been reported by Fiocco and DeWolf (unpublished report).)

The interesting range of heights for the detection of incoming extraterrestrial dust is, however, between 100 and 200 kilometers, where the contribution of molecular scattering decreases very rapidly; besides, the approaching scatterers, before slowing down, should be characterized by relatively large values of radial incoming speed and their echoes should be affected by large values of Doppler shift. At the ruby laser wavelengths ($\lambda = 0.694\mu$), the Doppler shift is 0.139\AA , 0.463\AA , and 1.39\AA for a radial component of the meteoroid velocity $v = 3.10^3 \text{ m-sec}^{-1}$, 10^4 m-sec^{-1} , and $3.10^4 \text{ m-sec}^{-1}$, respectively.

DESIGN FEATURES OF SYSTEM

We now consider some of the design features of a system capable of continuously monitoring the influx of extraterrestrial dust. The expected number of photoelectrons, n_R , emitted at the photocathode after each transmitted pulse, which are due to a distribution of scatterers of

radar cross section Σ per unit volume in the interval of ranges between R_1 and R_2 is

$$n_R = W_t \frac{\eta \lambda K A}{4\pi h c} \int_{R_1}^{R_2} \Sigma dR/R^2$$

where W_t is the transmitted energy per pulse, η is the quantum efficiency of the detector, λ is the wavelength, h is Planck's constant, c is the speed of light, K is an efficiency factor for transmission and instrumental losses, and A is the collecting aperture of the telescope.

The designer of an experiment would be greatly relieved if the scattering characteristics of the incoming particles and their size distribution were known. Figure 1 shows the normalized backscattering (radar) cross section of spheres as a function of the parameter $\alpha = \frac{2\pi a}{\lambda}$ for different values of the complex refractive index. From a perusal of these curves, it appears that in many cases the radar cross section exceeds the geometrical cross section; the appropriateness of assimilating these particles to spheres is, of course, open to question. For the purpose of our estimate, we shall assume that the influx on Earth is 4.4×10^3 tons/day ($10^{-13} \text{ kg-m}^{-2}\text{-S}^{-1}$) of particles typically of 0.1μ radius; with density,

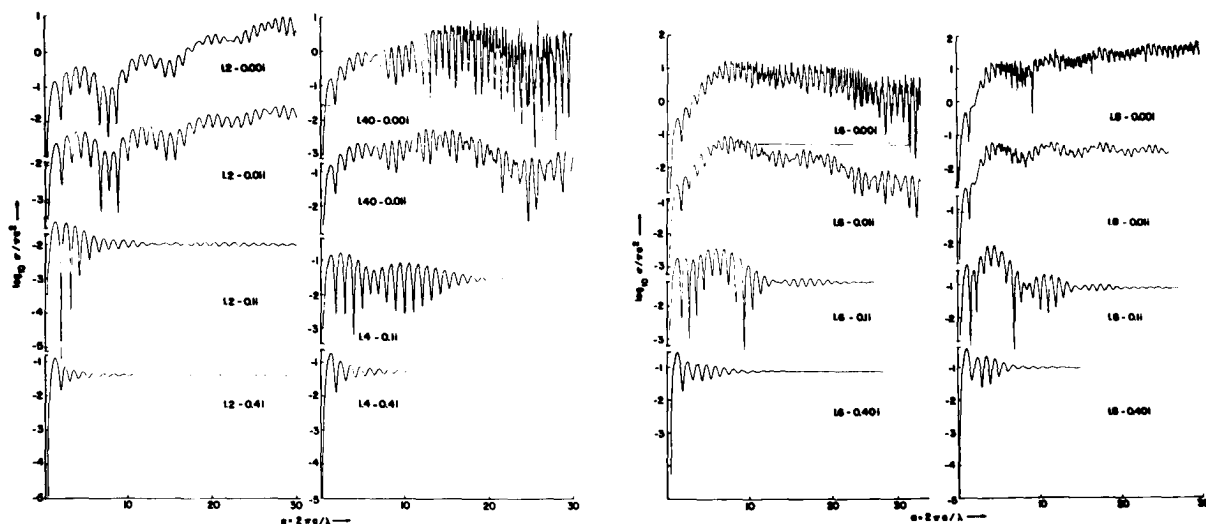


FIGURE 1.—Normalized radar cross section of spheres versus size parameter $\alpha = 2\pi a/\lambda$. Curves refer to different values of complex refractive index; horizontal lines indicate values of reflection coefficient for normal incidence.

$\delta = 10^3 \text{ kg}\cdot\text{m}^{-3}$; and vertical component of velocity, $v_1 = 10 \text{ km}\cdot\text{sec}^{-1}$. By taking the radar cross section of the particles equal to their geometrical cross section, a value $\Sigma = 0.75 \times 10^{-13} \text{ m}^2/\text{m}^3$ is obtained.

Since a range resolution of 15 kilometers is sufficient, in the corresponding 100- μ -second interval, a ruby laser ($\lambda = 0.694\mu$) can be made to radiate, at the rate of once a second, 20 joules and possibly as much as 50 joules. The receiver could utilize a collecting dish or a mosaic of collectors for a total aperture of 10 meters² that can be achieved at relatively low cost if the field of view is kept at 1 mrad. The spectral resolution would be achieved by the use of interference filters and a Fabry-Pérot interferometer; some frequency stabilization of the laser output would be required. Thus, radiating 20-joule pulses and assuming an efficiency $K = 10$ percent, we estimate that approximately 2000 photoelectrons

would be accumulated after 10 hours for the echoes in the range of 100 to 200 kilometers. The effective time of observation would be only 24 seconds, during which time the noise contribution would amount to approximately 240 electrons because of dark current and probably 15 000 electrons in a 0.5Å spectral window, because of sky background. The level of signal is therefore expected to exceed the fluctuations in noise level by a factor of approximately 16 and thus allow an ample margin of reliability. By the range distribution of the echoes, an estimate of the deceleration parameters would also be obtained.

CONCLUDING REMARKS

In conclusion, it appears possible to measure, on a nightly average, the influx of micrometeorites in the Earth's atmosphere and the gross features of their velocity distribution and of their ballistic characteristics.

REFERENCES

- FIOCCO, G., and L. D. SMULLIN, 1963, *Nature*, **199**, 1275.
FIOCCO, G., and G. COLOMBO, 1964, *J. Geophys. Res.*, **69**, 1795.
FIOCCO, G., and G. GRAMS, 1964, *J. Atmos. Sci.*, **21**, 323.
FIOCCO, G., 1965, *J. Geophys. Res.*, **70**, 2213.
FIOCCO, G., and G. GRAMS, 1966, *Tellus*, **18**, 34.
GRAMS, G., and G. FIOCCO, 1967, *J. Geophys. Res.*, **72**, 3523.

Page intentionally left blank

II

PARTICLE COLLECTION AND IMPACT

Page intentionally left blank

21. Characteristics of Interplanetary Dust (Abstract)

MAURICE DUBIN

*Office of Space Science and Applications, NASA
Washington, D.C.*

AND

C. L. HEMENWAY

*Dudley Observatory
Albany, New York*

An extensive review of the characteristics of interplanetary dust based on experimental and analytical investigations has been made. These investigations include measurements of flux and mass distributions and their time variations, as well as measurements of particle structures, densities, composition, crystal structure, and impact effects. These results have been obtained mainly from experiments carried out from balloons, rockets, satellites, and probes.

Descriptions of experimental methods and their limitations are presented. Flux distributions as a function of mass as obtained from impact detectors, collection methods, and other techniques are compared. The morphology of collected particles showing irregular shapes, conglomerate characteristics, ablation flow lines, and evidence of volatile constituents is discussed.

Page intentionally left blank

22. Satellite Measurements of Particles Causing Zodiacal Light

JOSE M. ALVAREZ
Langley Research Center, NASA
Hampton, Virginia

Early satellite measurements in near-Earth space showed that meteoroids were much more numerous than analysis of zodiacal-light measurements indicated. These early satellites employed microphones and sounding boards to obtain the meteoroid impact flux and mass distribution. The more recent Explorer XVI and XXIII and Pegasus I, II, and III satellites, using pressurized-cell and capacitor-type penetration detectors, respectively, have obtained measurements, also in near-Earth space, on the frequency of meteoroid penetration in metal test materials with thicknesses varying from 25 to 400 microns. Analysis of the penetration frequencies measured by these satellites gives a meteoroid population in space which is in agreement with results calculated by Beard (1959) and others using zodiacal-light data.

The satellite data refute the assumption that the number of particles in near-Earth space varies as r^{-p} where r is the particle radius and p is a constant. The data and theoretical considerations indicate instead that the concentration of particles in near-Earth space is given by

$$c(r) = 1.10 \times 10^{-16} r^{1.045 - 0.683 \log_{10} r} \quad (5.8\mu \leq a \leq 4.9 \text{ mm})$$

where r is particle radius in microns and $c(r)$ is calculated per cm^3 . The equation shows that the concentration of particles in near-Earth space is approximately 10^{-15} to $10^{-16}/\text{cm}^3$. This equation also indicates that the smallest particles in the vicinity of Earth are about 6 microns in radius which agrees with the 3-micron radius calculated as the minimum considering solar radiation pressure. An average particle density of 0.2 g/cm^3 was assumed.

THE NATIONAL AERONAUTICS AND SPACE ADMINISTRATION has long had a considerable interest in meteoroids as a result of the critical dependence of the design and construction of manned and unmanned spacecraft on the meteoroid environment. As late as December 1963 a spacecraft designer was faced with the uncertainty in the meteoroid environment depicted by figure 1. The ordinate of this plot is the meteoroid flux which is defined as the number of meteoroids of a given mass or greater passing through 1 square meter per second in near-Earth space. As can be seen, there were three main

sources of knowledge of the meteoroid environment, zodiacal-light measurements and early satellite microphone data which were concerned with very low-mass micrometeoroids and the meteor measurements which were associated with relatively large-mass meteoroids. Estimates of meteoroid flux from the zodiacal data varied about four orders of magnitude and the microphone data were about one or two orders of magnitude above the higher zodiacal estimate. The derived meteor flux estimates varied by about two orders of magnitude in the photographic range.

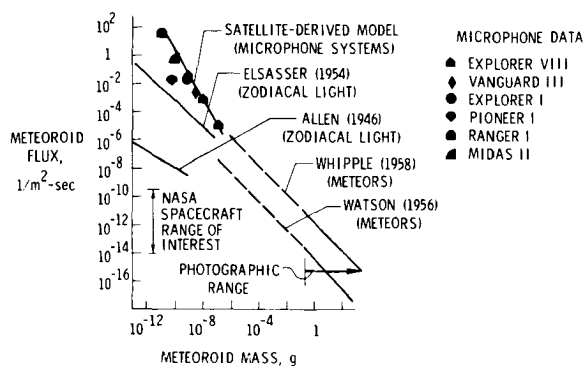


FIGURE 1.—The meteoroid environment in 1963.

The flux of critical interest to NASA and spacecraft designers was unfortunately beyond the range of the existing data as shown in the figure, and consequently, the data available with its broad uncertainties then had to be extrapolated to provide useful flux estimates. The Watson (1956) and Whipple (1958) estimates are two such extrapolations.

The uncertainty in interpreting the data available in terms of hazard to spacecraft led NASA to develop another class of satellites to specifically determine the damage potential of meteorites. This class of satellites exposes thin metal skins to the space environment and monitors the metal skins for penetrations. NASA has now orbited five successful spacecraft of the direct penetration type, two Explorer and three Pegasus satellites. The penetration rates obtained from these satellites have been very useful in constructing models of the meteoroid hazard for the spacecraft designer. The thinnest of the metallic skins obtain penetration-rate measurements which can also be made to yield valuable information about the small particles found in near-Earth space.

Figure 2 presents the penetration data from Explorer XVI and XXIII and Pegasus I, II, and III with the ordinate as the penetration rate and the abscissa as material thickness in microns. The apparent inconsistency in the data is due to differences in detector materials and physical differences in the detection process employed by the two satellite series. The Pegasus spacecraft used aluminum capacitor-type penetration detectors and the Explorers used pressurized-

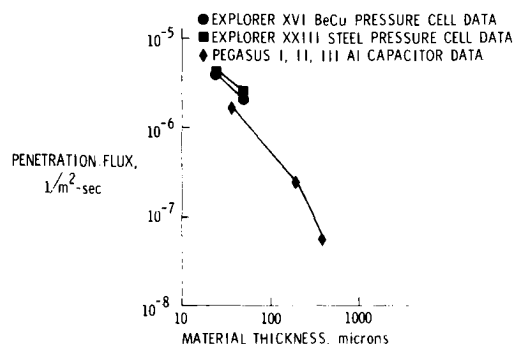


FIGURE 2.—Explorer and Pegasus data.

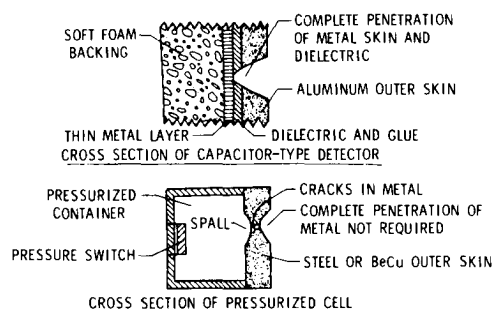


FIGURE 3.—Operation of penetration detectors.

cell penetration detectors of stainless steel and beryllium copper.

The following discussion presents an analysis of the Pegasus and Explorer data and the development of an equation for penetration rate in terms of material thickness. Hypervelocity impact theory is then used to interpret the penetration rate data in terms of particle concentration and particle radii.

As previously mentioned, differences in the penetration detectors used on the two satellite series exist and these differences must be recognized and reconciled.

The operation of the Pegasus aluminum capacitor-type penetration detector, schematically shown in figure 3, requires that a particle have sufficient kinetic energy upon impact to form a plasma between two charged plates of a capacitor mounted on the rear of the test material. The process naturally requires that the particle completely penetrate the aluminum skin and the capacitor dielectric. The stainless steel and beryllium copper pressure-cell detectors used on the Explorer satellites, on the other hand,

do not require that a particle penetrate the skin completely. This type of detector requires only that the damage to the skin be such that a gas leak is produced. Spallation and cracking can produce such leaks without the impacting particle entirely penetrating the metal skin as is also shown in figure 3.

The differences in detector operation just noted tend to make a pressurized-cell penetration detector more sensitive to penetrating particles than a capacitor-type penetration detector, both detectors being assumed to be of the same material. However, the detectors of the Explorer and Pegasus satellites exposed different materials; thus the differences are further increased.

Hypervelocity penetration theory and experiments indicate that material difference can be accounted for by a relation of the form

$$t(a) = k't(b) \quad (1)$$

where k' is a constant and $t(a)$ is a detector thickness of material a which is equivalent to thickness $t(b)$ of material b when identical types of detectors are used. Thicknesses are considered equivalent when they exhibit identical resistance to penetration.

Present hypervelocity theory is unfortunately not sufficiently sophisticated to accurately account for differences in detector operation such as those exhibited by the two different types of detectors. Since no laboratory calibrations of the penetration detectors are available as yet, it is assumed that a relation similar to equation (1) is true for two different types of detectors if they are constructed of identical materials. In the case of the capacitor-type detector, the dielectric thickness must be small compared to the skin thickness; such is the case for the two thickest Pegasus detectors. By letting A and B refer to capacitor- and pressure-cell-type detectors, respectively, and a and b refer to the different materials, the relation between Pegasus and Explorer thicknesses is assumed to be of the form

$$t(a, A) = k''t(b, B) \quad (2)$$

where k'' is a constant. By evaluating the constant

k'' , the Pegasus data can be transformed into equivalent Explorer data. The only difficulty encountered in this procedure is that the functional form of penetration flux is unknown as a function of thickness and must also be obtained from the data.

If the Pegasus thicknesses are converted to Explorer thicknesses by defining k'' in accordance with equation (2), it is impossible to draw a straight line which fits both sets of data. (See fig. 4.) Translation along the horizontal axis leaves the slope of a line invariant, and the thickness data points for Explorer and the two thickest for Pegasus define different slopes; thus the data cannot be fitted satisfactorily by an equation of the form

$$\log \psi = a_0 + a_1 \log t \quad (3)$$

where ψ is the meteoroid penetration rate $\left(\frac{\text{Penetration}}{\text{m}^2\text{-sec}}\right)$, t is the thickness of the sensor (microns) and a_0 and a_1 are constants. By assuming the logarithm of flux to be a continuous function of the logarithm of thickness, a series expansion in powers of the logarithm of thickness (see Courant and Hilbert, 1953) can be used to describe the relationship between flux and material thickness. Thus the logarithm of flux is given by

$$\log \psi = f(\log t) = \sum_{n=0}^{\infty} a_n \log^n t \quad n=0, 1, 2, \dots, \quad (4)$$

where t is particle thickness, a_n is a constant, and $f(\log t)$ is a function of the logarithm of t .

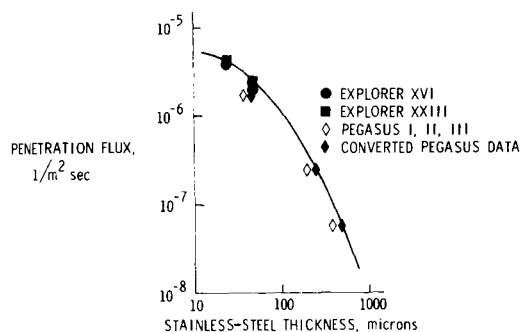


FIGURE 4.—Penetration satellite results.

The Pegasus thickness data for the thinnest material are not included in the present analysis because the dielectric is not thin in comparison with the aluminum skin and also because the aluminum alloy used differed from that used on the two thicker materials. Therefore, two Explorer and two Pegasus data points are available for the definition of the penetration rate as a function of thickness. Thus, since four data points are available, it is possible to determine four constants. The present analysis defines the constant k'' in equation (2) by using only the first three terms of the expansion given in equation (4). The logarithm of flux was therefore assumed to be of the form

$$\log \psi = a_0 + a_1 \log t(b, B) + a_2 \log^2 t(b, B) \quad (5)$$

for some range of t to be specified later. The solution was obtained by expressing equation (5) as a function of Pegasus thicknesses and k'' and by requiring that the constant k'' be such that the parabola goes through the average of the stainless steel and beryllium copper Explorer data points and the two thickest converted Pegasus data points. Table 1 presents the data used to define the four constants along with other pertinent information concerning the two satel-

lite series. The results of the parabolic fit is shown in figure 4 and is given by the following equation where thickness t is in microns

$$\log_{10} \psi = -5.966 + 1.364 \log_{10} t(b, B) - 0.683 \log_{10}^2 t(b, B) \quad 9.9\mu \leq t(b, B) \leq 8.3 \text{ mm} \quad (6)$$

The lower thickness limit (9.9μ) is obtained at the peak of the parabola. The upper thickness limit is obtained by going to the generally accepted meteor-derived slope of -4 and assuming the flux to be linear on a log-log scale after the parabola achieves this slope. Thus the following equation is assumed to be true for thicknesses greater than 8.3 mm :

$$\log \psi = 4.564 - 4 \log_{10} t(b, B) \quad t(b, B) > 8.3 \text{ mm} \quad (7)$$

The relation between the Pegasus material thicknesses $t(a, A)$ and the Explorer material thicknesses $t(b, B)$ is given by

$$t(a, A) = 0.82 t(b, B) \quad (8)$$

Equations (6) and (7) express the meteoroid flux in terms of the thickness of material that can be penetrated. To establish the concentration in

TABLE 1.—General Data

Satellite		Detector			Data		
Title	Launch date	Type	Material	Thickness, microns	Number of detected events	Measured penetration rate	Reference
Explorer XVI.	1962	Pressurized cells.	Beryllium copper	25	44 punctures	$3.88 \times 10^{-6}/\text{m}^2\text{-sec}$	Hastings (1963 a, b).
				51	11 punctures	$2.00 \times 10^{-6}/\text{m}^2\text{-sec}$	
				127	0	$10^{-6}/\text{m}^2\text{-sec (max)}$	
Explorer XXIII.	1964	Pressurized cells.	Stainless steel, type 302.	25	50 punctured cells	$4.40 \times 10^{-6}/\text{m}^2\text{-sec}$	O'Neal (1965, 1967).
				51	74 punctured cells	$2.50 \times 10^{-6}/\text{m}^2\text{-sec}$	
Pegasus I, II, III.	1965	Capacitor-type detector.	Aluminum 1100-0	38	582 penetrations	$2.18 \times 10^{-6}/\text{m}^2\text{-sec}$	Naumann (1965, 1966).
			Aluminum 2024-T3	200	49 penetrations	$2.43 \times 10^{-7}/\text{m}^2\text{-sec}$	D'Aiutolo et al. (1967).
				400	201 penetrations	$5.64 \times 10^{-8}/\text{m}^2\text{-sec}$	Clifton and Naumann (1966).

near-Earth space in terms of particle radius, a relationship of interest in studies of phenomena such as zodiacal light, the minimum particle radius required to penetrate respective material thicknesses must be established.

It is known experimentally that penetration equations are of the form

$$t/r = k(\zeta, V, \Gamma) \quad (9)$$

where t is the thickness of target plate having physical properties symbolized by Γ and penetrated by a particle of radius r whose density is ζ and whose velocity is V . A bigger particle having the same density and velocity will of course also penetrate the thickness t whereas a smaller particle will not. Substitution of equation (9) into equation (4) and integration thus yields the number of meteoroids having radius r or larger passing through 1 square meter of near-Earth space every second:

$$\log \psi(r) = \int f[\log r + \log k(\zeta, V, \Gamma)] \Pi_{\zeta} \Pi_V d\zeta dV \quad (10)$$

where Π_{ζ} and Π_V are probability density functions of the particle density and velocity. Unfortunately these probability density functions are not presently known in the range of the experimental data, therefore, the integral (eq. (10)) cannot be evaluated. One thing is generally true, however: the logarithm of the distribution function of particle radius is not a linear function of the logarithm of particle radius. This conclusion follows directly from equation (10) and is easily seen by replacing the function by its series expansion.

The lack of probability density functions for particle velocity and density forces the use of additional assumptions. Two approaches can be taken. One is to assume the probability density functions for the particle velocity and density and evaluate equation (10) directly. The other approach is to assume mean values for particle density and velocity. The latter approach is explored herein.

Table 2 presents the penetration equations used to obtain the possible range of particle sizes which penetrated the satellite detectors. The

TABLE 2.—Penetration Equations

Penetration equations	Assumed parameters	$\frac{t}{r}$	Reference
Charters $\frac{t}{r} = 6.84 \left(\frac{\zeta}{\zeta_t} \right)^{2/3} \left(\frac{v}{c} \right)^{2/3}$	c = Speed of sound in target = 5 km/sec	1.08 ($\zeta = 0.1$ g/cm ³) 1.71 ($\zeta = 0.2$ g/cm ³) 14.5 ($\zeta = 5$ g/cm ³)	Charters and Locke (1958) Anderson (1959)
Hermann-Jones $\frac{t}{r} = 1.8 \left(\frac{\zeta}{\zeta_t} \right)^{2/3} \ln T$ $T = 1 + \left(\frac{\zeta}{\zeta_t} \right)^{2/3} \frac{\zeta_t V^2}{4H}$	H = Brinell hardness = $10^{10} \frac{\text{dynes}}{\text{cm}^2}$	0.50 ($\zeta = 0.1$ g/cm ³) 0.75 ($\zeta = 0.2$ g/cm ³) 9.1 ($\zeta = 5$ g/cm ³)	Hermann and Jones (1962)
Walsh $\frac{t}{r} = 3KV^{0.58}$	K = Empirically determined constant = $0.96 \left(\frac{\text{sec}}{\text{km}} \right)^{0.58}$ (Langley hypervelocity experiments with aluminum spheres)	18.7 with particle density of 2.8 g/cm ³ implicitly assumed.	Walsh and Johnson (1965)
Fish-Summers $\frac{t}{r} = K \left(\frac{1}{\zeta_t} \right)^{1/2} V$	K = Empirically determined constant = $1.82 \left(\frac{\text{g}}{\text{cm}^3} \right)^{1/2} \frac{\text{sec}}{\text{km}}$ (From data in reference)	16.1 with particle density of 2.8 g/cm ³ implicitly assumed.	Fish and Summers (1964)

average velocity was assumed to be 25 km/sec (Clough and Lieblein, 1965); the average meteoroid density ζ was assumed to be between 0.1 g/cm³ and 5.0 g/cm³ for all the penetration equations; the target density ζ_t was taken to be 8 g/cm³. All equations in table 2 but the Fish-Summers equation were originally used for semi-infinite target and have been corrected for thin plates by multiplying the semi-infinite result by an empirically determined factor of 1.5.

Figure 5 presents a best estimate of particle concentration using a mean particle density of 0.2 g/cm³, a mean velocity of 25 km/sec. and the Charters penetration equation. This particular penetration equation was chosen since it is more in line with the recent observation of Fish and Summers (1964) who found relatively high ratios of thickness to particle radius for impacts resulting in leaks in pressurized containers. The Fish-Summers equation could not be used since a meteoroid density of 2.8 g/cm³ is incorporated into the equation. The particle density estimate was originally obtained by radiation pressure arguments; a recent paper by Verniani (1966), however, quotes an identical mean particle density from meteor data.

It was assumed that the Earth shields about one-fourth of the near-Earth space; therefore, the concentration was corrected by this factor. The particle concentration is given by the following equation in terms of particle radius r where r is in microns.

$$\log c = -15.958 + 1.045 \log_{10} r = 0.683 \log_{10}^2 r$$

$$5.8\mu \leq r \leq 4.8 \text{ mm} \quad (11)$$

Figure 5 also presents the extremes of the concentration obtained by using the highest and

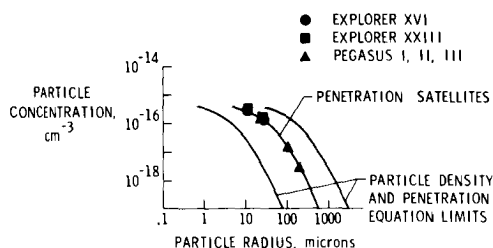


FIGURE 5. — Concentration model from penetration satellites.

lowest ratios of penetration depth to particle radius presented in table 2.

The conclusions obtained from figure 5 are as follows:

(1) The logarithm of the particle concentration is not a linear function of the logarithm of the particle radius. The conclusion follows directly from the fact that the Pegasus and Explorer data do not define this type of relation. This conclusion was perhaps to be expected. It is important, since it enables the experimental penetration data and meteor-derived penetration data to be compatible.

(2) If the rate of change of slope continues as the data indicate, the slope will be zero at about 6 microns indicating that the total near-Earth concentration of particles is about $10^{-15}/\text{cm}^3$.

(3) The estimate given by the penetration satellites suffers not so much from a choice of penetration equations but from lack of knowledge of particle densities. The mean particle density had to be assumed from meteor data and it is here that maximum error is to be expected.

(4) Regardless of the penetration equation used or the particle parameters assumed, the Explorer and Pegasus data clearly indicate a rather small value of slope at micron-sized particle radii.

Figure 6 shows the present estimate in comparison with various zodiacal-light results. Note that there is at least an order of magnitude agreement between the two sets of data. On the Explorer XXIII satellite, microphone data were obtained which did not agree with penetration data as also shown in figure 6. Tests conducted

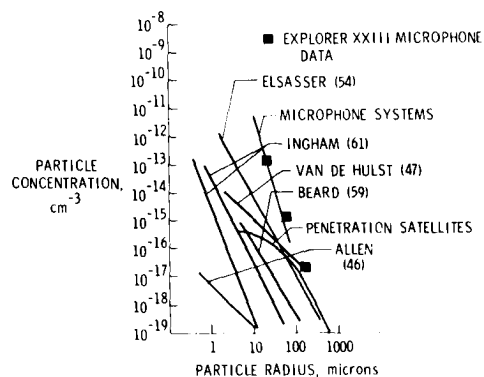


FIGURE 6. — Comparison of various models.

at Langley Research Center indicate that the Explorer microphone systems are sensitive to the thermal environment and give spurious data (O'Neal, 1967).

It is seen from the figure that the hypothesis of a dust cloud around the Earth may not be needed to obtain consistency between the results from zodiacal light and meteoroid penetration.

REFERENCES

- ALLEN, C. W., 1946, *Mon. Not. Roy. Astron. Soc.*, **106**, 137.
- ANDERSON, G. D., 1959, Studies in Hypervelocity Impact, Poulter Lab. Tech. Rept. 018-58, December.
- BEARD, D. B., 1959, *Astrophys. J.*, **129**, 496.
- CHARTERS, A. C., and G. S. LOCKE, JR., 1958, A Preliminary Investigation of High Speed Impact: The Penetration of Small Spheres into Thick Copper Targets, NACA RM A58B26.
- CLIFTON, S., and R. J. NAUMANN, 1966, Pegasus Satellite Measurements of Meteoroid Penetration (Feb. 16-Dec. 31, 1965), NASA TM X-1316, December.
- CLOUGH, N., and S. LIEBLEIN, 1965, Significance of Photographic Meteor Data in the Design of Meteoroid Protection for Large Space Vehicles, NASA TN D-2958, August.
- COURANT, R., and D. HILBERT, 1953, *Methods of Mathematical Physics*, Vol. 1, John Wiley & Sons, Inc., p. 65.
- D'AIUTOLO, C. T., W. H. KINARD, and R. J. NAUMANN, 1967, Proceedings of Symposium on Meteor Orbits and Dust, NASA SP-135 (SCA Vol. 11).
- ELSÄSSER, H., 1954, *Zeits. f. Astrophys.*, **33**, 274.
- FISH, R. H., and J. L. SUMMERS, 1964, The Effect of Material Properties on Threshold Penetration, Proceedings of the Seventh Hypervelocity Impact Symposium, Tampa, Florida, November 17-19.
- HASTINGS, E. C., 1963a, The Explorer XVI Micrometeoroid Satellite Supplement 3 Preliminary Results for the Period May 27, 1963, through July 22, 1963, NASA TM X-949.
- , 1963b, The Explorer XVI Micrometeoroid Satellite Supplement 2 Preliminary Results for the Period March 3 through May 26, 1963, NASA TM X-899.
- HERMANN, W., and A. H. JONES, 1962, Correlation of Hypervelocity Impact Data, Proceedings of the Fifth Symposium on Hypervelocity Impact, Vol. 1, Pt. 2, April, pp. 389-438.
- INGHAM, M. F., 1961, *Mon. Not. Roy. Astron. Soc.*, **122**, 157.
- NAUMANN, R. J., 1965, NASA Tech. Memo., X-1192.
- , 1966, NASA Tech. Note, D-3717.
- O'NEAL, R. L., 1965, NASA Tech. Memo., X-1123.
- , 1967, NASA Tech. Note, D-4284.
- VERNIANI, F., 1966, Smithsonian Astrophysical Observatory, Special Report, No. 219, August 26.
- VAN DE HULST, H. C., 1947, *Astrophys. J.*, **105**, 471.
- WALSH, J. M., and W. E. JOHNSON, 1965, On the Theory of Hypervelocity Impact, Vol. 2, 7th Hypervelocity Impact Symposium, February.
- WATSON, F. G., 1956, *Between the Planets*, rev. ed., Harvard Univ. Press, Cambridge.
- WHIPPLE, F. L., 1958, *Vistas in Astronautics*, Vol. 1, M. Alperin and M. Stern, eds., Pergamon Press, New York, 115.

Page intentionally left blank

23. Study of Particles Collected by the 1965 Luster Rocket*

N. N. GREENMAN, C. B. GILPIN,
S. K. ASUNMAA, AND R. G. INGERSOLL
*Douglas Missile and Space Systems Division
Santa Monica, California*

The NASA Ames Research Center's Luster micrometeorite-collecting rocket was successfully flown on November 16, 1965, during the Leonid meteor shower and collected for 206 seconds between altitudes of 63 and 144 kilometers. The Douglas collector surface, one of several guest experiments on board, consisted of titanium, tungsten, and molybdenum electron microscope screens each with a substrate of silicon monoxide and a shadow coat of nickel or indium; they were designed to withstand heating to 1000° C. The primary objective was to test, by heat annealing, whether radiation damage distinguished extraterrestrial from terrestrial particles; the secondary objective was to measure the abundance, composition, and other properties of the micrometeorites.

Heating tests were completed on one group of 58 particles and on 2 individual particles. Of these, only one particle showed evidence of possible radiation-damage annealing but it also showed some morphologic changes. It was concluded that all the studied particles could be contaminants and that more particles must be studied, together with composition and other data, before a conclusive answer can be given as to whether radiation damage is a criterion for micrometeorites. However, the heat-produced morphologic changes discovered in this study may also prove to be important in distinguishing micrometeorites from contaminants.

No chemical elements were identified in preliminary electron probe analyses.

Eight individual particles and two groups of particles were found in a total scanned area of 36 mm²; therefore, 0.3 particle per mm² of collector surface was collected if each group is counted as a single particle, or 2 particles per mm² if every particle in the groups is counted. These values do not include corrections for one-shadowed contaminants or for scanning efficiency.

THE IMPORTANCE OF COSMIC DUST, in general, and micrometeorites, in particular, hardly needs to be pointed out. These particles are of great interest to science and the space program because they are additions to, and erosional agents of, lunar and planetary surfaces; they are increments to the lithosphere and the atmosphere of the Earth; and they are potential erosional

and destructive agents of man-made space hardware.

Although nearly 100 years have passed since micrometeoritic contributions to the sediments of terrestrial oceans were first recognized (Murray, 1876), an intensive study of these particles has commenced only with the advent of high-altitude aircraft, rockets, and Earth-orbiting satellites during the past decade. The studies have used two general approaches. The first is the indirect approach in which particle flux,

*This study was performed for the National Aeronautics and Space Administration under contract NASw-1401.

velocity, and other characteristics are deduced from impacts on sensing devices usually flown on satellites. The second is the direct approach in which the particles themselves are collected and studied.

This investigation is in the second category; it presents the results of an investigation of particles collected with the Luster rocket which was successfully flown on November 16, 1965, from the White Sands Missile Range, New Mexico, during the Leonid meteor shower. The nose cone carried particle collectors mounted on arms that extended and retracted during flight, and the entire assembly was parachuted to the ground and recovered. Collection was carried out for 206 seconds between altitudes of 63 and 144 kilometers (Farlow and Blanchard, 1966). The experiment was under the direction of the NASA Ames Research Center and included collectors from guest scientists at Douglas and a number of other organizations.

A crucial problem in all direct particle studies is the problem of distinguishing extraterrestrial particles from terrestrial contaminants. Therefore, the primary purpose of this investigation was to test whether radiation damage, as revealed by resumption of the crystalline state with heating, could provide a criterion for making this distinction. A secondary purpose was to determine size, shape, abundance, composition, and other important characteristics of micrometeorites from electron microscope observations and from electron diffraction and electron probe analysis.

PREVIOUS WORK

The first successful collection of particles from high altitudes for direct study was made with the Venus flytrap rocket flown on June 6, 1961, by the Air Force Cambridge Research Laboratories (AFCRL). The AFCRL investigators, on the basis of controls built into the experiment, concluded that micrometeorites had been collected and were distinguishable from contaminant particles of terrestrial origin. They also found that micrometeorites displayed no diffraction patterns in the electron microscope, possibly because of radiation damage sustained in space (Soberman et al., 1961; Hemenway and Soberman, 1962). An alternative explanation,

that the particles may have been crystalline but too dense to yield diffraction patterns, was ruled out by Greenman and Gilpin (1967), who showed that particles of the silicates, olivine and enstatite, in the same size range yield distinct diffraction patterns.

AFCRL subsequently provided Douglas with samples from this collection. An attempt was made to test for the presence of radiation damage by heating the particles to see if crystallinity, as evidenced by the appearance of electron diffraction patterns, could be restored at temperatures below the melting point. This test was important because no positive criteria are known by which micrometeorites can be recognized without ambiguity in any particle collection. If radiation damage were present, it would constitute such a criterion because the bulk of the terrestrial contaminants in micrometeorite collections should be either crystalline or amorphous and not radiation damaged to any significant degree. Particles of extraterrestrial origin, on the other hand, could suffer radiation damage to the crystalline lattice, according to the calculations of Ryan (1964). Moreover, the damage could survive in small particles that fall too slowly through the atmosphere to undergo appreciable frictional heating.

Although several different substrate materials were used as collectors on the Venus flytrap flight, none were well suited for heating tests of this kind. The least faulty substrate, thin formvar double shadowed with aluminum, had the disadvantage that the low melting point of aluminum, about 660° C, prevented the tests from being carried out above about 500° C. In addition, at temperatures below 500° C, heating caused enough damage to the substrate to make it almost impossible to follow the same particle through every heating stage. For this reason, a statistical approach was used in which as many particles as possible were examined after each stage.

The results of heating to 250° C, 400° C, and 500° C were that, in general, the percentage of particles showing evidence of crystallinity increased with increasing temperature. Statistical analysis indicated that the crystallinity was probably produced by the heating, although the differences in the percentages were not great

enough to prove this. The d-spacings of the diffraction spots were found to correspond rather well with those of olivine and enstatite, the major minerals of the most abundant meteorite type; this correspondence indicates that annealing of radiation damage could have occurred. On the other hand, similar correspondence was found with other materials, such as mica and aluminum oxides and hydroxides, that could be contaminants or reaction products formed in the course of the heating tests. These studies are described by Greenman (1963, 1964).

The results of these first tests were thus suggestive, though inconclusive. Because the difficulties were caused chiefly by the inadequate heat resistance of the available substrates, a suitable substrate and supporting screen assembly for subsequent rocket collection flights was developed (Greenman and Gilpin, 1967). This assembly consisted of a titanium supporting screen with a substrate of silicon monoxide shadowed with nickel. Tests showed that this assembly had good collection efficiency and was able to withstand a temperature of 950° C with only a small amount of damage, although it was found that the nickel shadow disappeared. The disappearance of the nickel was considered an advantage in that it reduced the substrate thickness. For this reason, indium, which at 1000° C has a vapor pressure much greater than that of nickel, was also used as a shadowing metal on the Luster collecting substrates.

COLLECTOR PREPARATION AND CONTROL PROCEDURES

The Douglas collection surface was prepared by first casting a thin film of Parlodion on water. The Parlodion was then picked up on the titanium screens and dried. In addition to titanium, screens of tungsten and molybdenum (other high melting point metals) were also used to provide a variety of collector types for the heating experiments. The titanium and tungsten screens have keyed center holes and elongated openings which greatly facilitate the mapping of particles and finding them again after each stage of heating (fig. 1). The diameter of the screen shown is 3.05 mm. The silicon monoxide substrate was next deposited on the Parlodion, after which the Parlodion was dissolved with

amyl acetate. When dry, the screens and substrates were coated with approximately 25 Å of nickel or indium deposited in a vacuum evaporator at an angle of 15° to the surface. After preparation, several screens were examined in the electron microscope to make sure that the substrates were in good condition and that contamination was slight.

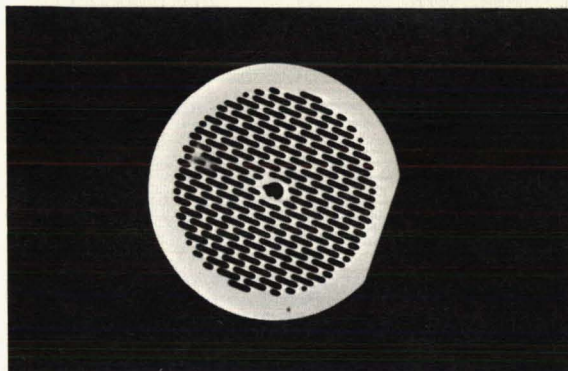


FIGURE 1.—Titanium supporting screen for Luster substrates; keyed center hole is shown.

The finished collector screens were mounted on a lucite base, 55 by 50 by 30 mm, with double-sided tape. An aluminum-coated shield was attached to one end of the lucite plate to cover three rows of screens with an air gap of about 1.5 mm. This arrangement was for the purpose of contaminant control; the covered screens were thus shielded from impact by particles during the collection phase of the flight but could accumulate contaminants carried in by air currents at other times. The circles in figure 2 indicate screens on which one-shadowed particles were found; squares indicate screens on which none were found. The letter-number coordinate system serves to identify the screens. The complete collection surface was shipped in a cleaned and sealed plastic box to NASA Ames Research Center for incorporation into the Luster flight package. Also, an identical surface was shipped to be used as a spare, and a set of slides with 10 substrates each was shipped to be exposed in the Ames laboratory and in the White Sands portable clean room where the final assembly of the flight instrument took place. These were to be used as contaminant controls.

After the flight, the flight sample, spare, and

controls were returned to Douglas. They were opened in a Class 100 clean room and a second nickel or indium coat was applied at 15° to the surface and at about 90° to the direction of the first coat. This double-shadowing technique served as a control to separate preflight contaminants, which should show two metal shadows, and postflight contaminants, which should show none, from particles collected in flight, which should show only one. Contaminants deposited during the time between shadowings should also show one shadow. Double-shadowing, in-flight shielding, and laboratory-exposed substrates thus were the three types of contaminant control used in this study.

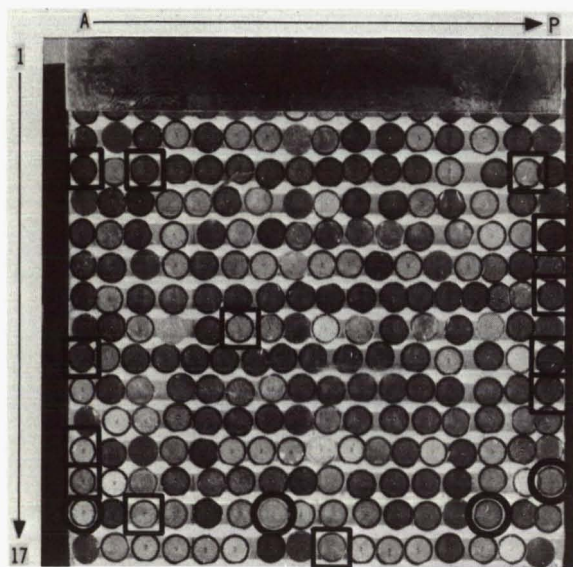


FIGURE 2.—Collection surface flown on 1965 Luster rocket.

HEAT ANNEALING EXPERIMENTS

All particles with one shadow were initially considered to be of possible extraterrestrial origin and were mapped and counted. The only exceptions were the few cases in which particles of distinctive morphology were found with both one and two shadows; all these particles were classed as contaminants. The particles were then heated in stages of increasingly higher temperatures and after each stage the electron diffraction patterns were examined for evidence of newly produced crystallinity. Test temperatures began at 200°C and were increased in 200°C intervals to a maximum of 1000°C or until diffraction

effects were observed in the particles. Heating was done in a three-zone resistance-heated tube furnace (fig. 3). Temperatures were maintained within 10° of the nominal setting for 1 hour, and the furnace was then allowed to cool slowly to room temperature. In the earlier heating tests, the screens were placed in a tungsten container which, in turn, was placed in an inconel tube that fitted into the furnace. At higher temperatures, some sticking of the titanium screen to the tungsten container and some diffusion of one metal into the other made it necessary to replace the inconel tube with one of quartz and the tungsten box with quartz boats to hold the screens.

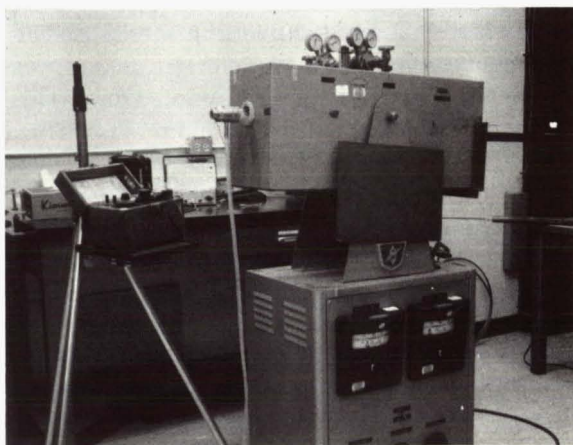


FIGURE 3.—Tube furnace used in heating experiments.

To prevent chemical reactions of the particles with atmospheric gases, especially oxygen and water vapor, the heating was carried out in an inert gas atmosphere. The tube was first purged for $\frac{1}{4}$ hour with high purity argon at a flow rate of 7 liters/min in the inconel tube and 2.4 liters/min in the quartz tube. These flow rates were reduced to 2.4 and 1.4 liters/min, respectively, in the inconel and quartz tubes during the heating and subsequent cooling.

Particles with one shadow were found on 4 of the 17 screens examined. These screens and the coordinate system by which they are designated are shown in figure 2. All four of the screens with one-shadowed particles are titanium with nickel shadow coats.

The one-shadowed particles found consist of 8 individual particles (2 of which were found

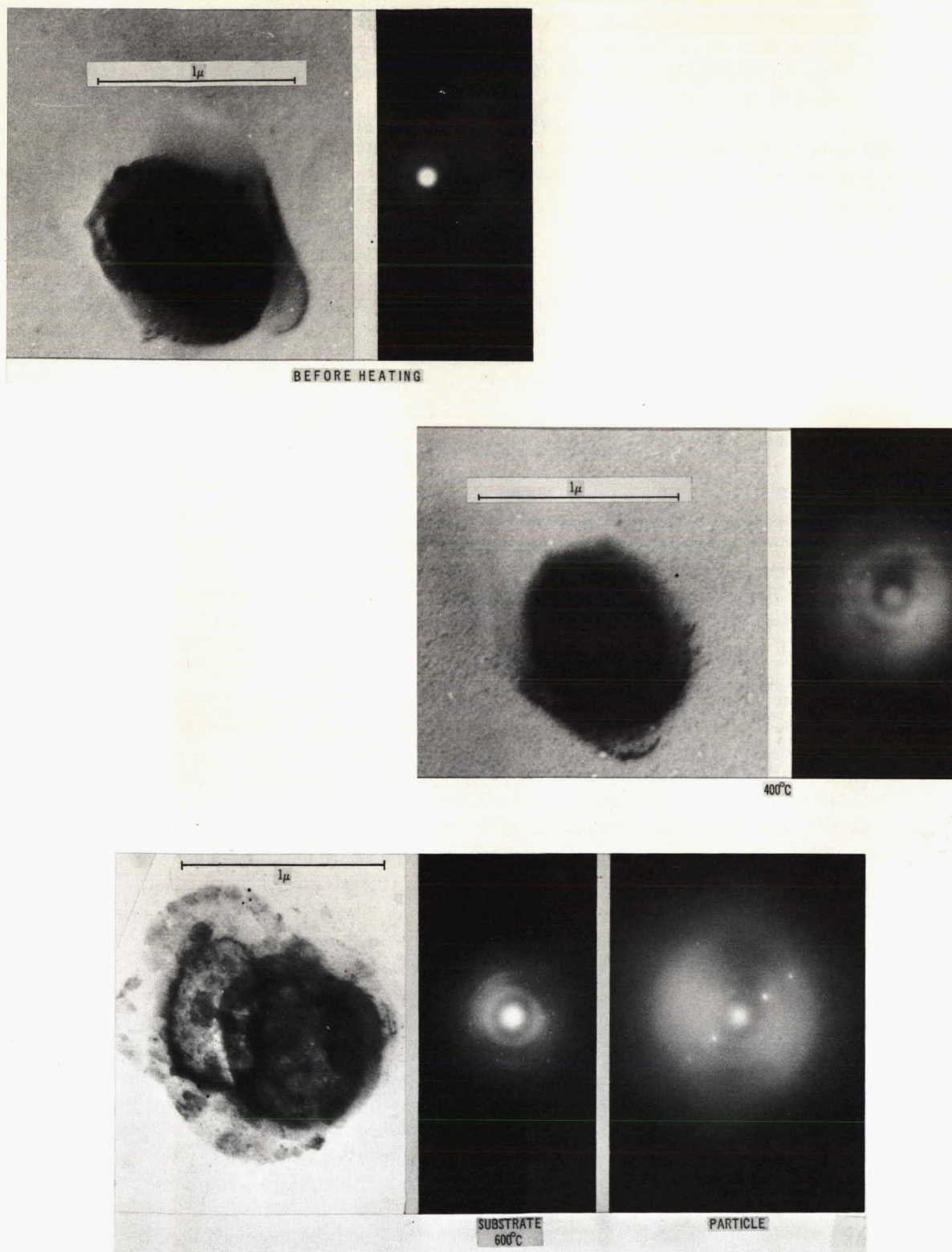


FIGURE 4.—Particle on screen G-16 and its diffraction patterns.

only after heat treatment), one group of 5, and one large group of 58 or more. Of these, the large group and 2 individual particles have been taken completely through the heating tests, 2 are still being tested, 2 have been lost or are otherwise not capable of being studied further, and the remaining group and 2 individual particles are available for additional investigations.

An electron diffraction pattern appeared after heat treatment in only one of the particles studied. This particle, from screen G-16, is shown in figure 4. It is about 0.9 micron in its longest dimension and, before it was heated, had a dense nucleus surrounded by a less dense rim. Essentially no change occurred after heating to 400 °C, nor were any electron diffraction effects observed that were associated with the particle (the broad diffuse rings are attributable to the substrate). After heating to 600° C, however, the nucleus became much less dense, and a dark mottled area appeared around the particle, although its original outlines were not greatly modified.

The diffraction pattern after heating to 600° C shows a symmetrical line of spots, an inner pair corresponding to a d-spacing of about 2.8 Å and an outer second-order pair corresponding to a d-spacing of about 1.4 Å. A single third-order spot of 0.9 Å d-spacing is also faintly seen. This pattern is associated with the particle because the diffraction pattern of the substrate is devoid of these spots, although the sharpening of the rings indicates that some recrystallization of the nickel shadow coat has taken place.

Because of the morphological change in the particle, it is not possible to conclude definitely

that annealing of radiation damage occurred. In fact, these changes at 600° C arouse suspicions as to whether the particle is of extraterrestrial origin at all, despite its single shadow. The possible use of heating to distinguish extraterrestrial from terrestrial particles will be discussed in a later section. The 2.8 Å d-spacing is close to that of prominent lines in both olivine and enstatite. However, definite identification cannot be made from only one d-spacing because other substances may also have lines with this value. It is also possible that the mottled area is caused by recondensation of material volatilized from the particle in the course of heating and that this crystallized material has given rise to the diffraction pattern. Hemenway and Soberman (1962) were able to produce a similar effect by heating with the electron beam in the electron microscope. A third possibility is that the particle may have simply changed position by sliding and left the mottled material as a residue. This possibility is suggested by examination of the stereo pair (fig. 5) taken with two different tilt positions of the particle on a tilting stage. This interpretation would lend support to the possibility that radiation-damage annealing has occurred, because the mottled residue in this case could be the result of physical causes and not necessarily of chemical reactions or vaporization phenomena.

Figure 6 shows particles from screen N-16. These are a large swarm of the type termed "fluffy" by Soberman et al. (1961) and considered by them to be of extraterrestrial origin. The particles have highly irregular outlines and appear to be composed of a mosaic of smaller polygonal units. The largest is about 1/4 micron and they range in size to less than 1/10 micron. The photograph before heating and the one after 600° C show the same particles; the photograph after 800° C is an adjoining group of the same type. No changes seem to have taken place in particle morphology and no diffraction effects were observed, even with a tilting stage. After the 800° C heating, it was found that some rupture of the substrate near the particles had occurred; it was decided, therefore, to subject the particles at this point to electron probe analysis in an attempt to obtain composition

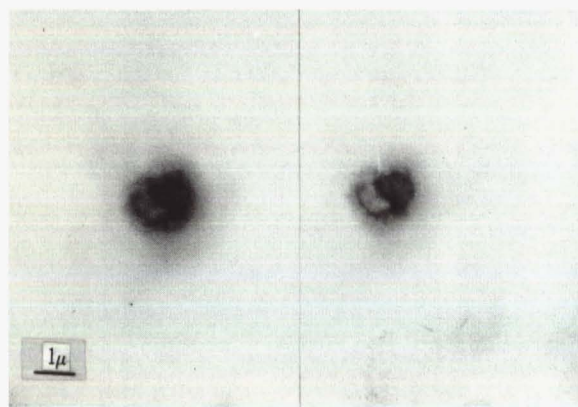


FIGURE 5.—Stereo photograph of particle on screen G-16.

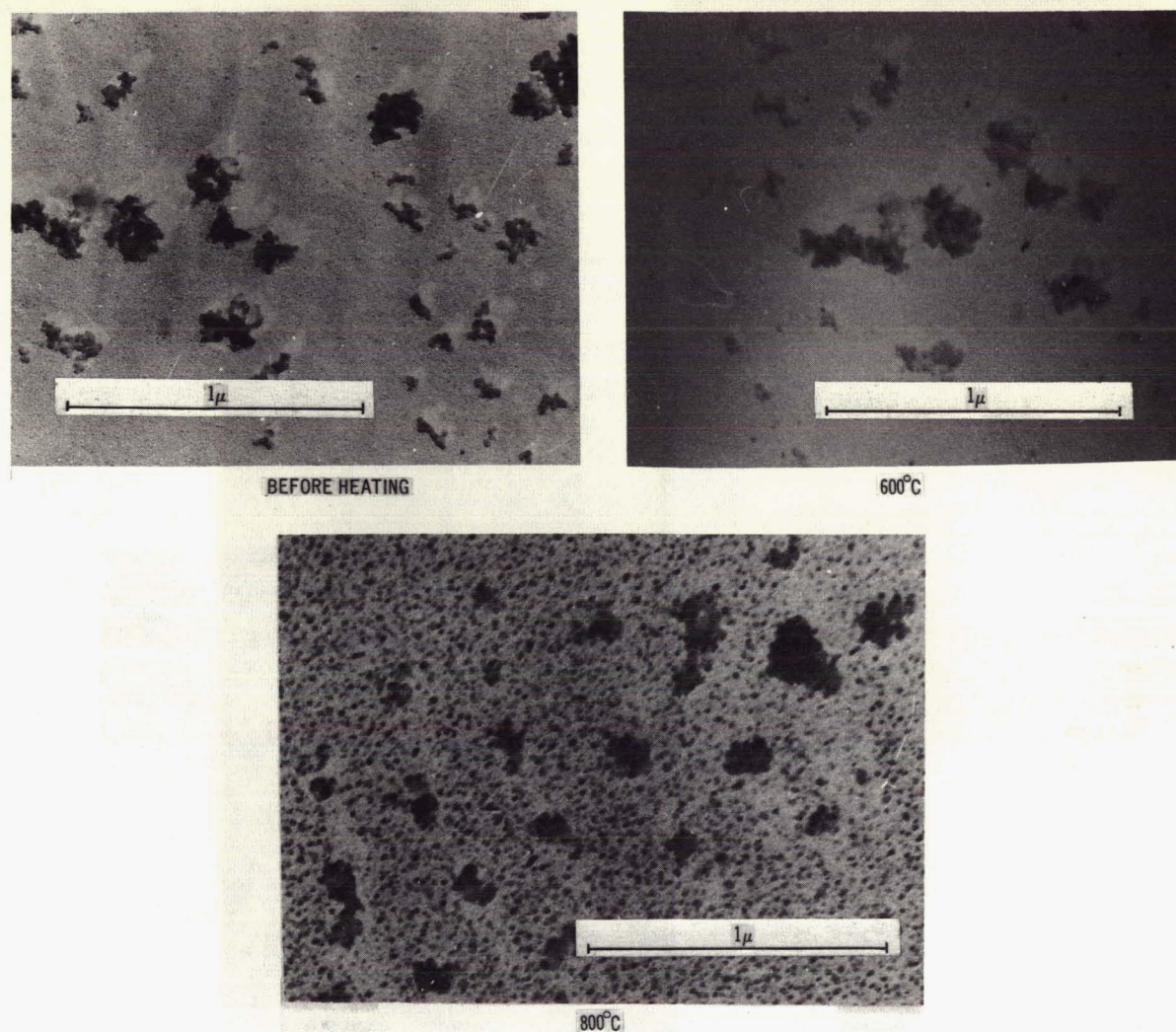


FIGURE 6.—Fluffy particles on screen N-16.

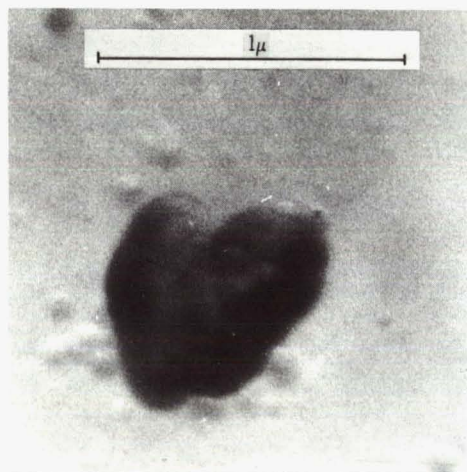
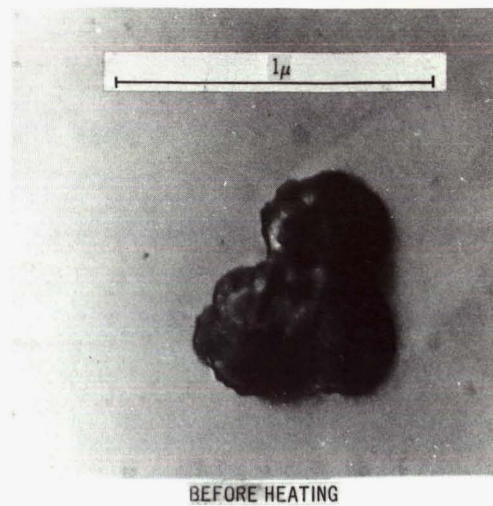
information before possibly losing them with further heating.

If these particles are indeed extraterrestrial, their failure to yield diffraction patterns results because (1) they are amorphous, (2) they are radiation damaged but must be heated above 800° C to be annealed, or (3) they are so intensely radiation damaged that they are not capable of being annealed, as Primak (1960) found to be the case with quartz that was intensely irradiated with fast neutrons. If the first case is true, the radiation-damage criterion for extraterrestrial origin would not be applicable universally. This principle also applies to the third case if heat annealing is used to detect radiation damage.

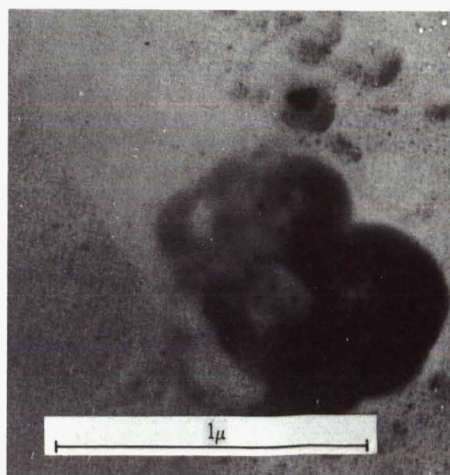
If these are contaminants, on the other hand, they have no bearing on the validity of the radiation-damage criterion. In this case, their diffraction behavior is explained by their amorphous nature.

A particle from screen P-15 is shown in figure 7. It is about 0.8 micron in its longest dimension and has a three-lobed form suggesting a merger of three more or less spherical particles. It showed little, if any, change after 200° C (the apparent distortion in the photograph is caused by its tilted position on the tilting stage). For temperatures higher than 400° C, however, the particle showed progressive disintegration until nothing but a faint residue was left after 1000° C.

FIGURE 7.—Three-lobed particle on screen P-15 and its diffraction patterns.



200°C



400°C

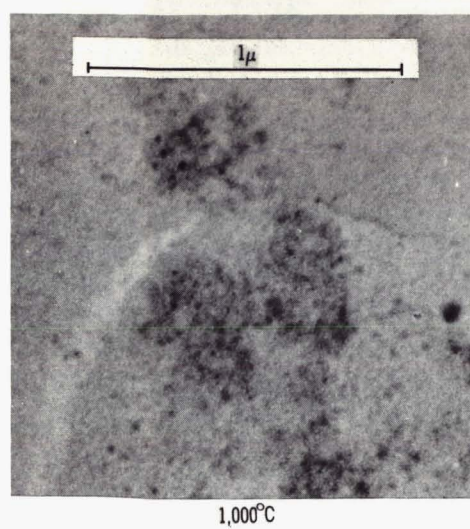
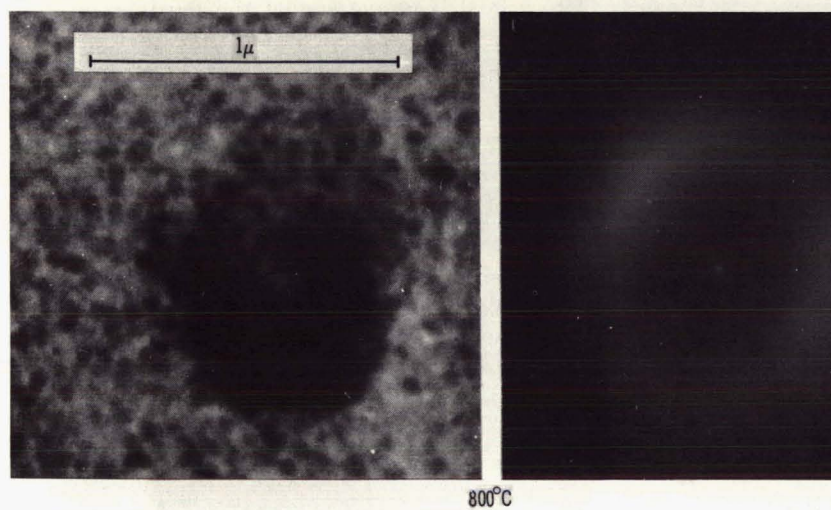
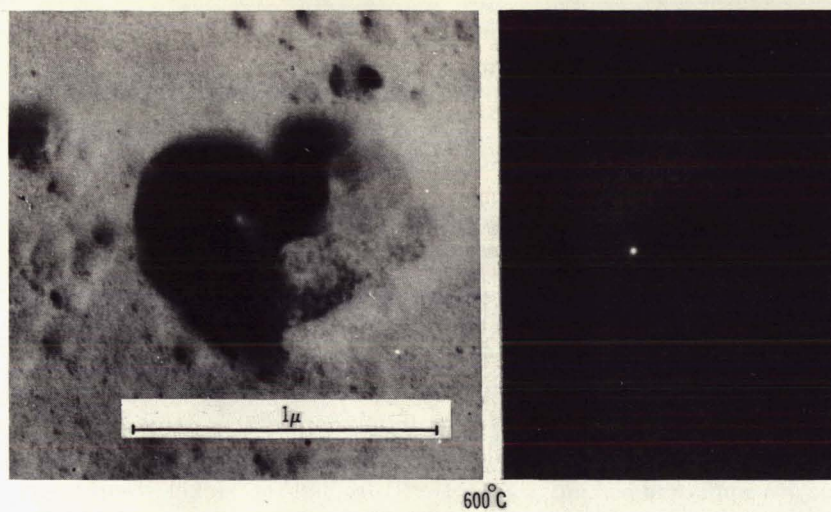


FIGURE 7. - Continued.

No diffraction effects were observed. The sporadic spots appearing in the 800° C diffraction pattern are probably associated with the nucleation of the nickel shadow coat to a more coarsely crystalline state.

Screen A-16 is still undergoing heating tests. Figure 8 shows a particle with a dense spherical core with a somewhat less dense rim providing a polygonal outline. It is about $\frac{1}{2}$ micron in diameter. Figure 9 shows a large fluffy particle, about 1.5 microns in its longest dimension, that was discovered only after the 400° C heating. It yielded no diffraction pattern after being heated to this temperature.

An interesting example of a spherical-looking

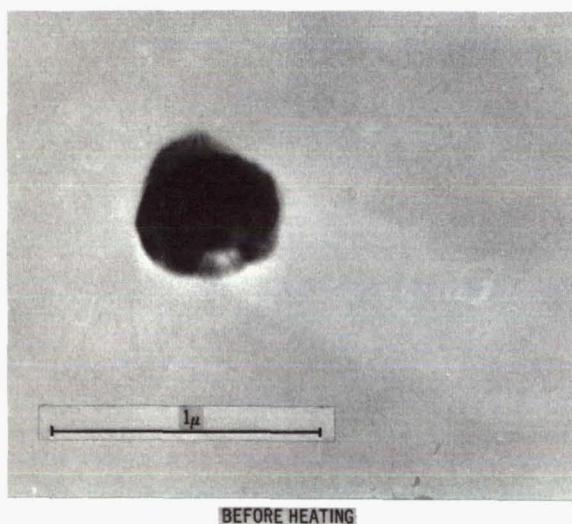


FIGURE 8. — Particle on screen A-16.

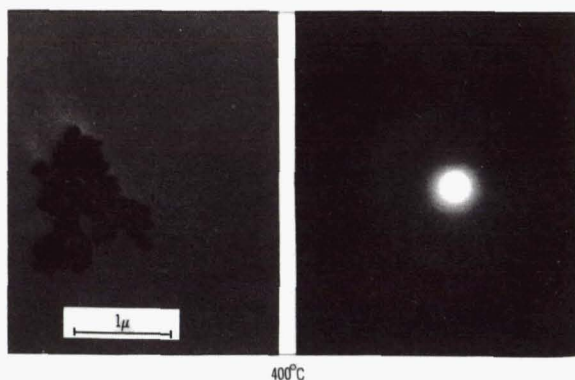


FIGURE 9. — Large fluffy particle on screen A-16 and its diffraction pattern.

one-shadowed contaminant changing with heating is afforded by the particles shown in figure 10 from screen C-16. These are a group of more or less spherical, in part polygonal, particles mostly between $\frac{1}{10}$ and $\frac{1}{5}$ micron. At every heating stage except that at 200° C, the particles photographed show only one shadow. The particles at the 200° C stage, from another mesh opening on the same screen, have two shadows. Such a close association of similar particles showing both single and double shadows strongly suggests that all particles are contaminants that entered during the deposition of the first shadow coat. Possibly, they are incompletely vaporized droplets of nickel some of which arrived just before, others just after, the shadow coat. Comparison of the particles in successive heating stages shows that they have become circular and have expanded in size, although the dark crescent shadow marking the original particle boundary maintains its size more or less unchanged. This screen shows good evidence of tungsten-titanium diffusion, which accounts for the highly crystalline substrate and the breaking up of the screen after 1000° C. It also accounts for the diffraction patterns which show not only sharpening of the nickel rings but also additional rings and the spot pattern at 1000° C, these patterns were probably caused by chemical reactions among the substrate materials.

ELECTRON PROBE ANALYSIS

Electron probe analysis was carried out with an Applied Research Laboratories Model EMX electron microprobe X-ray analyzer. The particle on screen G-16 was subjected to analysis; the fluffy particles on screen N-16 are presently being examined.

Because little work has been done on submicron particle analysis with the electron probe, much of the effort made in this study was devoted to developing successful techniques. One of the first difficulties encountered was the location of the particle with the probe, since the light microscope of the EMX does not give a magnification high enough to see the particle directly. With the use of the electron microscope to obtain a sequence of pictures of successively lower magnification, it was possible to localize the substrate area sufficiently so that the particle

could be picked up by the probe beam. Figure 11 shows the low-magnification electron microscope picture of the particle and of neighboring contaminants which assisted greatly in locating it. Figure 12 is the backscattered electron display of the probe showing particle A and three of its neighbors.

X-ray scans showed only that two of the contaminant particles contained Na (fig. 13) and one contained Fe (fig. 14), neither of which was found in the particle of interest. The beam was next set on the particle, and 10-second counts were made to detect the elements from Mg to Ti (atomic numbers 12 to 22), as well as Cr, Mn, Fe, Ni, Zn, Au, and Pb. None were found, possibly because the particle may have become too thin in the course of the heating tests. It is likely that with longer counting periods and with other improvements in technique, the major elements present in the particle will be detected.

ABUNDANCE AND SIZE MEASUREMENTS

A total of eight individual one-shadowed particles was found on the four screens circled in figure 2. In addition, groups of particles were found on two of these screens, the large swarm of at least 58 fluffy particles on N-16 and the group of 5 on P-15. Those not already pictured are shown in figures 15 to 18. Figure 16 is interesting with regard to the source of fluffy particles. Although the large particle shown is itself dense at the center, it is surrounded by a dozen or more small fluffy particles that appear to have been thrown off from its edges. The particle in figure 17 is also of interest because of its resemblance to the particle on screen G-16 (fig. 4) that yielded diffraction spots with heating.

To calculate the abundance data, the number of particles per unit area is needed. A central area of the screen of 2.1-mm diameter is open to view in the electron microscope. The open mesh area makes up 56 percent of the titanium screen and 70 percent of the tungsten, giving 1.9 and 2.4 mm², respectively, for the available scanning area of each screen. The total area of the 10 titanium and 7 tungsten screens scanned in this study is, then, 36 mm². If the 2 groups are counted each as a single particle, the total of one-shadowed particles is 10, and a value of 0.3 particle per mm² of collector area is obtained. If, on the other

hand, each particle of the groups is counted, the large fluffy group dominates the total, which now rises to 71. This gives a value of 2 particles per mm² of collector area.

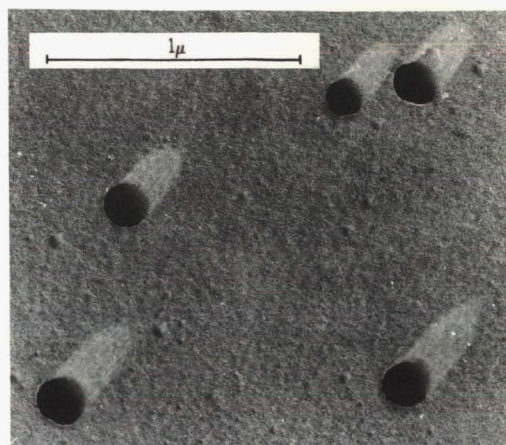
These figures can be compared with the value of 7 particles per mm² given by Soberman et al. (1961) for the Venus flytrap, which collected over a higher altitude range (88 to 168 km) and for a little longer time (236 sec) than the Luster. It must be remembered, however, that the Venus flytrap data are for particles estimated to have been extraterrestrial, the suspected one-shadowed contaminants having been eliminated from the count. For the present study, the count includes all one-shadowed particles, with the few exceptions mentioned earlier. Because of this difference and because the scanning efficiency is not known (the scanning efficiency of the Venus flytrap work is assumed to be 100 percent), the two abundance values are not strictly comparable. However, a rough estimate of the scanning efficiency of this study can be obtained from the fact that, of the total of eight particles and two groups, two particles were discovered during examination after the heating tests, not in the original preheating scans. This increase of 25 percent, taken as a measure of efficiency, gives maximum values of 0.4 and 2.5 instead of 0.3 and 2 particles per mm² in the two cases discussed previously. If the fluffy particles (one group of 58 and 2 individual) are taken to be the only extraterrestrial particles, the two values become 0.1 and 2 particles per mm². Evidently, the abundance of particles collected by the Luster collector during the Leonid meteor shower is, at most, less than half that of the Venus flytrap but may be much less, even zero, if the fluffy particles, too, are contaminants.

In size, the particles range from about 0.05 to 0.3 micron in the group of 58 fluffy particles and from 0.2 to 0.5 micron in the group of 5 particles on screen P-15. For the individual particles, the sizes are 1.5, 0.9, 0.8 (for 3 particles), 0.5, and 0.3 micron. Data are not available for one particle.

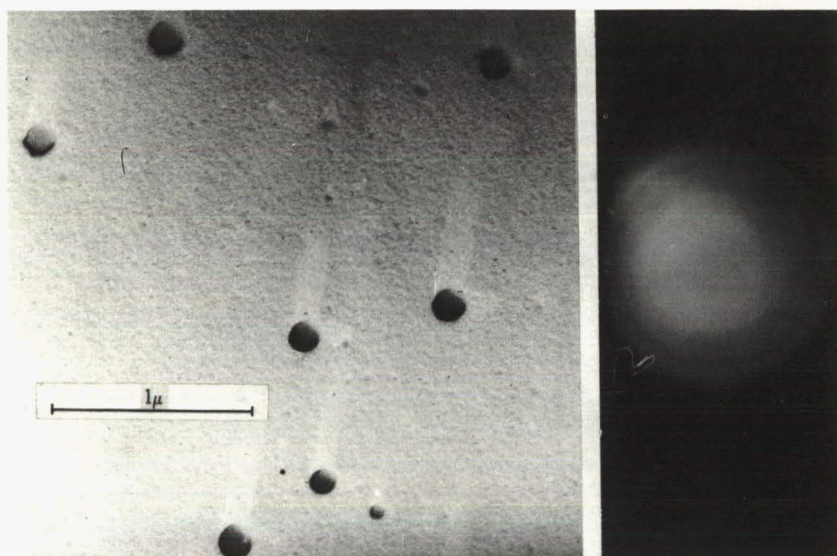
CONCLUDING REMARKS

One group of 58 particles and 2 individual particles went completely through the heat annealing tests; 2 individual particles are still

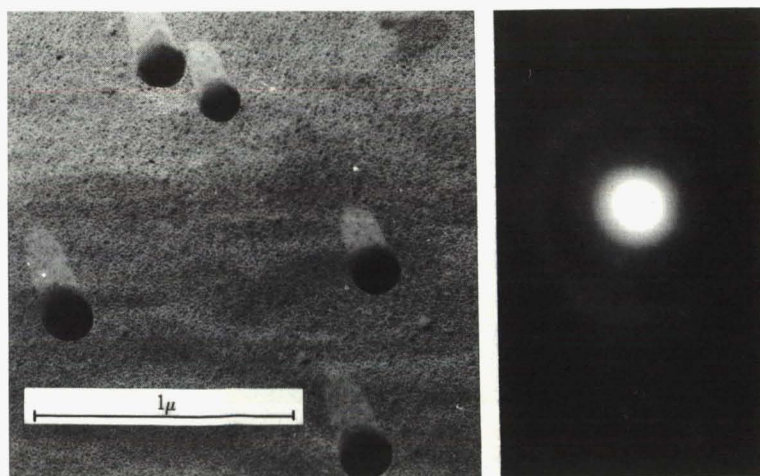
FIGURE 10.—Contaminant particles with both one. and two shadows on screen C-16 and their diffraction patterns.



BEFORE HEATING



200°C



400°C

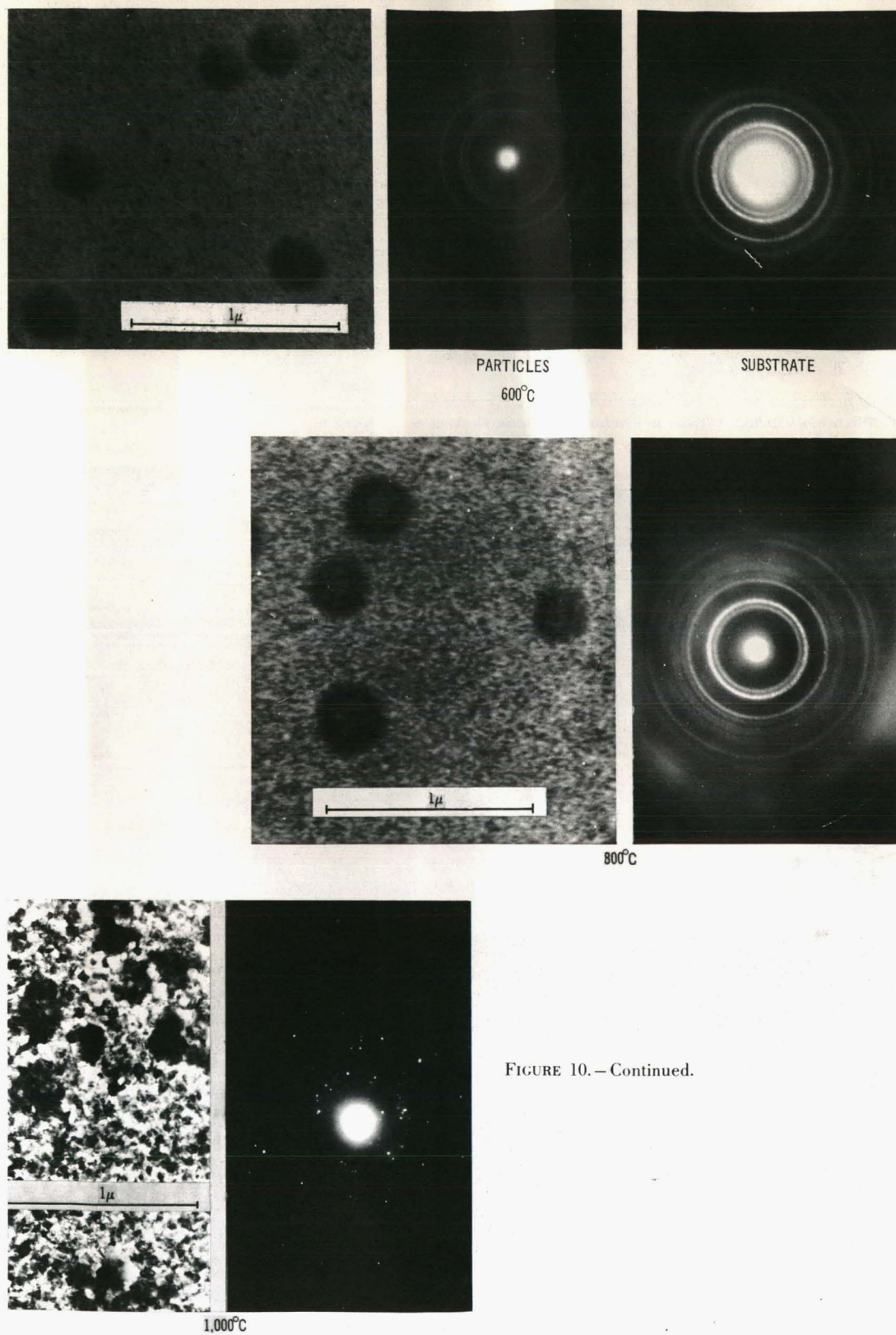


FIGURE 10.—Continued.

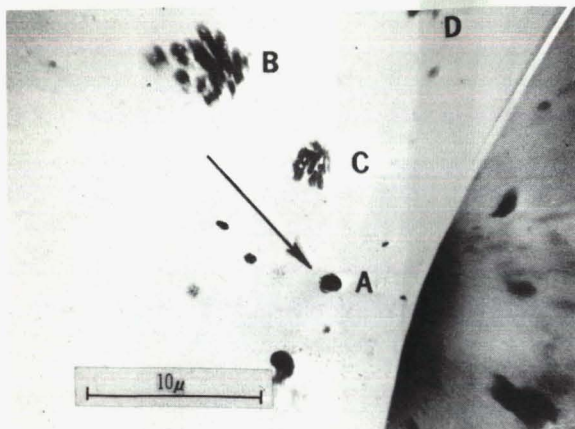


FIGURE 11.—Low-magnification photograph of particle shown in figure 4 (labeled A) used in locating particle in electron probe.

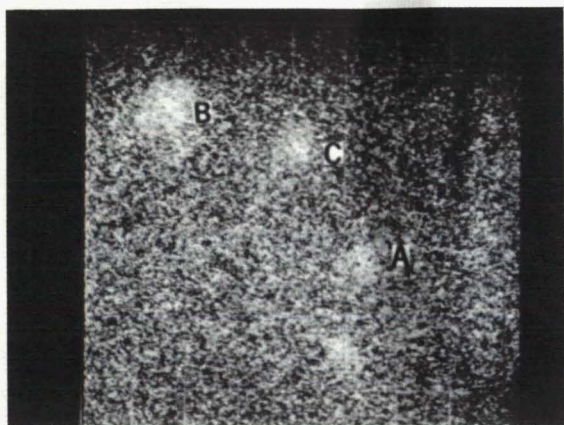


FIGURE 12.—Backscattered electron photograph of same area shown in figure 11. (Grid square side equals 3 microns.)

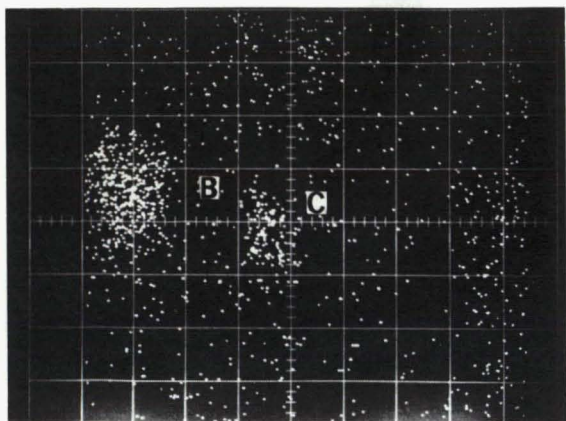


FIGURE 13.—Na K α X-ray scan of same area shown in figure 11. (Grid square side equals 3 microns.)

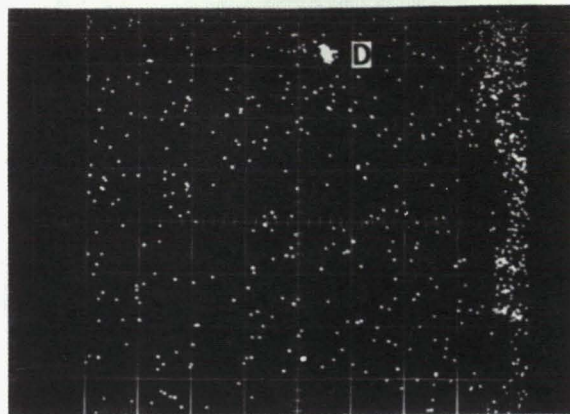


FIGURE 14.—Fe K α X-ray scan of same area shown in figure 11. (Grid square side equals 6 microns.)

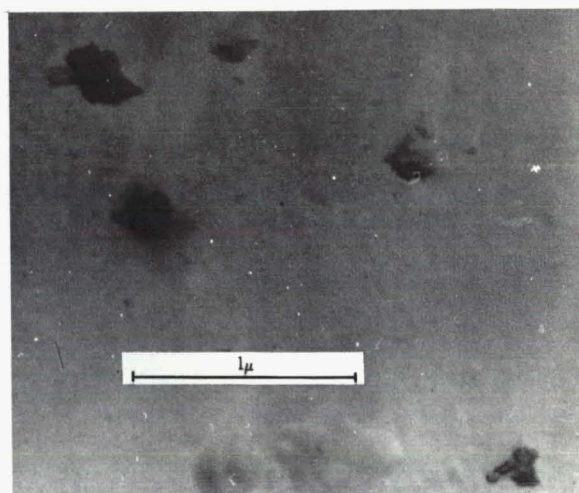


FIGURE 15.—Group of particles on screen P-15.

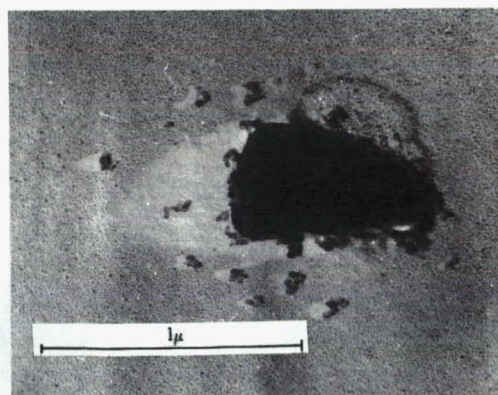


FIGURE 16.—Dense particle on screen N-16 with small fluffy particles.

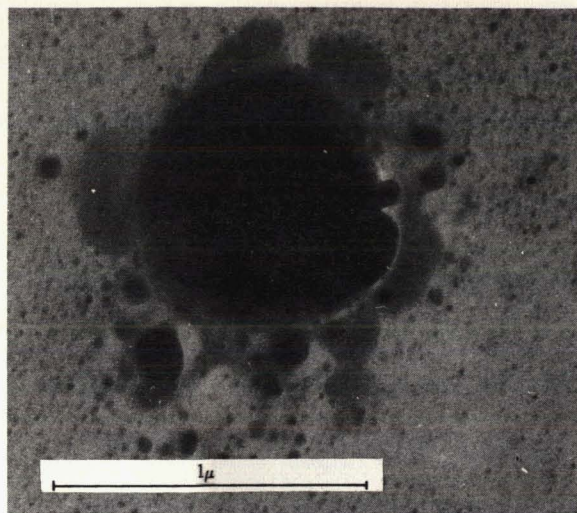


FIGURE 17.—Particle on screen N-16.

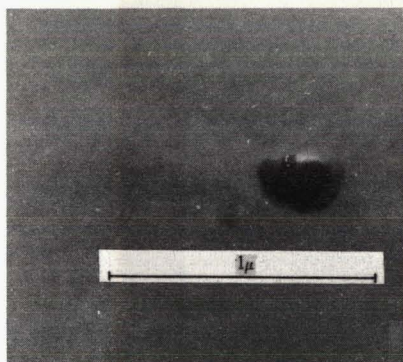


FIGURE 18.—Particle on screen P-15.

being tested. Of those for which the tests were completed, one individual particle (screen G-16) showed new diffraction spots after heating to 600° C but also showed morphologic changes, the second (screen P-15) showed morphologic changes and no diffraction after 1000° C, and the group of particles (screen N-16) showed neither morphologic changes nor diffraction after 800° C. Quite possibly, the two individual particles that changed in the course of heating are not of extraterrestrial origin because silicates and iron, of which, at first guess, micrometeorites may be largely composed, are stable at these temperatures. (It is assumed that they are also stable under these conditions in particles of submicron sizes, but this assumption should be tested.)

The heating technique may thus have diagnostic value beyond that of radiation-damage annealing alone. Contaminant particles of the type found with both one and two shadows on screen C-16, as well as organic substances and possibly hydrates and other materials, can easily be distinguished from stable materials by heat-produced morphologic changes even though all particles may have only one shadow.

If the group of fluffy particles tested are of extraterrestrial origin, their failure to show either morphologic changes or diffraction patterns may indicate that the radiation-damage criterion is not applicable to particles of this type. On the other hand, these, too, may be contaminants. To determine conclusively whether radiation damage is a criterion for extraterrestrial origin will, therefore, require tests on many more particles and, especially, the integration of data from these tests with composition information, as well as with morphologic and other information. Additionally, further investigation of heat-produced morphologic changes in silicates, iron, and other appropriate materials should be undertaken because these changes may well be of value in classifying certain particle types as contaminants.

No chemical composition data from the electron probe have yet been obtained from the particles except for the detection of Na and Fe in some of the contaminants. Success was achieved in the development of techniques for locating submicron particles in the probe.

Abundance values for the Luster flight, based on 8 individual particles and 2 groups of particles, are 0.3 and 2 particles per mm² of collector surface, the first value applying if each group is counted as a single particle, the second if every particle in the groups is counted. These values do not include corrections for one-shadowed contaminants or for scanning efficiency. Sizes are almost entirely in the range 0.1 to 1 micron, the particles in the groups being less than 0.5 micron, the individual particles being mostly greater than 0.5 micron.

ACKNOWLEDGMENTS

We wish to thank P. A. Larssen and E. L. Miller for help with the electron probe analysis and F. J. Moyers for help with the heating of the samples.

REFERENCES

- FARLOW, N. H., and M. B. BLANCHARD. 1966. *Trans., Amer. Geophys. Union*, **47**, 143-144.
- GREENMAN, N. N., 1963. *Trans., Amer. Geophys. Union*, **44**, 877.
- , 1964, *Ann. N.Y. Acad. Sci.*, **119**, 298-317.
- GREENMAN, N. N., and C. B. GILPIN, 1967, NASA SP-135 (SCA Vol. 11).
- , 1966, *Trans. Amer. Geophys. Union*, **47**, 480-481.
- HEMENWAY, C. L., and R. K. SOBERMAN. 1962. *Astron. J.*, **67**, 256-266.
- MURRAY, J., 1876. *Proceedings Royal Society of Edinburgh*, **9**, 247-261.
- PRIMAK, W., 1960. *Journal of Physics and Chemistry of Solids*, **13**, 279.
- RYAN, J. A., 1964, in *The Lunar Surface Layer* (J. W. Salisbury and P. E. Glaser, eds.), 265-312 (New York: Academic Press).
- SOBERMAN, R. K., C. L. HEMENWAY, T. G. RYAN, S. A. CHREST, J. FRISSORA, E. F. FULLAM, J. J. BALSAMO, J. COLE, D. HALLGREN, P. YEDINAK, A. GOODMAN, and G. HOFF, 1961. *GRD Research Notes*, 71.

24. Preliminary Micrometeorite Results From Gemini IX and XII*

C. L. HEMENWAY AND D. S. HALLGREN
*Dudley Observatory
Albany, New York*

AND
J. F. KERRIDGE
*Birkbeck College
London, England*

Micrometeorite collection and cratering experiments were successfully exposed to the space environment during the recent series of Gemini manned space flights. Preliminary results are presented, following an examination in an electron microscope, of some thin nitrocellulose collection and penetration films. A study of cratering effects in polished stainless steel using optical microscopy and a Stereoscan electron microscope is also presented. Some evidence is advanced that discrepancies between satellite microphone and penetration data may be due to the fragile nature of a portion of the interplanetary dust population.

THE S-12 MICROMETEORITE COLLECTION EXPERIMENT included aboard three of the manned Gemini spacecraft missions in 1966 consisted of 24 specimen slides, each measuring 1 inch by 1.125 inches by 0.0625 inch and contained within a box attached to the outside of the spacecraft adaptor section. The collector is constructed in two sections to enable one section to be sterilized for biological experiments. The unit measures 11 inches by 5 inches by 1 inch and weighs 6.5 pounds. The package (shown in fig. 1) was sealed before flight, opened at altitude for a specified period, sealed on completion of the exposure, and retrieved during an EVA exercise by an astronaut for stowage within the spacecraft for reentry. The box was internally powered and electrically operated with squib-actuated locking rods and was controlled by the astronauts by means of a switch panel located in the cabin on missions GT-IX and GT-X and by command from the ground on mission GT-XII. The sensitive collection surfaces were loaded and unloaded in the clean facility at Dudley Observa-

*This study was supported by National Aeronautics and Space Administration Grant NsG-155-61.

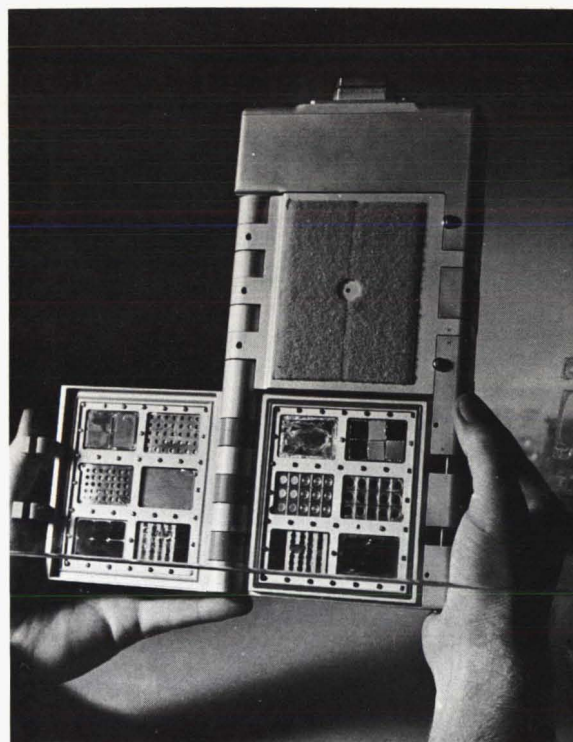


FIGURE 1.—The S-12 micrometeorite collection experimental package.

tory, the complete S-12 unit being hand-carried to and from Cape Kennedy.

In addition to surfaces prepared by Dudley Observatory, 11 other laboratories provided surfaces for inclusion on a guest experimenter basis. (See table 1.) This paper describes preliminary results from the host laboratory's surfaces, other workers' results being published elsewhere. The experiment included on mission GT-X was accidentally lost; the exposure conditions for the two successful experiments are given in table 2. The collections were made at an altitude of 300 kilometers. On the GT-IX-A mission the exposure took place during two sleep periods, the spacecraft being in a tumbling mode. In order to minimize contamination of the surfaces no material was dumped from the spacecraft nor were the attitude control thrusters

fired during a 1-hour period immediately preceding exposure. On mission GT-XII, however, the spacecraft was maintained in 0,0,0 orientation throughout the exposure by operation of the thrusters. Since the Gemini spacecraft was at that time docked with the Agena target vehicle, the thrusters used were those of the Agena; during the 6-hour 24-minute exposure, 2 pounds of a nitrogen-freon mixture were expended from the thrusters. In addition a urine dump was made approximately 1 minute before exposure. The spacecraft orientation resulted in the S-12 unit "looking" directly away from the Earth but tilted by about 10° toward the path of the spacecraft.

RESULTS

Several different surfaces were employed in the S-12 experiment with a number of investigative techniques in mind. This paper describes results obtained thus far from a study of some thin nitrocellulose films designed for examination in the transmission electron microscope. For the GT-IX-A experiment some films were shadowed with aluminum and some with palladium; for GT-XII only palladium was used. The shadowing served to identify contaminant particles by flagging them (Hemenway and Soberman, 1962). As an additional control some films were mounted in the collection unit facing downward, shielded from the micrometeorite flux, and these were surveyed in order to sample the contamination indigenous to the experiment.

A superficial difference between the surfaces returned from missions GT-IX-A and GT-XII was the considerable damage suffered by the exposed films flown aboard GT-IX-A. Both sets of controls and the exposed films from GT-XII were returned essentially intact.

Grids were punched from both exposed and control films and examined in the RCA EMU-3 electron microscope. Total exposed area examined to date is 5 mm² from GT-IX-A and 10 mm² from GT-XII; control areas examined are, respectively, 6 mm² and 11 mm². Study of the GT-IX-A surfaces has so far been confined to those shadowed with palladium.

In the electron microscope the grids were scanned at 3000X magnification and initially all phenomena visible at this magnification, except

TABLE 1.—*Guest Experimenters for S-12 Micrometeorite Collection*

Laboratory	Principal experimenter	Missions
Air Force Cambridge Research Laboratories.	Skrivanek	IX-A, X, XII
Ames Research Center ...	Farlow	IX-A, X, XII
University of Chicago.....	Fernandez-Moran	X
Max Planck Institut, Heidelberg.	Fechtig	IX-A, X, XII
Birkbeck College, London.	Kerridge	X, XII
Manned Spacecraft Center.	Burbank	IX-A, X, XII
Smithsonian Astrophysical Observatory.	Wright	X, XII
University of Washington	Hodge	X, XII
University of Tel-Aviv	Shafir	IX-A, X, XII
U.S. Geological Survey...	Carr	IX-A, X, XII

TABLE 2.—*Exposure Conditions for S-12 Micrometeorite Collection Experiments*

Mission	GT-IX-A	GT-XII
Date.....	6/3, 4/66	11/11/66
Duration.....	16 ^h 47 ^m	6 ^h 24 ^m
Orientation.....	Random	Directed

for unshadowed particles, were photographed at an appropriate magnification, generally about 8000X. Phenomena which were observed at this higher magnification but not at the lower setting were not intentionally photographed and were not included in the results. Later, when familiarity had been gained with the phenomenological background, certain readily identifiable artifacts were consciously omitted from the record. An example of this selection process is the omission of large holes which, although more frequent in the exposed surfaces than in the controls, were indistinguishable in the two cases. The result was an upper level cutoff in the size data for holes but it was not possible to define this cutoff point.

The two major species of phenomena observed were particles and holes. It was noticeable that the control grids were extremely clean of particles, most contamination being unshadowed and amounting to about the same on both exposed surfaces and controls. Single-shadowed particles predominated over double-shadowed particles on exposed and control grids, the exposed surfaces showing a significant excess of the former (relative to the controls) up to 1 micron in size at which point the signal fell below the noise level. The number of particles between 0.1 and 1 micron in size found on exposed and control surfaces for both missions, normalized to events per meter² of actual collection surface per second of exposure time, is shown in table 3. Clearly, some of the particles seen on exposed surfaces are contaminants picked up during flight but at this stage no attempt has been made to distinguish these from genuine micrometeorites.

TABLE 3.—*Numerical Results from Preliminary Study of Surfaces Included in S-12 Micrometeorite Collection Experiments*

	GT-IX-A	GT-XII
Total particles on exposed surfaces ...	73	272
Particles on control surfaces	40	220
Total holes on exposed surfaces.....	2400	60
"Real" holes on exposed surfaces.....	400	4
Total holes on control surfaces.....	194	12

At satellite altitudes micrometeorite collection is undoubtedly an improbable process in view of the high velocities involved; therefore, measurements of micrometeorite flux based on a count of particles collected intact by satellite should be treated with caution. This view was supported during the study of surfaces from GT-IX-A by the fact that holes in the film exceeded particles in number by a factor of 10. This factor was indicative of a great many particles having passed through the nitrocellulose film.

It was believed that the study of holes could not be conducted in the same overall statistical fashion as was employed for the particles. Instead, although the total number of holes in exposed surfaces greatly exceeded that in controls, an attempt was made to assess each hole in an exposed film and place it in either a "real" or "false" category on the basis of qualitative comparison with phenomena observed on the controls. The criteria for this selection were made conservative deliberately, and for any area considerably more holes were rejected from the exposed-surface results than occurred in the corresponding controls. Figure 2 illustrates two fairly typical "real" hole structures, that is, structures unlike any known indigenous artifacts and thought to be due, therefore, to the impact of a micrometeorite.

The width of each "real" hole was measured and in table 3 are given the numbers of holes larger than 0.1 micron found in exposed and control films for missions GT-IX-A and GT-XII. The difference between the results from the two missions is striking and this discrepancy will be discussed later in the paper.

Two phenomena observed on exposed films from GT-IX-A but not on either set of controls or on GT-XII exposed films are shown in figures 3 and 4. Each occurred at a rate of approximately 100 events per meter² per second. The cluster of holes shown in figure 3 is thought to be due to a relatively large particle with low cohesive strength breaking up on contact with the spacecraft atmosphere. No satisfactory explanation for the eyelike structure of figure 4 has yet been set forth.

The large difference between the hole count on the GT-IX-A films and that for GT-XII is

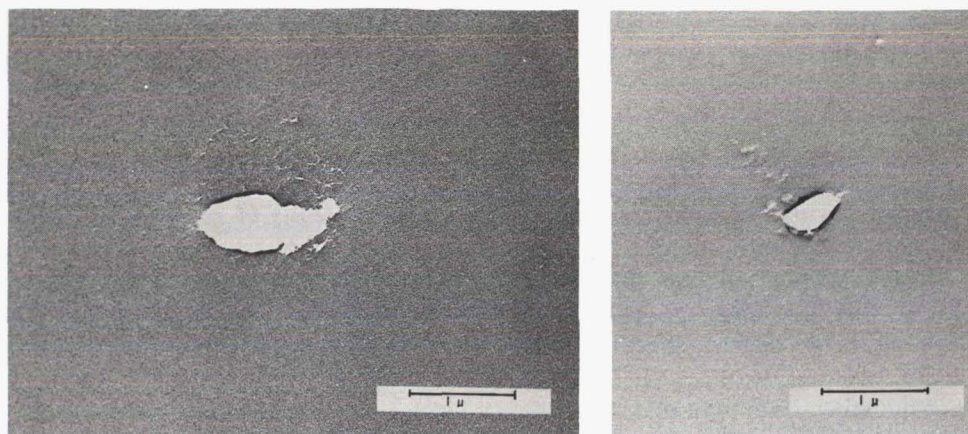


FIGURE 2.—Nitrocellulose film shadowed with palladium and exposed during mission GT-IX-A showing “real” hole structures.

hard to explain on instrumental grounds. Although the nitrocellulose films used in the latter experiment were slightly thicker than the earlier ones, it is not thought that this could produce such a striking effect. Doubts that the S-12 unit on GT-XII might not have opened (it was not visible to the astronauts during operation) were eliminated by four independent observations: all electrical and mechanical parts had apparently worked properly; photographic film monitors inside the boxes were blackened on recovery; results from biological survival experiments contained within the same unit were consistent

with earlier work; after the flight the interior of the box was under vacuum.

Three differences in the experimental conditions between the two missions might be noted in connection with this discrepancy. In the first place, the orientation of the collection surfaces differed between the two exposures. Secondly, the preexposure urine dump and the release of nitrogen-freon gas from the thrusters contributed to the spacecraft atmosphere for the GT-XII experiment. Finally, the GT-IX-A mission took place during the Zeta Perseid and Arietid radar meteor showers, whereas the GT-XII exposure

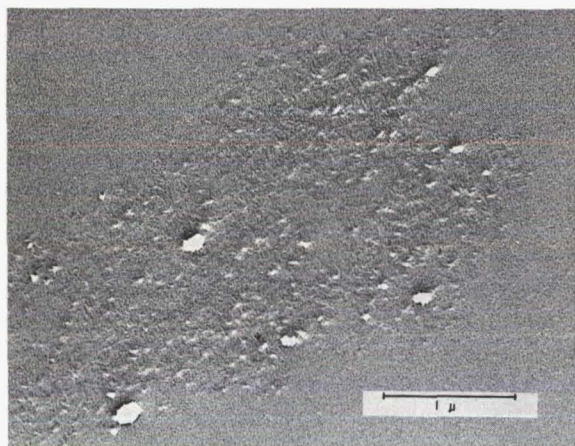


FIGURE 3.—Electron micrograph of a multiple-hole structure found in a nitrocellulose film shadowed with palladium and exposed during the GT-IX-A mission.

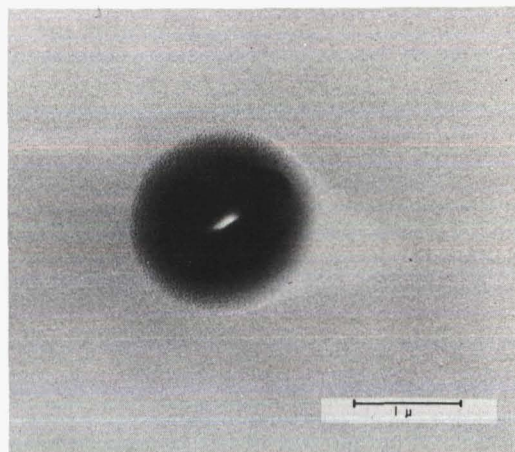


FIGURE 4.—Electron micrograph of a curious eyelike structure found in palladium-shadowed nitrocellulose films exposed during the GT-IX-A mission.

fell into the quiet period immediately preceding the Leonid shower. However, the effect of these factors on the experimental conditions is still uncertain.

It is hoped that work currently in progress will help to show which of the S-12 results more closely approximates the actual micrometeorite flux in the 0.1- to 1.0-micron range. This work is the S-10 micrometeorite cratering experiment which was flown on the outside of the Agena target vehicle (Gemini VIII mission) and retrieved some 4 months later by astronaut Collins during the Gemini X mission. This experiment consisted of four highly polished stainless-steel plates which were exposed to the space environment throughout the flight of the Agena. The unit measures 6¼ inches by 5½ inches by 1 inch and weighs 4 pounds. Each plate has an area of 21.5 cm². Figure 5 shows the experimental package after recovery. The stainless-steel plates are visibly dirty, much of the surface material being contamination due to thruster firings and astronaut handling. Clearly, distinguishing particulate matter from contaminants would be extremely difficult; therefore, the search for particles was begun by examining the stainless-steel plates for impact craters. Scanning with an optical microscope capable of resolving craters greater than 10 microns in diameter revealed three such craters, one of which is illustrated in figure 6. The same crater seen in the Stereoscan electron microscope is shown in figure 7 and a detail of

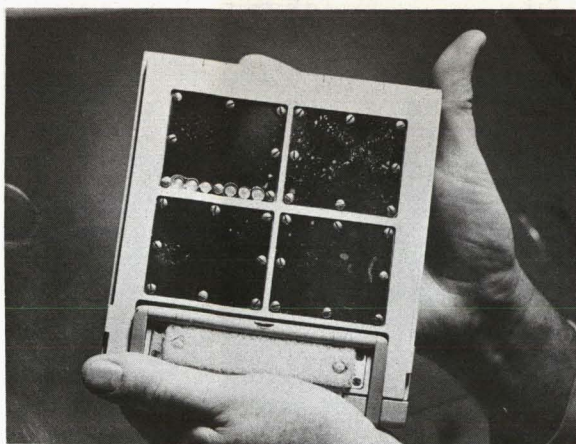


FIGURE 5.—The S-10 micrometeorite cratering experimental package after recovery.

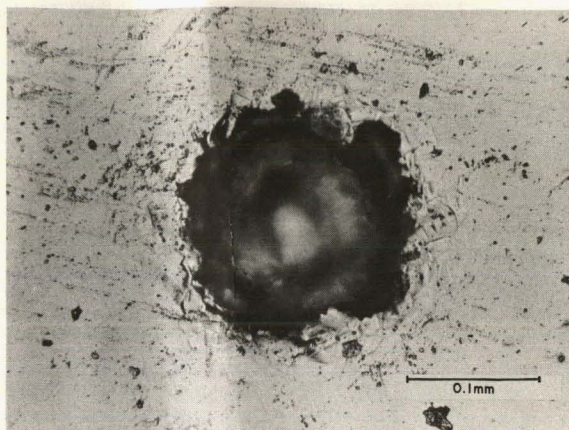


FIGURE 6.—Photomicrograph of a crater found in a stainless-steel plate exposed to space environment for 4 months on the S-10 experiment.

it in figure 8. This latter photograph reveals very clearly the flow structure on the inside of the crater indicative of intense local heating when the crater was formed by (it is thought) a particle impacting at high velocity. The other two craters found in the stainless steel are shown in figures 9 and 10 as they appear in the Stereoscan. The largest crater (fig. 9) measures 290 microns by 180 microns and is 32 microns deep; the smallest crater (fig. 10) measures 17 microns across and 7 microns in depth.

It is interesting to note that the crater in figure 9 is multiple, apparently caused by a loosely bound aggregate. This observation offers a possible explanation for the apparent discrepancy between micrometeorite flux measurements derived from satellite microphone data and from penetration experiments such as Pegasus. It seems probable that the penetrating power of such an aggregate would be comparatively small whereas its momentum as recorded by a microphone would be indistinguishable from that of a solid particle. Such a suggestion has been proposed by Jennison and McDonnell (1966).

These surfaces are being scanned at higher magnifications in the Stereoscan in a search for craters as small as 0.1 micron in diameter in order to relate this work with that of the S-12 experiment; to date few phenomena have been observed which support the S-12 results from GT-XII. However, the area examined thus far with the Stereoscan has been very small.

FIGURE 7.—The crater shown in figure 6 as it appears in the Stereoscan electron microscope. Width of the crater is 160 microns; depth is 65 microns.

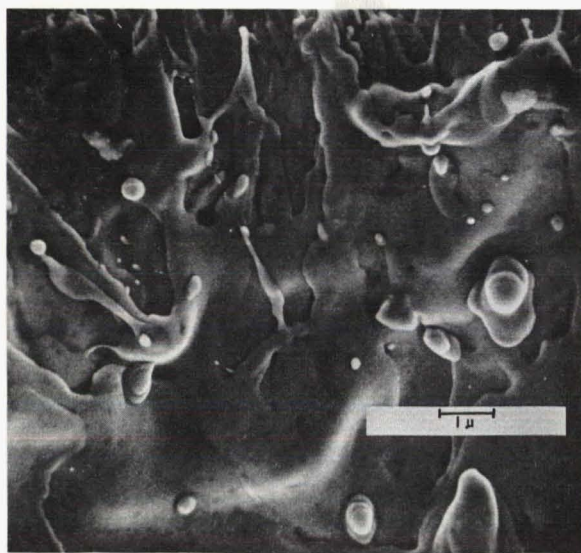
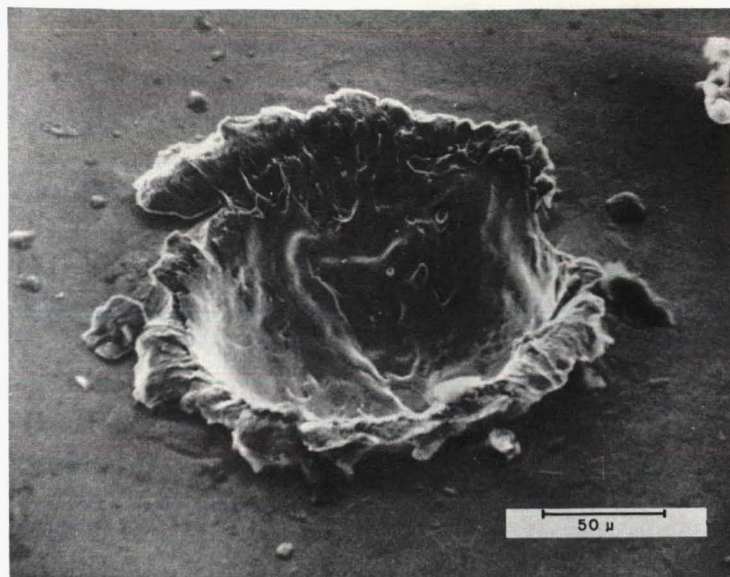


FIGURE 8.—A Stereoscan view of a detail within the crater shown in figures 6 and 7.

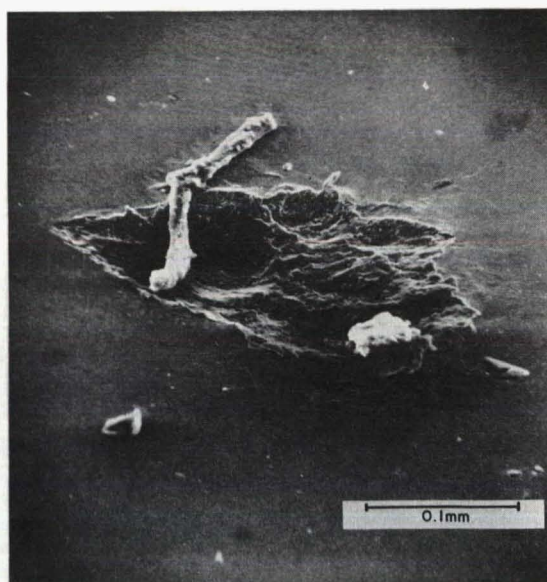


FIGURE 9.—The largest crater found on the S-10 stainless-steel surfaces.

FIGURE 10.—A Stereoscan photograph of the smallest crater found by optical microscopy in the S-10 stainless-steel plates.



REFERENCES

- HEMENWAY, C. L., and R. K. SOBERMAN, 1962, *Astron. J.*, **67**, 256.
JENNISON, R. C., and J. A. M. McDONNELL, 1966, in *Space Research VI*, 937.

Page intentionally left blank

25. Preliminary Results of a Micrometeoroid Collection Experiment in the Gemini Program

URI SHAFRIR AND AKIVA YANIV
Tel-Aviv University
Tel-Aviv, Israel

Results of a preliminary analysis of a micrometeoroid collection experiment are discussed. The collection surfaces were exposed for a period of approximately 17 hours to space environment at an altitude of about 250 kilometers during the Gemini IX mission in May 1966.

With the aid of optical and electron microscopy, surface phenomena, such as color changes of the copper grids, round holes in the 200-Å-thick formvar collecting film, and single-shadowed particles were observed and described.

Some speculations as to the possible causes of these phenomena are presented.

THE EXPERIMENT

THE EXPERIMENT was part of the Guest Experimenters Program for Micrometeoroid Collection in the Gemini IX mission. For a detailed description of the experiment as a whole, see paper No. 24 by Hemenway, Hallgren, and Kerridge. This experiment was flown on May 31, 1966, on the Gemini IX spacecraft and exposed for 16 hours and 47 minutes at an altitude of approximately 250 kilometers above the surface of the Earth.

For this study, 34 electron-microscope (EM) 200-mesh grids were mounted in a brass container approximately $2.5 \times 3.0 \times 0.15$ centimeters; the EM grids were covered with formvar films 200 Å wide, and 10 were mounted approximately 0.5 millimeter under a 6-micron Mylar film, as shown in figure 1.

RESULTS

The preliminary results are based on the following analysis:

(a) Scanning, by optical microscopy, of five grids and parts of the brass container.

(b) Scanning, with the aid of an electron microscope (GEM 7), of three grids.

(c) Mass spectrometry, with the aid of GCA argon ion micro-mass spectrometer, of one large particle.

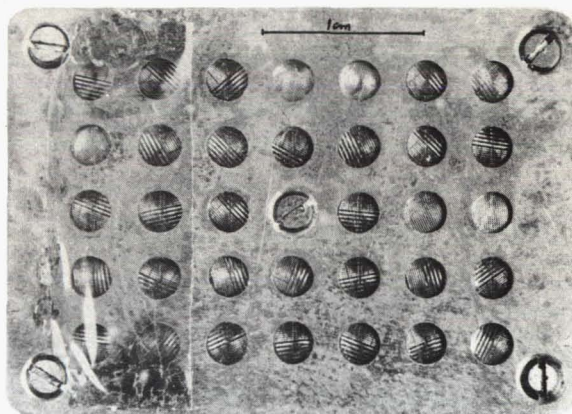


FIGURE 1.—General view of experiment.

Therefore, it should be clear that these results are obviously of a preliminary nature, and that any terminal conclusions based on this experiment will necessarily have to await further analysis of a larger number of grids.

Color Changes

Four or five of the copper grids were found to have undergone color changes during the exposure in space. The original yellowish color of the copper grids (which was preserved under the holdup frame) changed to red close to the exposure boundary of the grid and then to turquoise-blue, which was the color of most of the grid. It should be mentioned that all cases of color changes exhibit radial symmetry, that is, a turquoise-blue inner circle, covers most of the exposed area of the grid and is surrounded by a thin red circle, which is in turn surrounded by the original yellowish color of the copper grid extending to the outer circular boundary of the grid.

Superposed on this large-scale color change are small areas (a fraction of a millimeter in size) where rather extensive color changes occur. A typical case would be a red dot on the turquoise-blue background, or a small blue area on a red background.

In all cases of grids where color changes took place, extensive damage to the formvar film occurred. In addition, it should be noted that all color changes occurred on EM grids which were directly exposed to the space environment, that is, no color changes were found on the grids which were mounted under the 6-micron Mylar film. At least in one case, close examination of the bottom of the brass container, where a colored grid was found, showed a "photograph" of the grid pattern on the brass; in other words, areas of the brass container which were not covered by the grid mesh appeared definitely darker than the covered parts on the bottom of the container. Several color change phenomena are demonstrated in figures 2 to 5.

Particles

Many single-shadowed particles of sizes 100 Å to several microns were found both on the EM grids which were not covered by the 6-micron Mylar film and on the covered ones. Figures 6, 7, and 8 demonstrate various types of particles which were found on the 200-Å formvar film; none of the particles have regular shapes, some appear very fragile, and some are embedded in the film.

Since the results thus far rely on examination of only one covered and two uncovered grids, it is possible to get only preliminary statistics from the analysis. An attempt has been made, with the following rather surprising results: normalized to cumulative flux, the numbers for 0.1-micron-radius particles and 0.01-micron-radius particles (approximately 10^{-14} gram and 10^{-17} gram, respectively) fall between 10^4 and 10^5 particles per m^2 per second. These results apply only to the uncovered grids; the preliminary statistics from one covered grid, which was scanned with the aid of the electron microscope, yield numbers that are about one order of magnitude smaller than the number of particles on the uncovered grids.

Holes

Many holes, the number exceeding by about one order of magnitude the number of particles found both on the covered and uncovered grids, were discovered in the 200-Å formvar film. Most holes are round or slightly elliptical, and many of them are associated with a topography on the film which resembles, to some extent, a volcano crater or, as suggested in paper No. 24 by Hemenway, Hallgren, and Kerridge, the result of an interaction of a shock wave with the thin film. It should be noted, however, that virtually all round holes exhibit one bright rim, which may be interpreted as the equivalent of a single shadow for the case of a particle. According to this interpretation, the fact that the films were shadowed both before and immediately after the exposure to the space environment, from two opposite, low angles, means that the round holes were created between the two shadowing processes, i.e., most probably during the exposure in space. Most holes were found in the vicinity of single-shadowed particles. Figures 9, 10, and 11 show some of the typical holes found on the 200-Å formvar films.

Mass Spectrometry

Mass spectrometry was carried out on one giant particle (approximately 150 microns long by 30 microns wide) which was wrapped in the formvar film on one of the colored grids. This analysis was carried out through the courtesy of Geophysics Corporation of America, by Dr.

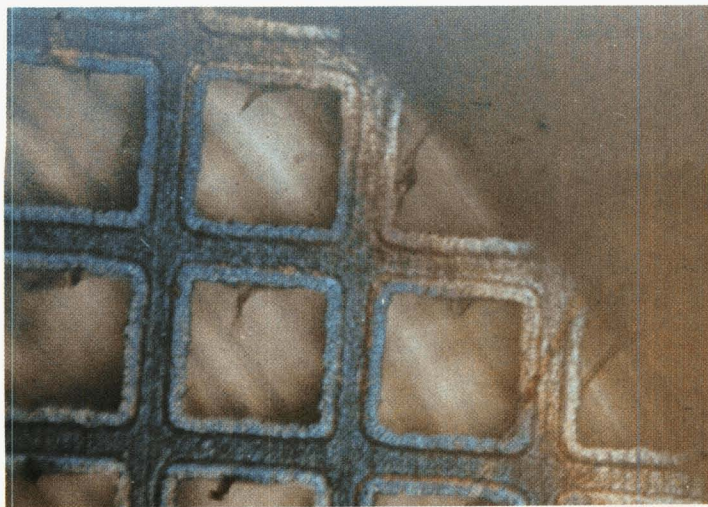


FIGURE 2.—General view of a 200-mesh copper grid showing color changes.

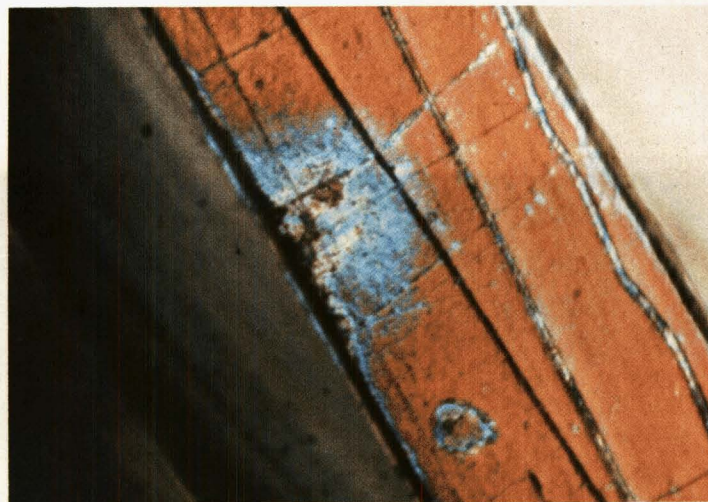


FIGURE 3.—Detail of a small-scale coloring.

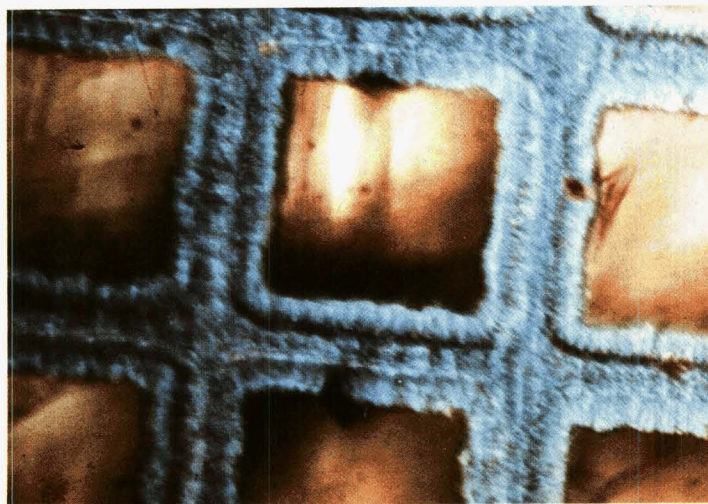


FIGURE 4.—Detail of a small-scale coloring.

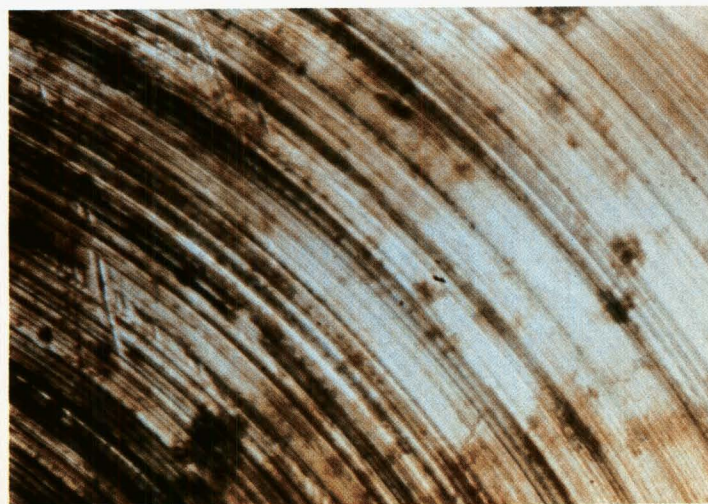


FIGURE 5.—Detail of "photograph" on bottom of brass container.

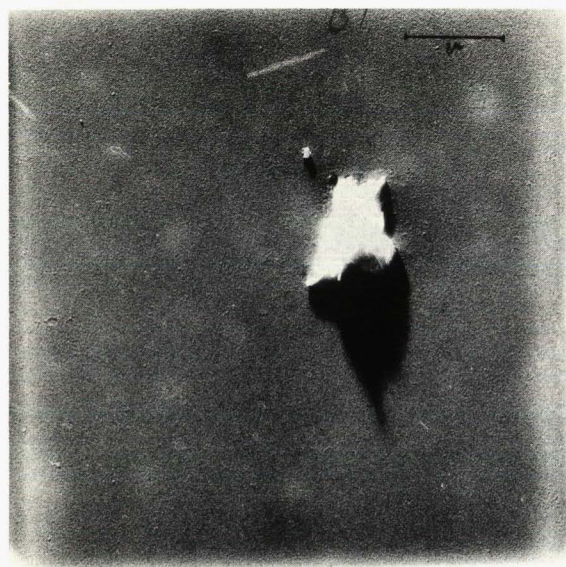


FIGURE 6.—Two single-shadowed particles found on 200-Å-thick formvar film.



FIGURE 7.—A fragile single-shadowed particle.



FIGURE 8.—Remains of a particle embedded in formvar film.

Satkiewicz, with the aid of their new argon ion micro-mass spectrometer. The results are undergoing quantitative analysis at present, but qualitatively it can be stated that relatively large amounts of Mg, Al, Fe, Si, and Ti were found in the sample.

Controls

The backup experiment, which served as the control, underwent treatment similar to that of the flight experiment both before and after the exposure. The postexposure analysis of the control grids can be summarized as follows:

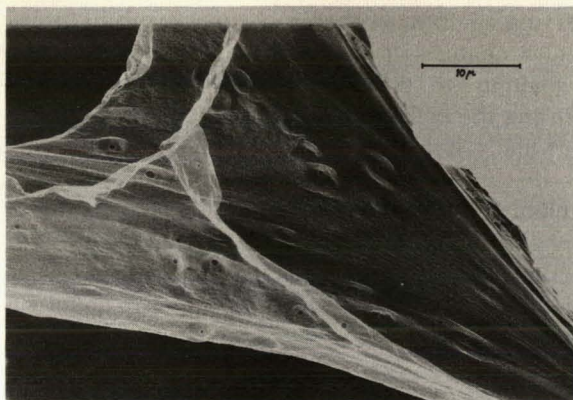


FIGURE 9.—General view of area with extensive round-hole population.

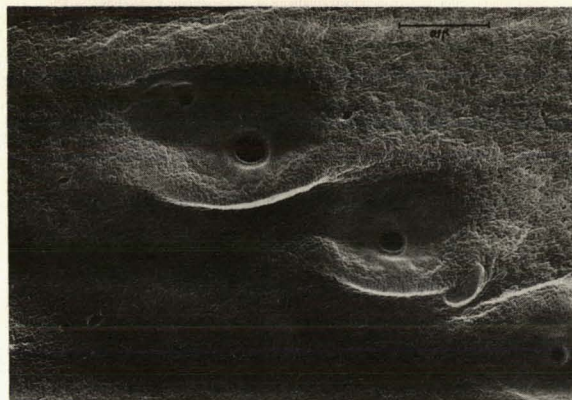


FIGURE 10.—Detail of figure 9 showing round holes with elliptical topography.

(a) No color changes were found on any of the control grids.

(b) No round holes were found in the control formvar films.

(c) Very few single-shadowed particles were found on the control films; in terms of these statistics, it can be stated that the number of single-shadowed particles found on the control was approximately two orders of magnitude less than that on the flight experiment.

SPECULATIONS

At this early stage of data reduction and analysis, there is no ground for a serious attempt to explain the observed phenomena; however, even though the nature of this report is preliminary, several speculations are offered for the causes of the observed phenomena. Such speculations may stimulate discussions and thus help to design and carry out better future experiments in this field.

A spacecraft atmosphere is useful in trying to explain the color changes on several (not all, and always uncovered) grids, as well as the nature of the round holes. According to this hypothesis, the spacecraft is carrying its own gaseous, as well as particulate, atmosphere, consisting of waste material, rocket output, and so forth, generated by the spacecraft in orbit. It is easy to see how such an atmosphere will accumulate near the spacecraft, provided (a) that the injected material has a small initial velocity relative to the spacecraft, and (b) that the relaxation time

for diffusion (the time that it takes for the density of the atmosphere near the spacecraft to fall to $1/e$ of its initial value) is of the same order of magnitude or smaller than the time for stock renewal; that is to say, that the rate of escape is equal to or smaller than the rate of supply of material to this atmosphere. Such a hypothesis may explain the color changes on several grids, by implying the possibility of "drops" of material impinging on some of the sampling surfaces; if such an atmosphere can be shown to be dense enough to reduce the velocity of the incoming interplanetary dust particles appreciably, the round holes in the 200-Å formvar collecting surfaces may be explained to be a result of a thermic interaction of the incoming hot particles with the thin plastic film. This

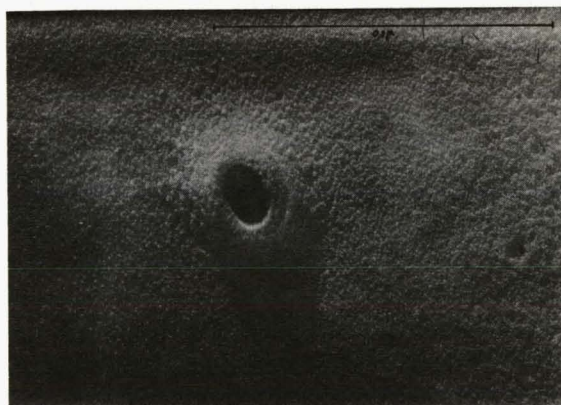


FIGURE 11.—Further enlargement of figure 9 showing one bright rim of a round hole.

speculation, if proved to be true to any appreciable extent, will of course raise severe questions with respect to the purity, or rather the contamination level, of the whole experiment.

However, it should be mentioned that the color changes on some grids may possibly be due to some residual effects from the treatment received in applying the 200-Å formvar films. It should be remembered that the formvar films were formed on a body of water, and were then "raised" on the copper grids and left to dry; slightly different

drying conditions, therefore, may result in future color changes, possibly in conjunction with the radiation to which the grids were exposed during the collection time.

Finally, if the spacecraft atmosphere hypothesis is discounted, two possible explanations for the round holes may be (1) surface defects, catalyzed by exposure to the space environment, or (2) a new kind of velocity signature of very high-speed particles, which was hitherto unknown in the laboratory.

26. Evidence of Dust Concentration in the Mesosphere

O. E. BERG AND L. SECRETAN
*Goddard Space Flight Center, NASA
Greenbelt, Maryland*

A COSMIC DUST IMPACT REGISTRATION EXPERIMENT has been exposed to space environment and recovered from three flights: Gemini XII and two Aerobee flights. This paper is concerned with the preliminary results of these exposures. It is more specifically concerned with an interesting anomaly which became manifest during the course of analyzing and comparing the data from the three exposures.

The experiment, briefly described, is one which utilizes a photometer system to scan metal-evaporated surfaces on glass before and after exposure to space in order to positively identify extraterrestrial impacts. The resolution capability of the experiment to detect perforations formed by hypervelocity dust particles has been determined with the dust particle accelerator at GSFC. Craters produced by carbonyl iron spheres having masses ranging from 10^{-10} to 10^{-12} gram and velocities from 1.4 to 8 km/sec were readily detectable in the scanning system.

Unfortunately, a practical detection capability for cosmic dust impacts cannot be ascribed from this calibration because (a) the physical characteristics of cosmic dust may vary widely from those of the iron spheres used in the laboratory (Donn, 1964), and accordingly, (b) the crater and penetration characteristics of low-density particles are not well known (Bjork, 1962).

As mentioned, the experiment has been flown in two Aerobee rocket flights (one launched December 16, 1964, at 0700 MST and one on October 25, 1966, at 0715 MST) and in Gemini XII on November 11, 1966. The exposure area-time factor for each of the Aerobee experiments

was 11 $\text{m}^2\text{-sec}$ and 10.6 $\text{m}^2\text{-sec}$, respectively, and for Gemini XII, 11 $\text{m}^2\text{-sec}$.

Although each experiment received comparable exposures, the Gemini experiment yielded no probable impacts, whereas the Aerobee experiments shared a total yield of 18 "probable impacts." The term "probable impacts" refers to surface perforations which were present in post-flight photometric scanning records only.

Although the discrepancy is certainly not great in view of existing variations in cosmic dust influx rates, there is a noteworthy difference in the exposure conditions which is interesting to consider as a possible solution to the discrepancy.

Figure 1 exhibits a major difference in exposure conditions between the Aerobee flights and Gemini XII. The entire Gemini XII exposure

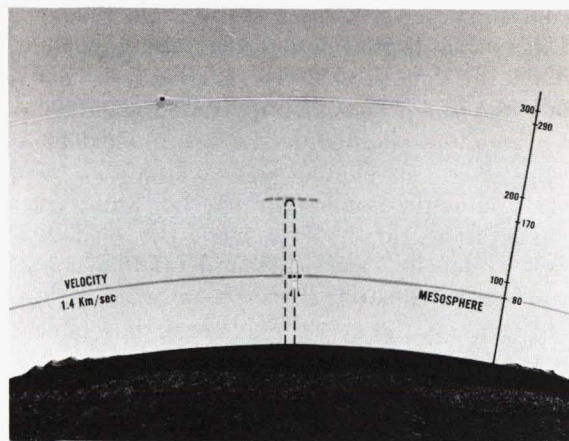


FIGURE 1.—Aerobee and Gemini XII trajectory altitudes.

occurred at an altitude of 290 kilometers (± 5 km). The Aerobee exposures began on ascent at an altitude of 65 km when the rocket-Earth velocity was 1.4 km/sec, continued up through peak at 170 kilometers where the rocket-Earth velocity was near zero, and terminated on rocket descent at 80 kilometers.

It is possible that the impacts recovered from the rocket flights were inflicted by quasi-stationary particles in the region of the mesosphere impinging upon the prepared surfaces which were in effect moving at a high velocity relative to the particles; that is, the surfaces were "ramming" the particles at velocities sufficiently high to perforate the metallic coating and thus produce detectable craters.

There is precedence to a conjecture that a "settling" dust layer exists in the region of the mesosphere. (The layer is not to be confused with a dust belt. The low-altitude layer is formed by extraterrestrial particulate matter entering and being decelerated in Earth atmosphere and settling to the surface.) Ionospheric rocket soundings of electron densities by Aiken and Whipple (personal communications) have shown anomalies in the 81-kilometer region which can most plausibly be explained by electron absorption in a concentration of dust. Ground-based radar measurements by Fiocco and Smullin (1963) support the existence of such a layer. And last, but certainly not of least importance, are the numerous sightings and measurements of the noctilucent clouds in that altitude region.

Figure 2 shows a hypervelocity crater formed by a carbonyl iron sphere having a mass of 10^{-11} gram and a velocity of 4.5 km/sec. The diameter of this crater is 9.5 microns. The target medium, similar to that used in the flight experiments, consisted of a glass substrate coated with 2500 Å of evaporated aluminum. The features exhibited in this impact are characteristic features observed over the entire velocity range for this target configuration: (a) the symmetry, (b) the rolled-back crater lip, and (c) the depth-to-diameter ratio of approximately 0.5.

In contrast, the next three figures show impact areas with features which are the largest, but otherwise typical, of the 18 probable impacts recovered from the Aerobee flights. The scale is noted on each figure.

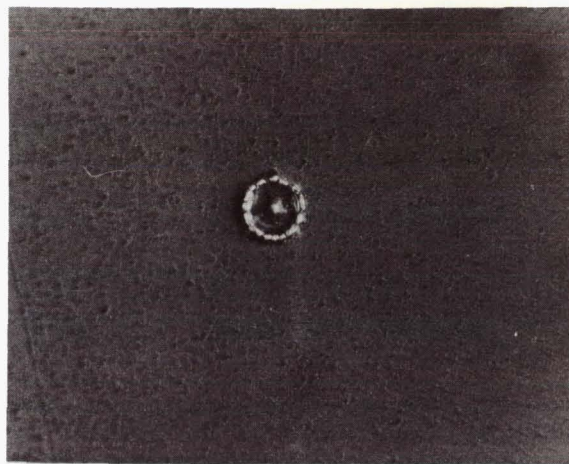


FIGURE 2.—Hypervelocity crater formed by carbonyl iron sphere.

The largest recovered crater is shown in figure 3. Note the asymmetry of the crater. Depth-to-diameter ratio is approximately 0.1.

The second largest impact area, shown in figure 4, has similar features of asymmetry and depth-to-diameter ratio.

The impact area shown in figure 5 is the most massive of four impacts of this type recovered from the Aerobee experiments. The impact area is characterized by the mass of material which has attached itself to the surface. The impacts were detected in the photometric scanner by the minute cracks and perforations in the film associated with the deposit. An analytical study of this mass of material is planned.

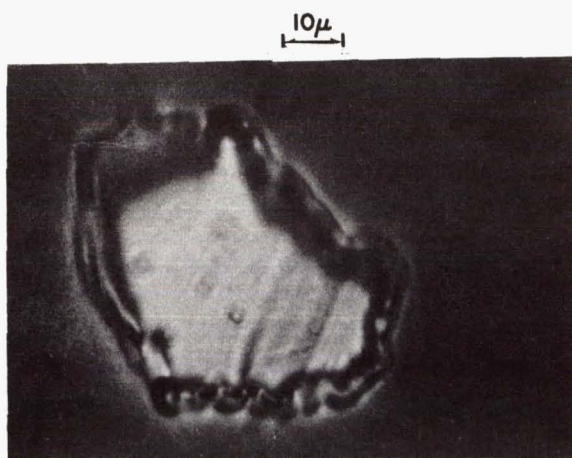


FIGURE 3.—Largest impact area.



FIGURE 4.—Second largest impact area.

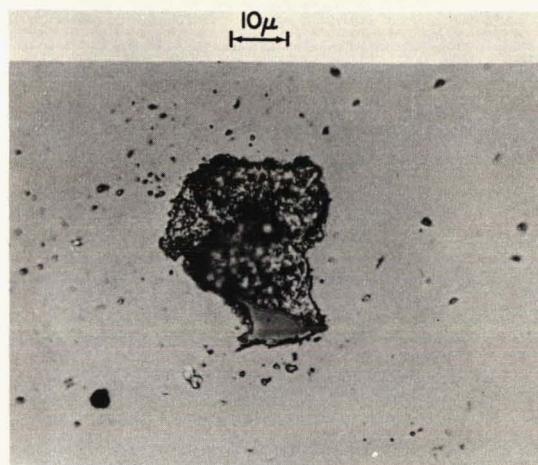


FIGURE 5.—Most massive impact area.

A comparison between the typical hypervelocity laboratory crater and the craters recovered from the Aerobee experiments suggests that the latter are formed by high-velocity, soft, irregular projectiles.

The following conclusions are based on the results of this experiment:

(1) The region of the mesosphere may well harbor an interesting concentration of decelerated cosmic dust particles which deserves further study.

(2) Penetration parameters for soft, irregular microparticles at high velocities may vary widely from accepted values derived from dissimilar laboratory models.

REFERENCES

- BJORK, R. L., 1962, "Review of Physical Processes in Hypervelocity Impacts and Penetration," Sixth Hypervelocity Symposium, Vol. 2, Part I, April.
 DONN, B., 1964, *Ann. N.Y. Acad. Sci.*, **119**, 5-16.
 FIOCCO, G., and L. D. SMULLIN, 1963, *Nature*, **199**, 1275.

Page intentionally left blank

27. Pegasus Results and Their Interpretation in Relation to Current Meteoroid Models (Abstract)

JAMES B. DOZIER AND ROBERT J. NAUMANN
George C. Marshall Space Flight Center, NASA
Huntsville, Alabama

A summary of the penetrating flux values for the 0.04-, 0.2-, and 0.4-mm thickness aluminum capacitor detectors of the Pegasus satellites is presented. Using threshold-penetration masses inferred for the Pegasus detectors, the penetration flux results have been interpreted in terms of a mass distribution function for spatial density. The distribution of meteoroids near the Earth obtained from this analysis is found to be very similar to the deep-space value inferred from interpretations of zodiacal-light measurements. The Earth accretion rate of meteoroid material implied by these results is found to be between 100 and 300 metric tons per day.

Page intentionally left blank

28. Particle Collection From the Luster Rocket

ROBERT A. SKRIVANEK
*Air Force Cambridge Research Laboratories
Bedford, Massachusetts*

A PROJECT LUSTER Aerobee particle collection rocket was successfully launched and recovered on November 16, 1965, at the White Sands Missile Range (Blanchard, Farlow, and Ferry, 1966). Project Luster is the name given to a rocket-borne particle collection experiment conducted by the NASA Ames Research Center. The nose cone opened during ascent at an altitude of 64 kilometers, exposing various particle collection devices on each of its four large retractable arms. Upon descent, at 84 kilometers, the arms were retracted and the collection experiments were sealed within the nose cone. The nose cone reached an apogee of 144 kilometers and the time of exposure was 206 seconds. All preflight preparations were conducted with standard clean-room techniques in a Class 100 Clean Room (Federal Standard No. 209, 1963; Blanchard and Farlow, 1966).

The systematic scanning for collected particles was performed in two ways: optical microscopy and electron microscopy. Optical microscopy has the advantage of being able to scan very large areas in a given amount of time. The minimum detectable particle size for optical microscopy depends upon the magnification used, but, for practical purposes in this type of work, it is never less than 1 micron. Scans were made at 500X, for which particles greater than 1 micron were reported; 200X, particles greater than 2 microns; 100X, particles greater than 5 microns. Equal areas of exposed flight sample and control sample were scanned. The single-shadow criteria for identification of contamination was employed for this work. The particle counts and the areas scanned are shown in table 1.

The particle counts (table 1) are low and this attests to both the number of particles collected

TABLE 1. — *Observed Particle Counts Using Optical Microscopy*

Magnification	Minimum detectable size, microns	Area scanned, cm ²	Control—sample particles	Flight—sample particles
500X	1	0.232	0	0
200X	2	.640	0	1
100X	5	4.000	0	2

in space and to the relative efficiency of the clean-room techniques for particles in this size range. Furthermore, these values would tend to be upper limits because these particles counted could still be contaminants. If these particle counts are normalized to 1 meter² of area, they can then be compared with the results obtained by other workers. Table 2 shows the results of the particle count normalized for 1 meter², and the particle fluxes based on a true collection time of 206 seconds.

TABLE 2. — *Normalized Particle Counts and Calculated Flux*

Particle size, microns	Number, particles/m ²	Flux, particles/m ² ·sec
1	43 000	210
2	12 000	56
5	4 200	20

Scanning with the electron microscope was performed on the same type of surface used in the optical work. The range of magnification was varied between approximately 1000X and 25 000X. Particles greater than 0.1 micron were

counted and grouped into 0.1-micron increments because the numbers were very low.

Scanning with an electron microscope is a very slow process and consequently the total area scanned was quite small. One group scanned $7.18 \times 10^{-2} \text{ cm}^2$ and the other scanned $6.5 \times 10^{-2} \text{ cm}^2$. However, because the number of particles increases as the diameter decreases, it is possible to see many more events with the electron microscope than in the optical range.

Figure 1 shows the results of the particle-size frequency distribution for single-shadowed particles. The curves are the results of two

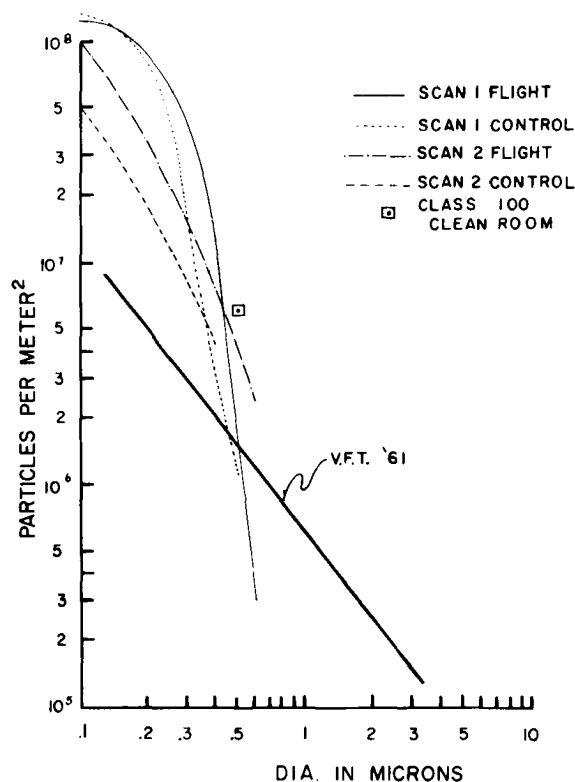


FIGURE 1.—Particle-size frequency distribution for single-shadowed particles.

independent scans, neither scanner being aware of the results of the other. The discrepancy in the two sets of curves can easily be explained because the scans were performed at two different magnifications. At the higher magnification more smaller particles will be counted. The important point here is that the control surfaces have very nearly the same number of particles as the flight surfaces. At 0.1 micron, on one scan, the number

of particles on the control actually exceeds the number of particles on the flight sample.

Further examination of the constraints on this experiment shows that these results are not entirely unexpected. As mentioned previously, the entire experiment was prepared in a Class 100 Clean Room which specifies less than 100 particles per cubic foot of air greater than 0.5 micron. If a particle collection surface were exposed for only 1 hour in a laminar-flow clean room, it would collect approximately 6×10^6 particles/meter² greater than 0.5 micron. This value, plotted in figure 1, is where the experimental curves converge. Thus it is not unusual that surfaces prepared in this environment are contaminated with particles of less than 0.5 micron. In fact, a laminar-flow clean room with an air velocity of approximately 100 feet per minute tends to concentrate particles of less than 0.5 micron.

In 1961, when the Venus flytrap was flown, no clean room was used, and the number of particles per unit area (particles less than 0.5 micron) was less for this flight than on the Luster flight (Hemenway and Soberman, 1962). For particles greater than 0.5 micron the particle count on the Venus flytrap was much higher than on the Luster rocket. This again attests to the efficiency of the clean room in controlling contamination in this size range.

CONCLUDING REMARKS

It is probable that the flux of cosmic dust particles measured on several previous particle collection rockets is several orders of magnitude too high. With the particle collection techniques presently in use, it is not possible to accurately determine the flux of particles of less than 0.5 micron. Before this question can be settled, it will be necessary to reduce the contamination level of particles in this size range. This will require the adoption of cleanliness techniques radically different from the laminar-flow clean-room concepts presently being used. For particles greater than 1 micron, the contamination controls are adequate, but because the expected fluxes are rather low, it is necessary to either examine very large areas or expose small collection areas for longer periods of time. The particles in this size range found on this experiment can only

constitute an upper limit. If additional tests were applied to the particles, i.e., chemical analysis, it might be possible to disprove their cosmic origin. In any case, the flux is considerably lower than that previously reported for the Venus flytrap experiment.

For particles between 0.5 and 1.0 micron, it is very difficult to obtain any reliable experimental data. These particles are too small to be seen

optically. In order to find a statistically meaningful number when scanning with an electron microscope, it would be necessary to scan for very long periods of time. The best approach to this problem appears to be to increase of exposure times by several orders of magnitude, and thereby increase the number of particles per unit area. Admittedly, this is not easy to do with a small probe rocket.

REFERENCES

- BLANCHARD, M. B., and N. H. FARLOW, 1966, *Contamination Control*, **5**, 22-25.
BLANCHARD, M. B., N. H. FARLOW, and G. V. FERRY, 1966, *J. Geophys. Res.*, **71**, 5689.
Federal Standard, No. 209, 1963.
HEMENWAY, C. L., and R. K. SOBERMAN, 1962, *Astron. J.*, **67**, 256.

Page intentionally left blank

29. Preliminary Results of Investigations of Solid Interplanetary Matter in the Vicinity of the Moon*

T. N. NAZAROVA, A. K. RYBAKOV,
AND G. D. KOMISSAROV
*U.S.S.R. Academy of Sciences
Moscow, U.S.S.R.*

INVESTIGATIONS OF METEORITIC MATERIAL from the Luna 10 satellite were performed by means of piezoelectric sensors glued to the satellite skin. These sensors were sensitive to the impacts of meteoritic particles with masses of 7×10^{-8} gram and larger at a particle velocity assumed to be 15 km/sec. The area sensitive to impacts was 1.2 meter².

From April 3 to May 12, 1966, for a time period of 11 hours and 50 minutes, 198 impacts (particles of 7×10^{-8} gram or larger) were recorded which amounts to 5×10^{-3} impacts per meter² per second and exceeds the average for interplanetary space by two orders of magnitude. Supplementary experimental data obtained until May 29, 1966, do not change the result. The average impact rate per meter² per second is the same.

It is known that in interplanetary space meteoric particles are mostly amalgamated into individual aggregations whose extension varies within wide limits and whose particle spatial density is nonuniform and may exceed the average value by one or two orders of magnitude. However, registration of increased particle density in the vicinity of the Moon during a long period of time, as it was during the Luna 10 experiments, gives a basis for believing that this aggregation is of a local character and is related to the Moon.

The observations covered a region which represents an envelope 650 kilometers in thickness which surrounds the Moon and is 355 kilometers

from its surface with the exception of a small section of the envelope not visible from the Earth.

Figure 1 shows the satellite trajectories and indicates the frequency of recorded particle impacts. Recorded particles were observed at heights from 355 to 1050 kilometers and mostly formed condensations which varied from 100 to 900 kilometers. In this case the dependence of the spatial density of particles on the distance from the Moon was not discovered.

The increased density of matter in the vicinity of the Moon may be explained if an assumption is made that the Moon itself serves as a particle source. During collisions of meteoric bodies with the lunar surface, an explosion takes place resulting in the ejection of a lunar rock mass which exceeds the mass of an impinging particle many times. The degree of fragmentation of ejected matter depends on the composition and structure of the lunar surface. After explosion part of the matter returns to the lunar surface while another part leaves the vicinity of the Moon and passes into interplanetary space. However, part of the rock ejected during the explosion, under the combined effect of the Earth's and Moon's fields and solar pressure, can exist for some time in orbits around the Moon.

If this hypothesis is correct, instrumentation installed aboard an artificial Moon satellite must record particles of lunar origin (those passing into interplanetary space and those orbiting around the Moon) as well as meteoric particles whose quantity is small as compared with lunar particles.

*Previously published in *Kosmicheskie Issledovaniia*, Vol. IV, issue 6, 1966.

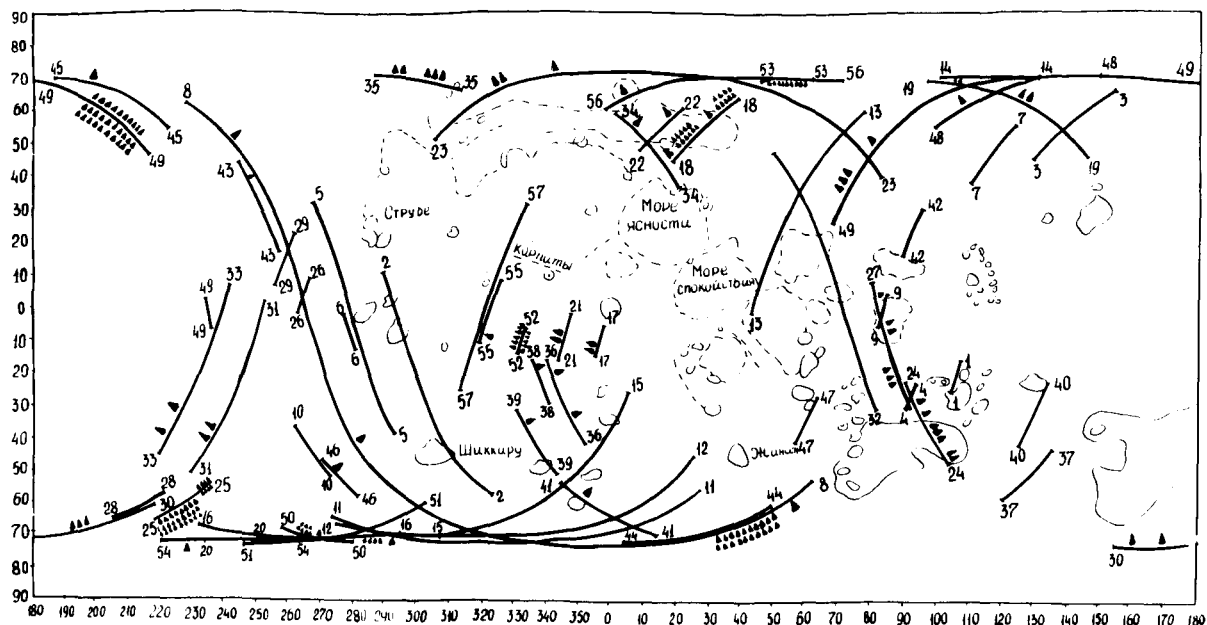


FIGURE 1.—Projection on the lunar surface of the satellite trajectories. (The symbol ▲ indicates a recorded particle impact.)

The velocity of the majority of these particles should be assumed to be 3 to 9 km/sec, rather than 15 km/sec as is assumed for sporadic meteoric particles in near-Earth cosmic space. Since the dependence $I \sim E$ is used (where I is the pulse recorded by the sensor and E is the

energy of a particle), the magnitude of the limit recorded mass of a particle in this case increases and spatial density of dust matter in the vicinity of the Moon will differ already by more than three to four orders of magnitude from the average density for interplanetary space.

30. Elemental Abundances in the Interplanetary Dust

PAUL W. HODGE

*University of Washington
Seattle, Washington*

AND

FRANCES W. WRIGHT

*Smithsonian Astrophysical Observatory
Cambridge, Massachusetts*

Data on the elemental abundances of particles believed to be interplanetary in origin are derived from chemical analyses of several hundred small particles collected in remote regions. The agreement with general cosmic abundances of the heavier elements is good, with a few exceptions.

THE BULK CHEMICAL COMPOSITION of the interplanetary dust is still not known from direct interplanetary sampling programs, although progress in obtaining appropriate samples is accelerating. A review of all available data from satellite and space probe samples shows that information from these sources is still not sufficiently good to be used as a source of data on the elemental abundances of the interplanetary dust. For instance, our experience with a surface exposed to the interplanetary medium by the meteoritic dust experiment on the spacecraft Gemini XII has shown that at least the majority, if not all, of the particles found are contaminants, and that only the very few crater-producing particles are possibly of extraterrestrial origin. In this type of experiment, great difficulties are encountered when an uncontaminated sample of interplanetary dust is wanted.

It has been shown, for instance by Sitte (1966), that even data obtained from study of microcraters in space-exposed surfaces are insufficient at present to allow a comprehensive conclusion on the elemental abundances in the general interplanetary dust. The only elements reported from the analyses of craters that can be ascribed to interplanetary dust particles are Si, Al, Fe, Mn, and Mg, and no quantitative data on any of these elements are available.

Because it is still technically extremely difficult to obtain information on elemental abundances in interplanetary dust in this state, richer sources of data have been used. These sources of information are the ancient ice deposits in central Greenland and the ice cores at the South Pole from which several hundred particles have been obtained. These samples are less easily identified as definitely extraterrestrial, perhaps, but are much more easily handled and are much more abundant. All the particles used in the present study are among those reported in a series of papers describing attempts to identify extraterrestrial dust (Wright, Hodge, and Langway, 1963; Wright and Hodge, 1964; Hodge, Wright, and Langway, 1964; Hodge and Wright, 1967; Hodge, Wright, and Langway, 1967; Franklin, Hodge, Wright, and Langway, 1967).

IDENTIFICATION

Identification of the extraterrestrial dust in a given sample is not a simple matter, even when the sample is made by an exposure in a space environment, as has been amply demonstrated by the experience of those working with space-vehicle-meteoritic-dust experiments. It is expected that in the fairly near future, however, the problem of contamination of space vehicle sampling devices will be overcome. Until such

time, contamination remains to be about as bad a problem for samples obtained in a space environment as for those obtained in some of the clean environments on the surface of the Earth.

It has been amply shown (Brocas and Picciotto, 1967; McCorkell, Fireman, and Langway, 1967; Fireman, De Felice, and Langway, 1967) that the ice cores obtained in central Greenland and at the South Pole are relatively free of terrestrial dust and are particularly usable as sources of extraterrestrial material, which is concentrated together in a way that would be difficult to reproduce in space. The He^3 measurements (Fireman, De Felice, and Langway, 1967) show conclusively that the dust of central Greenland does contain a significant extraterrestrial component, and the chemical analyses of various elements (McCorkell, Fireman, and Langway, 1967; Brocas and Picciotto, 1967) indicate that this extraterrestrial component probably makes up the major portion of the dust collected at these sites.

However, it has been shown many times that identification of extraterrestrial dust in any terrestrial sample cannot be made reliably on the basis of the chemical composition of that dust alone because there is no deduced information concerning the expected chemical composition. The chemical composition cannot be assumed to be identical to that of meteorites, because the possibility exists that the majority of the dust particles have a cometary origin, or perhaps some other origin. Furthermore, because of the difficulty of quantitative chemical analyses in spectra of comets, there is very little information about what to expect in elemental abundances for cometary material. In addition, it has been shown that because of the encounter of particles with the atmosphere, those that are melted or partially evaporated may become chemically differentiated in the process. There is evidence from laboratory experiments that nickel, for instance, can be lost from a nickel-iron pellet passing at high velocity through the atmosphere. There is a wide variety of chemical compositions found in the Sikhote-Alin meteorite spherules (Wright, Hodge, and Langway, 1963; Hodge, Wright, and Langway, 1964) and also a variety of compositions produced when artificial meteoritic spherules are

made in the laboratory (Wright and Hodge, 1965a). Because of these difficulties, the chemical composition of particles cannot be used as the criterion for identifying them as extraterrestrial. Certainly, in any case, it would be a contradiction of purpose to identify particles on the basis of their composition and then to conclude anything about the elemental abundances of interplanetary dust. Therefore, identification has been obtained on the basis of other evidence.

Hodge, Wright, and Langway (1964) made an attempt to eliminate from the polar ice samples all particles that could be identified as definitely of terrestrial origin. The most conspicuous of these are the particles that could be assigned a volcanic origin on the basis of comparison with chemical abundances of particles collected from volcanic samples (Hodge and Wright, 1964; Wright and Hodge, 1965b; Wright, Hodge, and Allen, 1966). Other sources of contamination are also identified and discussed by Hodge and Wright (1964). Therefore, with the process of elimination (admittedly dangerous because of possible omissions of unrecognized contaminants and because the identification is based on compositions of contaminants) a pure sample of interplanetary dust was selected. The relative numbers and relative masses of particles of different types are estimated on the basis of counts of the polar samples. Table II of Hodge and Wright (1964) gives data on the relative estimates of the rates of fall of the different kinds of particles; the estimates are integrated over the size distributions and over the surface of the Earth for a year. It is seen that the total rate of fall so derived, about 1 million tons per year, is in good agreement with the influx rate determined in other recent studies (Brocas and Picciotto, 1967; McCorkell, Fireman, and Langway, 1967).

ELEMENTAL ABUNDANCES

Table 1 summarizes the relative elemental abundances for the dust obtained in the polar regions after identifiable contaminants have been removed from the sample. Only elements of atomic number 12 and greater were included in the measurements. Table 1 also compares the abundances of the elements in the polar dust with relative abundances in chondrites and in cosmic

material as deduced primarily from stellar spectroscopy. All three cases have been normalized to agree at a value of 100 for iron. In all cases, the abundances are by weight.

TABLE 1.—*Comparison of Elemental Abundances from Present Study (Relative to Iron)*

Element	Polar dust	Chondrites	Cosmic
Mg	1.7	90	680
Al	4.1	10	45
Si	76	130	850
P	0.01	0.6	6.8
S	0.7	12	600
K	0.3	0.4	1.8
Ca	5.8	12	42
Ti	1.0	0.6	2.1
Cr	2.7	2.6	6.5
Mn	0.7	1.3	3.5
Fe	100	100	100
Co	1.0	0.5	1.5
Ni	2.4	7.1	24
Zn	0.07	0.002	0.5

Even though uncertainties exist in the identifications, the agreement between the polar-dust abundances and that for chondrites and cosmic material is extremely good. It is noticeable, in fact, that the polar-dust abundances agree as well with the other two as they agree with each other, a reflection on the accuracy of the values as well as on the extent to which each is representative of any true or general cosmic abundance. There are three conspicuous exceptions to the general agreement. These are magnesium, phosphorus, and sulfur, for which the abundances measured in polar dust are very considerably smaller than those measured for cosmic material (solar abundances), and somewhat smaller than abundances measured in chondrites. In all three cases the abundances increase in the order: polar dust, chondrites, cosmic material; this order is possibly indicative of a normalization problem. Possibly the iron abundances in the three samples differ in the reverse sense.

It is of interest to compare the present results with other recent measurements of the chemical

composition of possible cosmic material in polar-ice deposits. Table 2 summarizes a comparison with measurements made by McCorkell, Fireman, and Langway (1967), who determined the nickel, cobalt, and iron ratios in bulk samples of melted ice from central Greenland. The table also compares these ratios with those for chondrites and for the crust of the earth. The agreement between the bulk polar analyses and the present analyses of individual particles is quite good in the case of the iron-cobalt ratio. About 10 times as much nickel was found in samples of this study as was found in those of McCorkell, Fireman, and Langway (1967). The agreement between present ratios and ratios for chondrites is also quite good; however, for our polar measurements, agreement is very poor with the ratios for the Earth crust material.

TABLE 2.—*Comparison of Elemental Abundances from Greenland Bulk Analyses (Relative to Iron)*

Element	Polar dust	Bulk polar	Chondrites	Earth crust
Fe.....	100	100	100	100
Co.....	1.0	0.09	0.5	0.04
Ni.....	2.4	0.2	7.1	0.12

Table 3 gives another comparison, the analyses of Brocas and Picciotto (1967) who measured certain abundance ratios in ice from the South Pole. Again, very poor agreement is noted with material from the crust of the Earth, and much closer correspondence is found between the particle measurements of the present study and the bulk measurements.

TABLE 3.—*Comparison of Elemental Abundances from South Pole Bulk Analyses*

Element	Present study	Brocas and Picciotto (1967)	Earth crust
Mg/Ni.....	0.7	4	260
K/Ni.....	0.14	5.4	320
Ca/Ni.....	2.4	5.4	455

ACKNOWLEDGMENTS

We are greatly indebted to Dr. C. C. Langway, Jr., Dr. Henri Bader, and Dr. R. A. Schmidt, who allowed us to use

samples of particles collected at the poles, and to Dr. F. L. Whipple, Dr. E. L. Fireman, and Dr. E. Picciotto, for important discussions.

REFERENCES

- BROCAS, J., and E. PICCIOTTO, 1967, *J. Geophys. Res.*, **72**, 2229.
FIREMAN, E. L., J. DE FELICE, and C. C. LANGWAY, 1967, paper given at the annual meeting of the A.G.U., March.
FRANKLIN, F. A., P. W. HODGE, F. W. WRIGHT, and C. C. LANGWAY, 1967, *J. Geophys. Res.*, **72**, 2543.
HODGE, P. W., and F. W. WRIGHT, 1967, NASA SP-135 (SCA Vol. 11).
HODGE, P. W., and F. W. WRIGHT, 1964, *J. Geophys. Res.*, **69**, 2449.
HODGE, P. W., F. W. WRIGHT, and C. C. LANGWAY, 1964, *J. Geophys. Res.*, **69**, 2919.
HODGE, P. W., F. W. WRIGHT, and C. C. LANGWAY, 1967, *J. Geophys. Res.*, **72**, 1404.
McCORKELL, R., E. L. FIREMAN, and C. C. LANGWAY, 1967, paper given at the annual meeting of the A.G.U., March.
SITTE, K., 1966, report submitted to ESRO "PLA" Ad Hoc Working Group.
WRIGHT, F. W., and P. W. HODGE, 1964, *Ann. N.Y. Acad. Sci.*, **119**, 287.
WRIGHT, F. W., and P. W. HODGE, 1965a, Smithsonian Observatory Special Report, No. 192.
WRIGHT, F. W., and P. W. HODGE, 1965b, *J. Geophys. Res.*, **70**, 3889.
WRIGHT, F. W., P. W. HODGE, and R. A. ALLEN, 1966, Smithsonian Observatory Special Report, No. 228.
WRIGHT, F. W., P. W. HODGE, and C. C. LANGWAY, 1963, *J. Geophys. Res.*, **68**, 5575.

III

METEOR OBSERVATIONS

Page intentionally left blank

31. Space Density of Radio Meteors*

RICHARD B. SOUTHWORTH

*Smithsonian Astrophysical Observatory
Cambridge, Massachusetts*

The space-density distribution of dust in the solar system is estimated from the orbits of approximately 13 000 radar meteors observed by the Harvard-Smithsonian Radio Meteor Project. Approximate corrections are made for unobservable classes of orbits and for other observational selection effects. Within the limits 0.1 to 10 AU, the space density decreases monotonically outward from the Sun. The distribution in heliocentric latitude has a very broad maximum centered on the ecliptic and a deep minimum over the ecliptic poles. There is no evidence for any substantial enhancement of density in the asteroid belt. The distribution shows the effects of planetary perturbations and collisional destruction.

THIS REPORT presents the distribution of relative space densities of observed radio meteors, and also a distribution that is approximately corrected for inherent deficiencies in observation. Briggs (1962) computed densities by assuming observed photographic meteor orbits as an injection distribution and then assuming breakup into smaller particles which would spiral into the Sun under the Poynting-Robertson effect. These are the first published space densities of meteors known to the author. The author believes that this paper gives the first density distributions derived from observed meteors alone.

METEOR OBSERVATIONS

The data used here comprise the observations of 13 672 meteors between November 1962 and November 1965 by the six-station radar network of the Radio Meteor Project, operated in Havana, Ill., by the Harvard College and Smithsonian

Astrophysical Observatories, and supported by the National Bureau of Standards, the National Science Foundation, and the National Aeronautics and Space Administration. The orbit of each meteor was computed from its observed speed and trajectory in the atmosphere, and its mass was computed from the observed distribution of electrons left behind the meteor. Verniani and Hawkins' (1964) luminous efficiency was used in the latter computation.

Each meteor is assigned a weight proportional to the product of five factors. Factor 1 is the 1.33 power of the observed mass; this is proportional to the total mass of all sizes of particles down to any given limiting mass in a distribution of the form found by Hawkins and Upton (1958) for photographic meteors. Factor 2 depends on the altitude and azimuth of the observed radiant. It is the reciprocal of the probability found by Elford (1964) for observing the radiant, except that radiants with less than 10-percent relative probability of detection have been assigned zero weight. Such inherently improbable radiants are likely to result from observational or computational errors and should not be given their high theoretical weights. Factor 3 depends upon the

*This work was supported in part by grants NSR 09-015-033 and NSR-158 from the National Aeronautics and Space Administration, grant NAS 9-4875 from Manned Spacecraft Center, NASA, Houston, Texas, and Contract AF 19(628)-3248 from the U.S. Air Force Cambridge Research Laboratories.

declination of the observed radiant. It is inversely proportional to the fraction of the sidereal day during which a point at any given declination remains within the 10-percent contour of Elford's distribution. Factor 4 is unity for radiants north of the ecliptic and zero for radiants south of it, and thus the incompletely observed southern sky is eliminated from this analysis. Factor 5 is inversely proportional to a slight refinement of Öpik's (1951) probability that a body in an orbit of given semimajor axis a , eccentricity e , and inclination i will collide with the Earth during one revolution of the body. This probability is

$$P = R_E^2 \frac{V_c^2}{\pi V_G V_R \sin i} \quad (1)$$

where R_E is the Earth's radius, V_c is the geocentric velocity outside the atmosphere, V_G is the geocentric velocity after the Earth's attraction is deducted, and V_R is the radial component of the heliocentric velocity. The refinement consists in the eccentricity of the Earth's orbit not being neglected when computing

$$V_R = \left[\frac{2}{r} - \frac{1}{a} - \frac{a}{r^2} (1 - e^2) \right]^{1/2} \quad (2)$$

where r is the Earth's distance from the Sun at the time the meteor is observed. Neglecting the refinement yields imaginary weights on a few meteors. In practice, if the difficulty is not recognized, these meteors may be grotesquely misweighted.

The weighted distribution of radio-meteor orbits represents, as accurately as the data permit us to determine it, the total orbital distribution down to a certain limiting mass of all meteors in orbits that have perihelia at ≥ 1 AU and aphelia at ≤ 1 AU. Figure 1 gives the *weighted* distribution of the logarithms of observed masses. The optimum limiting mass representing these observations will be in the range $10^{-3.5}$ to 10^{-4} grams.

UNCORRECTED RELATIVE SPACE DENSITY

Space density is discussed here as a function of two dimensions in a plane normal to the ecliptic through the Sun. Any dependence of space

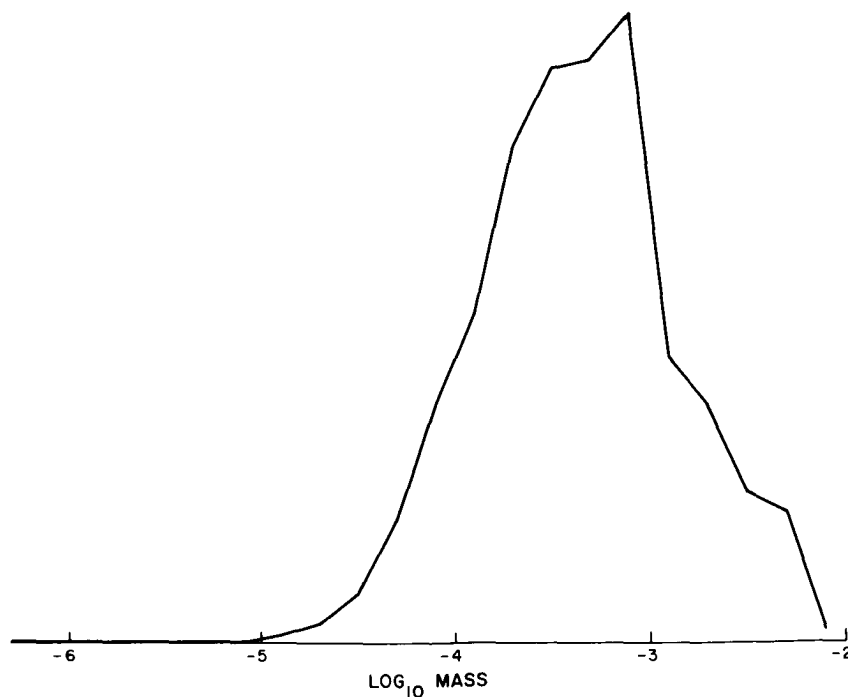


FIGURE 1.—Relative frequency of mass (grams) in the weighted sample.

density of ecliptic longitude has been averaged out. The two dimensions used are r , the distance from the Sun in astronomical units, and $\sin \beta$, the sine of the heliocentric ecliptic latitude.

For this computation, distance from the Sun in the range $0.1 \leq r \leq 10$ is divided into 20 intervals, and sine latitude is also divided into 20 intervals. This yields 200 cells, with boundaries

$$\left. \begin{array}{l} \log_{10} r \\ \sin \beta \end{array} \right\} = -1.0, -0.9, -0.8, \dots, +1.0 \quad (3)$$

The cell volumes are proportional to r_b^3 , where r_b is either bounding r .

In each cell the relative space density is computed from the weighted sum of the residence times of all meteors passing through the cell, divided by the volume of the cell. The residence time is the time each meteor spends within a cell in the course of one orbital revolution. The residence times in the intervals of radius vector are computed exactly, but the subdivision into intervals of sine latitude within each radius-vector interval is approximate. The approximation used is to apportion the time within each interval of radius vector as if the meteor's sine latitude had varied linearly with time from its value at one boundary of the interval to its value at the other boundary. However, if the meteor passed through perihelion or aphelion in any interval of radius vector, the time was apportioned as if the sine latitude had varied linearly from entering the interval to perihelion or aphelion, and then linearly at a different rate after that. Table 1 presents decimal logarithms of these uncorrected relative space densities.

AVERAGES WITH RESPECT TO ARGUMENT OF PERIHELION

All the observed orbits necessarily intersect the Earth's orbit, and table 1 shows a correspondingly large peak in density near the Earth's orbit. A much better approximation to reality can be achieved by assuming that the longitudes of the nodes Ω are independent of the arguments of perihelion ω . In the present context, this is equivalent to assuming that ω is uniformly distributed from 0° to 360° independent of a , e , or i . In fact, complete uniformity is not expected, as

will be discussed below, but the true distribution of ω cannot be calculated without numerous further assumptions and a great deal of effort.

To compute the space-density average over ω , we implicitly replace each observed meteor by a set of meteors that are similar except for a uniform distribution of ω . Thus each observed meteor will contribute to all cells between its perihelion and aphelion, and between latitudes $\pm i$. From the well-known relation

$$\sin \beta = \sin i \sin (\omega + v) \quad (4)$$

where v is true anomaly (invariant under the averaging), it can easily be found that the relative frequency of values of $\sin \beta$ in the range

$$B_1 \leq \sin \beta \leq B_2$$

is

$$F_{12} = \frac{1}{\pi} \left[\arcsin \left(\frac{B_2}{\sin i} \right) - \arcsin \left(\frac{B_1}{\sin i} \right) \right] \quad (5)$$

Table 2 presents space densities averaged over ω . They were computed from equation (5) without approximations. Since these densities are symmetric about the ecliptic, only northern latitudes are presented.

UNOBSERVABLE ORBITS

Orbits with aphelia < 1 AU or perihelia > 1 AU cannot be observed from the Earth. A reasonable correction for these unobservable orbits is essential. The approximation used here is to extrapolate the observed two-dimensional distribution of $1/a$ and e into the range of unobservable orbits. It is assumed, for this purpose only, that the distribution of angular elements i , ω , and Ω is independent of a and e . Table 3 gives the weighted distribution of the 13 672 meteors with respect to $1/a$ and e . The relative density D in this array is approximately fitted by the following empirical formulas:

$$\left. \begin{array}{l} D = AE \\ A = \begin{cases} 15a & (a < 1) \\ 250 - 800a^{-1} + 955a^{-2} - 390a^{-3} & (a > 1) \end{cases} \\ E = 4 + 6e + 3e^2 - 16e^3 + 4e^4 \end{array} \right\} \quad (6)$$

TABLE 1.—*Logarithms of Uncorrected Relative Space Density*

		Radius vector																				
		0.100	0.126	0.158	0.199	0.251	0.316	0.398	0.501	0.631	0.794	1.00	1.26	1.58	1.99	2.51	3.16	3.98	5.01	6.31	7.94	10.0
Sine latitude	1.0	4.474	4.566	4.335	4.258	4.166	3.861	3.830	3.802	3.686	3.507	3.418	3.061	2.917	2.853	2.523	2.301	2.039	1.984	1.781	1.400	
		4.851	4.623	4.680	4.590	4.652	4.630	4.581	4.517	4.351	4.222	4.047	3.823	3.607	3.298	3.164	2.801	2.412	2.262	2.253	2.124	
		5.134	5.121	5.096	5.000	4.931	4.927	4.878	4.734	4.603	4.507	4.356	4.115	3.847	3.661	3.333	3.148	2.988	2.711	2.281	2.018	
		5.129	5.102	5.091	5.099	5.084	4.985	4.869	4.861	4.790	4.630	4.482	4.420	4.150	3.898	3.567	3.307	3.016	2.699	2.436	2.153	
	0.5	5.289	5.185	5.171	5.155	5.140	5.039	4.998	4.945	4.957	4.819	4.660	4.496	4.275	4.028	3.784	3.480	3.043	2.854	2.256	2.133	
		5.212	5.312	5.275	5.231	5.241	5.140	5.105	5.048	5.125	4.942	4.772	4.722	4.469	4.194	3.937	3.509	3.237	2.908	2.489	2.365	
		5.339	5.200	5.170	5.225	5.323	5.221	5.199	5.239	5.186	5.142	4.983	4.815	4.509	4.289	4.071	3.668	3.340	2.942	2.686	2.145	
		5.374	5.193	5.209	5.186	5.264	5.277	5.303	5.320	5.411	5.313	5.204	5.064	4.801	4.452	4.263	3.900	3.500	3.157	2.763	2.507	
	0.0	5.354	5.185	5.298	5.233	5.320	5.229	5.304	5.359	5.437	5.465	5.328	5.117	4.920	4.632	4.346	4.014	3.687	3.032	2.704	2.169	
		5.337	5.245	5.295	5.253	5.291	5.272	5.236	5.291	5.435	5.701	5.618	5.109	4.795	4.422	4.255	3.833	3.545	2.922	2.450	1.873	
		5.426	5.305	5.299	5.278	5.357	5.305	5.257	5.395	5.492	5.754	5.580	4.992	4.607	4.431	4.039	3.740	3.418	3.145	2.740	2.501	
		5.459	5.414	5.318	5.263	5.355	5.334	5.413	5.485	5.553	5.434	5.310	5.053	4.718	4.449	4.142	3.860	3.459	3.132	2.842	2.544	
	-0.5	5.305	5.478	5.323	5.312	5.328	5.341	5.480	5.431	5.349	5.240	5.075	4.963	4.793	4.479	4.179	3.932	3.549	3.115	2.936	2.872	
		5.311	5.433	5.326	5.287	5.300	5.225	5.225	5.210	5.222	5.016	4.974	4.852	4.514	4.212	3.961	3.596	3.228	3.042	2.495	2.224	
		5.400	5.352	5.366	5.269	5.205	5.071	5.238	5.161	5.022	5.013	4.794	4.563	4.391	4.098	3.708	3.433	3.257	2.814	2.460	2.195	
		5.316	5.297	5.296	5.253	5.151	5.097	5.083	5.034	4.917	4.853	4.590	4.463	4.230	3.970	3.616	3.340	3.132	2.792	2.488	2.146	
	-1.0	5.284	5.282	5.201	5.101	5.109	5.037	4.921	4.930	4.772	4.652	4.379	4.284	3.990	3.719	3.511	3.180	2.907	2.611	2.045	1.872	
		5.095	5.148	5.135	5.191	5.013	4.903	4.790	4.771	4.568	4.430	4.251	4.071	3.735	3.466	3.252	3.055	2.833	2.359	2.172	1.979	
		4.722	4.812	4.836	4.749	4.755	4.590	4.563	4.486	4.332	4.067	3.900	3.696	3.561	3.296	3.069	2.775	2.453	2.345	1.910	1.661	
		4.348	4.234	4.203	4.223	4.132	4.069	4.073	3.828	3.775	3.557	3.303	3.176	3.008	2.772	2.592	2.136	2.023	1.846	1.632	1.170	

TABLE 2.—*Logarithms of Relative Space Density Averaged with Respect to ω*

		Radius vector																				
		0.100	0.126	0.158	0.199	0.251	0.316	0.398	0.501	0.631	0.794	1.00	1.26	1.58	1.99	2.51	3.16	3.98	5.01	6.31	7.94	10.0
Sine latitude	1.0	4.423	4.290	4.259	4.195	4.106	4.095	4.150	4.114	4.060	4.059	3.892	3.473	3.127	2.806	2.484	2.202	1.994	1.811	1.582	1.269	
		4.735	4.708	4.753	4.707	4.631	4.578	4.549	4.524	4.470	4.465	4.314	3.935	3.600	3.308	3.008	2.719	2.457	2.193	1.931	1.668	
		5.115	5.036	5.058	4.976	4.884	4.836	4.759	4.775	4.693	4.716	4.574	4.223	3.852	3.524	3.228	2.986	2.732	2.420	2.134	1.908	
		5.201	5.081	5.112	5.038	5.003	4.905	4.854	4.846	4.791	4.844	4.691	4.378	4.047	3.744	3.464	3.162	2.829	2.575	2.265	2.038	
	0.5	5.301	5.215	5.156	5.095	5.127	4.992	4.991	4.949	4.948	4.997	4.838	4.538	4.226	3.919	3.634	3.360	3.057	2.751	2.383	2.115	
		5.367	5.329	5.251	5.184	5.183	5.085	5.071	5.032	5.055	5.104	4.947	4.652	4.345	4.082	3.788	3.492	3.175	2.811	2.461	2.167	
		5.336	5.387	5.286	5.259	5.290	5.203	5.192	5.167	5.159	5.202	5.057	4.789	4.473	4.195	3.941	3.588	3.250	2.910	2.590	2.191	
		5.363	5.364	5.340	5.302	5.335	5.295	5.345	5.345	5.356	5.378	5.254	4.974	4.734	4.418	4.144	3.818	3.449	3.117	2.817	2.595	
	0.0	5.375	5.357	5.344	5.329	5.382	5.345	5.377	5.401	5.430	5.438	5.306	5.036	4.801	4.531	4.264	3.928	3.585	3.154	2.782	2.559	
		5.364	5.351	5.354	5.372	5.401	5.383	5.425	5.482	5.537	5.507	5.370	5.108	4.860	4.587	4.329	3.976	3.652	3.198	2.776	2.540	

TABLE 3.—*Weighted Relative Distribution of l/a and e in the Observed Sample of Meteors*

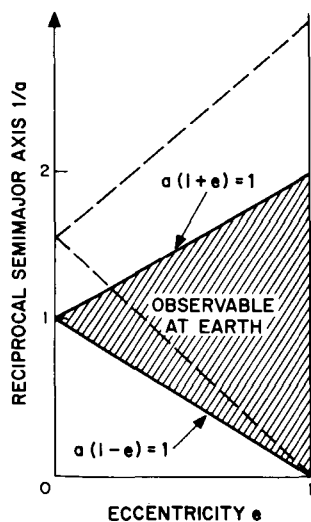
[illegible]

FIGURE 2.—The region \otimes in the $(1/a)-e$ distribution that can be observed at a distance r from the Sun is a triangle bounded above by $a(1+e)=1/r$ and below by $a(1-e)=1/r$.

Figure 2 shows the region in the $(1/a)-e$ distribution that can be observed at any given value of radius vector. The correction factor for unobservable orbits is computed as a function of radius

vector \mathbf{r} , and is the ratio of the integral of D over the region observable at \mathbf{r} to the integral over the common region observable both at \mathbf{r} and at the Earth. These ratios were computed by numerical integration for the logarithmic midpoints of the radius vector cells used for computing density. They are printed in table 4 in logarithmic form. Numerical experiments in fitting formulas other than those in equation (6) to the data yielded correction factors whose logarithms agreed with table 4 to about 10 percent. They included formulas where the eccentricity distribution was made to depend upon the major axis, giving proportionately more low eccentricities in small orbits and high eccentricities in large orbits.

TABLE 4.—*Correction Factors for Unobservable Eccentricities*

$\log_{10} r$	$\log_{10} \text{ correction}$	$\log_{10} r$	$\log_{10} \text{ correction}$
-1.0	1.099	0.0	0.048
-0.9	.962	.1	.150
-.8	.828	.2	.260
-.7	.695	.3	.375
-.6	.566	.4	.488
-.5	.443	.5	.597
-.4	.326	.6	.706
-.3	.219	.7	.818
-.2	.122	.8	.935
-.1	.038	.9	1.055
.0		1.0	

CORRECTED RELATIVE SPACE DENSITIES

Table 5 presents the logarithms of the final corrected relative space densities computed. Figure 3 shows these space densities as functions of radius vector in the ecliptic and at latitude $\pm 30^\circ$. Figure 4 shows them as functions of latitude for three different values of radius vector. Finally, figure 5 shows contours of space density

TABLE 5. — *Logarithms of Corrected Relative Space Density*

		Radius vectors—																					
		1.0	0.100	0.126	0.158	0.199	0.251	0.316	0.398	0.501	0.631	0.794	1.00	1.26	1.58	1.99	2.51	3.16	3.98	5.01	6.31	7.94	10.0
Sine latitude	0.9	5.522	5.252	5.087	4.890	4.672	4.538	4.476	4.333	4.182	4.097	3.940	3.623	3.387	3.181	2.972	2.799	2.700	2.629	2.517	2.324		
	0.8	5.834	5.670	5.581	5.402	5.197	5.021	4.875	4.743	4.592	4.503	4.362	4.085	3.860	3.683	3.496	3.316	3.163	3.011	2.866	2.723		
	0.7	6.214	5.998	5.886	5.671	5.450	5.279	5.085	4.994	4.815	4.754	4.622	4.373	4.112	3.899	3.716	3.583	3.438	3.238	3.069	2.964		
	0.6	6.300	6.043	5.940	5.733	5.569	5.348	5.180	5.065	4.913	4.882	4.739	4.528	4.307	4.119	3.952	3.759	3.635	3.393	3.200	3.093		
	0.5	6.400	6.177	5.984	5.790	5.693	5.435	5.317	5.168	5.070	5.035	4.886	4.688	4.486	4.294	4.122	3.957	3.763	3.569	3.318	3.170		
	0.4	6.466	6.291	6.079	5.879	5.749	5.528	5.397	5.251	5.177	5.142	4.995	4.802	4.605	4.457	4.276	4.089	3.881	3.629	3.396	3.222		
	0.3	6.435	6.349	6.114	5.954	5.856	5.646	5.518	5.386	5.281	5.240	5.105	4.939	4.733	4.570	4.429	4.185	3.956	3.728	3.525	3.246		
	0.2	6.462	6.326	6.168	5.997	5.901	5.738	5.671	5.564	5.478	5.416	5.302	5.124	4.994	4.793	4.632	4.415	4.155	3.935	3.752	3.650		
	0.1	6.474	6.319	6.172	6.024	5.948	5.788	5.703	5.620	5.552	5.476	5.354	5.186	5.061	4.906	4.752	4.525	4.291	3.972	3.717	3.614		
	0.0	6.463	6.313	6.182	6.067	5.967	5.826	5.751	5.701	5.659	5.545	5.418	5.258	5.120	4.962	4.817	4.573	4.358	4.016	3.711	3.595		

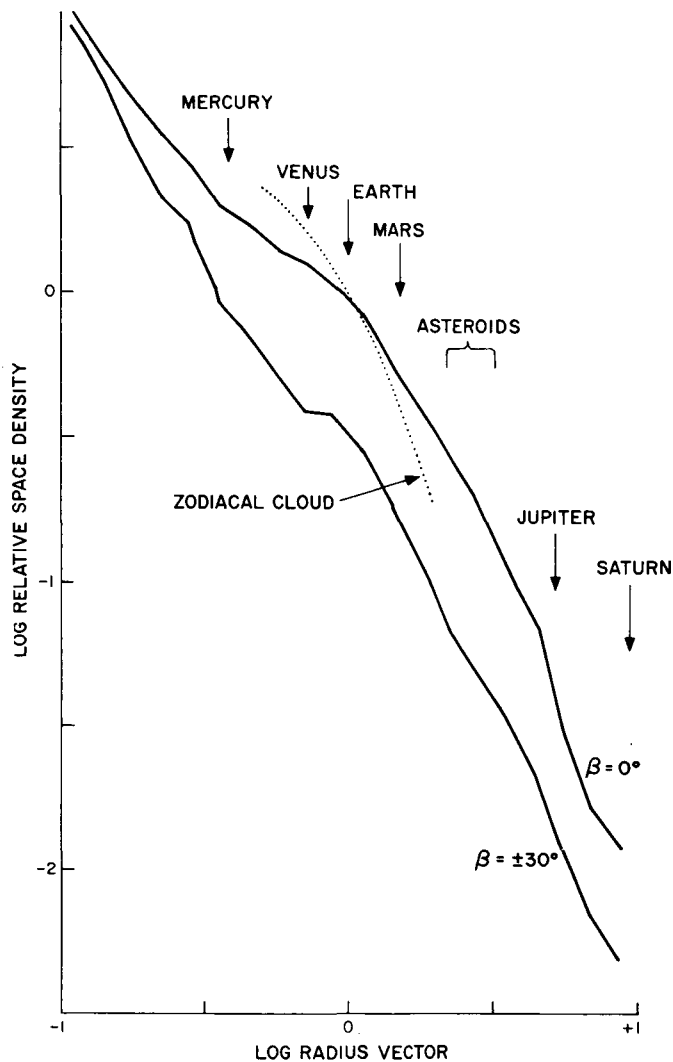


FIGURE 3.—Relative space density of radio meteors as functions of r and of zodiacal particles.

in a plane normal to the ecliptic at two different scales. Generally speaking, the vicinity of the Earth is not an exceptional region in any of these figures; this fact may be taken as one qualitative confirmation that appropriate corrections have been made to the observations. One exception to this generalization is the bump appearing in figure 3 near $r=1$, on the curve for $\beta=\pm 30^\circ$. This bump is probably to be understood as the result of a correlation between i and e in meteor orbits, contrary to the assumption made when the correction was being made for unobservable orbits. A more exact correction would be ex-

pected to raise the rest of the curve so that the bump is eliminated.

Only a very modest relative increase in space density appears in the asteroid region—perhaps 15 percent over a smooth distribution, and perhaps only a statistical fluctuation. Of course, this does not mean that there is no considerable excess in meteor space density in the asteroid belt, because asteroidal orbits cannot be observed on Earth and table 3 cannot be safely extrapolated to such orbits. The absence of a concentration near the asteroids does mean, however, that less than the order of 5 percent of the radar meteors

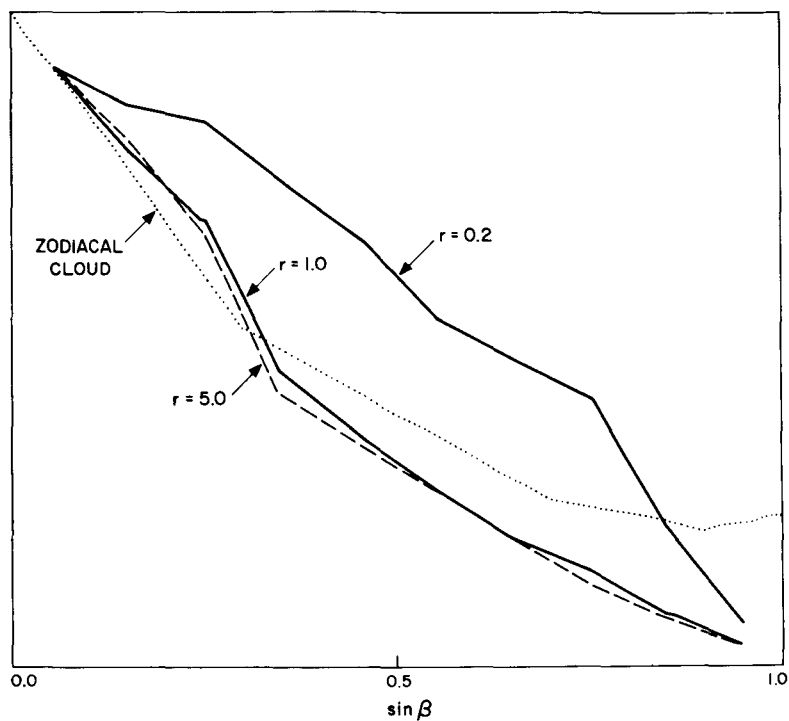


FIGURE 4.—Relative space density of radio meteors as a function of $\sin \beta$, and zodiacal particles.

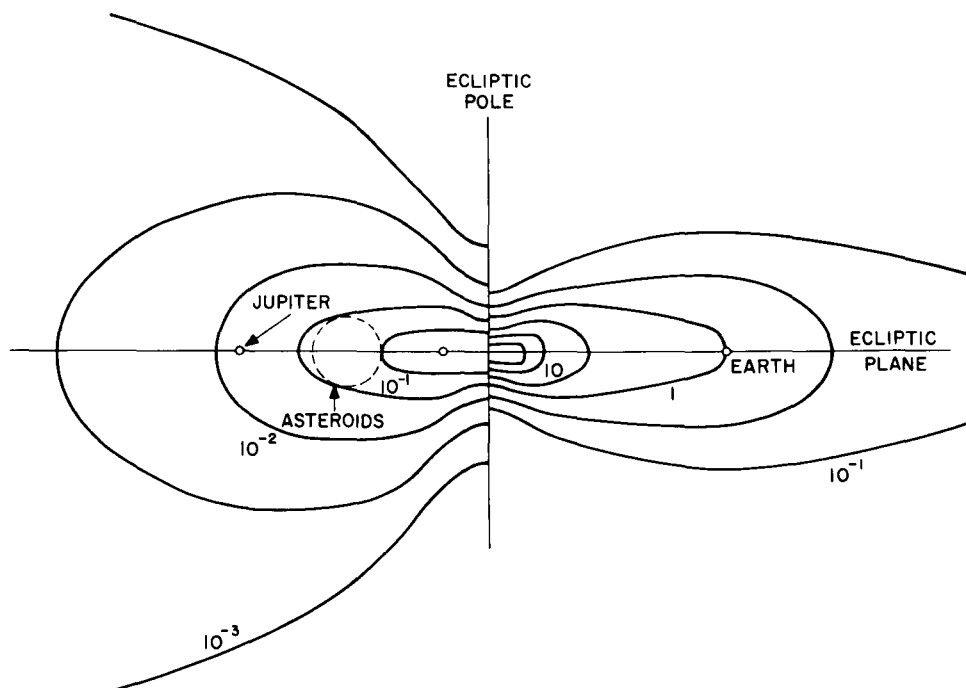


FIGURE 5.—Relative space density of radio meteors.

originated in the asteroid belt and have also kept nearly their original orbits.

Observed orbits of short-period comets are a most instructive parallel for meteor orbits. Whether the meteors are supplied from long-period or short-period comets, their orbits will tend to resemble those of short-period comets, because "capture" by Jupiter has similar effects either on the comet orbits or on the meteor orbits after the meteors have left the comet. The dip in space density that is evident in figure 3 beyond Jupiter's orbit is readily understood as a concentration of aphelia near Jupiter, just as in Jupiter's "family" of comets.

Outside the initial perihelion distance, a particle spiraling into the Sun under the Poynting-Robertson effect has a radial-density distribution with a slope at least as steep as -2.5 in figure 3 (cf., Southworth, 1964). The curves in figure 3 are appreciably flatter, which strongly suggests that these meteors do not, on the average, persist long enough to spiral in. Presumably they are destroyed by collisions.

Another aspect of the concentration of aphelia to Jupiter's orbit is the concentration of values of ω for comets toward 0° and 180° (Porter, 1963). Meteors may be expected to show some such concentration of values of ω , partly because of initial capture by Jupiter, and partly because the regression of the nodes under later Jupiter perturbations is not at uniform speed. As Moulton (1914) remarked, and as Whipple (1950) showed specifically for Comet Encke, the rate of change of ω is faster when ω is near 90° or 270° than when ω is near 0° or 180° .

The effect on space density of a concentration of values of ω near 0° and 180° is to shrink the density distribution far from the Sun to low latitudes, because the meteors are then near their aphelia, which are near the ecliptic. The author has discussed (paper No. 37) the mean space distribution when the orbits evolve under the Poynting-Robertson effect and ω is concentrated in this way. The conclusion reached there is that, at distances from the Sun greater than twice or three times the mean of the original perihelion distances, the distribution of latitudes will be compressed toward the ecliptic. Nearer the Sun,

the distribution of latitudes will reflect the distribution of inclinations without bias. Figure 4 clearly shows that the distribution of latitudes of radio meteors is broader near the Sun, confirming the argument stated above. The spread in latitude in the innermost curve reflects a broad distribution of inclinations, and helps to confirm that the orbits are comparable to those of short-period comets.

COMPARISON WITH ZODIACAL CLOUD

Figures 3 and 4 also show curves of density distribution derived from observations of the zodiacal light (Southworth, paper No. 37). When they were derived it was assumed for convenience that the latitude distribution was independent of distance from the Sun. Thus each latitude curve in figure 3 is necessarily a blending of latitude curves appropriate to different distances. All the information came from distances between 0.5 and 2 AU, but while the low latitudes were mostly seen in the neighborhood of the Earth, the high latitudes were mostly observed nearer the Sun. Moreover, the region nearer the Sun seems to have been contaminated by extra strong light. Thus the zodiacal-cloud curve could be plausibly reconciled with the meteor curves: they agree at low latitudes near the Earth, they agree at higher latitudes nearer the Sun, and the zodiacal curve is probably wrong at the highest latitudes.

The radial distribution of density fitted to the zodiacal light has been drawn in figure 4 so that it intersects the low-latitude meteor curve at the Earth. (This does not imply anything about their absolute densities.) The zodiacal distribution is appreciably steeper than the meteor distributions. It is not certain that the difference is statistically significant, because the zodiacal light was nearly as well fitted by radial distributions almost exactly matching those of the meteors. Nonetheless, the difference supports the hypothesis made previously that meteors are eliminated by collisions (or other processes) as well as by the Poynting-Robertson effect. Since the zodiacal particles spiral in faster and have less cross section for collisions, they will be more concentrated to the Sun than are the meteors.

CONCLUSIONS

The relative space density in the range 0.1 to 10.0 AU from the Sun of meteors in the mass range 10^{-3} to 10^{-4} grams has been computed. It shows a broad maximum near the ecliptic plane,

and a deep minimum near the ecliptic poles.

There is little evidence for an asteroidal origin for these meteors. Planetary perturbations and collisional destruction appear important in their evolution.

REFERENCES

- BRIGGS, R. E., 1962, *Astron. J.*, **67**, 710.
ELFORD, W. G., 1964, Harvard-Smithsonian Radio Meteor Project Research Report No. 8.
HAWKINS, G. S., and E. K. L. UPTON, 1958, *Astrophys. J.*, **128**, 727.
MOULTON, F. R., 1914, *An Introduction to Celestial Mechanics* (New York: The Macmillan Co.).
OPIK, E. J., 1951, *Proc. Roy. Irish Acad.*, **54**, Sec. A, No. 12.
PORTER, J. G., 1963, *The Moon, Meteorites, and Comets* (B. M. Middlehurst and G. P. Kuiper, eds.) (Chicago: Univ. of Chicago Press), 550.
SOUTHWORTH, R. B., 1964, *Ann. N.Y. Acad. Sci.*, **119**, 54.
VERNIANI, F., and G. S. HAWKINS, 1964, *Astrophys. J.*, **140**, 1590.
WHIPPLE, F. L., 1950, *Astrophys. J.*, **111**, 375.

32. The Orbits of Meteor Bodies and the Origin of the Hard Component of the Interplanetary Medium

B. L. KASHCHEYEV AND V. N. LEBEDINETS
*Astronomical Council
Moscow, U.S.S.R.*

FROM NOVEMBER 1959 TO DECEMBER 1960 an annual cycle of radar measurements of radiants and velocities of individual meteors was performed at the Kharkov Polytechnical Institute by Kashcheyev, Lebedinets, and Lagutin (1965 and 1966) and Lebedinets and Kashcheyev (1966). Meteor velocities were measured by the pulse-diffraction method of Davies and Ellyett (1949), and radiant coordinates were measured, by reception, at three spaced points, of radio waves reflected from meteor trails in the process of formation (Gill and Davies (1956)). For this purpose equipment for 8-meter waves was used. The equipment was described by Lebedinets and Kashcheyev (1966) and Kashcheyev and Lebedinets (1961), together with a procedure of measured data treatment. Measurement accuracy was determined by analysis of different error sources and also by an inner convergence of measurement data for known meteor streams. Root mean square error in the radiant declination δ of an individual meteor was about $\pm 2.5^\circ$. The same error in the right ascension was $\pm 2.5^\circ \sec \delta$, and in the extra-atmospheric velocity it was ± 2.0 km/sec.

Velocities, radiants, and orbits of 12 500 meteor bodies were measured. They were bodies generating meteors brighter than approximately $+7^m$.

When performing a statistical treatment of the catalog of measured orbits, considerable attention was paid to the selectivity effect of meteor radar observation, and a due account of that effect was made. To change from a measured orbit distribution to a real one, the following factors must be taken into account: The first is

the geometrical factor I/P_1 characterizing the relative noticeability of meteors having different values of the radiant declination. That factor is determined by geometrical parameters of radiowave reflection from meteor trails and the directivity diagram of an antenna set. The second is the physical factor I/P_2 , characterizing relative noticeability of meteors moving at different velocities. The physical factor is determined by the dependence of the ionization coefficient, the height h and ionization distribution along a meteor trail upon the initial mass M_0 and velocity V_0 of the meteor body and also by the dependence of the initial radius of the ionized trail on h and V_0 . The third is the astronomical factor I/P_3 , which characterizes the dependence of the probability of a meteor's encounter with the Earth upon the orbit elements of the meteor body. A procedure for calculating the geometrical and physical factors was suggested by Lebedinets and Kashcheyev (1966) and Lebedinets (1963). The astronomical factor was calculated by Öpik (1951). By ascribing a certain statistical weight $P_1 P_2 P_3$ to each meteor, one can change from the measured distribution of orbit elements to an effective distribution for a whole set of meteor bodies whose masses exceed a certain minimum value M_0^x and whose orbits have a perihelion distance q equal to or less than 1 AU and an aphelion distance $1 - q$ equal to or greater than 1 AU. For our measurement equipment the M_0^x value was about $2 \cdot 10^{-4}$ gram.

THE ORBITS OF METEOR BODIES

A semimajor axis distribution of radio-meteor orbits is shown in figures 1 to 4. Eccentricity,

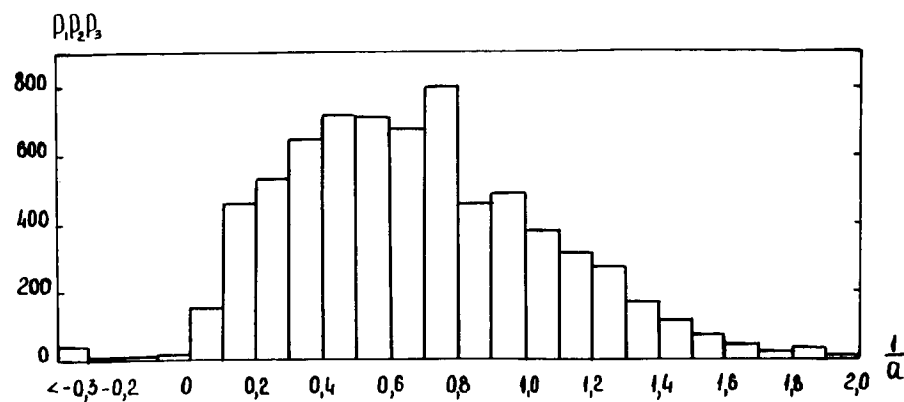


FIGURE 1.—Semimajor axis distribution corrected for the observation selectivity.

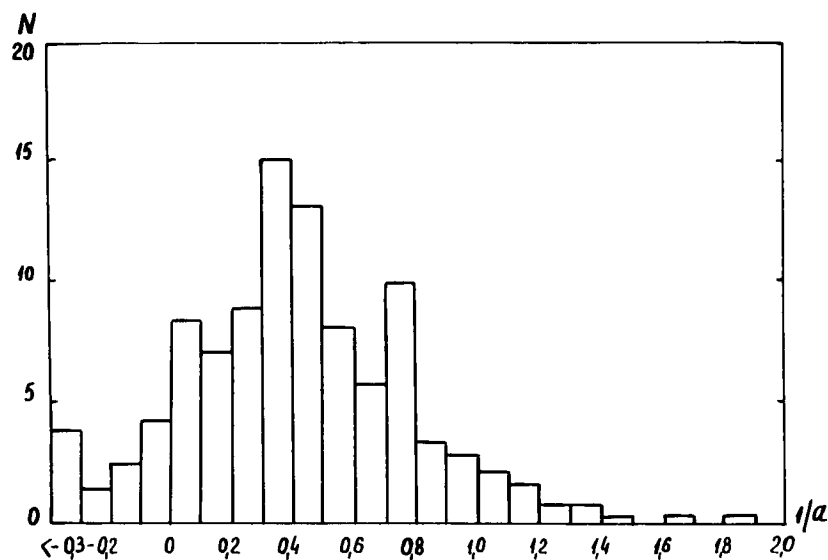


FIGURE 1.—Continued.

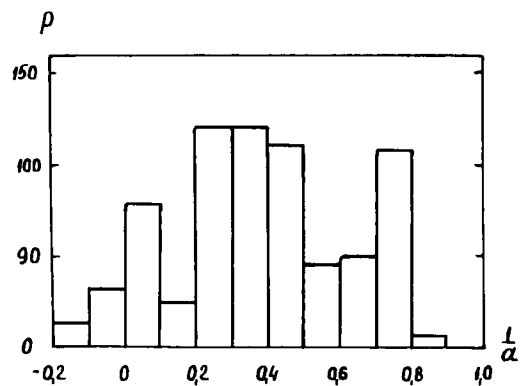
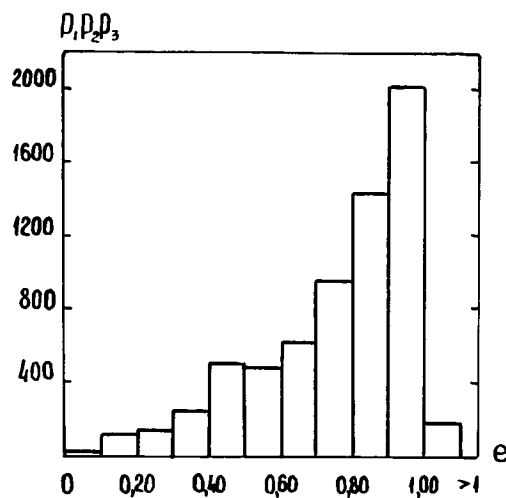


FIGURE 1.—Concluded.

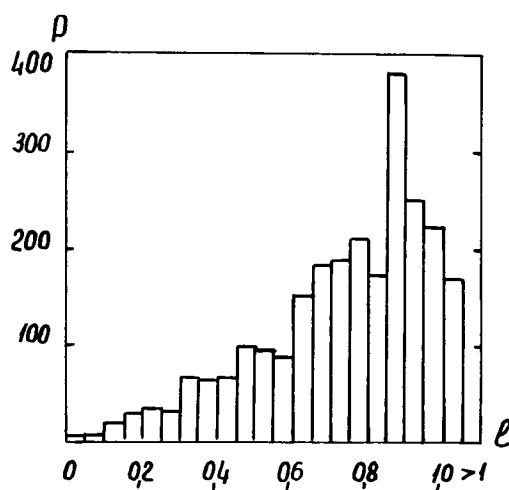
(a) Radio meteors

FIGURE 2. — Eccentricity distribution corrected for observation selectivity.



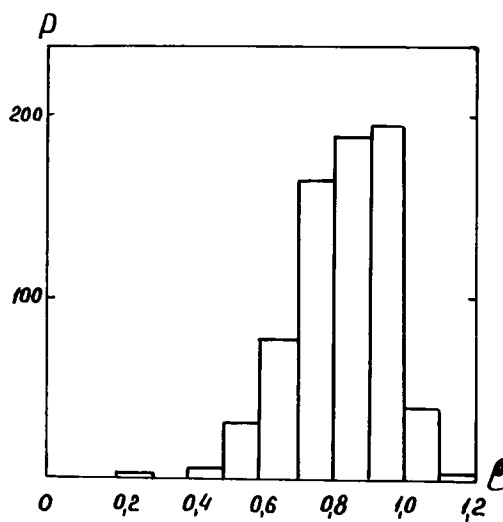
(b) Faint photographic meteors

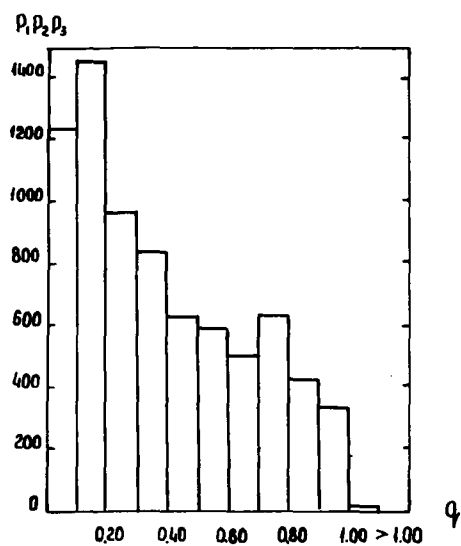
FIGURE 2. — Continued.



(c) Bright photographic meteors

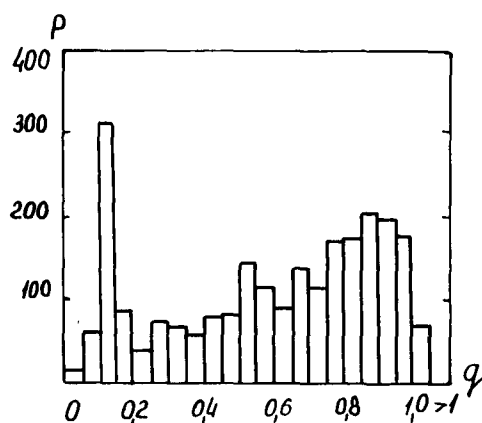
FIGURE 2. — Concluded.





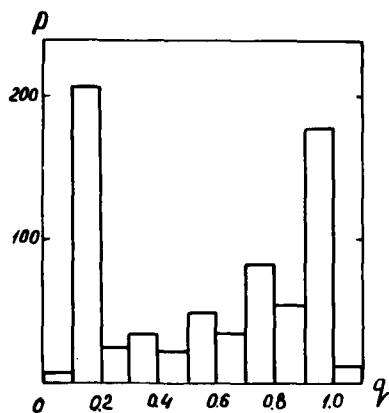
(a) Radio meteors

FIGURE 3.—Perihelion-distance distribution corrected for observation sensitivity.



(b) Faint photographic meteors

FIGURE 3.—Continued.

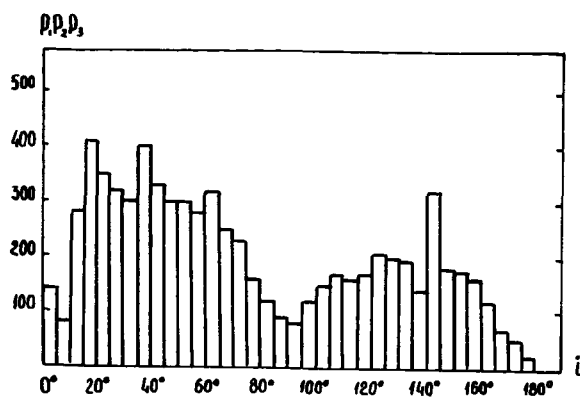


(c) Bright photographic meteors

FIGURE 3.—Concluded.

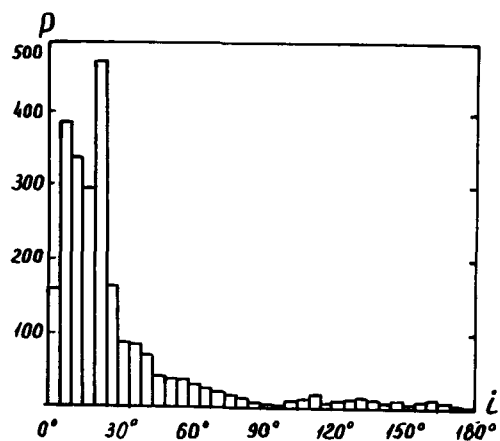
(a) Radio meteors

FIGURE 4. — Inclination distribution corrected for observation sensitivity.



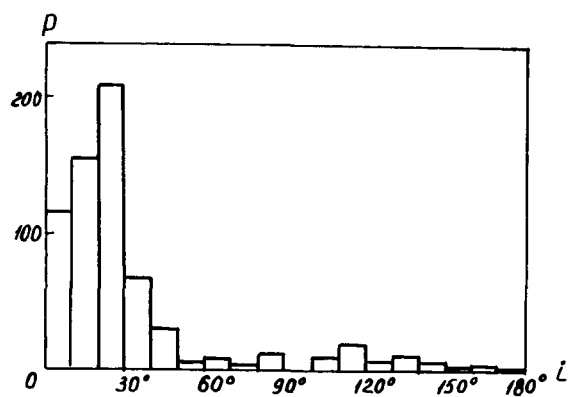
(b) Faint photographic meteors

FIGURE 4. — Continued.



(c) Bright photographic meteors

FIGURE 4. — Concluded.



perihelion, and inclination distributions of the same orbits are also shown. All those distributions were corrected for the observation selectivity. For the sake of comparison, a distribution of 2529 orbits of weak photographic meteors is also given, together with the distribution of 144 orbits of bright photographic meteors. The data on the weak meteors were borrowed from McCrosky and Posen (1961) who used Super-Schmidt cameras for their observations. The data on the bright meteors are those of Whipple (1954) who used small cameras. Two-dimensional distributions of radio-meteor orbits are given in figures 5 to 7. They are i and q , i and a , i and e distributions. Circled areas in figures 5 to 7 are proportional to orbit numbers in corresponding intervals of i , q , a , and e . Distributions for $1/a$, q , e , and i of orbits of sporadic and stream radio meteors calculated on the basis of our observations are compared in figures 8 to 11.

We calculated orbits of 12 500 meteors, including orbits of 3500 meteors belonging to meteor streams.

We observed mainly meteors of $+5^m$ to $+7^m$ absolute visual magnitude. Meteors observed by McCrosky and Posen (1961) had a $+1^m$ to $+3^m$ magnitude (the middle of their observed interval was $+2^m$). Whipple (1954) observed meteors in an interval of 0^m to -3^m (the middle of his interval was -2^m).

Figure 1 shows that mean dimensions of meteor body orbits decrease steadily with meteor masses, the eccentricity distributions of radio meteors and photographic ones being roughly the same. Respective distributions of perihelion distances are substantially different (fig. 3): when q increases from 0.05 to 1 AU, the distribution function of radio meteors decreases steadily and that of photographic meteors increases steadily (if we neglect meteors of the Geminid stream). The mean q value for radio-meteor orbits is approximately two times smaller than that for photographic meteors. Orbit distributions according to their inclinations are also substantially different for the radio and photographic meteors. A strongly pronounced concentration near the ecliptic plane is characteristic of photographic meteors: a large majority of their orbits

have i less than or equal to 30° . The concentration near the ecliptic plane is most sharply pronounced for smaller meteor orbits having $a \leq 5$ AU. The distribution of larger orbits, that is, those with $a > 10$ AU, according to i , is ap-

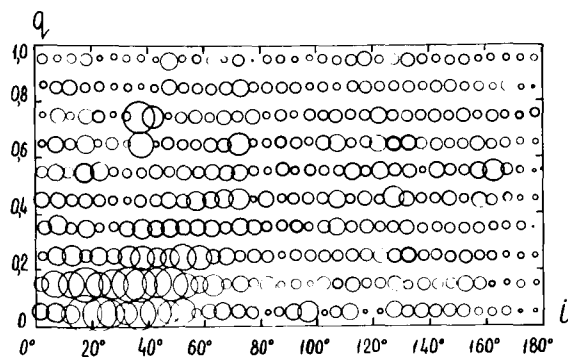


FIGURE 5.—Distribution of radio meteor orbits for inclination and perihelion distance.

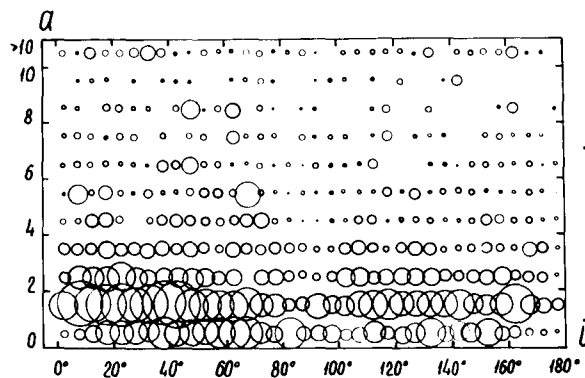


FIGURE 6.—Distribution of radio meteor orbits for semimajor axis and inclination.

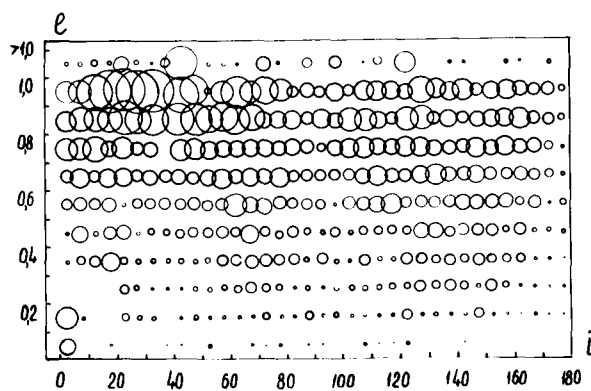


FIGURE 7.—Distribution of radio meteor orbits for eccentricity and inclination.

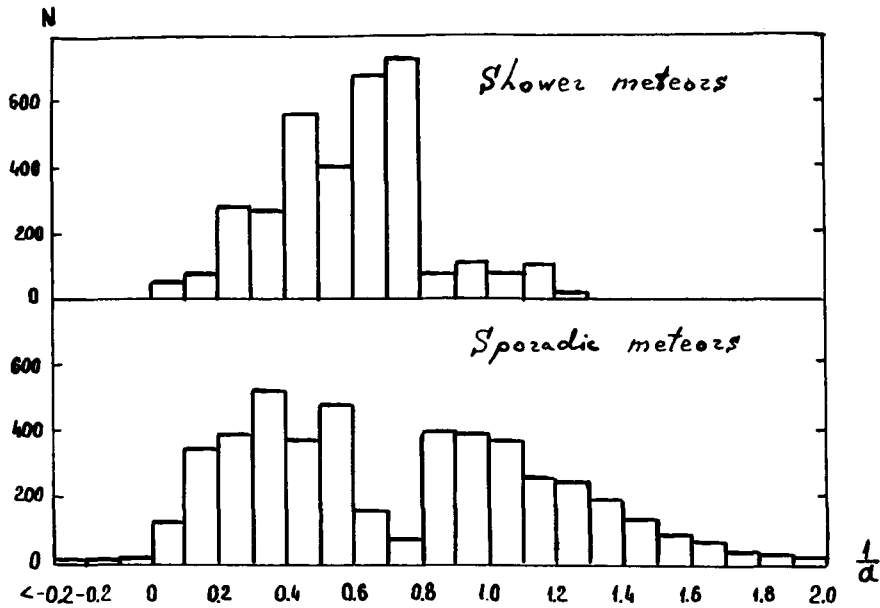


FIGURE 8.—Distribution of the semimajor axis for orbits of stream and sporadic radio meteors.

proximately uniform. Orbit concentration near the ecliptic plane is substantially less pronounced in case of radio meteors; the i -distribution of orbits having $a > 3$ AU is also roughly uniform.

Orbits of sporadic and stream meteors are appreciably different. Stream meteors rarely have orbits of very small sizes, that is, with a smaller than 1.25 AU, whereas nearly half the sporadic meteors have orbits of that small size. Orbits with $a > 2.5$ AU are also substantially more frequent for sporadic meteors than for meteor streams. More than 70 percent of the stream meteors have orbits with $1.25 < a < 2.5$ AU. Nearly two-thirds of the stream meteor orbits have eccentricities $e > 0.8$, but only less than 30 percent of sporadic meteors have orbits with the same eccentricity value. Only 5 percent of the stream meteor orbits have e less than 0.4, but the same eccentricity is characteristic of nearly 20 percent of sporadic meteors. Nearly 45 percent of the stream meteors have orbits with very small perihelion distances, that is, with $q < 0.2$ AU, whereas only 12 percent of the sporadic meteors have such orbits. No orbit concentration near the ecliptic plane is observed in the case of sporadic meteors, and, what is more, i -values close to 0° or 180° are particularly rare

for these meteors. More than 80 percent of the sporadic meteors have orbits with an i -value of 30° to 165° . An appreciable concentration of the meteor orbits near the ecliptic plane is observed in case of stream meteors.

A comparison of orbits obtained on the basis of photographic and radar observations reveals some general regular features of the motion of

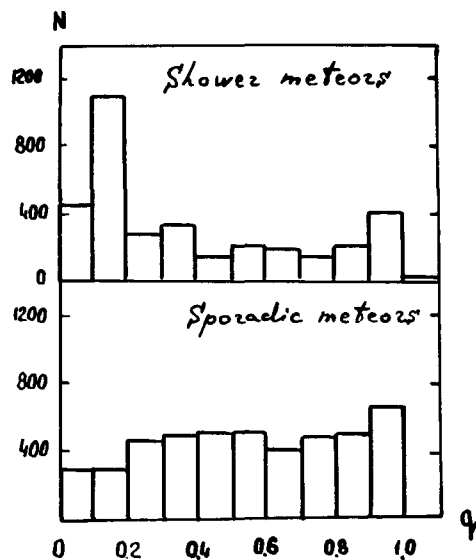


FIGURE 9.—Distribution of the perihelion distance for orbits of stream and sporadic radio meteors.

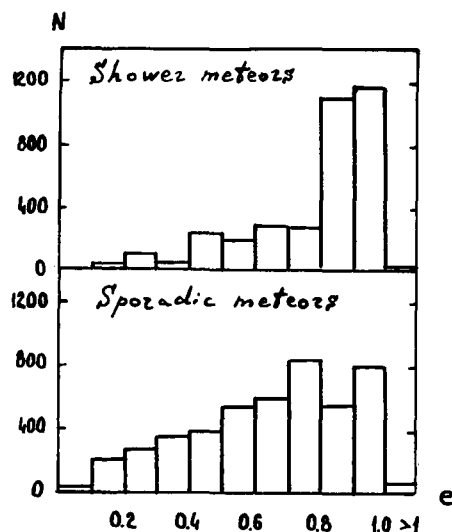


FIGURE 10.—Distribution of the eccentricity for orbits of stream and sporadic radio meteors.

meteor bodies in the solar system, with those features being different for meteors of different sizes.

Using small cameras for photographic observations, Whipple (1954) has found that a great majority of large-size meteor bodies generating meteors brighter than 0^m have orbits of two main kinds: (a) Orbits similar to those of the long-period comets. Orbits of this kind have very large dimensions ($a > 10$ AU), arbitrary inclinations to the ecliptic plane, and eccentricities close to 1. (b) Orbits similar to those of the short period comets. These orbits have relatively small sizes ($a \leq 5$ AU), large eccentricities ($e > 0.7$), and small inclinations (less than 30°). Meteor bodies having short-period-type orbits are four times more numerous than those having long-period-type orbits. Some 10 percent of meteors have asteroidal-type orbits with small eccentricities and small inclinations.

Photographic observations by means of Super-Schmidt cameras permitted 2529 orbits of smaller meteor bodies generating meteors brighter than $+3^m$ to be obtained (McCrosky and Posen (1961)), and a much greater variety of orbits was revealed in this case. Almost circular orbits, that is, orbits with a smaller than 1 AU, were found, together with a small number of orbits having small eccentricities and large

inclinations. But a large majority of meteor bodies had orbits belonging to one of the two previously discussed types of comet orbits.

It is easy to see in figures 1 to 7 that a complex of orbits, obtained as a result of radio observations of meteors brighter than $+5^m$ to $+7^m$, may be represented as a superposition of two following components: (c) orbits with arbitrary inclinations (their number is appreciably smaller in cases of $i < 30^\circ$ and $i > 165^\circ$), with arbitrary eccentricities varying from 0 to 1 and with arbitrary perihelion distances that vary from 0 to 1 AU; and (d) orbits with small inclinations. In most cases such orbits have moderate dimensions, that is, $a \leq 3$ AU, small perihelion distances of $q < 0.3$ AU, and large eccentricities ($e > 0.7$). A majority of the sporadic meteor bodies and a small number of the stream bodies have (c) type orbits, but a majority of the stream meteor bodies and a small number of sporadic ones have orbits of the (d) type.

Origin of the Meteor Substance

Due to the Poynting-Robertson effect and resistance of the interplanetary medium, dimensions and eccentricities of the orbits of meteor bodies steadily decrease, and the particle finally falls onto the Sun (Poynting (1903) and Robertson (1937)). It is easy to show that the lifetime of the majority of smaller meteor bodies that generate radio meteors and move along orbits calculated by us never exceeds 10^7 years. The lifetime of greater particles generating photographic meteors is also very short compared with the age of the solar system. A great number of meteor bodies are captured by planets; therefore, the meteor substance in inner regions of the solar system must be constantly supplied by some unknown sources.

Different authors suggest three main sources of the meteor substance: disruption of comets, disintegrations of asteroids due to their collisions and penetration of hard particles into the inner regions of the solar system from its outer periphery under the action of the Poynting-Robertson effect.

According to Whipple (1954), a similarity of orbits of the great majority of large-size meteor bodies to those of comets (mainly short-period

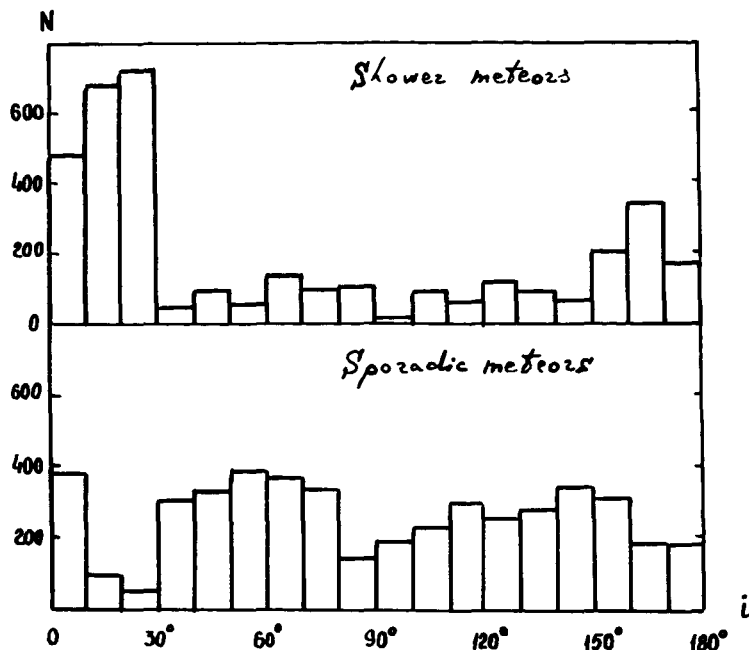


FIGURE 11. — Distribution of the inclination for orbits of stream and sporadic radio meteors.

ones) is evidence that the above meteor bodies are almost exclusively a product of the disintegration of short-period comets and that only a small number of meteor bodies are generated as a result of the disruption of asteroids. McCrosky and Posen (1961) analyzed a catalog of orbits obtained by them and came to the conclusion that a majority of meteor bodies generating weak photographic meteors are also of comet origin.

Radar observations of meteors in Jodrell Bank (Davies and Gill (1960)) and in Kharkov (Kashcheyev and Lebedinets (1961)) revealed a great number of small orbits having $a \leq 2$ AU, small eccentricities ($e < 0.7$), and large inclinations

$$(30^\circ < i < 165^\circ)$$

Nearly 30 percent of the radio meteors and less than 10 percent of the faint photographic ones have such orbits, but only approximately 1 percent of the bright photographic meteors have orbits of this kind. To explain a great number of orbits of the last type, Davies and Gill (1960) suggested that there is a large dust cloud at great distances from the Sun and that the cloud particles move along large orbits with arbitrary inclina-

tions. A majority of those orbits lie entirely beyond the Jupiter orbit, but due to the Poynting-Robertson effect dimensions of the cloud particle orbits are steadily decreasing. After a certain period of time a particle orbit may come near that of Jupiter, and the particle may sometimes come very close to this planet and be captured by it or transferred from the initial orbit to another one, belonging to the (b) type. Öpik (1951) has shown that of all the meteor bodies moving along orbits with small eccentricities and inclinations, only those that are small and generate meteors weaker than $+9^m$ can cross the Jupiter barrier.

According to estimations of Davies and Gill (1960), somewhat larger particles generating meteors up to 5^m can also cross the Jupiter barrier without any appreciable perturbation if their orbits have sufficiently large inclinations. A further decrease of the orbit sizes brings it close to the Earth's orbit, and the particle may encounter the Earth. Thus, according to Davies and Gill (1960) a substantial number of small particles (generating radio meteors) approach the Earth's orbit under the action of the Poynting-Robertson effect. These particles come from a

dust cloud situated beyond the Jupiter orbit, and experience no appreciable perturbation on the part of Jupiter or other planets.

Wyatt and Whipple (1950) have investigated changes of meteor-body orbits under the influence of the Poynting-Robertson effect. For $e \neq 0$ they have obtained the following formula:

$$\frac{e^{4/5}}{a(1-e^2)} = \frac{e_0^{4/5}}{a_0(1-e_0^2)} = C_1 \quad (1)$$

In this equation a_0 and e_0 are initial values of a and e , and C is a constant.

Using the initial relation $q = a(1-e)$ we can get from equation (1)

$$\frac{e^{4/5}}{q(1+e)} = \frac{e_0^{4/5}}{q_0(1+e_0)} = C \quad (2)$$

It is easy to see from the last relation that at $q_0 > 5$ AU and $e_0 \leq 1$, $q \leq 1$ AU and $e < 0.06$. Therefore, particles that had initially moved along orbits lying entirely beyond the Jupiter orbit and then, due to the Poynting-Robertson effect, came close to the Earth's orbit, must have almost circular orbits with $e < 0.06$. Nevertheless, according to the results of our radio observations and also of those by Davies and Gill (1960), less than 1 percent of radio meteors have orbits with $e < 0.06$. Thus, an insignificant number of meteor bodies generating radio meteors may be those particles that initially belonged to the dust cloud, situated at a distant periphery of the solar system, which then penetrated into its inner regions under the influence of the radiative deceleration, experiencing no substantial perturbation on the part of the giant planets. Therefore the origin of the small meteor bodies moving along short-period orbits with large inclinations and generating radio meteors cannot be explained by the mechanism suggested by Davies and Gill (1960).

Of all the large bodies of the solar system that are known at present (planets, their satellites, asteroids, and comets), only long-period comets have orbits with arbitrary inclinations. In view of this fact disintegration of long-period comets moving along orbits with relatively short peri-

helion distances is, to all appearances, the only source of meteor bodies with orbits of the (c) type.

The distribution of (d) type radio-meteor orbits according to their a , e , and q is substantially different from that of short-period comet orbits (Porter (1961)). Nearly two-thirds of radio-meteor orbits with small inclinations have $a < 2.5$ AU, $e > 0.8$, and $q < 0.3$ AU. At present, no comet is known to have such an orbit. A large majority of radio-meteor orbits with small inclinations have $a < 2.5$ AU. Only two comets are known to have $a < 2.5$ AU. A large majority of radio-meteor orbits with small inclinations have $q < 0.3$ AU. Only one short-period comet is known at present that has $q < 0.3$ AU, but its orbit is far too large ($a = 27$ AU). For the short-period comets a mean value of the orbit eccentricity is $\bar{e} \approx 0.6$. For the radio-meteor orbits with small inclinations, the mean value is $\bar{e} \approx 0.85$. Smaller a and e values of the meteor body orbits as compared with those of the short-period comet orbits can be explained by the radiative deceleration, but the eccentricity increase cannot be explained in this way. It is even less probable that the radiative deceleration may explain a simultaneous decrease in perihelion distance and the increase of eccentricity. Thus we see that it is unlikely that the observed complex of radio-meteor orbits having small inclinations to the ecliptic plane could be a disintegration product of comets having orbits similar to those of the short-period comets known at present.

For 40 meteor streams, we obtained orbits with $a < 2.5$ AU, $e > 0.8$, and $q < 0.3$ AU. Orbits of that type have active meteor streams of Geminid and Arietid showers for which no fore-mother comet is known. This is an evidence that a great number of comets (or some other large bodies which generate meteor streams when disintegrating) having orbits of the type mentioned above must constantly appear in the solar system. If we accept the ice model of the comet nuclei (Vsekhsviaty (1948) and Whipple (1950 and 1951)), the lifetime of comets having $q < 0.3$ AU and $a < 2.5$ AU will be very short because entire orbits lie near the Sun and comets will often come very close to it at perigee. Therefore, the nuclei of such comets will very likely disintegrate after few revolutions around the Sun, and it is only

natural that we know no comets having orbits of this type. If we assume that a decay time of meteor streams of the Geminid and Arietid type is approximately equal to a time of the fall onto the Sun of the small meteor bodies that generate radio meteors, we may roughly estimate an occur-

rence time of the short-period comets that move along orbits with very small perihelion distances. In order to explain the observed number of the radio-meteor streams, it is necessary to assume that one comet of this kind appears every 100 to 1000 years.

REFERENCES

- DAVIES, J. G., and C. D. ELLYETT, 1949, *Phil. Mag.*, **40**, 614.
 DAVIES, J. G., and J. C. GILL, 1960, *Mon. Not. Roy. Astron. Soc.*, **121**, 437.
 GILL, J. C., and J. G. DAVIES, 1956, *Mon. Not. Roy. Astron. Soc.*, **116**, 105.
 KASHCHEYEV, B. L., and V. N. LEBEDINETS, 1961, *Radar Investigations of the Meteoric Phenomena*, edited by *Acad. Sci. USSR*.
 KASHCHEYEV, B. L., V. N. LEBEDINETS, and M. F. LAGUTIN, 1965, *Doklady Acad. Sci. USSR*, **164**, N. 6.
 —, 1966, Works collection: *Issledovaniya meteorov* (Investigations of Meteors) edited by "Nauka," Moscow.
 LEBEDINETS, V. N., 1963, *Ast. Zhur.*, **40**, N. 4, 719.
 LEBEDINETS, V. N., and B. L. KASHCHEYEV, 1966, *Ast. Zhur.*, **43**, N. 4, 854.
 McCROSKY, R. E., and A. POSEN, 1961, *Smithson. Contrib. Astrophys.*, **4**, 15.
 ÖPIK, E. J., 1951, *Proc. Roy. Irish Acad.*, **1754**, N. 12, 165.
 PORTER, J. G., 1961, *Mem. B.A.A.*, **39**, N. 3, 1.
 POYNTING, J. H., 1903, *Phil. Trans. Roy. Soc.*, **A202**, 525.
 ROBERTSON, H. P., 1937, *Mon. Not. Roy. Astron. Soc.*, **97**, 423.
 VSEKHSVIATSKY, S. K., 1948, *Ast. Zhur.*, **25**, N. 4, 256.
 WHIPPLE, F. L., 1950, *Astrophys. J.*, **3**, 375.
 —, 1951, *Astrophys. J.*, **113**, 464.
 —, 1954, *Astron. J.*, **59**, 501.
 WYATT, S. P., and F. L. WHIPPLE, 1950, *Astrophys. J.*, **3**, 134.

Page intentionally left blank

33. Orbital Distributions of Meteors of Limiting Magnitude +6 Observed From the Southern Hemisphere

CARL S. NILSSON

*Smithsonian Astrophysical Observatory
Cambridge, Massachusetts*

A radio survey of orbits of meteors of limiting magnitude +6 was made at Adelaide, South Australia, during 1961. Each orbit has been weighted for observational and astronomical selection, and the distributions of 1900 orbits are compared with those of other surveys, particularly with those of the faint photographic survey of McCrosky and Posen (1961). The distributions for stream orbits and sporadic orbits are given separately.

The two most noteworthy distributions are those with perihelion distance and longitude of perihelion. The latter shows evidence of Jupiter alinement for the sporadic meteor orbits; this evidence, however, still does not differentiate between an asteroidal or cometary source.

THIS PAPER PRESENTS THE ORBITAL DISTRIBUTIONS of 1900 meteors detected during a radio survey of meteor orbits made at Adelaide, South Australia, during 1961. Several surveys of this type have been undertaken in the Northern Hemisphere at varying magnitudes. Davies and Gill (1960) measured the orbits of over 2000 meteors of limiting radio magnitude +8; McCrosky and Posen (1961) analyzed the trails of 2500 meteors of limiting magnitude +3 photographed simultaneously from two camera stations; and Hawkins (1962) has extended radio measurements of meteor orbits to magnitude +10. Kashcheyev, Lebedinets, and Lagutin (1960) have also made a similar radar survey of meteor orbits to a limiting magnitude of about +7, but none of these northern surveys has been able to include radiants south of declination -20° . Our observations extend to meteors of radio magnitude +6 and include both overdense and underdense meteor trails. Our results are briefly compared to those of the northern surveys mentioned previously.

OBSERVATIONAL TECHNIQUE

The radio equipment consists of a combination of continuous wave and radar on 27 Mc/s; the continuous-wave transmitting power was only 300 W, and this limited the survey to meteors giving rise to line densities greater than 3×10^{13} electrons/m. This limit corresponds to a radio magnitude of about +6 (McKinley, 1961). The equipment has been described in detail by Weiss and Elford (1963). One feature of the system is that not only are the velocity and trail orientation measured for each meteor, but the actual positions of the three specular reflection points are also uniquely determined. The heights of each reflection point are measured to ± 2 kilometers.

We have corrected the apparent reflection-point positions for wind shear from the measures of Doppler drift at each reflection point. Also, having measured the antenna radiation patterns, we are able to determine the electron line density at each reflection point. Thus, assuming a certain vaporization theory, the mass of each meteor could be calculated. A more complete description

of the observational method, data processing, geocentric corrections, and accuracy of results has been published previously (Nilsson, 1964).

Weighting against selection effects is of the greatest importance in attempting to derive real distributions of meteor orbits in space, so the weights applied to these data are described briefly.

First, there are the selection factors inherent in the radio method of observation. Electron line density depends heavily on meteor velocity, the relationship probably being of the form

$$q_{\max} \propto V_{\eta_{\max}}^{\eta} \quad (1)$$

where the subscript refers to the point of maximum ionization. The value of η has been variously determined to be between 3 and 5; the most recent work (Verniani and Hawkins, 1964) confirms the value 4.0 chosen to weight the orbits of this survey.

Because of the location of the observing station, certain radiant declinations are more favored than others; from the known equipment parameters it has been possible to calculate directly the expected echo rate as a function of declination. This is shown in figure 1. The observed diurnal rate variations of various showers have been used to verify the equipment response as a function of radiant position, and each orbit has been weighted according to the declination of its radiant.

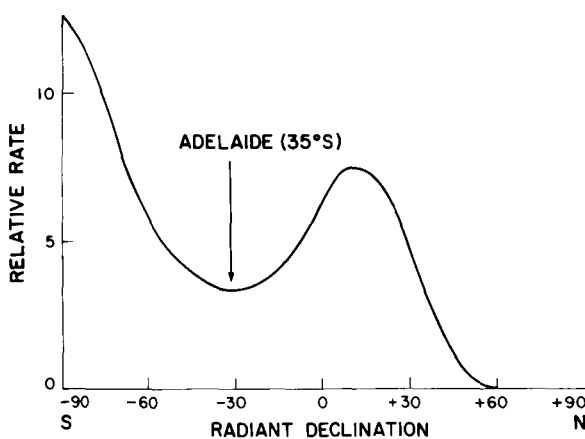


FIGURE 1. — The calculated meteor echo rate for the Adelaide equipment as a function of radiant declination.

Some other selection factors have also been considered: certain hours of observation were more frequently interrupted than others, and there was some dependence of the number of echoes reduced on the Fresnel diffraction frequency. These factors were included. Whipple (1955) has suggested that rapid diffusion of the ion column of high-altitude meteors inhibits their observations by radio techniques. The height of maximum ionization increases with velocity; hence the high-velocity meteors will be selectively discriminated against, with a concomitant effect on the orbit distributions. This effect does not seem as serious in practice as theory suggests. The velocity distribution in figure 2 does not differ markedly from the faint photographic meteor velocity distribution found by McCrosky and Posen (1961). From classical vaporization theory (Weiss, 1959) we expect that the atmospheric density at the height of maximum ionization ρ_{\max} will be given by

$$\rho_{\max} \propto \cos \chi \cdot V_{\infty}^{-2} \quad (2)$$

where χ is the zenith angle of the radiant. From a study of the distributions of echo heights of the meteors observed at Adelaide, the author found (unpublished data) that the exponent of V_{∞} in equation (2) was about -1.1 rather than -2 . This value held for the slow meteors as well as for the fast ones and is consistent with the results of Greenhow and Hall (1960) who found the ex-

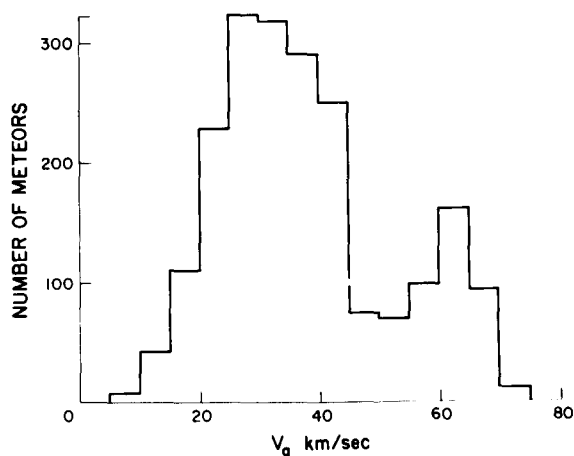


FIGURE 2. — The observed distribution with geocentric velocity V_g for all meteors.

ponent of V_∞ in equation (2) to be between -1.0 and -1.5 . Thus the height of maximum ionization does not vary as markedly with velocity as theory suggests.

Finally, there is the astronomical weighting factor, which involves the probability that a meteor of given orbital elements will collide with the Earth. Fortunately, all the meteor distributions shown here from various radio and photographic surveys have used the same factor, the original derivation of which is due to Öpik (1951).

$$W \propto \frac{V_g \sin i}{V_\infty^2} \cdot \left(\frac{2}{r} - \frac{1}{a} - \frac{p}{r^2} \right)^{1/2} \quad (3)$$

where W is the weight, V_g is the geocentric velocity of the meteor, V_∞ is the velocity at the top of the atmosphere, i is the inclination of the orbit, r is the Sun-Earth distance, a is the semimajor axis, and $p = a(1 - e^2)$.

DISTRIBUTIONS OF ORBITAL ELEMENTS

The distributions are presented as double histograms, with the shaded area representing the contribution due to meteor streams, both major and minor. By analyses of orbit associations (Nilsson, 1964), about 29 percent of the weighted total of orbits can be significantly associated into groups of three or more orbits. The top histogram, in each case, represents all the meteors observed in the survey, the lower one represents the sporadic, or unresolvable, background, and the shaded area in between shows the contribution of all the streams. Figure 2 shows the unweighted distribution with geocentric velocity, V_g , of 2040 meteor velocities observed at Adelaide. The observed values of velocity have been corrected for retardation through the Earth's atmosphere, diurnal motion of the observer, and the Earth's gravitational attraction. This distribution is consistent with those of other surveys, the modal value being about 30 km/sec. It is the only Adelaide radio survey distribution presented here which has not been weighted for selection, as it is more useful for comparison in this form.

A comparison of various distributions with reciprocal semimajor axis, $1/a$, is given in figures 3(a) to 3(e). The distributions are arranged in

order of decreasing brightness and clearly show a steady increase in the proportion of short-period orbits as one proceeds to fainter magnitudes. Negative values of $1/a$ signify orbits which have been calculated to be hyperbolic. In view of the known experimental error of the order of 0.1 in $1/a$, no significant number of hyperbolic orbits were found in the Adelaide data, shown in figure 3(c). This distribution appears to fit quite consistently between the faint photographic survey of McCrosky and Posen (1961) at limiting magnitude +3, and the radio survey of Davies and Gill (1960) at limiting magnitude +8. The similarity of the latter distribution with that of the Harvard Radio Meteor Project (Southworth, unpublished data) is quite noticeable.

As Davies and Gill (1960) allowed for observational selection in a manner quite different from Southworth, this suggests that the distributions with $1/a$ are not very sensitive to observational weighting.

Figure 4 shows the weighted distribution with eccentricity; it is normal in appearance and shows the usual tendency of the streams to have high eccentricities.

Two distributions with inclinations are given in figure 5 for the Adelaide data. In figure 5(a), for all values of eccentricity, one can see that the streams are generally, but not entirely, concentrated in direct orbits within 40° of the ecliptic plane. Figure 5(b) gives the distribution with inclinations for the 130 orbits for which $e < 0.5$. It seems to be of the same form as that for all values of eccentricity, although the median value of inclination for the low-eccentricity orbits is 50° compared with 36° for all the orbits. This difference is brought about by the stream content of the orbits with $e > 0.5$; the median values of inclination for the sporadic content are the same for each distribution, namely 42° . There are a few minor associations of orbits at high inclinations, the most noticeable being the Puppis stream at 70° . This stream, of low eccentricity, belongs to the class of orbits described by Hawkins (1962) as "toroidal."

The distribution with perihelion distance for the Adelaide data, given in figure 6(d), is quite different from that obtained by other surveys.

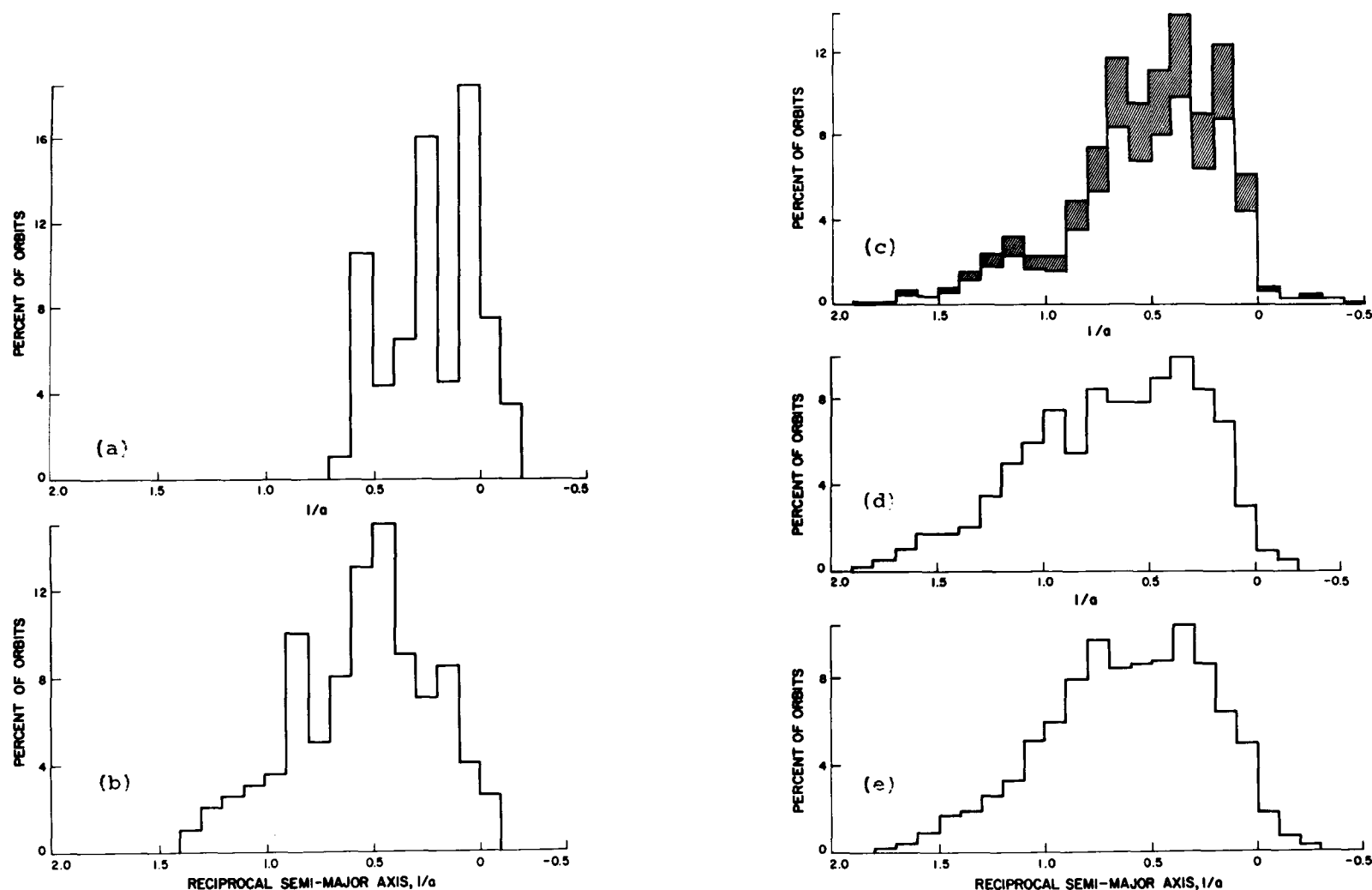


FIGURE 3.—Distributions with reciprocal semimajor axis, $1/a$, for various meteor surveys in order of limiting magnitude: (a) bright photographic survey, 144 meteors (Whipple, 1954, from McCrosky and Posen, 1961); (b) faint photographic survey, 2529 meteors (from McCrosky and Posen, 1961); (c) Adelaide radio survey, about 1900 meteors; (d) Jodrell Bank radio survey, 2510 meteors (from Davies and Gill, 1960); (e) Harvard radio survey, about 12 500 meteors (Southworth, unpublished data).

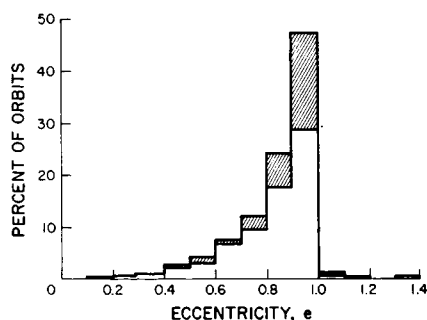


FIGURE 4.—The variation of weighted distribution for all orbits of Adelaide data with eccentricity e .

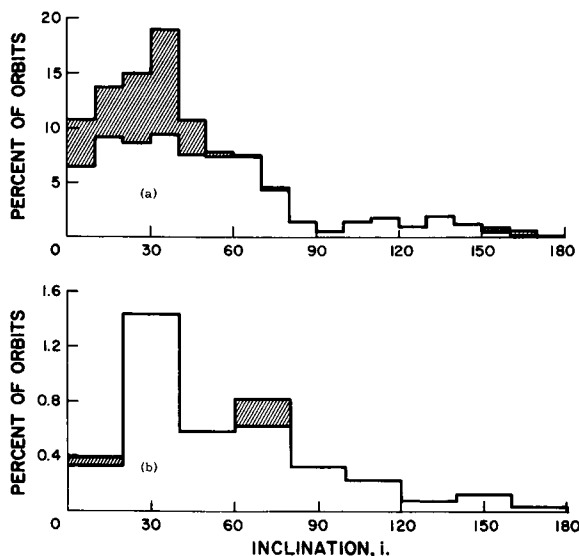


FIGURE 5.—Distributions with inclination i for (a) all orbits; (b) orbits with $e < 0.5$.

Figure 6(a) shows an observed distribution for 369 comets with perihelia < 1.9 AU compiled by McCrosky and Posen (1961) from the Baldet and De Obaldia catalog. From a study of absolute brightness as a function of perihelion distance, McCrosky and Posen (1961) concluded that the distribution was reasonably true out to 1 AU. It seems obvious, however, that the peak at 1 AU is due to observational selection. The distribution for faint photographic meteors is certainly similar out to 1 AU, and it is supported by the Harvard Radio Meteor data, shown in figure 6(c). The Adelaide data, in contrast with the above, show a marked decrease in weighted numbers as the perihelion distance increases out

to 1 AU. The stream contributions are quite marked at small perihelion distances, corresponding to orbits of moderate size and high eccentricities. Incomplete separations of stream orbits are not responsible for this major difference between surveys, as the other distributions contain both sporadic and stream orbits, so we can simply compare the distributions for all the meteors observed. It thus appears that the Adelaide survey observed more short-period, high-eccentricity orbits than the other surveys, and it will be interesting to see if this distribution is confirmed by any other surveys around limiting magnitude +6.

Figure 7 shows the variation of weighted distribution for 1900 meteor orbits with aphelion distance. This distribution, of course, is strongly influenced by the fact that a meteor orbit must cross that of the Earth to be observed. Hence $q < 1.0$ and $q' > 1.0$ AU for all observed orbits, and the bulk of the orbits have aphelia q' between the orbits of Mars (1.5 AU) and Jupiter (5.2 AU). This suggests that we may be able to detect the influence of Jupiter on the aphelion alignment of the low-inclination members of these orbits, such as that observed for the short-period comets and the asteroids. The latter two sets of bodies both show pronounced maximums in number against longitude of perihelion around 13° , the longitude of perihelion of Jupiter's orbit. This can be clearly seen in figure 8(a) (McCrosky and Posen, 1961) and figure 8(b) (Porter, 1952).

Jacchia and Whipple (1961) and McCrosky and Posen (1961) have looked for signs of this alignment in their data, shown in figures 9(a) and 9(b), respectively, but without success. If a sufficient number of comets, or asteroids, are sources of these meteors, we should expect to see a similar distribution for meteors, since the longitude of perihelion is not perturbed very quickly.

McCrosky and Posen (1961) suggested that the bright meteor distributions could be explained if only relatively few comets which approach close to the Earth's orbit were responsible for most of the meteor population. Thus, the distribution with longitude of perihelion would vary from time to time depending on the particular sources at hand. The perihelion longitudes of

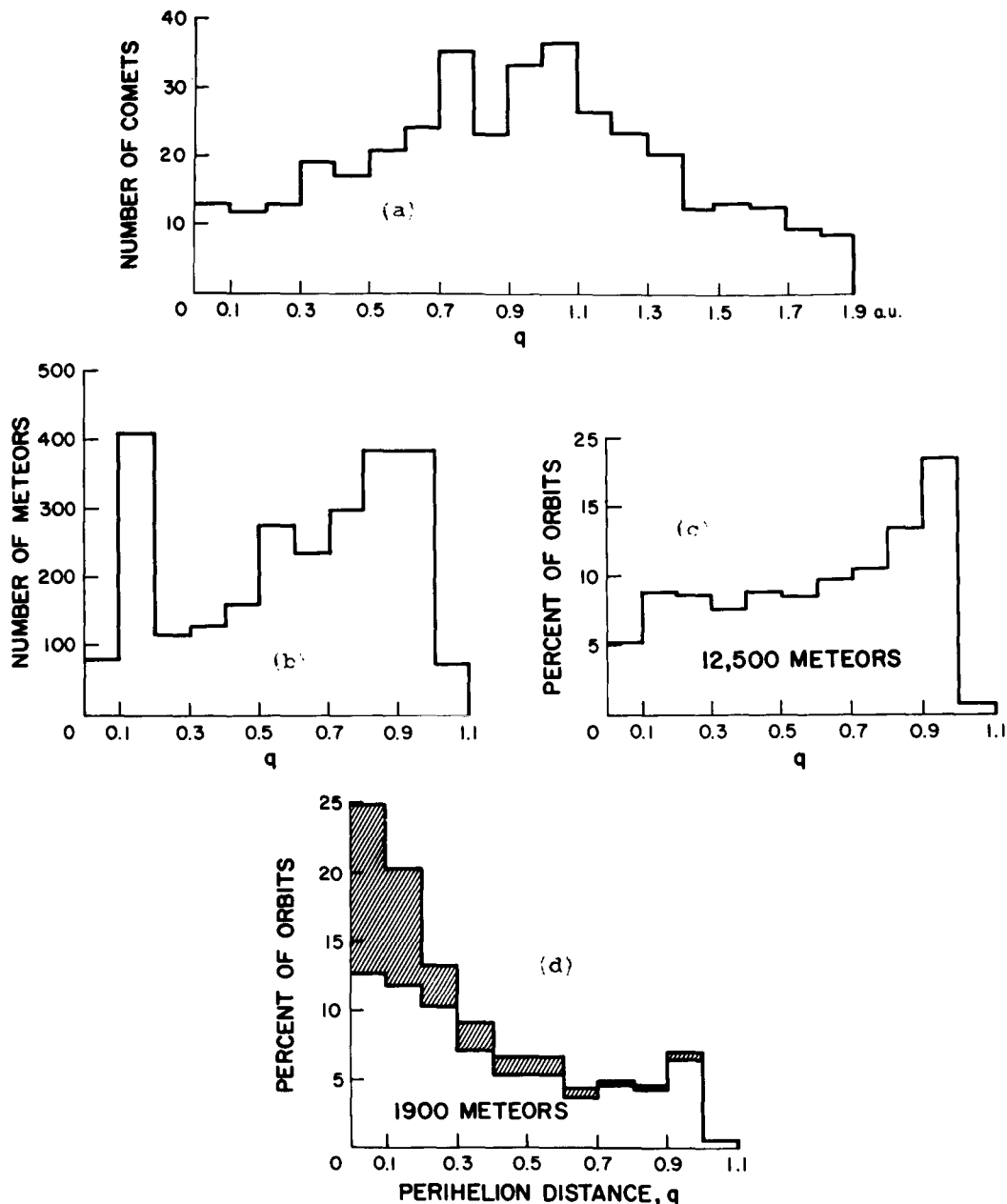


FIGURE 6. —Distributions with perihelion distance q : (a) the distribution for 369 comets with $q < 1.9$ AU (from McCrosky and Posen, 1961); (b) faint photographic survey (from McCrosky and Posen, 1961); (c) Harvard radio survey (Southworth, unpublished data); (d) Adelaide radio survey. The shaded portion shows the contribution of streams.

the six close-approach comets satisfying their conditions of observation for the Northern Hemisphere do, in fact, lie near the maximums of the bright meteor distribution. These longitudes are marked by arrows underneath the abscissa in figure 9(a). There appears to be little

correlation, however, with the distribution for the faint photographic meteors shown in figure 9(b). The Adelaide data are rather instructive in this study. The orbits selected are those within 30° of the ecliptic plane with aphelia between 3 and 5 AU from the Sun. It can be seen

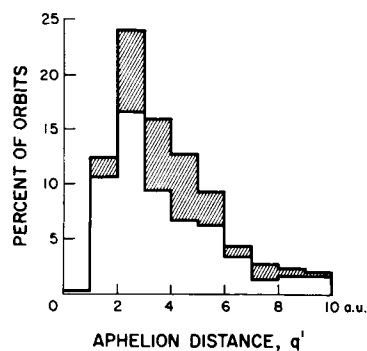


FIGURE 7.—The distribution with aphelion distance q' .

from figure 9(c) that the total distribution for all orbits shows a maximum-to-minimum range similar to the bright meteor distribution, although there is only one pronounced peak, not two. The streams are heavily concentrated in the region $70^\circ < \pi < 180^\circ$. Observations were made reasonably uniformly throughout the year, so this concentration is real, at least for 1961. When the stream orbits are subtracted, however, the remaining sporadic distribution does indeed show a simple maximum near the expected longitude of 13° . This could either show the origi-

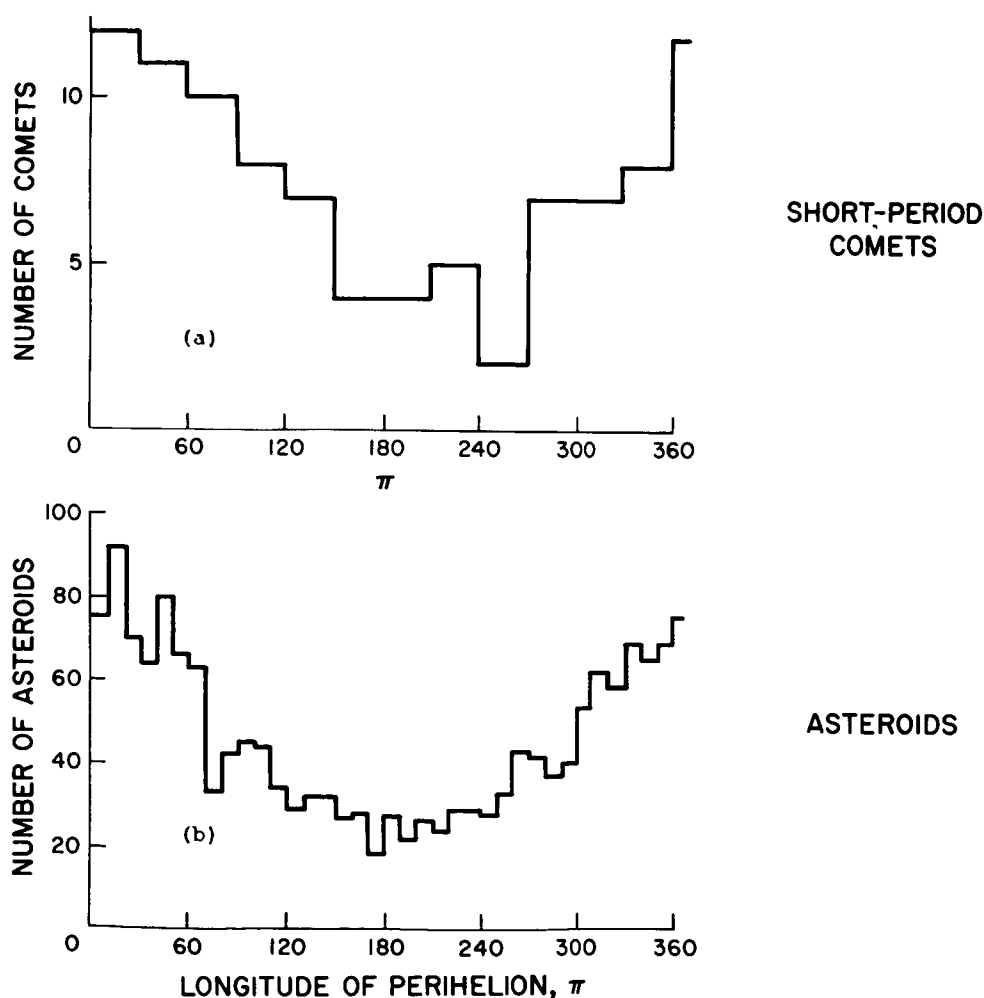


FIGURE 8.—Distributions with longitude of perihelion π for (a) short-period comets (from Porter, 1952); (b) asteroids (from McCrosky and Posen, 1961).

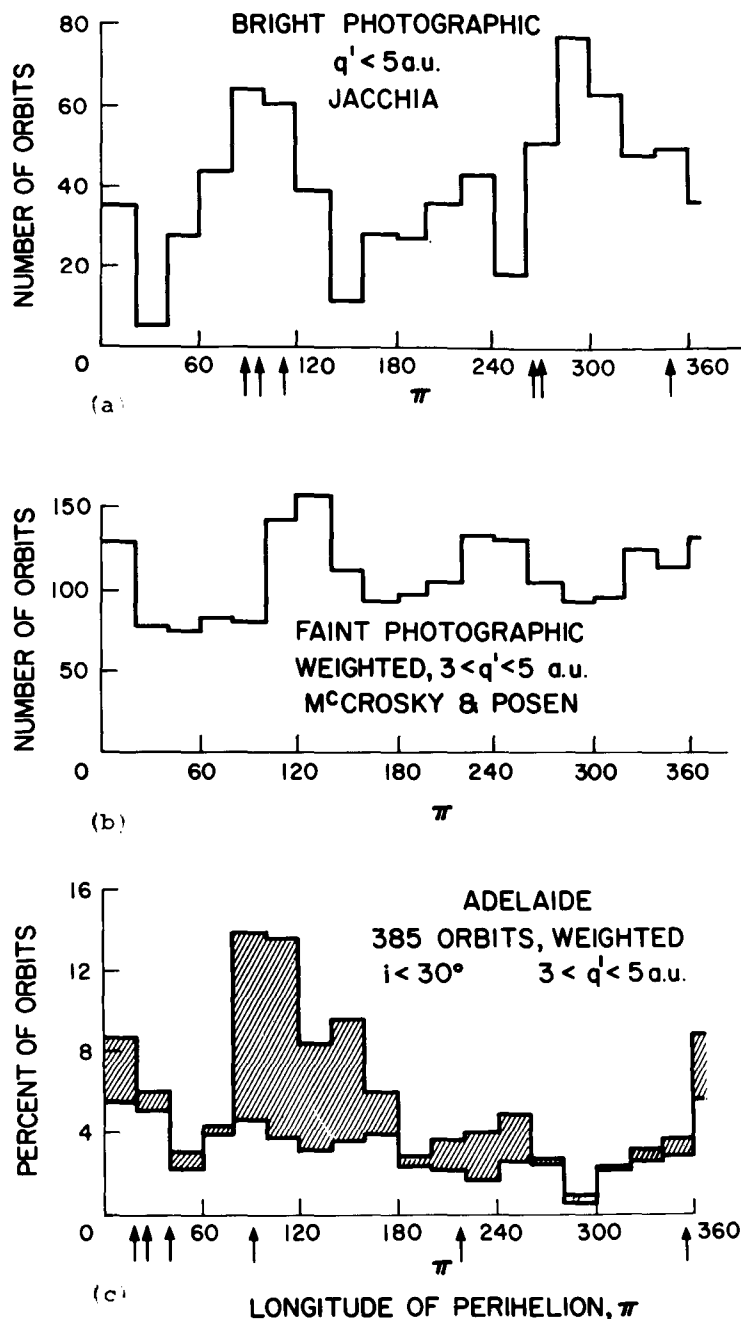


FIGURE 9.—Distributions with longitude of perihelion π for (a) bright photographic meteors reduced by Jacchia (from McCrosky and Posen, 1961); (b) faint photographic meteors (from McCrosky and Posen, 1961); (c) Adelaide radio meteors.

nal alinement, consistent with short-period cometary injection, for example, or it could be the result of aphelion capture by Jupiter from some other original distribution. In the latter case, longer meteor lifetimes are required, as this

alinement would probably take at least approximately 10^5 years to eventuate.

For completeness, the longitudes of the six short-period comets from Porter's (1952) list which closely approach the Earth's orbit and

could give rise to meteor radiants visible in the Southern Hemisphere are included in figure 9(c). These, not unexpectedly, are grouped near 13° and do not correlate with the total maximum between 70° and 180° . There is thus little support from the Adelaide data for the suggestion that these particular comets determine the total distribution with longitude of perihelion. Other classes of comets, such as the long-period comets which have more random distributions with longitude of perihelion, may indeed contribute a significant proportion of the meteor population.

Whipple (1954) has introduced an empirical comet-asteroid criterion K defined by

$$K = \log_{10} \left[\frac{a(1+e)}{1-e} \right] - 1 \quad (4)$$

which is positive for most comet orbits and negative for most asteroid orbits. This index is thus quite helpful in any discussion of the general characteristics of meteor orbits and their origin, and it is interesting to see how the orbits are distributed with respect to this criterion. Figure 10 gives the weighted distribution for the Adelaide data. Most of the orbits have $K > 0$, particularly those associated with streams, but a significant proportion have $K < 0$. This proportion

appears to increase as one considers fainter magnitudes. Whipple's (1954) analysis of bright meteors showed 6 percent with $K < 0$; McCrosky and Posen found 26 percent of their faint photographic meteors with orbits for which $K < 0$. From the Adelaide data about 22 percent of the observed numbers of orbits have $K < 0$, but only 17 percent of all the weighted orbits have $K < 0$.

The proportion is greater, however, if streams are excluded; about 21 percent of the weighted sporadic orbits have $K < 0$. It is surprising that this figure is a little less than that found for the faint photographic meteors, in view of the fainter limiting magnitude of the Adelaide data, but further comments on this are better left until figures from other surveys are available.

It remains to look at the distributions of the orbits for which $K < 0$. By definition, they will be smaller and of lower eccentricity than those for which $K > 0$. This is obvious in figures 11(a) and 11(b). The distribution with inclination is shown in figure 11(c). The orbits are predominantly direct with inclinations $< 70^\circ$; however, the distribution does not drop between 0° and 20° , as do the two distributions in figure 5 for orbits with all values of K . The distribution can be described quite well by a simple cosine law

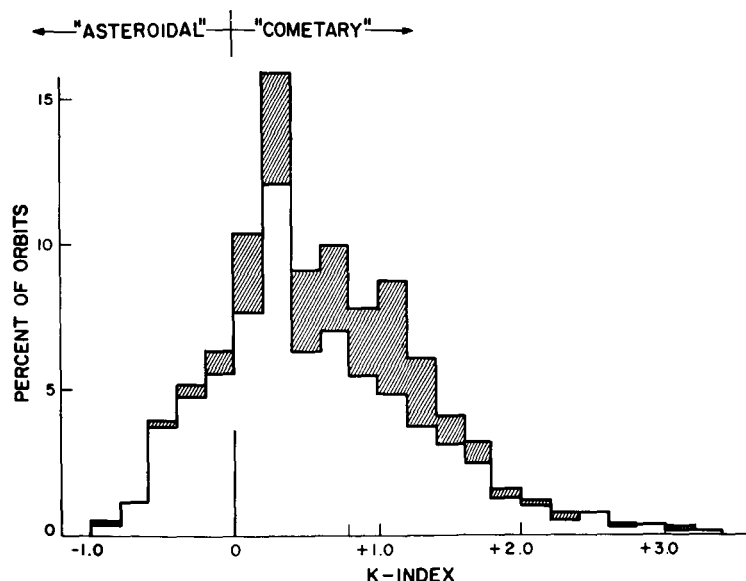


FIGURE 10.—Distribution of Adelaide data with K -index (1900 weighted meteor orbits for radio magnitude of +6).

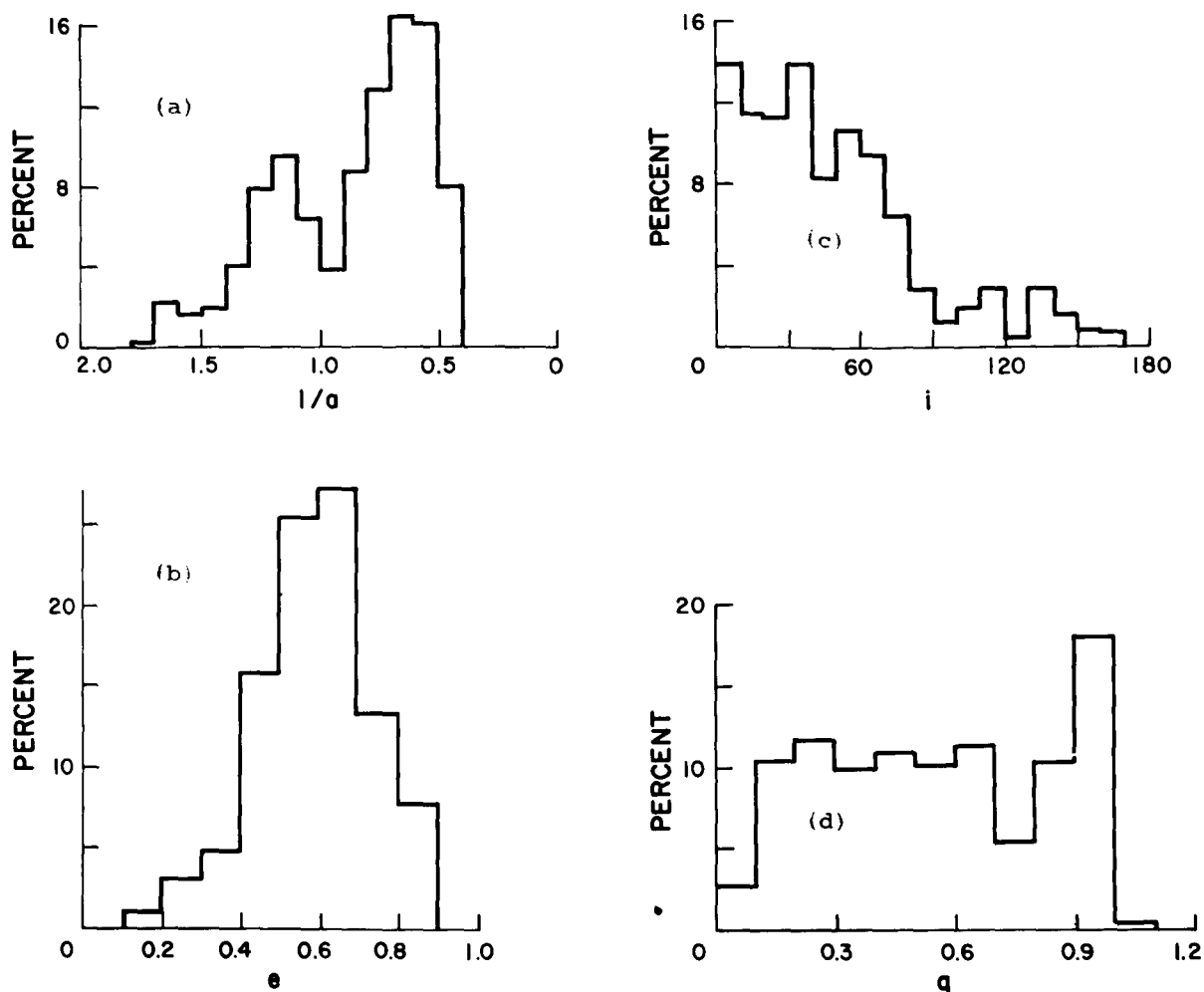


FIGURE 11.—Distributions of all Adelaide meteor orbits (430) for which $K < 0$ with (a) reciprocal semimajor axis $1/a$; (b) eccentricity e ; (c) inclination i ; (d) perihelion distance q .

out to an inclination of 90° . Now, both the short-period comets and the asteroids are generally confined to within 30° of the ecliptic plane. The distribution of stream meteors, however, does not show a maximum until 30° and extends out to 60° . If the stream meteors originate mostly from the short-period comets, perturbations must have extended the distribution with inclination out and away from the ecliptic. The distribution in figure 11(c) for the “asteroidal” orbits seems to indicate, therefore, that either the source or the age, or both, of at least some of these meteors is different. In fact, they may well be asteroidal in origin.

Figure 11(d) shows the distribution with perihelion distance for these orbits. By definition of K , we have excluded orbits with $e > 0.9$, so it is not surprising to see that the peak at small perihelion distance shown in figure 6(e) has disappeared, and the distribution for the “asteroidal” orbits is essentially flat out to 1.0 AU.

ACKNOWLEDGMENT

This survey was carried out at the University of Adelaide, first under the direction of L. G. H. Huxley and later under J. H. Carver. The author wishes to acknowledge particularly the guidance of W. G. Elford, University of Adelaide, and the late A. A. Weiss, CSIRO, Sydney, who jointly supervised the project. Financial support for the survey was provided

by the Radio Research Board of Australia and a University Research Grant. The author was supported by a General Motors-Holden Pty., Ltd., Post Graduate Research Fellowship and a CSIRO Senior Research Studentship.

This paper was written during the author's tenure at the Harvard College Observatory and the Smithsonian Astro-

physical Observatory, Cambridge, on the Radio Meteor Project under the coordination of G. S. Hawkins. This project is supported by the National Aeronautics and Space Administration under Contract NSR-09-015-033. The author also thanks R. B. Southworth for valuable assistance and the use of unpublished data.

REFERENCES

- DAVIES, J. G., and J. C. GILL, 1960, *Mon. Not. Roy. Astron. Soc.*, **121**, 437.
 GREENHOW, J. S., and J. E. HALL, 1960, *Mon. Not. Roy. Astron. Soc.*, **121**, 174.
 HAWKINS, G. S., 1962, *Astron. J.*, **67**, 241.
 JACCHIA, L. G., and F. L. WHIPPLE, 1961, *Smithson. Contrib. Astrophys.*, **4**, 97.
 KASHCHEYEV, B. L., V. N. LEBEDINETS, and M. F. LAGUTIN, 1960, *Meteory* (Sbornik Statei No. 1, issued by Dept. of Basic Radio-Engineering, V. I. Lenin Polytechnic Institute of Kharkov).
 MCCROSKY, R. E., and A. POSEN, 1961, *Smithson. Contrib. Astrophys.*, **4**, 15.
 MCKINLEY, D. W. R., 1961, *Meteor Science and Engineering* (New York: McGraw-Hill).
 NILSSON, C. S., 1964, *Australian J. Phys.*, **17**, 205.
 ÖPIK, E. J., 1951, *Proc. Roy. Irish Acad.*, **54a**, 165.
 PORTER, J. G., 1952, *Comets and Meteor Streams* (London: Chapman and Hall).
 VERNIANI, F., and G. S. HAWKINS, 1964, *Astrophys. J.*, **140**, 1590.
 WEISS, A. A., 1959, *Australian J. Phys.*, **12**, 54.
 WEISS, A. A., and W. G. ELFORD, 1963, *Proc. Inst. Radio Engrs. Aust.*, **24**, 197.
 WHIPPLE, F. L., 1954, *Astron. J.*, **59**, 201.
 —, 1955, *Astrophys. J.*, **121**, 249.

Page intentionally left blank

IV

SCATTERING PROPERTIES

Page intentionally left blank

34. Small Particles in Space

J. MAYO GREENBERG
Rensselaer Polytechnic Institute
Troy, New York

The scattering of radiation by small spherical and nonspherical particles is discussed in relationship to studies of interstellar and interplanetary grains. A survey is made of the theories of the origin of the interstellar particles and their physical interactions with the gas atoms and radiation in space. Theoretical and observational evidence is presented for the various interstellar-grain models. The present state of affairs seems to indicate that the interstellar particles are at least optically similar to the interplanetary particles responsible for producing the zodiacal light. A preliminary investigation is made to show the possible kinds of orientation appropriate to nonspherical interplanetary particles.

THE FORMATION AND GROWTH of interstellar particles have been subjected to considerable analysis for the past 35 years or so. At present there is still no definitive answer to the questions of their origin and chemical composition. Probably the most reliable information concerning the interstellar particles comes from a study of their optical properties. The suggestion that there may be a generic relationship between the interstellar particles and the interplanetary particles has certainly been made and discussed. Whether or not the interplanetary material owes its origin or is related in some way to the interstellar material is an open question, and the final answer may simply be that *some* of the interplanetary material is of interstellar origin or vice versa. In any case, many of the physical processes which involve the two kinds of particles are the same. It may indeed turn out that both kinds of particles have similar optical properties in that they are both dielectric. This does not necessarily imply identical chemical composition.

We shall summarize here a possible theory of dielectric interstellar grains. On the basis of cosmic abundance alone we would expect the interstellar particles to be almost pure hydrogen. However, it can be shown on the basis of grain temperature alone that such a particle would readily evaporate. If we still assume that the grains grow by accretion of "condensable" gas

atoms and subsequent molecule formation induced by ultraviolet photon bombardment, we are led to a grain composition which is largely of molecules of H_2O , CH_3 , and NH_3 with perhaps a trace of iron and its oxides plus other atoms and molecules in roughly their relative cosmic abundance. This sketchy picture might suffice to define what we mean by "ice"-like or "dirty-ice"-like grains whose optical properties are those of a dielectric in the visible with absorption bands in the infrared and the ultraviolet. A more complete account of the various possibilities, including metallic and graphite particles, may be found in a review article (Greenberg, 1963, 1967). In the subsequent section we shall mainly, but not exclusively, concern ourselves with application of the dielectric-grain model to the explanation of the interstellar-dust observations.

In the last two sections we shall give simple preliminary results of some calculations related to both interstellar and interplanetary particles.

INTERSTELLAR EXTINCTION AND POLARIZATION

The extinction and polarization of star light are readily observed characteristics of the interstellar medium. If one observes a star whose spectral-energy distribution is reduced in the blue relative to the red, one is quite sure that the light from this star has undergone attenuation in passing through interstellar space. In the range

of wavelengths between $1 \leq \lambda^{-1} \leq 3 \mu^{-1}$ the extinction or attenuation in wavelengths is roughly linear with inverse wavelength. In figure 1 we show a measured extinction curve which may be taken as relatively standard in the aforementioned range of wavelengths and which also shows the results of observations in the far ultraviolet. Beyond $\lambda^{-1} = 5 \mu^{-1}$ it is not yet

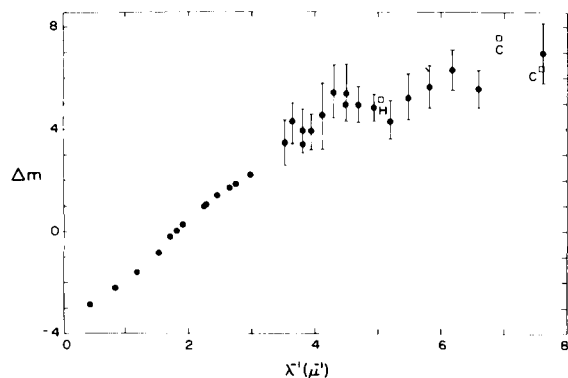


FIGURE 1.—Observed interstellar extinction through the visible to the ultraviolet. Points up to $\lambda^{-1} = 3$ from Bogess and Borgman (1964). Points marked C from Chubb and Byram (1963). Point H from Alexander et al. (1964). Points with error bars from Stecher (1965).

resolved whether the extinction is continuing its increase or not. In figure 2 we show a collection of averaged polarizations by several observers for a large number of stars. Note that the polarization has a maximum somewhere in the visible region of the spectrum, and on the average this appears to be at about $\lambda^{-1} = 1.8 \mu^{-1}$.

The extinction in magnitudes may easily be shown to be directly proportional to the sum of extinction cross sections of all the particles along

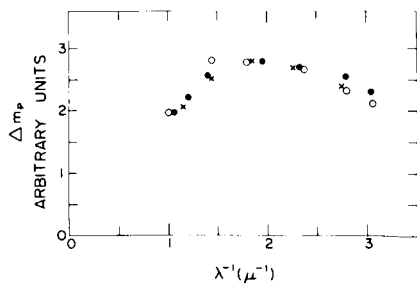


FIGURE 2.—Averages of various observed polarizations as a function of inverse wavelength. Open circles, Gehrels (1960); solid circles, Coyne and Gehrels (1966); crosses, Visvanathan (1965).

the line of sight to the star. Similarly the polarization, in magnitudes, is directly proportional to the maximum difference in the extinction which can be obtained by observing the plane-polarized components along orthogonal directions. If we define the optical depths, τ_1 and τ_2 , where τ_1 is the greater, then the attenuation factors for light polarized along these two directions are, respectively, $\exp(-\tau_1)$ and $\exp(-\tau_2)$. The extinction and polarization are given by

$$\left. \begin{aligned} \Delta m &= \frac{1.086}{2} (\tau_1 + \tau_2) \\ \Delta m_p &= 1.086 (\tau_1 - \tau_2) \end{aligned} \right\} \quad (1)$$

where the expression for Δm is actually an approximate one based on the assumption (generally valid) that $(\tau_1 - \tau_2)/(\tau_1 + \tau_2) \ll 1$.

It is obvious that the interstellar particles must be both nonspherical and preferentially oriented in order to produce polarization via extinction. It is generally believed that the orientation mechanism is magnetic. However, the magnetic fields in interstellar space are at most of the order of $B = 10^{-5}$ gauss and because the grains are continually subjected to collisions by the gas atoms at a temperature of about 100° K, the degree of orientation treated as in thermodynamic equilibrium would be exceedingly minute.

However, the orientation is actually produced by a magnetic relaxation phenomenon (Davis and Greenstein, 1951), and, when a steady-state distribution is considered (Jones and Spitzer, 1967), it is possible to have a degree of orientation consistent with observations (Greenberg, 1966). A qualitative description of the type of orientation produced by magnetic relaxation is that nonspherical particles tend to spin about their short axes which in turn tend to line up with the direction of the magnetic field. Thus a cigar-shaped particle perfectly oriented by the Davis-Greenstein mechanism would spin so that its long axis lies in a plane whose normal is along the magnetic field. Lesser orientation implies wobble of the rotation axis.

If the interstellar grains are dielectric in character, then their sizes must be of the order of the wavelength. The only nonspherical particles for which complete scattering data for

all sizes may be obtained are infinite cylinders. In figure 3 we present an example of calculations of the total cross sections of cylinders which are

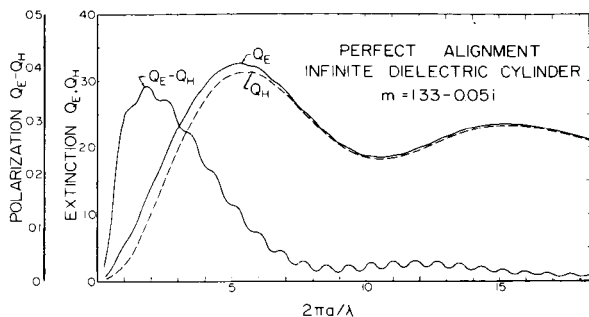


FIGURE 3.—Calculated extinction efficiencies for dielectric ($m = 1.33 - 0.05i$) cylinders oriented normal to incident radiation: Q_E for E parallel axis, Q_H for H parallel axis.

lined up with their axes normal to the direction of propagation of the radiation. The extinction efficiency is defined as the cross section per unit length divided by the cylinder diameter. The indices E and H refer to the cases in which the

radiation is polarized along and transverse to the cylinder axis. We note that if the interstellar grains were cylinders all of one size and perfectly aligned normal to the line of sight (like a picket fence), then the optical depths of equations (1) would be simply given (for unit-length cylinders) by $\tau_1 = N2aQ_E$ and $\tau_2 = N2aQ_H$ where N is the number of particles per unit area along the line of sight and a is the cylinder radius. With this grossly oversimplified model we get a fair simultaneous representation of both the observed extinction and polarization if we chose a cylinder size given by $a = (2\pi)^{-1}$ microns; i.e., $\frac{2\pi a}{\lambda} = 2$

corresponds approximately to $\lambda^{-1} = 2$ (actually 1.8) if we use the peak of the polarization as is shown in figure 2. The extinction (which follows the sum, $Q_E + Q_H$) for such a particle size would appear not to rise beyond $\lambda^{-1} \approx 5\mu^{-1}$.

It should be clearly realized that we are making only optical models of interstellar grains and that the use of infinite cylinders is dictated by the

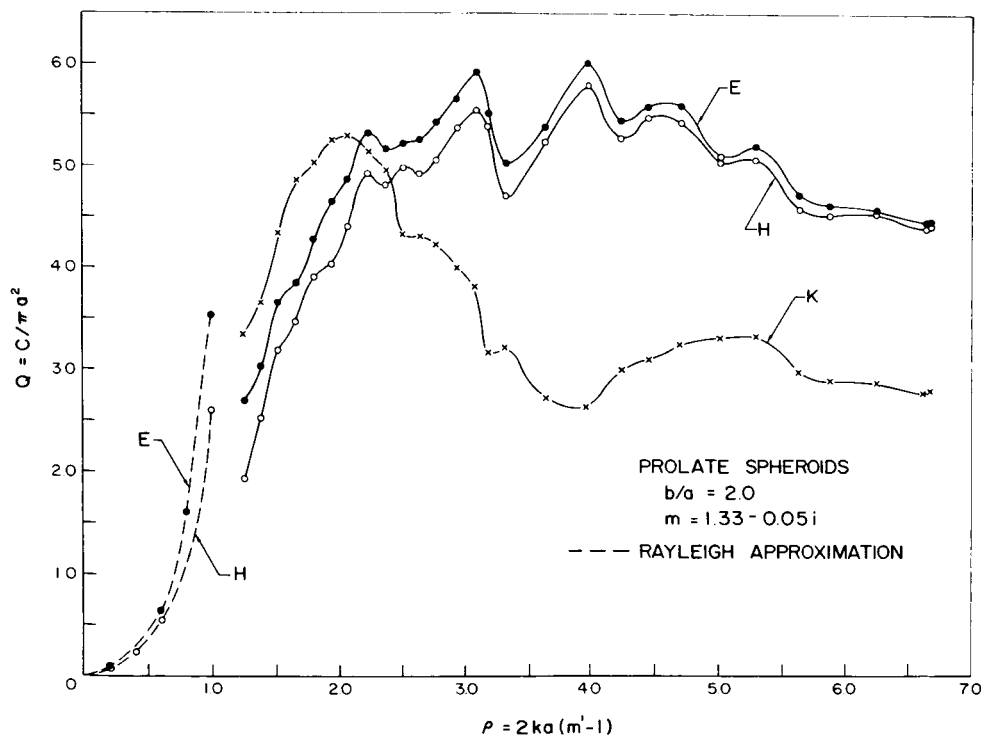


FIGURE 4.—Experimental extinction efficiencies for three orthogonal orientations of prolate spheroids. Elongation, $b/a = 2$, index of refraction, $m = 1.33 - 0.05i$. E , H , and k refer, respectively, to particle axis parallel to electric, magnetic, and propagation vectors of incident radiation. Calculated values of Q_E and $Q_H (= Q_k)$ are shown as broken curves for small values of ka .

limited availability of computational procedures for arbitrary nonspherical particles. Most likely the actual grains do not possess such a high symmetry and probably also have irregular surfaces which might introduce significant modifications in their optical properties.

At present it seems that the only way to obtain scattering information on irregular (by design) particles is by a microwave analog method. Most of the work we have done has been on total cross sections although the angular distributions are certainly attainable with the present equipment. Just as a demonstration of the fact that detailed scattering data are available and also that the infinite cylinders are not qualitatively different from finite particles, we present some samples of experimental results for prolate spheroids in figures 4 to 6. The results for three orthogonal particle orientations relative to an incident linear

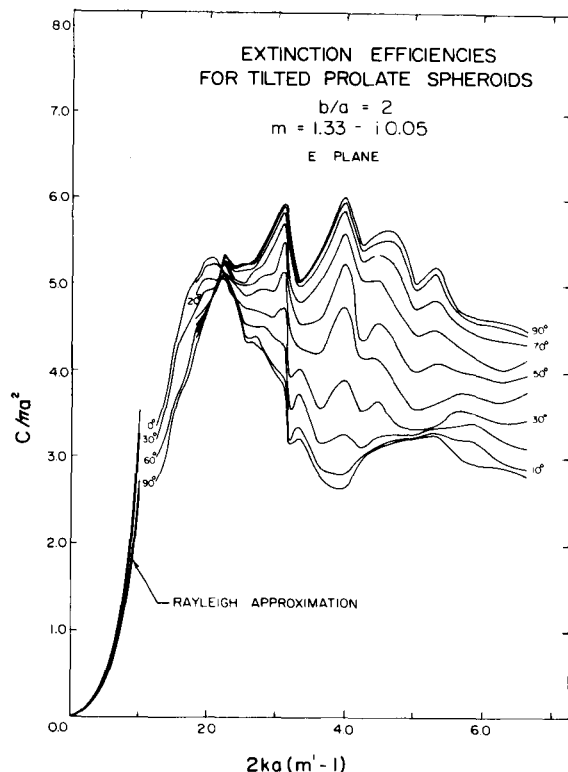


FIGURE 5.—Experimental extinction efficiencies for prolate spheroids obliquely oriented in plane containing particle axis and electric vector of incident radiation. The 90° curve corresponds to Q_E and the 0° curve to Q_k in figure 4. Calculated values according to Rayleigh approximation are shown for small values of ka .

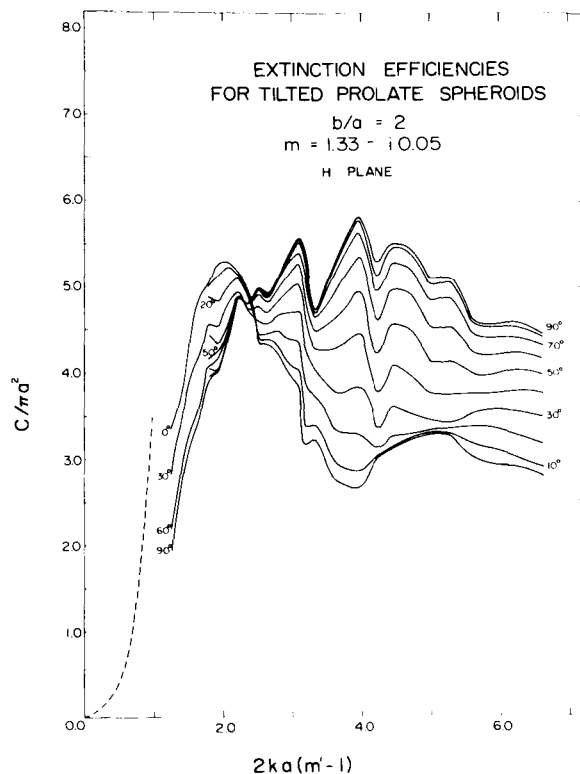


FIGURE 6.—Experimental extinction efficiencies for prolate spheroids obliquely oriented in plane containing particle axis and magnetic vector of incident radiation. The 90° curve corresponds to Q_H and the 0° curve to Q_k in figure 4. Calculated values for small values of ka are shown as dashed curve.

polarized radiation field are shown in figure 4. Figures 5 and 6 demonstrate the variations with cross section as the particle axis is rotated in the k, E and k, H plane, respectively.

Detailed calculations based on the measurements of finite elongated or flattened particles have not yet been made. However, the infinite cylinder has been subjected to very detailed analysis with consideration of particle size distributions, variation of refractive index with wavelength, and varying degrees of orientation. Even effects of varying elongation have been simulated. The details have been published elsewhere (Greenberg, 1967) and are beyond the scope of this limited summary report.

ANGULAR-SCATTERING PROPERTIES OF INTERSTELLAR GRAINS

From a purely optical point of view, the studies (both theoretical and observational) of reflection

nebulae and the diffuse galactic light are most closely related to zodiacal-light investigations.

As an example we present an outline of some calculations made of models of reflection nebulae and a comparison with some observational results. In figure 7 is shown a star and nebula configuration which served as the basis of the theoretical calculations. The star light penetrates the nebula and the radiation which reaches

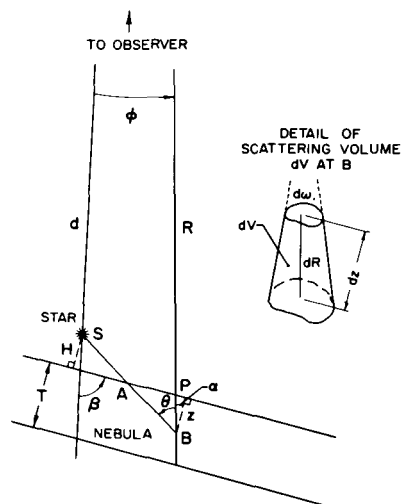


FIGURE 7.—Geometrical configuration of a plane-parallel model of a reflection nebula. Case pictured is that in which star is between observer and front surface of nebula. Perpendicular distance between star and nebula is H , nebular thickness is T , distance to star is d , variable distance to a nebular volume element dV is R , nebular-tilt angle is β , scattering angle for nebular particles is $\Theta = \pi - \theta$, and observation or telescope offset angle is ϕ . Solid angle subtended by telescope is $d\omega$.

the observer is that which is scattered by particles within the nebula which are along the lines of sight defined by line PB in the diagram. These scattering contributions are given by (Greenberg and Roark, 1967)

$$I_N(\phi, \lambda) = I_s(\lambda) \frac{\gamma^2}{4k^2} \sec \alpha \, d\omega \times \int_0^T \int_{a_1}^{a_2} \frac{1}{r^2} F(\Theta, \lambda, a) n(a) \, da \, dz \exp[-\kappa(\lambda)(L_s + L_N)] \quad (2)$$

where $F(\Theta, \lambda, a)$ is the angular-scattering factor as defined in the notation of van de Hulst (1957) by $F(\Theta) = \frac{1}{2}[i_1(\Theta) + i_2(\Theta)]$, where Θ is the angle

between incident and scattered radiation and i_1 and i_2 correspond to radiation polarized within and perpendicular to the scattering plane, and I_N is the nebular light intensity, I_s is surface light intensity of the star, γ is stellar radius, r is distance from the star to the scattering element of volume dV , $n(a) \, da$ is number of grains per unit volume of size a in da , and $\kappa(\lambda)$ is extinction per unit length within the nebula.

The intensity given by equation (2) is for monochromatic light at wavelength λ . In practice one generally, or at least often, is required for light-gathering purposes to use a finite bandwidth. The observed and calculated results shown in figure 8 are for the B and V colors as given by the B and V filter in the UBV system.

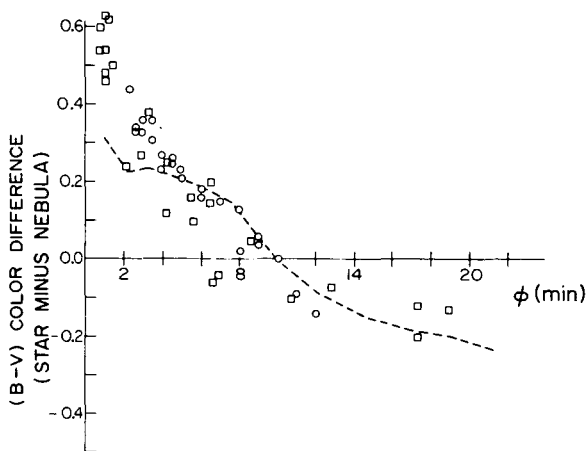


FIGURE 8.—Observed $B-V$ color differences in Merope nebula. Circles from Greenberg and Roark (1967), squares from Hall and Elvius (1965). Broken line represents computed color difference for $\beta = 90^\circ$, $T = 1.0$ pc. Star in front of nebula and dielectric nebular grains distributed according to $n(a) = \exp[-5(a/0.6)^3]$ with $\kappa(5540 \text{ Å}) = 1.2 \text{ mag/pc}$.

We show the comparison between the observed color difference of the star Merope and its associated nebulosity with a calculated color difference for a particular nebular model. These color differences are plotted for varying telescope offset angles (viewing angle relative to the star). The agreement appears to be close enough for one to infer that the theoretical nebular parameters in the undoubtedly oversimplified model are qualitatively correct. One of these parameters, $\kappa(\lambda)$, defines the grain density within the nebula. With the assumption of dielectric (dirty-

ice) grains and a value of $\kappa(5540\text{\AA}) = 1.2 \text{ mag/pc}$, one finds that the mass density in Merope is about 10^{-23} gm/cm^3 . This mass density is within a factor of 10 of the density which has been suggested for the small interplanetary particles producing the zodiacal light. It is not suggested here that interstellar grains are the main source of interplanetary particles. It is, however, to be noted that if we happen to be passing through a cloud with such a high grain density as Merope, some of these could well contribute to scattering of light from the Sun.

PHYSICAL INTERACTIONS OF INTERSTELLAR GRAINS

The interstellar grains are undoubtedly subject in a general way to the same physical interactions as the interplanetary particles. Actually we have much more direct information about the events in our solar system but the extension to the interplanetary particles is not too great. The electromagnetic radiation impinging on a grain produces elevated grain temperatures and radiation-pressure forces. The atoms and electrons impinging on a grain may cause sputtering of the grain material, produce charges on the grains, and, if the atoms are streaming, may produce a degree of grain orientation if the grains are elongated or flat.

The basic formulation of some of these problems may be found elsewhere in this symposium as well as in a review article (Greenberg, 1967).

We will here briefly illustrate some examples of calculational results and procedures pertaining to radiation effects in a form which we believe will offer some convenience in usefulness.

Assuming that the grain reaches temperature equilibrium by balancing the radiation absorbed with the radiation emitted, one may write (for spheres)

$$\int_0^\infty C_{\text{abs}}(a, \lambda) R(\lambda) d\lambda = \int_0^\infty C_{\text{abs}}(a, \lambda) B(\lambda, T_g) d\lambda \quad (3)$$

where $C_{\text{abs}}(a, \lambda)$ is the absorption cross section of a grain of radius a at wavelength λ , $R(\lambda)$ is average radiation field incident on the grain (average over particle orientation), $B(\lambda, T_g)$ is the Planck blackbody radiation at temperature T_g , and T_g is the grain temperature.

In figure 9 we present the absorption (or emission) curves for a spherical blackbody of radius $a = 0.5\mu$ (the upper straight-line curve) and for a "dirty-ice" sphere of the same radius whose complex index of refraction is as shown in figure 10. The lower curve in figure 9 is obtained by numerical integration of the Mie theory absorption cross sections for the wavelengths within the Planck blackbody distribution $B(\lambda, T)$ at the appropriate temperatures. The use of these curves in obtaining grain temperatures when the grain is subject to a blackbody radiation field at temperature, T_R , and dilution factor, W , is shown by the vertical and horizontal lines. Thus a grain in a 4000° K field diluted by a factor

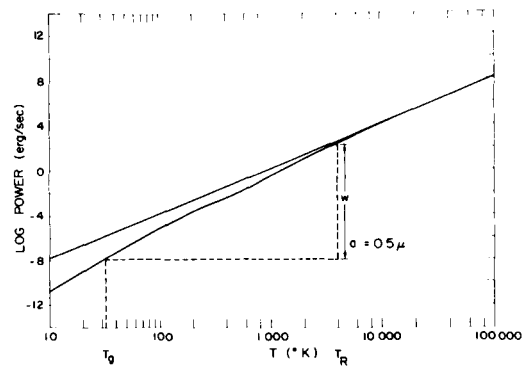


FIGURE 9.—Energy absorbed or emitted (curved line) by a "dirty-ice" grain of $0.5\text{-}\mu$ radius. Straight line corresponds to perfect blackbody law (T^4). Dotted lines indicate procedure for calculating temperature of grain (T_g) subjected to a blackbody radiation field at temperature $T_R = 4000^\circ \text{ K}$ diluted by a factor $W = 10^{-8}$.

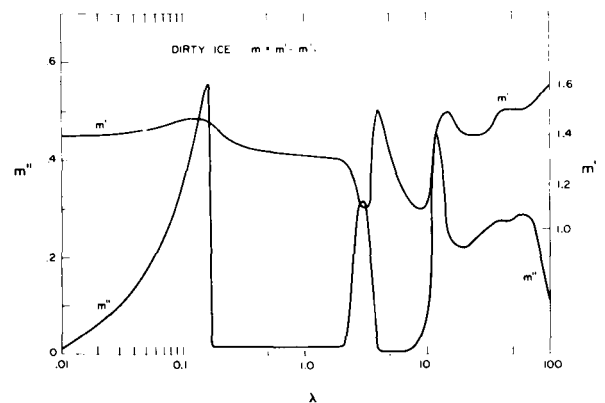


FIGURE 10.—"Dirty-ice" complex refractive indices used in computation of absorption (fig. 9) and scattering (fig. 11) of spherical grains.

$W=10^{-8}$ would arrive at a temperature $T_g=32^\circ\text{K}$.

In figure 11 we present the Mie theory results for the radiation pressure (shown actually as Force/a^3) for "dirty-ice" spheres of radii $a=0.1\mu$, 1.0μ , and 10.0μ . Comparison is made with the results for a blackbody shown on a straight line.

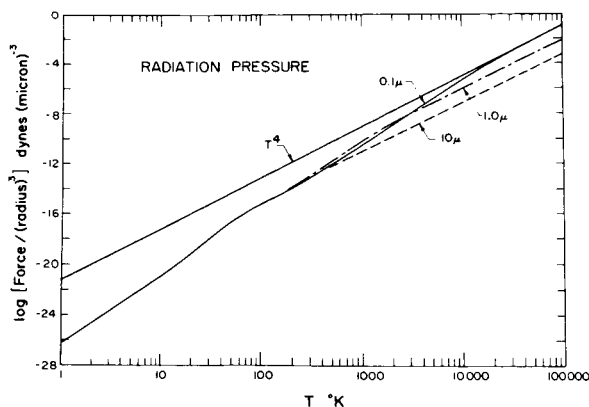


FIGURE 11.—Radiation forces (curved lines) on spherical "dirty-ice" grains of radii 0.1μ , 1.0μ , and 10.0μ . Straight line labeled T^4 is force on a blackbody.

SCATTERING BY SMALL NONSPHERICAL PARTICLES

The scattering by a distribution of nonspherical particles may, for random orientation, be represented fairly well by some appropriate distribution of spherical particles (Donn and Powell, 1961). This is certainly not true for selectively oriented particles and work is in progress at Rensselaer on the effects of selectively oriented cylinders on the angular-scattering distributions and particularly the polarization of reflection nebulae.

For very small particles—small enough to satisfy the Rayleigh approximation—it turns out that random orientation of ellipsoids is equivalent to single-size sphere scattering with however the condition that the total particle volume (or number) is different.

We omit the derivation of the following result which is the ratio of the total scattering by randomly oriented ellipsoids to the total scattering by a sphere of equal volume:

$$\frac{\langle C \rangle_{\text{el.}}}{C_{\text{sp}}} = \frac{[(m^2-1)L_1+1]^{-2} + [(m^2-1)L_2+1]^{-2} + [(m^2-1)L_3+1]^{-2}}{27(m^2+2)^{-2}} \quad (4)$$

where the quantities L_1 , L_2 , and L_3 are defined in van de Hulst's book, and where m is the index of refraction. If the ellipsoids are axially symmetric and very elongated (rods) or very flat (disks), equation (4) becomes respectively

$$\left. \begin{aligned} \frac{\langle C \rangle_{\text{rod}}}{C_{\text{sp}}} &= \frac{(m^2+1)^2+8}{(m^2+1)^2} \frac{(m^2+2)^2}{27} \\ \frac{\langle C \rangle_{\text{disk}}}{C_{\text{sp}}} &= \frac{2m^4+1}{m^4} \frac{(m^2+2)^2}{27} \end{aligned} \right\} \quad (5)$$

In the limit $m \rightarrow 1$ these ratios approach unity. However, for $m=2$ the rods are 1.8 times as efficient and the disks are 2.7 times as efficient as spheres per unit volume.

The ratio of area to volume for very elongated particles and for very flat particles approaches zero so that for *large particles* the volume-scattering efficiency in these extremes is infinitely greater than for spheres. The reason for this is that the cross sections for random orientation are proportional in all cases to the total surface area—a result which is readily proven in the geometrical optics limit.

ORIENTATION OF NONSPHERICAL PARTICLES

In interstellar space the most generally accepted mechanism for orientation of small particles is that produced by magnetic relaxation (Davis and Greenstein, 1951). The refinements and modifications by Cugnon (1963) and Jones and Spitzer (1967) on the theory of this orientation process have been applied to the problem of interstellar polarization (Greenberg, 1966, 1967).

While other processes leading to orientation of interstellar particles by gas streaming motion have been proposed (Gold, 1952), there has generally seemed to be ample evidence to preclude them on either observational or theoretical grounds. The situation in interplanetary space is, in this respect, quite different. The streaming of solar particles (solar wind) is a well-established phenomenon and it will be shown to produce at least some degree of particle orientation. A full treatment of this problem is not given here. We will, however, show by an analytical example

how the solar wind may orient elongated particles. A limited analysis will also be given of the additional effect of the Davis-Greenstein mechanism.

Consider the elongated grain as shown in figure 12. Its length is $2a$ and width is $2b$. Let a stream of particles be incident at an angle, Θ , with respect to the long axis of the grain. Let the number density of the streaming particles be N , their mass m , and their velocity v . If we consider

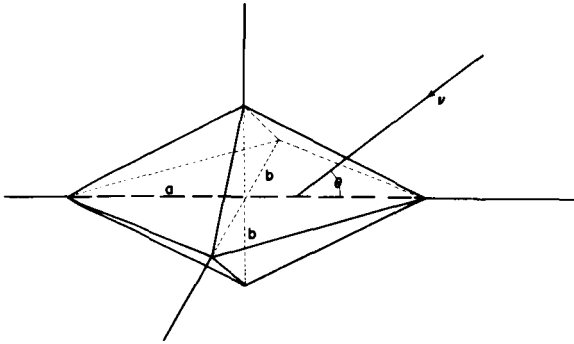


FIGURE 12.—Diagram of a “diamond”-shaped grain particle being bombarded by particles with velocity, v , making an angle, θ , with respect to long axis of grain.

that each particle is specularly reflected off the grains it may be shown that the average torque exerted is given by

$$L = -\frac{4Nmv^2 ab^2}{3(2a^2 + b^2)} (a^2 - b^2) \sin 2\Theta \quad (6)$$

Note that in the calculation of this torque it has been assumed that the incident particles act like a continuous stream whereas, as we shall show, each incident particle may impart enough angular momentum to the grain to set it into rather violent motion.

The dependence of this torque (eq. (6)) on the angle between the grain axis and the incident particle current shows that the grain tends to line up with its axis normal to the streaming motion. If each collision were to produce a sufficiently small rotation of the grain, one could properly average the effects and show that the result (eq. (6)) leads to a distribution of grain axis “tending” to lie in a plane whose normal is along the direction of streaming motion.

If, on the other hand, the particle collisions are such that the overall effect cannot be treated

as a continuous phenomenon, the kind (or degree) of orientation is quite different. There is still a symmetry axis for the orientation, namely, the particle-current direction. All grain-rotation axes in the plane normal to this vector are equivalent. The grains may then be visualized as spinning about their short axes all of which lie in a plane. Although this is not a high degree of orientation, it is certainly significantly different from random orientation.

The solar magnetic field would produce a torque via the Davis-Greenstein mechanism tending to make the grains rotate about an axis perpendicular to the field. Thus, within the plane-of-rotation axes defined above, there is a *further* reduction in the degree of randomness.

An estimate of the criterion of stream continuity with respect to grain orientation is readily obtained. Let the angular motion of the grain be given by equipartition of energy as in thermodynamic equilibrium with a gas whose temperature corresponds to the kinetic energy of the solar wind particles. A lower limit on the particle size for which stream continuity may be assumed is that for which the angle of grain rotation is small in the time between particle impacts. The moment of inertia is approximately given by $I \approx 4ab^4$ if the grain has elongation $\frac{a}{b} = 2$ and a mass density $\rho = 1$ gm/cm³. Let the solar wind be represented qualitatively by $N = 3$ cm⁻³ and $v = 300$ km/sec $= 3 \times 10^7$ cm/sec. The time between impacts is given by $T = (NvA)^{-1}$ where A is grain area. The angle of rotation between proton impacts is then

$$\Delta\Theta = \omega T = m^{1/2}(2b)^{-9/2}$$

For $b = 10\mu$, $\Delta\Theta \approx 1$ radian. Therefore it appears that 10μ is at least the minimum particle dimension for which equation (6) applies.

The preceding argument leads perhaps to a too severe limitation on the range of validity of equation (6). A less fundamental validity argument which, however, is physically reasonable is based on consideration of grain rotation induced by a single proton collision. If we let the angular momentum imparted by a single collision be given by $mva/2$ and equate this to $I\omega$, the rotation angle is given by $\Delta\Theta = m(64Nb^6)^{-1}$. With this relation-

ship $\Delta\Theta \approx 1$ for $b \approx 0.4\mu$. This is undoubtedly too small but may indicate that the lower limit of $b = 10\mu$ obtained is too large.

The grain sizes appropriate to the different kinds of orientation seem to span a range of particle sizes over which the optical properties vary considerably. Therefore the preceding analysis certainly must be done more carefully before definite conclusions can be drawn.

What we have done here is very preliminary but it does indicate a possibility that the properties of the scattered light of the zodiacal-light

particles may be modified by orientation effects produced by the solar wind and that variation in the solar wind may conceivably produce variations in the zodiacal light via changing orientation effects.

ACKNOWLEDGMENTS

The author would like to express his appreciation to Dr. R. M. Lichtenstein for a clarifying discussion. This work has been supported in part by grants from the National Aeronautics and Space Administration and the National Science Foundation.

REFERENCES

- BOGGESE, A., and J. BORGMAN, 1964, *Astrophys. J.*, **140**, 1636.
 COYNE, G., and T. GEHRELS, 1966, *Astron. J.*, **71**, 355.
 CUGNON, P., 1963, *Bull. Soc. R. Sci. Liège*, **32**, 228.
 DAVIS, L., Jr., and J. L. GREENSTEIN, 1951, *Astrophys. J.*, **114**, 206.
 DONN, B., and R. S. POWELL, 1961, in *ICES Electromagnetic Scattering* (M. Kerker, ed.), 151 (New York: Pergamon Press).
 GEHRELS, T., 1960, *Astron. J.*, **65**, 470.
 GREENBERG, J. M., 1963, in *Annual Review of Astronomy and Astrophysics, Volume 1* (L. Goldberg, ed.), 267 (Palo Alto: Annual Reviews, Inc.).
 —, 1966, *Astron. J.*, **71**, 856.
 —, 1967, in *Stars and Stellar Systems*, ch. 6, vol. 7 (G. P. Kuiper and B. M. Middlehurst, eds.) (University of Chicago Press).
 GREENBERG, J. M., and T. P. ROARK, 1967, *Astrophys. J.*, **147**, 917.
 JONES, R. V., and L. SPITZER, Jr., 1967, *Astrophys. J.*, **147**, 943.
 LIND, A. C., R. T. WANG, and J. M. GREENBERG, 1966, *Applied Optics*, **4**, 1555.
 STECHER, T. P., 1965, *Astrophys. J.*, **142**, 1683.
 VAN DE HULST, H. C., 1957, *Light Scattering by Small Particles* (New York: J. Wiley and Sons).
 VISVANATHAN, S., 1965, unpublished thesis, Mt. Stromlo Observatory.

Page intentionally left blank

35. Analysis of All Available Zodiacal-Light Observations

R. S. POWELL, P. E. WOODSON III, M. A. ALEXANDER,
R. R. CIRCLE, A. G. KONHEIM, D. C. VOGEL,
AND T. W. MCELFRESH
Melpar, Inc.
Falls Church, Virginia

A model of the interplanetary-dust ensemble is derived which explains many of the inconsistencies in the zodiacal-light observations. It is shown that the number density of particles is nearly independent of distance from the Sun in the region between Mercury and Mars but is possibly zero beyond Mars. Further, it is shown that the size distribution of the interplanetary dust changes slightly with time and distance from the Sun. Finally, it is shown that the ensemble consists of particles with radii less than 1.1 micron. A few larger particles certainly exist but they do not affect the zodiacal light. The electron density in the region beyond Mercury is arbitrary.

ALL PREVIOUS ANALYSTS of the zodiacal-light observations have made two drastic assumptions concerning the nature of interplanetary dust ensemble. The first assumption is that the size distribution of the interplanetary dust is the same at all points throughout the solar system. The second is that the number density of the particles at a given distance, r , from the Sun can be represented by a monotonic function of r . These assumptions have been necessary in order to simplify the scattering equations which relate the measured brightness and polarization of the zodiacal light to the theoretical functions which describe the optical properties of small particles (Mie, 1908; Born and Wolf, 1964).

Both assumptions are embodied in the mathematical expression for the number density of the interplanetary dust used in the detailed analysis of Blackwell and Ingham's and Weinberg's observations by Giese and Siedentopf (1962a), Giese (1963), and Little et al. (1965). The expression is

$$N(r,a) = N(a_0)(a/a_0)^{-p}(R/r)^v \quad (1)$$

where $N(r,a)$ is the number density of particles with radius a at distance r from the Sun and a_0 , p , and v are constants deduced from the observations. This expression was initially used by Allen (1946) and van de Hulst (1947) to demonstrate the necessity of considering the diffraction component of the light scattered by the dust and it has no fundamental significance.

The model of the interplanetary dust corresponding to equation (1) can be rationalized to fit the models derived from dynamic considerations (see, for example, Southworth, 1964; Harwit, 1963; Wyatt and Whipple, 1950), but any number of more complicated models are possible. For example, the Mariner IV data indicate that the number density may be an oscillating function of r (Alexander et al., 1965). Even more complicated models seem reasonable on the basis of observations supporting the hypothesis of an Earth-centered belt (Divari, 1964). Equation (1) does not account for observed meteor showers nor does it seem reasonable in view of the fact that forces due to radiation pressure and the Poynting-Robertson effect are very sensitive to

particle size (Wyatt and Whipple, 1950; Beard, 1959).

There is a third assumption usually made that the interplanetary dust does not contain a significant number of submicron-size particles. Particles with radii less than 0.1 to 0.8 micron (depending on the absorption coefficient and mass density) are supposedly blown out of the solar system by the Sun's photon and corpuscular radiation. However, as pointed out by Shapiro et al. (1966), Belton (1966), and others, the calculation of the resultant forces on an interplanetary particle is not so simple as some of us pretend. They mention several mechanisms which modify the effects of radiation pressure. Also, there are several possible sources which give a continual supply of submicron particles. For example, the fluffy particles of Hemenway and Soberman (1962) can be pulled toward the Sun by the Poynting-Robertson effect and broken up (Giese, 1963) possibly by charge effects induced as they approach the region of the electron corona or converted to small particles by surface evaporation (Belton, 1966). Fesenkov (1963) alludes to the idea that there exist many asteroid-like bodies orbiting throughout the solar system. These bodies could continually produce particles with radii smaller than those set by radiation pressure. Although the possibility that comets are a source of submicron particles has been questioned (Southworth, 1964), such particles fit the available observations of comet Arend-Roland and Mrkos (Donn et al., 1967).

Another objection to submicron interplanetary dust is based on the argument that such particles are incompatible with the observed color of the F-corona (Elsässer, 1965; Southworth, 1964). However, there is no reason to assume that the size distribution of dust close to the Sun is the same as that in the zodiacal light. (In fact, large particles are continually being "pulled" into smaller and smaller volume around the Sun by the Poynting-Robertson forces. Submicron particles are not.)

Many investigators assume that the zodiacal light would be much bluer than sunlight if the interplanetary ensemble contained large numbers of submicron particles. Tanabe and Huruwata in paper 6 and Karyagina (1961) have shown that

the zodiacal light is bluer than sunlight at elongations of 15° to 40° and 40° to 50° , respectively. As we will show later, a submicron particle model of the interplanetary dust is compatible with their spectral measurements.

Having cast aspersions on all the usual assumptions used for analysis of the zodiacal-light observations and thereby adding more confusion to an already confusing problem, we now proceed to present a model of the interplanetary dust which is just as arbitrary. We do this for two reasons: first, we want to test the uniqueness of previous analytic fits to the zodiacal-light observations, and second, we want to demonstrate that the apparent disagreement among various observers (as reviewed by Weinberg, 1964a, and Gillett, 1966) may not be as serious as we thought. We shall present a model of the interplanetary dust which fits most of the available observations.

BELT MODEL OF INTERPLANETARY DUST

Let us arbitrarily separate the interplanetary space (in the ecliptic) into a system of belts so that the boundary of each belt coincides with the orbits of the planets as shown in figure 1. Let us assume that the k th belt is populated with particles having any size distribution at all, i.e., we assume that all particle sizes and refractive indices (real and complex) are possible and that the size distribution, number density, and chemical composition of particles in one belt are completely independent of the same quantities in another. We will assume for now that the particles are spherical.

Using such a model, it is possible to deduce the size distribution of particles in each belt from the many single-color observations of the zodiacal light. The inversion is based on the mathematical method of Powell and Donn (unpublished report). Although the necessary inversions of the familiar integral equations (Giese, 1963; van de Hulst, 1947) are accomplished through approximations, the results are as accurate as the Mie theory allows. We point out that the method has been applied to observations of comet Arend-Roland and Mrkos by Donn and Powell (unpublished report) and the results checked according to the exact Mie theory by Remy-Battiau (unpublished report). We found that the particles in both

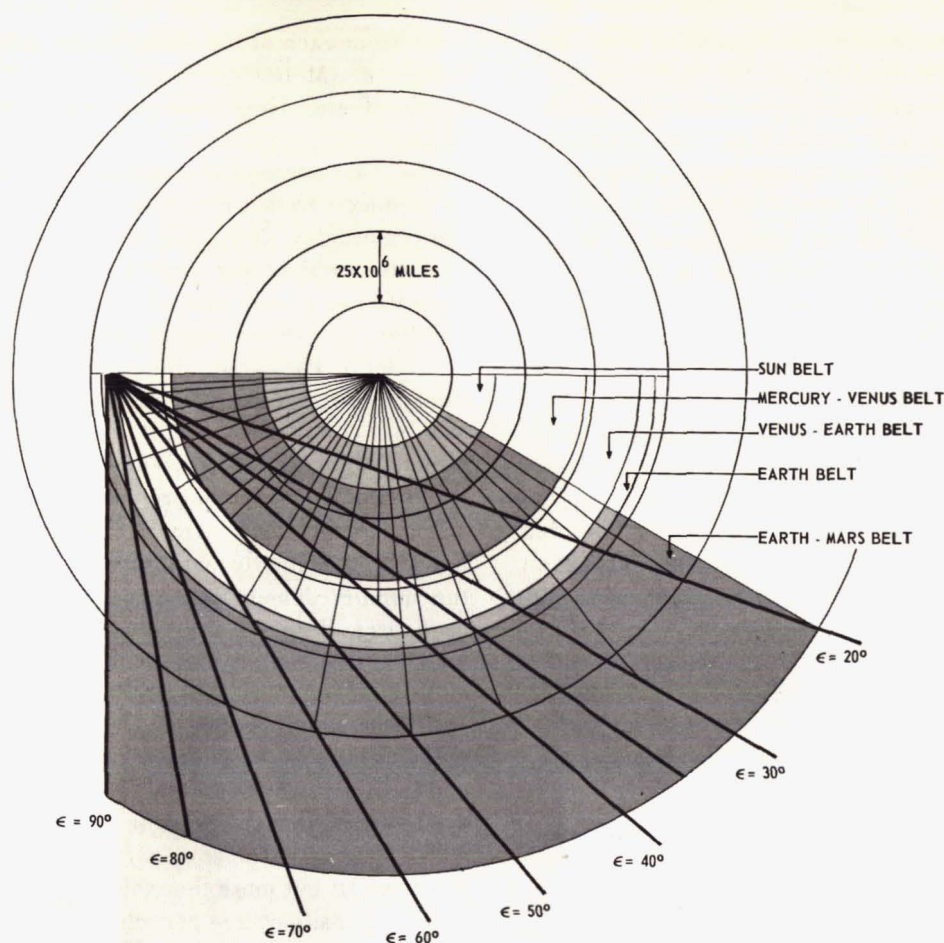


FIGURE 1.—Belt-distribution map. Size distribution of particles in each belt as derived from various zodiacal-light observations are shown in figures 8 to 11.

comets were dielectric—definitely not iron as Liller (1960) suggested. The method has been checked further by reproducing the analytic results of Giese and Siedentopf (1962a).

Our method does not allow a direct fit of the polarization function

$$P = \frac{B_1 - B_2}{B_1 + B_2} \quad (2)$$

as used in the review of observations by Weinberg (1964a). Instead, we use the delta parameter:

$$\Delta = B_1 - B_2 = PB_3 \quad (3)$$

which is the difference between the brightnesses measured with electric vectors perpendicular and parallel to the scattering plane, respectively.

The delta parameter is also the product of the measured polarization, P , and the measured brightness, $B_3 = B_1 + B_2$.

The delta parameter corresponds more closely to the quantities actually measured than does the polarization in the sense that the delta parameter is a combination of two separately measured variables, whereas the polarization is a combination of three. In this regard we point out that the experimental corrections for the measured brightness, B_3 , are radically different than those for the measured delta, $B_1 - B_2$, and that the brightness is an absolute measurement, whereas the delta parameter is relative. These factors may lead to large discrepancies in various observations of the polarization but small discrepancies in various observations of

the delta parameter. For example, overcorrection of the measured brightness, B_3 , leads to a value for the polarization, $(B_1 - B_2)/B_3$, which is too low and vice versa. This correlation might be expected to show up in the observations and it does in a general way. The polarization measured by Blackwell and Ingham and Elsässer is much higher than Weinberg's, but Weinberg's brightness is higher (Weinberg, 1964b). When one corrects the polarization measured by Blackwell and Ingham and Elsässer by the ratio of their brightness to Weinberg's, the large discrepancies disappear. Of course, the correction is not as simple as the preceding discussion indicates. On the other hand, we emphasize that theoretical fits to the delta parameter are probably more realistic than fits to the polarization. A comparison of observations, $\Delta(\epsilon)$, according to various representative observers is shown at the bottom of figure 2(a). The corresponding brightness observations are shown in the left-hand graph of figure 2(b).

DEDUCTIONS FROM OBSERVATIONS USING THE BELT MODEL

The observations of Weinberg (1964b), Blackwell and Ingham (1961), Divari and Asaad (1960), Robley (1962), and Behr and Siedentopf (1953) are shown in figures 3 to 7. The theoretical curves from the belt model are shown superimposed on the observational curves. We have been able to match Weinberg's and Blackwell and Ingham's curves exactly. The observations of Robley and Divari and Asaad can be matched approximately within the experimental error. Behr and Siedentopf's observations cannot be matched precisely unless one assumes that Venus sweeps out particles near its orbit.

The observations shown in figures 3 to 7 and the conclusions drawn therefrom are representative of all other available observations (e.g., Elsässer, 1958; Huruata, 1951; Barbier, 1955; Smith et al., 1965; Beggs et al., 1964; Wolstencroft and Rose, 1967; and Gillett/Ney, 1966). We have not analyzed the data of Peterson (1961) and Dufay (1925). Peterson's data do not extend close enough to the Sun for our purposes and Dufay's measurements were made before there was sufficient knowledge of atmospheric corrections.

The size distribution and refractive indices of the particles in each belt as derived independ-

ently from each of the observations are shown in figure 8 (Mercury-Venus), figure 9 (Venus-Earth), figure 10 (Earth), and figure 11 (Earth-Mars).

The characteristics of the interplanetary dust as deduced from all zodiacal-light observations are remarkably similar. All observations indicate that the radii of the particles lie in the range from 0.08 to 1.5 microns and that the decrease in number density with increasing particle size is very steep. The large differences in the observations can be explained by slight differences in the size and composition of the interplanetary particles. (Of course, there is no way to determine whether or not electrons are present from analysis of single-color observations. Particles with radii less than 0.08 micron scatter like electrons. Thus, the number density of such particles as plotted in figures 8 to 11 may be multiplied by 10^7 to 10^{10} (depending on size) to estimate the equivalent number of electrons.)

In the region between Mercury and Venus (fig. 8), the observations of Weinberg, Blackwell and Ingham, and Divari and Asaad all require the existence of iron particles in addition to dielectrics. Most of these iron particles have radii of less than 1μ but more than 0.08μ . Notice that the number density of iron particles is lower than that of dielectrics and that the iron particle size is larger. Notice also that the observations of Blackwell and Ingham and Behr and Siedentopf require the existence of a large number of very small particles with radii less than 0.1μ —at least a factor of 100 more than required by the other observers. The refractive index of dielectric particles is between $m=1.4$ and $m=1.8$ for all observers.

In the region between Venus and Earth the dielectric particles ($1.4 \leq m \leq 1.8$) have radii $0.08\mu \leq a \leq 0.3\mu$. Behr and Siedentopf, Divari and Asaad, and Robley require a higher proportion of small particles than either Weinberg or Blackwell and Ingham. Weinberg and Blackwell and Ingham require iron particles. Again, these are larger and less numerous than the dielectrics.

All observations also lead to similar conclusions concerning the nature of the dust near Earth's orbit. The particles are all dielectrics

$$(1.4 \leq m \leq 1.8)$$

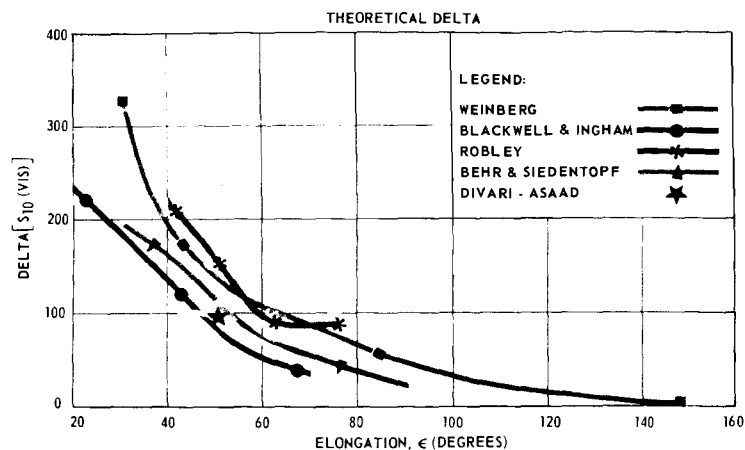
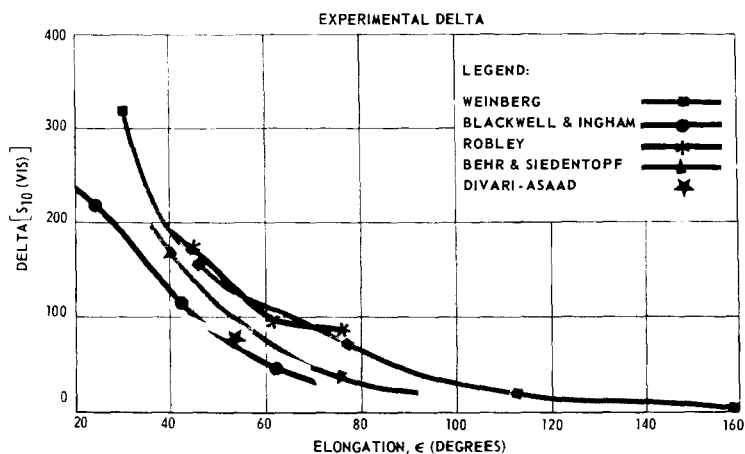
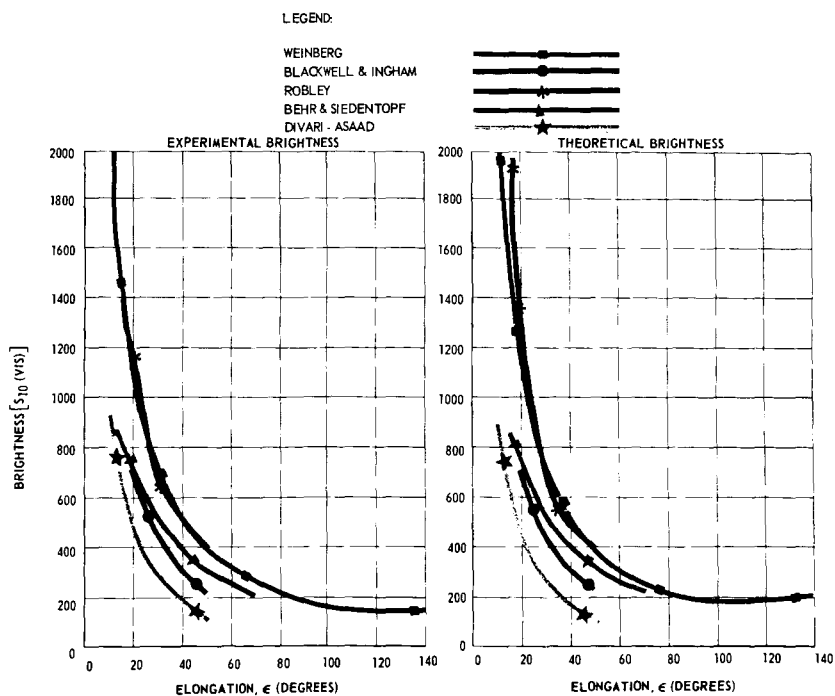


FIGURE 2.—Comparative theoretical and observational plots for various parameters.

(a) $\Delta = B_1 - B_2$ versus elongation ϵ .(b) Brightness B_3 versus elongation ϵ .

(a)



(b)

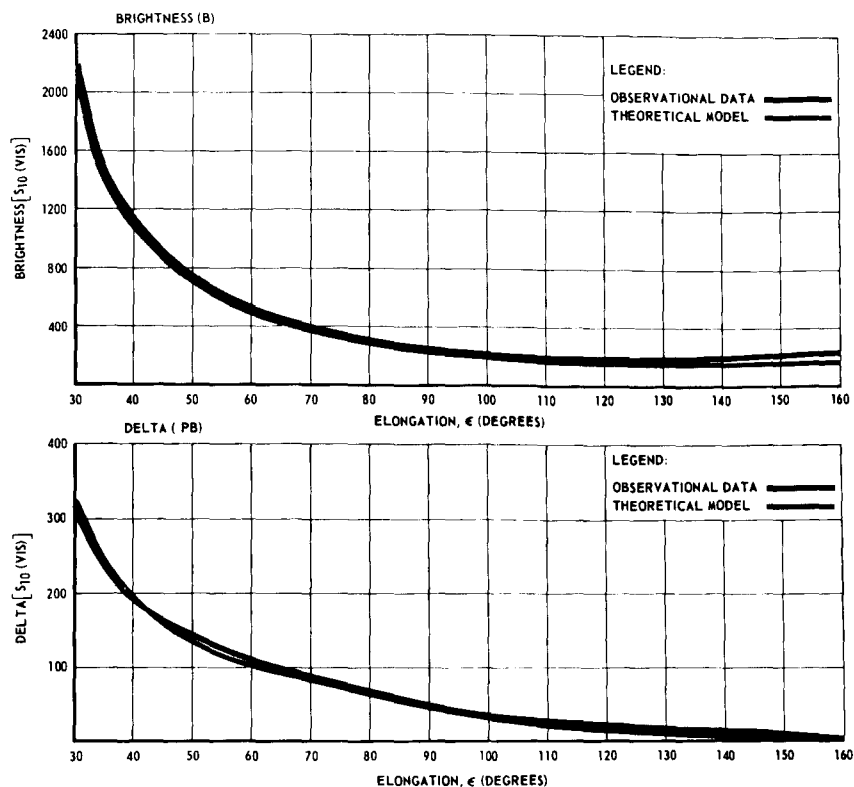


FIGURE 3. — Comparison of observations of Weinberg (1964b) and theoretical model.

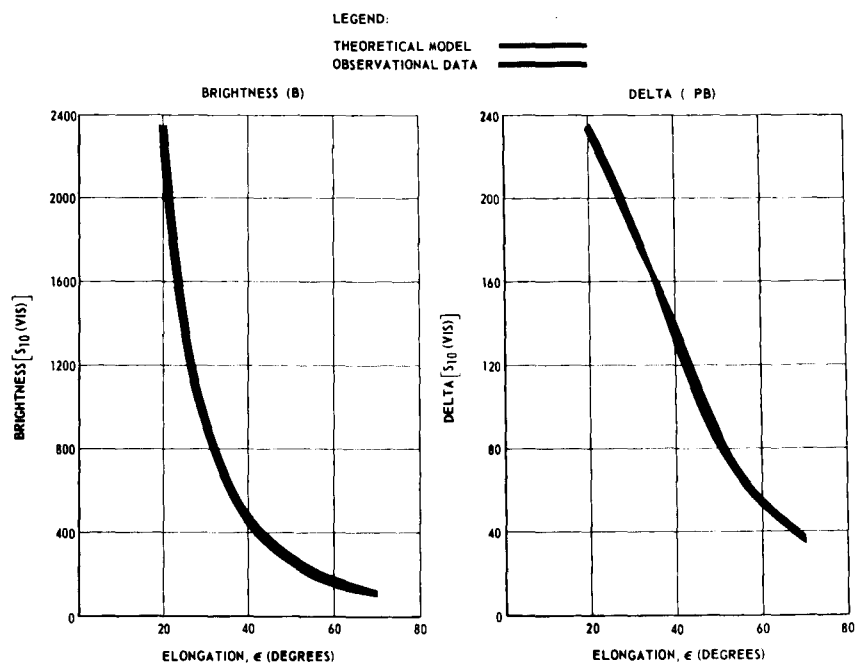


FIGURE 4. — Comparison of observations of Blackwell and Ingham (1961) and theoretical model.

FIGURE 5.—Comparison of observations of Divari and Asaad (1960) and theoretical model.

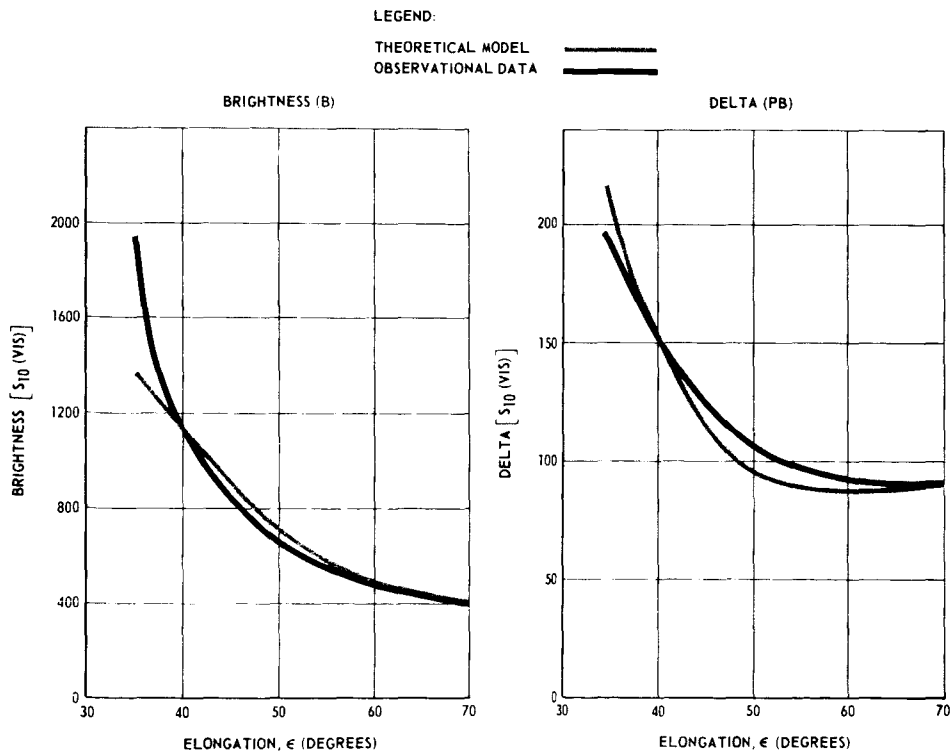
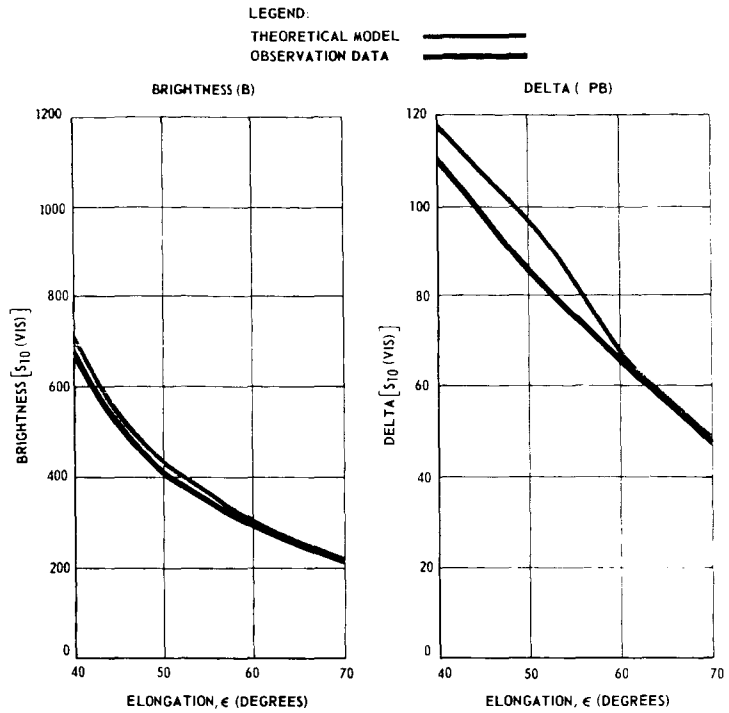


FIGURE 6.—Comparison of observations of Robley (1962) and theoretical model.

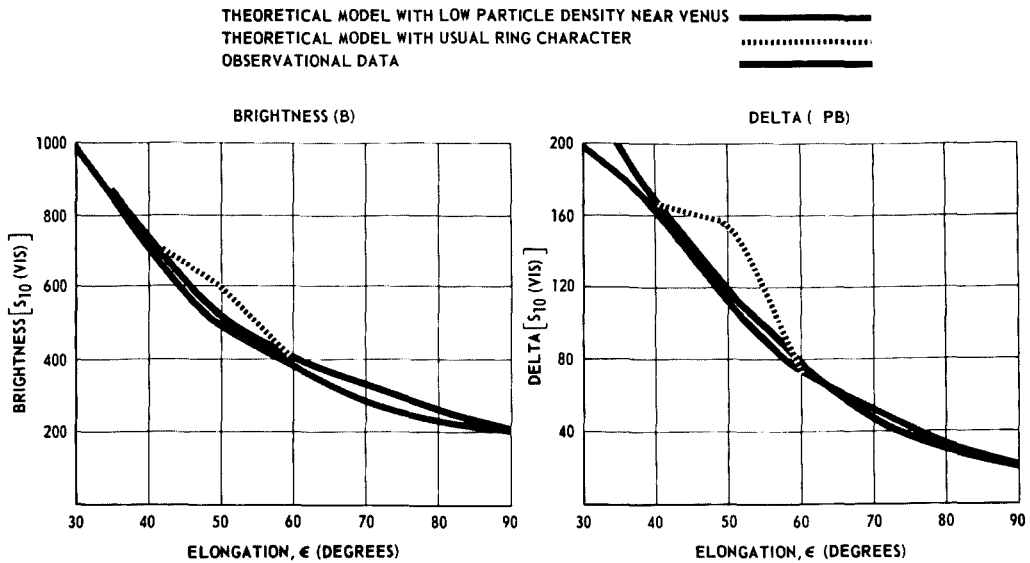


FIGURE 7.—Comparison of observations of Behr and Siedentopf (1952) and theoretical model.

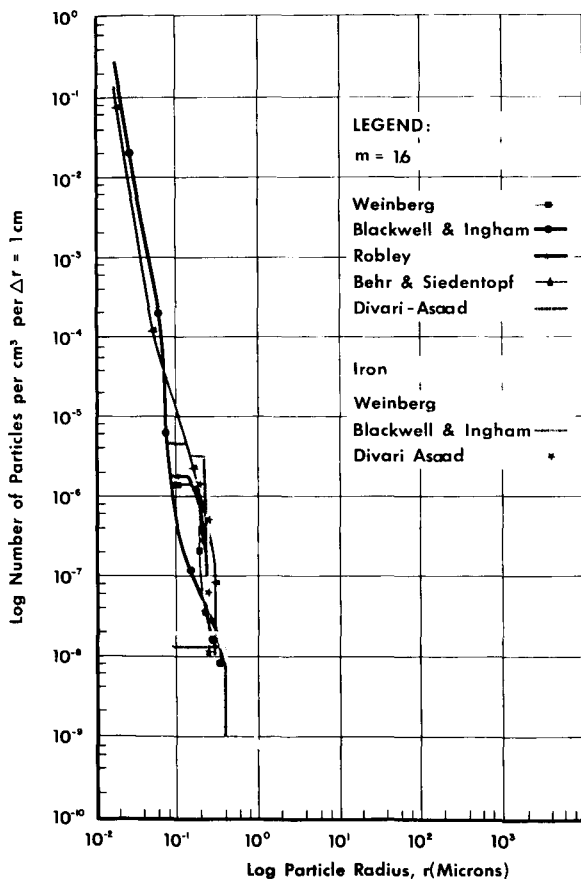


FIGURE 8.—Theoretical model—Mercury-Venus belt.

and very small (0.08μ to 0.2μ in radius). Weinberg's observations require that particles near the Earth's orbit ($0.9 \leq r \leq 1.1$ AU) have a slightly different size distribution than those in the Venus-Earth belt. The slope (number density versus particle size) is steeper than previously estimated. For comparison we present our results with previous estimates in figure 12.

In the region between Earth and Mars (fig. 11) we find again that all particles are dielectric with radii in the range of 0.08μ to 0.6μ . The size distribution which fits Robley's observations has the highest proportion of small particles. The size distributions corresponding to the observations of Weinberg and Blackwell and Ingham require the same narrow range of particle radii,

$$0.1 \leq a \leq 0.2$$

but Weinberg's number density is greater by a factor between 7 and 20.

No particles are required in the space beyond Mars to explain the existing observations. On the other hand, the size and radial distribution of particles beyond Mars may be similar to those interior to Mars, but the number density must be less by at least a factor of 10.

As can be seen by comparing figures 8 to 11, the size distribution is roughly the same through-

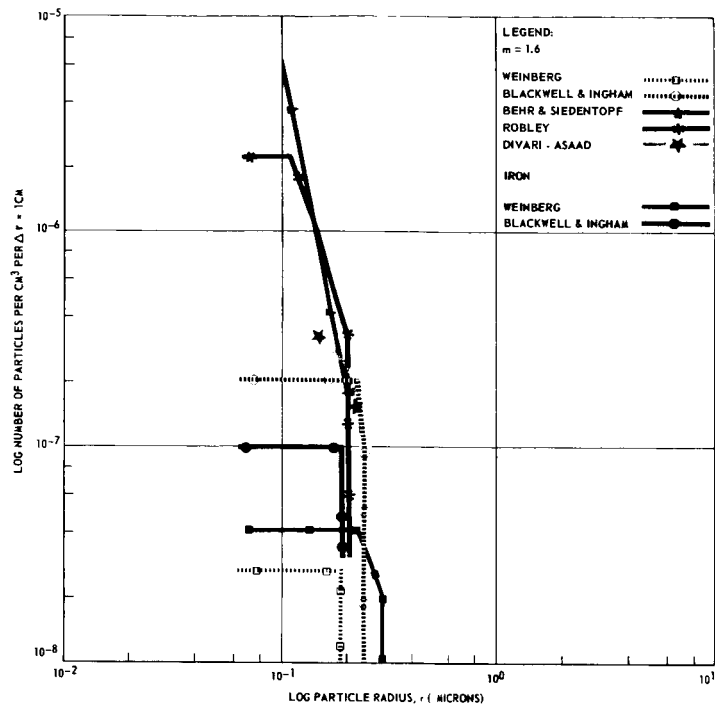


FIGURE 9. — Theoretical model—Venus-Earth belt.

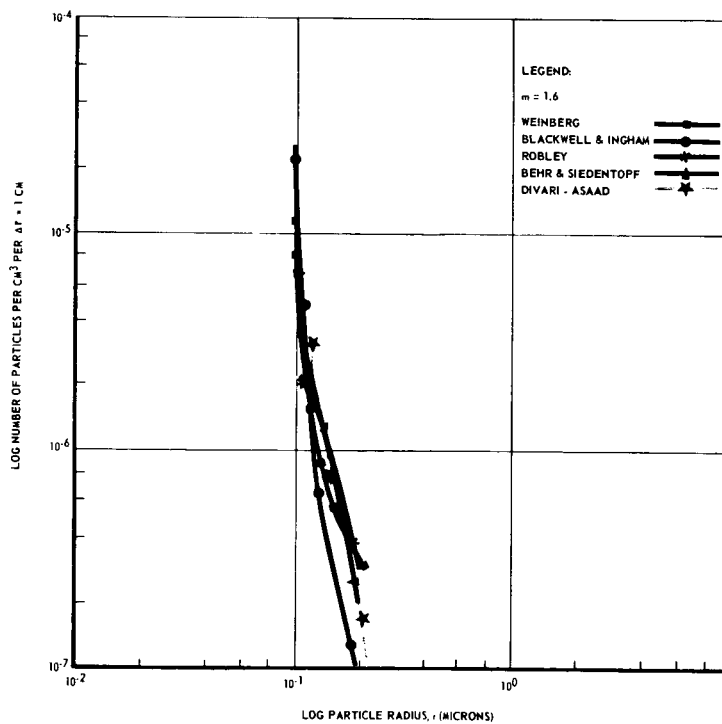


FIGURE 10. — Theoretical model—Earth ring.

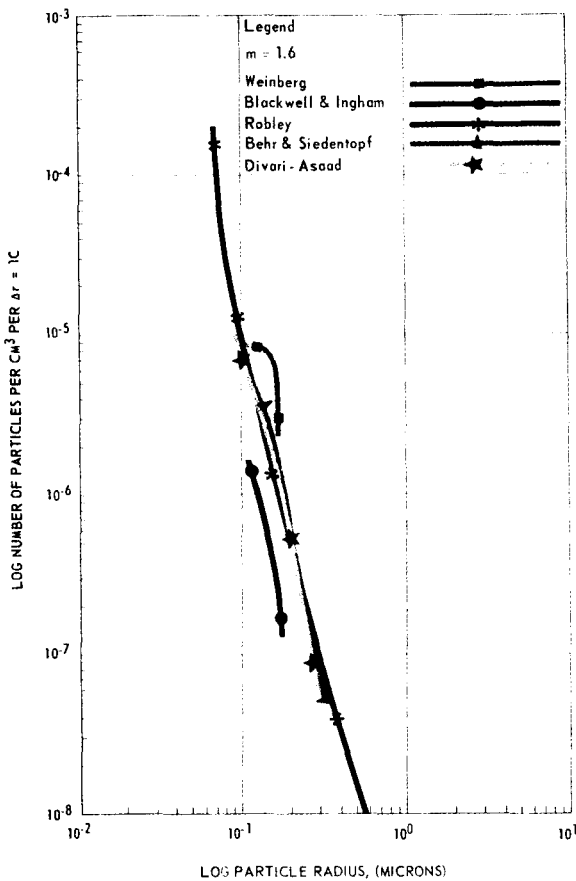


FIGURE 11.—Theoretical model—Earth-Mars belt.

out the region from Mercury to Mars. Furthermore, the number density is nearly independent of distance from the Sun. The accuracy of these two statements can be judged from figure 13 where the size distributions derived from all observations in all belts are superimposed.

COLOR OF ZODIACAL LIGHT AS ESTIMATED FROM BELT MODEL

A unique model of the interplanetary dust can only be derived from "monochromatic" ($\Delta\lambda \leq 50\text{\AA}$), three-color observations of the brightness and polarization at all elongations $30^\circ \leq \epsilon \leq 160^\circ$. Such complete observations are not yet available. The validity of our belt model is, therefore, open to question since it was derived from single-color or wideband measurements. However, Tanabe and Huruwata in paper 6 have measured the absolute brightness of the zodiacal light at elongations $15^\circ \leq \epsilon \leq 40^\circ$ at three wave-

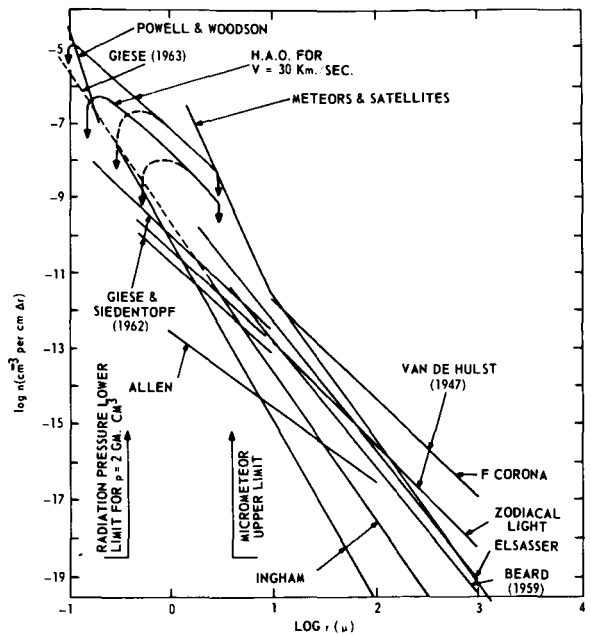


FIGURE 12.—Average size distribution derived from belt model compared with previous estimates.

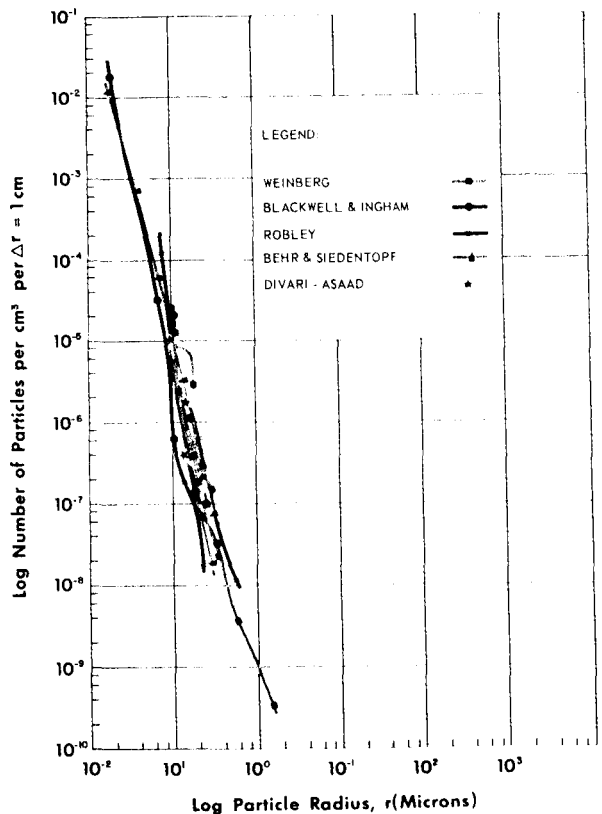


FIGURE 13.—Superposition of all derived size distributions.

lengths (4300Å, 5300Å, 6000Å) and Karyagina (1961) has made relative three-color measurements at $\epsilon = 40^\circ$ to 50° .

Thus, it is possible to test the validity of the belt model in a preliminary manner by comparing the color of the zodiacal light predicted from the belt model with the measurements of Tanabe and Huru-hata and Karyagina at elongations where the single-color observations are in coincidence. In this section we give the results

of such a comparison made by using the size distributions derived from the observations of Weinberg.

According to the belt model, the color of the zodiacal light should appear as shown in figure 14. Note that it is bluish at all elongations—slightly bluer than the average measured by Tanabe and Huru-hata. However, a comparison with their measurements is only valid at $\epsilon = 30^\circ$ where the absolute brightness measured by

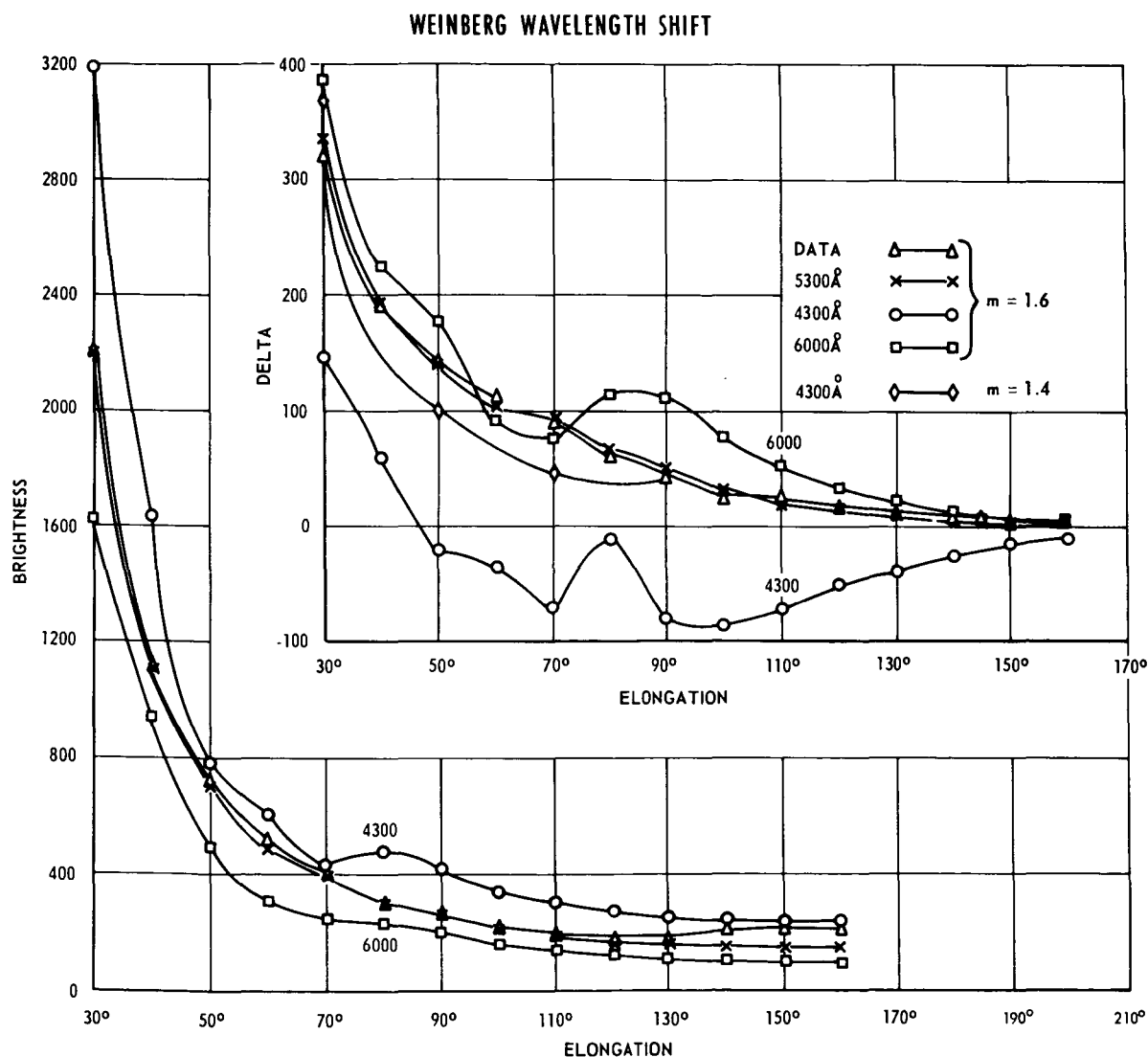


FIGURE 14.—Color of zodiacal light as predicted from belt model (as derived from Weinberg's single-color observations).

Tanabe and Huruata and Weinberg at $\lambda = 5300\text{\AA}$ is the same. At $\epsilon = 30^\circ$ the color as predicted from the belt model can be represented by a color matrix, $Q(30^\circ)$, the elements of which represent the relative brightness at $\lambda = 4300\text{\AA}$ (top), $\lambda = 5300\text{\AA}$ (middle), and $\lambda = 6000\text{\AA}$ (bottom):

$$Q(30^\circ) = \begin{bmatrix} 1.45 \\ 1.00 \\ 0.84 \end{bmatrix} \text{ (Predicted from Weinberg)}$$

Tanabe and Huruata's measurements at $\epsilon = 30^\circ$ can be represented by three such matrices depending on whether one considers the maximum or minimum measured values possible within the constraints of their experimental error.

$$\begin{array}{ccc} \begin{bmatrix} 1.45 \\ 1.00 \\ 0.55 \end{bmatrix} & \begin{bmatrix} 1.15 \\ 1.00 \\ 0.68 \end{bmatrix} & \begin{bmatrix} 0.86 \\ 1.00 \\ 0.91 \end{bmatrix} \\ \text{Maximum blue} & \text{Average} & \text{Minimum blue} \end{array}$$

(Tanabe and Huruata, $\epsilon = 30^\circ$)

At $\epsilon \approx 45^\circ$ the color matrix predicted from the belt model is:

$$Q(45^\circ) = \begin{bmatrix} 1.16 \\ 1.00 \\ 0.75 \end{bmatrix} \text{ (Predicted from Weinberg)}$$

Karyagina's measurements over the interval $40^\circ < \epsilon < 50^\circ$ give:

$$\begin{array}{ccc} \begin{bmatrix} 1.25 \\ 1.00 \\ 0.35 \end{bmatrix} & \begin{bmatrix} 0.91 \\ 1.00 \\ 0.53 \end{bmatrix} & \begin{bmatrix} 0.71 \\ 1.00 \\ 0.75 \end{bmatrix} \\ \text{Maximum blue} & \text{Average} & \text{Minimum blue} \end{array}$$

(Karyagina, $\epsilon \approx 45^\circ$)

Thus, the belt model as derived from Weinberg's observations is compatible with the color measurements of both Tanabe and Huruata and Karyagina and we must tentatively accept the possibility that the zodiacal light is dominated by submicron-size particles. The real test will occur when the polarization is measured at three wavelengths over a wide range of elongations.

If the dielectric particles have a refractive index greater than $m = 1.5$, the polarization at $\lambda = 4300\text{\AA}$ should be negative for $\epsilon > 50^\circ$. If the polarization at $\lambda = 4300\text{\AA}$ turns out to be positive for $\epsilon < 130^\circ$, the average refractive index of the particles must be $m < 1.5$ or the particles must be nonspherical.

NONSPHERICAL PARTICLES

The foregoing analysis is based on the assumption that the interplanetary dust particles are spherical. But particles formed through natural processes such as collision, grinding, explosion, thermal stress, nucleation-condensation, and coagulation are rarely spherical. Consequently, there is some question regarding the accuracy of the deduced size distributions, radial distributions, absolute number density, and refractive index of the interplanetary dust as derived from the belt model. Since the mathematical difficulties involved in solving Maxwell's equations for nonspherical particles are enormous, it is easier to examine the question by comparison with laboratory experiments.

One approach is to measure the scattering from single, nonspherical particles and compare the results with calculations from the Mie theory. Greenberg et al. (1961) and Giese and Siedentopf (1962b) have approached the problem in this manner by using microwave analog techniques. Napper and Ottewill (1963) used optical techniques. Unfortunately, an enormous number of measurements for various sizes, refractive indices, shapes, and orientations are required before we can apply single-particle experiments to the general problem of analyzing the zodiacal light.

Another approach is to measure the scattering from ensembles containing randomly oriented, polydisperse particles. This approach has been used by Richter (1956, 1962, 1966), Hodkinson (1963), Donn and Powell (1962), and Powell et al. (1967), for example, by one of two methods.

The first method is to assume that each nonspherical particle in the measured laboratory-size distribution can be characterized by its volume, its longest dimension, or some combination of geometric parameters. The scattering from spheres with similar dimensions is then calculated and compared with the measured

scattering. Little et al. (1965) used this method to compare Richter's data with the Mie theory. Napper and Ottewill (1963) used the same technique. The discrepancies in the resulting scattering diagrams for nonspheres and spheres are unpredictable. These discrepancies do not indicate that nonspherical particles scatter differently than spheres. They only indicate that spheres and nonspheres cannot be compared on the basis of a linear relationship between their respective geometric properties.

The single-particle measurements show that it is probably impossible to find a single sphere of any size and refractive index which scatters like a single nonsphere of given size and orientation. The resonant peaks in the angular and spectral distribution of the scattered irradiance and polarization, each of which corresponds to the stimulation and interaction of many high-order multipoles, are much too sensitive to asymmetries in the boundary conditions (van de Hulst, 1957).

On the other hand, the scattering from an ensemble containing many nonspheres with different alignments and sizes may average out in such a way that it compares almost exactly with the scattering from some other size distribution of spheres. This has been shown for cubes by Donn and Powell. In their experiments, the scattering was measured from various known size distributions of cubes and fourlings. Most of the particles in these distributions were submicron in size. An equivalent size distribution of spherical particles was then determined by inverting the scattering equations according to the Mie theory. In general, it was rather easy to find an equivalent size distribution of spheres which matched the angular distribution of the scattered irradiance and polarization at one wavelength. The equivalent size distribution of spheres was, in general, different from the measured size distribution of nonspheres. Although these experiments were limited to only a few size distributions and particle shapes, the conclusions are interesting:

(a) Large-volume shapes, such as cubes, scatter like spheres (fig. 15). The equivalent sphere size distributions derived by inverting the measured angular irradiance and polariza-

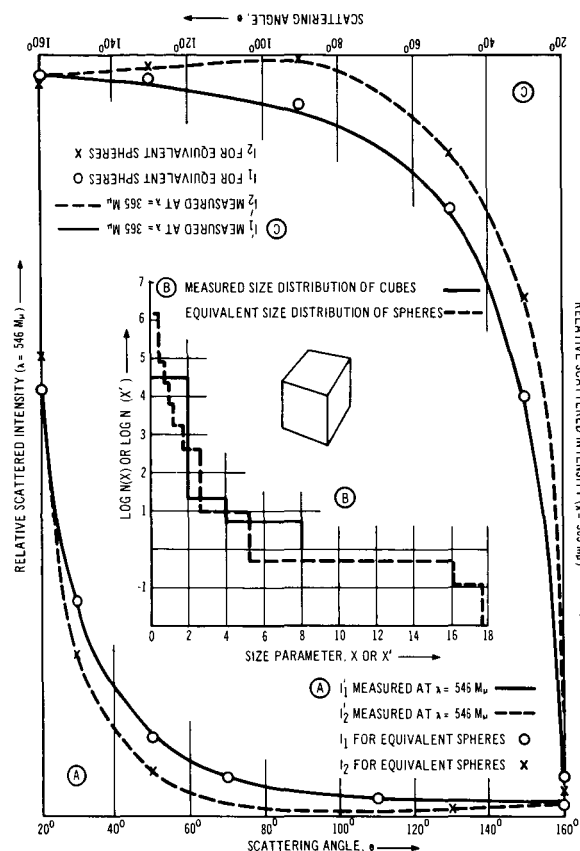


FIGURE 15.—Optical character of MgO cubes.

tion at two wavelengths are nearly identical, thus demonstrating that both the angular and wavelength dependence of large-volume particles are similar to spheres. Furthermore, the equivalent sphere size distributions are very close to the actual, measured size distributions of cubes. (On the average, a cube scatters like a sphere with diameter such that the sphere just encloses the cube.)

(b) On the other hand, small-volume shapes such as needles and fourlings (fig. 16) exhibit single-color scattering diagrams like spheres, but the equivalent sphere size distribution may differ markedly from the actual size distribution (figs. 16 and 17). The fourlings scatter like smaller spheres but there is no linear relationship.

(c) Although large-volume particles exhibit the same wavelength dependence as spheres, small-volume particles do not; i.e., a size distribution of spheres which is equivalent to fourlings at

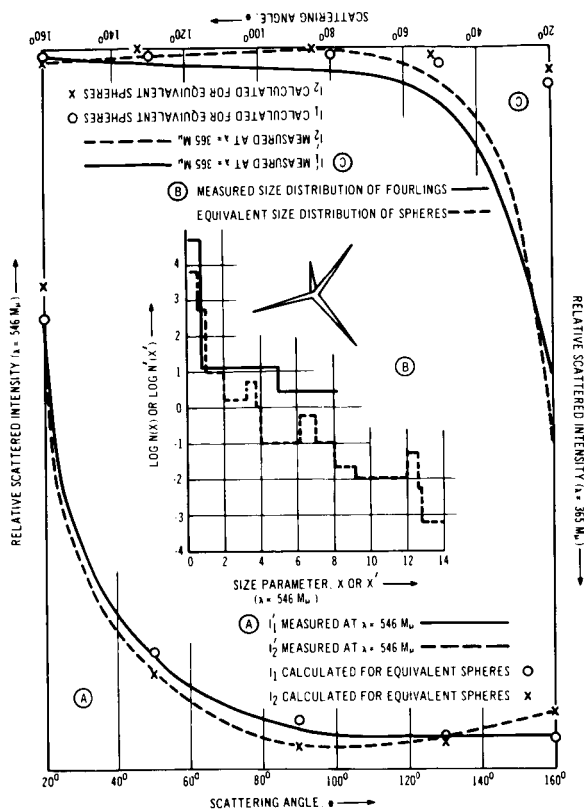


FIGURE 16.—Optical character of ZnO fowlings. Equivalent sphere size distribution was constructed to match angular scattering measured from fowlings at $\lambda = 546 \mu$. Notice that scattering from fowlings at $\lambda = 365 \mu$ is not the same as predicted from equivalent spheres.

one wavelength is not equivalent at another (figs. 16 and 17). Thus, small-volume particles may look like smaller spheres insofar as single-color measurements are concerned, but the wavelength dependence would not be consistent with the Mie theory. In this regard, the optical test for highly nonspherical particles is as follows: first, determine the size distribution of spheres which matches the angular character of the scattered irradiance and polarization as measured at wavelength, λ_1 . Increase the size of all spheres in the equivalent size distribution by λ_1/λ_2 . Compare the resulting scattering diagram with angular measurements at λ_2 . If the two compare favorably, the particles are spheres, cubes, octahedrons, etc. If there are large discrepancies, especially in the ratio of forward-to-backward

scattering, the particles are probably needle-like. We emphasize again that this test only applies to a broad size distribution of randomly oriented particles.

The very small size of the particles derived from the belt model could be due to the fact that the particles are large but needle-like. If so, the usual radiation-pressure arguments would be inappropriate because the equivalent ratio of scattering cross section to mass is unknown for such particle shapes. On the other hand, if the particles are needle-like, the observed color dependence would be incompatible with the Mie theory. Unfortunately, there are not sufficient data concerning the color of the zodiacal light and the wavelength dependence of the polariza-

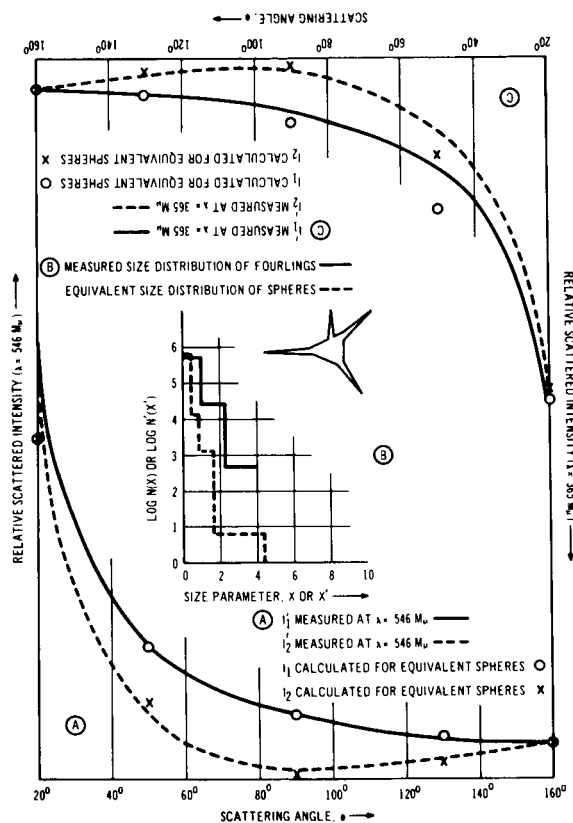


FIGURE 17.—Optical character of imperfect ZnO fowlings. Although angular character and wavelength dependence of light scattered by imperfect fowlings is the same as equivalent spheres (except at $30^\circ < \theta < 80^\circ$ where wavelength dependence deviates), the equivalent spheres are larger.

tion to test for needle-like particles. However, the available data are compatible with the idea that most of the particles are large-volume types: spheres, cubes, fat ellipsoids, and octahedrons. Our tentative conclusion is that the particles are not needle-like and that the Mie theory is therefore applicable.

CONCLUSIONS

The general arguments presented are compatible with the following conclusions:

(a) All observations indicate that the zodiacal-light phenomenon is due to scattering from sub-micron particles with radii in the range from 0.08 to 1.5 micron.

(b) The number density of particles in each size range is approximately constant throughout the ecliptic in the region between Venus and Mars.

(c) Differences in observations can be explained by minor changes in the size distribution and composition of the particles in each or all the belts between Venus and Earth, Earth and Mars, and especially between Mercury and Venus.

(d) All observations can be explained by the presence of a dominant fraction of dielectric particles ($1.4 < m < 1.8$) in the regions between Venus and Mars.

(e) There is evidence that some iron particles exist in the regions between Mercury and Earth but not beyond Earth. The iron particles tend to be larger (radii between 0.08 and 1.5 microns) than the dielectrics (radii less than 0.3 micron) and the number density of iron particles tends to be less than the number density of dielectrics by a factor of 100.

(f) There is evidence that the planets have some effect on the size distribution of the dust near them. Behr and Siedentopf's data cannot be explained without assuming that Venus sweeps out many of the particles near its orbit. More interesting, perhaps, is the fact that an exact fit to Weinberg's data requires a slightly different size distribution of particles near the Earth's orbit than in the regions of space interior and exterior to Earth.

(g) In general, the slope of the curve of number density versus particle size is steeper than previously expected.

(h) The total mass of dust required to explain the zodiacal-light observations is in the range from 10^{-24} to 10^{-26} grams per cubic centimeter.

(i) The number density of particles in the region beyond Mars is not sufficient to affect the character of the zodiacal light.

(j) Until more accurate three-color observations are made, there is no reason to assume highly nonspherical particle shapes. Spheres, cubes, fat ellipsoids, and octahedrons scatter in the same manner. The radiation-pressure limit for such shapes should be estimated more accurately.

(k) The observations analyzed can be explained without any assumptions concerning the number of electrons in the region beyond Mercury. The electron number density as derived from analysis of continuum observations is arbitrary.

(l) Further analysis of the presently available zodiacal-light observations will not yield unique results. A unique and reliable model of the interplanetary dust ensemble can only be derived from three-color monochromatic measurements of the brightness and polarization at all elongations, $25^\circ \leq \epsilon \leq 160^\circ$. Measurements in the blue are most important. Monitoring the three-color brightness and polarization at elongations $25^\circ \leq \epsilon \leq 40^\circ$ over a period of several months would be valuable. Simultaneous three-color observations from a satellite and a good Earth site, such as Haleakala, would be very valuable.

(m) There is no reason to compare the results from direct-impact measurements with deductions from zodiacal-light observations in the hope of determining the nature of the near-Earth ensemble. The zodiacal light is due to very small particles. Light from particles larger than 1.1 micron is swamped by light from smaller particles. Direct-impact devices are only sensitive to particles larger than 1 micron (depending on velocity).

(n) Giese's analysis (1963) of Blackwell and Ingham's observations using submicron particles is not merely an academic exercise as claimed by Elsässer (1965). Only submicron particles fit all the observations in a consistent manner.

(o) Obviously, a more detailed analysis of effects which counteract radiation pressure should be performed.

ACKNOWLEDGMENTS

We wish to thank Dr. B. Donn and M. Dubin of National Aeronautics and Space Administration for general guidance and criticism. We also wish to thank Drs. J. L. Weinberg and C. W. McCracken whose comments regarding their mistrust of the constant size-distribution assumption led to the belt

model; and Dr. R. H. Giese whose work gave us the courage to disregard the radiation-pressure limit. We also wish to acknowledge the gracious contribution of Mrs. Patricia Lightfoot who programmed the computer. Most of the research was supported by National Aeronautics and Space Administration under contracts NASw-1198 and NASw-1206. The remainder was supported by Melpar, Inc.

REFERENCES

- ALEXANDER, W. M., C. W. MCCrackEN, and J. L. BOHN, 1965, *Science*, **149**, 1240-1241.
 ALLEN, C. W., 1946, *Mon. Not. Roy. Astron. Soc.*, **106**, 137-150.
 BARBIER, D., 1955, *Mém. Soc. Roy. Sci. Liège*, **15**, 55.
 BEARD, D. B., 1959, *Astrophys. J.*, **129**, 496-507.
 BEGGS, D. W., D. E. BLACKWELL, D. W. DEWHIRST, and R. D. WOLSTENCROFT, 1964, *Mon. Not. Roy. Astron. Soc.*, **127**, 319.
 BEHR, A., and H. SIEDENTOPF, 1953, *Zeits. f. Astrophys.*, **32**, 19-50.
 BELTON, M. J. S., 1966, *Science*, **151**, 35-44.
 BLACKWELL, D. E., and M. F. INGHAM, 1961, *Mon. Not. Roy. Astron. Soc.*, **122**, 113-127.
 BORN, M., and E. WOLF, 1964, *Principles of Optics* (2d ed., London: Pergamon Press), 633-664.
 DIVARI, N. B., 1964, *Soviet Ast. J.*, **7**, 547-548.
 DIVARI, N. B., and A. S. ASAAD, 1960, *Soviet Astron.—AJ*, **3**, 832-838.
 DONN, B., and R. S. POWELL, 1962, *Electromagnetic Scattering* (M. Kerker, ed.) (Pergamon Press), 151-158.
 DONN, B., R. S. POWELL, and L. REMY-BATTIAU, 1967, *Nature*, **213**, 379.
 DUFAY, J., 1925, *Compt. Rend.*, **181**, 399.
 ELSÄSSER, H., 1958, *Die Sterne*, **34**, 166-169.
 —, 1965, *Introduction to Solar Terrestrial Relations* (Oriner and Maseland, eds.) (Dordrecht: D. Reidel Publ. Co.), 149-166.
 FESENKOV, V. G. 1963, *AIAA J.*, **1**, 1250-1253.
 GIESE, R. H., 1963, *Space Science Reviews*, **1**, 589-611.
 GIESE, R. H., and H. SIEDENTOPF, 1962a, *Zeits. f. Astrophys.*, **54**, 200-216.
 —, 1962b, *Zeitschf. f. Naturforsch.*
 GILLET, F. C., 1966, Report No. 2, Contract NASA (NsG-281-62) and NONR 710(22), Univ. of Minnesota.
 GREENBERG, J. M., N. E. PEDERSON, and J. C. PEDERSON, 1961, *J. Appl. Phys.*, **32**, 233.
 HARWIT, M., 1963, *J. Geophys. Res.*, **68**, 2171.
 HEMENWAY, C. L., and R. K. SOBERMAN, 1962, *Astron. J.*, **67**, 256.
 HODKINSON, J. R., 1963, *Electromagnetic Scattering* (M. Kerker, ed.) (Pergamon Press), 87-100.
 HURUHATA, M., 1951, *Publ. Astron. Soc. Japan*, **2**, 156-171.
 KARYAGINA, Z. V., 1961, *Soviet Astron.—AJ*, **4**, 828-832.
 LILLER, W., 1960, *Astron. J.*, **132**, 867-882.
 LITTLE, S. J., B. J. O'MARA, and L. H. ALLER, 1965, *Astron. J.*, **70**, 346-352.
 MIE, G., 1908, *Ann. Physik* **4**, **25**, 577.
 NAPPER, D. H., and R. H. OTTEWILL, 1963, *Electromagnetic Scattering* (M. Kerker, ed.) (Pergamon Press), 377-386.
 PETERSON, A. W., 1961, *Astrophys. J.*, **133**, 668-674.
 POWELL, R. S., B. DONN, R. R. CIRCLE, D. C. VOGEL, and P. D. WOODSON III, 1967, *Planetary Space Sci.*, **15**, 1641-1652.
 RICHTER, N. B., 1956, *Veröff. Sternwarte Sonneberg* **2**, Heft 6.
 —, 1962, *Veröff. Sternwarte Sonneberg* **5**, Heft 4.
 —, 1966, *Quart. J. Roy. Astron. Soc.*, **3**, 179.
 ROBLEY, R., 1962, *Ann. de Geophys.*, **18**, 341-350.
 SHAPIRO, I. I., D. A. LAUTMAN, and G. COLOMBO, 1966, *J. Geophys. Res.*, **71**, 5695-5741.
 SMITH, L. L., F. E. ROACH, and R. W. OWEN, 1965, *Planetary Space Sci.*, **13**, 207.

- SOUTHWORTH, R. B., 1964, *Ann. N.Y. Acad. Sci.*, **119**, 54-57.
- VAN DE HULST, H. D., 1947, *Astrophys. J.*, **105**, 471.
- , 1957, *Light Scattering by Small Particles* (John Wiley & Sons, Inc.).
- WEINBERG, J. L., 1964a, Hawaii Institute of Geophysics Report, HIG-64-11.
- , 1964b, *Ann. d'Astrophys.*, **27**, 718-738.
- WOLSTENCROFT, R. D., and L. J. ROSE, 1967, *Astrophys. J.*, **147**, 271-292.
- WYATT, S. P., and F. L. WHIPPLE, 1950, *Astrophys. J.*, **111**, 134-141.

Page intentionally left blank

36. Some Models of the Zodiacal Cloud

L. H. ALLER, G. DUFFNER, M. DWORETSKY,
D. GUDEHUS, S. KILSTON, D. LECKRONE,
J. MONTGOMERY, J. OLIVER, AND E. ZIMMERMAN
*University of California, Los Angeles
Los Angeles, California*

NUMEROUS OBSERVATIONAL STUDIES have been made of the zodiacal light (cf., e.g., Barbier (1955), Beggs, Blackwell, Dewhirst, and Wolstencroft (1964), Behr and Siedentopf (1953), Blackwell (1955, 1956), Blackwell and Ingham (1961), Divari and Asaad (1960), Divari, Krylova, and Moroz (1964), Dumont (1965), Elsässer (1963), Elvey and Roach (1937), Fesenkov (1958), Gillett, Huch, Ney, and Cooper (1964), Hoffmeister (1930, 1932), Huruata (1951), Peterson (1961), Regener (1955), Robley (1962), Roach (1964), Smith, Roach, and Owen (1965), and Weinberg (1964). Interpretations of the zodiacal light have been published by Allen (1946), van de Hulst (1947), Whipple (1955), Beard (1959), Harwit (1963, 1964), Ingham (1961), Giese (1961, 1963), Giese and Siedentopf (1962), Southworth (1964), Little et al. (1965), and Belton (1966). Some of these papers have tried to explain the optical properties of the zodiacal light; others have dealt with the dynamics of the cloud.

In this investigation, we confine our attention to an examination of certain simplified heliocentric models which attempt to reproduce the observed polarization, brightness, and color distribution in the zodiacal light.

Five steps are involved:

- (1) Calculation of the Mie coefficients which are needed to obtain the scattering function
- (2) Adoption of an assumed particle size distribution and evaluation of the resultant scattering function
- (3) Evaluation of radiation-pressure effects and determination of what size particles can be retained in the solar system

(4) Calculation of observed intensity distribution, polarization distribution, and colors for sundry models

(5) Identification of the influence of each model parameter on the results and specifications of observations needed to determine unique properties of interplanetary material.

Briefly, the assumptions underlying the calculation are as follows:

- (1) The particles scatter according to the Mie theory for spheres.
- (2) The particle size distribution is determined by a power law—an assumption inspired by work on faint meteors.
- (3) The spatial distribution of the particles is smooth, i.e., the number density goes as a simple power law as a function of distance from the Sun and shows an exponential decrease with distance from the plane.
- (4) The particle size distribution and the optical properties do not change with distance from the Sun.

The investigation constitutes an extension of an earlier effort by Little, O'Mara, and Aller (1965) to provide a model for the zodiacal cloud; an attempt is made here to predict colors, isophotes, and isopolarization contours. The chief conclusions of this study are:

- (a) Small, solid spheres with refractive indices similar to ice or SiO_2 can be retained in the solar system, but a lower limit exists for the sizes of particles of metal, graphite, or fluffy particles of any kind.
- (b) A simple power law form, a^{-p} , for particle size distribution does not seem possible, unless

p assumes different values above and below some critical size, a_B .

(c) A low index of refraction (as suggested by earlier work) is indicated.

(d) The spatial distribution of the particles indicates that they probably do not increase in density or may actually thin out near the Sun.

(e) The zodiacal light should be slightly bluer than the Sun; the color excess changes slowly with position in the sky.

CALCULATION OF THE MEAN SCATTERING FUNCTION

To calculate the mean scattering function, let a be the radius of the particle and define

$$\alpha = \frac{2\pi a}{\lambda} \quad (1)$$

in the usual way.

The density and particle-size-distribution function is assumed to be of the form:

$$N(r, z, a) = N_0 \left(\frac{R_0}{r} \right)^\nu \exp \left[-K \left(\frac{z}{R_0} \right) \right] \left(\frac{a}{a_0} \right)^{-p} \quad (2)$$

where r is the distance of the particle from the Sun, R_0 is 1 AU, z is the height above the ecliptic plane, and ν and K are parameters of the model. The particle-size-distribution factor can be written in the form

$$N = N_{a_0} \left(\frac{a}{a_0} \right)^{-p} \sim N_{\alpha_0} \left(\frac{\alpha}{\alpha_0} \right)^{-p} \quad (3)$$

where, naturally, α_0 changes as the wavelength, λ , changes. We can represent any reasonable particle size distribution by a "broken" power law of the form:

$$\begin{aligned} p_1 & \text{ for } a_{\min} < a < a_1 \\ p_2 & \text{ for } a_1 < a < a_2 \\ p_i & \text{ for } a_{i-1} < a < a_i, \text{ etc.} \end{aligned} \quad (4)$$

The computer program is written to accommodate as many as 10 different values of p . In actual practice we used two values of p , viz

$$\begin{aligned} p &= p_L \text{ for } a_{\min} < a < a_B; \\ p &= p_U \text{ for } a_B < a < a_{\max} \end{aligned} \quad (5)$$

where a_{\min} is some minimum particle size, a_B is

the "breakpoint" in the size distribution and a_{\max} is some maximum size. Physically, a_{\min} may be identified with the particle size that is blown out of the solar system or with some size that is so small that there is no longer any effect on the scattering. For sufficiently small particles, i.e., for α much less than 1, Rayleigh scattering occurs, but then the efficiency is so low that the contribution is negligible.

Note that at 5000Å, $a = 0.1\mu$ and $\alpha = 1.25$, while for $a = 2\mu$, $\alpha = 25.5$. Larger particles are too rare, presumably, to affect the scattering much. The physical parameters assumed for the particles are:

$$\begin{aligned} \text{Density, } \rho &= 4.0 \text{ (usually), Complex index of} \\ & \text{refraction, } \tilde{n} = 1.33 - 0.01i, \\ & \text{Magnetic permeability, } \mu = 1 \end{aligned} \quad (6)$$

This choice of the index of refraction was based on previous work (Little, O'Mara, and Aller, 1965). A more rigorous treatment would require inclusion of the wavelength variation of the complex index of refraction. This refinement would introduce a color term in addition to that set by choice of other parameters, a_{\min} , a_B , etc.

The scattering functions $S_1(\alpha, \theta)$ and $S_2(\alpha, \theta)$ are calculated by the Mie theory. The basic scheme, due to Giese (1961, 1963) and to Giese and Siedentopf (1962), was modified by O'Mara and further revised for this particular project. We have to calculate the ratio of two integrals for the two planes of polarization.

$$\sigma_i(\theta) = \frac{\int_{\alpha_{\min}}^{\alpha_{\max}} S_i(\alpha, \theta) \left(\frac{\alpha}{\alpha_0} \right)^{-p} d\alpha}{\int_{\alpha_{\min}}^{\alpha_{\max}} \left(\frac{\alpha}{\alpha_0} \right)^{-p} d\alpha} \quad i = 1, 2 \quad (7)$$

Note that α_{\min} , α_{\max} , and α_B (the value of α corresponding to the breakpoint) all vary with wavelength in accordance with equation (1).

Comments on Computational Program

The computational program is written with a viewpoint of versatility. All parameters and variable quantities are read in as data, rather than being built into the code. The range of integration, α_{\min} to α_{\max} , is chosen so as to

represent the actual range of particle sizes that contribute significantly to the mean scattering function, $\sigma_i(\theta)$. In practice, the integrand is computed for 50 integration steps and the calculation is carried out by Simpson's rule. The results are expressed as a table of σ as a function of θ , with intervals of 2° . In the course of the integration at every fifth value of the argument, α , a table of $S_{1,\alpha}(\theta)$ and $S_{2,\alpha}(\theta)$ is printed out and can be plotted by the machine if required. The time needed to run this program depends on the upper limit of α and the number of integration steps. For $\alpha_{\max}=26$ and $N=50$, the program required 2.5 minutes for one set of parameters independent of the range of p values used.

Figure 1 shows the normalized scattering function for the two planes of polarization σ_1 and σ_2 , for $\lambda=3800\text{\AA}$, 5000\AA , and 6500\AA . Figure 2 shows the corresponding curves for polarization as a function of θ for the same wavelengths, $p=4$, and an index of refraction given by equation (6). The particle range was chosen as $a=0.1\mu$ to 2.0μ .

The scattering functions and resultant polarizations depend on the lower limit, α_{\min} ; the dependence is more marked the larger the value of p (as indeed one would expect) and the shorter the wavelength. The polarization is always larger the smaller the value of α_{\min} . In figure 3, the results for 3800\AA and 6500\AA are compared for $p=4$ and for $\alpha_{\min}=0.1\mu$ and 0.01μ .

Figure 4 shows polarization as a function of θ for $\lambda=5000\text{\AA}$ when $p=4$ and for $a > 1.0\mu$ and $p=0, 2, 3$, or 4 when $a < 1.0\mu$. Notice the increasing oscillations the smaller the value of p . Similar calculations show that, for the smaller values of p , the oscillations become more numerous the larger the value of α_B . Essentially, particles over a limited range of sizes tend to dominate the scattering. These calculations give the dependence of $\sigma_{1,2}$ and the polarization on the angle, θ . They do not give results that can be compared immediately with observations, since what we observe is not $p(\theta)$ or $I(\theta)$, but rather $p(\epsilon)$ and $I(\epsilon)$, where ϵ is the elongation.

MINIMUM PARTICLE SIZES FOR ZODIACAL CLOUD

It is evident from considerations of the preceding section that one must establish the lower

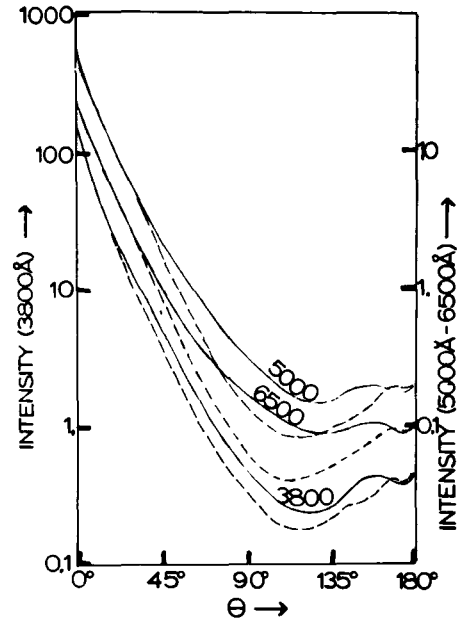


FIGURE 1.—Normalized scattering functions σ_1 and σ_2 for two planes of polarization for 3800 \AA , 5000 \AA , and 6500 \AA as functions of the scattering angle θ . Particle size distribution is given by a^{-4} , $0.1\mu < a < 2.0\mu$, $\bar{n}=1.33-0.01i$.

limit for the sizes of the particles that might be found in the zodiacal cloud. Assuming that the particles carry negligible charges or that the influence of magnetic or electric fields can be ignored, the critical factor will be the ratio of the force of gravity, F_g , to the radiation pressure, F_p . If $F_p/F_g > 1$, the particle presumably will be ejected from the solar system by radiation. Since both the energy intercepted and the force of gravity fall off as r^{-2} , the ratio is essentially independent of distance, unless the particle approaches so close to the Sun, that the effect of the solid angle subtended by the solar disk becomes important. If the radius of the particle is a and its density is ρ , the gravitational force on the particle is

$$F_g = \frac{4\pi a^3 \rho}{3} \frac{GM_o}{R^2} \quad (8)$$

where M_o is the mass of the Sun, G is the gravitational constant, and R is the distance of the particle from the Sun. The radiation pressure is given by

$$F_p = \frac{\pi a^2}{c} \left(\frac{R_o}{R} \right)^2 \int_{\lambda=0}^{\infty} Q_{pr} F(\lambda) d\lambda \quad (9)$$

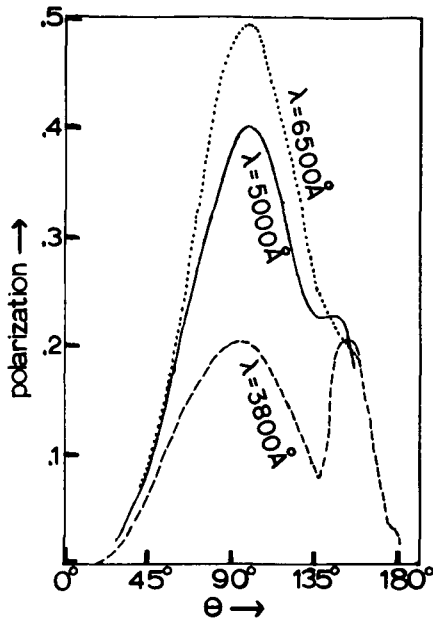


FIGURE 2.—Polarization as a function of scattering angle θ for 3800 Å, 5000 Å, and 6500 Å. Particle size distribution assumed to be a^{-4} for $0.1 \mu < a < 2.0 \mu$. $\bar{n} = 1.33 - 0.01i$.

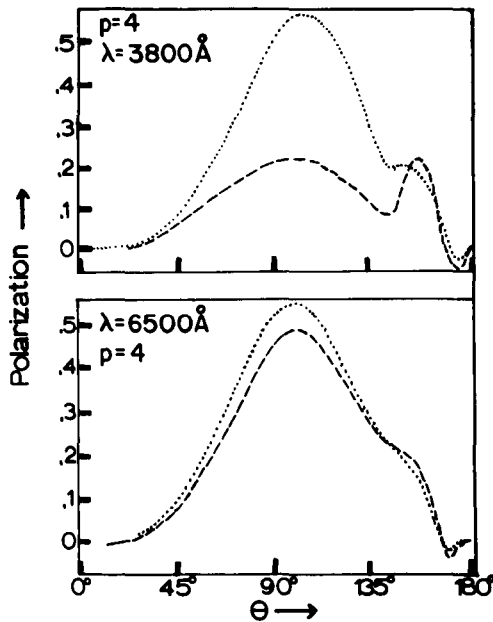


FIGURE 3.—Dependence of polarization on lower limit of particle size. Curves for 3800 Å and 6500 Å are shown for $a_{\min} = 0.01 \mu$ and $a_{\min} = 0.1 \mu$. In each instance the $a_{\min} = 0.1$ micron curve lies higher; we assume $p = 4$.

where R_0 is the distance from the Earth to the Sun, $F(\lambda)d\lambda$ is the flux of solar energy in the interval from λ to $\lambda + d\lambda$ at the top of the Earth's

atmosphere, and Q_{pr} is the efficiency of absorption (essentially the ratio of the effective area for absorption to the true area). The ratio F_p/F_g is

$$\frac{F_p}{F_g} = \frac{3}{4} \frac{R_0^2}{apcGM_0} \int_{\lambda=0}^{\infty} Q_{pr} F(\lambda) d\lambda$$

$$= 4.221 \times 10^{-11} \frac{\int_0^{\infty} Q_{pr} F(\lambda) d\lambda}{a\rho} \quad (10)$$

The problem is to evaluate this expression numerically. The calculation of the integral

$$\int_{\lambda_1}^{\lambda_2} Q_{pr}(\lambda, a_0, \bar{n}) F(\lambda) d\lambda$$

involves the calculation of $Q_{pr}(\lambda, a_0, \bar{n})$ from Mie theory; $F(\lambda)$ may be taken from Allen's "Astrophysical Quantities," p. 172. A Gaussian quadrature which involves an optimization of abscissae and weights in numerical integration turns out to be the most convenient.

All calculations were carried out for a range of particle sizes $0.05\mu < a_0 < 1\mu$. Some of the results are shown in figure 5. To obtain the minimum sized particle with a given complex index of refraction (that may yet be retained in the solar system), one proceeds as follows: Select the density of the particle on the ordinate, move to the intersection with the complex-index-

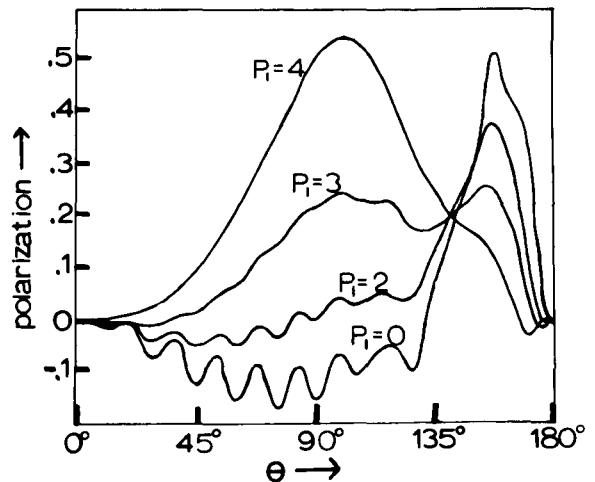


FIGURE 4.—Dependence of polarization on scattering angle for different size distributions. Particle size distribution of the form a^{-p} is assumed but with $p = 4$ for all values of a greater than 1.0μ , and $p_i = 0, 2, 3$, or 4 for $a < 1.0 \mu$.

of-refraction curve for that particle, and then from the intersection down to the abscissa where the particle radius is given in microns. We selected this type of presentation to enable a range of densities to be compared for each complex index of refraction. We have discussed the substances selected by Giese (1961) and by Giese and Siedentopf (1962) in similar research and shall compare our results with theirs.

Giese's results for nickel correspond closely to our own; $a_{\min} = 0.14\mu$ and 0.16μ , respectively. The results differ considerably for ice, however. Also, Giese's curve crosses the $\rho = 1$ line at $a_{\min}(\text{H}_2\text{O}) = 0.85\mu$ while our curve fails to cross it at all, reaching a maximum at a density of 0.7; we cannot find any reason for this discordance. See table 1.

TABLE 1.—Limiting Sizes of Small Particles in the Solar System

Material	Complex index of refraction	Density, ρ , gm/cm ³	a_{\min} , μ
Iron.....	1.27 to 1.37i 1.38 to 1.50i 1.70 to 1.84i	7.86	0.18 to 0.19
Melted iron droplets.....	1.27 to 1.37i 1.38 to 1.50i 1.70 to 1.84i	6.88	0.19 to 0.21
Nickel.....	1.46 to 2.68i 1.50 to 3.10i	8.9	0.16
Zinc.....	1.41 to 4.10i	7.15	0.19
Carbon (graphite crystals).....	1.59 to 0.66i	2.25 3.52	0.43 0.30
Absorbing particles.....	1.33 to 0.50i 1.33 to 0.05i	$\rho \leq 7.5$ $\rho \leq 1.45$	
SiO ₂	1.55 to 0.00	2.1	{ Does not exist
H ₂ O.....	1.33 to 0.00	1.0	

Throughout all these calculations, the permeability of the material is taken as $\mu = 1.00$.

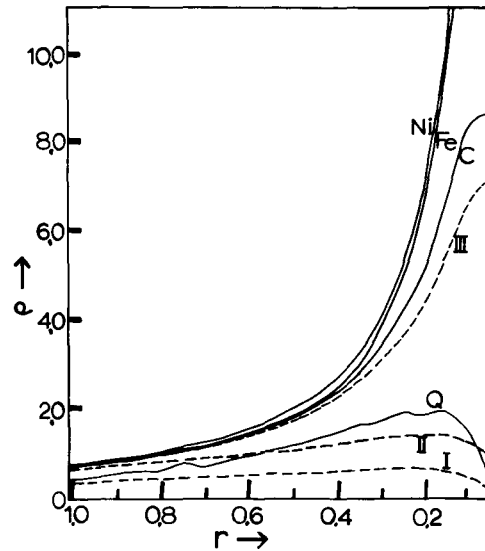


FIGURE 5.—Minimum particle sizes for retention against radiation pressure. Curves are presented for different substances. At the radius, r , where curve reaches density, ρ , of the material involved, the particle can no longer be retained in solar system. Curves I, II, and III correspond to ice with indices of refraction of 1.33 (pure ice), $\tilde{n} = 1.33 - 0.05i$ and $1.33 - 0.50i$ (dirty ice). Q refers to silicon dioxide, SiO_2 , $\tilde{n} = 1.55$; C, to graphite crystals, $\tilde{n} = 1.59 - 0.66i$, and Ni and Fe, to selected curves for iron and nickel. See table 1.

Slight changes in μ appear to have little effect. Changes from $\mu = 1.0$ to $\mu = 55$ for insulated, powdered, iron particles (Handbook of Chemistry and Physics) produce too large an effect for the present computing program. Although Giese's results indicate that without a finite absorption coefficient, k , definite a_{\min} values existed for H_2O and SiO_2 , we find that no a_{\min} exists for these substances if their densities correspond to solid crystals. For dirty ice with $\tilde{n} = 1.33i$ to $0.04i$ and unit density, $a_{\min} = 0.55\mu$. Similarly, with the inclusion of a finite k for SiO_2 , an a_{\min} will exist.

Of course, the interplanetary particles cannot be ice. We have assumed a substance with the same optical constants as ice merely as a matter of convenience, since it appeared to give a reasonably good representation of the general behavior of the $I(\epsilon)$ and $p(\epsilon)$ curves. Actually we are probably concerned with a radiation-damaged substance of some kind, whose optical properties are characterized by a small value of the real part, n , of the refractive index.

The results in table 1 suffer from yet another limitation; we have assumed a constant index of refraction for each material. No known substance has a constant index of refraction over a wavelength range from $0.2\mu < \lambda < 3\mu$. Data on indices of refraction over wide wavelength intervals are not available for many of the most likely substances.

Notice that for all materials, some a_{\min} exists if the mean density of the "dust particle" is sufficiently low. Our mode of presentation of the results shows this effect of reducing the density or a_{\min} very clearly. An a_{\min} can be seen to exist for any sufficiently "fluffy" particle. Indeed if the net density for any aggregate of materials (i.e., a fluffy accumulation) is less than 0.25 cm/cm^3 , the aggregate will be ejected from the solar system even for very large particle sizes beyond the range of our calculations, at least insofar as one is justified in using the Mie theory for such aggregates.

We will see that, in practice, the absence of very large polarizations and a distinct blue coloration of the zodiacal cloud indicate that there exists some lower limit to the particle size—or at least that small particles apparently cannot exist in very large numbers.

Precise values of the cutoff radii would be impossible to give—even if we knew exactly what substances were present. The particles are almost certainly irregular in shape and Mie theory calculations can give only rough approximations.

MONOCHROMATIC SURFACE BRIGHTNESS OF ZODIACAL LIGHT

We have now to calculate the monochromatic surface brightness $I_\lambda(\epsilon, \beta)$ of the zodiacal light as seen from the Earth. Here ϵ is the elongation along the ecliptic (the celestial longitude of the point in the sky minus the celestial longitude of the Sun) and β is the celestial latitude of the point.

In our model the zodiacal light is presumed to arise from the scattering of sunlight by small interplanetary particles, whose density follows the spatial distribution $N(r, z)$. Here, r denotes the projected distance from the Sun in the ecliptic plane and z is the height above that plane.

Figure 6 depicts the geometry of the problem.

Consider radiation falling upon a small-volume element at a distance from the Sun. The Sun will occupy a solid angle, $d\omega$, and have a mean intensity I' . The flux reaching P will be:

$$I' d\omega = E_\lambda R_0^2 / \rho^2 \quad (11)$$

where E_λ is the monochromatic solar flux at the Earth. Radiation is scattered in all directions. Let the average flux of radiation scattered by a particle toward the Earth in a solid angle, $d\omega$, be given by $\delta I_\lambda^{(1)} d\omega$ and $\delta I_\lambda^{(2)} d\omega$ where $I_\lambda^{(1)}$ and $I_\lambda^{(2)}$ are the components of I_λ along and perpendicular to the direction to the Sun, i.e., in the plane SPE and perpendicular thereto. Then

$$\begin{aligned} \delta I_\lambda^{(1)} d\omega &= \frac{I'_\lambda}{2} d\omega' \frac{\lambda^2}{4\pi^2 \Delta^2} \sigma_1(\theta, p) d\omega \\ &= \frac{E_\lambda R_0^2}{2} \frac{\lambda^2}{\rho^2 4\pi^2 \Delta^2} \sigma_1(\theta, p) d\omega \quad (12) \end{aligned}$$

where $\sigma_1(\theta, p)$ and $\sigma_2(\theta, p)$ are the mean scattering functions defined in equation (7), the factor 2 arises because two planes of polarization are involved, $\lambda^2/4\pi^2$ is a "normalization" factor introduced in the scattering function, and $1/\Delta^2$ represents the geometrical attenuation.

The number of scattering particles in the volume element $\Delta^2 d\omega d\Delta$, subtending an angle, $d\omega$, at a distance Δ will be $N(r, z) \Delta^2 d\Delta$. The

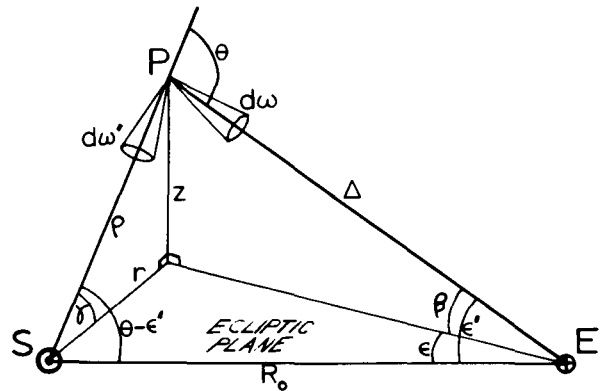


FIGURE 6.—Relation between Sun-particle distance, ρ , particle-Earth distance, Δ , and scattering angle, θ . S represents Sun, E, Earth, and P, scattering particles.

net surface brightness will be

$$I_{\lambda}^i d\omega = E_{\lambda} \frac{\lambda^2}{8\pi^2} \int_0^{\infty} \frac{R_o^2}{\rho^2} N(r, z) \sigma_i(\theta, p) d\Delta d\omega \quad (13)$$

For the present calculations we assumed a distribution law of the form (2), and

$$N(r, z) = N_o \left(\frac{R_o}{r} \right)^{\nu} \exp(-Kz/R_o) \quad (14)$$

where we have integrated over the size distribution of the particles (compare eq. (7)). Here N_o is the density at the Earth, ν is a density-distribution parameter, and $1/K$ is an assumed scale height for distribution above the ecliptic plane—expressed in astronomical units. Equation (14) is intended as an interpolation formula only. Any mechanical model of the zodiacal cloud based on orbit theory, radiation pressure, electric-charge effects, etc., would certainly lead to a different density distribution, which could be then incorporated into the theory as needed.

With equation (14) introduced into equation (13), we get

$$I_{\lambda}^{(i)}(\epsilon, \beta) d\omega = E_{\lambda} N_o \frac{\lambda^2}{8\pi^2} \int_0^{\infty} \left(\frac{R_o}{\rho} \right)^2 \left(\frac{R_o}{r} \right)^{\nu} \exp(-Kz/R_o) \sigma_i(\theta, p) d\Delta d\omega \quad (15)$$

In the special case, $\epsilon = 180^\circ$, $\beta = 0$, equation (15) can be evaluated readily since $z = 0$, $\rho = r = \Delta + R_o$, and $d\Delta = dr$. Then

$$I_{\lambda}^{(i)}(180^\circ, 0^\circ) = E_{\lambda} N_o \frac{\lambda^2}{8\pi^2} \int_0^{\infty} \frac{R_o^{\nu+2}}{r^{\nu+2}} \sigma_i(180^\circ, p) dr \quad (16)$$

or

$$I_{\lambda}^{(i)}(180^\circ, 0^\circ) = E_{\lambda} N_o \frac{\lambda^2}{8\pi^2} \frac{1}{\nu+1} \sigma_i(180^\circ, p) \quad (17)$$

where ($\nu = -1$). For all other angles, equation (15) is integrated best by making the following trigonometric transformations. By use of the sine law and figure 6 we get

$$\frac{\rho}{\sin \epsilon} = \frac{R_o}{\sin \theta} = \frac{\Delta}{\sin(\theta - \epsilon')} \quad (18)$$

or

$$\frac{R_o}{\rho} = \frac{\sin \theta}{\sin \epsilon'} \quad (19)$$

$$\frac{\Delta}{R_o} = -\frac{\sin(\theta - \epsilon')}{\sin \theta} \quad (20)$$

Also from figure 6,

$$z = \Delta \sin \beta \quad (21)$$

and from equation (20)

$$\frac{z}{R_o} = \frac{\Delta}{R_o} \sin \beta = \frac{\sin(\theta - \epsilon')}{\sin \theta} \sin \beta \quad (22)$$

Again from figure 6,

$$\frac{z}{R_o} = \frac{\rho}{R_o} \sin \gamma \quad (23)$$

or by equations (19) and (22)

$$\frac{\sin(\theta - \epsilon')}{\sin \theta} \sin \beta = \frac{\sin \epsilon'}{\sin \theta} \sin \gamma \quad (24)$$

or

$$\sin \gamma = \frac{\sin(\theta - \epsilon')}{\sin \epsilon'} \sin \beta \quad (25)$$

From figure 6 and equation (19)

$$\frac{r}{R_o} = \frac{\rho}{R_o} \cos \gamma = \frac{\sin \epsilon'}{\sin \theta} \cos \gamma \quad (26)$$

where it is convenient to use

$$\cos \gamma = \sqrt{1 - \sin^2 \gamma} \quad (27)$$

for the machine computation. From figure 6, one sees that

$$\rho d\theta = d\Delta \sin \theta \quad (28)$$

or by equation (18)

$$d\Delta = R_o \frac{\sin \epsilon'}{\sin^2 \theta} d\theta \quad (29)$$

Now substitute equations (19), (22), and (26) into equation (15) to get

$$I_{\lambda}^{(i)}(\epsilon, \beta) = E_{\lambda} N_o R_o \frac{\lambda^2}{8\pi^2} \int_{\epsilon'}^{\pi} \frac{(\sin \theta)^{\nu}}{(\sin \epsilon')^{\nu+1} (\cos \gamma)^{\nu}} \times \sigma_i(\theta, \tilde{n}, p) \exp \left[-K \frac{\sin(\theta - \epsilon')}{\sin \theta} \sin \beta \right] d\theta \quad (30)$$

where, by equations (27) and (25) we get

$$\cos \gamma = \sqrt{1 - \frac{\sin^2 (\theta - \epsilon)}{\sin^2 \beta}} \sin^2 \beta \quad (31)$$

and by Napier's rule and figure 6,

$$\cos \epsilon' = \cos \epsilon \cos \beta \quad (32)$$

In the ecliptic plane, where $\beta = 0$, $\cos \gamma = 1$, $\sin \epsilon = \sin \epsilon'$, we recover the expression

$$I_{\lambda}^{(i)}(\epsilon, 0) = E_{\lambda} N_0 R_0 \frac{\lambda^2}{8\pi^2} \int_{\epsilon}^{\pi} \frac{(\sin \theta)^{\nu} \sigma_i(\tilde{n}, p)}{(\sin \epsilon)^{\nu+1}} d\theta \quad (33)$$

Now σ is a function not only of the parameters \tilde{n} and p but also of the cutoff values, α_{\min} and α_{\max} , which in turn depend on a_{\min} and a_{\max} and on λ . It is from this wavelength dependence and $\tilde{n}(\lambda)$ that the zodiacal light may get a color different from the Sun. Hence, it will be of interest to find the surface brightness of the zodiacal light in different colors to test the validity of our assumed particle size distributions and a_{\min} values.

PREDICTED COLORS AND POLARIZATIONS FOR SOME ZODIACAL-CLOUD MODELS

The substantial choice of parameters available means that one may select a wide range of models subject to the usual restrictions of geometrical and physical plausibility. In the first approximation, we may compute $I(\epsilon)$ and $p(\epsilon)$ in the plane of the ecliptic. If the model looks promising, we may then compute isophotic contours and polarizations at high celestial latitudes.

The necessary integrations may be performed numerically using Simpson's rule. Tables of $\sigma_i(\Theta, \tilde{n}, p)$ have been provided for equal intervals in Θ , so this interval is chosen as the integration step length. An advantage of the trigonometric transformations is that the integration step length becomes smaller near the Sun where the intensity contribution is the greatest. Since one end point of the integration is at $\Theta = \epsilon'$, one chooses ϵ' and β as independent coordinates, but we compute ϵ since $I(\epsilon, \beta)$ is the quantity

ultimately wanted for comparison with observation.

Once $I_{\lambda}^{(i)}$ is computed for several wavelengths, the color of the zodiacal light may be computed. The wavelengths chosen are

$$\begin{aligned} 3800\text{\AA} \quad V &= -2.5 \log (I_{3800}^1 + I_{3800}^2) \\ 5000\text{\AA} \quad G &= -2.5 \log (I_{5000}^1 + I_{5000}^2) \\ 6500\text{\AA} \quad R &= -2.5 \log (I_{6500}^1 + I_{6500}^2) \end{aligned} \quad (34)$$

so that the colors computed are $(V-G)$ and $(G-R)$. Furthermore, it is of interest to determine the color excesses or differences between the color of the zodiacal cloud and that of the Sun as a function of (ϵ, β) .

$$\begin{aligned} \Delta(V-G) &= (V-G) + 2.5 \log \frac{E_{3800}}{E_{5000}} \\ \Delta(G-R) &= (G-R) + 2.5 \log \frac{E_{5000}}{E_{6500}} \end{aligned} \quad (35)$$

where the solar monochromatic fluxes E_{3800} , E_{5000} , and E_{6500} are taken from Allen's "Astrophysical Quantities."

Finally, for any color chosen, the polarization is given by

$$p_{\lambda} = \frac{I_{\lambda}^{(1)} - I_{\lambda}^{(2)}}{I_{\lambda}^{(1)} + I_{\lambda}^{(2)}}$$

Note that the polarization can be obtained for different colors. In the present study, results are tabulated for the green 5000Å.

Since the computational choices were open-ended, only a limited number of examples could be studied. For certain of the models we calculated isophotes and polarization contours for the entire range of ϵ and β . We computed colors only for points along the ecliptic.

Computational Procedure and Results

Consider first the isophote problem. We computed the integral (eq. (30)) for values of β chosen at 2° intervals from 0° to 88°. For each value of β , $\epsilon'(\text{start}) \geq \beta \geq 5^\circ$. At each cycle ϵ' was chosen and incremented by 4° and the integral was computed for each ϵ' . We also computed ϵ for each value of ϵ' and β . The loop ended when $\epsilon = 180^\circ$. Then β was stepped to $\beta + \Delta\beta$, a new ϵ' was chosen and the cycle was repeated.

Further, developments of appropriate subroutines permitted one to display computer output in a graphical form; these subroutines plot graphs of the intensity and polarization of the scattered light all as functions of ϵ and β . The intensity or amount of polarization is represented in 41 levels; hence to construct isophotes or polarization isocontours, all one needs to do is to draw graphs through the symbolic characters on the graphs.

Table 2 gives an abstract of one calculation for a model with two values of p , viz

$$\begin{aligned} 0.01\mu < a < 0.40\mu, p = 2.0 \\ 0.40\mu < a < 2.00\mu, p = 4.00 \end{aligned}$$

The first column gives the elongation, ϵ , in degrees. The columns headed V , G , and R give the logarithms of the surface brightnesses at 3800\AA , 5000\AA , and 6500\AA , respectively, in cgs units. For convenience in tabulation all logarithms of intensities have been increased by 10; thus, for example, the reading 5.408 should actually be -4.592 . The absolute values depend

of course on the particle density assumed. By changing the number density, the values can be increased or decreased to permit optimum adjustment to an observed intensity distribution. The color differences, $\Delta(V-G)$ and $\Delta(G-R)$, are in *magnitudes*. The last column gives polarizations in percentages.

Rather early in the course of the calculations it became apparent that changes in particle space distribution had only small effects on the polarization and color of the zodiacal light; such changes as were obtained affected the intensity distribution along the ecliptic quantitatively—only slightly—not qualitatively. Sudden drops in intensity near the center of the gegenschein, for example, cannot be removed by juggling the value of ν in equation (2) for the particle size distribution. On the other hand, it should come as no surprise that the parameter, p , does have a substantial influence on the predicted intensity and polarization distributions.

Clearly, as figures 7–10 show, a large number of possible models exist and one must isolate,

TABLE 2.—*Model of the Zodiacal Cloud*

$[\bar{n} = 1.33 - 0.010i; \nu = 1.0; \mu = 1.00; N_0 = 2.206 \times 10^{-11} \text{ cm}^{-3}; 0.01\mu < a < 0.40\mu, p = 2.0; 0.40\mu < a < 2.00\mu, p = 4.0]$

Elongation, ϵ , deg	V (^a)	G (^a)	R (^a)	$\Delta(V-G)$	$\Delta(G-R)$	Polariza- tion, percent
10.....	5.408	5.530	5.304	-0.262	-0.347	4.74
20.....	4.598	4.772	4.584	-0.132	-0.252	6.33
30.....	4.034	4.228	4.090	-0.079	-0.126	9.05
40.....	3.617	3.783	3.672	-0.152	-0.061	12.9
50.....	3.340	3.446	3.317	-0.175	-0.108	17.7
60.....	3.015	3.183	3.028	-0.148	-0.170	21.8
70.....	2.803	2.967	2.810	-0.169	-0.173	23.6
80.....	2.644	2.793	2.643	-0.197	-0.157	23.6
90.....	2.516	2.664	2.513	-0.197	-0.162	22.9
100.....	2.424	2.570	2.410	-0.203	-0.181	21.3
110.....	2.359	2.506	2.337	-0.201	-0.205	17.2
120.....	2.315	2.467	2.290	-0.187	-0.228	10.2
130.....	2.313	2.449	2.270	-0.237	-0.230	1.49
140.....	2.328	2.446	2.275	-0.273	-0.211	-6.10
150.....	2.314	2.645	2.295	-0.191	-0.206	-8.75
160.....	2.298	2.503	2.321	-0.054	-0.239	-6.76
170.....	2.322	2.527	2.330	-0.024	-0.273	-4.40

^a Values are logarithms of the intensity (surface brightness) plus 10, i.e., 10.000 is to be subtracted from these numbers to give the correct intensities.

if possible, the domain of parameter values embracing the most likely solutions. In practice, the polarization curves seemed to supply the first necessary condition for the validity of a model. Hence, we required first that the computed polarizations fit Weinberg's observations (1964) reasonably well. Second, it was required that the computed intensity distribution have a shape similar to the curves obtained by Smith, Roach, and Owen (1965) or of Weinberg. Finally, the colors must not differ greatly from that of the Sun.

In our initial calculations, we assumed that p was constant over the entire range of particle radius, a , from 0.01μ or 0.1μ to 2μ , beyond which dimension the particles were not sufficiently numerous to have much effect. The results are shown in figures 7 and 8. None of these models proved satisfactory. They all had intensity minima in the center of the gegenschein, and those which yielded plausible polarization curves had

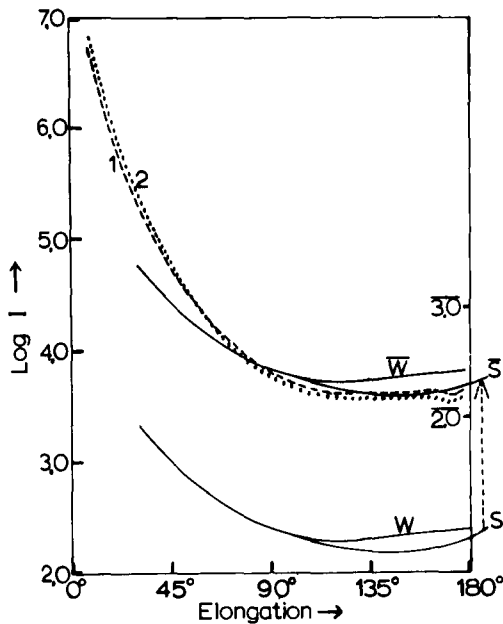


FIGURE 7.—Intensity distribution for a^{-4} particle-size-distribution law. Solid lines represent observed intensity distribution (Smith et al.) and Weinberg (W); dotted curve, space-distribution parameter ($\nu=1.0$); dashed curve, space-distribution parameter ($\nu=0$). On left-hand scale, $N_0 = 2.206 \times 10^{-11}$ particles/cm³. On right-hand scale, N_0 is adjusted to 0.92×10^{-12} particles/cm³ so as to secure a fit with observations. Note that predicted curve rises steeply toward the Sun. Throughout, a_{\min} is assumed to be 0.1μ .

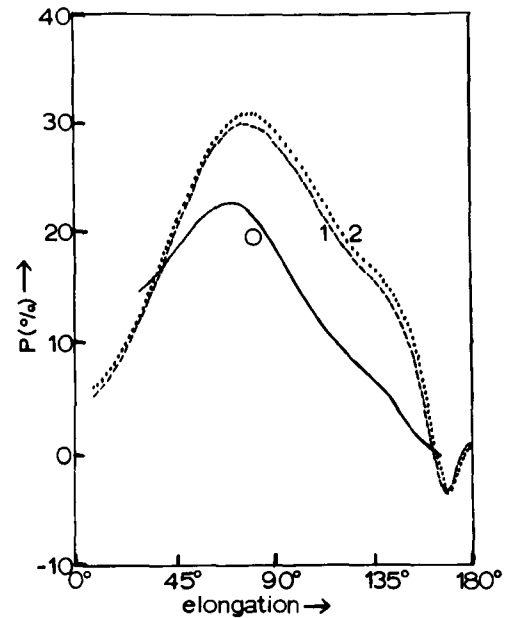


FIGURE 8.—Ecliptic polarization for an a^{-4} particle-size-distribution law. Solid curve represents observed polarization according to Weinberg; dashed curve, $\nu=1.0$; dotted curve, $\nu=0.8$. \tilde{n} is assumed to be $1.33 - 0.01i$. Note that predicted polarization is larger than the observed polarization.

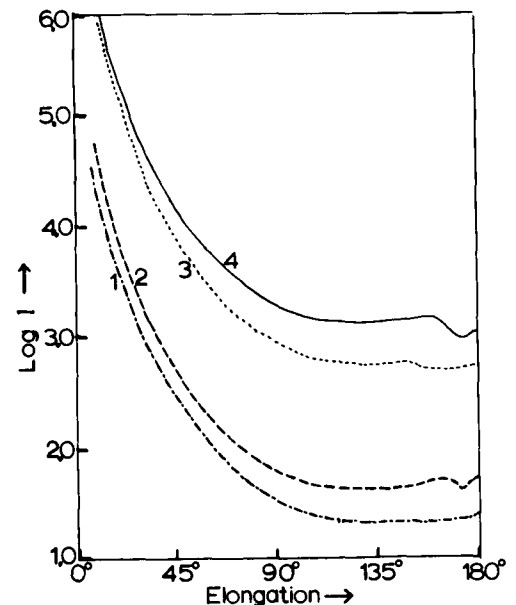


FIGURE 9.—Predicted intensity distributions for models with different values of p and a_B . For each model, $\nu=1.00$, $a_{\min}=0.01\mu$, $a_{\max}=2.00\mu$. For $p=4$ for $a > a_B$, but $p=p_1$ for $a < a_B$, $\tilde{n}=1.33 - 0.01i$; $N_0=2.21 \times 10^{-11}$. For curve 1, $p_1=3$, $a_B=0.50\mu$. For curve 2, $p_1=3$, $a_B=1.50\mu$. For curve 3, $p_1=2$, $a_B=0.60\mu$. For curve 4, $p_1=2$, $a_B=1.00\mu$.

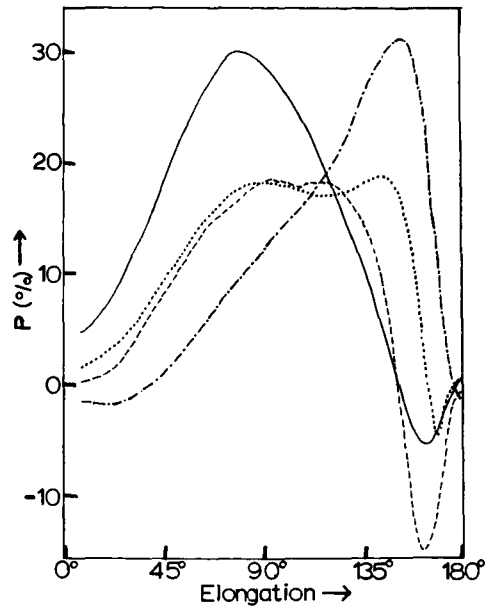


FIGURE 10.—Predicted ecliptic polarizations for models with different values of p and a_B . Choices of parameters are the same as for figure 9, $a_{\min}=0.01\mu$, $a_{\max}=2.00\mu$, $\nu=1.00$, $\tilde{n}=1.33-0.01i$, $p=4$ for $a > a_B$. Solid curve, $p_1=3$, $a_B=0.50\mu$; dotted curve, $p_1=3$, $a_B=1.50\mu$; dashed curve, $p_1=2$, $a_B=0.60\mu$; dot-dash curve, $p_1=2$, $a_B=1.00\mu$.

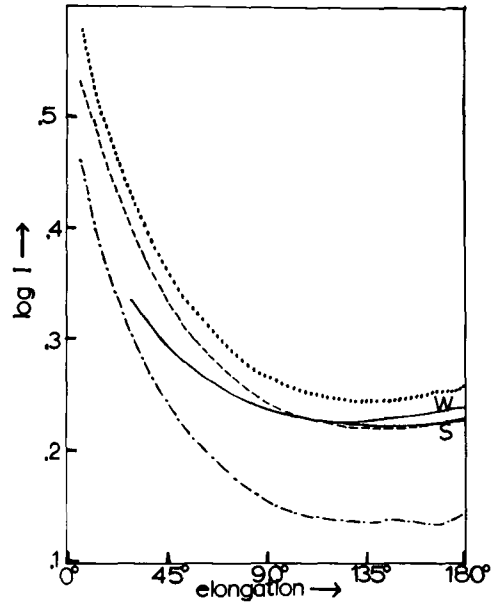


FIGURE 11.—Ecliptic intensity distribution for selected models. Solid curve, observed values (Smith et al. and Weinberg). Theoretical curves are computed for $a_{\min}=0.01\mu$, $a_{\max}=2.00\mu$, $\nu=1.00$, and $\tilde{n}=1.33-0.01i$, $p=4$ for $a > a_B$. Dotted curve, $p_1=2.0$, $a_B=0.40\mu$; dashed curve, $p_1=2.3$, $a_B=0.50\mu$; dot-dash curve, $p_1=3.0$, $a_B=0.60\mu$.

unacceptable colors. The best case, with $p=4.0$, predicted too high a polarization peak. We also calculated a set of isophotes for this model.

Next, we tried a distribution law of the form of equation (3) with two values of p (eq. 5). For radii, $a > a_B$, $p=p_U$ was always chosen as 4.0. For $a < a_B$, $p=p_L$ was assigned a series of values, -6.0 , -4.0 , -2.0 , 0.0 , 1.0 , 2.0 , and 3.0 and a_B values $=0.40, 0.50, 1.0$, and 1.50 . Investigation of a fair number of a_B-p_L pairs soon showed that certain combinations of the parameters would not work. If a_B was too large, or if p_L was too small, the maximum polarization always occurred near elongations of 150° (with large negative polarizations near the Sun). The transition from a peak near 90° to one near 150° occurred rather suddenly; for $p_L=3$, $a_B=1.50$ and $p_L=2$, $a_B=0.60$, a double peak occurred. Hence models with too few small particles must be avoided. Increasing a_B or decreasing p_L produces these effects. The best models obtained so far are those given in figures 11 and 12. They correspond to $a_{\min}=0.01\mu$, $p_U=4.0$ (a greater than a_0) and $a_B=0.40\mu$, $p_L=2.0$; $a_B=0.50\mu$, $p_L=2.3$;

$a_B=0.60\mu$, $p=3.0$. The predicted polarizations are almost within the observational error limits of Weinberg's results. Furthermore, there is no sudden dip in the gegenschein intensity near 180° . We notice, however, that the observed curve rises much less steeply at small elongations than does the curve predicted by our model. The spatial distribution of the particles will have to be somewhat revised. Although, by setting ν below 0.5, it might be possible to obtain intensity curves that will fit the observations, a better model might be obtained by postulating no particles near the Sun, or a steep decline in particle number somewhere within the Earth's orbit. With the present model, the best we can do is juggle the value of ν until there results a fit with the intensity distribution and N_0 can be found.

The next step is to adjust the value of K to get the best representation of the isophotes. In figures 13 and 14 we give both the predicted isophotal contours and the polarization contours. These calculations have been plotted for the $p=0$ model, only. Comparison with observa-

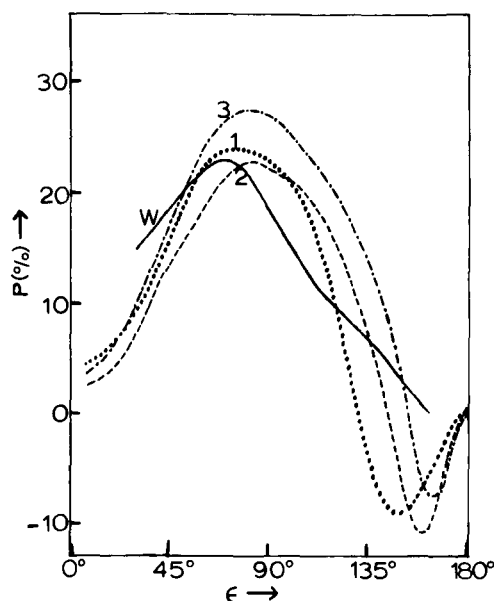


FIGURE 12.—Polarization for selected models with different values of p and a_B . Solid curve is observed polarization (Weinberg). Theoretical curves are computed with theoretical parameters assumed as follows: $p=4.0$, $a > a_B$, $\nu=1.00$, $\tilde{n}=1.33-0.01i$, $a_{\min}=0.01\mu$. Dotted curve, $p_1=2.0$, $a_B=0.40\mu$; dashed curve, $p_1=2.3$, $a_B=0.50\mu$; dot-dash curve, $p_1=3$, $a_B=0.60\mu$.

tions suggest that further adjustments in the size parameters and spatial distributions are required. In particular, the very large polarizations predicted at high celestial latitudes do not appear to be substantiated by the observations.

It appears that a large number of models can be made to fit the observations about equally well. One can generate a family of models by taking any reasonably good model, slightly decreasing p_L and reducing a_B at the same time (by an appropriate amount) or by increasing both. Of course, by assuming different analytical forms for size and space distribution, we may be able to get a better representation of the data.

All of our Mie theory models that come close to fitting the observed polarization and intensity curves suggest one conclusion: On the average, the zodiacal light is about 0.2 magnitude bluer than the Sun in both the $V-G$ and $G-R$ color indices. Such a color difference is probably not easily observable with present techniques, but good color observations eventually will become available. Ideally, different refractive indices could lead to different predicted color differences,

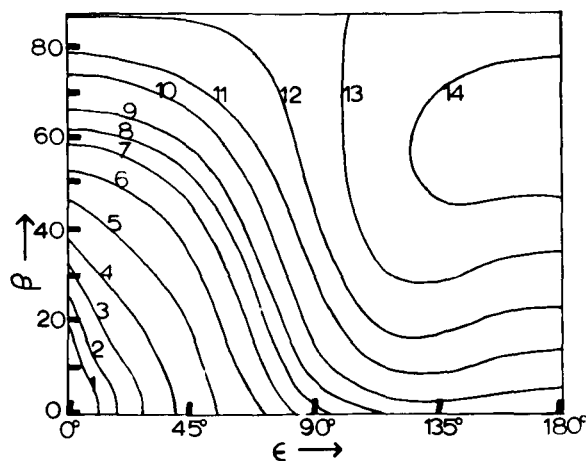


FIGURE 13.—Predicted zodiacal-light isophotes. Isophotes are plotted as functions of celestial latitude, β , and elongation, ϵ . Data are uncertain for values of β exceeding 70° , near the Sun where the intensity rises rapidly, and near the gegenschein. Parameter values are $p=4.0$ (all particle sizes), $\nu=1.00$, and $K=5.0$. Intensity contours are as follows:

Curve	Intensity
1	4.54×10^{-4}
2	1.50×10^{-4}
3	4.98×10^{-5}
4	1.64×10^{-5}
5	5.45×10^{-6}
6	2.38×10^{-6}
7	1.37×10^{-6}
8	1.04×10^{-6}
9	7.75×10^{-7}
10	5.96×10^{-7}
11	4.52×10^{-7}
12	3.43×10^{-7}
13	2.60×10^{-7}
14	1.97×10^{-7}

and color-dependent polarizations, so that color observations might help decide between possible compositions of the zodiacal cloud. In practice, the particles may be irregular and comparisons with Mie theory predictions may be of limited usefulness. The Mie particles require a large number of very small contributors which will give a distinctly bluish zodiacal cloud. The same intensity distribution and polarization may be produced with larger particles that do not scatter at all according to the Mie theory (cf., e.g., Southworth, 1964).

ACKNOWLEDGMENT

We acknowledge, with thanks, advice from B. J. O'Mara, and help from John Ross, D. Locke, James Vanyo, and Robert Wolfe. The program was supported in part by NASA.

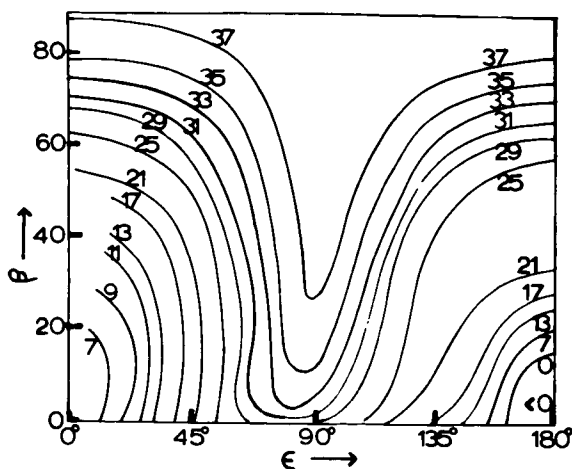


FIGURE 14.—Predicted zodiacal-light contours of equal polarization. Notice that this model, with $p=4.0$, for all values of a , $\nu=1.00$, $K=5.0$, predicted very high polarizations at high celestial latitudes.

REFERENCES

- ALLEN, C. W., 1946, *Mon. Not. Roy. Astron. Soc.*, **106**, 137.
 BARBIER, D., 1955, *Mém. Soc. Roy. Sci. Liège*, **15**, 55.
 BEARD, D. B., 1959, *Astrophys. J.*, **129**, 496.
 BEGGS, D. W., D. E. BLACKWELL, D. W. DEWHIRST, and R. D. WOLSTENCROFT, 1964, *Mon. Not. Roy. Astron. Soc.*, **127**, 319.
 BEHR, A., and H. SIEDENTOPF, 1953, *Zeits. f. Astrophys.*, **32**, 19.
 BELTON, M. J. S., 1966, *Science*, **151**, 35.
 BLACKWELL, D. E., 1955, *Mon. Not. Roy. Astron. Soc.*, **115**, 629.
 —, 1956, *Mon. Not. Roy. Astron. Soc.*, **116**, 365.
 BLACKWELL, D. E., and M. F. INGHAM, 1961, *Mon. Not. Roy. Astron. Soc.*, **122**, 113.
 DIVARI, N. B., and A. S. ASAAD, 1960, *Soviet Astron.—AJ*, **3**, 832.
 DIVARI, N. B., S. N. KRYLOVA, and W. L. MOROZ, 1964, *Geomag. and Aeron.*, **4**, 684.
 DUMONT, R., 1965, *Ann. d'Astrophys.*, **28**, 265.
 ELSÄSSER, H., 1963, *Planetary Space Sci.*, **11**, 1015.
 ELVEY, C. T., and F. E. ROACH, 1937, *Astrophys. J.*, **85**, 213.
 FESENKOV, V. G., 1958a, *Soviet Astron.—AJ*, **2**, 299.
 —, 1958b, *Soviet Astron.—AJ*, **2**, 475.
 GIESE, R. H., 1961, *Zeits. f. Astrophys.*, **51**, 119.
 —, 1963, *Space Science Reviews*, **1**, 589.
 GIESE, R. H., and H. SIEDENTOPF, 1962, *Zeits. f. Astrophys.*, **54**, 200.
 GILLET, F. C., W. F. HUCH, E. P. NEY, and G. COOPER, 1964, *J. Geophys. Res.*, **69**, 2827.
 HARWIT, M., 1963, *J. Geophys. Res.*, **68**, 2171.
 —, 1964, *Mém. Soc. Roy. Sci. Liège*, ser. 5, **IX**, 506.
 HOFFMEISTER, C., 1930, *Veröff. Univ.-Sternw. Berlin-Babelsberg*, **VIII**, Heft 2, 63 pp.
 —, 1932, *Veröff. Univ.-Sternw. Berlin-Babelsberg*, **X**, Heft 1, 111 pp.
 HURUHATA, M., 1951, *Publ. Astron. Soc. Japan*, **2**, 156.
 INGHAM, M. F., 1961, *Mon. Not. Roy. Astron. Soc.*, **122**, 157.
 LITTLE, S. J., B. J. O'MARA, and L. H. ALLER, 1965, *Astron. J.*, **70**, 346.
 PETERSON, A. W., 1961, *Astrophys. J.*, **133**, 668.
 REGENER, V. H., 1955, *Astrophys. J.*, **122**, 520.
 RICHTER, N. B., 1962, *Quart. J. Roy. Astron. Soc.*, **3**, 179.

- ROACH, F. E., 1964, *Space Science Reviews*, **3**, 512.
ROBLEY, R., 1962, *Ann. de Geophys.*, **18**, 341.
SMITH, L. L., F. E. ROACH, and R. W. OWEN, 1965, *Planetary Space Sci.*, **13**, 207.
SOUTHWORTH, R. B., 1964, *Ann. N.Y. Acad. Sci.*, **119**, 54.
VAN DE HULST, H. C., 1947, *Astrophys. J.*, **105**, 471.
WEINBERG, J. L., 1964, *Ann. d'Astrophys.*, **27**, 718.
WHIPPLE, F. L., 1955, *Astrophys. J.*, **121**, 750.

37. Phase Function of the Zodiacal Cloud

RICHARD B. SOUTHWORTH
Smithsonian Astrophysical Observatory
Cambridge, Massachusetts

Smith, Roach, and Owen's zodiacal-light photometry has been analyzed for the phase function and distribution of the particles. It is assumed that (1) there is a unique phase function, (2) the space density is the product of a distribution in heliocentric latitude and another in radius vector, and (3) all the observed light is scattered by interplanetary particles symmetrically distributed about the Sun, except for the enhancement at 65° elongation (possibly this is double scattering by ice in the high atmosphere). Various distributions in radius vector are tried, each yielding a phase function and a latitude distribution, and a predicted zodiacal-light distribution. Good fits to the observations are found with radial-density distributions similar to that found from radar meteors; these also yield latitude distributions comparable to the meteor distribution. For scattering angles above 60°, the phase functions resemble a Lambert law, except for an extra peak near 180°, which could be caused by particle roughness.

A COMPLETE GENERAL ACCOUNT of the relationship between the observed brightness of the zodiacal light and the cloud of interplanetary particles that scatter the Sun's light to the Earth must consider a particle distribution with several degrees of freedom. The cloud doubtless contains many types of particles, each with a distinct scattering (phase) function, distributed in three dimensions. Time, polarization, and color are other variables that will not be considered here. On the other hand, the observed zodiacal-light brightness (with time, polarization, and color again neglected) has only two dimensions. Thus, the observations alone are not sufficient to specify all the properties of the cloud. Nonetheless, with reasonable simplifications, the observations are enough to deduce some important average properties.

Hapke (1965) has shown that the effect of low-energy proton bombardment on a wide variety of substances is to make their scattering functions nearly similar. Thus, we can expect that

all except the newest zodiacal particles in fact have approximately the same scattering function, as a consequence of the solar wind. For this paper, however, it is sufficient to assume that there is a homogeneous mixture of particles. The scattering function to be found here is, then, a mean scattering function.

It will be assumed here that the zodiacal light is scattered primarily by a heliocentric, and not a geocentric, cloud. It is then clear that the cloud is symmetric about an axis through the Sun and the ecliptic poles. Large or small deviations from symmetry must occur, but they will be neglected. The space-density distribution is thus a two-dimensional one. A point in this distribution will be specified here by its radius vector, r , and its heliocentric latitude, β .

The particles in the cloud spiral toward the Sun under the influence of the Poynting-Robertson effect (Whipple, 1955). Figure 1 (from Southworth, 1964) shows the time average of the relative space density of a single particle, as a

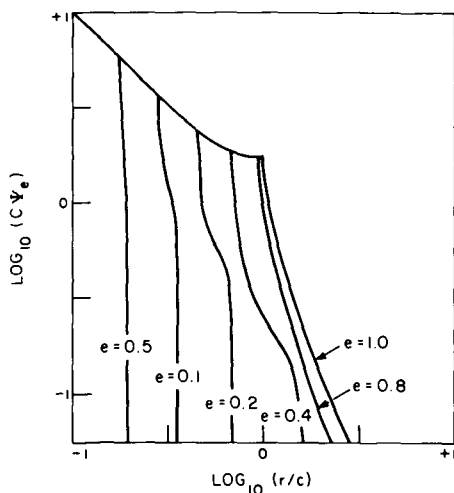


FIGURE 1.—Average space density, Ψ_e of particles spiraling toward Sun under Poynting-Robertson effect, as a function of radius vector, r , orbital invariant $C = (a/2)(1-e^2)e^{-4/5}$, and initial eccentricity, e . For any value of e the graph of Ψ_e consists of a nearly vertical curve (interpolated if necessary) marked with the value of e , and also of that part of the upper diagonal curve that lies to the left of the nearly vertical curve. Intersection of the two curves occurs at the perihelion distance of the initial orbit.

function of r . Figure 2 shows schematically the relative space density to be expected from many such particles injected into the cloud as cometary

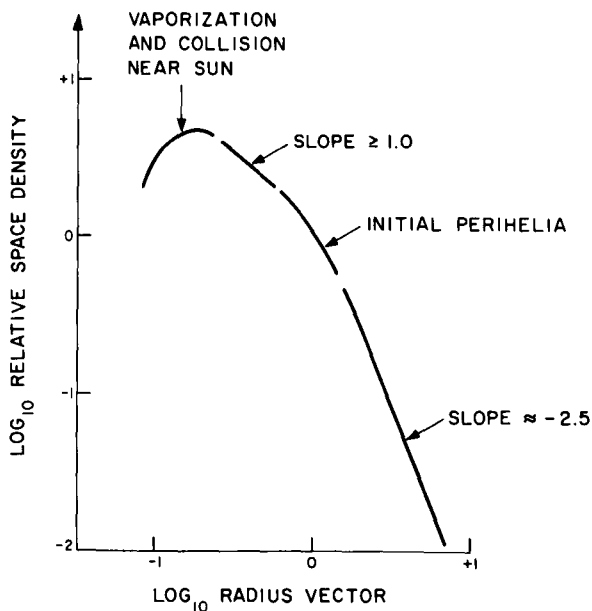


FIGURE 2.—Schematic drawing of density distribution under the Poynting-Robertson effect.

debris. These are released near the perihelia of the comets, with nearly parabolic initial orbits (Southworth, 1964). The initial perihelia of the particles are thus the same as those of the comets, roughly half of which (Richter, 1963) lie between 0.5 and 1.5 AU.

The Poynting-Robertson effect does not alter the plane of a particle's orbit, but it gradually alters the distribution of true anomalies in the orbit. Initially, when the orbit is highly eccentric, the particle spends most of its time near aphelion, with true anomaly in the neighborhood of 180° . Later, when the orbit is less eccentric, true anomalies are more uniformly spread. Since this will also change the distribution of heliocentric latitudes, an estimate of the magnitude of the change is needed here. On the hypothesis of a cometary origin for the zodiacal particles (and also on some other hypotheses), it is expected that the initial orbits of the particles will be similar to the orbits of short-period comets. This is because a few of the particles will be released from short-period comets, and many of the rest, released from bright long-period comets, will soon be perturbed by Jupiter into short-period orbits in exactly the same way that the comets themselves are perturbed. Like the comets (Porter, 1963), the particles will have values of the argument of perihelion clustered near 0° and 180° ; i.e., their aphelia and perihelia will tend to be at lower heliocentric latitudes than the intermediate sections of their orbits.

Figure 3 is a contour diagram of the time average of the relative space density of a particle under the Poynting-Robertson effect, as a function of both radius vector and true anomaly, computed by numerical integration. It shows how the space densities in figure 1 are distributed over true anomaly. To see how the Poynting-Robertson effect will alter the distribution of heliocentric latitudes, we should compare the average of the densities near perihelion and aphelion (which will be at relatively low latitudes) with the densities in the neighborhood of true anomaly 90° (which will be at relatively high latitudes). We find that, at distances more than two to three times the initial perihelion distance, the particles are concentrated toward aphelion, and hence toward low latitudes. At less than

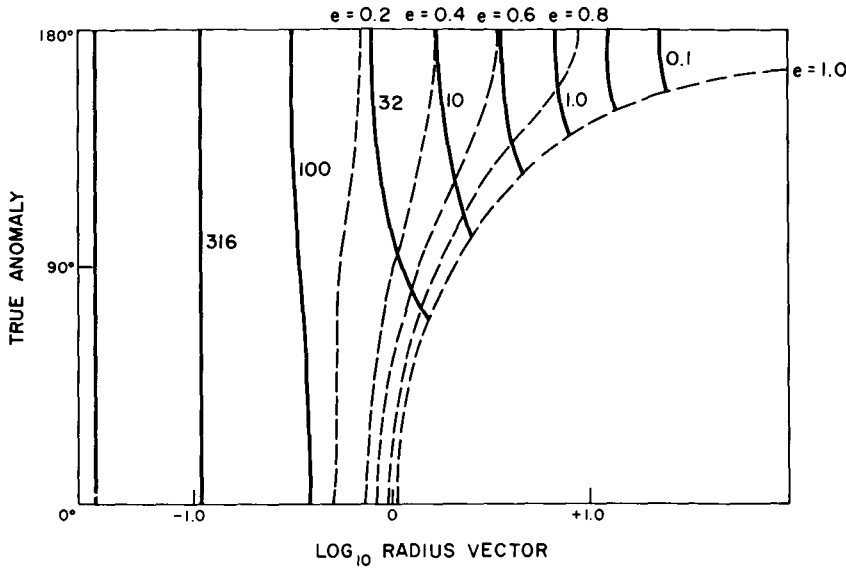


FIGURE 3.—Relative density contours under the Poynting-Robertson effect.

twice the initial perihelion distance, however, the distribution of latitudes will not be significantly biased by the distribution of true anomalies. It follows that the zodiacal cloud should be appreciably more concentrated at low latitudes at roughly 2 or more astronomical units from the Sun than at roughly 1 or less astronomical unit.

MODEL CLOUD

The model of the zodiacal cloud used in the computations to be reported here is defined by three one-dimensional distributions. The scattering function phase function, $T(\theta)$, denotes the light intensity scattered at an angle θ by a unit particle space density and is assumed to be the same in all parts of the cloud. The light scattered is taken to be proportional to the space density, ρ , which is assumed to depend only on r and β and to be of the form

$$\rho(r, \beta) = R(r)S(\beta) \quad (1)$$

Thus, the expected dependence of the latitude distribution on distance from the Sun is not included in the model. Since no observations at less than 30° elongation from the Sun have been used, and since contributions to the observed zodiacal light from more than about 2 AU from the Sun are small, the latitude distribution to be found here represents an average over the range from 0.5 to 2 AU.

In order not to spend a disproportionate amount of computing time on the relatively small volume of space at high heliocentric latitudes, the distribution, S , is treated as a function of $\sin \beta$ rather than of β ; equal intervals of $\sin \beta$ represent equal volumes in space.

A variety of distributions $R(r)$, of a form suggested by figure 2, are assumed. Given R , S , and T , we can formally compute zodiacal-light intensities as

$$I = \int_{\text{Line of sight}} RST \, ds \quad (2)$$

where ds is the differential of distance along the line of sight from the Earth. Since I is a two-dimensional distribution, it suffices to determine a two-dimensional distribution of S and T . For simplicity and numerical stability, however, S and T were assumed to be independent one-dimensional distributions. They are found by successive approximations, as described in the following section.

COMPUTING

The radial-density distribution was taken to be of the form

$$\log_{10} R(r) = C_1 \log_{10} r + C_2 (\log_{10} r)^2 \quad (3)$$

This distribution is smooth (which is essential) and adequately versatile. Table 1 shows the values used for C_1 and C_2 .

TABLE 1.—Numerical Results for 11 Radial-Density Distributions

Case	Radial distribution coefficients		Rms residual in intensity	Latitude-distribution coefficients for—							Phase-function coefficients at—						
	C_1	C_2		0.0	0.1	0.3	0.5	0.7	0.9	1.0	30°	54°	79.2°	104.4°	129.6°	154.8°	180°
1	−0.6	−4	0.492	1.0	0.83	0.52	0.35	0.20	0.16	0.18	2.50	0.29	0.42	0.45	0.61	0.77	1.0
2	−0.6	−2	0.499	1.0	0.85	0.54	0.36	0.21	0.17	0.19	2.52	0.31	0.48	0.49	0.69	0.77	1.0
3	−0.6	0	0.540	1.0	0.87	0.57	0.38	0.22	0.19	0.21	2.72	0.35	0.60	0.56	0.76	0.75	1.0
4	−1.2	−4	0.393	1.0	0.83	0.51	0.36	0.22	0.18	0.20	1.59	0.12	0.32	0.41	0.64	0.76	1.0
5	−1.2	−2	0.383	1.0	0.84	0.52	0.37	0.23	0.19	0.21	1.41	0.12	0.36	0.44	0.66	0.76	1.0
6	−1.2	0	0.399	1.0	0.87	0.54	0.39	0.24	0.20	0.23	1.22	0.13	0.42	0.48	0.70	0.76	1.0
7	−1.8	−4	0.313	1.0	0.83	0.50	0.37	0.24	0.20	0.22	0.85	0.00	0.24	0.38	0.63	0.76	1.0
8	−1.8	−2	0.297	1.0	0.84	0.51	0.38	0.25	0.20	0.23	0.52	0.00	0.26	0.40	0.64	0.76	1.0
9	−1.8	0	0.302	1.0	0.86	0.53	0.40	0.27	0.21	0.24	0.10	0.00	0.28	0.44	0.66	0.76	1.0
10	−2.4	−2	0.419	1.0	0.85	0.51	0.38	0.27	0.21	0.23	0.00	0.00	0.13	0.41	0.59	0.75	1.0
11	−2.4	0	0.582	1.0	0.88	0.54	0.39	0.27	0.23	0.26	0.00	0.00	0.11	0.44	0.60	0.76	1.0

The functions S and T are each taken to be the sum of seven triangular functions, multiplied by coefficients

$$\begin{aligned} S(\sin \beta) &= \sum_j^7 S_j s_j(\sin \beta) \\ T(\theta) &= \sum_k^7 T_k t_k(\theta) \end{aligned} \quad (4)$$

Figure 4 shows how the sum forms a function defined at seven points whose ordinates are the coefficients S_j or T_k , with straight-line segments joining the points.

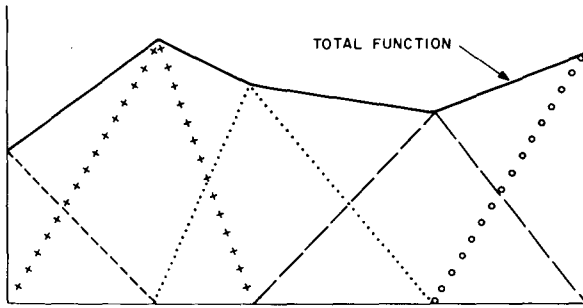


FIGURE 4. — Resolution of a function consisting of n connected straight-line segments into a sum of $n+1$ triangular functions.

The observational equations (2) now become

$$I = \sum_j S_j \sum_k T_k \int_{\text{Line of sight}} s_j t_k R \, ds \quad (5)$$

The integrals in equations (5) are evaluated numerically. The integration was continued to $r=5$ AU, beyond which contributions are negligible.

Initial trial values are assumed for both S_j and T_k , and then equations (5) are solved by least squares for improved values of S_j and T_k , alternately. However, the least-squares solution is not allowed to make any coefficient negative or to make any very large change that might cause unstable iteration. When a coefficient would have exceeded one of these bounds, it is set equal to that bound, and a new least-squares solution is carried out for the remaining variables. Ten iterations or fewer were sufficient in each case to reach a stable solution.

OBSERVATIONS

Smith, Roach, and Owen's (1965) observations have been used. Following their estimates of observational errors, the standard error, σ , of an intensity, I , was taken to be

$$\sigma = (361 + 0.01I^2)^{1/2} \quad (6)$$

They note an excess brightness in their observations at an elongation of about 65° . This excess was not observed by Wolstencroft and Rose (1967) and cannot be reconciled with a model of zodiacal particles under the Poynting-Robertson effect. Accordingly, smooth curves have been empirically drawn through the observations and have removed this excess. The appendix describes a possible, but not very probable, cause for the excess brightness. Table 2 contains the observations used, as corrected.

Table 2 presents observations used for all cases, and includes detailed results for case 8. The observations were corrected for the excess brightness observed at 65° elongation from the Sun. Three hundred were then chosen to represent the distribution over the whole sky, with comparatively few in the region of small elongation, which was not so well observed as other regions.

The table is arranged in rows by latitude. For each point, the quantities printed are: the longitude measured from the Sun, the corrected intensity, the residual from the final fit, and the residual divided by the standard error assigned to the observation.

LATITUDE DISTRIBUTION

Table 1 shows the radial-density distributions used and the resulting rms error of an individual observation in units of the expected observational error. All these radial distributions make acceptable fits to the observations, but the best fit is case 8, which is also the best fit to figure 2. Table 2 includes the individual residuals of each observation for case 8—both in the original units and in terms of the estimated observational error.

Table 1 shows all values found for the latitude coefficients S_j , which are remarkably insensitive to the radial distribution. Figure 5 shows the latitude distribution for case 8; the others hardly

TABLE 2.—*Reticuled Results for Case 8*

Lat., deg.	Long., deg.	30.	35.	40.	45.	50.	55.	60.	65.	70.	75.	80.	85.	90.	95.	100.	105.	110.	115.	120.	125.
0	INT	2330.	1595.	1185.	945.	745.	600.	500.	425.	370.	320.	290.	265.	250.	235.	220.	210.	200.	190.	185.	180.
	O-C	228.7	77.2	51.8	70.2	45.5	19.9	6.7	-2.1	-5.3	-14.1	-10.9	-9.4	-3.4	-1.8	-3.7	-3.8	-5.8	-9.2	-8.4	-8.3
	*/SIG	0.98	0.48	0.43	0.73	0.59	0.32	0.12	-0.04	-0.13	-0.38	-0.31	-0.29	-0.11	-0.06	-0.13	-0.13	-0.21	-0.34	-0.32	-0.32
5	Long., deg.	130.	135.	140.	150.	160.	170.	180.													
	INT	175.	175.	175.	170.	175.	185.	205.													
	O-C */SIG	-8.4 -0.32	-4.1 -0.16	-1.0 -0.04	-4.1 -0.16	-5.3 -0.20	-5.6 -0.21	1.4 0.05													
10	Long., deg.	35.	40.	45.	50.	55.	60.	65.	70.	75.	80.	85.	90.	95.	100.	105.	110.	120.	130.	140.	150.
	INT	1145.	870.	735.	610.	505.	425.	370.	335.	300.	275.	255.	235.	215.	205.	200.	190.	180.	175.	170.	165.
	O-C */SIG	-41.2 -0.35	-44.7 -0.50	9.1 0.12	15.9 0.25	1.6 0.03	-10.7 -0.23	-12.7 -0.31	-5.5 -0.14	-6.4 -0.18	-3.3 -0.10	-0.6 -0.02	-2.5 -0.08	-8.2 -0.28	-7.0 -0.25	-3.4 -0.12	-6.6 -0.24	-6.0 -0.23	-2.0 -0.08	-0.3 -0.01	-3.6 -0.14
15	Long., deg.	160.	170.	180.																	
	INT	170.	175.	195.																	
	O-C */SIG	-4.5 -0.18	-8.8 -0.34	3.6 0.13																	
20	Long., deg.	30.	35.	40.	45.	50.	55.	60.	65.	70.	75.	80.	85.	90.	95.	100.	110.	120.	130.	140.	150.
	INT	905.	690.	505.	425.	370.	330.	305.	285.	265.	245.	230.	215.	200.	190.	185.	175.	170.	165.	160.	155.
	O-C */SIG	110.8 1.20	53.8 0.75	-14.8 -0.27	-12.1 -0.26	-10.6 -0.25	-13.2 -0.35	-9.1 -0.25	-4.0 -0.12	-1.9 -0.06	-2.5 -0.08	-0.6 -0.02	-1.1 -0.04	-4.3 -0.16	-4.8 -0.18	-2.4 -0.09	-2.4 -0.09	-0.3 -0.01	0.9 0.04	1.3 0.05	-1.7 -0.07

Lat., deg.	Long., deg.	160.	170.	180.																	
	INT O-C */SIG	155. -4.6 -0.19	160. -5.4 -0.22	175. 6.8 0.26																	
20	Long., deg.	30.	35.	40.	45.	50.	55.	60.	65.	70.	75.	80.	85.	90.	95.	100.	120.	150.	180.		
	INT O-C */SIG	545. -40.9 -0.71	450. -40.7 -0.83	390. -25.6 -0.59	345. -14.3 -0.36	315. -5.6 -0.15	290. -3.6 -0.10	270. -0.9 -0.03	255. 3.4 0.11	240. 5.0 0.16	225. 4.4 0.15	210. 2.0 0.07	195. -2.1 -0.08	185. -3.2 -0.12	180. -1.0 -0.04	175. -0.2 -0.01	165. 2.4 0.10	150. -1.0 -0.04	165. 7.1 0.28		
25	Long., deg.	25.	30.	35.	40.	45.	50.	55.	60.	65.	70.	75.	80.	85.	90.	95.	110.	120.	130.	140.	150.
	INT O-C */SIG	520. 27.1 0.49	465. 36.5 0.73	410. 33.7 0.75	360. 27.9 0.68	315. 16.8 0.46	285. 10.4 0.30	255. -1.4 -0.04	240. 0.2 0.01	225. -0.2 -0.01	210. -2.2 -0.08	200. -0.7 -0.02	190. -0.2 -0.01	180. -1.6 -0.06	175. 0.6 0.02	170. 1.3 0.05	165. 6.3 0.25	160. 5.1 0.20	155. 3.5 0.14	155. 7.5 0.31	150. 4.7 0.19
	Long., deg.	160.	170.	180.																	
	INT O-C */SIG	145. -0.3 -0.01	150. 3.1 0.13	155. 7.0 0.28																	
30	Long., deg.	30.	40.	50.	60.	70.	80.	90.	100.	120.	150.	180.									
	INT O-C */SIG	300. -24.7 -0.70	250. -17.6 -0.56	230. -7.6 -0.26	200. -14.6 -0.53	180. -14.1 -0.54	160. -16.5 -0.67	155. -8.5 -0.35	155. -0.3 -0.01	145. -3.3 -0.14	145. 4.2 0.18	150. 9.3 0.38									
35	Long., deg.	25.	30.	35.	40.	45.	50.	55.	60.	65.	70.	75.	80.	85.	90.	95.	110.	120.	130.	140.	150.
	INT O-C */SIG	245. -37.4 -1.21	230. -27.7 -0.93	225. -12.2 -0.41	215. -7.3 -0.25	205. -8.8 -0.31	200. -7.7 -0.28	195. -5.7 -0.21	185. -8.3 -0.31	180. -5.9 -0.23	175. -3.7 -0.14	170. -1.7 -0.07	170. 5.1 0.20	165. 5.8 0.23	160. 5.5 0.22	155. 4.4 0.18	150. 5.7 0.23	150. 7.5 0.31	145. 4.1 0.17	145. 6.2 0.26	140. 3.4 0.14

TABLE 2.—Reticuled Results for Case 8—Continued

Lat., deg.	Long., deg.	160.	170.	180.																	
	INT O-C */SIG	135. -0.6 -0.03	135. -0.4 -0.02	140. 4.6 0.20																	
	Long., deg.	15.	25.	35.	45.	55.	65.	75.	85.	120.	150.	180.									
40	INT O-C */SIG	235. -26.2 -0.87	225. 0.2 0.01	215. 13.7 0.48	205. 15.4 0.55	190. 9.7 0.36	170. -0.6 -0.02	160. -0.1 -0.00	155. 4.5 0.18	135. -2.3 -0.10	125. -8.2 -0.36	125. -6.4 -0.28									
	Long., deg.	10.	15.	20.	25.	30.	35.	40.	45.	50.	55.	60.	65.	70.	75.	80.	90.	100.	110.	120.	130.
45	INT O-C */SIG	210. -8.2 -0.29	205. -3.9 -0.14	205. 6.8 0.24	200. 11.2 0.40	195. 12.8 0.47	190. 11.5 0.43	185. 9.8 0.37	180. 8.2 0.31	170. 1.5 0.06	165. -0.1 -0.00	155. -6.5 -0.26	145. -12.9 -0.54	140. -14.1 -0.60	135. -15.1 -0.65	135. -11.4 -0.49	135. -5.0 -0.21	135. -0.7 -0.03	135. 1.5 0.07	135. 2.3 0.10	135. 2.9 0.12
	Long., deg.	140.	150.	160.	170.	180.															
	INT O-C */SIG	135. 3.5 0.15	130. -0.5 -0.02	130. 0.7 0.03	130. 1.3 0.06	130. 1.5 0.06															
	Long., deg.	0.	10.	20.	30.	40.	50.	60.	70.	100.	140.	180.									
50	INT O-C */SIG	180. -5.2 -0.20	180. -1.2 -0.05	175. 2.4 0.09	170. 4.5 0.18	165. 4.4 0.17	160. 4.1 0.16	155. 4.3 0.17	145. 0.0 0.00	135. 4.1 0.18	130. 1.9 0.08	125. -1.4 -0.06									
	Long., deg.	0.	5.	10.	15.	20.	25.	30.	35.	40.	45.	50.	55.	60.	65.	70.	75.	90.	105.	120.	135.
55	INT O-C */SIG	165. 1.7 0.07	165. 2.1 0.08	165. 3.2 0.13	160. -0.1 -0.00	160. 2.0 0.08	155. -0.8 -0.03	150. -3.5 -0.15	150. -1.4 -0.06	145. -4.5 -0.19	145. -2.8 -0.12	140. -6.0 -0.25	140. -7.0 -0.17	135. -4.9 -0.30	135. -7.5 -0.21	130. -5.1 -0.33	130. 0.7 -0.22	130. 0.3 0.03	130. 4.1 0.18	125. 0.1 0.00	120. -4.9 -0.22

Lat., deg.	Long., deg.	150.	165.	180.																	
	INT O-C */SIG	125. 0.2 0.01	125. 0.4 0.02	125. 0.5 0.02																	
	Long., deg.	0.	15.	30.	45.	60.	75.	100.	140.	180.											
60	INT O-C */SIG	155. 5.1 0.21	150. 1.9 0.08	145. 1.0 0.04	140. 0.5 0.02	135. -0.1 -0.00	125. -4.7 -0.21	125. 1.8 0.08	125. 3.1 0.14	125. 3.0 0.13											
	Long., deg.	0.	10.	20.	30.	40.	50.	60.	70.	80.	90.	100.	110.	120.	130.	140.	150.	160.	170.	180.	
65	INT O-C */SIG	150. 9.9 0.41	150. 10.4 0.43	145. 6.7 0.28	140. 3.6 0.15	140. 5.8 0.25	135. 3.2 0.14	130. 0.7 0.03	130. 3.5 0.15	125. 1.0 0.04	125. 3.1 0.13	120. -0.4 -0.02	120. 0.6 0.03	125. 6.0 0.27	125. 5.9 0.26	125. 5.8 0.25	125. 5.6 0.25	125. 5.5 0.24	125. 5.4 0.24	125. 5.4 0.24	
	Long., deg.	0.																			
70	INT O-C */SIG	145. 12.5 0.52																			
	Long., deg.	0.	15.	30.	45.	60.	75.	90.	105.	120.	135.	150.	165.	180.							
75	INT O-C */SIG	135. 8.7 0.37	135. 9.0 0.39	130. 5.2 0.23	130. 7.1 0.31	130. 9.0 0.39	125. 6.0 0.26	125. 7.6 0.33	120. 3.8 0.17	120. 4.5 0.20	115. -0.2 -0.01	115. -0.1 -0.01	115. -0.2 -0.01	115. -0.3 -0.01							
	Long., deg.	0.	20.	40.	60.	80.	100.	120.	140.	160.	180.										
80	INT O-C */SIG	130. 8.8 0.38	130. 9.2 0.40	125. 5.3 0.23	125. 6.8 0.30	125. 8.3 0.37	115. -0.5 -0.02	115. 0.4 0.02	115. 0.8 0.04	115. 1.1 0.05	115. 1.1 0.05										

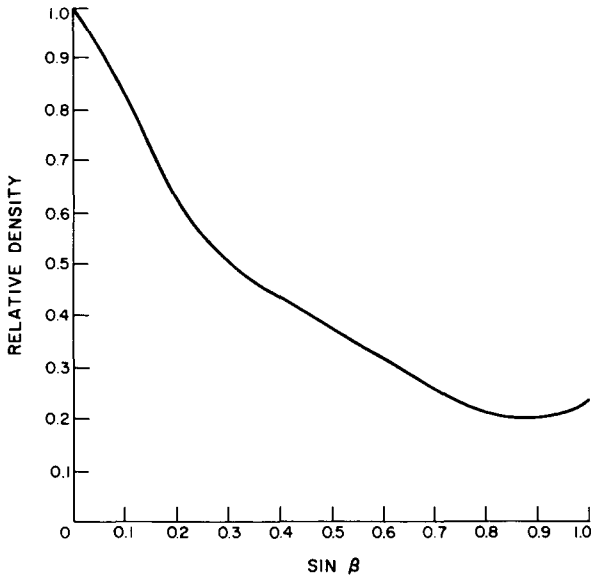


FIGURE 5.—Latitude distribution for case 8.

differ. The minor maximum at 90° latitude is not likely to be real. It possibly results from inadequate correction of the observations for the peak at elongation 65° , or more probably from the known inadequacy of the assumption expressed in equation (1).

The width of the latitude distribution is a very satisfactory confirmation that the zodiacal particles are in orbits like those of the short-period comets.

PHASE FUNCTION

Table 1 further gives all values for the phase-function coefficients T_k ; the distributions are plotted in figure 6, with the scale successively displaced upward 0.1 for each distribution. The distribution found between 30° and 54° depends strongly on the assumed radial density. It is likely that this part of the phase function (if it is real) can be explained by classical diffraction.

The major part of the phase function found here is not very sensitive to the assumed radial-density distribution, and consequently merits some attention. It is doubtless possible to produce a similar curve with several different sorts of particles, especially as this is only an average curve. However, it should be pointed out that the function found is very similar to a Lambert law, which is the phase function in diffuse reflection by smooth spherical particles much

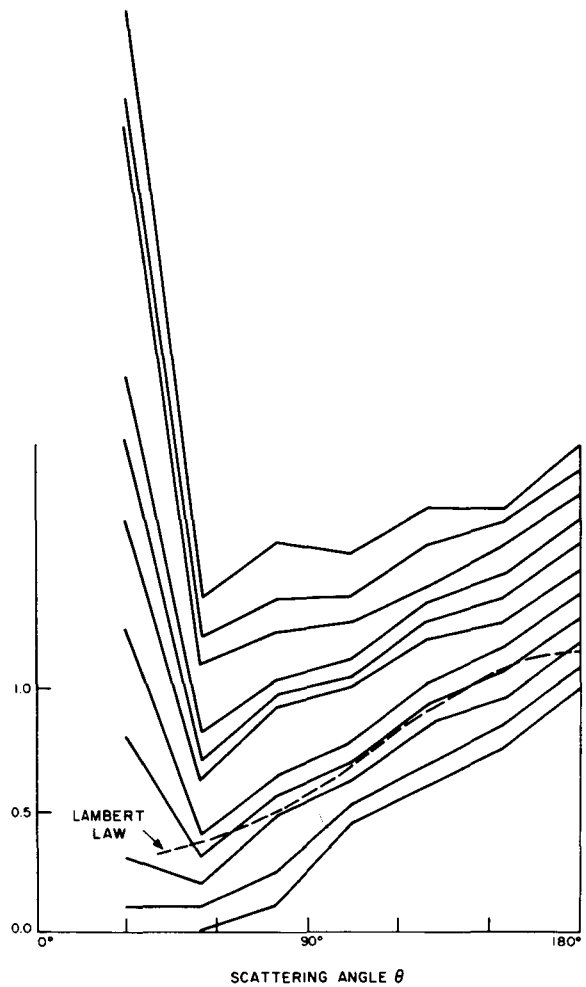


FIGURE 6.—Phase functions.

larger than a wavelength of light. Figure 6 includes a Lambert law curve fitted to case 8. Rough particles would be expected to show an extra peak in the phase function at 180° because shadows are then eliminated. The phase function found here, in fact, has just such a peak. It would be expected that particles from comets should be rough, in harmony with the phase function found.

One more confirmation is still available. According to classical theory (van de Hulst, 1957), the luminous intensity at wavelength, λ , diffracted at an angle, θ , to a distance, r , by a spherical particle of radius, a , under incident intensity, I_o , is

$$I_D = \frac{a \lambda I_o}{2 \pi^2 r^2 \sin^3 \theta} \quad (7)$$

if θ is outside the first few diffraction rings and if the rings have been smoothed out. The corresponding scattered intensity from a Lambert law particle that scatters a fraction, A , of the total light incident on it is

$$I_L = \frac{2a^2 A I_0 (\sin \theta - \theta \cos \theta)}{3\pi r^2} \quad (8)$$

Evaluating I_D at $\theta = 30^\circ$ and I_L at $\theta = 150^\circ$, with $\lambda = 5300\text{\AA}$ and $A = 0.07$ as for the Moon, and comparing with the results of case 8, we find

$$a \sim 6\mu$$

This value can be no more than an order-of-magnitude estimate, both because we actually must consider distributions of particle sizes and because the phase-function results are uncertain. Nonetheless, it tends to confirm that the zodiacal particles are large compared with the wavelength of light, in harmony with the appearance of a phase function appropriate to large particles.

CONCLUSIONS

The latitude and radius-vector distributions deduced here are compared with the meteor space-density distribution in paper 31. The radius-vector distribution of the meteors is not as steep as that for case 8 or as the equilibrium Poynting-Robertson distribution. Presumably this is caused by collisions of the meteors with zodiacal dust, while collisions would be much less important for the zodiacal dust itself, which spirals in faster. The meteor latitude distribution is similar in character to that of the meteors, although the meteors have a wider distribution in latitude near the Sun than far out. This characteristic was also theoretically expected in the zodiacal distribution, but had been omitted from the model for simplicity.

The space distribution of the zodiacal particles as found here is entirely accordant with a come-

tary origin and with subsequent evolution under planetary perturbations and the Poynting-Robertson effect.

The mean phase function of the zodiacal particles has a broad peak in the backscatter direction. The phase function is consistent with opaque, rough particles much larger than the wavelength of light.

APPENDIX—POSSIBLE CAUSE OF EXCESS BRIGHTNESS

The anomalous excess of brightness that Smith, Roach, and Owen (1965) found at approximately 65° elongation off the ecliptic could be explained by double scattering of sunlight in ice crystals at the noctilucent-cloud level. The light would be scattered twice, once into the common 22° halo and once into the 46° halo. (See, for example, Minnaert, 1954.) Figure 7 is a schematic diagram for the double scattering. Clouds B and D are approximately 82 km above sea level. Sight lines A and C pass above the tropopause (roughly 15 km above sea level), but they do not pass much above it because cloud B must be in sunlight at the same time that the Sun is more than 18° below the horizon at F. The maximum depression of the Sun at F, when A and C graze the tropopause and when D is 10° above the horizon at F, is 29° . Sight lines A and C are necessarily in different vertical planes. The azimuth difference between the planes is from 14° to 19° when the scattering angle at B is 22° , and from 43° to 46° when the scattering angle at B is 46° . Sight lines C and E are generally in different vertical planes.

When skew rays are considered, both the 22° and 46° halos are actually a few degrees wide even for monochromatic light. For simplicity, however, their width is neglected in figure 8, which is a schematic diagram of the celestial sphere for the case of 22° scattering at B. A comparable diagram for the case of 46° scattering at B can be readily imagined. The Sun is depressed 18° to 29° below the horizon at F.

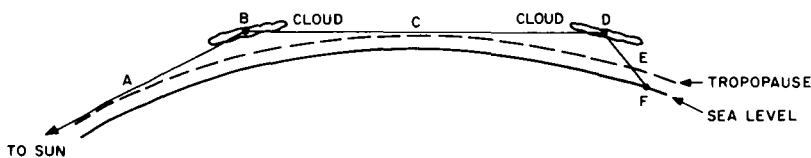


FIGURE 7.—Schematic drawing of model for scattering of sunlight by ice clouds.

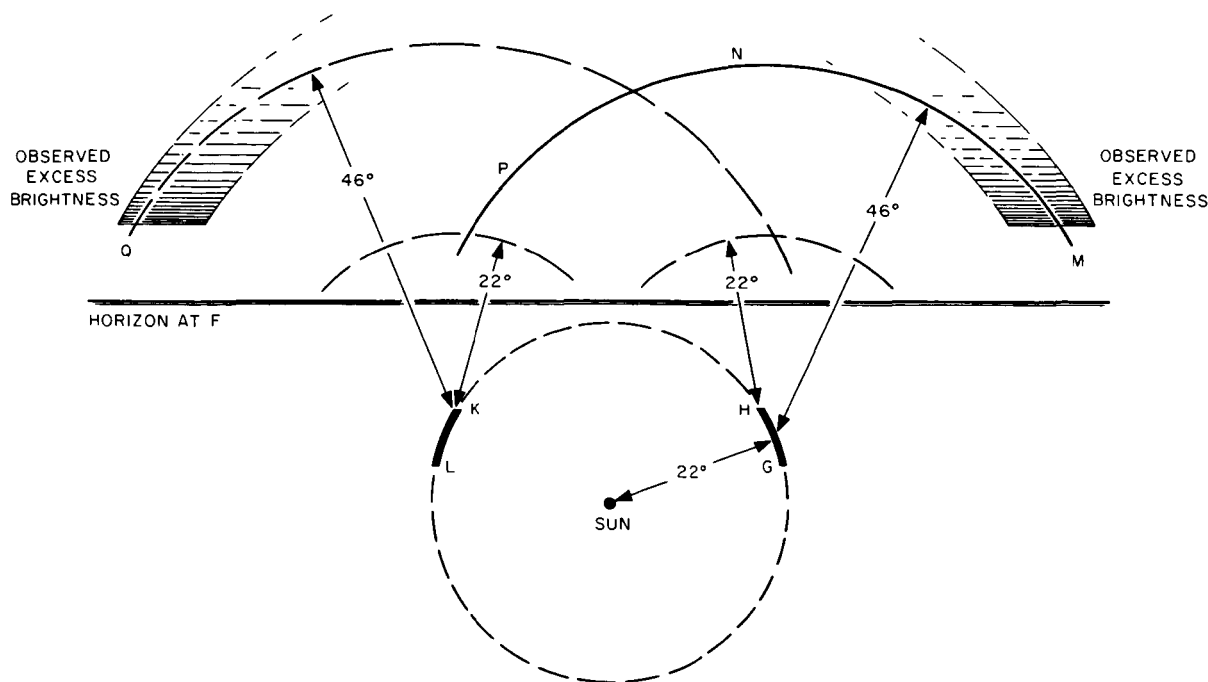


FIGURE 8.—Relationship between ice-crystal halos and observed excess brightness in zodiacal light.

Light scattered in the 22° halo at cloud B reaches cloud D only if it is in arc GH (or KL); the exact position depends on the distance from B to D. Point G is 5° nearer the horizon than the Sun, and point H is 11° nearer. Light scattered in the 46° halo at cloud D reaches the observer at F anywhere on the arc MNP, but preferentially at low elevation because sight line E then has a longer path in cloud D. The observed excess brightness corresponds to light scattered to points near M or Q. Smith, Roach, and Owen (1965) did not observe below 10° elevation.

Light scattered to P and light scattered in the 22° halo at cloud D form a broad band of excess brightness superposed on the brightest part of the zodiacal light and will not be readily distinguishable from other light.

The principal merit of this hypothesis of ice clouds is that the scattered light 60° to 70° from the Sun would be strong only where it is actually observed—mostly at comparatively low elevation and at a different azimuth from the depressed Sun. Under the circumstances of observation, this corresponds to high ecliptic latitude.

Only ice crystals that are large compared with the wavelength of light will form the halos. We

can estimate the number density, $N \text{ cm}^{-3}$, of crystals 5μ in diameter that would reproduce the observed excess brightness, as follows: Assume light paths 100 km long in clouds B and D (fig. 7) and ice-crystal cross sections $2 \times 10^{-7} \text{ cm}^2$, so that the fraction of light intercepted by ice crystals in each cloud is approximately $2N$. Estimate that 0.1 of the light incident on a crystal is scattered into the 22° halo, and 0.05 into the 46° halo. Further, estimate that cloud D subtends a vertical angle of roughly 1° at B; then the fraction of the 22° halo light reaching D is 0.02, and the fraction of 46° halo light is 0.009. When the 46° scattering occurs at D, roughly 0.4 of the light is scattered toward the ground. However, only half this amount contributes to the excess brightness, because the shift at D in the azimuth of the ray must be in the same sense as the shift at B if the final elongation of the ray from the Sun is to be about 65° . When the 22° scattering occurs at D, roughly 0.2 of the light is scattered toward the ground and half contributes to the excess brightness. Estimate that 0.7 of 5300\AA light is absorbed along each of paths A and C; absorption in path E is accounted for in original data reductions.

The total excess brightness observed by Smith, Roach, and Owen in the whole sky is approximately 1.15×10^5 10th-magnitude stars, or 2×10^{-10} of the Sun's brightness. Only half of this is actually observed at one time. Thus,

$$(2N)^2(0.1)(0.05)[(0.02)(0.2) + (0.009)(0.1)](0.3)^2 = 10^{-10}$$

and

$$N = 3 \times 10^{-3}$$

These ice crystals constitute 1.6×10^{-5} of the atmospheric mass density at 82 km. They may be compared with the noctilucent-cloud material collected by Hemenway, Soberman, and Witt (1964). If it is assumed that their "halos" are ice and that the cloud they sampled was near 82 km in height and 3 km thick, then their "halos" contained from 1×10^{-5} to 4×10^{-5} of the atmospheric density as ice. The hypothetical cloud of 5μ particles thus seems comparable in ice content to noctilucent clouds, but it would scatter less sunlight because its total cross section is 0.1 to 0.3 of that of the noctilucent cloud.

The principal fault with the hypothetical clouds is the lack of real noctilucent clouds at the same latitudes. The hypothetical clouds would presumably be formed under conditions similar to noctilucent clouds, except for a much smaller number of condensation nuclei. The first scattering cloud (B) ought to be observable in the Pacific Ocean at 30° to 35° north latitude, but it would be considerably fainter than normal noctilucent clouds. The second cloud (D) would be hard to detect except as the excess brightness found by Smith, Roach, and Owen. It is clear that these

clouds might not have been seen previously even if they existed. However, the only noctilucent clouds so far observed at latitudes less than 45° were caused artificially by rocket launchings at Point Mugu, California (Fogle and Haurwitz, 1966). I have not investigated whether the artificial clouds themselves might be important here.

From present knowledge of atmospheric temperature at noctilucent-cloud heights, it seems unlikely, but not impossible, that the hypothetical ice clouds at 20° to 30° latitude actually exist. The necessary temperature for persistence of depends on the water-vapor content of the atmosphere, which is ill known. If water vapor is as abundant as ice in the hypothetical cloud, i.e., 2×10^{-5} by mass of the atmosphere, then the frost point at 82 km is 159° K. However, for a preliminary measurement of water-vapor pressure at 79 km by Fedynski (quoted by Fogle and Haurwitz, 1966), the frost point is 179° K. According to CIRA (1965), the mean temperature at 80 km and 30° north latitude is 199° K on September 1, which is a representative date for Smith, Roach, and Owen's excess-brightness observations. Mean temperature at 60° N in June and July (representative for noctilucent clouds) is about 170° K. However, since measurements in noctilucent clouds reach down to 135° K (Fogle and Haurwitz, 1966), it is possible that variation from the mean temperature is necessary for the formation of a noctilucent cloud. A comparable variation might then cause one of the low-latitude ice clouds hypothesized here.

REFERENCES

- CIRA, 1965 (COSPAR International Reference Atmosphere, Amsterdam: North-Holland Publ. Co.).
 FOGLE, B., and B. HAURWITZ, 1966, *Space Science Reviews*, **6**, 279.
 HAPKE, B., 1965, *Ann. N.Y. Acad. Sci.*, **123**, 711.
 HEMENWAY, C. L., R. K. SOBERMAN, and G. WITT, 1964, *Tellus*, **16**, 84.
 MINNAERT, M., 1954, *The Nature of Light and Colour in the Open Air* (New York: Dover Publ.), 362.
 PORTER, J. G., 1963, in *The Moon, Meteorites, and Comets* (B. M. Middlehurst and G. P. Kuiper, eds.), 550-572 (Chicago: University of Chicago Press).
 RICHTER, N. B., 1963, *The Nature of Comets* (London: Methuen and Co.), 221.
 SMITH, L. L., F. E. ROACH, and R. W. OWEN, 1965, *Planetary Space Sci.*, **13**, 207.
 SOUTHWORTH, R. B., 1964, *Ann. N.Y. Acad. Sci.*, **119**, 54.
 VAN DE HULST, H. C., 1957, *Light Scattering by Small Particles* (New York: John Wiley and Sons), 470.
 WHIPPLE, F. L., 1955, *Astrophys. J.*, **121**, 750.
 WOLSTENCROFT, R. D., and L. J. ROSE, 1967, *Astrophys. J.*, **147**, 271.

38. On Optical Models Approximating Observations of the Zodiacal Light Outside the Ecliptic

R. H. GIESE AND C. V. DZIEMBOWSKI
*Max-Planck-Institut für Physik und Astrophysik
Munich, West Germany*

SOME EARLIER OBSERVATIONS of the zodiacal light in the ecliptic plane (see, Blackwell and Ingham, 1961; Elsässer, 1958) caused difficulties in the interpretation of the results by spherical-particle models. Although it was always easy to fit models to the observed brightness distribution, only the assumption of either an unrealistically high electron density or of the existence of very small ($\leq 0.1\mu$) particles allowed the reproduction of the observed polarization curves. This difficulty is removed, if one takes the more recent results of Weinberg (1964), which present a maximum polarization of 23 percent (instead of about 35 percent) near 70° of elongation. As Weinberg has shown, his observed brightness and polarization curves might be reasonably approximated by models favoring the presence of very small particles. However—contrary to the observations referred to above—Weinberg's results can be approximated also by a second type of model, which derives the polarization not from the Rayleigh-like scattering behavior of very small particles but from the polarization caused by much larger absorbing spheres (see Giese and Lüst, 1966). Starting from these two types of models, which fit Weinberg's observations in the ecliptic plane, we try to derive models approaching the observational data as presented by Smith, Roach, and Owen (1965) for the zodiacal light outside the ecliptic.

METHOD

For our computations the average scattering functions

$$\sigma_j(\vartheta) = \frac{\int_{\alpha_1}^{\alpha_2} \alpha^{-k} i_j(\alpha, \vartheta) d\alpha}{\int_{\alpha_1}^{\alpha_2} \alpha^{-k} d\alpha} \quad j=1; 2 \quad (1)$$

as defined by Giese and Siedentopf (1962) are used to represent the typical average scattering properties of one particle out of a mixture of spherical particles ranging from a lowest (α_1) to an upper size parameter (α_2). As usual, the size parameter is defined according to the Mie theory by

$$\alpha = \frac{2\pi a}{\lambda} \quad (2)$$

where a and λ represent the particle radius and the wavelength of light, respectively. The scattering functions i_j follow the definition by van de Hulst (1957) as used by Giese (1961) and (1963). They give the intensity of scattered light of an individual particle as a function of the refractive index (m), size (α), and scattering angle (ϑ) with the electrical vector perpendicular ($j=1$) and parallel ($j=2$) to the plane of vision. Although the size distribution function $\sim \alpha^{-k} d\alpha$ is a rather special case, more complicated models and even models of different materials (dielectric and metallic particles) can be treated by superposition of the single components, each represented by a scattering function as defined in formula (7).

For the spatial distribution of particles, the

number density $n(x, y, z)$ of each component is assumed to decrease with the distance from the Sun corresponding to a law

$$n(x, y, z) = n_0 \left(\frac{A}{\rho} \right)^\beta \quad (3)$$

where $A = 1$ astronomical unit.¹

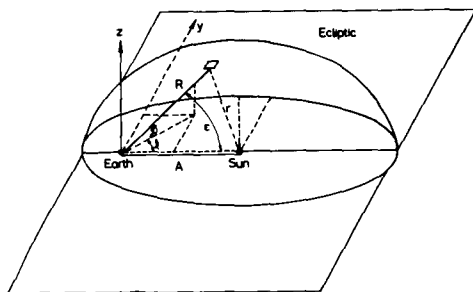


FIGURE 1.—Geometric relations.

Here n_0 is the number density of the particles near the Earth's orbit. The particles are assumed to have equal number densities along the surfaces of ellipsoids (fig. 1) defined by

$$\frac{(x-A)^2}{\rho^2} + \frac{y^2}{\rho^2} + \frac{z^2}{(\rho/\sqrt{\gamma^2+1})^2} = 1 \quad (4)$$

Here ρ is the parameter characterizing the ellipsoid surface corresponding to the number density, $n_0 \left(\frac{A}{\rho} \right)^\beta$. As can be seen from equation (3) and figure 1, ρ represents in the ecliptical plane—but not outside the ecliptic—the distance of the corresponding equidensity surface from the Sun. The flatness of the ellipsoids is determined by γ . A spherical distribution of particle number densities would correspond to $\gamma=0$, while large values ($\gamma \gg 1$) of γ correspond to a strong concentration of interplanetary dust toward the ecliptic plane.

By use of the symbols and geometry shown in figure 1, one arrives from equations (3) and (4) at

¹ In all figures the unit of length is taken as 1 astronomical unit ($A=1$). In this case it follows that $(\rho/A) = \rho$.

$$n = \frac{n_0}{\left(\frac{r}{A} \right)^\beta \left[1 + \left(\gamma \frac{z}{r} \right)^2 \right]^{\beta/2}} \quad (5)$$

Using the geometric relations

$$r = A \frac{\sin \epsilon}{\sin \vartheta} \quad (6)$$

$$R = \frac{\sin(\vartheta - \epsilon)}{\sin \vartheta} \quad (7)$$

$$dR = A \frac{\sin \epsilon}{(\sin \vartheta)^2} d\vartheta \quad (8)$$

$$z = R \sin \delta \quad (9)$$

we can transform the integral (see Giese and Siedentopf, 1962)

$$I_j = \frac{L\lambda^2}{8\pi^2} \int_{R=0}^{\infty} \frac{n(r, z) \sigma_j(\vartheta)}{(r/A)^2} dR \quad j=1; 2 \quad (10)$$

which presents the surface brightness of the zodiacal light (after integration along the line of sight, L = Solar flux at 1AU) into the form

$$I_j = \frac{n_0 L \lambda^2}{8\pi^2 (\sin \epsilon)^{\beta+1}} \int_{\vartheta=\epsilon}^{\pi} \frac{(\sin \vartheta)^\beta \sigma_j(\vartheta) d\vartheta}{\left\{ 1 + \left[\gamma \frac{\sin \delta \sin(\vartheta - \epsilon)}{\sin \epsilon} \right]^2 \right\}^{\beta/2}} \quad (11)$$

which can be evaluated by numerical integration. The angular distance ϵ between the Sun and the direction of the observer's line of sight is known by the relation

$$\cos \epsilon = \cos \delta \cos \ell \quad (12)$$

if the ecliptical latitude (δ) and the difference of the ecliptical longitude between the Sun and the direction of the line of sight (ℓ) are given.

RESULTS

The observational data of Smith et al. (1965) are plotted in figure 2 for ecliptic latitudes $\delta = 0^\circ, 20^\circ, 40^\circ, 60^\circ$, and 80° . In the upper curve

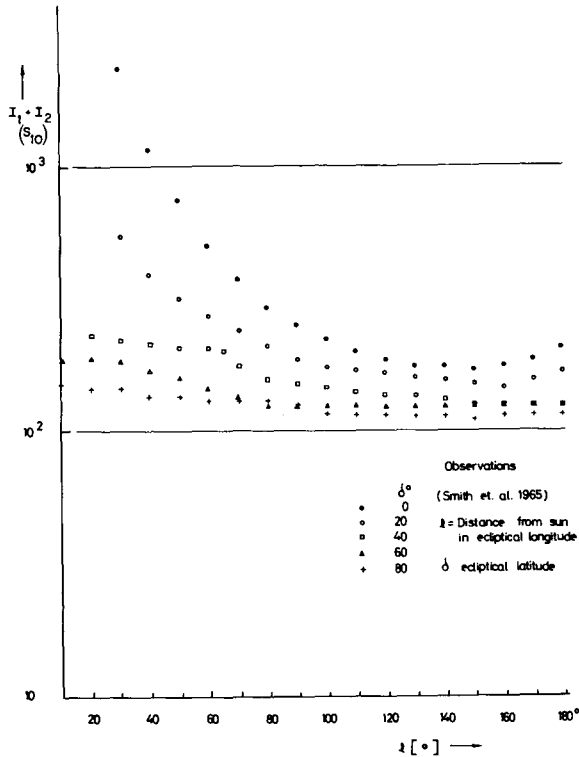


FIGURE 2.—Plot of observational data by Smith et al. (1965).

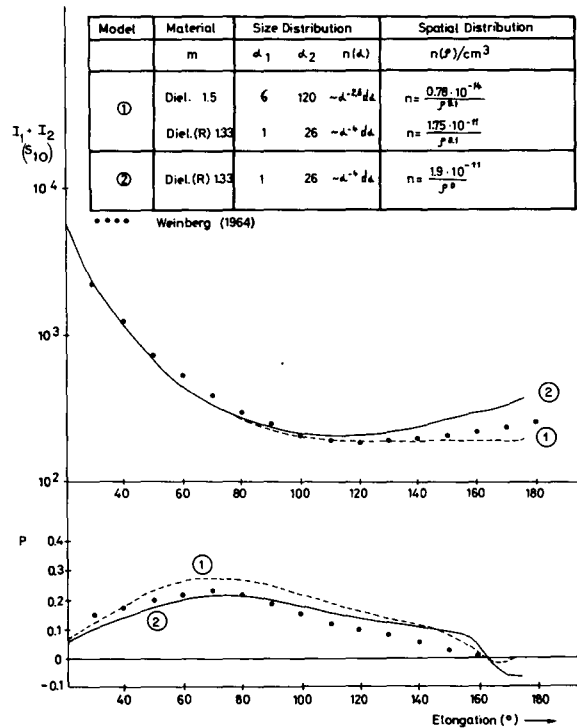
($\delta = 0^\circ$) there is a decrease of brightness ($I_1 + I_2$) of more than a factor of 13 between 30° and 155° of elongation. On the other hand, the curves for $\delta = 40^\circ$, 60° , and 80° present a decrease of brightness by less than a factor of 2 in the corresponding region ($\ell = 30^\circ$ to $\ell = 160^\circ$), and all arrive at a brightness of 125 to 115 stars of 10th magnitude per square degree ($S_{10}(\text{vis})$) in the region near $\ell \approx 160^\circ$. For discussion of the computed curves it should be noted that the observed curve for $\delta = 20^\circ$ is for all angles of ℓ between the curves corresponding to $\delta = 0^\circ$ and $\delta = 40^\circ$.

Rayleigh Particle Models

Figure 3 presents the curve of brightness ($I_1 + I_2$) and polarization (p) in the ecliptic plane for two models, which favor the existence of a large percentage of very small ($r \approx 0.1\mu$) particles. Model 2 is identical with a model (computed earlier by Giese (1963)), which Weinberg (1964) has shown to be in reasonable agreement with his observed values. By adding a small fraction of larger particles, which contribute only about $1/8$ of the observed brightness, one can modify

this model to obtain an even better approach to the observed data (model 1). Both models produce the polarization mainly by the existence of very small particles, whose scattering functions are already close to the case of Rayleigh scattering. In model 2 the minimum or average or maximum particle radius is 0.08μ or 0.12μ or 2.1μ for a wavelength of $\lambda = 0.5\mu$. In order to investigate the resulting brightness curves out of the ecliptic we adopt in figure 4 a model very close to model 2 of figure 3. The slight decrease of spatial density ($\beta = 0.1$) is taken in order to distinguish ellipsoids of individual, equal densities by means of equations (3) and (4). The exponent $\beta = 0$ would better approach the observations (see Weinberg (1964), fig. 9), but correspond to an equal number density of dust particles over the whole planetary system. On the other hand, a large value of β would result in a much higher polarization than observed in the ecliptic plane (see Weinberg (1964), fig. 9, $\beta \geq 0.5$).

Figure 4 shows the range of brightness as a function of ℓ for a value $\gamma = 500$, presented in

FIGURE 3.—Rayleigh particle models. Approximation of Weinberg's brightness ($I_1 + I_2$) and polarization (p) measurements for two models.

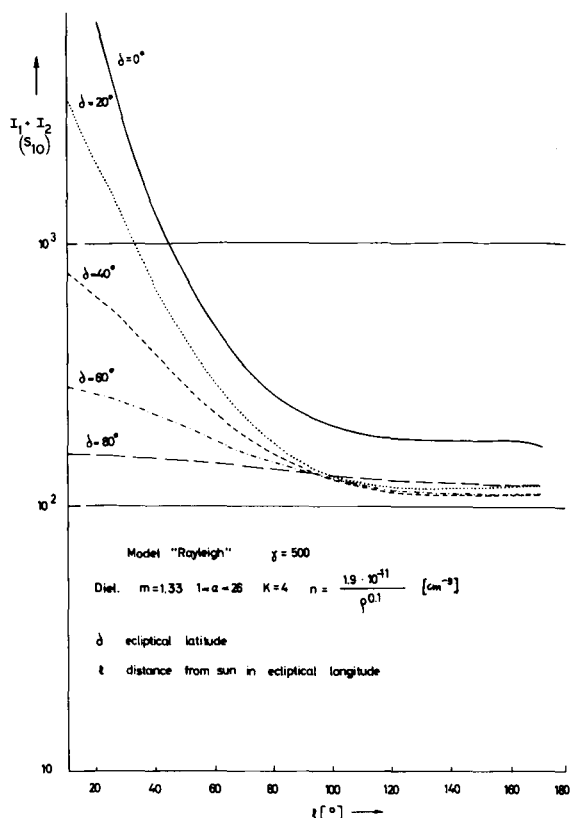


FIGURE 4.—Brightness produced by a Rayleigh model at different ecliptic latitudes (δ).

the same way as the observational data in figure 3. As can be seen by comparing the diagrams, the computed curve for $\delta = 20^\circ$ is too close to the curve for $\delta = 0^\circ$ in the region $l < 60^\circ$ and—contrary to the observations—mixed with the other curves for $l > 90^\circ$. If we lower the concentration of dust toward the ecliptic plane by adopting smaller values of γ , the brightness for the backward regions of all curves $\delta \neq 0^\circ$ becomes too high and the curve for $\delta = 20^\circ$ approaches even more closely the curve $\delta = 0^\circ$. On the other side, increasing γ would result in a decrease of brightness of all curves $\delta \neq 0^\circ$ in the region $l > 90^\circ$ below the observed values without reaching a satisfying agreement in the region $l < 90^\circ$.

Metallic Particle Models

In the models referred to previously it was not necessary to assume the existence of metallic particles, since for $\alpha \leq 1$ both metallic and

dielectric particles produce a considerable polarization, especially at scattering angles near $\vartheta = 90^\circ$. (See fig. 2 of Giese (1963).) The scattering functions of larger particles ($\alpha \geq 5$), however, differ markedly for different materials. As has been shown in an earlier paper (figs. 2, 3, and 5(a) of Giese, 1963) metallic particles show a pronounced and always positive polarization ($I_1 > I_2$), practically for all scattering angles $20^\circ \leq \vartheta \leq 160^\circ$. In spite of this fact it was not possible to reproduce the results of Blackwell and Ingham (1961) and Elsässer (1958) by spherical dust particles of a typical size parameter $\alpha \approx 5$. The reason was that the size and density distributions fitting the observed brightness data, after integration over the line of sight, resulted in a polarization much below 35 percent near $\epsilon = 70^\circ$, even for mixtures of pure metallic particles. Contrary to this result, the polarization of only 23 percent, as observed by Weinberg, can be produced by metallic particles. (See Giese and Lüst, 1966.) Figure 5 (model 3) shows an example where an approximation to both the observed brightness and polarization in the ecliptic plane is obtained by a mixture of metallic

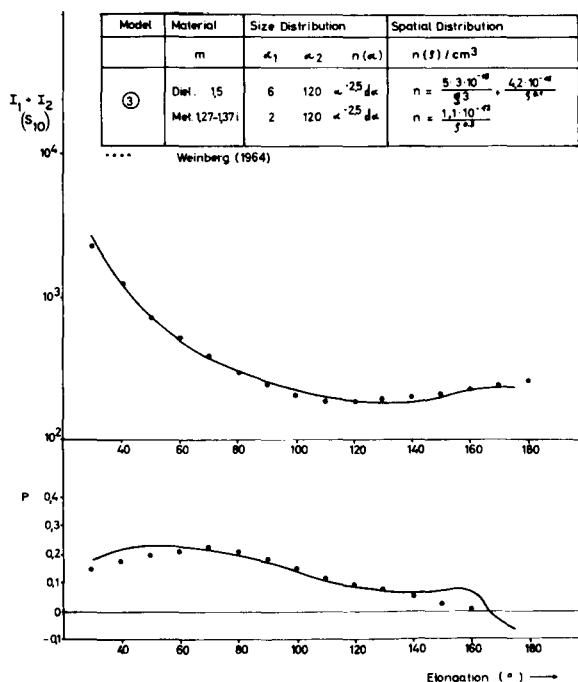


FIGURE 5.—Metallic particle model. Approximation of Weinberg's observations by a metallic particle model.

and dielectric particles. The exponent of the size distribution function ($k=2.5$) is lower than in the case of Rayleigh particle models and closer to the values given by van de Hulst (1947) and Elsässer (1955). The average particle radius is 0.42μ for the metallic component

$$(0.16\mu \leq a \leq 9.6\mu)$$

and 1.3μ for the dielectric component

$$(0.48\mu \leq a \leq 9.6\mu)$$

if we adopt for the wavelength of light $\lambda=0.5\mu$. Since the corresponding average size parameters are $\alpha=5.3$ and $\alpha=16.7$ for the metallic and the dielectric component, respectively, most particles of this model do not behave like Rayleigh scatterers. The polarization is mainly caused by the presence of metallic particles. The dielectric component must be added in order to decrease the polarization at low elongations, since the polarization of the metallic component alone would produce a polarization much higher than that observed at elongations near $\epsilon=30^\circ$ and would therefore not follow the observed polarization curve.

In figure 6 the brightness curves for different ecliptical latitudes resulting from a dust composition as in model 3 (fig. 5) are plotted as a function of ℓ . Although there is no exact agreement with the observed curves (fig. 3), the metallic-particle model shows most of the general features, which are mentioned in the beginning of this section about the observational data of Smith et al. (1965). Especially the curve for $\delta=20^\circ$ is well separated from the other curves, and the brightness at $\delta=20^\circ$ differs more from the brightness in the ecliptic plane at $\ell < 60^\circ$ than in the case of the Rayleigh particle model. In figure 6 the characteristic parameter for the dust concentration toward the ecliptic plane has been adopted as $\gamma=10$. For $\gamma=1$ the curve $\delta=20^\circ$ would be too close to the curve for $\delta=0^\circ$ in the region $\ell < 90^\circ$ and the brightness values of all curves outside the ecliptic would be too high. On the other side, the computations for $\gamma \geq 20$ arrived at brightness values outside the ecliptic which were much below the observed ones, especially for $\ell > 90^\circ$.

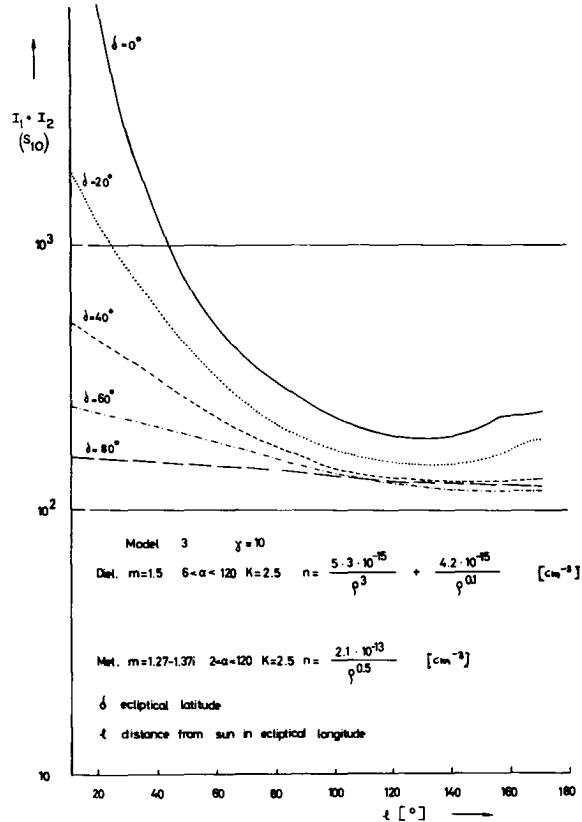


FIGURE 6.—Brightness produced by a metallic particle model at different ecliptical latitudes.

CONCLUDING REMARKS

As long as computations and observations are restricted to the ecliptical plane, no reliable distinction may be possible between the Rayleigh and the metallic-particle model. Differences in the brightness and polarization curves at higher elongations ($\epsilon > 130^\circ$) should not be overestimated, since models based on spherical particles show peculiar effects (i.e., caused by the "haze bow") especially in this region. They are too closely related to the spherical shape to be absolutely significant in the interpretation of light scattering by real interplanetary dust grains. The discussion of the brightness at very low elongations (Fraunhofer corona) by Elsässer (1955) arrives at a size distribution ($k=2$), which does not support the Rayleigh particle model ($k=4$). Extraterrestrial observations below $\epsilon=20^\circ$ and close to the Sun should be helpful in learning more about the real sizes of the scattering particles (diffraction part of the scattering func-

tion). The same is true for color measurements and the discussion of the properties of different models in several wavelength bands. (See paper 36 by Aller et al.)

Very useful information seems to come from the photometric observations outside the ecliptic. The Haleakala data of Smith et al. (1965) are better approximated by the metallic-particle model. The reason might be that this type of model produces—compared with the Rayleigh models—a steeper decrease of brightness from $\delta = 0^\circ$ to $\delta = 20^\circ$ in the region $\ell < 60^\circ$ due to the steeper decrease in both the scattering and the density-distribution function. This property makes it easier to adjust the brightness curves for $\ell < 90^\circ$ and at the same time for $\ell > 90^\circ$ to the observations.

Certainly the special examples discussed in

this paper do not present the real distribution of interplanetary dust particles. They only demonstrate the general features of the Rayleigh and metallic (absorbing) particle models. Neither models which only reproduce the optical properties of interplanetary dust (as above) nor models derived from mechanical arguments, but not reproducing brightness and polarization, can be considered as a solution for the real interplanetary dust composition and distribution. Since, however, the polarization of larger absorbing particles (at least spheres) is rather independent of size, it is not impossible that a synthesis of models taking into account both optical and mechanical arguments can be more easily obtained by the metallic-particle model than by Rayleigh models, which are necessarily bound to extremely small particle radii.

REFERENCES

- BLACKWELL, D. E., and M. F. INGHAM, 1961, *Mon. Not. Roy. Astron. Soc.*, **122**, 129.
 ELSÄSSER, H., 1955, *Zeits. f. Astrophys.*, **37**, 114.
 —, 1958, *Die Sterne*, **34**, 166.
 GIESE, R. H., 1961, *Zeits. f. Astrophys.*, **51**, 119.
 —, 1963, *Space Science Reviews*, **1**, 589.
 GIESE, R. H., and H. SIEDENTOPF, 1962, *Zeits. f. Astrophys.*, **54**, 216.
 GIESE, R. H., and R. LÜST, 1966, First LIL Symposium Proceedings, Research in Geosciences and Astronomy, Athens, 1965, 103, Springer Verlag, Wien, New York.
 SMITH, L. L., F. E. ROACH, and R. W. OWEN, 1965, *Planetary Space Sci.*, **13**, 207.
 VAN DE HULST, H. C., 1947, *Astrophys. J.*, **105**, 471.
 —, 1957, *Light Scattering by Small Particles* (New York: John Wiley and Sons).
 WEINBERG, J. L., 1964, *Ann. d'Astrophys.*, **27**, 718.

V

DYNAMICS

Page intentionally left blank

39. Theoretical Considerations of Small Particles in Interplanetary Space

L. BIERMANN

Max-Planck-Institut für Physik und Astrophysik
Munich, Germany

The lifetime of dust particles in interplanetary space as a function of the particles' radius a , the composition, and the shape is discussed for the size range of $0.01 \mu \leq a \leq$ several μ , for which cometary origin is assumed to predominate. Near both the upper and lower limits, the lifetime becomes directly proportional to a , but with coefficients differing in the ratio of approximately 1000 to 1. In the middle range ($0.03 < a < 0.3$) the lifetime is determined essentially by radiation pressure and gravity; it is approximately independent of a and equal to 10^7 seconds. The sharp drop of the lifetime by ≥ 3 powers of 10 from the upper range, where the Poynting-Robertson effect and (possibly) sputtering dominate, to the middle range is somewhat smoothed out by the initial conditions given for particles of cometary origin, by differences of the composition and optical properties and of the particle shapes and (possibly) by electromagnetic effects, provided a purely statistical increase of the particle energy with time can be assumed. The transition from the middle to the lower range, in which electromagnetic effects dominate and cause spherical particles with $a \approx 0.01 \mu$ to escape in $\leq 10^6$ seconds, is continuous. If the supply from comets is continuous over this range, say $\sim a^{-m} da$, the stationary number density would, in the simplest possible picture, be $\sim a^{-(m-1)} da$ near the upper and lower limits, while the sharp drop in the lifetime around $1/2 \mu$ to 1μ should be reflected in a similar, although smaller, drop in the number density. As a consequence, comparisons between observed zodiacal light data and theoretical models become meaningful only if the latter are consistent in their mathematical forms with the discontinuous character of the distribution function to be expected, if submicron particles are supplied over the whole range considered here.

WE SHALL CONSIDER a solid particle in interplanetary space as "small" if the force resulting from the pressure of solar light acting on it becomes equal within a factor 2 or 3 to that of solar gravitation. For spherical particles the upper limit of this range of particle radii depends on the density and on the optical properties, being generally between 1 and some fraction of a micron. Particles which are more than 10 times smaller ($<$ some hundred Å) are removed so

rapidly that they can probably be disregarded in our present discussion. The range of particle sizes which we shall consider is hence characterized by values of the parameter $2\pi a/\lambda$ (a is particle radius) between 13 or 25 (upper limit) and $1/2$ or 1. This range is of interest in connection with the observed polarization to which such particles, if they exist in sufficient number, could well contribute; we note that for particles with $2\pi a/\lambda \leq 1$, a space density of $\geq 10^{-25}$

g/cm^3 would contribute to the polarization about as much as 300 electrons per cm^3 (cf. Elsässer and Schmidt, 1966).

It happens that in this same range, the influence of the solar wind on the particle's lifetime has to be taken into account. The influence of the latter is threefold: The solar-wind particles act simultaneously by the Poynting-Robertson effect, which causes the particles to spiral inward toward the Sun; by sputtering, which reduces their size; and by the force exerted by fluctuating magnetic fields embedded in the solar wind plasma, by which the particles are gaining energy in one step or statistically until they are removed out of the inner parts of the solar system. At least the first two effects as such have been known for a long while, but the necessary data on the solar wind have become available only in recent years.

In earlier work (Behr and Siedentopf, 1953; Ingham, 1961; Giese, 1961 and 1963; Parker, 1964; and Elsässer and Schmidt, 1966), particles for which the force resulting from solar radiation pressure is larger than the Sun's gravitational attraction have usually been regarded as nonexistent in interplanetary space, while it was realized that dielectric particles with moderate refractive index and with radius below 500 \AA ($2\pi a/\lambda < 0.8$) for which the radiation pressure is again small could again move in elliptical orbits, if nongravitational effects were absent.

The lifetimes of the particles in the whole range of sizes considered here are important for every discussion of how the approximately stationary state of the interplanetary medium is maintained. The supply of new particles for this size range appears to come mainly from comets. In this connection we draw attention to the observations of strong polarization in comets.

The subsequent discussion shows that the lifetime in interplanetary space of "small" particles, as specified above, as a function of the particle radius, permits us to draw certain conclusions regarding the possible size-distribution laws of such particles.

Dielectric particles of spherical shape are used as a first example of how gravitation, radiation pressure, the solar wind, and the initial conditions affect the lifetime. The results are then

extended to metallic particles and to nonspherical particles.

In the literature on the subject, ordinary ice and SiO_2 have often been taken as examples for dielectric particles, although it was, of course, realized that the lifetime of ice particles of the sizes of interest is determined by ordinary evaporation and hence is extremely short (a minute or two from similar discussions for cometary nuclei by Huebner, 1965, and by Delsemme, 1966). Here we fix attention, as far as dielectric particles are concerned, to small stony particles with a purely real refractive index.

The upper limit of the radius of such particles for which the radiation pressure balances solar gravity (which we call a_0) is taken to be smaller than that for ordinary ice (0.8μ ; Giese, 1961) in the ratio of the densities. Assuming a value of 2.5 for the latter, we find for spherical particles $a_0 \approx 3200 \text{ \AA}$ ($10^{-4.5} \text{ cm}$); since $2\pi a/\lambda \approx 4$, this procedure should not introduce too great an error.

Before proceeding to the discussion of the aforementioned mechanisms, we observe that for particles released into the zodiacal cloud by comets, the initial conditions are such that the effective limiting radius is somewhat larger than a_0 . This holds both for dielectric and for metallic particles. Consider, for example, a comet which has an aphelion near the orbit of Jupiter and which releases dust particles near the orbit of the Earth. When it is in the neighborhood of the Earth's orbit, its kinetic energy differs from its potential energy by less than 20 percent. Radiation pressure need compensate for only the 20 percent of gravity for the particle to escape in a hyperbolic orbit. As another example, we consider a moderately elliptical orbit with a semi-major axis equal to 1. In that case the kinetic energy in the neighborhood of the Earth's orbit is about 50 percent of the escape energy. If the 50 percent is compensated by radiation pressure, the particle will escape.¹

If one could assume that the ratio of the force resulting from radiation pressure to that due to gravity were $\sim 1/a$, the effective limiting radius

¹ During the meeting, Dr. Harwit kindly drew the attention of the author to his paper, *J. of Geophys. Res.*, **68**, 2171 (1963), in which the same problem is discussed in more detail.

would be $5a_0$ in the first of these two cases, but $2a_0$ in the second. Published work indicates, however, that this ratio often varies somewhat faster than $1/a$; no generally valid figure for the factor by which a_0 has to be increased can be given even if the orbital characteristics were the same for all comets. We shall assume here that $3a_0$ is the effective limit of the radius, and that below this limit a dust particle released from a comet will go into a parabolic or hyperbolic orbit.

If this does occur, the time the dust particle takes to pass through the inner parts of the planetary system, where it could contribute to the zodiacal light and the gegenschein, is of the order of 10^7 seconds. This is so, because the radiation pressure is never large compared with the gravitational attraction.

For dielectric particles, the ratio of radiation pressure to gravitational force again becomes small for radii of the order of some 100 \AA ; for such size, however, electromagnetic forces prevent the particle from describing an elliptical orbit around the Sun.

We turn now to the other effects limiting the lifetime of a small particle. First we have the Poynting-Robertson effect, which causes the particles to spiral inward toward the Sun and to which, as is now known, the Sun's corpuscular radiation contributes, in addition to the classical effect due to the flux of solar light. In order to have the same expression for both kinds of radiation, we observe that it is the mass flux F ($\text{g}/\text{cm}^2\text{-sec}$) which enters into the expression for the time scale of the change of the orbit. For solar light this amounts to $1.51 \times 10^{-15} \text{ g}/\text{cm}^2\text{-sec}$, which is equivalent to a flux of 9×10^8 protons/ $\text{cm}^2\text{-sec}$. The Sun's corpuscular radiation under generally quiet conditions is equivalent to $2^{1/2}$ or $3 \times 10^8 \text{ m}_\text{H}/\text{cm}^2\text{-sec}$ (Ferraro and Parker, 1966; Ness, 1966), but it is estimated to increase almost 100 times before the biggest geomagnetic storms (Ferraro and Parker, 1966); since the angular width of the corpuscular eruptions causing such storms is $\approx \pi/2$, there must be approximately four times as many solar events of this type as indicated by geophysical data. It is obvious that the influence of the solar winds and storms on the lifetime of interplanetary dust particles by

the Poynting-Robertson effect is of the same order of magnitude as that of solar light; we assume that their combined mass flux is $10^{-14.6} \text{ g}/\text{cm}^2\text{-sec}$ (or more if the active periods and storms more than double the value assumed here for the quiet-time corpuscular flux). The time scale of the variation of the orbital angular momentum of the particle is then

$$t_{\text{P.R.}} = \frac{m}{F(\pi a^2)_{\text{eff}}} = \frac{\rho}{F} \frac{4}{3} \frac{a^3}{(a^2)_{\text{eff}}} \\ = 1.3 \times 10^{11} \left(\frac{\rho}{2.5} \right) \frac{a^3/(a^2)_{\text{eff}}}{1\mu}$$

Here $(a^2)_{\text{eff}}$ is a weighted mean, allowing for the fact that for light the cross section in the Poynting-Robertson effect may be somewhat larger or considerably smaller than the geometrical cross section, depending on $2\pi a/\lambda$ and the optical properties. The effective lifetime is the inverse sum of individual reciprocal lifetimes; the dependence of $t_{\text{P.R.}}$ on a should therefore be weaker than for the radiative effect alone. More accurate work of Wyatt and Whipple (cf. Jacchia, 1963) indicates that this figure could (assuming the same ratio of radiation to gravity) be lower, for example, by a factor of 4 for a circular orbit of the particle, and that the coefficient $10^{11.1}$ given above holds for a particle moving on an orbit with $e=0.75$ and perihelion distance $q=0.7$.

The next effect to be considered is the sputtering, that is to say, the progressive abrasion of the particles' surface layers by the solar wind ions of $\approx 1 \text{ keV}$ to 4 keV for quiet-time protons or α particles, but of $\approx 10 \text{ keV}$ to 40 keV emitted during storms. Obviously, the ions emitted during storms should be more effective than those emitted in periods of low solar activity. In the absence of a more detailed analysis of existing data (which the author has unfortunately not yet been able to carry out) and of data on the particle flux in storms (which do not yet seem to exist), we shall assume here that an average solar ion disrupts, per unit mass, the equivalent of 13 mass units or $10^{-22.7} \text{ g}$ and that the average flux over the solar cycle is $5 \times 10^8 \text{ m}_\text{H}/\text{cm}^2\text{-sec}$ (at 1 AU). This would lead to an average surface abrasion of $10^{-14} \text{ g}/\text{cm}^2\text{-sec}$ or a decrease of the

radius of 3 Å/year for the particle density of $\rho = 2.5$ assumed here.² This means a time scale of $10^{11.0}$ seconds for particles of 1 μ radius, which is comparable to the one found for the Poynting-Robertson effect. The dependence on the particles' radius is essentially the same; the combined time scale would be $\approx 10^{11}$ seconds.

We turn now to the electromagnetic effects due to the magnetic fields frozen into and carried by the solar-wind plasma (cf. Parker, 1964). The validity of the concept of frozen-in fields has for quiet-time conditions been confirmed by the observations from space vehicles such as Mariners II and IV and interplanetary monitoring platforms (IMP) 1 to 3, and there is no reason to doubt its applicability also for disturbed periods, although conditions may be more complicated then. This means that a dust particle in interplanetary space, the velocity of which is necessarily small compared with that of solar wind, is subject to the electric field:

$$\mathbf{E} = -\frac{1}{c}(\mathbf{v} \times \mathbf{B})$$

where \mathbf{v} is the velocity of the solar-wind plasma seen from the dust particle, and \mathbf{B} the intensity of the interplanetary magnetic field. The prevailing component of \mathbf{v} is radial with respect to the Sun; there are other components resulting from fluctuations of the direction of the solar wind (usually by only a few degrees of arc, but near the edges of sectors of the same direction of the magnetic flux (cf. Ness and Wilcox, 1964) or in storms up to 10° or more) and also from the motion of the dust particle with respect to the Sun. The magnetic vector \mathbf{B} appears to have a tendency to be aligned parallel to the equatorial plane of the Sun; the component perpendicular to this plane is experimentally less well known, and the measured values are less well understood than is the case for the components parallel to the equatorial plane. We shall therefore not discuss the several consequences of the possible presence of a perpendicular component of \mathbf{B} of one sign over extended periods of time.

The equatorial component of \mathbf{B} gives rise to

² However, cf. Wehner (1963) who finds only ≈ 0.4 Å/yr.

an electric field perpendicular to both \mathbf{v} and \mathbf{B} , that is, perpendicular to the equatorial plane. Assuming for average conditions $v/c = 10^{-2.8}$ and for the component of \mathbf{B} perpendicular to \mathbf{v} a value of $10^{-4.5}$ oersted (or 3 γ in the usual units), we have $E = 10^{-7.3}$ esu. The importance of this component of \mathbf{E} is due to the fact that it tends to have, from the observed behavior of the interplanetary magnetic field, the same sign over substantial fractions of the rotation period of the Sun of 25 days.

The force acting on the particle is given by its electric charge, which is determined by its electric potential and its effective radius. All the older estimates of the electric potential have been superseded since the actual conditions in interplanetary space have become known. Recent estimates give values of the order of 5 to 20 volts; the most detailed work known to the author is that of J. W. Rhee (paper 41 of this volume). On the basis of Rhee's work, we take 7 volts as typical for quiet conditions at 1 AU, whereas at the higher electron temperatures prevailing under disturbed conditions, 8 volts might be more representative. At smaller distances from the Sun, the potential should be slightly higher. We shall take 7.5 volts or 0.025 esu as an overall average. For a spherical particle, the charge is given by the product of the potential and the radius; we note that for nonspherical particles, the charge may be smaller, for example, by a factor π in the extreme case of a spherical disk.

For a spherical particle of radius a the force is then

$$\begin{aligned} |K_z| &= 10^{-1.6} a \times 10^{-2.8} \times 10^{-4.5} \\ &= 10^{-8.9} \times a \text{ dyn} \end{aligned}$$

and the resulting acceleration is

$$b_z = 10^{-9.5} \frac{1}{\rho} \frac{1}{a^2} \text{ cm-sec}^{-2}$$

We assume, furthermore, that a typical period of time, during which the sign of \mathbf{K} remains the same, is $\approx 10^{5.9}$ seconds. The velocity gained in this time is then

$$v_z = 10^{-3.6} \frac{1}{\rho} \frac{1}{a^2} \text{ cm-sec}^{-1}$$

For the particle with $\rho = 2.5$ and $a = 10^{-4.0}$ cm considered above, we find $10^{-1.9}$ cm/sec² and

$10^{4.0}$ cm/sec = 0.1 km/sec; if the velocity would increase statistically, after $\approx 10^5$ reversals (10^{11} sec), the additional velocity needed for escape would be reached. After reaching the escape velocity, the particle would be lost fast. The time of 10^{11} seconds is again comparable to the ones found before. It is difficult to say, however, by how much it should be increased in order to allow for the deviation from statistical conditions obviously present; on the other hand, for the reasons stated previously the energy needed will normally be only a fraction of that needed for large bodies. We conclude that 10^{11} sec is an adequate estimate; we note that for larger particles electromagnetic effects become rapidly unimportant, the time scale being $\approx a^4$ as compared to a^1 for the Poynting-Robertson effect and for sputtering.

Turning now to very small particles, we see that for a particle size of $a = 10^{-5.1} = 800$ Å, we have $v_z = 10^{6.2}$ cm/sec. The effective escape velocity would approximately be reached in one step; since the distance covered in this time is only $10^{11.8}$ cm or 0.04 AU, at least 25 times as many time intervals would be needed before the particle would indeed be lost (the simultaneous diffusion in velocity and in real space does not seem to have been discussed in the literature; we take the distances covered to be $\sim t^1$ under these circumstances). The resulting time scale is $\geq 10^7$ seconds. The distance reached in the first step increases $\sim 1/a^2$, so that for $a = 10^{-5.8}$ cm, 1 AU is reached by one step and the "lifetime" has decreased to $10^{5.9}$ seconds. From there on it decreases further only $\sim a$.

Comparing this time scale with the ones found for the Poynting-Robertson effect and for sputtering, we see that whereas for $a = 10^{-4}$ cm = 1 μ , all these time scales are the same within their range of uncertainty; for $a < 10^{-5}$ cm, the effect last discussed dominates.

We now collect our results on the lifetime t_l of spherical dielectric particles of a density of $\rho = 2.5$ as a function of their radius a in table 1, in which they are compared with the figures for nonspherical particles and for metallic particles of spherical or nonspherical shape. In each case, the particle mass and the assumed ratio of radiation pressure to gravity K_r/K_g which deter-

mines, for a given particle orbit, $t_{P.R.}$ precedes the lifetime. The radius is given in μ .

The actual size limit, below which the majority of particles injected from a comet should get lost, was estimated above as 3 a_0 or 1 μ . The limit below which *all* injected particles get lost would, from the considerations given above, be near that one for which $K_r = \frac{1}{2} K_g$; we put it at $a = 0.5 \mu$. Between 0.5 μ and 1 μ , even the order of magnitude of the lifetime depends on the initial conditions; this is indicated by the entry $\frac{1}{2} \times 10^{11}$ or 10^7 seconds. For $a \leq 0.03 \mu$, the electromagnetic effects result in accelerations so large, compared with solar gravity ($10^{-0.2}$ cm/sec at 1 AU), that distances of ≈ 1 AU are reached within a time shorter than 10^7 seconds; near $a = 0.01 \mu$ time intervals of $\leq 10^6$ seconds are reached.

The general dependence of t_l on a is therefore such that both for larger radii ($a > 1 \mu$) and for very small radii ($a < 0.16 \mu$) t_l is proportional to a , but with a factor of proportionality different by roughly three powers of 10; in the transition region, t_l is approximately constant, being $\leq 10^7$ seconds. The drop from $\leq 10^{11}$ seconds to $\leq 10^7$ seconds around 0.8 μ takes place in a range of a , which corresponds only to a factor of 2 or 3, such that $d \log t_l / d \log a$ is of order 10.

If we assume tentatively that the supply of such particles from comets is a smooth function of a , say $\sim a^{-4} da$, down to 0.01 μ , and furthermore if only supply and elimination were to be considered, the stationary number of particles actually present in interplanetary space, considered as a function of a only, should exhibit a kind of gap in the interval $0.5 \mu < a < 0.1 \mu$; the stationary number density per unit interval of da would be in the ratio of 1:10 for $a \approx 1 \mu$ and $a \approx 0.03 \mu$, but approximately $a^{-3} da$ for $a > 1 \mu$ and $< 0.03 \mu$.

Spherical metallic particles and nonspherical particles of both kinds remain to be considered. As an example of the first, we use published figures for iron and nickel ($\rho \approx 8$), which lead to $a_0 \approx 0.16 \mu$. In contrast to the behavior of dielectric particles, K_r does not again become small compared with K_g at small radii; since, however, at such small values of a , the electromagnetic forces dominate in any case, the gen-

TABLE 1.—*Lifetimes of Particles*[The spacing of the lines corresponds approximately to the differences of the logarithms of a]

(a) Spherical particles

a, μ	Dielectric ($\rho = 2.5$)				Metallic ($\rho = 8$)		
	$\frac{2\pi a}{\lambda}$	m	K_r/K_g	t_l, sec	m	K_r/K_g	t_l, sec
1	13	$10^{-11.0}$	$\geq .2$	$\sim a$ $\approx 10^{11}$ $\frac{1}{2} \times 10^{11} \text{ or } 10^7$			
.5	6	$10^{-11.9}$	$\approx \frac{1}{2}$	$\approx 10^7$	$10^{-11.4}$	$\geq .2$	$\sim a$ $\approx 10^{11}$ $\frac{1}{2} \times 10^{11} \text{ or } 10^7$
.32	4	$10^{-12.5}$	1	.			
.25	3.2			.	$10^{-12.3}$	$\approx \frac{1}{2}$	$\approx 10^7$
.16	2	$10^{-13.4}$	> 1	.	$10^{-12.9}$	1	.
				.			.
.063	.8	$10^{-14.6}$	≈ 1	$\approx 10^7$	$10^{-14.1}$	> 1	.
							.
.032	.4	$10^{-15.5}$	< 1	$\approx 10^{6.5}$	$10^{-15.0}$	≈ 1	$\approx 10^7$
.016	.2	$10^{-16.4}$		$\approx 10^6$	$10^{-15.9}$.	$\approx 10^{6.5}$
.010	.13			$\sim a$	$10^{-16.5}$.	$\approx 10^6$ $\sim a$

(b) Nonspherical particles

a, μ	Dielectric				Metallic		
	$\frac{2\pi a}{\lambda}$	m	K_r/K_g	t_l, sec	m	K_r/K_g	t_l, sec
3.2	40			$\sim a$		$\approx .2$	$\sim a$ $\approx 10^{11}$ $\frac{1}{2} \times 10^{11} \text{ or } 10^7$
2	25	$10^{-10.5}$	$\approx .2$	$\approx 10^{11}$ $\frac{1}{2} \times 10^{11} \text{ or } 10^7$		$\approx \frac{1}{2}$	$\approx 10^7$
1	13	$10^{-11.4}$	$\approx \frac{1}{2}$	$\approx 10^7$.
.8	10				$10^{-11.7}$	≈ 1	.

eral behavior of t_l as a function of a remains the same, with the transition region of constant t_l being displaced to somewhat smaller radii.

For nonspherical particles³ the ratio of cross section to volume is larger than for spherical particles; if a now relates to the cross section, this may be allowed for in a rough approximation by using an artificially reduced density in the expression; for the mass, the value of the density would be chosen equal to 1 both for dielectric particles and for metallic particles. In the latter case, the observations of the "fluffy" particles in the high atmosphere suggested a somewhat extreme assumption of the effective ratio cross section to volume. The ratio K_r/K_g which determines $t_{P.R.}$ was taken to be larger than that for spherical particles in the ratio 2.5:1 to 8:1. For very small particles, where electromagnetic effects dominate, the effective ratio of radius to volume has to be considered; for nonspherical particles, the effect of the larger radius for given mass is somewhat reduced by the fact that the electric charge may be smaller (see above). In the range of radii of the order 0.01μ no separate entries have been made for particles of nonspherical shape, t_l being mainly determined by the mass.

Returning to the question of which quasi-stationary distributions of particle sizes in interplanetary space are plausible and should be used for comparison in the observational data (e.g., the polarization as a function of position), it is seen that in the range below $a \approx 1 \mu$, no pure power law is likely to be realized. If particles with $a \leq 0.1 \mu$ are assumed to exist, as has been assumed several times, their size distribution function should be regarded as being effectively

separated⁴ from that for particles with $a \geq 1 \mu$, because the change (by a factor 10^4 or so) of the lifetime with decreasing size should have the consequence that there is a minimum in the stationary distribution function of particles below 1μ , although this could partially be filled in by variations in the particle properties and shapes. Hence, no firm conclusions regarding the possible existence of submicron particles seem possible without using size distribution functions which allow for this.

It is clear that the short lifetime of very small particles of $\approx 10^7$ seconds leads to at least two questions. One refers to the amount of the supply of cometary particles required, and the other refers to the variations of the zodiacal-light data with time and position to be expected. It was mentioned already that mass densities in space of very small particles of 10^{-25} g/cm^3 should produce observable effects. Assuming an effective volume of $\frac{4\pi}{3} \times \frac{1}{5} (1 \text{ AU})^3 = 10^{39.4} \text{ cm}^3$ and a lifetime of 10^7 sec , we find $\approx 10^{15} \text{ g/year}$. Restricting attention to the fairly large number of periodic rather faint comets, we note that cometary masses are usually thought⁵ to be of the order 10^{16} to 10^{18} g ; 1 percent of 10^{17} g/year would just seem to be consistent with the cometary data. With regard to the variations of particle densities with space and time, we observe that the relatively rapidly changing accelerations resulting from the electromagnetic forces, which for small particles are large compared with solar gravity, should result in a dispersion, which together with the effect of the long path length of integration would seem to make it difficult to detect correlations with individual comets. Both questions obviously require further study.

REFERENCES

- BEHR, A., and H. SIEDENTOPF, 1953, *Zeits. f. Astrophys.*, **32**, 19.
 DELSEMME, A. H., 1966, *Mém. Soc. Roy. Sci. Liège*, **12**, 69-111.
 ELSÄSSER, H., and T. SCHMIDT, 1966, *Z. für Naturforschung*, **21a**, 1116.

³ After the meeting, L. Davis, Jr., informed me about still unpublished work of his which tends to indicate that asymmetrical particle shapes should by solar radiation pressure result in so rapid rotation that small particles are destroyed even faster than they would be eliminated by the process discussed here. I am indebted to Dr. Davis for drawing my attention to his results which are to be published soon.

⁴ The only published distribution function of at least approximately this character known to the author is that of Elsässer and Schmidt (1966).

⁵ In this connection, attention should be drawn to the work of Huebner (1965) who showed that the gas production of comets, which is thought to be comparable in mass with that of dust, varies with the root only of the visual luminosity.

- FERRARO, V. C. A., and E. N. PARKER, 1966, Reprint No. EFINS 66-50, Univ. of Chicago Press, 149.
- GIESE, R. H., 1961, *Z. für Astrophysik*, **51**, 119.
- , 1963, *Space Science Reviews*, **1**, 589.
- HARWIT, M., 1963, *J. Geophys. Res.*, **68**, 2171.
- HUEBNER, W. F., 1965, *Z. für Astrophysik*, **63**, 22.
- INGHAM, M. F., 1961, *Mon. Not. Roy. Astron. Soc.* **122**, 157.
- JACCHIA, L. G., 1963, *The Solar System*, Vol. IV (B. M. Middlehurst and G. P. Kuiper, eds.), 774-798 (Chicago: Univ. of Chicago Press).
- NESS, N. F., 1966, *Observations of the Solar Wind Interaction With Geomagnetic Field: Conditions Quiet*, 1.
- NESS, N. F., and J. M. WILCOX, 1964, *Phys. Rev. Letters*, **13**, 461.
- PARKER, E., 1964, *Astrophys. J.*, **139**, 951.
- WEHNER, G. K., C. KENKNIGHT, and D. L. ROSENBERG, 1963, *Plan Space Sci.*, **11**, 885.
- General: The articles of Porter, Whipple, Millman, McKinley, and Jacchia, 1963, *The Solar System*, Vol. IV (B. M. Middlehurst and G. P. Kuiper, eds.) (Chicago: Univ. of Chicago Press).

40. Dynamics of Submicron Particles ($a < 10^{-5}$ cm) in Interplanetary Space

THOMAS SCHMIDT AND HANS ELSÄSSER
*Landessternwarte
Heidelberg, Germany*

IN THIS PAPER the question of whether submicron particles could be present in interplanetary space is discussed. One reason for investigating this problem was to learn whether the polarization of the zodiacal light could be at least partially due to light scattering by such particles. The results of sampling experiments during the last few years have indicated the existence of particles with diameters less than 10^{-5} cm.

Some aspects of this problem are also discussed by Parker (1964), but our results are not in full agreement with his considerations. We study dynamic problems of particle motion only. Destroying of submicron-charged particles by internal electrostatic forces is not discussed.

RADIATION AND PARTICLE PRESSURE

In the planetary system particles can be present for a longer interval of time if radiation pressure of the solar light and corpuscular pressure of the solar wind are less than the gravitational attraction

$$F_g = 2.5 \rho a^3 r^{-2} \quad (1)$$

(ρ and a are the particle density and radius in $\text{g}\cdot\text{cm}^{-3}$ and cm, respectively; r is the distance from the Sun in AU).

The radiation pressure of submicron Rayleigh-like particles is

$$F_r = \frac{\pi a^2}{c} \int \left\{ \frac{8}{3} x^4 \mu^2 - 4x \operatorname{Im}(\mu) \right\} I_\nu d\nu, \quad \left(x = \frac{2\pi a}{\lambda}, \mu = \frac{m^2 - 1}{m^2 + 1} \right) \quad (2)$$

Therefore, only for dielectric particles in the

submicron range—or for such particles with a small imaginary part of the refractive index—does the radiation pressure become less than the gravitational attraction. If we refer to ice or quartz particles, we get the result that only particles with radii less than 6×10^{-6} cm may be stable against radiation pressure.

The corpuscular pressure of the solar wind is given by

$$F_c = \pi a^2 k f_c m_c v_c \quad (3)$$

This equation sets a lower limit of orbit stability near about $a = 10^{-7}$ cm, if we assume that the solar particle flux is $f_c = 10^9 \text{ cm}^{-2} \text{ sec}^{-1}$, the particle velocity $v_c = 400 \text{ km/sec}$, the efficiency factor $k = 1$, and the corpuscular mass

$$m_c = m_p = 1.67 \times 10^{-24} \text{ g}$$

THE POYNTING-ROBERTSON EFFECT

The tangentially directed Poynting-Robertson force is given by

$$F_{pr} = - \left(\frac{F_r}{c} + \frac{F_c}{v_c} \right) u \quad (4)$$

where u is the tangential component of the orbital velocity of the dust particles. The lifetime t_{pr} of an interplanetary particle due to the radiation and corpuscular Poynting-Robertson effect, until its angular momentum becomes zero, is therefore

$$t_{pr} = M / \left(\frac{F_r}{c} + \frac{F_c}{v_c} \right) \quad (5)$$

where M is the mass of the particle. The following

table gives some results; t_{pr}^r is the lifetime computed without the corpuscular component of the Poynting-Robertson effect:

a , cm	t_{pr}^r , yr	t_{pr} , yr
10^{-7}	3.4×10^8	2.4
10^{-6}	3.4×10^5	24
10^{-5}	340	140
10^{-3}	7×10^3	6×10^3

We see that the particle lifetimes for $a \leq 10^{-5}$ are determined by the solar wind and are very small compared with the lifetimes of greater particles.

THE LORENTZ FORCE OF THE INTERPLANETARY MAGNETIC FIELD

The Lorentz force of the interplanetary magnetic field is given by

$$\mathbf{F}_L = -\frac{q}{c} \mathbf{v}_c \times \mathbf{B} \quad (6)$$

The electrostatic potential of interplanetary dust particles may be about $\Phi = 6$ volts, after Rhee (1966). The resulting electric charge is given by $q = 2 \times 10^{-2} a \chi$ [cgsu], where χ is a parameter of particle geometry. It is $\chi = 1$ for spheres and $\chi = 1/\pi$ for flat circular disks. We take into account a tangential component of the interplanetary magnetic field of $B = 3 \times 10^{-5}$ gauss only; therefore, the following particle lifetime computations are for lower limits only.

Thus we get, in cgs units,

$$F_L = 0.2 \times 10^{-16} \kappa a v_c \quad (7)$$

where κ describes the deviation of χ from 1 and of Φ and B from the figures given above.

We now consider the influence of magnetic fields with statistically alternating signs on dust particles moving on circular orbits around the Sun. According to space-probe measurements, we take a mean time interval of $\Delta t = 10^6$ seconds between sign changes of the magnetic field.

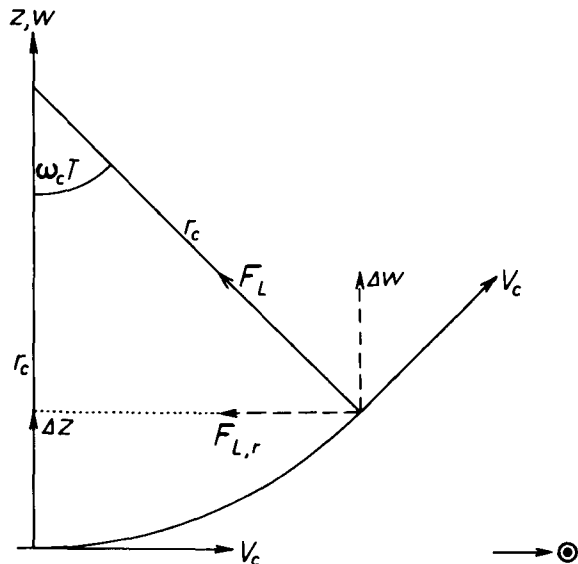


FIGURE 1.—The Lorentz force of the interplanetary magnetic field, where z and w are the spatial and velocity coordinates, respectively, perpendicular to the ecliptic plane.

The particle will be swept out from the planetary system at least after the epoch t_L , when the deviation of the particle motion from the tangential direction has led to a radial component of the Lorentz force $F_{L,r}$ (see fig. 1) greater than the gravitational attraction. We get

$$F_{L,r} = \omega_c F_L \sqrt{t \Delta t} \quad (8)$$

ω_c is the gyration frequency of the particle. Comparing $F_{L,r}$ with the gravitational attraction, we find

$$t_L = 1.1 \times 10^{63} \frac{a^8 \rho^4}{v_c^2 \kappa^4} \quad (9)$$

Figure 2 shows the results of the computations for different values of κ . The upper limit of sub-micron particle lifetimes in the planetary system thus becomes not more than 10 years.

In summarizing the results of our considerations, it must be stated that a considerable number of dust particles with $a < 10^{-5}$ cm in the interplanetary system could exist only if there is a very effective production mechanism. To get no unreasonably high densities of long-lived particles with $a > 10^{-4}$ cm, this production mechanism should generate particles exclusively

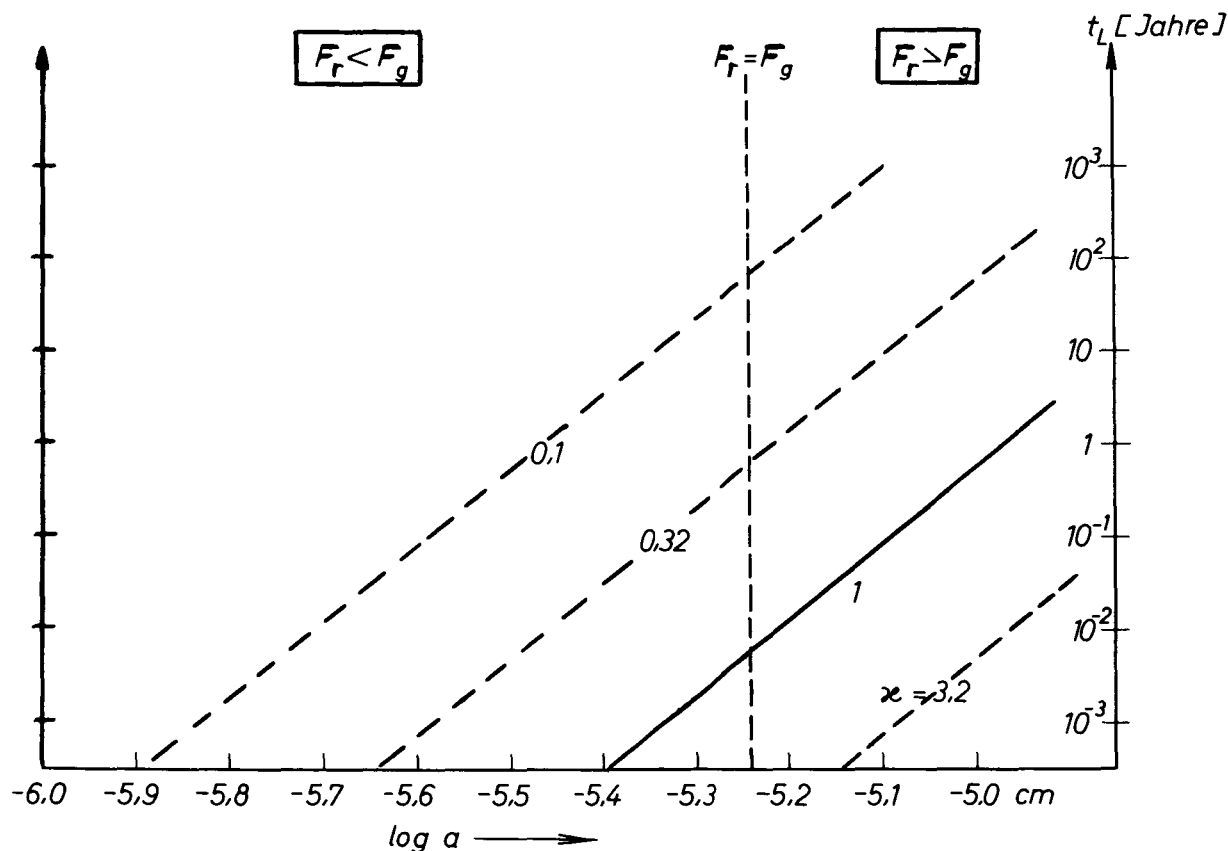


FIGURE 2.—Lorentz force lifetimes t_L of interplanetary dust particles with density $\rho = 1 \text{ g}\cdot\text{cm}^{-3}$ for different values of κ .

in the submicron range. A mechanism of this type is not known.

CIRCUMTERRESTRIAL DUST CLOUD

Is there a possibility for a circumterrestrial concentration of these submicron particles caused by trapping within the Earth's magnetosphere? A particle could be captured if the gyration radius r_g of motion in the magnetic field is less than the dimension of the magnetosphere of about $r_m = 10^5 \text{ km}$. The following table shows particle velocities v_p relative to the Earth with $r_g = r_m$ ($\Phi = 6 \text{ volts}$, $B = 3 \times 10^{-4} \text{ gauss}$).

$a, \text{ cm}$	$v_p, \text{ km/sec}$
10^{-5}	0.05
10^{-6}	5
10^{-7}	500

Therefore, Lorentz capture of interplanetary dust particles by the magnetosphere may be possible if the particles are smaller than 10^{-6} cm .

For details of this investigation, see Elsässer and Schmidt (1966).

REFERENCES

- ELSÄSSER, H., and T. SCHMIDT, 1966, *Z. für Naturforschung*, **21a**, 1116.
 PARKER, E. N., 1964, *Astrophys. J.*, **139**, 951.
 RHEE, J. W., 1966, Univ. of Maryland, Dep. of Physics and Astronomy, Technical Report, No. 596.

Page intentionally left blank

41. Electrostatic Potential of a Cosmic Dust Particle*

JOHN W. RHEE
*Rose Polytechnic Institute
Terre Haute, Indiana*

An attempt has been made to compute the equilibrium potential of a cosmic dust particle in interplanetary space. The equilibrium potential is determined by the balance of the photoelectrons and thermal plasma only. The contribution to the potential from the protons is shown to be small and can be neglected in interplanetary space. The preliminary data seem to indicate that the maximum potential is 6.6 volts at 1 AU, 5.7 volts at 2 AU, and 5.3 volts at 3 AU. The potential must be of the same order of magnitude at the other distances.

THE MOTION OF A SMALL DUST PARTICLE moving in the solar system usually has been considered only in relation to the gravitational force and solar radiation pressure. In actuality, it can be expected that they do have certain electric charges due to the solar wind and photoelectric effect produced by the solar radiation. In such cases, the magnetic field carried in the solar wind will exert a Lorentz force on the cosmic dust particles which are responsible for the zodiacal light. For particles smaller than about 10^{-5} cm the electromagnetic force dominates the Poynting-Robertson effect, thus forming the principal perturbation to the Keplerian orbits (Singer, 1965).

A cosmic dust particle can be charged by a number of the following physical processes:

- (1) Loss of electrons due to the photoelectric effect
- (2) Accretion of electrons in interplanetary space
- (3) Capture of positive ions or protons
- (4) Loss of electrons and protons by interaction with the cosmic rays
- (5) Loss of electrons by thermionic emission.

Only the first three processes are important. The cosmic dust particles probably have a net positive charge due to the excessive loss of the electrons. The charged dust particles may be trapped in the magnetic field of the Earth. The electrostatic force can break up the fluffy "dust balls" and inject them into closed orbits around the Earth.

A number of authors have considered the potential of a dust particle located in interplanetary space, and the values obtained in these papers range from a few tenths of a volt to several kilovolts (Öpik, 1956; Whipple, 1940; Shklovskii, 1958; Spitzer, 1941; Sonett, 1960; Singer, 1961; Parker, 1964; Kurt and Moroz, 1962; Peale, 1966; and Divari, 1966). It has been predicted by Whipple (1940) and Singer (1961) that meteoric charges would be positive in interplanetary space because of the photoelectric effect and the possible interaction with the interplanetary magnetic field. The problem of the electric potential on interplanetary dust grains was first formulated by Spitzer (1941). Subsequent demonstrations of interplanetary gas and plasma indicate that meteoric orbits might be appreciably affected. The electric charge must become less positive as the particle approaches the Earth and must become negative in the ionosphere.

*The results presented in this paper represent one phase of research conducted at the University of Maryland under Grant NSF-GY-670 from the National Science Foundation.

Öpik (1956) showed that solid particles in interplanetary space would carry an electric potential of about 200 volts, caused by the photoelectric effect of the radiation from the solar corona. Assuming an interplanetary gas temperature of 10^4 K and a photocurrent density of 2.5×10^{-9} A/cm², Kurt and Moroz (1962) demonstrated that the equilibrium potential for a metallic sphere with a radius of 65 cm must be in the range between -2.4 and 4 volts. The perturbation of the cosmic dust particles by the solar wind has already been examined, and it is expected that the photoemission from the dust grains would lead to a positive potential of the order of 10 volts on each grain (Parker, 1964). Using the experimental data obtained by Hinteregger et al. (1959), Peale (1966) proved that the equilibrium potential of the dust particles must be less than 10 volts at 1 AU.

Our main objective here is to derive a relationship between the equilibrium potential and electron density and to show that the equilibrium potential in interplanetary space cannot be greater than about 7 volts.

CALCULATION OF POTENTIAL

The electrostatic potential of a dust particle in interplanetary space is established by the equilibrium between photoelectrons and secondary electrons leaving the particle and plasma electrons and ions sticking to the particle. The secondary emission coefficient of normal metals and alloys is appreciably less than unity. However, for a given particle flux and plasma density, the potential cannot rise above a few volts due to the secondary emission. Therefore, the contribution to the equilibrium potential from the secondary emission must be small and can be neglected. This means that the equilibrium potential will be determined by the photoelectrons and thermal plasma only. Because of the unknown efficiencies of the two processes, a direct approach to this problem seems to be rather difficult. Nevertheless, we will attempt to derive the equation of balance by assuming that the plasma electrons and protons are in thermal equilibrium and the dust particles are at rest relative to the plasma particles.

Let us consider a spherical dust particle of radius a , at a distance r from the Sun, and far from the Earth. The threshold frequency ν_t of a photon which can eject an electron from the particle is

$$\nu_t = \frac{1}{h} \left(W + \left| \frac{Qe}{a} \right| \right) \quad (1)$$

where h is the Planck's constant, W is the work function, e is the electronic charge, and Q is the positive charge on the dust particle. The charge Q in esu is related to the equilibrium potential, Φ in statvolts by

$$\Phi = \frac{Q}{a} \quad (2)$$

The photoelectric effect is efficient for the dust particles only when they are bombarded by the photons having a wavelength shorter than $\lambda_0 = 2000 \text{ \AA}$ (Spitzer, 1941). Hence we shall assume that $W = \frac{hc}{\lambda_0}$ where c is the speed of light.

The number of photons incident on the particle per second and which can ionize the dust particle is equal to

$$N_+ = \pi a^2 \left(\frac{R_\odot}{r} \right)^2 \int_{\nu_t}^{\infty} \frac{P(\nu) d\nu}{h\nu} \quad (3)$$

where R_\odot is the radius of the Sun, $P(\nu)$ is Planck's radiation function, and

$$4\pi R_\odot^2 \int_0^{\infty} P(\nu) d\nu = 4 \times 10^{33} \text{ ergs/sec} \quad (4)$$

For the purpose of simplicity, we shall also assume that $P(\nu)$ can be approximated by Wien's formula

$$P(\nu) \propto \nu^3 \exp \left(-\frac{h\nu}{KT_s} \right) \quad (5)$$

where T_s is the surface temperature of the Sun (6000° K) and K is the Boltzmann constant. After some manipulations, we find that

$$N_+ = \frac{a^2 \times 10^{33}}{6r^2 KT_s} (x^2 + 2x + 2) [\exp(-x)] \quad (6)$$

where

$$x = \frac{h\nu_t}{KT_s} = \frac{W}{KT_s} + \frac{|e\Phi|}{KT_s}$$

Along with this, we must investigate the rate at which the free electrons and protons stick to the particle. Under stationary conditions, both rates must be identical, and this determines the equilibrium potential Φ .

Let us assume that there are N_e electrons per cm^3 in space and that these electrons are characterized by the kinetic temperature T_e according to the corresponding Maxwellian velocity distribution. The electron flux N_- incident on the particle has been given by Singer (1956) and is equal to

$$N_- = \frac{N_e \int_0^\infty \sigma(v) v f(v) dv}{\int_0^\infty f(v) dv} \quad (7)$$

where $\sigma(v)$ is the capture cross section and given by Singer (1956)

$$\sigma(v) = \pi a^2 \left(1 + \frac{2|Qe|}{M_e v^2 a} \right) \quad (8)$$

and

$$f(v) = \frac{1}{v^2} \exp \left(-\frac{M_e v^2}{2KT_e} \right) \quad (9)$$

where M_e is the mass of the electron.

Integration of equation (7) yields

$$N_- = \pi a^2 \left(\frac{8KT_e}{\pi M_e} \right)^{1/2} N_e \left(1 + \frac{|e\Phi|}{KT_e} \right) \quad (10)$$

Similarly, we write the following expression for the protons:

$$N'_+ = \pi a^2 \left(\frac{8KT_p}{\pi M_p} \right)^{1/2} N_p \left(1 - \frac{|e\Phi|}{KT_p} \right) \quad (11)$$

where N'_+ is the proton flux, N_p is the proton density, T_p is the proton temperature, and M_p is the mass of the proton.

A stationary condition is achieved if

$$\eta N_+ = N_- - N'_+ \quad (12)$$

where η is the ejection probability (quantum yield).

If the plasma is neutral, we have

$$N_e = N_p$$

and

$$T_e = T_p$$

Therefore, we get

$$\begin{aligned} & \frac{10^{33}\eta}{6r^2KT_s} (x^2 + 2x + 2) \exp(-x) \\ &= N_e (8\pi KT_e^{1/2}) \left[(M_e)^{-1/2} \right. \\ & \quad \left. - (M_p)^{-1/2} + \frac{|e\Phi|}{KT_e} (M_e^{-1/2} + M_p^{-1/2}) \right] \quad (13) \end{aligned}$$

But $M_e^{-1/2} \gg M_p^{-1/2}$, so we can rewrite equation (13) as

$$\begin{aligned} & \frac{10^{33}\eta}{6r^2KT_s} (x^2 + 2x + 2) \exp(-x) \\ &= N_e \left(\frac{8\pi KT_e}{M_e} \right)^{1/2} \left(1 + \frac{|e\Phi|}{KT_e} \right) \quad (14) \end{aligned}$$

According to equation (14), the contribution to Φ from the protons is small and can be neglected in interplanetary space.

ALTERNATE APPROACH

To evaluate the electron and proton fluxes of interplanetary plasma to the dust particle in a slightly different way, we make use of the theory developed by Mott-Smith and Langmuir (1926) and Bettenger (1965). The electron flux to the positively charged dust particle is

$$\begin{aligned} N_- = \pi b^2 N_e (V_e)_{av} & \left[1 - \frac{(b^2 - a^2)}{b^2} \right. \\ & \left. \exp \left(-\frac{a^2}{b^2 - a^2} \left| \frac{e\Phi}{KT_e} \right| \right) \right] \quad (15) \end{aligned}$$

where b is the Langmuir radius, $(V_e)_{av}$ is the mean velocity of the electrons. The proton flux is given by

$$N'_+ = \pi a^2 N_e (V_p)_{av} \exp \left(-\left| \frac{e\Phi}{KT_e} \right| \right) \quad (16)$$

where $(V_p)_{av}$ is the mean velocity of the protons.

For the dust particles of a few microns in diameter,

$$\frac{a^2}{b^2 - a^2} \left| \frac{e\Phi}{KT_e} \right|$$

is rather small. Hence, we may write

$$N_- = \pi a^2 N_e (V_e)_{av} \left(1 + \left| \frac{e\Phi}{KT_e} \right| \right) \quad (17)$$

and

$$N'_+ = \pi a^2 N_e (V_p)_{av} \left(1 - \left| \frac{e\Phi}{KT_e} \right| \right) \quad (18)$$

which are identical with equations (10) and (11) if we substitute $(V_e)_{av}$ and $(V_p)_{av}$. The equilibrium potential determined by equation (14) is seen to be independent of the particle radius, provided the particle radius is small in comparison with the Debye shielding length.

In the absence of photoelectrons the plasma will charge the particle to a small negative potential due to the difference in the electron and proton velocities. If the space charge layer is neglected, this potential is equal to

$$\Phi_0 = \frac{KT_e}{e} \ln \left(\frac{M_p}{M_e} \right)^{1/2} \quad (19)$$

and $\Phi_0 = -3.2$ volts for $T_e = 10^4$ °K. For small electron density Φ_0 is somewhat higher (-2.1 volts).

DISCUSSION AND CONCLUSION

Using equation (14), we have computed the equilibrium potential (volts) as a function of electron density for three different electron temperatures (10^3 , 10^4 , and 10^5 °K) and for the three Sun-particle distances (1, 2, and 3 AU); they are tabulated in tables 1, 2, and 3. The result is also plotted in figures 1 to 9.

The estimates of the electron density in interplanetary space (at 1 AU) have ranged from a value of 600 electrons/cm³ down to the current best estimates of 1 to 10 electrons/cm³. These values are obtained from both the direct measurements and the recent results from the zodiacal light studies. The low electron density indicates that the polarization of the zodiacal light is due to the interplanetary dust particles rather than to the electrons. In addition to the electron density, we have to know the ejection probability and this is not well known at the present time. According to the recent work, the ejection probability for $\lambda = 584$ Å and 740 Å is equal to 0.13, and near L_α ($\lambda = 1215$ Å) it attains a value of 0.02 (Kurt and Moroz, 1962). Therefore, we

TABLE 1.—*Equilibrium Potential as a Function of Electron Density and Temperature at 1 AU*
[Ejection probability η is assumed to be unity]

Equilibrium potential, Φ , volts	Electron density, N_e , electrons/cm ³ , at—		
	Electron temperature, $T_e = 10^3$ °K	Electron temperature, $T_e = 10^4$ °K	Electron temperature, $T_e = 10^5$ °K
1.0	2.29×10^5	4.23×10^5	2.59×10^5
1.2	1.38×10^5	2.73×10^5	1.81×10^5
1.4	8.55×10^4	1.78×10^5	1.27×10^5
1.6	5.37×10^4	1.16×10^5	8.86×10^4
1.8	3.42×10^4	7.67×10^4	6.19×10^4
2.0	2.20×10^4	5.07×10^4	4.32×10^4
2.2	1.43×10^4	3.37×10^4	3.02×10^4
2.4	9.32×10^3	2.25×10^4	2.10×10^4
2.6	6.12×10^3	1.50×10^4	1.46×10^4
2.8	4.04×10^3	1.01×10^4	1.02×10^4
3.0	2.67×10^3	6.76×10^3	7.10×10^3
3.2	1.78×10^3	4.55×10^3	4.94×10^3
3.4	1.18×10^3	3.06×10^3	3.43×10^3
3.6	7.91×10^2	2.07×10^3	2.39×10^3
3.8	5.30×10^2	1.40×10^3	1.66×10^3
4.0	3.55×10^2	9.44×10^2	1.15×10^3
4.2	2.39×10^2	6.39×10^2	7.98×10^2
4.4	1.61×10^2	4.33×10^2	5.54×10^2
4.6	1.08×10^2	2.93×10^2	3.84×10^2
4.8	7.31×10^1	1.99×10^2	2.66×10^2
5.0	4.94×10^1	1.35×10^2	1.84×10^2
5.2	3.34×10^1	9.21×10^1	1.28×10^2
5.4	2.26×10^1	6.29×10^1	8.84×10^1
5.6	1.53×10^1	4.26×10^1	6.12×10^1
5.8	1.04×10^1	2.90×10^1	4.23×10^1
6.0	7.03	1.99×10^1	2.93×10^1
6.2	4.77	1.34×10^1	2.02×10^1
6.4	3.24	9.15	1.40×10^1
6.6	2.20	6.24	9.67
6.8	1.50	4.25	6.68
7.0	1.02	2.90	4.61
7.2	6.92×10^{-1}	1.98	3.19
7.4	4.71×10^{-1}	1.35	2.20
7.6	3.20×10^{-1}	9.20×10^{-1}	1.52
7.8	2.18×10^{-1}	6.28×10^{-1}	1.05
8.0	1.48×10^{-1}	4.28×10^{-1}	7.22×10^{-1}
8.2	1.01×10^{-1}	2.92×10^{-1}	4.98×10^{-1}
8.4	6.89×10^{-2}	2.00×10^{-1}	3.43×10^{-1}
8.6	4.70×10^{-2}	1.39×10^{-1}	2.37×10^{-1}
8.8	3.20×10^{-2}	9.31×10^{-2}	1.63×10^{-1}
9.0	2.18×10^{-2}	6.35×10^{-2}	1.12×10^{-1}
9.2	1.49×10^{-2}	4.34×10^{-2}	7.75×10^{-2}
9.4	1.01×10^{-2}	2.96×10^{-2}	5.34×10^{-2}
9.6	6.91×10^{-3}	2.02×10^{-2}	3.68×10^{-2}
9.8	4.71×10^{-3}	1.38×10^{-2}	2.53×10^{-2}
10	3.21×10^{-3}	9.44×10^{-3}	1.74×10^{-2}

TABLE 2.—*Equilibrium Potential as a Function of Electron Density and Temperature at 2 AU*
[Ejection probability η is assumed to be unity]

Equilibrium potential, Φ , volts	Electron density, N_e , electrons/cm ³ , at—		
	Electron temperature, $T_e = 10^3$ °K	Electron temperature, $T_e = 10^4$ °K	Electron temperature, $T_e = 10^5$ °K
1.0	5.73×10^4	1.06×10^5	6.47×10^4
1.2	3.46×10^4	6.82×10^4	4.53×10^4
1.4	2.14×10^4	4.44×10^4	3.17×10^4
1.6	1.34×10^4	2.91×10^4	2.22×10^4
1.8	8.55×10^3	1.92×10^4	1.55×10^4
2.0	5.50×10^3	1.27×10^4	1.08×10^4
2.2	3.70×10^3	8.42×10^3	7.54×10^3
2.4	2.33×10^3	5.62×10^3	5.26×10^3
2.6	1.53×10^3	3.75×10^3	3.66×10^3
2.8	1.01×10^3	2.52×10^3	2.55×10^3
3.0	6.68×10^2	1.69×10^3	1.77×10^3
3.2	4.44×10^2	1.14×10^3	1.23×10^3
3.4	2.96×10^2	7.66×10^2	8.58×10^2
3.6	1.98×10^2	5.17×10^2	5.96×10^2
3.8	1.32×10^2	3.49×10^2	4.14×10^2
4.0	8.88×10^1	2.36×10^2	2.88×10^2
4.2	5.99×10^1	1.60×10^2	2.00×10^2
4.4	4.02×10^1	1.08×10^2	1.38×10^2
4.6	2.71×10^1	7.35×10^1	9.60×10^1
4.8	1.83×10^1	4.99×10^1	6.65×10^1
5.0	1.23×10^1	3.39×10^1	4.61×10^1
5.2	8.35	2.30×10^1	3.19×10^1
5.4	5.65	1.56×10^1	2.21×10^1
5.6	3.83	1.06×10^1	1.53×10^1
5.8	2.59	7.24	1.06×10^1
6.0	1.76	4.93	7.32
6.2	1.19	3.36	5.06
6.4	8.10×10^{-1}	2.29	3.50
6.6	5.50×10^{-1}	1.56	2.42
6.8	3.74×10^{-1}	1.06	1.67
7.0	2.54×10^{-1}	7.25×10^{-1}	1.15
7.2	1.73×10^{-1}	4.94×10^{-1}	7.96×10^{-1}
7.4	1.18×10^{-1}	3.37×10^{-1}	5.50×10^{-1}
7.6	8.01×10^{-1}	2.30×10^{-1}	3.79×10^{-1}
7.8	5.45×10^{-2}	1.57×10^{-1}	2.62×10^{-1}
8.0	3.71×10^{-2}	1.07×10^{-1}	1.81×10^{-1}
8.2	2.53×10^{-2}	7.31×10^{-2}	1.24×10^{-1}
8.4	1.72×10^{-2}	4.99×10^{-2}	8.59×10^{-2}
8.6	1.17×10^{-2}	3.41×10^{-2}	5.92×10^{-2}
8.8	8.00×10^{-3}	2.33×10^{-2}	4.08×10^{-2}
9.0	5.45×10^{-3}	1.59×10^{-2}	2.81×10^{-2}
9.2	3.72×10^{-3}	1.08×10^{-2}	1.94×10^{-2}
9.4	2.54×10^{-3}	7.41×10^{-3}	1.33×10^{-2}
9.6	1.73×10^{-3}	5.06×10^{-3}	9.19×10^{-3}
9.8	1.18×10^{-3}	3.46×10^{-3}	6.33×10^{-3}
10	8.03×10^{-4}	2.36×10^{-3}	4.36×10^{-3}

TABLE 3.—*Equilibrium Potential as a Function of Electron Density and Temperature at 3 AU*
[Ejection probability η is assumed to be unity]

Equilibrium potential, Φ , volts	Electron density, N_e , electrons/cm ³ , at—		
	Electron temperature, $T_e = 10^3$ °K	Electron temperature, $T_e = 10^4$ °K	Electron temperature, $T_e = 10^5$ °K
1.0	2.55×10^4	4.70×10^4	2.87×10^4
1.2	1.54×10^4	3.03×10^4	2.01×10^4
1.4	9.50×10^3	1.97×10^4	1.41×10^4
1.6	5.97×10^3	1.29×10^4	9.85×10^3
1.8	3.80×10^3	8.52×10^3	6.88×10^3
2.0	2.45×10^3	5.64×10^3	4.80×10^3
2.2	1.59×10^3	3.74×10^3	3.35×10^3
2.4	1.04×10^3	2.50×10^3	2.34×10^3
2.6	6.80×10^2	1.67×10^3	1.63×10^3
2.8	4.49×10^2	1.12×10^3	1.13×10^3
3.0	2.97×10^2	7.51×10^2	7.89×10^2
3.2	1.97×10^2	5.05×10^2	5.49×10^2
3.4	1.32×10^2	3.40×10^2	3.81×10^2
3.6	8.79×10^1	2.30×10^2	2.65×10^2
3.8	5.89×10^1	1.55×10^2	1.84×10^2
4.0	3.95×10^1	1.05×10^2	1.28×10^2
4.2	2.65×10^1	7.11×10^1	8.87×10^1
4.4	1.79×10^1	4.81×10^1	6.15×10^1
4.6	1.20×10^1	3.27×10^1	4.27×10^1
4.8	8.12	2.22×10^1	2.96×10^1
5.0	5.49	1.51×10^1	2.05×10^1
5.2	3.71	1.02×10^1	1.42×10^1
5.4	2.51	6.95	9.82
5.6	1.70	4.73	6.80
5.8	1.15	3.22	4.70
6.0	7.82×10^{-1}	2.19	3.25
6.2	5.30×10^{-1}	1.49	2.25
6.4	3.60×10^{-1}	1.02	1.55
6.6	2.45×10^{-1}	6.93×10^{-1}	1.07×10^{-1}
6.8	1.66×10^{-1}	4.72×10^{-1}	7.42×10^{-1}
7.0	1.13×10^{-1}	3.22×10^{-1}	5.13×10^{-1}
7.2	7.69×10^{-2}	2.20×10^{-1}	5.34×10^{-1}
7.4	5.23×10^{-2}	1.50×10^{-1}	2.44×10^{-1}
7.6	3.56×10^{-2}	1.02×10^{-1}	1.69×10^{-1}
7.8	2.42×10^{-2}	6.98×10^{-2}	1.16×10^{-1}
8.0	1.65×10^{-2}	4.76×10^{-2}	8.03×10^{-2}
8.2	1.12×10^{-2}	3.25×10^{-2}	5.53×10^{-2}
8.4	7.66×10^{-3}	2.22×10^{-2}	3.81×10^{-2}
8.6	5.22×10^{-3}	1.51×10^{-2}	2.63×10^{-2}
8.8	3.55×10^{-3}	1.03×10^{-2}	1.81×10^{-2}
9.0	2.42×10^{-3}	7.06×10^{-3}	1.25×10^{-2}
9.2	1.65×10^{-3}	4.82×10^{-3}	8.61×10^{-3}
9.4	1.13×10^{-3}	3.29×10^{-3}	5.93×10^{-3}
9.6	7.68×10^{-4}	2.25×10^{-3}	4.08×10^{-3}
9.8	5.23×10^{-4}	1.54×10^{-3}	2.81×10^{-3}
10	3.57×10^{-4}	1.05×10^{-3}	1.94×10^{-3}

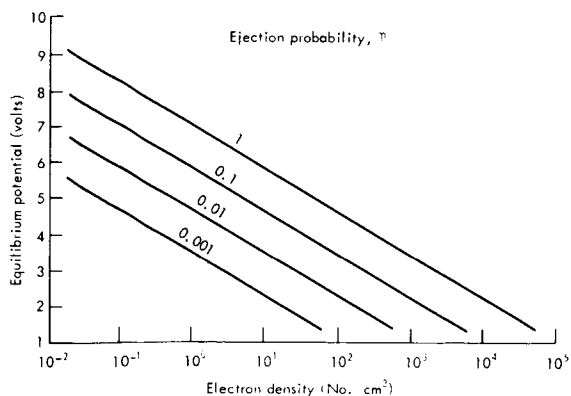


FIGURE 1.—Equilibrium potential as a function of electron density at an electron temperature of 10^3 °K at 1 AU.

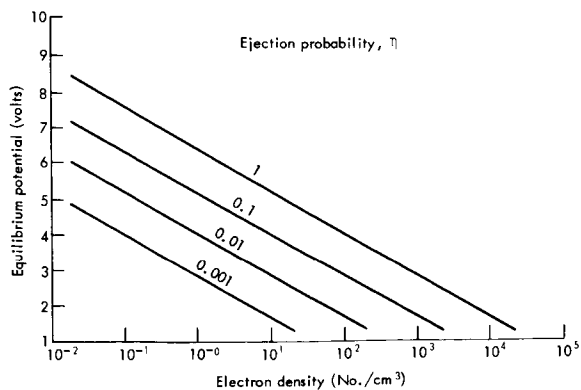


FIGURE 4.—Equilibrium potential as a function of electron density at an electron temperature of 10^3 °K at 2 AU.

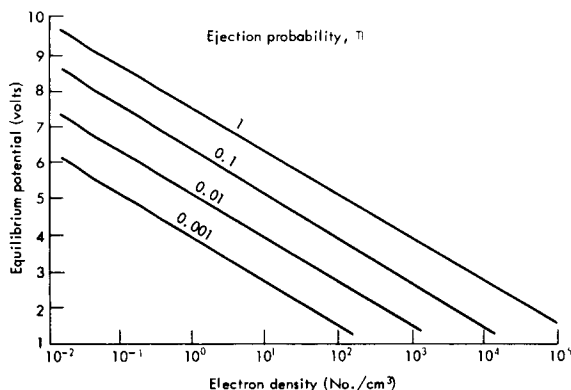


FIGURE 2.—Equilibrium potential as a function of electron density at an electron temperature of 10^4 °K at 1 AU.

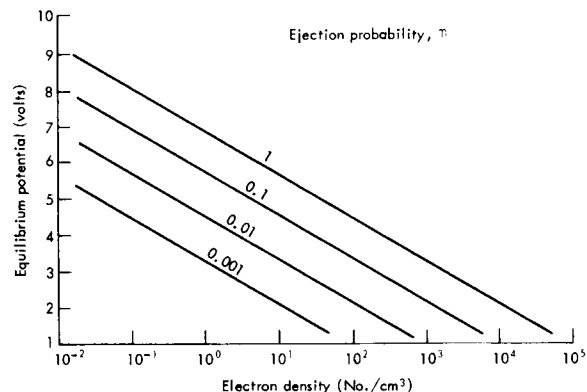


FIGURE 5.—Equilibrium potential as a function of electron density at an electron temperature of 10^4 °K at 2 AU.

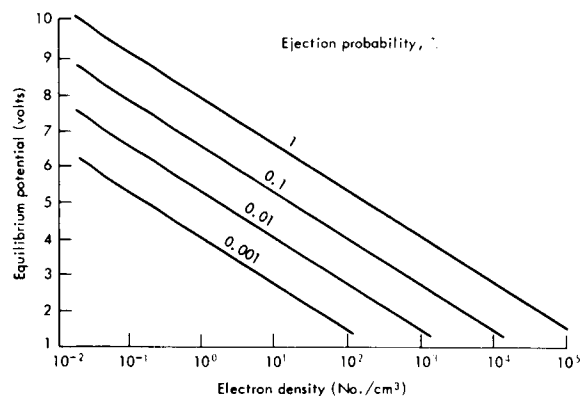


FIGURE 3.—Equilibrium potential as a function of electron density at an electron temperature of 10^5 °K at 1 AU.

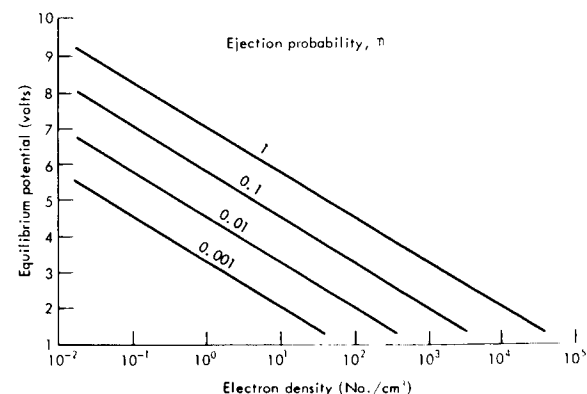


FIGURE 6.—Equilibrium potential as a function of electron density at an electron temperature of 10^5 °K at 2 AU.

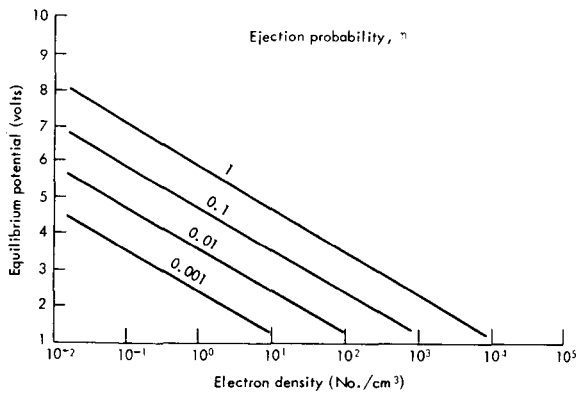


FIGURE 7.—Equilibrium potential as a function of electron density at an electron temperature of 10^3 °K at 3 AU.

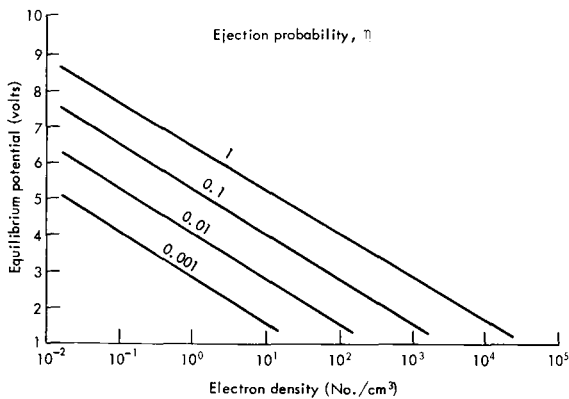


FIGURE 8.—Equilibrium potential as a function of electron density at an electron temperature of 10^4 °K at 3 AU.

assumed four different values for η and plotted Φ as a function of η .

An examination of the figures shows that the maximum potential is 6.6 volts at 1 AU, 5.7 volts at 2 AU, and 5.3 volts at 3 AU. It should be noted that the equilibrium potential is insensitive to great changes in the electron density and the probability of the photoelectric effect. It can therefore be assumed that the possible potential does not exceed 6 ~ 7 volts even for large meteoric particles at 1 AU. As can be seen from the

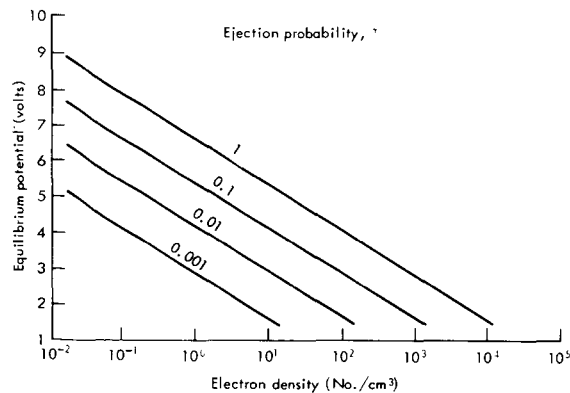


FIGURE 9.—Equilibrium potential as a function of electron density at an electron temperature of 10^5 °K at 3 AU.

tables and figures, the potential must be of the same order of magnitude at the other distances.

At high electron densities, the high temperature results in lower positive potential; for low density the reverse is true because as the plasma particle energy increases, the potential has less influence upon the capture cross section. The cross section decreases rapidly as the particle energy goes up.

In summary, an attempt has been made to estimate the equilibrium potential of an interplanetary dust particle, and it is shown that the potential in interplanetary space cannot exceed 7 volts. The existence of a high value of positive potential is most unlikely. Even though it seems impossible to measure charge of a dust particle at the present time, it is hoped that one can carry out an experiment to detect a charge of this magnitude in the future (Jennison and McDonnell, 1964).

ACKNOWLEDGMENT

The author was greatly stimulated by the encouragement and advice given by Howard Laster, E. J. Opik, and S. F. Singer. He is also grateful to Richard T. Bettinger for interesting discussions. The computing facility was also made available by Richard T. Bettinger.

REFERENCES

- BETTINGER, R. T., 1965, *Rev. Sci. Instr.*, **36**, 630.
DIVARI, N. B., 1966, *Soviet Astron.—AJ*, **10**, 151.
HINTEREGGER, H. E., K. R. DAMON, and L. A. HALL, 1959, *J. Geophys. Res.*, **64**, 961.
JENNISON, R. C., and J. A. M. McDONNELL, 1964, *Planetary Space Sci.*, **12**, 627.
KURT, P. G., and V. I. MOROZ, 1962, *Planetary Space Sci.*, **9**, 259.
MOTT-SMITH, H. M., and I. LANGMUIR, 1926, *Phys. Rev.*, **28**, 727.
ÓPIK, E. J., 1956, *Irish Astron. J.*, **4**, 84.
PARKER, E. N., 1964, *Astrophys. J.*, **139**, 951.
PEALE, S. J., 1966, *J. Geophys. Res.*, **71**, 911.
SHKLOVSKII, I. S., 1958, *Astron. Zh.*, **35**, 557.
SINGER, S. F., 1956, *Scientific Uses of Earth Satellites* (Univ. of Michigan Press), 301.
—, 1961, *Nature*, **192**, 303.
SONETT, C. P., 1960, *Advances in Space Science*, **2**, 89 (New York: Academic Press).
SPITZER, L., 1941, *Astrophys. J.*, **93**, 369.
WHIPPLE, F. L., 1940, *Proc. Am. Phil. Soc.*, **83**, 711.

42. The Thermal Emission of the Zodiacal Cloud* (Abstract)

C. KAISER AND G. NEWKIRK, JR.
High Altitude Observatory
Boulder, Colorado

The simultaneous influence of gravitation, Poynting-Robertson acceleration, and sublimation on interplanetary particles is examined in order to describe their evolution. A model for the interplanetary medium is constructed in which the particles are assumed to originate in an "asteroid mill" and subsequently to spiral into the Sun. Particular attention is paid to the sublimation of the material as it approaches the Sun and to the role this sublimation plays in determining the size and spatial distribution of semitransparent and opaque particles in the inner reaches of the solar system. The thermal radiation emitted by our models of the interplanetary medium is described.

*The complete text of this research will appear as a doctor's thesis, University of Colorado, by C. Kaiser.

Page intentionally left blank

43. Dynamics of Interplanetary Dust Particles Near the Sun*

MICHAEL J. S. BELTON
Kitt Peak National Observatory
Tucson, Arizona

Vaporization in the neighborhood of the Sun is generally considered as the primary sink for zodiacal dust particles. However, detailed consideration of the physical and dynamical behavior of the dust particles in the immediate vicinity of the Sun shows that this view is too facile.

In this contribution it is shown that the majority of the smaller grains are not destroyed by the process of vaporization. After approaching a certain minimum distance from the Sun under the influence of the usual drag forces, the onset of vaporization stabilizes the orbits of the particles and then causes them to move out into interplanetary space once more.

The grains are reduced in size but do not in general become so small that radiation pressure overcomes gravity.

The interaction of the electrically charged grains with the magnetized interplanetary gas is included in the dynamical treatment. First-order perturbation theory (variation of elements) is used to make quantitative estimates of the effects of Lorentz forces on the orbits of the particles.

The observed component of the interplanetary magnetic field perpendicular to the ecliptic has important consequences for the zodiacal particles if its direction is stable over time scales comparable with the period of the solar cycle.

THE INTERPRETATION of photometric and polarimetric observations of the zodiacal light with the help of simple, but highly parameterized, physical models has yielded a considerable amount of information about the general physical and optical characteristics of zodiacal particles. Unfortunately the very nature of the models that have been used has precluded the possibility of gaining much useful insight into such problems as: Where do the particles come from? What are their dynamics, and how are they destroyed or removed from the system?

In order to advance our understanding of these intriguing problems not only new and better observations are required, but also a better technique of building models with which to analyze

them. In order to extract information about the sources, sinks, and dynamics of interplanetary particles, we must use models which are based on specific assumptions about the nature of these properties. What is advocated in this contribution is therefore the replacement of the "variation of arbitrary parameters" technique, which is presently widely used, with a kind of "variation of physical assumptions" technique.

Such an approach has been tried in the past, notably by Fesenkov (1959) and also by Briggs (1962). Unfortunately it has not been too successful, the isophotes of the zodiacal light being reproduced, for example, in analyses based on three distinct origins for the particles (cf. Belton, 1966).

The lack of success, however, does not seem to be an indication of an intrinsic weakness in

*Kitt Peak National Observatory Contribution No. 237.

the method itself but merely a reflection of the quality and restricted nature of the observations that were available to the above investigators. With the increasing quality of photometric observations, the possibility of space observations giving information about the stability of the cloud and with direct information about the velocity distribution of the particles almost within grasp (see James, paper 13 of these proceedings), the careful development of this type of approach should, in the future, be very rewarding.

Unfortunately the physical and dynamical theory of the zodiacal dust cloud, on which this approach must be based, is not in a very satisfactory state at the present. It is the purpose of this contribution to consider two limited aspects of the dynamical problem: The importance of the interaction of the particles with the interplanetary magnetic field and also the behavior of the particles as they get very close to the Sun.

INTERACTION OF THE PARTICLES WITH THE INTERPLANETARY MAGNETIC FIELD

In considering this topic two difficulties immediately present themselves: The estimation of the electric charge on the particles as a function of their position in space and the choice of a suitable model for the interplanetary magnetic field.

The Electric Charge on Interplanetary Dust

Figure 1 illustrates the results of some rather extensive and detailed calculations of the equilibrium potential of interplanetary dust as a function of heliocentric distance. The calculations, which are extensions of some earlier work (Belton, 1964), include the effects of electronic and ionic accretion, secondary electron emission, photoelectric effect, and high-field and thermionic emission. The potential is plotted since, for positive charge at least, it is independent of the dimensions of the particle.

The decrease in potential near the Sun is due to both the increase in temperature of the interplanetary gas and to the rapid increase in electron density in the outer part of the corona. The negative values which are indicated are extremely uncertain because of the difficulty of evaluating the effects of lowering of the work

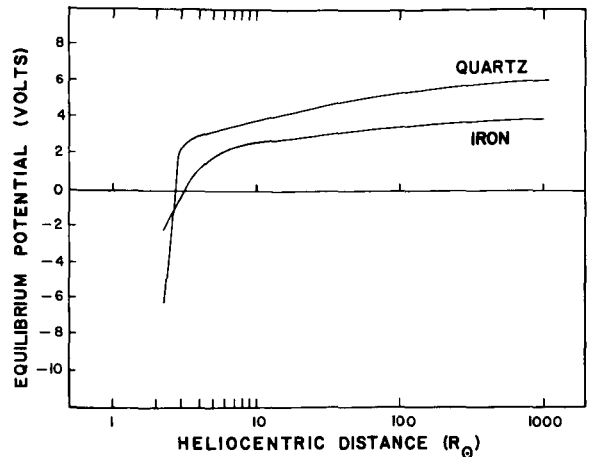


FIGURE 1.—The electrostatic potential of two types of dust particle in interplanetary space.

function at the surface of the grains caused by their own charge and high-field and thermionic emission. As particles will probably not exist this close to the Sun, these problems are largely academic. Of course, the potentials are not really as well defined as figure 1 might indicate. Considerable modulation of the potential may occur due to transient disturbances and large-scale inhomogeneities in the interplanetary medium (Belton, 1966).

In the simple calculations which follow I shall always assume that the particles are at a positive potential of 5 volts with respect to the interplanetary gas. It should be noted that at least two other detailed calculations of the equilibrium potential on interplanetary dust have appeared in the last two years (Notni, 1964; and Whipple, 1965). The results of these calculations are not at variance with those presented here.

The Interplanetary Magnetic Field

The choice of a suitable model for the interplanetary magnetic field poses one of the more difficult problems in this discussion. Parker (1964) and more recently Shapiro, Lautman, and Colombo (1966) have considered the problem in terms of an extended dipole configuration. In this contribution I shall make use of a rather different but equally simple model, first considered by Ahluwalia and Dessler (1962), in which the field is considered to consist of tubes of flux emanating from the Sun, supported by the solar

wind and twisted into "Parkerian" spirals due to the rotation of the sources of the field with the photosphere. The polarity in the tubes is determined by the photospheric fields at their bases. This model appears to fit the general features of the interplanetary field observed near the ecliptic (Dessler, 1967).

This representation of the magnetic field, which assumes an underlying radial expansion for the interplanetary gas at constant velocity, does not include a B_θ , or polar component.¹ Nevertheless, such a component may have been observed over an extended period of time by the magnetometers on Mariner II, IMP 1, and Mariner IV. On the average it is found to be directed southward with a magnitude of about 10^{-5} gauss. If it exists and is not simply the result of spacecraft fields or calibration error, this component presents a considerable problem for the theorist since it represents a gigantic drain of magnetic energy from the photosphere (Davis, 1966; and Dessler, 1967). From the point of view of the study of interplanetary dust such a long-lived B_θ component leads to rather spectacular effects which are discussed subsequently.

In the following sections we shall always consider the dynamics of the particles from the point of view of an observer whose frame of reference is nonaccelerating and centered at the Sun. Thus, two electromagnetic forces are involved in the dynamics: (1) a Lorentz force, due to the particles' motion with respect to the magnetic field, and (2) an electric force, due to the divergence-free electric field which must exist in our frame of reference so that the flow of interplanetary plasma may take place across the magnetic field. It was Parker (1964) who first pointed out the probable importance of this electric field in the dynamics of interplanetary dust.

The Influence of B_θ

From an elementary consideration of the resulting force acting on a charged dust particle, it is clear that it will suffer secular changes in both its orbital energy and angular momentum. For the positive charge which is expected, particles moving in a direct sense will find their

orbits to be shrinking and becoming more circular. The reverse will be the case for retrograde particles.

By using the technique of the "variation of the elements" (Moulton, 1914) or directly from the equations of motion, it is a simple matter to deduce the rate of change of a (the semimajor axis) and e (the eccentricity) of the osculating orbit. Taking the average over an orbit, the results are:

$$\left. \begin{aligned} da/dt &= (2wB_0K/\mu)a^{1/2} \cos i \\ de/dt &= (wB_0K/2\mu)e(1-4e^2)a^{-1/2} \cos i \end{aligned} \right\} \quad (1)$$

where w is the solar wind velocity; $K = V/\rho s^2$, where V is the electric potential, ρ is the mass density of the particle, and s is the particle radius; i is the orbital inclination; $\mu = (GM - \alpha)^{1/2}$, where G is the gravitational constant, M is the mass of the Sun, and $\alpha = (3QE_\odot/16\pi c s \rho)$ where c is the velocity of light, Q is a radiative efficiency factor for the transfer of radial momentum to the particle, and E_\odot is the solar constant.

These expressions are considerably different from those recently published by Shapiro et al. (1966) who assumed that $B_\theta = B_0/r^2$ where r is the heliocentric distance. In the work reported here, it is assumed that $B_\theta = B_0/r$ which has the appropriate r dependence for a constant solar wind velocity. Shapiro, Lautman, and Colombo's assumed form for $B_\theta(r)$ implies a solar-wind velocity which increases linearly with distance from the Sun in apparent contradiction to their own assumptions regarding the flow.

To give an indication of the magnitude of the effect of B_θ , it is natural to make a comparison with the effects induced on the orbit by the Poynting-Robertson drag. For a spherical particle of 1-micron radius in a circular orbit at 1 AU, the induced electromagnetic effect is 400 times that of Poynting-Robertson. The lifetime of such a particle ($\sim s^2 a^{1/2}$) is a mere 30 years, compared with 3500 years under Poynting-Robertson drag ($\sim s a^2$). Thus the presence of a steady B_θ component with the magnitude suggested by space observations will have very important consequences for the zodiacal particles. Its existence over times comparable with the solar cycle could cause strong variations of

¹ The fundamental plane of this coordinate system is taken as the solar equator.

the polarization and brightness of the cloud. The demand on the injection process would be increased by two orders of magnitude if a steady state existed under the influence of this field. One other interesting point connected with this, perhaps mythical, B_θ component, is that if a steady state did exist, then the space density of the particles would necessarily fall off as $r^{-2.5}$. This dependence is far stronger than is apparently allowed by the observations.

The Influence of B_r and B_ϕ

In this discussion the effects of B_θ will be ignored. As it moves, the particle responds to two kinds of variations in the magnetic field. It experiences the effects of reversals of polarity in the background field as it moves from one flux tube to another. For particles farther than 100 solar radii from the Sun, the characteristic period of the fluctuations is effectively determined by the solar rotation period and the number of flux tubes. The observations of the magnetic field show that this period is of the order of 10^6 seconds. For particles closer to the Sun, the period depends more and more on their sense of revolution. For direct particles, the period increases while the reverse is the case for those in retrograde orbits. The second type of fluctuation is due to transient disturbances propagating in the medium. It is assumed that these fluctuations are at sufficiently high frequencies and low magnitude to be effectively negligible in this discussion.

The gyration period of interplanetary dust particles is much larger than 10^6 seconds, and the effects of the electromagnetic forces can be treated in terms of a diffusion or random walk through a series of electromagnetic scattering cells. This rough type of calculation has been done by Parker (1964), who found that the scattering should only be important for submicron-size particles. The refinement which is presented here is to make use of the "variation of orbital elements" technique and to look at the problem as a random walk in orbital-element space. The object was an investigation of the possibility that certain of the orbital elements might be affected far more strongly than others. This, however, did not turn out to be the case. Relaxation times were computed for a , e , and i .

In each case the time was found to be of the same magnitude and proportional to (as^4/V^2P) where P is the period of the fluctuations as seen by the particles. Thus, the influence of the interplanetary electromagnetic field is seen to be a very strong function of the particle size. Using the effects of Poynting-Robertson drag as a criterion for the relative importance of interaction, we finally arrive at the same conclusion as did Parker: Within 1 AU from the Sun, magnetic effects are negligible for particles with dimensions of 1 micron or greater. The effects very rapidly increase in importance as smaller particles are considered.

It has already been mentioned that for direct particles the period of the electromagnetic fluctuations increases as the particles approach the Sun. When the particle is corotating with the Sun (at approximately 30 solar radii) the lifetime associated with the underlying magnetic field is the same as that of the photospheric fields. It would, therefore, appear that the electromagnetic forces could severely perturb the motion of the particles. In actual fact, this is probably not the case. In the corotation zone, our model for the magnetic field predicts that the Lorentzian force will precisely cancel the electric force; thus the net effect (for a circular orbit) is zero. This result serves as an extreme example, but points out that the effects induced by the particles' orbital motion cannot always be neglected in the dynamical problem.

BEHAVIOR OF INTERPLANETARY DUST PARTICLES AS THEY APPROACH THE SUN

Vaporization in the neighborhood of the Sun is generally considered to be the primary sink for zodiacal dust particles. It is therefore rather surprising that no detailed account of their behavior in the vicinity of this sink has appeared in the astronomical literature. Recently, Low and Smith (1966) have reported observations of thermal emission from a dust cloud surrounding the star R Mon. The model with which they have analyzed their observations indicates that the behavior of the material in the vaporization zone close to the star is of primary importance for an understanding of the observations. These reasons, plus the added stimulus provided by

the announcement at this conference that thermal emission has been observed from interplanetary dust within a few solar radii from the Sun, suggest that the fate of a particle as it approaches the Sun should receive careful consideration.

The particles get hot as they approach the Sun and begin to vaporize. They are therefore reduced in size. The problem of the correct choices of temperature and vapor pressure is a difficult problem by itself which it will not be useful to enlarge upon here. The relationships that have been used in the ensuing calculations are merely noted. If T is the temperature and p is the vapor pressure, then

$$T(r) = 120/r^{0.5}; \log p = -22200/T + 13.66 \text{ (dielectric)} \quad (2a)$$

$$T(r) = 418/r^{0.27}; \log p = -20040/T + 12.78 \text{ (metallic)} \quad (2b)$$

The temperature law used for dielectrics is that suggested by Over (1958), while the law used for metallic particles is based on the remarkable observations of comet 1965f by Becklin and Westphal (1966). The predicted temperature law for iron spheres (van de Hulst, 1949) is very similar to that deduced from the observations of Becklin and Westphal.

The evaporation will at first remove sharp surface protuberances and the particle will become roughly symmetrical in shape. Because of the small dimensions of the particles that we are considering, the temperature of the dark side will be within a very small fraction of a degree of that of the illuminated side, even for the worst conductors of heat. After a short time the evaporation can be assumed to be *effectively* isotropic. These statements are necessarily somewhat qualitative but can be justified by simple order-of-magnitude calculations.

As a result of its reduction in size, radiation pressure increasingly buoys up the particle against the force of gravity. In terms of potential, we can say that the particle's potential energy per unit mass increases as its radius decreases. The particle is not accelerated, however, since we have assumed that the evaporation is isotropic in the particle's rest frame. The total energy per

unit mass of the particle therefore increases with the potential energy. This implies that the semi-major axis of the osculating orbit is also increasing. Considering now only the effects of the evaporation of the grain, the assumption of isotropic evaporation requires that the angular momentum per unit mass of the particle must also remain constant. This result, together with an increasing semimajor axis, implies that the eccentricity of the orbit must also be increasing. All of these results can be deduced in a straightforward manner from the equations of motion of the particle.

The final stages of the development of a dust particle's orbit are therefore pictured as follows: The orbit of the particle, gently buffeted by the interplanetary magnetic field, first becomes circular and smaller in size under the action of various drag forces. At a small distance from the Sun, evaporation sets in, and the particle diminishes in size. The effects of the drags are at first stabilized and then overcome. The particle moves on to larger and more eccentric orbits until the orbit finally becomes hyperbolic and leaves the system. All of this only happens, of course, if the particle is not completely evaporated on one of its passes through perihelion. In order to check this, it has been necessary to perform a number of numerical integrations. A typical example is shown in figure 2.

Based on the calculations that have been performed, the following statements may be made with a fair degree of certainty:

(1) Metallic and dielectric particles in the size range of 1 to 10 microns will all eventually be ejected from the solar system on hyperbolic orbits providing their initial perihelion distance is greater than a certain minimum distance from the Sun. This distance is quite uncertain but was found to be 2.5 solar radii for dielectrics and 7 solar radii for metallic particles.

(2) When ejected from the system the particles are usually somewhat larger than the critical size at which radiation pressure exactly balances the force of gravity.

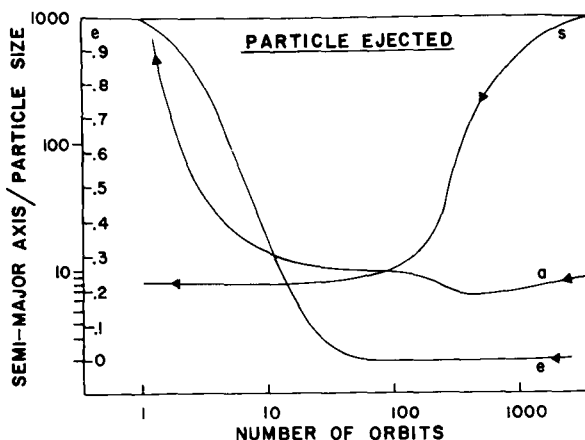
(3) Particles larger than about 10 microns are evaporated completely.

(4) The distance of closest approach to the Sun depends strongly on the precise optical and

physical properties of the particles. It also depends on the initial size of the particles. In our calculations, which did not incorporate the complications of the Mie theory, the distance of

closest approach for an initially 1-micron particle was 2.5 and 7 solar radii for dielectric and metallic particles, respectively.

FIGURE 2.—The development of the orbit of an evaporating dust particle. The particle is metallic and has an initial radius of $10\ \mu$. The integration is started with the particle in a circular orbit at 8 solar radii. The abscissa measures the number of orbits remaining before ejection. The ordinate displays a scale for a and s . The semimajor axis can be read directly in terms of solar radii. The scale is in units of 0.01 micron for s , the particle radius. The development of the orbit is fully described in the text.



REFERENCES

- AHLUWALIA, H. S., and A. J. DESSLER, 1962, *Planetary Space Sci.*, **9**, 195.
 BECKLIN, E. E., and J. A. WESTPHAL, 1966, *Astrophys. J.*, **145**, 445.
 BELTON, M. J. S., 1964, Thesis, Univ. of California, Berkeley.
 —, 1966, *Science*, **151**, 35.
 BRIGGS, R. E., 1962, *Astron. J.*, **67**, 710.
 DAVIS, L., 1966, *The Solar Wind* (New York: Pergamon Press), 148.
 DESSLER, A. J., 1967, *Reviews of Geophysics*, **5**, 1–42.
 FESENKOV, V. G., 1959, *Ann. Astrophys.*, **22**, 820.
 LOW, F. J., and B. J. SMITH, 1966, *Nature*, **212**, 675.
 MOULTON, F. R., 1914, *An Introduction to Celestial Mechanics* (2d ed., New York: Macmillan Publ. Co.).
 NOTNI, P., 1964, *Veröff. Sternwarte Babelsberg*, No. 1, **15**.
 OVER, J., 1958, *Koninkl. Ned. Akad. Wetenschap. Proc.*, **51B**, 74.
 PARKER, E. N., 1964, *Astrophys. J.*, **139**, 951.
 SHAPIRO, I. I., D. A. LAUTMAN, and G. COLOMBO, 1966, *J. Geophys. Res.*, **71**, 5695.
 VAN DE HULST, H. C., 1949, *Res. Astron. Obs. Utrecht*, **XI**, Part 2.
 WHIPPLE, E. C., JR., 1965, Thesis, George Washington University.

44. The Cloud of Interplanetary Boulders*

MARTIN HARWIT
Cornell University
Ithaca, New York

An attempt is made to evaluate the density of boulders (roughly 10-meter-sized objects) in interplanetary space. Such bodies cannot be directly observed and the most direct evidence comes from impacts on the Earth. We show that the most plausible density, consistent with various types of data, is $\sim 4 \times 10^{-28} \text{ cm}^{-3}$. This is about three orders of magnitude higher than the density usually quoted. The difference arises because we postulate that the boulders have orbits of low eccentricity and their approach rate toward the Earth is slow because the weak Poynting-Robertson effect is the only means by which the boulders are impelled into orbits of smaller diameter. The low orbital eccentricity is consistent with an asteroidal origin of boulders. We show that the unusually high concentration of boulders postulated here can indirectly produce interplanetary dust at a rate high enough to compensate the Poynting-Robertson losses. The high concentration of boulders can also explain the observed rate of splitting among parabolic comets and is consistent with the observation that these comets split near the ecliptic plane.

WE KNOW A GREAT DEAL about two types of interplanetary objects, the very small and the very large. We observe the small meteors and meteorites which impact on the Earth and make themselves known through atmospheric trails and impact craters. Their diameters normally are below a meter. The much larger asteroids, at the other extreme of the size range, are observed through telescopes. Their diameters range from 1 kilometer to more than 100. In the size range between these limits—the range from 10 to several hundred meters—we have little first-hand knowledge of interplanetary objects. Our only clue comes from a handful of craters on the Earth and a much larger number visible on the Moon.

For simplicity we call the 10-meter- to 0.5-kilometer-sized projectiles “boulders,” and we examine the available evidence to show that boulders may be far more abundant than pre-

viously thought. Current estimates on boulder densities in space are based on two types of data: (1) the number and size distribution of lunar craters and (2) a simple interpolation between estimated number densities of observable asteroids and meteorites. These two sets of data cannot be directly intercompared because the lunar data are cumulative over a long period of time and give little information about current boulder densities, while the asteroidal and meteorite studies are related to current number densities in interplanetary space. Even here, there is an important difficulty. The orbits of meteorites before impact are not yet well known, although the data being gathered by the Prairie Network will give the information we need. Meteorite trajectories—just as the orbits of meteors—may well turn out to be quite different from asteroidal orbits. And the orbits of boulders may be quite different from both asteroidal and meteoritic orbits.

We argue here that the orbits of boulders may have low values of eccentricity and inclination so that a dense cloud of boulders may survive

*The research reported in this paper was sponsored by the National Science Foundation under Grant GP-1338 and by the National Aeronautics and Space Administration under Grant NSG-382 and Contract NSP 33-010-026.

in interplanetary space for many eons without appreciable self-destruction. Further, we postulate that those boulders which initially had trajectories intersecting the Earth's orbit about the Sun soon were eliminated by collisions with the Earth or Moon. The boulders impacting on the Earth or Moon at the present epoch are the few objects which, at any given time, are slowly drawn in toward the Sun by virtue of the Poynting-Robertson effect. Because the boulders are massive and the Poynting-Robertson effect is weak, relatively few boulders approach the Earth in this way. Those that do come close are predominantly scattered into orbits of greater eccentricity and inclination (Arnold, 1963, 1965a) where they can be rapidly destroyed through collisions with other boulders in the cloud. Only those few boulders that escape this fate can eventually impact on the Earth to give rise to craters. We will show that an interplanetary cloud of boulders with an overall number density $g \text{ cm}^{-3}$, and total mass of $\sim 5 \times 10^{23} \text{ g}$ is consistent with information obtained from—

- (1) Impact rates on the Earth and Moon
- (2) Zodiacal light observations
- (3) Apparently required dust supply rates for replenishing dust lost from the zodiacal cloud through the Poynting-Robertson or other loss mechanisms
- (4) Celestial mechanical effects
- (5) Possibly observable impact rates on asteroids and comets.

THE CLOUD OF BOULDERS

We think of a cloud of boulders whose members have typical diameters d , mass density ρ , mass m , and spatial number density n . These boulders move in eccentric orbits about the Sun. From time to time, they collide and the rate of collision is determined by the relative velocity v , which in turn depends on the semi-major axis a , the eccentricities e , and the inclinations i of the orbits involved. If the boulders were moving randomly, the time T_c moved by an individual boulder before colliding with another boulder would be of order

$$T_c = (4nd^2v)^{-1} \quad (1)$$

This collision time is a minimum in the sense that boulders moving in nonintersecting orbits cannot collide no matter what the value of v may be. If a dense cloud of boulders is to survive long in the solar system, the boulders must move on non-intersecting or seldom-intersecting orbits. This is the situation when all the orbits are direct and when the eccentricities and inclinations of the orbits are low. Parenthetically, these are the same features that one usually holds responsible for the survival of planets and the stability of the solar system.

IMPACTS OF BOULDERS ON THE EARTH

We are in the habit of thinking of the Earth and Moon as impact counters for all kinds of interplanetary debris ranging from submicroscopic and microscopic grains all the way up to boulder-size objects, asteroids, and comets. Hand in hand with this concept goes the assumption that impacts on the Earth and Moon represent some kind of random sampling of the cloud of interplanetary debris. This postulate is deeply ingrained in our thinking and is seldom stated explicitly. We assume that impact of interplanetary debris on the Earth constitutes a random process and that the impact rates can be used to derive true interplanetary densities of debris near the Earth's orbit.

For small grains, the random sampling postulate can be partially justified. We know that the Poynting-Robertson effect shrinks the orbital diameter of small grains at such a fast rate that a large fraction of these grains can cross the Earth's orbit without ever coming close enough to the Earth to be strongly perturbed. A grain that does impact on the Earth presumably will then do so the very first time that it enters the Earth's sphere of gravitational influence. It therefore represents an essentially unperturbed orbit from the cloud of grains which, guided by solar gravitational attraction and light pressure, slowly drifts inward through the Earth's orbit, and into the Sun.

The orbits of boulders, on the other hand, need not lead to collisions with the Earth similar to those expected on the basis of random collisions, provided that the eccentricity of boulder orbits is low. We will present the detailed argument for this in the following paragraphs.

If a boulder has orbital eccentricity $\epsilon \ll 1$ and its perihelion distance q is close to the Earth's orbit, the velocity at perihelion is

$$v_q \sim v_E(1 + \epsilon/2) \quad (2)$$

where v_E is the mean orbital velocity of the Earth.

We wish to calculate the impact parameter s for a boulder whose approach velocity to the earth is $v = \epsilon v_E/2$. If the Earth's radius is r and the velocity for Earth grazing particles is v , at closest approach, conservation of angular momentum gives

$$rV = sv \quad (3)$$

Conservation of energy gives

$$\frac{v^2}{2} \sim \frac{V^2}{2} - \frac{M\gamma}{r} \quad (4)$$

For the Earth, $M\gamma/r \gg \epsilon^2 v_E^2/8$ as long as $\epsilon < 1/3$. For this reason $V \sim (2M\gamma/r)^{1/2}$ and from equation (3),

$$s \sim \frac{(8M\gamma r)^{1/2}}{\epsilon v_E} \sim 4.8 \times 10^8 / \epsilon \text{ cm} \quad (5)$$

This means that for low-eccentricity orbits the capture cross section of the Earth πs^2 can be much larger than its geometrical cross section.

We can now compute the capture probability of a boulder per orbit about the Sun. The Earth's eccentric orbit precesses about the Sun, sweeping out a torus whose projected area on the ecliptic plane is

$$A = 2\pi a(2a\epsilon_E) = 5 \times 10^{25} \text{ cm}^2 \quad (6)$$

If the boulder passes through the torus, once per revolution, it has probability

$$\frac{\pi s^2}{A} \sim \frac{1.4 \times 10^{-7}}{\epsilon^2} \quad (7)$$

of colliding with the Earth. For eccentricities as low as $\epsilon \sim 0.1$, the collision probability reaches unity in a time of the order of 7×10^4 years. For more highly eccentric orbits, this time interval may increase by two orders of magnitude, but the mean life of a boulder, once it crosses the

Earth's orbit, cannot well exceed 10^7 years in the absence of other effects.

This result appears to hold well enough for boulders which at some initial time were injected into trajectories that crossed the Earth's orbit about the Sun. Such boulders would soon be removed from the solar system through impact on the Earth (or, to lesser extent, the Moon).

The situation is quite different for a boulder which first approaches the Earth's orbit along a slow Poynting-Robertson spiral into the Sun. Such a boulder's orbit initially must be altered primarily through scattering. In this process, the perihelion distance cannot be appreciably altered, but the aphelion distance is increased because the scattering process systematically leads to acceleration of the boulder. This comes about through a process first described by Arnold (1965a). Essentially it works on the same principle as Fermi's mechanism for the acceleration of cosmic-ray particles in encounters with cosmic clouds.

A boulder interacting with the Earth in this way will not be able to impact on the Earth, until the Poynting-Robertson effect has sufficiently decreased the boulder's perihelion distance. For a boulder in a low-eccentricity orbit, the complete Poynting-Robertson trajectory into the Sun would be traversed (cf. Wyatt and Whipple, 1950) in a time

$$T = 3.5 d \rho a^2 \text{ years} \quad (8)$$

where d is the boulder's diameter measured in centimeters, ρ is its density, and a is the semi-major axis measured in AU. The time required to alter the semimajor axis by an amount Δa is therefore

$$\Delta T = 7 \times 10^6 \rho d a \Delta a \quad (9)$$

and the rate of perihelion decrease therefore is roughly

$$\Delta a / \Delta T \sim (7 \times 10^6 \rho d a)^{-1} \quad (10)$$

for a boulder in a low eccentricity orbit.

If one sets Δa equal to 10 capture radii of the Earth (cf. Arnold, 1965a, b)

$$\Delta a \sim 5 \times 10^9 / \epsilon \text{ cm} \sim \frac{3.3 \times 10^{-4}}{\epsilon} \text{ AU} \quad (11)$$

The time between initial onset of appreciable scattering by the Earth, and eventual impact through crossing of the Earth's trajectory, will be as long as

$$\Delta T \sim \frac{2.3 \times 10^3}{\epsilon} \rho d \quad (12)$$

If $\epsilon \sim 0.1$, $d \sim 10^3$ cm, and $\rho \sim 3$ to 8, one finds that $\Delta T \sim 7 \times 10^7$ to 1.8×10^8 years

This is an interval long compared with the previously computed impact time of 7×10^4 years.

During this time interval, impact on the Moon has a probability of order unity, and the probability of collision with other boulders may also be significant, provided the density of the cloud of boulders is high. Both these factors tend to decrease the probability of eventual impact on the Earth.

The destruction rate through collision with other boulders becomes significant when the number density of boulders (see eq. (1)) is such that

$$(4nd^2v) \sim 3 \times 10^{-16} \text{ sec}^{-1}$$

The least certain quantity here is v . We will assume that perturbations (scattering) by the Earth increase the eccentricity of a boulder's orbit to 0.2 and produce an inclination angle of the order of 0.3 rad. Then $v \sim 10^6$ cm-sec $^{-1}$ and

$$n \sim 8 \times 10^{-29} \text{ cm}^{-3}$$

If the destruction rate of boulders scattered by the Earth is to be appreciable, n should be at least half an order of magnitude greater. One then has the somewhat surprising situation in which an increase in n decreases the absolute number of boulders that impact on the Earth. This can be understood by considering that the approach rate of boulders to the Earth is then proportional to n , while the removal of scattered boulders through intercollision proceeds exponentially with n , for the 10^8 -year interval before the Poynting-Robertson effect makes possible direct impacts on the Earth.

In summary, one sees that a count of direct impacts on the Earth, as conducted, say, by Brown (1960) must always lead to a deceptively low computed number density of large inter-

planetary boulders, if one chooses to disregard the possibility of low eccentricity orbits and instead invokes a random impact hypothesis. Two factors contribute to this feature. First, the Poynting-Robertson approach rate of large boulders toward the Earth will occur at a rate inversely proportional to the boulder diameter. This alone will lead to a factor as large as 10 when 10-meter-sized boulders are compared to meter-sized meteorites. Second, the slower approach rate toward the Earth's orbit, once appreciable perturbations due to the Earth's gravitational influence have commenced, makes impact on the Moon or destruction through collision with other boulders a much stronger possibility. The effect of these alternate fates may be to reduce present-day impact rates on the Earth by another factor which might be as high as 10^2 . Thus, the total rate of impact of boulders on the Earth may be a factor as high as 10^3 less than one might compute on the expectation that impact on the Earth was equally probable for interplanetary debris of all sizes. A number density of boulders in interplanetary space as high as $n \sim 4 \times 10^{-28} \text{ cm}^{-3}$ should therefore be taken as a serious possibility.

SELF-DESTRUCTION AND THE ORIGIN OF THE CLOUD OF BOULDERS

The previous argument shows that there are two acceptable models of an interplanetary cloud of boulders. One model of such a cloud is very dense, $n \sim 4 \times 10^{-28} \text{ cm}^{-3}$, with corresponding mass density of $\sim 2 \times 10^{-18} \text{ g cm}^{-3}$ and a total mass of the order of $M \sim 3 \times 10^{23}$, which is a small mass compared with the mass in the asteroidal belt. It is clear that such a small mass would in no way significantly perturb the orbits of planets nor would it lead to other observable celestial mechanical effects.

The self-destruction rate, however, is quite rapid for such a cloud. Even if the inclination and eccentricity of boulder orbits were as low as those of planetary orbits, appreciable self-destruction of the cloud would be expected in a time of the order of 10^8 years. Such a cloud would then have to be continually replenished, presumably through occasional collisions of boulders with asteroids.

The alternate model of the cloud of boulders

takes a boulder density which is one and a half orders of magnitude lower, roughly $n \sim 10^{-29}$. The impact rate on the Earth is then the same as for the denser cloud because we still have the same low approach rate dictated by the Poynting-Robertson effect, and, in addition, a loss factor of the order of 2 to 3 is possible through collision with the Moon. A further reduction in impact rates by a factor of 30 is due to the reduction of the number density of boulders.

For each of these models the impact rate of boulders roughly 10 meters in diameter is

$$\frac{dn}{dt} \sim \left[2\pi a^2 n^2 (\sin i) \frac{\Delta a}{\Delta t} \right] x \sim 0.08 \quad (13)$$

per year for the whole Earth. About one boulder per century would fall on land. The expression in brackets in equation (13) gives the approach rate of boulders toward the Earth's orbit, and x is the probability that an approaching boulder will eventually impact on the Earth. A typical inclination i of a boulder orbit was chosen as ~ 0.15 rad, and we take $\epsilon \sim 0.1$. We have taken $x \sim 1/30$ for $n \sim 10^{-29}$, and $x \sim 10^{-3}$ for $n \sim 4 \times 10^{-28}$.

The self-destruction rate for the more tenuous cloud of boulders is consistent with a primordial origin. Such a cloud could have formed at the inception of the solar system. If it had been much denser at that time, its density would have rapidly decreased through the intercollision of boulders until it reached its present density for which the destruction time constant is just equal to the cloud's age. This equality is a characteristic of most self-destructive systems.

ABRASION OF BOULDERS

The abrasion rate of boulders in interplanetary space must be considered in order to determine whether or not boulders of a given size and composition can survive for several eons. Whipple and Fireman (1959) first pointed out that the cosmic-ray ages of meteorites could be used to place an upper limit on the abrasion rates of interplanetary bodies. Current estimates made on the basis of this technique give abrasion rates well below 10^{-8} cm/year both for iron and stony meteorites.

In order to survive for the full 4×10^9 years

since the birth of the solar system, a boulder would only have to be a meter in diameter. Ten-meter-sized boulders would be virtually unaffected by the abrasion process. This mechanism therefore appears to have little importance in determining the evolution of the cloud of interplanetary boulders. There will be a small drag on the boulders due to continual collisions with fine dust, but this drag is small compared to the Poynting-Robertson process.

THE ZODIACAL LIGHT

The cloud of boulders can make a direct and an indirect contribution to the zodiacal glow. The direct contribution comes from light directly scattered off boulders. The indirect contribution is due to intercollision of boulders that can produce debris which in turn scatters radiation.

Direct Contribution

If the spatial density of boulders is n out to a distance $h \ll r$ from the ecliptic plane, the total scattered light received from a direction perpendicular to the ecliptic plane is of the order of

$$\int_0^h \frac{L_{\odot}}{4\pi r^2} \sigma n \frac{d\Omega}{4\pi} dh \sim 7 \times 10^{19} n \text{ erg/cm}^2\text{-sq}^\circ\text{-sec}$$

where r is the Earth's distance from the Sun, σ is the scattering cross section of a boulder, n is the number density in cm^{-3} , and the cloud of boulders is taken to extend out to 0.15 AU from the ecliptic, at the Earth's distance from the Sun.

Even for the denser cloud of boulders discussed in the section entitled "Self-Destruction and the Origin of the Cloud of Boulders," the number density is only $n \sim 4 \times 10^{-28} \text{ cm}^{-3}$, so that the flux received is $3 \times 10^{-8} \text{ erg/cm}^2\text{-sec-sq}^\circ$, an order of magnitude less than the brightness of the zodiacal light at high declination. We have assumed here that all the light incident on a boulder is isotropically scattered. This is a conservative assumption, and the actually scattered light from boulders would probably be considerably less than the value calculated.

Indirect Contribution

In the section entitled "Self-Destruction and the Origin of the Cloud of Boulders," we com-

puted that the destruction of the dense model of the interplanetary cloud of boulders would take place with a time constant of about 10^8 years, while that of the less dense cloud would take place in about 4×10^9 years. These destruction rates are considerably higher than the abrasion rates computed in the section entitled "Abrasion of Boulders." If small-scale interplanetary debris is produced in the destruction of boulders, the relative contribution from the two models would be 300 tons/sec and 0.1 ton/sec, respectively. This compares to a minimum supply rate of the order of 1 ton/sec required to keep the zodiacal cloud intact against elimination by the Poynting-Robertson effect. The dense cloud can, therefore, easily account for the required supply rate, even if only a small fraction of the intercollision debris produced is retained in the solar system as fine dust. The more tenuous cloud cannot maintain the required dust supply rate.

COLLISIONS OF BOULDERS WITH COMETS

While boulders with low orbital eccentricity and inclination are not likely to collide with the Earth or other planets, they do have a high probability of impacting on parabolic comets.

Consider a new (parabolic) comet approaching the solar system for the first time. Such a comet may have spent several eons in a circumsolar cloud at some 10^5 AU from the Sun. The comet's diameter is ~ 50 km. During its transit across the inner solar system, it sweeps out a volume of order 3×10^{26} cm³. If the density of boulders is $n \sim 4 \times 10^{-28}$ cm⁻³, as suggested in the section entitled "The Cloud of Boulders," every tenth comet will suffer a collision with a boulder.

The relative velocity of the two objects just prior to collision is of the order of 10^7 cm/sec, so that the total kinetic energy made available on impact by the boulder is of the order of 10^{23} erg. It is not clear how this large amount of energy is used up. Since comets are believed to be rather loosely packed aggregates of ices and grains, it is possible that a boulder could penetrate to a depth of several hundred meters. (On the Earth it would penetrate well over 100 meters—particularly if atmospheric effects are neglected.) An explosion in the interior of the comet nucleus

could then occur, and it is possible that the comet would split into two or more fragments. Figure 1 taken from another publication (Harwit, unpublished report) shows that comets which split through nontidal effects undergo fission close to the ecliptic plane. The paper argues that the most plausible explanation for the concentration toward the ecliptic lies in the hypothesis that boulders impacting on comets can trigger a large enough energy release to cause fracture.

DISCUSSION

The purpose of this paper has been to show that one can place useful bounds on the concentration of roughly 10-meter-diameter boulders in interplanetary space. Two types of clouds are consistent with impact rates for boulders colliding with the Earth. Very roughly, the boulder concentration in these clouds is $n_1 \sim 4 \times 10^{-28}$ and $n_2 \sim 10^{-29}$ cm⁻³. These values are, respectively, 10^3 and 25 times higher than one would estimate on the basis of meteorite impact craters if boulders moved in random orbits through interplanetary space. The high densities suggested by the present paper arise from the consideration that boulders in Earth-crossing orbits are eliminated rapidly (in a time of the order of 10^7 years) from the solar system and only those boulders having low eccentricity can survive. These spiral slowly toward the Sun, and therefore enter Earth-crossing orbits infrequently.

Boulder densities between the two limits

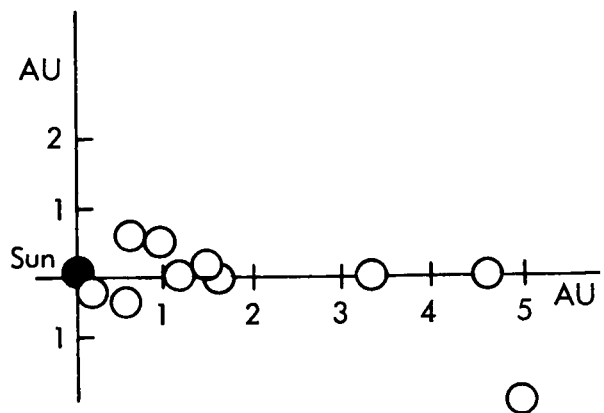


FIGURE 1.—Distances from the ecliptic plane at which comets are observed to split (Harwit, unpublished data).

n_1 and n_2 are unlikely, because the impact rates on the Earth would be too high. When the concentration exceeds n_1 the self-destruction rate through boulder intercollisions becomes so high that impacts on the Earth become unlikely, leading to the curious result that at higher boulder densities, impact rates on the Earth actually decrease.

If the concentration is as high as n_1 , two interesting results are obtained. First, there is then little difficulty in explaining the origin of interplanetary debris of the kind that gives rise to zodiacal scattered light. In the past, there has been great difficulty in accounting for a source which could supply enough dust to compensate the Poynting-Robertson loss which compels interplanetary debris to spiral into the Sun (Harwit, 1963). Second, collisions with boulders could account for the observed splitting of parabolic comets as they traverse the ecliptic plane (the comets in question are those that

cannot have split through the tidal action of the Sun).

The self-destruction rate of a cloud of this density is high, and typical boulders cannot survive for more than $\sim 10^8$ years. This means that a periodic replenishment of boulders would be required. This replenishment could come about through collisions of boulders with larger objects, mainly asteroids. In each such collision, a large amount of new material is liberated and injected into orbits of relatively low inclination and eccentricity, as required by the models described throughout this paper.

Neither the proper zodiacal dust supply rate nor the correct probability of comet splitting can apparently be obtained from the more tenuous model having spatial density n_2 . If all these considerations are appropriate, the most likely density of interplanetary boulders, consistent with most of the observed data, seems therefore to be of the order of $4 \times 10^{-28} \text{ cm}^{-3}$.

REFERENCES

- ARNOLD, J. R., 1963, "Isotopic and Cosmic Chemistry," 346 (H. Craig et al., eds.) (Amsterdam: North Holland).
—, 1965a, *Astrophys. J.*, **141**, 1536.
—, 1965b, *Astrophys. J.*, **141**, 1548.
BROWN, H., 1960, *J. Geophys. Res.*, **65**, 1679.
HARWIT, M., 1963, *J. Geophys. Res.*, **68**, 2171.
WHIPPLE, F. L., and E. L. FIREMAN, 1959, *Nature*, **183**, 1315.
WYATT, S. P., Jr., and F. L. WHIPPLE, 1950, *Astrophys. J.*, **111**, 134.

Page intentionally left blank

45. Collisional Model of Meteoroids

J. S. DOHNANYI
Bellcomm, Inc.
Washington, D.C.

A COLLISIONAL MODEL OF METEORIODS is formulated. Meteoroids collide with each other inelastically, and this process is accompanied by fragmentation. The net result is particle removal from a given mass range as well as particle creation in the same mass range due to collisions between other larger objects. If these two competing processes are set equal and a steady-state distribution results, a number density function of a population index type is obtained which is in qualitative agreement with observation.

The physical model employed is based on the following assumptions:

(1) All objects collide with a certain average relative velocity.

(2) All masses are spherical.

(3) All masses have the same material properties, for example, density.

(4) All collisions are center to center, that is, the impact parameter is zero.

(5) The total ejected mass during (hypervelocity) cratering into a semi-infinite target is proportional to the incident particle mass.

(6) Cratering into finite objects is given by assumption (5) provided the target is not completely shattered.

(7) The largest object completely shattered by an incident particle has a mass about two or three orders of magnitude larger than the total ejected mass from a semi-infinite target for a similar incident particle.

(8) The mass of the largest fragment is proportional to the mass of the incident particle (namely, proportional to the total ejected mass).

(9) The "comminution law," that is, the number density of particles in the mass range m to $m + dm$ included in the fragments ejected during impact has a form

$$Cm^{-n} dm \quad (1)$$

where the coefficient C is a function of the masses of the colliding objects.

(10) The mass of the smallest particle present is given by the radiation pressure limit.

The simplifying assumptions (1) to (4) are introduced in order to render the mathematics tractable without seriously compromising physical reality. Assumptions (5) and (7) to (9) are based on experiments by Gault, Shoemaker, and Moore (1963). Assumption (6) is arbitrary, but in the absence of experimental information it appears to be the safest one to make. Assumption (10) is self-evident and is listed only for completeness.

By using assumptions (1) to (10) it is possible to describe the mass distribution of a system of particles undergoing collisions and fragmentation at relative speeds in the high or hypervelocity range. More specifically, given that $f(m, t)dm$ is the number of particles having a mass in the range m to $m + dm$ at a time t , expressions corresponding to the terms in the following equation have been derived by the writer:

$$\frac{\partial}{\partial t} f(m, t) = \begin{array}{l} \boxed{\text{time rate of change of } f(m, t)dm \text{ due to} \\ \text{the erosive action of collisions with very} \\ \text{small objects}} \\ + \\ \boxed{\text{time rate of change in } f(m, t)dm \text{ due to} \\ \text{catastrophic, that is, completely dis-} \\ \text{ruptive collisions}} \\ + \\ \boxed{\text{time rate of change in } f(m, t)dm \text{ due to} \\ \text{particle creation, in this same mass} \\ \text{range, by the fragmentation of larger} \\ \text{objects}} \end{array} \quad (2)$$

An additional term due to the influence of radiation damping on the particle number density is also considered and dismissed because of particle lifetime considerations. Evidence of erosion rates in space, discussed by Whipple (1963), indicates that the approximate lifetime of an object imposed by collisions is about two orders of magnitude shorter than the lifetime imposed by radiation damping on the same object.

The mathematical problem of solving equation (2) for $f(m, t)$ is complicated. However, under the simplifying assumption that the population has reached a steady-state value, that is,

$$\frac{\partial f(m, t)}{\partial t} = 0 \quad (3)$$

a solution of the form

$$f(m, t) = f(m) \propto m^{-\alpha} \quad (4)$$

satisfies equation (2) in the following range of values of m and α

$$\Gamma' \mu \ll m \ll \Lambda M_x / \Gamma' \quad (5)$$

and

$$\frac{1}{2}(\eta + 5/3) < \alpha < 2 \quad (6)$$

where μ is the smallest mass not blown away by radiation pressure; $\Gamma' \mu$ is the largest mass completely disrupted by a collision with μ , and therefore the mass below which the erosion term is not valid; Γ' is a constant of proportionality according to assumption (7); M_x is the largest mass in the distribution; $\Lambda M_x / \Gamma'$ is the largest mass that can be produced under assumption (5) and is, therefore, the upper limit to which this formalism applies; Λ is a constant of proportionality according to assumption (8); η is the population index for the comminution process according to assumption (9).

Outside the limits of equation (6), steady-state solutions of the population-index type do not exist. For $\alpha > 2$ erosion by the smallest particles (of size μ) dominates; for $\alpha < \frac{1}{2}(\eta + 5/3)$ collision products from the most massive objects (M_x) cause evolution of the mass distribution with time. Experiments by Gault indicate that the population index η for the comminution process

(eq. (1)) is about 1.8; in this case, the lower limit for α is ~ 1.7 .

The results (eqs. (5) and (6)) are compared with near-Earth meteoroid data in figure 1, in which the shaded region represents the values of α allowed by equation (6). It can be seen from the figure that the radio meteors have a population index at the lower limit of $-\alpha$; this is also true for the McCrosky and Posen (1961) photographic meteors analyzed by the writer. Photographic meteor data analyzed by Hawkins and Upton (1958) and radio data by Kaiser (1961) are somewhat low by comparison.

An interesting feature of the theory is that as $m \rightarrow \Gamma' \mu$, $-\alpha$ should increase approaching ∞ as $m \rightarrow \mu$, reflecting the fact that the population is "empty" when the radiation pressure limit is reached.

Gault (private communication) observed that a basalt object is completely shattered by a projectile having a mass 10^{-3} times the mass of the target object at impact velocities of 2 km/sec. At near-Earth meteoric velocities of about 20 km/sec this would imply (using "energy scaling") that

$$\Gamma' \approx 10^5 \quad (7)$$

or even higher if the meteoroids have a lower cohesive strength than basalt.

It can be seen from the figure that satellite data indicate the same trend in α and in about the same mass region, as would be expected from the present model.

Stony meteorites have, according to Hawkins (1960), a population index $\alpha = 2$, and irons have $\alpha = 1.5$. Comparison with figure 1 indicates approximate agreement between the present model and the distribution of stones; irons are, however, somewhat high.

Lunar craters of a nonequilibrium distribution have a population index in the approximate range (see, e.g., Dodd, Salisbury, and Smalley, 1963)

$$1.5 \leq \alpha \leq 1.7$$

which is somewhat low compared with equation (6).

Figure 2 is a cumulative plot of asteroids cataloged by Kuiper et al. (1958). The straight line

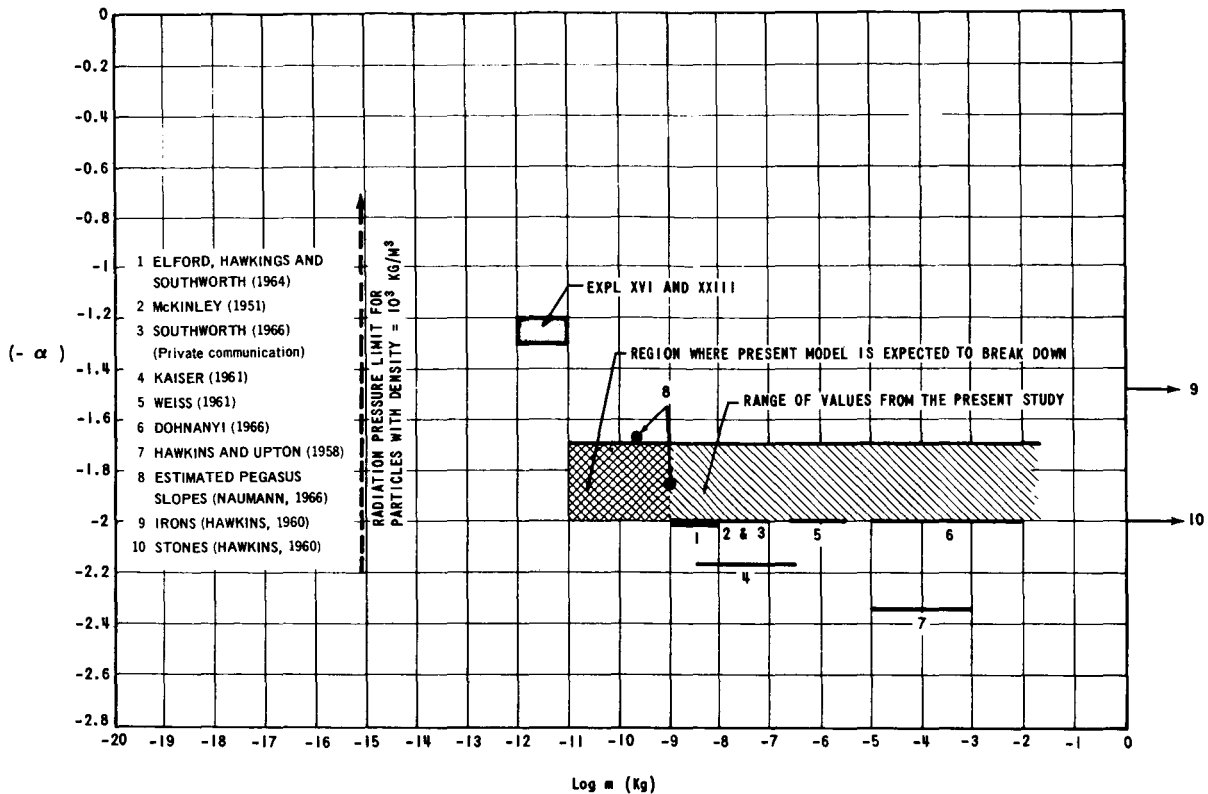


FIGURE 1.—Observed values of the population index α versus mass of interplanetary particles as reported by various investigators. Shaded region in the range of values for α is consistent with a steady-state distribution discussed in the text.

is a least-squares fit to the distribution and has a population index

$$\alpha = 1.80 \pm 0.04 \quad (8)$$

Since these masses are near the high mass limit of the distribution, a more detailed treatment is necessary before the good agreement between

the results of the steady-state theory and observation can be considered meaningful. Such an analysis is now in progress.

ACKNOWLEDGMENTS

The writer is particularly indebted to B. G. Smith for some important suggestions; thanks are also due to R. H. Hilberg, N. W. Hinnners, A. N. Kontaratos, and G. T. Orrok for valuable discussions and suggestions.

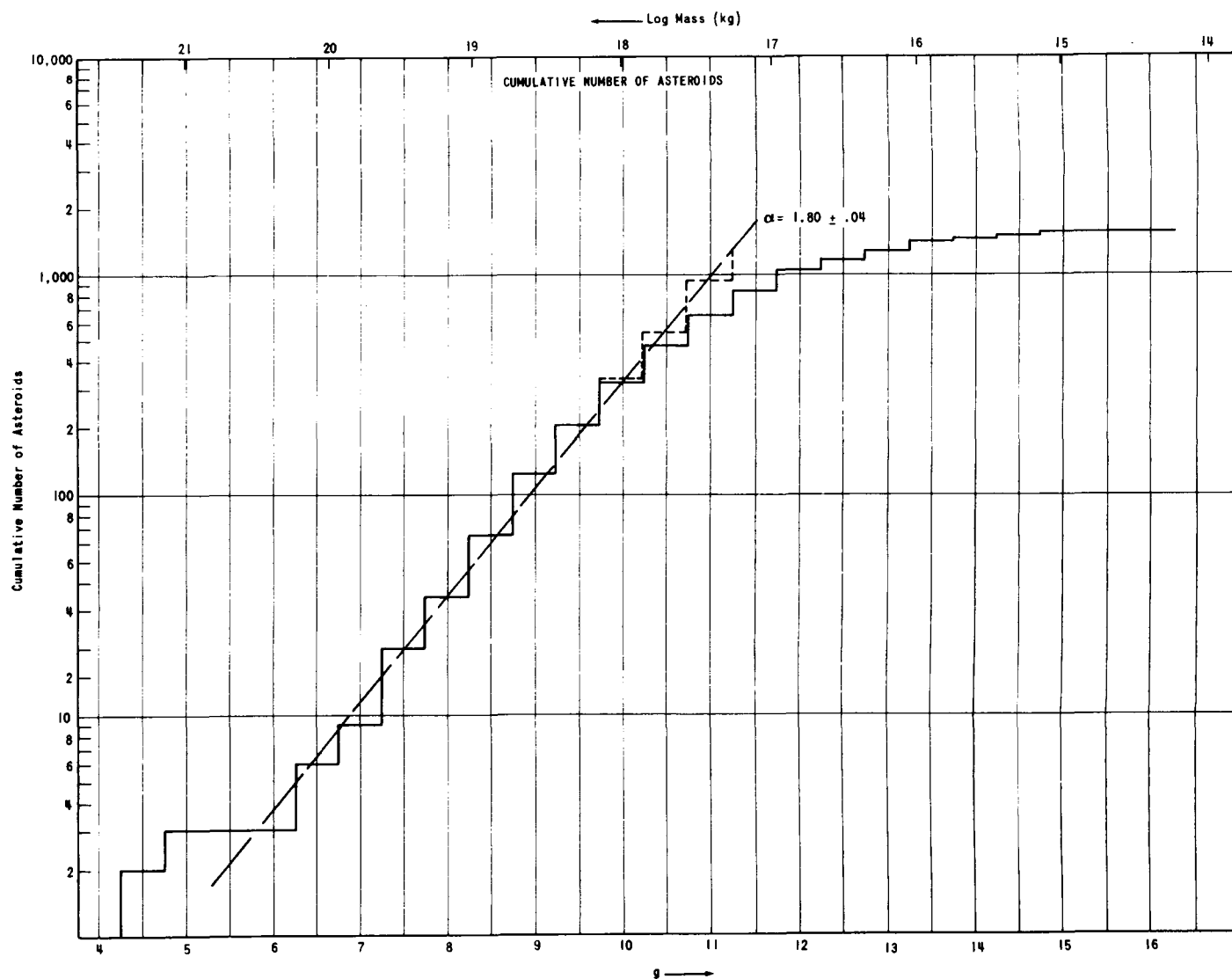


FIGURE 2.—Cumulative number of asteroids having an absolute photographic magnitude of g or smaller versus g (in half-magnitude intervals) as reported by Kuiper et al. (1958).

REFERENCES

- DODD, R. T., JR., J. W. SALISBURY, and V. G. SMALLEY, 1963, *Icarus*, **2**, 466.
- DOHNANYI, J. S., 1966, Bellcomm TR-66-340-1.
- ELFORD, W., G. S. HAWKINS, and R. B. SOUTHWORTH, 1964, Harvard Radio Meteor Project Res. Rept., No. 9.
- GAULT, D. E., E. M. SHOEMAKER, and H. J. MOORE, 1963, NASA Tech. Note, D-1767.
- HAWKINS, G. S., 1960, *Astronomical J.*, **65**, 318.
- HAWKINS, G. S., and E. K. L. UPTON, 1958, *Astrophys. J.*, **128**, 727.
- KAISER, T. R., 1961, *Monthly Not. Roy. Astron. Soc.*, **123**, 265.
- KUIPER, G. P., Y. FUJITA, T. GEHRELS, I. GROENEVELD, J. KENT, G. VAN BIESBROECK, and C. J. VAN HOUTEN, 1958, *Astrophys. J.*, Suppl. Ser. **3**, 289.
- MCCROSKY, R. M., and A. POSEN, 1961, *Smithsonian Contributions to Astrophysics*, **4**, 15.
- MCKINLEY, D. W. R., 1951, *Canadian J. of Phys.*, **29**, 403.
- NAUMANN, R. J., 1966, NASA Tech. Note, D-3717.
- WEISS, A. A., 1961, *Australian J. of Phys.*, **14**, 102.
- WHIPPLE, F. L., 1963, *Smithsonian Contributions to Astrophysics*, **7**, 239.

Page intentionally left blank

46. Light Scattered by the Earth's Dust Cloud

N. B. DIVARI

*Odessa Polytechnic Institute
Odessa, U.S.S.R.*

THE POSSIBLE CONTRIBUTION to the zodiacal light from the light scattered by the Earth's dust cloud was discussed by Fesenkova (1964) and Divari (1965a). It was shown that dust particles present near the Earth can partially contribute to the brightness of zodiacal light and F-corona. However, since neither space density nor space distribution of dust is known, it is interesting to consider different possible models of the Earth's dust cloud, keeping in mind the necessity, after studying the main regularities in the distribution of light scattered by the dust cloud on the basis of different suppositions about its structure, of comparing the calculations with the results of measurements of night-sky brightness in the continuum. The results of such a comparison will make it possible to estimate the contribution of the Earth's dust cloud to the night-sky brightness and to make conclusions about the structure of the dust cloud.

In this paper, we give the results of calculations for the intensity of sunlight scattered by Earth's dust cloud, carried out on the basis of different suppositions about the space distribution of the dust in the vicinity of the Earth.

Taking the rectangular coordinate system with origin in the Earth's center and with axes directed to the ecliptic pole (OZ -axis), to the Sun (OY -axis), and perpendicular to the plane OYZ (OX -axis), we suppose that the space dust density $n(x, y, z)$ is determined in terms of the coordinates x, y, z as follows:

$$n(x, y, z) = C(\sqrt{k'^2x^2 + y^2 + k^2z^2} - 1)^{-m} \quad (1)$$

where $[n] = \text{cm}^{-3}$, and the coordinates x, y, z are expressed in units of the Earth's radius. Then the surfaces of equal space density will be defined by the equations

$$k'^2x^2 + y^2 + k^2z^2 = \text{Constant} \quad (2)$$

that is, they will be three-axis ellipsoids.

The constant factor C of equation (1) is the space density (cm^{-3}) of particles at the point $x=0, y=2$, and $z=0$; that is at a point 2 Earth radii from the Earth's center in the direction of the Sun

$$C = n(0, 2, 0) \quad (3)$$

In the direction to the Sun ($x=z=0$), the space density changes as follows:

$$n(0, y, 0) = \frac{C}{(y-1)^m} = \frac{C}{h^m} \quad (4)$$

where h is the distance from the Earth's surface.

The intensity $I(\beta, \epsilon)$ of sunlight scattered in the given direction ($\beta; \epsilon$) into a unit of solid angle is defined by

$$I(\beta, \epsilon) = I_0 CR \gamma (\pi a^2)_m f(\theta) \int_{l_1}^{l_2} (\sqrt{k'^2x^2 + y^2 + k^2z^2} - 1)^{-m} dl \quad (5)$$

if the integration variable l (the distance from the observer to the scattering element in the point $(x; y; z)$) is expressed in Earth radii. Here $f(\theta)$ is the phase function of dust, γ is the albedo of the dust particles, $R = 6.37 \times 10^8$ cm is the Earth's radius, I_0 is the flux of solar radiation at 1 AU from the Sun, and $(\pi a^2)_m$ is the mean cross section of particles with radii in the range (a_1, a_2) defined by the formula

$$(\pi a^2)_m = \pi \int_{a_1}^{a_2} a^{2-\nu} da / \int_{a_1}^{a_2} a^{-\nu} da \quad (6)$$

if we take for the radius distribution $N(a)$ of the particles the relationship:

$$\frac{dN(a)}{da} \sim a^{-\nu} \quad (7)$$

The phase function of the dust particles is taken as follows:

$$f(\theta) = \frac{1}{18.3} [1 + 11.1(e^{-3\theta} - 0.009)] \quad (8)$$

which is obtained from Piaskovskaya-Fesenkova's (1959) observations of atmospheric aerosols. If we let $I_0 = 6.8 \times 10^{-5}$, the brightnesses $I(\beta, \epsilon)$ from equation (5) will be expressed in units of the mean brightness of the solar disk.

For the purpose of investigating the probable contribution of the Earth's dust cloud to the zodiacal light and night sky brightness, we computed the quantities

$$L(\beta, \epsilon) = \int_{l_1}^{l_2} (\sqrt{k'^2 x^2 + y^2 + k^2 z^2} - 1)^{-m} dl \quad (9)$$

and

$$f(\theta)L(\beta, \epsilon) \quad (10)$$

for different values of the parameters k' , k , and m with different inclinations i of the ecliptic to the horizon. (About 100 different models were considered in all.) Equation (9) was computed by the Runge-Kutta method with the value of the upper integral limit l_2 , corresponding to the Earth's gravity radius, equal to $41 R_\oplus$. Special calculations have shown that increasing the upper limit from $41 R_\oplus$ to $100 R_\oplus$, the law of space-density distribution of particles being as adopted, introduces very little change in the result and has no importance for the purposes of our investigation. The value of the lower limit l_1 of equation (9) was determined by the point of the outlet from the Earth's shadow for which a shielding height of 50 km was adopted.

For the given values of the ecliptic coordinates (β, ϵ) and the angle i of inclination of the ecliptic to the horizon and the Sun depression g , we computed the azimuthal coordinates (ζ, A) of the view direction; after that, for every l_i along the view path, the coordinates of point x' , y' , z' in the

azimuthal geocentric system are computed successively from the formulas

$$\left. \begin{aligned} x'_i &= l_i \sin \zeta \sin A \\ y'_i &= l_i \sin \zeta \cos A \\ z'_i &= l_i \cos \zeta + 1 \end{aligned} \right\} \quad (11)$$

Then the coordinates x_i , y_i , z_i of the scattering point in the geocentric ecliptic coordinate system can be found from the following formulas

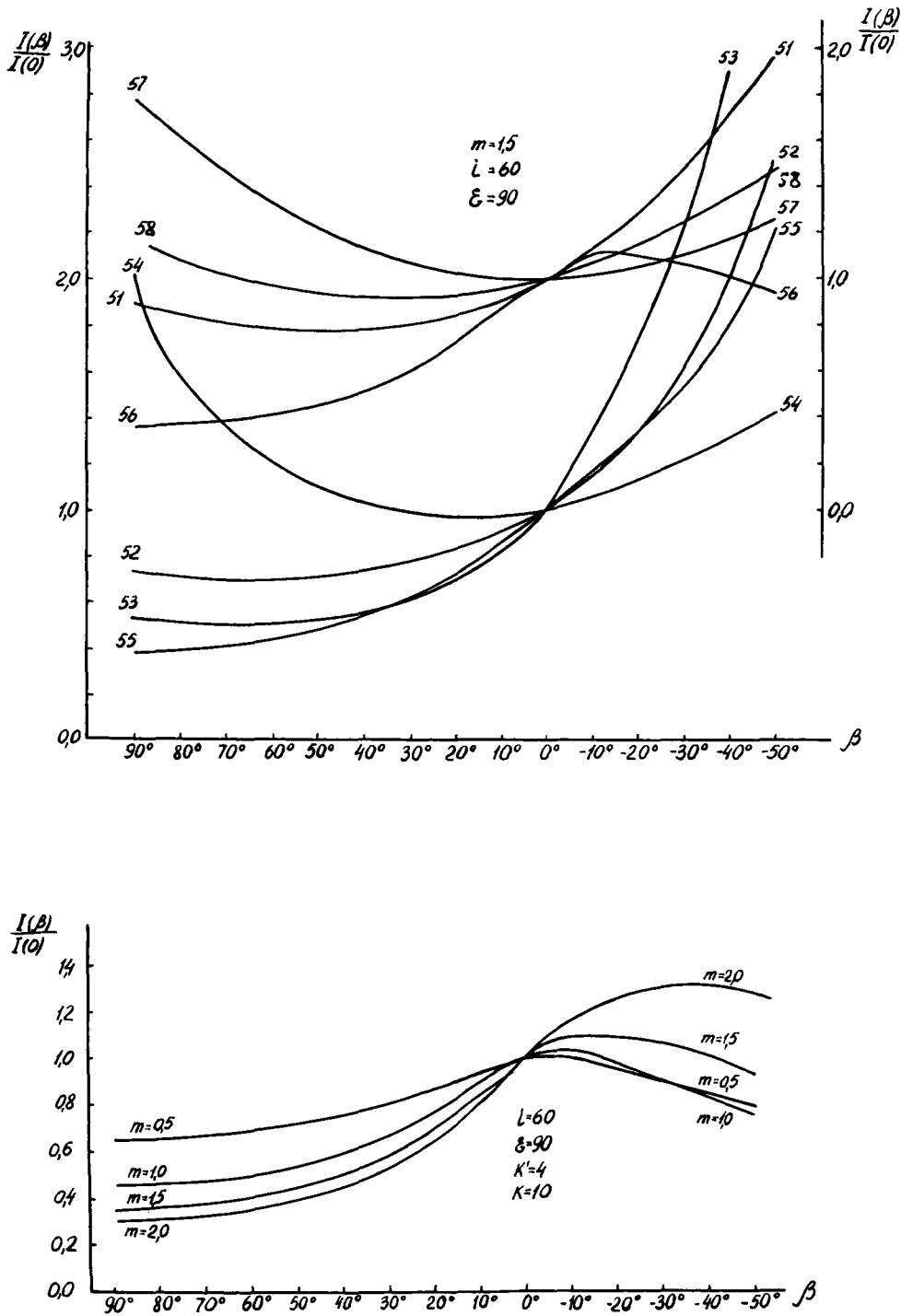
$$\left. \begin{aligned} x_i &= x'_i \cos i \cos g \\ &\quad + y'_i \sin g \sin i \sqrt{1 - \tan^2 g \operatorname{ctn}^2 i} \\ &\quad + z'_i \cos g \sin i \sqrt{1 - \tan^2 g \operatorname{ctn}^2 i} \\ y_i &= y'_i \cos g - z'_i \sin g \\ z_i &= -x'_i \sin i \sqrt{1 - \tan^2 g \operatorname{ctn}^2 i} \\ &\quad + y'_i \cos i \tan g + z'_i \cos i \end{aligned} \right\} \quad (12)$$

Taking into account the values x_i , y_i , z_i , we computed the values of the integrand in equation (9). The calculations were carried out both for constant and variable k' and k ; their dependence on the distance z of the scattering point from the Earth's center was taken as linear

$$\left. \begin{aligned} k' &= \delta'(Z - 1) + k'_0 \\ k &= \delta(Z - 1) + k_0 \end{aligned} \right\} \quad (13)$$

Below, we give a general description of the results obtained.

At $i = 90^\circ$, it is possible, on the whole, to choose the parameters k , k' , and m in such a manner that the computed distribution of brightness be near to the observed one. However, at inclined positions of the ecliptic relative to the horizon, the situation becomes quite different. The fact is that when the inclination i decreases, the maximum of the computed brightness is displaced to the south of the ecliptic. That was pointed out by Fesenkov (1964) and it particularly manifests itself at great values of k and m , that is, at the high flattening of the dust cloud


 FIGURE 1.—Computed course of brightness along the circle $\epsilon=90^\circ$ at $i=60^\circ$ for different models.

(a) Models with $m=1.5$: model 51: $k'_0=1$, $k_0=1$, $\delta'=5$, $\delta=10$; model 52: $k'_0=1$, $k_0=1$, $\delta'=10$, $\delta=10$; model 53: $k'_0=1$, $k_0=1$, $\delta'=1$, $\delta=10$; model 54: $k'_0=1$, $k_0=1$, $\delta'=5$, $\delta=5$; model 55: $k'_0=1$, $k_0=2$, $\delta'=0$, $\delta=0$; model 56: $k'_0=4$, $k_0=10$, $\delta'=0$, $\delta=0$; model 57: $k'_0=3$, $k_0=2$, $\delta'=0$, $\delta=0$; model 58: $k'_0=1$, $k_0=1$, $\delta'=0$, $\delta=0$. (b) Models with $k'=4$, $k=10$, and different values of m .

relative to the ecliptic and at the rapidly decreasing space density with distance h from the Earth's surface. Hence, for the selection of the parameters of equation (1), it is convenient to start from the consideration of the brightness distribution at angles of inclination i of the ecliptic to the horizon differing from 90° .

First of all, it is necessary to consider the (course) variation of the brightness along the circle $\epsilon = 90^\circ$. Along this circle, the angle of scattering θ for particles of the Earth's dust cloud does not change practically and is equal to 90° . Therefore, the form of the phase function does not influence the relative course of computed brightnesses. This is a very important consideration because the real phase function of cosmic-dust particles is not known, and it is very difficult to say to what degree of adequacy it is represented by equation (8). The course of the brightness along the circle $\epsilon = 90^\circ$ depends only on the space density of dust particles.

The course of brightness variation along the circle $\epsilon = 90^\circ$ for $i = 60^\circ$ is shown in figure 1 for some models. As may be seen from this figure, at $m > 1$ there is an essential parallax displacement of the maximum zodiacal-light brightness from the ecliptic. Therefore, it is clear that at great values of m it is not possible to obtain concordance with observations. It may also be seen from figure 2, where the relative course of brightness along the ecliptic ($\beta = 0^\circ$) at $k' = k = 1$ and at the different values of m is shown, together with the observed course of brightness (dashed line), which was presented by Divari (1965b) according to the observations of many authors. At the greater values of m the brightness increases very much with decreasing of angular distance from the Sun; it increases so much that it cannot be brought to conformity with the observed increase by means of possible changes of phase function. From this figure it is clear that, for example, the value $m = 7.2$, which was obtained by Divari (1964) by means of twilight observations for the law of distribution of atmospheric dust at heights of the order of 100 km, cannot be used for interpretation of the zodiacal light. Moreover, the great values of m lead to an appreciable dependence of the brightness on the Sun depression at a given point with fixed values of β and ϵ . Thus, only small values of m , near

$m = 1$, can be used for the explanation of zodiacal light.

To make this quantity more exact, let us consider, for $i = 90^\circ$, the course of brightness along the circle $\epsilon = 90^\circ$ for different combinations of values k and k' at $m = 1$. The corresponding curves, representing the dependence of computed brightness on ecliptic latitude β , are shown in figure 3 (solid lines), together with the observed ones (dashed line) found by Smith, Roach, and Owen (1965). It is necessary to point out that there is ground for supposing that the results presented by Smith, Roach, and Owen (1965) give some overstated values of zodiacal-light brightness in the ecliptic pole, because the tropospheric scattering of different components of night sky is not very exactly taken into account. Therefore, the dashed line representing the observed dependence must be considered as defining the upper limit of zodiacal-light brightness. Taking this into account, we can select for further specification the values $k' \geq 1$ and $k > 3$. The curve with $k' = 4$ and $k = 10$ is very close to the curve of the observed data. At the values of k' close to the values of k (for example, curve 2), we get a very slow decrease of brightness in the direction to the ecliptic pole, and at $k' > k$ there

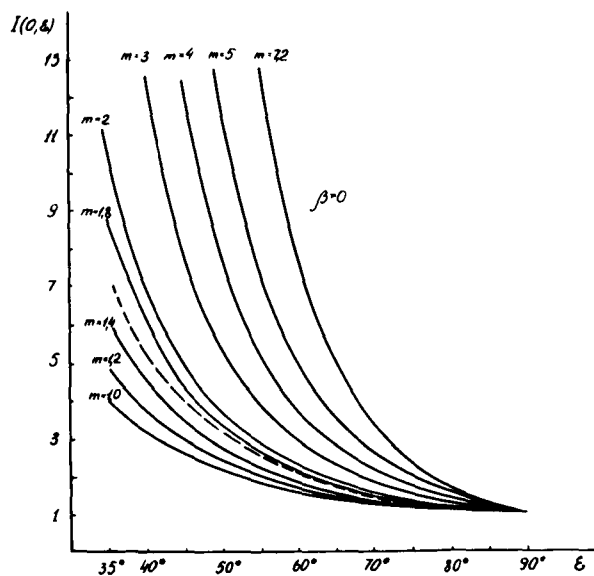


FIGURE 2.—Comparison of the observed course of zodiacal-light brightness along the ecliptic (dashed line) with the computed one for different values of m at $k' = k = 1$ and $i = 90^\circ$.

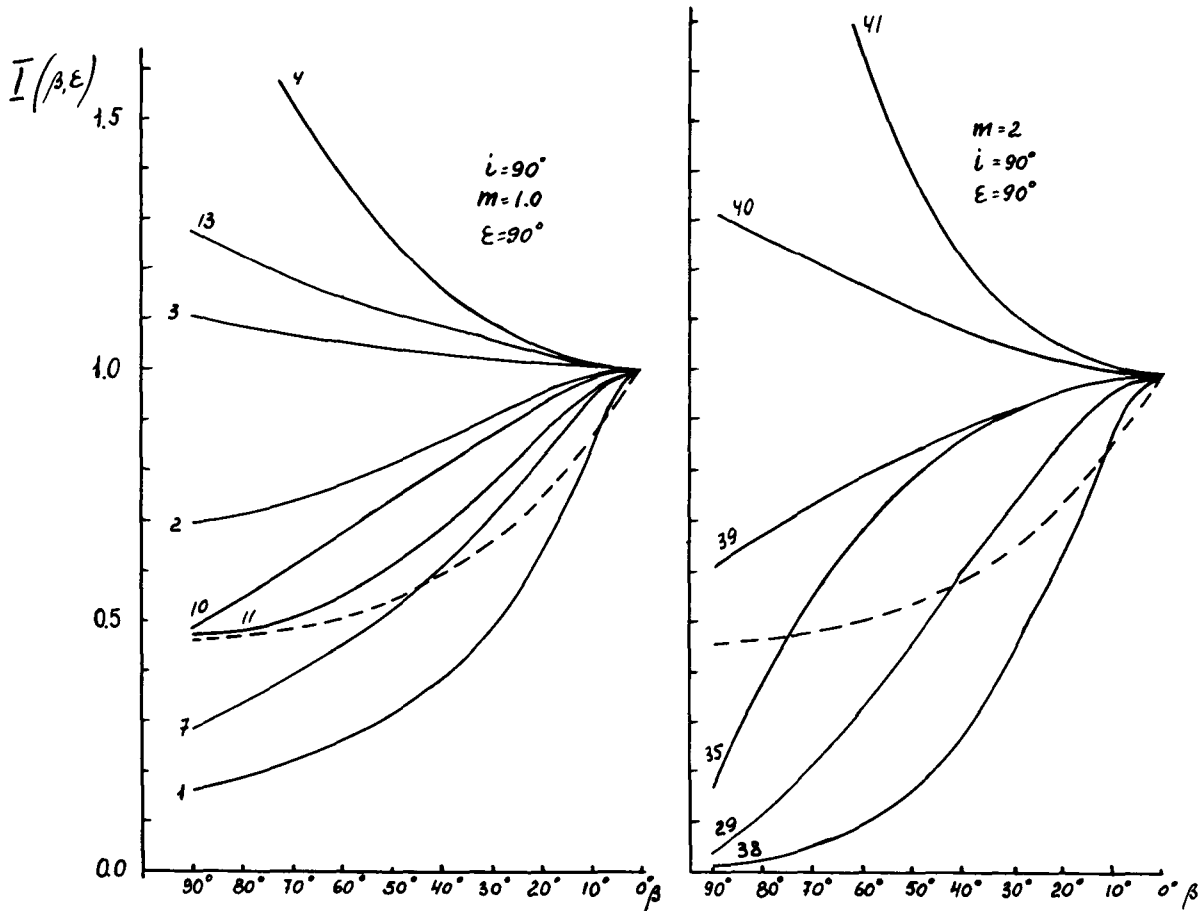


FIGURE 3.—Comparison of the observed course of zodiacal-light brightness (dashed line) along the circle $\epsilon=90^\circ$ with computed ones for different models at $i=90^\circ$. (a) Models with $m=1$: model 1: $k'=1, k=5$; model 2: $k'=3, k=5$; model 3: $k'=5, k=5$; model 4: $k'=10, k=5$; model 7: $k'=1, k=3$; model 10: $k'=1, k=2$; model 11: $k'=4, k=10$; model 13: $k'=1, k=1$. (b) Models with $m=2$: model 29: $k'=1, k=3$; model 35: $k'=1, k=2$; model 38: $k'=1, k=5$; model 39: $k'=3, k=5$; model 40: $k'=5, k=5$; model 41: $k'=10, k=5$.

is a strong increase of brightness in the direction to the ecliptic pole. Thus, the Earth's dust cloud can provide every kind of variation of brightness along the circle $\epsilon=90^\circ$, depending on values of parameters k' and k . If we want to explain the zodiacal light, it is clear that the condition $k' < k$ must hold, which provides the decrease of brightness in the direction to the ecliptic pole; that is, the surfaces of equal space density must be ellipsoids with the greater axis directed toward the Sun and the smallest directed toward the ecliptic pole.

To have a more precise value of k' , consider the brightnesses in the ecliptic, which at $i=90^\circ$ do not depend on k , because in this case $z=0$.

The values of $f(\theta)L(\beta, \epsilon)$ for the point $\beta=0^\circ$ and $\epsilon=35^\circ$ at $m=2$ and at four values of k' are shown in table 1. As seen from the table, at $k'=1.0$ there is a strong dependence of the brightness on the Sun depression. At $k' \geq 1.4$, the computed brightnesses do not depend on Sun depression. Thus, it is necessary to let $k' \geq 1.4$ and $k > k'$. Furthermore, as seen from figure 3, the brightness at the ecliptic pole cannot be equal to zero, but must contribute more than 0.1 of the brightness in the ecliptic at $\epsilon=90^\circ$.

Proceeding from the condition $k' \geq 1.4$, according to the data of figure 3, one can let $k'=4$; $k=10$; and $m=1.0$ for a model which provides

TABLE 1.—Values of $f(\theta)L(\beta, \epsilon)$ for the point $\beta=0^\circ$ and $\epsilon=35^\circ$ at $m=2$

g, deg	$f(\theta)L(\beta, \epsilon)$ for—			
	$k'=1.0$	$k'=1.4$	$k'=2.0$	$k'=4.0$
16	10.45	0.385	0.113	1.98×10^{-2}
18	9.35	.386	.113	1.98×10^{-2}
20	8.51	.386	.113	1.98×10^{-2}
22	7.85	.386	.113	1.98×10^{-2}
24	7.35	.386	.113	1.98×10^{-2}
32	6.35	.385	.113	1.98×10^{-2}

a dependence very close to the observed one of the zodiacal light brightness on the latitude β along the circle $\epsilon=90^\circ$. However, such a model does not give a sufficiently fast increase of the brightness along the ecliptic when ϵ decreases. The observed and computed relative values of brightness along the ecliptic for ϵ from $\epsilon=35^\circ$ to $\epsilon=90^\circ$ are compared in table 2. As the phase function $f(\theta)$ of dust particles in interplanetary space is not exactly known, it is possible to bring the data of the second line into correspondence with the data of the first line of table 2 by varying the phase function, that is, to use the observations along the circle $\beta=0^\circ$ for the determination of the phase function. Taking the phase function as

$$f(\theta) = \kappa[1 + \mu(e^{-3\theta} - 0.009) + \nu \cos^2 \theta] \quad (14)$$

we find by the method of the least squares the values of μ and ν on condition that the function $f(\theta)L(\beta, \epsilon)$ must correspond in the best way to observed dependence. It was found that

$$f(\theta) = \frac{1}{17.9} [1 + 22.3(e^{-3\theta} - 0.009) + 0.02 \cos^2 \theta] \quad (15)$$

(the factor κ before the square brackets is defined from the condition of normalization $\iint f(\theta)d\omega=1$). The relative brightnesses, obtained with the new phase function (15), which correspond quite well to the observed ones, are given in the last line of table 2. The obtained phase function (15) was used for computations of the intensity of light scattered by the Earth's dust cloud. The computations were carried out for different models of the space density distribution of the dust particles of the Earth's cloud, taking into account the limits found before for the parameters m , k' , and k . To compare the calculated brightness distribution with the observed one, we found the ratios of computed values of $f(\theta)L(\beta, \epsilon)$ to observed brightness $I_n(\beta, \epsilon)$ for different points of the sky with ecliptic coordinates β and ϵ . The constancy of the values of these ratios for the considered region of the zodiacal light serves as a criterion of agreement between the computed and observed brightnesses and shows how well the considered model can explain the zodiacal light. In table 3, these ratios are given for one of the models selected by us (the model 12: $m=1.0$, $k'_0=4.0$, $\delta'=0.0$, $k_0=10.0$, $\delta=1.0$) at an inclination of the ecliptic to the horizon $i=90^\circ$.

As seen from this table, the ratios $f(\theta)L(\beta, \epsilon)/I_n(\beta, \epsilon)$ for the considered model in the region $0^\circ \leq \beta \leq 50^\circ$, $35^\circ \leq \epsilon \leq 90^\circ$ do not change more than twofold. Such an agreement between computations and observations must be considered as a good one, taking into account the inaccuracies of the values of brightness deduced from observations and the possibilities of improving the models. In any case, it is not worse than that of the representation of zodiacal light by a heliocentric dust cloud of cometary or meteoroid nature. Thus, one can conclude that there exists a model of the Earth's dust cloud, which, at

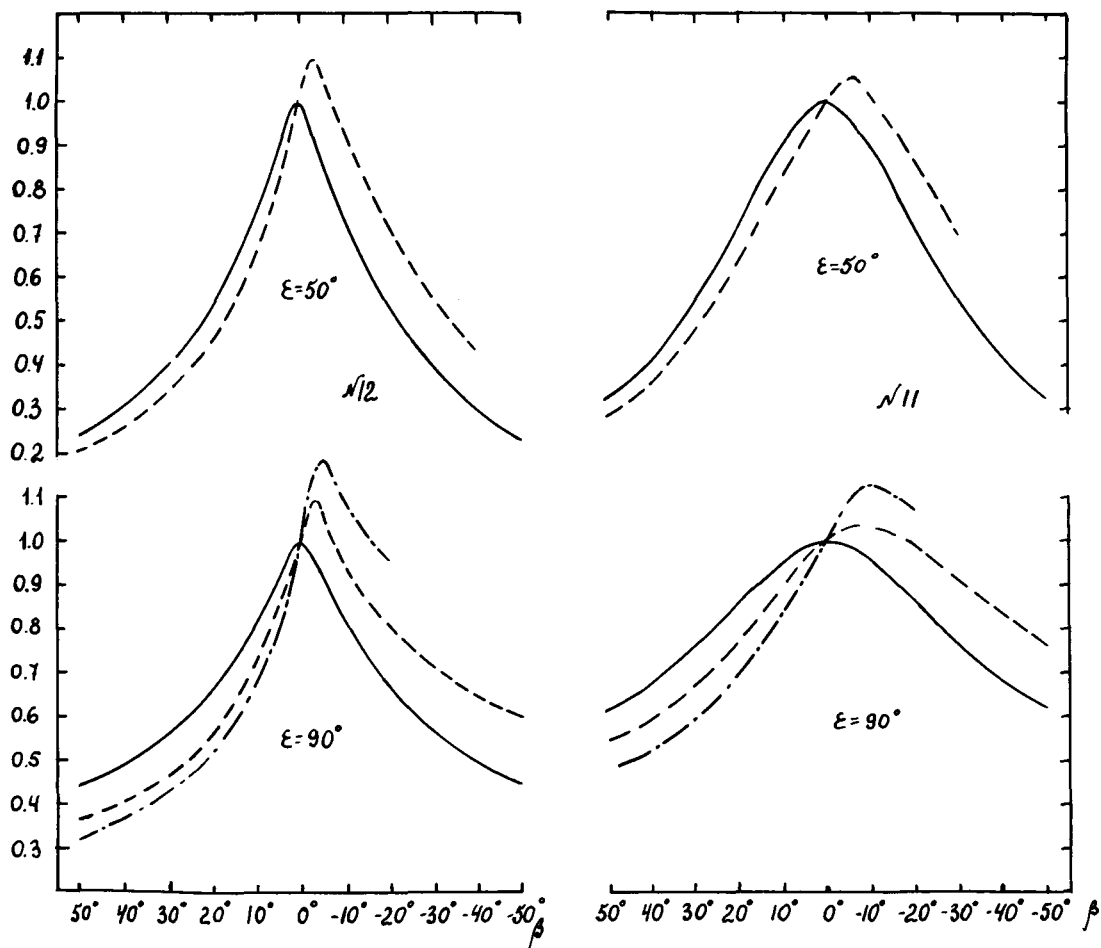
TABLE 2.—Relative Course of Brightness Along the Ecliptic

	$\epsilon=35^\circ$	$\epsilon=40^\circ$	$\epsilon=45^\circ$	$\epsilon=50^\circ$	$\epsilon=55^\circ$	$\epsilon=60^\circ$	$\epsilon=70^\circ$	$\epsilon=80^\circ$	$\epsilon=90^\circ$
Observations (Smith, Roach, and Owen, 1965)	6.38	4.74	3.78	2.98	2.40	2.00	1.48	1.16	1.00
Models:									
$k'=4, k=10, m=1.0, i=90^\circ$	3.91	3.09	2.49	2.06	1.76	1.53	1.24	1.08	1.00
$L(\beta, \epsilon)$	1.46	1.36	1.28	1.21	1.15	1.11	1.05	1.01	1.00
Brightness with new phase function.....	6.39	4.81	3.72	2.93	2.36	1.95	1.43	1.15	1.00

TABLE 3.—Ratios $\frac{f(\theta)L(\beta, \epsilon)}{I_n(\beta, \epsilon)}$ for Model 12 at $i=90^\circ$

 [$m=1.0$, $k'_0=4$, $\delta'=0$, $k_0=10$, $\delta=1.0$]

β , deg	$f(\theta)L(\beta, \epsilon)/I_n(\beta, \epsilon)$, for—								
	$\epsilon=35^\circ$	$\epsilon=40^\circ$	$\epsilon=45^\circ$	$\epsilon=50^\circ$	$\epsilon=55^\circ$	$\epsilon=60^\circ$	$\epsilon=70^\circ$	$\epsilon=80^\circ$	$\epsilon=90^\circ$
0	224	227	220	220	220	218	217	222	223
10	279	285	270	251	235	224	207	205	213
20	331	318	298	275	255	236	208	198	198
30	356	334	302	276	247	230	196	208	197
40	296	269	249	231	210	191	191	189	177
50	237	212	189	177	188	193	195	184	176
90	153								


 FIGURE 4.—Course of brightness along $\epsilon=50^\circ$ (upper) and $\epsilon=90^\circ$ (lower) at different inclinations of the ecliptic to the horizon for two models. Model 11: $m=1$, $k'=4$, $k=10$; model 12: $m=1$, $k'_0=4$, $k_0=10$, $\delta'=0$, $\delta=1$. Legend: — $i=90^\circ$; --- $i=60^\circ$; -.- $i=30^\circ$.

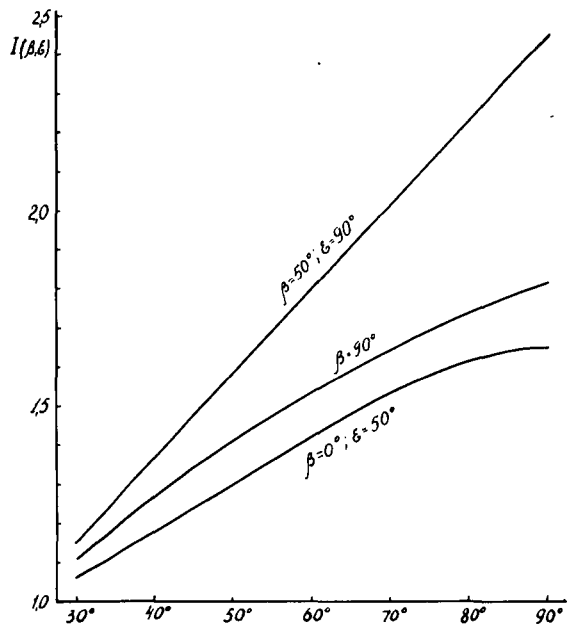


FIGURE 5.—Dependence of the computed brightness on the inclination i of the ecliptic to the horizon at three points for model 12 ($m = 1$, $k'_0 = 4$, $k_0 = 10$, $\delta' = 0$, $\delta = 1$).

$i = 90^\circ$, can provide a relative distribution of zodiacal-light brightness quite close to the observed one.

However, the characteristic feature of the models of the Earth's dust cloud with concentration of dust in the ecliptic plane is the presence of the parallax at inclinations to the horizon less than 90° . In figure 4, the computed brightnesses are shown along the sections $\epsilon = 50^\circ$ and $\epsilon = 90^\circ$ for two models: 11 ($m = 1$, $k' = 4$, $k = 10$) and 12 ($m = 1$, $k'_0 = 4$, $\delta' = 0$, $k_0 = 10$, $\delta = 1$). As seen from these curves, at an inclination of the ecliptic $i = 60^\circ$, the axis of zodiacal light is displaced some degrees to the south from the ecliptic and the symmetry of the curve is appreciably disturbed. It must be noticed that the displacement of the maximum for some degrees relative to the ecliptic and the disturbance of the symmetry of the brightness curve along the section $\epsilon = \text{constant}$ was often noted during observations. However, these displacements of the maximum were observed not only to the south of the ecliptic but also to the north of it.

Another characteristic feature of the Earth models is the dependence of zodiacal-light bright-

ness $I(\beta, \epsilon)$ at a given point with ecliptic coordinates β and ϵ on the inclination i of the ecliptic to the horizon, which is shown in figure 5 for the model 12 at three points of the sky. As seen from this figure, the brightness $I(\beta, \epsilon)$ increases with the increase of the inclination i ; the kind of increasing is different for different points of the sky, which is connected with the dependence of the brightness on zenith distance. This dependence of brightness on zenith distance is clearly shown for the spherical model of the Earth's dust cloud (model 13), for which $k' = k = 1$. It is obvious that in this case the distribution of the brightness is not connected with the ecliptic, but depends only on zenith distance and azimuth relative to the Sun's azimuth. The apparent dependence of the brightness $I(\beta, \epsilon)$ on the ecliptic inclination i is determined by the dependence of the zenith distance of the point ($\beta; \epsilon$) on the inclination of the ecliptic to the horizon.

Unfortunately, the results of specially organized observations for the comparison of zodiacal light brightnesses at different inclinations of the ecliptic to the horizon are not published. However, the results of observations, published by Elvey and Roach (1937) and Divari (1955a), show that there is a seasonal variation of the zodiacal-light brightness, according to which the zodiacal-light brightness in middle latitudes increases in average with the inclination of the ecliptic to the horizon. Nevertheless, there is proof of a direct connection between the zodiacal-light brightness and the inclination of the ecliptic to the horizon.

It seems that the component of the night sky found by us (Divari, 1955b), which depends on the inclination of the ecliptic to the horizon, is of great interest in connection with this. This component was obtained by the method of observation of a given point at different zenith distances, its change resulting from daily sky movement. It can have a direct relation to the Earth's dust cloud.

Let us consider now what must be the space density of the dust near the Earth for the component of the Earth's dust cloud to be apparent in the measurements of the night sky brightness. This evaluation can be made by equating the observed brightness to equation (5) for computed brightness, that is,

$$I_n(\beta, \epsilon) = I_0 CR \gamma (\pi a^2)_m f(\theta)$$

$$\int_{l_1}^{l_2} (\sqrt{k'^2 x^2 + y^2 + k^2 z^2} - 1)^{-m} dl \quad (16)$$

Or, letting $I_0 = 6.8 \times 10^{-5}$, $R = 6.37 \times 10^8$ cm and taking into account the designation (9)

$$I_n(\beta, \epsilon) = C(\pi a^2)_m \gamma 4.33 \times 10^4 f(\theta) L(\beta, \epsilon) \quad (17)$$

Hence we get the space density C of dust particles at the distance of 1 Earth radius from the Earth's surface

$$C = \frac{I_n(\beta, \epsilon)}{4.33 \times 10^4 (\pi a^2)_m \gamma f(\theta) L(\beta, \epsilon)} \quad (18)$$

The mean value $(\pi a^2)_m$ of the cross section of the dust particle depends on the dimension distribution $N(a)$, that is, on the parameter p in equation (7) and on the supposed range (a_1, a_2) of the particle radii. We computed the function $L(\beta, \epsilon)$ for different models. For models which can have a real significance the quantity $f(\theta)L(\beta, \epsilon)$ at the ecliptic pole has a value of the order of 10^{-1} to 10^{-2} . The values of C , found for some selected models by means of observations and calculations for the ecliptic pole, are given in table 4. These values of space density C at a distance of 1 Earth radius from the Earth's surface were compared with the values of space density N_1 , found by Ingham (1961) for a heliocentric dust cloud at a distance of 1 AU from the Sun by means of zodiacal-light observations.

The ratios $\frac{C}{N_1}$ of space density C of the Earth's dust cloud particles at a distance of 1 Earth radius from the Earth's surface to the space

density N_1 of the heliocentric zodiacal cloud particles at a distance of 1 AU from the Sun are given in the last column of table 4. These values are found on condition that the Earth's dust cloud completely explains the observed zodiacal-light brightness. As seen from table 4, it is necessary for this that C be from three to five orders of magnitude higher than N_1 .

The results of some experiments (see, for example, Whipple, 1961), performed on rockets and satellites with direct counting of meteoroid impacts, lead to the conclusion that the space density of dust near the Earth is three orders of magnitude higher than the space density in free interplanetary space at a distance of 1 AU from the Sun. However, papers have been recently published (for example, Nilsson, 1966) in which such as enhancement near the Earth is questioned, as well as the reliability of measurements of dust flux performed by means of some rockets and satellites. In connection with this, zodiacal-light observations acquire special significance for the solution of the problem of space density of dust particles near the Earth and in the interplanetary space.

First of all, it must be noted that the ratios C/N_1 listed in table 4 establish the upper limit for space density enhancement in the Earth's dust cloud. If this enhancement had been stronger than the values C/N_1 , the intensity of light scattered by the Earth's dust cloud would have exceeded the intensity of the zodiacal light and immediately would have been detected. From this point of view, the enhancement of space density of dust at a distance of 1 Earth radius found by Whipple (1961) by means of

TABLE 4. — Space Density C for $a_1 = 3 \times 10^{-5}$ cm and $\gamma = 0.2$

Model	p	$(\pi a^2)_m$	C	N_1	C/N_1
No. 10 ($m=1, k'=1, k=2$)	5	5.5×10^{-9}	5.1×10^{-9}	6×10^{-13}	9×10^3
	4	8.5×10^{-9}	3.4×10^{-9}	5×10^{-13}	7×10^3
No. 11 ($m=1, k'=4, k=10$)	5	5.5×10^{-9}	3.4×10^{-8}	6×10^{-13}	6×10^4
	4	8.5×10^{-9}	2.3×10^{-8}	5×10^{-13}	5×10^4
No. 12 ($m=1, k'_0=4, k=10$, $\delta'=0, \delta=1$)	5	5.5×10^{-9}	4.8×10^{-8}	6×10^{-13}	8×10^4
	4	8.5×10^{-9}	3.1×10^{-8}	5×10^{-13}	6×10^4
No. 13 ($m=1, k'=1, k=1$)	5	5.5×10^{-9}	2.0×10^{-9}	6×10^{-13}	3×10^3
	4	8.5×10^{-9}	1.3×10^{-9}	5×10^{-13}	3×10^3

TABLE 5.—*Comparison of Observed Zodiacal Light Brightness With Brightness Provided by Spherical Model of Earth's Dust Cloud*

	$\epsilon = 35^\circ$	$\epsilon = 40^\circ$	$\epsilon = 45^\circ$	$\epsilon = 50^\circ$	$\epsilon = 60^\circ$	$\epsilon = 70^\circ$	$\epsilon = 80^\circ$	$\epsilon = 90^\circ$
Model 13, $i = 60^\circ$	185	146	119	99	74	59	51	46
Zodiacal light (Divari, 1965a).....	1360	973	766	603	404	313	252	188

rocket and satellite data does not contradict the computed results because $\frac{C}{N_1} > 10^3$. On the other hand, if we proceed from these values of enhancement obtained from rocket data, it must be concluded that the Earth's cloud cannot be completely responsible for the zodiacal light. Model 12, which provides the best relative distribution of brightness, cannot contribute more than 10 percent to the zodiacal-light brightness.

One of the important objections against the Earth cloud model of zodiacal light is the character of variation of the degree of polarization along the ecliptic. According to results of many observations (Divari, 1965b), the degree of polarization along the ecliptic has a maximum near the elongation of $\epsilon = 60^\circ$. Such a course of variation of polarization can be explained by the heliocentric cloud. But it is very difficult to explain it by the Earth's dust cloud, because this cloud cannot provide a maximum of polarization degree at that elongation but leads instead to a maximum near $\epsilon = 90^\circ$.

The spherical model of the Earth's dust cloud (model 13) cannot be responsible for the zodiacal light, but it can introduce some contribution to the distribution of night sky continuum. Let us suppose, for example, that at the ecliptic pole this component provides a brightness of 50 stars of 10th magnitude per square degree, that is, practically all the brightness measured in the continuum. Then, in the ecliptic, the brightness of this component will be much less than the observed zodiacal-light brightness, as seen from table 5, where the observed zodiacal-light brightnesses are compared with the brightnesses for the spherical component, computed at an inclination of the ecliptic to horizon $i = 60^\circ$. Thus, the spherical model of the Earth's dust cloud can

provide the observed brightness at the ecliptic pole and can contribute a small part to the zodiacal-light brightness, slightly disturbing its cones.

The accomplished analysis of different models of the Earth's dust cloud shows that it cannot be completely responsible for the zodiacal-light phenomenon, but it can introduce some contribution of the order of some percent to the observed brightness in the region of the zodiacal cones. This component can be important in regions far from the ecliptic. The fact that, in the observed zodiacal light brightness, matter situated near the Earth manifests itself in some way follows from the relation obtained between the Moon's position, on the one hand, and the zodiacal light brightness and the position of its axis, on the other hand (Divari, 1963; and Divari and Komarnitskaya, 1965). Moreover, there are indications of an effect by the dust accumulated at the libration points of the Earth-Moon system and by the dust situated along the lunar orbit Gingerich (1966).

An explanation of the zodiacal light by means of the Earth's dust cloud set up by dust particles of submicron dimensions raises a particular problem. These particles are not investigated by satellites because the apparatus used until now is not sufficiently sensitive to such small particles. However, there are reasons to suppose (Divari, 1966), that such particles may exist in the Earth's magnetosphere if they have an electric charge which provides a potential of several volts. Since the action of sunlight pressure is not effective enough on the dielectric particles of submicron dimensions, these particles will not be driven out of the solar system. If we suppose that the minimum radius of particles is $a_1 = 3 \times 10^{-6}$ cm, then to explain zodiacal light

by model 12 of the Earth's dust cloud at $p=3$, the space density at a distance of $1 R_0$ from the Earth's surface must be equal to 10^{-7} cm^{-3} , which is three orders of magnitude higher than the space density at a height of 100 km above the Earth's surface as established by means of twilight observation (Divari, 1964). It is difficult to say now to what extent this space density of submicron dust is real, because there are no direct measurements of such small particles. However, it does not seem impossible.

In connection with this, it seems very important to establish the dependence of the degree of polarization on the scattering angle for submicron particles with the hope for an explanation of the observed course of the degree of polarization of zodiacal light by means of the light scattered by this fine dust of the Earth's cloud.

The real picture can be obtained only by observations. The computations carried out show what effects might be discovered if the Earth's dust cloud is important in the distribution of night-sky brightness in the continuum. In this respect, the decisive factor belongs to special observations which must be carried out at different inclinations of the ecliptic to the horizon.

At the same time, it is necessary to study other models of the dust distribution in the vicinity of the Earth, in particular models providing a space density maximum at some distance from the Earth's surface (torus or ring-shaped models).

ACKNOWLEDGMENT

I have to express my deep gratitude to Mrs. V. P. Marchenko who made the calculations on an electronic computing machine "Ural-2."

REFERENCES

- DIVARI, N. B., 1955a, *Ast. Zhur.*, **32**, 79.
 —, 1955b, *Izvestia Astrophys. Inst. Acad. Sci. (Alma-Ata)*, **1**, 179.
 —, 1963, *Ast. Zhur.*, **40**, 717, and 1963, *Soviet Astron.—AJ*, **7**, 547.
 —, 1964, *Geomagnetizm i. Aeronomiya*, **4**, 886.
 —, 1965a, *Ast. Zhur.*, **42**, 645, and 1965a, *Soviet Astron.—AJ*, **9**, 493.
 —, 1965b, *Usp. Fiz. Nauk*, **84**, 75, and 1965b, *Soviet Physics Uspekhi*, **7**, 681.
 —, 1966, *Ast. Zhur.*, **43**, 192.
 DIVARI, N. B., and N. I. KOMARNITSKAYA, 1965, *Ast. Zhur.*, **42**, 817.
 ELVEY, C. T., and F. E. ROACH, 1937, *Astrophys. J.*, **85**, 213.
 FESENKOV, V. G., 1964, *Ast. Zhur.*, **41**, 1001, and 1965, *Soviet Astron.—AJ*, **8**, 803.
 GINGERICH, O., 1966, *IAU Circ. No. 1985*.
 INGHAM, M. F., 1961, *Mon. Not. Roy. Astron. Soc.*, **122**, 157.
 NILSSON, C., 1966, *Science*, **153**, 1242.
 PIASKOVSKAYA-FESENKOVA, E. V., 1959, *Izvestia Astrophys. Inst. Acad. Sci. (Alma-Ata)*, **8**, 82.
 SMITH, L. L., F. E. ROACH, and R. W. OWEN, 1965, *Planetary Space Sci.*, **13**, 207.
 WHIPPLE, F., 1961, *Nature*, **189**, 127.

Page intentionally left blank

47. The Possibility of Dust Concentration Near the Earth

THOMAS SCHMIDT
*Landessternwarte
Heidelberg, Germany*

AS A RESULT OF THE Poynting-Robertson effect, interplanetary dust particles are continuously crossing the Earth's orbit from the outer planetary system. A concentration of dust near the Earth or the Earth's orbit may be caused by capture of those particles. This was investigated by numerical orbit computations.

Taking into account the radiation and corpuscular pressure and the radiation and corpuscular Poynting-Robertson effect, the differential equation of particle motion is given by

$$\frac{4}{3} \pi \rho a^3 \frac{d^2 \mathbf{r}}{dt^2} = \mathbf{F}_g + \mathbf{F}_{1r} + \mathbf{F}_{1c} + \mathbf{F}_{2r} + \mathbf{F}_{2c} \quad (1)$$

where ρ is the particle density, a is the particle radius, and \mathbf{F}_g is the resulting gravitational force of the Sun, Earth, and Moon. The Earth and the Moon are assumed to move on circular orbits; the gravitational forces of the other planets are neglected. The equations for radially directed forces of radiation and corpuscular pressure, \mathbf{F}_{1r} and \mathbf{F}_{1c} , for particle orbits which are not extremely eccentric are

$$\left. \begin{aligned} \mathbf{F}_{1r} &= \frac{\pi a^2}{c} \int Q_{pr} I_\nu d\nu \\ \mathbf{F}_{1c} &= \pi a^2 f_c v_c m_c k \end{aligned} \right\} \quad (2)$$

where Q_{pr} is the efficiency factor of the radiation pressure; I_ν is the solar radiation; f_c , v_c , and m_c are the flux, velocity, and mass of the solar-wind particles; and k is an efficiency factor for the corpuscular pressure.

The tangentially directed Poynting-Robertson forces \mathbf{F}_{2r} and \mathbf{F}_{2c} are given by

$$\left. \begin{aligned} \mathbf{F}_{2r} &= -\mathbf{F}_{1r} \frac{u}{c} \\ \mathbf{F}_{2c} &= -\mathbf{F}_{1c} \frac{u}{v_c} \end{aligned} \right\} \quad (3)$$

where u describes the tangential component of the particle velocity.

The differential equations (1) were solved numerically by the Runge-Kutta method. All computations refer to the particle mass density $\rho = 1 \text{ g-cm}^{-3}$ and the refractive index $m = 1.33$, but they are also valid for other particle properties with respectively varied parameters. Only particles with $a > 10^{-4} \text{ cm}$ are considered, which are not seriously affected by Lorentz forces of interplanetary magnetic fields. For these particles the corpuscular pressure itself is negligible; however, the corpuscular Poynting-Robertson effect is not.

The numerical values for the physical constants of equation (2) are as follows:

$$\begin{aligned} \int Q_{pr} I_\nu (1 \text{ AU}) d\nu &= 1.9 \times 10^6 \text{ erg-cm}^{-2}\text{-sec}^{-1} \\ &\quad (a = 10^{-4} \text{ cm}) \\ &= 1.6 \times 10^6 \text{ erg-cm}^{-2}\text{-sec}^{-1} \\ &\quad (a = 10^{-3} \text{ cm}) \\ f_c &= 9 \times 10^8 \text{ cm}^{-2}\text{-sec}^{-1} \\ v_c &= 300 \text{ km/sec} \\ m_c &= 1.67 \times 10^{-24} \text{ g} \\ k &= 1 \end{aligned}$$

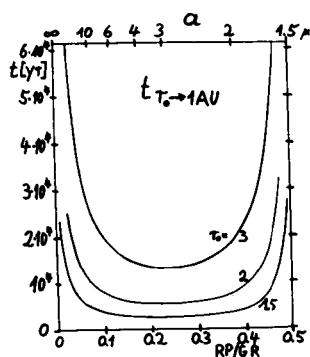


FIGURE 1.—Drifting times of particles generated from parent bodies on circular orbits at distances r_0 in AU down to the Earth orbit are plotted against the ratio RP/GR and the particle radius a (10^{-4} cm), respectively (particle density $\rho = 1 \text{ g-cm}^{-3}$).

RADIATION PRESSURE AND POYNTING-ROBERTSON FORCE

It is assumed that the particles under consideration are generated by parent bodies not affected by the radiation pressure and moving on circular orbits. In this case all generated particles with a ratio of radiation pressure and gravitation $RP/GR \geq 0.5$ will escape from the planetary system. Therefore, only particles with radii $a > 1.5 \times 10^{-4}$ cm can reach the Earth's orbit (see fig. 1). For noncircular parent orbits this limit is varied by small values only. The following computations are carried out in general with particle radii between 2×10^{-4} cm and 10^{-3} cm.

CAPTURE ORBITS OF THE EARTH'S GRAVITATIONAL FIELD

If particles of such kind generated at distances of 1.5 up to 3 AU from the Sun approach the Earth's orbit, they have velocities relative to the Earth from about 1 to 4 km/sec (assuming corotational and circular orbits of the parent bodies). In this velocity region, capture by the gravitational field of the Earth can occur. Altogether 134 different particle orbits have been computed passing the Earth's gravitational sphere of influence within 100 Earth radii. Particles remaining near the Earth at least two times longer than those without the gravitational attraction of the Earth have to fulfill very special initial conditions. For a total of 30 computed orbits with particle radii $a = 6 \times 10^{-4}$ cm, such conditions could be found only if the particle enters the Earth's sphere of influence between

0.0030 and 0.0038 AU outside, 0.0007 AU inside, or 0.0001 AU above or below the Earth's orbit. Not one of these particles remained more than 90 days in an orbit around the Earth. In the case of other particle radii, the results are qualitatively the same. (See also Shapiro, Lautman, and Colombo, 1966.) It seems almost impossible to explain in this way a dust concentration around the Earth of only three times the concentration of the deep interplanetary space. As Shapiro et al. (1966) have already shown, the number of capture orbits from lunar ejecta are insufficient in just the same way.

A DUST RING NEAR THE EARTH'S ORBIT

The computations have shown that indeed another effect may cause not a circumterrestrial dust cloud, but a dust ring around the Sun, just outside the Earth's orbit. The gravitational field of a planet seems to prevent particles affected by the Poynting-Robertson force with a small orbital eccentricity from passing the planetary orbits into the inner part of the solar system. Figures 2 and 3 show this effect. The perihelion distance r_p of the particle in AU is plotted against time in years. The dashed lines show the action of the Poynting-Robertson effect without the influence of the Earth, causing a steady decrease

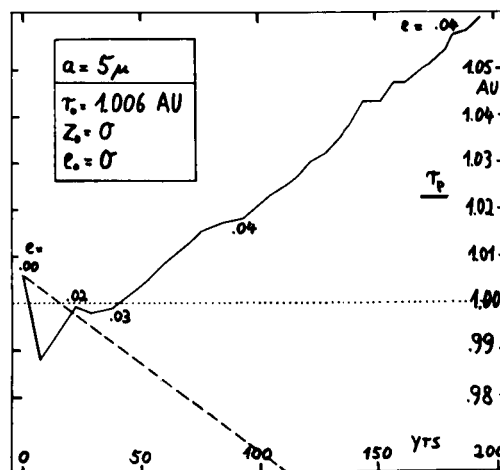


FIGURE 2.—The gravitational action of the Earth on the orbital motion of a particle affected by the radiation pressure and the Poynting-Robertson effect. The perihelion distance is plotted against the time. The dashed line shows the normal Poynting-Robertson drift. The key gives the particle radius ($\rho = 1 \text{ g-cm}^{-3}$) and the initial particle orbit (z_0 is the distance from the ecliptic plane).

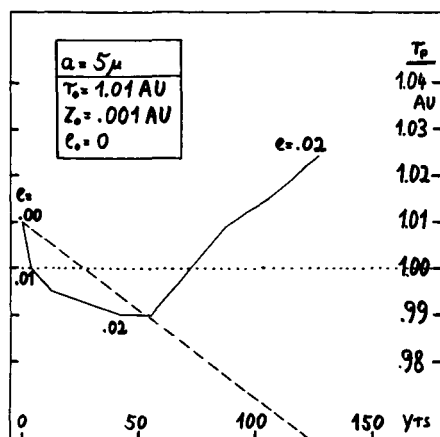


FIGURE 3.—The gravitational action of the Earth on the orbital motion of a particle affected by the radiation pressure and the Poynting-Robertson effect. The perihelion distance is plotted against time. The dashed line shows the normal Poynting-Robertson drift. The key gives the particle radius ($\rho = 1 \text{ g-cm}^{-3}$) and the initial particle orbit (z_0 is the distance from the ecliptic plane).

of the perihelion distance. The solid lines give computed perihelion distances affected by the gravitational field of the Earth. Each discontinuity in the curve refers to a single particle approach to the Earth. The evolution of the orbital eccentricity e is also shown. It is evident that the steady inward drift caused by the Poynting-Robertson effect is interrupted by an increasing perihelion distance. This inward drift may continue only when the increase of the orbital eccen-

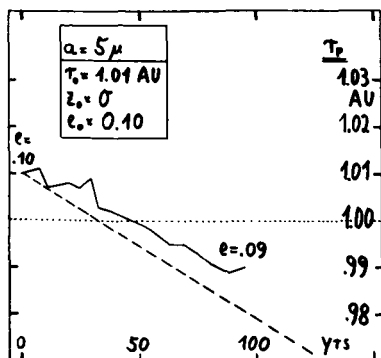


FIGURE 4.—The gravitational action of the Earth on the orbital motion of a particle affected by the radiation pressure and the Poynting-Robertson effect. The perihelion distance is plotted against time. The dashed line shows the normal Poynting-Robertson drift. The key gives the particle radius ($\rho = 1 \text{ g-cm}^{-3}$) and the initial particle orbit (z_0 is the distance from the ecliptic plane).

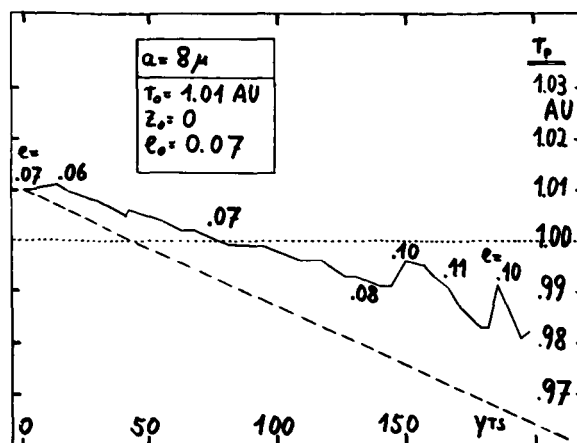


FIGURE 5.—The gravitational action of the Earth on the orbital motion of a particle affected by the radiation pressure and the Poynting-Robertson effect. The perihelion distance is plotted against time. The dashed line shows the normal Poynting-Robertson drift. The key gives the particle radius ($\rho = 1 \text{ g-cm}^{-3}$) and the initial particle orbit (z_0 is the distance from the ecliptic plane).

tricity by disturbances from the Earth has become great enough to diminish significantly the number of near-Earth transits. This case is shown in figure 4: A particle starting with an orbital eccentricity $e = 0.1$ is no more affected seriously by the gravitational field of the Earth. Figure 5 shows the situation of a particle with an initial eccentricity $e = 0.07$. The effect can be seen, but it is already significantly smaller than that for circular orbits.

CONCLUSION

The computations were conducted on the computer Siemens 2002 of the University of Heidelberg, which unfortunately is not fast enough to follow a sufficient number of particle orbits from the first influence of the Earth until the final passing into the inner part of the solar system. Computations of such kind will be done in the near future, but it is not yet possible to present distinct density determinations of such a dust ring near the Earth's orbit. However, to obtain at least a very radical lower limit of this dust concentration, the assumption may be made that the particle of figure 2 from the upper right end of the curve would drift immediately with the normal Poynting-Robertson shift into the inner part of the planetary system. A further

assumption is that the radial extension of the dust ring is given by $\bar{e}r_p$, the product of the mean eccentricity of particle orbits $\bar{e}=0.04$ and the perihelion distance $r_p=1$ AU. Thus, the concen-

tration of particles just outside the Earth's orbit with orbital elements similar to those of figure 2 should be about 5 times the concentration in the surrounding interplanetary space.

REFERENCES

- COLOMBO, G., D. A. LAUTMAN, and I. I. SHAPIRO, 1966, *J. Geophys. Res.*, **71**, 5705.
COLOMBO, G., I. I. SHAPIRO, and D. A. LAUTMAN, 1966, *J. Geophys. Res.*, **71**, 5719.
LAUTMAN, D. A., I. I. SHAPIRO, and G. COLOMBO, 1966, *J. Geophys. Res.*, **71**, 5733.
SHAPIRO, I. I., D. A. LAUTMAN, and G. COLOMBO, 1966, *J. Geophys. Res.*, **71**, 5695.

48. The Zodiacal Light and Earth-Orbiting Dust

S. J. PEALE

*University of California, Los Angeles
Los Angeles, California*

Dynamical and observational properties of a geocentric dust cloud are discussed and compared with observations of the zodiacal light. The geocentric contribution to the zodiacal light is shown to be negligible.

THE POSSIBILITY OF A MAJOR CONTRIBUTION to the zodiacal light by small dust particles concentrated near the Earth has been discussed by several authors (Jones, 1856; Divari, 1965; Peale, 1966). There have also been several observations which may support this hypothesis either directly or by inference (Divari and Komarnitskaya, 1966; Dubin and McCracken, 1962) (see also Dubin and Hemenway, paper 21; and Tousey and Koomen, paper 19). Other observations seem to be more consistent with only a small concentration of dust near the Earth and hence a heliocentric source of zodiacal light (Nilsson, 1966; Alvarez, paper 22; Dozier and Naumann, paper 27; Gillett, paper 2). In the light of these apparently contradictory results, we propose to examine the recent observations and theory related to the properties of a geocentric dust cloud. It is shown that, whereas the recent observations by themselves make the geocentric hypothesis less likely, the restrictions that are placed on the characteristics of geocentric dust by theoretical and numerical work in conjunction with these observations essentially destroy the hypothesis of a large geocentric contribution to the zodiacal light.

GROUND BASED OBSERVATIONS OF THE ZODIACAL LIGHT IN THE ECLIPTIC PLANE

Included here are the measurements of the zodiacal light brightness, color, and polarization as a function of elongation from the Sun and the

measurement of a Doppler shift of the Fraunhofer absorption lines in the zodiacal-light spectrum. Careful measurements of the brightness, color, and polarization have been made by numerous observers and have been until recently the only source of information about the nature of the particles which scatter sunlight to the Earth. However, observations with different color filters and the use of different methods of reducing the raw data to eliminate starlight and atmospheric contributions to the night-sky brightness have resulted in widely different estimates of the zodiacal-light parameters. These estimates, in turn, have been used to generate an even higher dispersion of the derived properties of the scattering dust grains. The dispersion of the observational estimates is more pronounced in the polarization measurements than in the integrated brightness distribution. Weinberg (1963) has discussed the difficulties of using wide-band filters for polarization measurements, and this accounts for some of the discrepancies. But even a given set of observational data can be matched by several plausible but fundamentally different models of the zodiacal dust. This idea was stretched to a logical extreme when it was shown that most of the known features of the zodiacal light could be reproduced with dust particles orbiting the Earth if the geocentric dust were distributed symmetrically with respect to the ecliptic plane (Peale, 1966). Such a diversity of possible models is understandable if one

realizes the existence of the large number of free parameters which have wide ranges of plausible values and that the simple theories used for scattering by small particles (the Mie theory and approximations to it) may have only a limited application.

The difficulties inherent in the measurement of a Doppler shift of the Fraunhofer lines in the zodiacal light spectrum have been discussed by Peale (1966) (see also James, paper 13). In spite of these difficulties an attempt to measure this Doppler shift was made by Ring et al. (1964). A blue shift was detected in the spectrum which was two to three times that expected for particles in circular orbit about the Sun, whereas no red shift was detected on the other side of the Sun. Particles with velocities consistent with the blue shift would not be bound in the solar system. This unlikely result therefore cannot be used as an indication of a heliocentric dust source for the zodiacal light.

In summary, it appears that current theoretical interpretations of the existing ground-based observations of the zodiacal light in the ecliptic plane cannot, by themselves, rule out a geocentric contribution. However, future measurements with extremely narrow-band filters which exclude atmospheric emission lines will furnish more conclusive evidence (see Weinberg, paper 1). In addition, the brightness of the zodiacal light as a function of position in the sky off the ecliptic plane, in conjunction with a recent theoretical treatment of the symmetry of the spatial distribution of particles orbiting the Earth, places conditions on the dust near the Earth which prove too restrictive for a substantial contribution to the zodiacal light (see the section entitled "Dynamics").

SATELLITE AND ROCKET OBSERVATIONS

A few years ago rocket (Hemenway and Soberman, 1962) and satellite (Alexander, 1962; Dubin and McCracken, 1962; and Hibbs, 1961) measurements indicated that the flux density of dust particles near the Earth was several orders of magnitude above that estimated for interplanetary space from the zodiacal-light brightness. Singer (1961) showed that this apparently anomalous flux density caused no grave

theoretical difficulties if one accounted for the peculiar characteristics of the microphone detectors and required the particles to have very small velocities at the surface of the Earth's sphere of influence. However, a more realistic distribution of velocities leaves the high flux densities without a sound theoretical justification. This led Hibbs (1961) to propose that the measured flux density was due to orbiting particles which would not be part of the direct flux from interplanetary space. But the sensitive microphone detectors were always placed on satellites with orbits close to the Earth's surface. The short lifetimes of orbiting dust particles at these altitudes prohibit the major fraction of the microphone impacts from being due to anything other than the direct influx to the Earth. Hibbs' explanation was, therefore, not sufficient to account for the observations, and the mystery remained. Although the satellite microphones had detected essentially no orbiting particles, the apparent anomalously high influx of particles indicated that perhaps particles orbiting the Earth in higher, more stable orbits also had anomalously high densities. This possibility motivated several studies of the properties of such particles (Fesenkov, 1964, 1965; Peale, 1966).

More recently, dust-particle detectors of a different type have been flown in low orbits with results which do not support an anomalous flux of particles near the Earth. In fact, the counting rates were quite consistent with those which would be expected from estimated interplanetary densities (Nilsson, 1966; see also J. M. Alvarez, paper 22; and Dozier and Naumann, paper 27). Since these measurements remove the theoretical problems involved with a high concentration of particles near the Earth, they are at once easily accepted. (However, see Dubin and Hemenway, paper 21.) If the later measurements are indeed correct, then the existence of a high density of orbiting particles is less likely. At the same time, it should be emphasized that these experiments were also performed in relatively low orbits and hence do not explicitly exclude a major orbiting component at higher altitudes. We shall consider such an absence of nearby particles in the following section.

DYNAMICS

A major difficulty with the hypothesis of a substantial contribution to the zodiacal light by orbiting geocentric dust is the fact that the group of particles orbiting relatively close to the Earth will have a spatial distribution which is symmetric with respect to the Earth's equatorial plane. The zodiacal light is nearly symmetric with respect to the ecliptic plane, however. If we assume that the Earth's equatorial bulge is the only perturbation experienced by the particles; the node of each particle orbit on the equatorial plane will vary according to the equation (Kozai, 1959)

$$\frac{d\Omega}{dt} = -2 \times 10^{-6} \left(\frac{R_E}{a} \right)^{7/2} \cos i (1 + 2e^2)$$

where R_E is the radius of the Earth and a , e , i , Ω are, respectively, the semimajor axis, eccentricity, inclination, and longitude of the node of the particle orbit. If we place a large number of particles in a toroidal ring about the Earth which is inclined at an angle i relative to the equatorial plane, the initial spatial distribution will, of course, be symmetric about the plane of the ring. However, the particles will each have unique values of the orbital parameters a , e , and i ; so by the above equation the positions of the nodes of these particles on the equatorial plane will change at unique rates. At some time in the future one would expect to see the particle orbit nodes scattered completely around the equatorial plane. The spatial distribution would consist of a cylindrical sheet of particles with an angular width of $2i$ relative to the Earth, and the sheet would be symmetric with respect to the equatorial plane. Particle interactions would tend to reduce the angular width, but the equatorial symmetry would be maintained. If we account for the other perturbing forces which act on the particles, the equatorial symmetry will still be obtained provided that the perturbation due to the oblate Earth is much larger than the others.

In addition to the gravitational perturbation of the oblate Earth, the corotating magnetosphere will also tend to symmetrize and concentrate particles with respect to the equatorial plane (Gold, 1962). However, these effects are com-

pletely negligible for particles orbiting the Earth when compared with other perturbations (Peale, 1966) and will not be considered further.

For particles orbiting relatively far from the Earth, the most important gravitational perturbations become those due to the Moon and Sun. By an argument which is entirely analogous to that above, one can show that the spatial distribution of these particles will be symmetric with respect to the ecliptic plane. Light scattered by such particles could contribute to the zodiacal light.

The other major perturbation which small particles will experience is that due to radiation pressure. The perturbing acceleration is proportional to the area-to-mass ratio, so radiation pressure can become the dominant perturbation for very small particles. The spatial distribution which would be established by the radiation pressure perturbation would be symmetric with respect to the ecliptic plane. Hence, this perturbation tends to place geocentric particles in the proper symmetry for a contribution to the zodiacal light. For the smallest particles likely to be found in Earth orbit, the radiation pressure dominates the oblateness perturbation if $a \gtrsim 1$ to $2 R_E$. This led Peale (1966) to propose that perhaps a considerable fraction of the dust orbiting the Earth had the necessary ecliptic symmetry to contribute to the zodiacal light.

Allan and Cook (1967) have shown, however, that a plane of symmetry exists for Earth orbiting particles which changes gradually from the equator to the ecliptic plane. For larger particles (radiation pressure being unimportant) the symmetry plane does not approach within 1° of the ecliptic unless $a \gtrsim 14 R_E$. This value is reduced to about $12 R_E$ if the area-to-mass ratio of the particles is near $200 \text{ cm}^2/\text{g}$. An area-to-mass ratio of $200 \text{ cm}^2/\text{g}$ is near the limit of validity of the approximations used in this analysis such that the symmetry plane for smaller particles could remain close to the ecliptic at smaller geocentric distances.

One might argue that the position of the axis of the zodiacal light is known to no better than a few degrees and thereby relax somewhat the symmetry restrictions on the larger particles. However, the observations which indicate non-

ecliptic symmetry for the zodiacal light favor the equatorial plane of the Sun and not the equatorial plane of the Earth. (Huruhata, 1965; see also Dumont, paper 11; and Saito and Huruhata, paper 7.) The lines of intersection of each of these planes with the ecliptic plane are separated by about 74° , so symmetries favoring one or the other plane would not be confused. If the observations of a component of the zodiacal light symmetric with respect to the Sun's equatorial plane prove to be accurate, the geocentric dust contribution to this component must necessarily be negligible.

The analysis of van de Hulst (1947) used by Peale (1966) for geocentric dust requires a considerable number of large particles to account for the increase in zodiacal-light brightness as the line of sight approaches very close to the Sun. These large particles would have to be highly dispersed about their symmetry planes for $a \leq 14 R_E$ in order to avoid a band of scattered light off the ecliptic plane (see Allan and Cook, 1967). On the other hand, if small particles alone ($< 10^{-2}$ cm) are adequate for the observed brightness and polarization as a function of elongation, one might consider this requirement of high dispersion to be unimportant for a substantial geocentric contribution for two reasons. First, the small particles are not covered by the Allan and Cook analysis, and second, the smaller particles tend to be controlled by radiation pressure and would display the necessary ecliptic symmetry. But these smaller particles will have relatively short lifetimes even if they are initially placed in the most stable orbits (Peale, 1966); so their presence in large numbers would require an unreasonable rate of supply (see the section entitled "Capture"). In addition, the small particles would still have to be considerably dispersed for $a \leq 4$ to $6 R_E$ (see fig. 4 of Peale, 1966). Let us examine this necessary high dispersion of the nearby particles more closely.

The purpose of the high spatial dispersion of the particles near the Earth is, of course, to maintain an overall symmetry of the scattered light relative to the ecliptic plane even though the symmetry plane established by the perturbations lies between the equatorial plane of the Earth and the ecliptic plane. More distant par-

ticles would have to be concentrated toward the ecliptic plane for a substantial zodiacal-light contribution. This axially symmetric distribution for the *geocentric particles* would lead to a dependence of the brightness in the ecliptic plane on elongation from the Sun ϵ , which is proportional to the scattering function of the particles. On the other hand, the brightness of the geocentric particles in a plane perpendicular to the ecliptic and containing the Earth and the Sun would have a relatively low value at the ecliptic pole but would increase at a higher rate than the scattering function for decreasing ϵ . This is a necessary consequence of the fact that the projected areal density of the geocentric particles is constant as a function of ϵ in the ecliptic plane but is minimal at $\epsilon = 90^\circ$ in the perpendicular plane. The ratio of the brightness of the geocentric particles in the ecliptic plane to that in the perpendicular plane would be a maximum at $\epsilon = 90^\circ$. However, Smith et al. (1965) find this ratio for the zodiacal light to be maximal at $\epsilon = 35^\circ$ —a result which is inconsistent with a substantial geocentric contribution to the zodiacal light.

If the brightness of the zodiacal light at the ecliptic pole proves to be somewhat lower than the present measurements, a large geocentric contribution would then require a virtual elimination of the nearby dispersed component of the geocentric dust, whereas the more distant particles would be somehow maintained. This is necessary because the depth of the dispersed component is a nonnegligible fraction of the likely maximum depth of about 50 to 60 R_E for any possible dust cloud. On the one hand, a low zodiacal-light brightness at the ecliptic pole would be required to give the proper dependence of brightness of a large geocentric contribution on elongation; on the other hand, such a low brightness at the pole would also require a spatial distribution about the Earth which is impossible to justify. For example, radiation pressure would drive the particle pericenters into the forbidden region.

CAPTURE

The difficult problem of the capture of small particles into geocentric orbit has been con-

sidered by Colombo et al. (1966a), Colombo et al. (1966b), and Lautman et al. (1966). They conclude that the three-body Jacobi capture from the interplanetary reservoir of particles is too rare to be of significance, whereas the lifetimes of captured lunar ejecta and interplanetary particles captured by dissipation in the upper atmosphere rarely exceed a year. The lunar ejecta are short lived because the orbits cross the orbit of the Moon. The small particles which are captured by grazing the atmosphere can have their orbit perigees raised by radiation pressure, and the orbit is thus stabilized. However, this effect is periodic, and the perigee returns to low altitudes about once a year. The resulting dissipation will cause rapid orbit decay. The larger particles captured by this process do not get their orbit perigees raised significantly, and the orbits start to decay immediately. An encounter with the Moon could stabilize the orbits of some atmosphere-grazing particles, but these particles would then fall in the same class as the lunar ejecta.

If the average lifetime of all the particles orbiting the Earth is at most a few years because of the marginal stability of the initial orbits, one can easily calculate the influx of mass to the Earth for any assumed brightness of the scattered sunlight from these particles. (The entire mass in the dust cloud must be replaced every few years.) A surface brightness for the geocentric dust which is a major fraction of the zodiacal-light surface brightness would lead to an influx of mass from orbiting particles that would exceed the estimated direct influx of several hundred tons per day. This result is obviously absurd, for the probability per unit time that a particle in heliocentric orbit will strike the Earth directly must be much greater than that for an intermediate capture into a stable orbit about the Earth before impact. Finally, the spatial distribution predicted by the highly eccentric initial orbits is incompatible with a high spatial density, since the corresponding flux would have been detected by the recent low satellites.

SUMMARY

We have indicated several difficulties with the hypothesis of a large geocentric contribution

to the zodiacal light. Measurements of the surface brightness of the zodiacal light off the ecliptic plane are not compatible with a large geocentric contribution to the zodiacal light. If one argues that these observations are in error by a sufficient amount to permit a large geocentric contribution, the nearby dispersed component of geocentric dust would have to be virtually absent. The spatial distribution would have to be limited to an approximate toroid with inner radius greater than $12 R_E$ —a distribution incompatible with the perturbations of radiation pressure. The short lifetimes of the marginally stable orbits which are likely to result from known capture processes require an excessively large rate of supply for a large geocentric contribution to the zodiacal light. Besides the problem with the zodiacal-light brightness off the ecliptic plane, the presence of these particles coming into the Earth would also have shown up as an anomalously high flux density on the recent low satellites.

It is seen that rationalization of some difficulty associated with a major geocentric contribution to the zodiacal light (e.g., the brightness of the zodiacal light off the ecliptic plane) sometimes leads to another problem which is just as damaging to the geocentric dust hypothesis. Other problems resist even the first step of rationalization (e.g., the initially unstable orbits). It is therefore difficult to believe at the present time that a geocentric contribution to the zodiacal light is at all significant.

ADDITIONAL NOTE

F. Gillett (private communication, March 1967) has offered another argument against a geocentric contribution to the zodiacal light, which is an effective *coup de grace* for the hypothesis. At the time of a solar eclipse, the F corona is observed to increase in brightness at an ever-increasing rate as the line of sight approaches the limb of the Moon. This observation eliminates any substantial contribution to the F corona by dust particles within the orbit of the Moon. The segment of the line of sight within the lunar orbit is partially within the shadow cone of the Moon. The fraction of this

segment which is contained in the shadow increases as the line of sight approaches the limb of the Moon. Therefore, the brightness of the F corona, if due to particles within the lunar orbit, would tend to level out or even decrease as the line of sight approaches the Moon. A rationalization to save the geocentric hypothesis would require that the orbiting particles be largely confined to the region beyond the Moon in order to contribute to the F corona and zodiacal light.

But such a distribution is dynamically unstable, for radiation pressure would periodically reduce the geocentric distance of the perigees of such orbits. Not only would this effect populate the forbidden region with particles, but it would also allow close encounters with the Moon which would rapidly deplete the hypothetical cloud. Again an obvious rationalization of an argument against the geocentric hypothesis leads to other difficulties just as damaging.

REFERENCES

- ALEXANDER, W. M., 1962, *Science*, **138**, 1098.
 ALLAN, R. R., and G. E. COOK, 1967, *J. Geophys. Res.*, **72**, 1124.
 COLOMBO, G., D. A. LAUTMAN, and I. I. SHAPIRO, 1966a, *J. Geophys. Res.* **71**, 5705.
 COLOMBO, G., I. I. SHAPIRO, and D. A. LAUTMAN, 1966b, *J. Geophys. Res.*, **71**, 5719.
 DIVARI, N. B., 1965, *Soviet Astron.—AJ*, **9**, 493.
 DIVARI, N. B., and N. I. KOMARNITSKAYA, 1966, *Soviet Astron.—AJ*, **9**, 632.
 DUBIN, M., and C. W. MCCracken, 1962, *Astron. J.*, **67**, 248.
 FESENKOV, V. G., 1964, *Astron. Zh.*, **41**, 1001.
 —, 1965, *Soviet Astron.—AJ*, **8**, 803.
 GOLD, T., 1962, *J. Phys. Soc. Japan*, **17**, Suppl. A-1, 187.
 HEMENWAY, C. L., and R. K. SOBERMAN, 1962, *Astron. J.*, **67**, 256.
 HIBBS, A. R., 1961, *J. Geophys. Res.*, **66**, 371.
 HURUHATA, M., 1965, *Planetary Space Sci.*, **13**, 237.
 JONES, G., 1856, *United States Japan Expedition*, Vol. III (Commodore M. C. Perry), Washington, D.C.
 KOZAI, Y., 1959, *Astron. J.*, **64**, 367.
 LAUTMAN, D. A., I. I. SHAPIRO, and G. COLOMBO, 1966, *J. Geophys. Res.*, **71**, 5733.
 NILSSON, C., 1966, *Science*, **153**, 1242.
 PEALE, S. J., 1966, *J. Geophys. Res.*, **71**, 911.
 RING, J., J. F. JAMES, M. DAEHLER, and J. E. MACK, 1964, *Nature*, **202**, 167.
 SINGER, S. F., 1961, *Nature*, **192**, 321.
 SMITH, L. L., F. E. ROACH, and R. W. OWEN, 1965, *Planetary Space Sci.*, **13**, 207.
 VAN DE HULST, H. C., 1947, *Ap. J.*, **105**, 471.
 WEINBERG, J. L., 1963, *Nature*, **198**, 842.

49. The Meteoroid Environment Near the Ecliptic

JOHN K. WALL
Douglas Aircraft Company, Inc.
Huntington Beach, California

A new model of the distribution of solid particles near the ecliptic is developed. The particle distribution function f is expressed as the product of three functions in the form

$$f = f_s f_v f_m$$

where f_s is the distribution with respect to distance from the Sun, f_v is the distribution with respect to particle speed, and f_m is the distribution with respect to particle mass. The spatial distribution function is evaluated by combining Mariner IV micrometeoroid flux data with the observed spatial distribution of the asteroids, corrected for the variation in the size of the smallest observable asteroid with distance from the Sun. The velocity distribution function is evaluated from meteor data, corrected for the nonequilibrium radiation from the gas cap. The mass distribution function is evaluated by combining zodiacal-light data corrected for the spatial distribution of particles, microphone, and penetration meteoroid detector data; reinterpreted optical and radio meteor data; and the size distributions of meteorites, lunar craters, and the asteroids. It is found that the near-Earth particle flux is $10^{-13.8} m^{-0.9}$ particles/ m^2 sec when the particle mass m is in grams.

NUMEROUS INVESTIGATIONS have shown that the solar system contains a large number of solid bodies ranging in size from cosmic dust particles as small as 10^{-15} g to asteroids larger than 10^{15} g. It is generally believed that the concentration of these bodies is greatest near the ecliptic and that most of them are in direct orbits about the Sun.

If it is assumed that the mechanisms involved in the formation and breakup of these bodies are independent of their size and location, it is reasonable to assume that the number density distribution function f of solid bodies near the ecliptic plane can be expressed as the product of three distribution functions in the form

$$f = f_s f_v f_m \quad (1)$$

where f is the number of particles per unit

volume at a distance s between s and $s + ds$ from the Sun, having a speed v between v and $v + dv$, and with a mass m between m and $m + dm$. The particle number distribution functions (f_s , f_v , and f_m) are given with respect to distance from the Sun, speed, and mass. For convenience and without loss of generality, f_s and f_v will be chosen in such a way that

$$f_s = 1 \quad (2)$$

at $s = 1$ AU, and

$$\int_{-\infty}^{\infty} f_v dv = 1 \quad (3)$$

when v is the heliocentric speed or the speed relative to a massless Earth. A reasonable approximation to the spatial distribution function f_s can be deduced from the data gathered by the

Mariner IV zodiacal-dust experiment and from the spatial distribution of the asteroids. The distribution function for particle speed v can be deduced from optical meteor data.

All past studies of the mass distribution of solid particles in the solar system have indicated that the mass distribution function f_m can be expressed in the form

$$f_m = Bm^{-\beta} \quad (4)$$

where B and β are constants, at least over the range of mass covered by each individual experiment, and $\beta > 1$. If the average particle density ρ_p and f_s and f_c are known, values of B and β can be deduced by combining the data from the zodiacal-light observations, the various microphone and penetration detector experiments, the meteor rate and magnitude-distribution observations, the meteorite-mass distribution, the size distribution of the lunar craters, and the apparent distribution of the asteroids. The average particle density can be determined from meteor data.

SYMBOLS

A	cross-section area of particle
B	mass-distribution constant
C	weak-wave speed
D	diameter of impact crater
F	flux or number of events/unit area-unit time
f	number density distribution function
G	normalizing constant
g	observed distribution function
H	atmospheric scale height
h	altitude
I	light intensity
K	constant characteristic of experiment
M	meteor magnitude
m	particle mass
N	number of events
p	pressure or pulse height
Q	number of events per unit area
r	particle radius
S	shock constant
s	distance from the Sun
T	plate thickness
t	time
U	shock speed

v	particle speed
w	interface speed
x	dummy integration variable
y	distance from point of impact to crystal of microphone detector
α	elongation angle
β	mass distribution exponent
γ	optical meteor velocity exponent
δ	heliocentric latitude
ϵ	optical meteor density exponent
ζ	fraction of original meteorite mass surviving passage through the atmosphere
η	strength of lunar surface rock
θ	entry angle
λ	wavelength
ϕ	scattering angle
ξ	interface speed fraction
ρ	density
σ	standard deviation
$\langle \rangle$	average value

Subscripts:

A	asteroids
a	air
C	lunar craters
D	lunar dust
e	with respect to a massless Earth
g	Earth escape
h	with respect to the Sun
M	meteorites
m	mass
max	point of maximum meteor light
O	optical meteors
P	penetration detectors
p	particle
Q	microphone detectors
R	radio meteors
r	reference or calibration particle or condition
s	spatial distribution
t	threshold
v	velocity
Z	zodiacal light
∞	condition just outside the Earth's atmosphere

SPATIAL DISTRIBUTION FUNCTION

The results of the Mariner IV interplanetary dust experiment (Alexander et al., 1965; and

Sloan, 1966) indicate that the flux of 10^{-14} g particles increases rapidly with distance from the Sun. By assuming that the particle impact speed varies as $s^{-1/2}$, these Mariner data can be easily converted to the relative particle number density, as shown in figure 1.

If we assume f_s is independent of m , the variation of f_s with s for $s > 1.5$ AU can be estimated from the observed number density distribution of the asteroids g_s . If it is assumed that all asteroids larger than some threshold mass m_t are seen, independent of their distance from the Sun, then

$$f_s \sim g_s \quad (5)$$

This is certainly a lower limit on f_s because the size threshold of visible asteroids must increase with distance from the Sun. Assuming that the average surface area of observed asteroids is proportional to $m^{2/3}$, that the optical properties and density of all asteroids are approximately the same, and that all asteroids just large enough to be seen are detected when at conjunction, then when $(s-1)^2$ is much larger than the surface area, the threshold mass m_t which can just be detected must vary with distance from the Sun as

$$m_t \sim s^3(s-1)^3 \quad (6)$$

where s is in AU.

Correspondingly, integrating the distribution function over all detectable asteroids yields

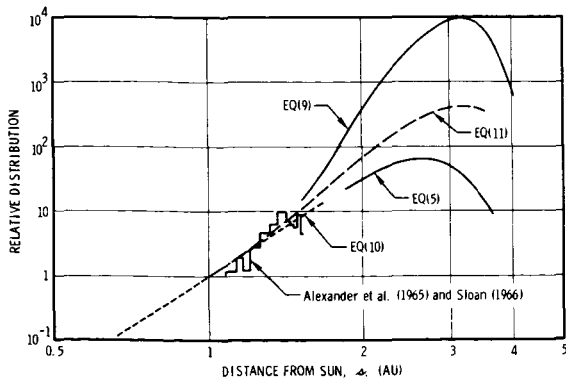


FIGURE 1.—Spatial distribution of cosmic dust and asteroids.

$$g_s = G_s f_s \int_{m_t}^{\infty} \int_{-\infty}^{\infty} f_m f_v dv dm \quad (7)$$

where G_s is a scaling constant. Combining equations (3), (4), and (7)

$$f_s = \frac{\beta-1}{BG_s} m_t^{\beta-1} g_s \quad (8)$$

and thus with equation (6),

$$f_s \sim [s(s-1)]^{3(\beta-1)} g_s \quad (9)$$

Using Narin's (1966) distribution of 1563 numbered asteroids averaged for the period 1954 to 1974, converted to the relative number of asteroids per unit volume for g_s , the upper and lower bounds on f_s determined by equations (5) and (9) are shown in figure 1. A value of $\beta = 1.9$ was assumed. This value of β is discussed in a subsequent section.

Using the Mariner IV data for $s < 1.5$ AU, f_s must vary approximately as

$$f_s = s^5 \quad (10)$$

For $s < 1.5$ AU, the asteroid distribution data suggests that f_s reaches a maximum value near $s = 3$ AU. Assuming that f_s lies approximately midway between the two bounds discussed above, then a reasonable approximation for f_s which is consistent with equations (2) and (10) is

$$f_s = s^{-2} 10^{3.65} e^{-(1.46)(s-3.4)^2} \quad (11)$$

DISTRIBUTION IN SPEED

The distribution of particles by speed f_v can be obtained from the observed speed distribution g_v of meteors. The observed distribution is related to f_v by

$$g_v = G_v f_v \int_{m_t}^{\infty} f_m dm \quad (12)$$

where m_t is the mass of the smallest detectable meteor, or the threshold mass, and G_v is a normalizing constant. Since the form of f_m is given by equation (4), equation (12) can be integrated and solved for f_v as a function of B , β , G_v , and the observed distribution, g_v . As in the previous sec-

tion, it is assumed at this point, and discussed in a later section, that $\beta = 1.9$. By choosing G_r in such a way that equation (3) is satisfied, B and G_r can be eliminated. Thus, if the variation of m_t with observed quantities such as meteor speed can be determined, then f_r can be calculated from the observed variation of g_r .

To determine m_t , it is assumed that the light intensity I_0 emitted by an optical meteor can be expressed in the form

$$I_0 = K_0 \rho_a^\epsilon v^\gamma A \quad (13)$$

where K_0 , ϵ , and γ are constants, ρ_a is the density of air, A is the frontal area of the particle, and v is the speed of the meteor relative to the Earth.

Assuming that the angle between the meteor's flight path and the local vertical θ is constant, the air density varies exponentially with altitude h in the form

$$\rho_a = \rho_{ar} e^{-h/H} \quad (14)$$

where ρ_{ar} and H are constants chosen to give the best fit to the true density variation over the altitude band of interest. Assuming the meteor's ballistic coefficient, $m/C_D A$, is approximately constant, where C_D is the drag coefficient of the particle referenced to area A , the equation of motion of the meteor particle can be integrated to yield

$$v = v_\infty e^{-\frac{C_D A H \rho_{ar}}{2m \cos \theta}} \quad (15)$$

where v_∞ is the speed of the meteor relative to the Earth just outside the atmosphere.

Although it is unusual to assume that $m/C_D A$ is approximately constant, it does not introduce a significant error because it is used only up to the point of maximum light, which occurs well before significant heating of the particle. Observational data on meteor acceleration are quite limited, but the data on Meteors 1242 and 19816 given by Cook, Jacchia, and McCrosky (1963) strongly support this approximation.

At the point of maximum light

$$\frac{dI_0}{dh} = 0 \quad (16)$$

By combining equations (13) to (16), it can be

shown that the air density at the point of maximum light intensity $\rho_{a, \max}$ and the particle speed at the same point v_{\max} are given by

$$\rho_{a, \max} = \frac{2m\epsilon \cos \theta}{\gamma C_D A H} \quad (17)$$

$$v_{\max} = v_\infty e^{-\epsilon/\gamma} \quad (18)$$

The maximum light intensity, I_{\max} , is obtained by combining equations (13), (17), and (18).

$$I_{\max} = K_0 A v_\infty^\gamma \left(\frac{2m\epsilon \cos \theta}{\gamma C_D A H} \right)^\epsilon \quad (19)$$

It is assumed that, on the average, meteoroids have the shape of a sphere. Consistent with this, it is assumed that

$$m = \frac{3}{4} \rho_p A^{3/2} \quad (20)$$

where ρ_p is the density of the particle.

By combining equations (19) and (20), the threshold particle mass m_t corresponding to the threshold light intensity which is just detectable I_t is

$$m_t = \left[\left(\frac{I_t}{K_0} \right) \left(\frac{\gamma C_D H}{2\epsilon \cos \theta} \right)^\epsilon \left(\frac{3}{4} \rho_p \right)^{\frac{2}{3}(1-\epsilon)} \right]^{\frac{3}{2+\epsilon}} v_\infty^{-\frac{3\gamma}{2+\epsilon}} \quad (21)$$

By combining equations (4) and (21) with equation (12), and by assuming average values for C_D , H , and $\cos \theta$, equation (12) can be integrated to yield the number distribution of particles with respect to v_∞ .

$$g_{r_\infty} = \frac{G_{r_\infty} B}{\beta - 1} \left[\left(\frac{\gamma C_D H}{2\epsilon \cos \theta} \right)^\epsilon \left(\frac{I_t}{K_0} \right) \left(\frac{3}{4} \rho_p \right)^{\frac{2}{3}(1-\epsilon)} \right]^{\frac{3(1-\beta)}{2+\epsilon}} v_\infty^{\frac{3\gamma(\beta-1)}{2+\epsilon}} f_{r_\infty} \quad (22)$$

If β , ϵ , and γ are known, and if G_{r_∞} is chosen appropriately, the velocity distribution function f_{r_∞} satisfying equation (3) can be determined from the measured velocity distribution of randomly selected meteors.

Page and Arnold (1964) have measured the light intensity from meteor-sized particles moving at speeds up to 12 km/sec in air at densities approximately equivalent to a 70-km altitude.

It was found that the air in the gas cap has high translational temperatures, but that this air is not in equilibrium as it does not have time to distribute its energy to the vibration, dissociation, and ionization modes before sweeping past the body into the wake. As a consequence, most of the light observed from particles at meteor speeds and altitudes is continuum radiation from the gas cap and not line emission as is assumed in the classic theory of meteors. The data from Page and Arnold suggest that

$$\gamma \approx 4 \quad (23)$$

$$\epsilon \approx 1/3 \quad (24)$$

It should be noted that ϵ is dependent on the ratio of the mean-free-path length to the characteristic dimension of the meteor. Thus, for very large particles, ϵ may approach 1, and for very small particles it may be nearly zero (Arnold, Reis, and Woodward, 1965). The value of ϵ given by equation (24) is a reasonable average value, but the effect of variations in ϵ should be examined carefully when additional experimental data become available.

To obtain the distribution function with respect to v_x , the meteor data given by McCrosky and Posen (1961) have been used to determine g_{v_x} , and equation (22) has been solved for f_{v_x} . The resulting empirical variation of f_{v_x} is shown in figure 2.

A good approximation to the particle distribution by speed with respect to a massless Earth at $s = 1$ AU, f_{v_e} , is given by

$$f_{v_e} = (0.117)e^{-\frac{1}{2}\left(\frac{v_e - 11}{3.4}\right)^2} \quad (25)$$

where v_e , the speed relative to a massless Earth, is in km/sec. Corresponding to equation (25), if v_g is the Earth-escape speed and the Earth's shielding effect is neglected, f_{v_∞} is

$$f_{v_\infty} = 0.117[1 - (v_g/v_\infty)^2]^{-3/2}e^{-\frac{1}{2}\left[\frac{(v_\infty^2 - v_g^2)^{1/2} - 11}{3.4}\right]^2} \quad (26)$$

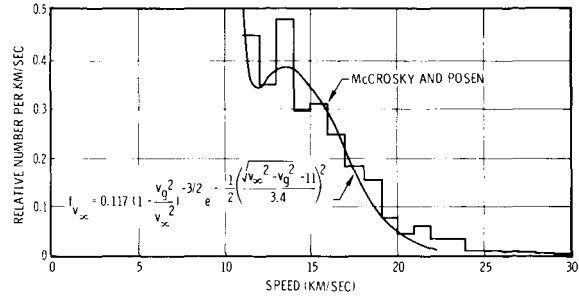


FIGURE 2.—Distribution of the speed of meteor particles just outside the Earth's atmosphere.

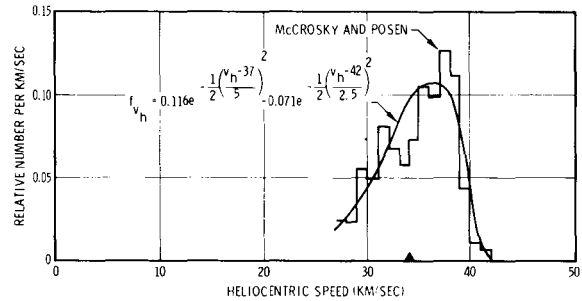


FIGURE 3.—Distribution of the heliocentric speed of meteors.

and $f_{v_\infty} \equiv 0$ when $v_\infty < v_g$. Equation (26) is compared with the observational data in figure 2.

It should be noted that equation (3) is not satisfied by f_{v_x} because of the concentration of low-speed particles at low altitudes near the Earth. This effect is reflected by the term $[1 - (v_g/v_\infty)^2]^{-3/2}$ in equation (26). Obviously, this term is singular when $v_\infty = v_g$. Because other forces in addition to the Earth's gravity affect particle motion, this singularity is artificial. To avoid the difficulties associated with this singularity, it has been assumed that $f_{v_\infty} = 0$ when the difference between v_∞ and v_g is so small that forces other than the Earth's gravity dominate the particle motion.

The particle distribution with respect to heliocentric speed v_h can also be estimated from the McCrosky and Posen data (1961). For $s = 1$ AU, the resulting function f_{v_h} is shown in figure 3. A reasonable fit to these data is given by

$$f_{v_h} = 0.116e^{-\frac{1}{2}\left(\frac{v_h - 37}{5}\right)^2} - 0.071e^{-\frac{1}{2}\left(\frac{v_h - 42}{2.5}\right)^2} \quad (27)$$

The available data do not indicate how v_h and f_{v_h} vary with distance from the Sun. However,

it is reasonable to expect all speeds to vary approximately as $s^{-1/2}$. With this assumption, equation (27) can be generalized as

$$f_{v_h} = 0.116s^{1/2}e^{-\frac{s}{2}\left(\frac{v_h - \langle v_{h,1} \rangle}{5}\right)^2} - 0.071s^{1/2}e^{-\frac{s}{2}\left(\frac{v_h - \langle v_{h,2} \rangle}{2.5}\right)^2} \quad (28)$$

where:

$$\langle v_{h,1} \rangle = 37s^{-1/2} \quad (29)$$

$$\langle v_{h,2} \rangle = 42s^{-1/2} \quad (30)$$

PARTICLE DENSITY

To determine the average density of meteoric particles, it is assumed that the average particle is spherical in shape. Thus, as assumed in equation (20)

$$\rho_p \approx \frac{4}{3} m A^{-3/2} \quad (31)$$

By definition, the peak magnitude, M , of a meteor is given by

$$M = M_r - 2.5 \log I/I_r \quad (32)$$

where M_r and I_r are the peak magnitude and intensity of a reference meteor.

Combining equations (13), (18), and (32) yields

$$\frac{1}{A} = \left(\frac{v_x}{v_{x,r}}\right)^\gamma \left(\frac{\rho_{a,\max}}{\rho_{a,\max,r}}\right)^\epsilon 10^{0.4(M-M_r)} \frac{1}{A_r} \quad (33)$$

where the subscript r denotes the reference meteor.

Neglecting variations in C_D , equation (17) can be rewritten in the form

$$\frac{m}{A} = \left(\frac{H}{H_r}\right) \left(\frac{\cos \theta_r}{\cos \theta}\right) \left(\frac{\rho_{a,\max}}{\rho_{a,\max,r}}\right) \left(\frac{m_r}{A_r}\right) \quad (34)$$

where equation (34) has been nondimensionalized for convenience.

Combining equations (31), (33), and (34) gives

$$\rho_p = \frac{4}{3} \left(\frac{H}{H_r}\right) \left(\frac{\cos \theta_r}{\cos \theta}\right) \left(\frac{\rho_{a,\max}}{\rho_{a,\max,r}}\right)^{1+\epsilon/2} \left(\frac{v_x}{v_{x,r}}\right)^{\gamma/2} 10^{0.2(M-M_r)} \frac{m_r}{A_r^{3/2}} \quad (35)$$

Using the Trailblazer I_g experiment (Jewell and Wineman, 1964) as the reference meteor, the average particle density has been calculated from the Hawkins and Southworth data (1958). The resulting average particle density is 1.6 g/cm³.

ZODIACAL LIGHT

It has been shown by van de Hulst (1947) that the light observed in the outer solar corona is largely the result of diffraction from small solid particles surrounding the Sun. Following his approach, the intensity of the light falling on a particle at distance s in AU from the Sun and at elongation α from the Earth is $(I_h s^{-2})$, where I_h is the intensity of the solar radiation at $s = 1$ AU. Assuming the particle is a sphere of radius r , the distribution of light of wavelength λ scattered by the particle is $J_1^2(2\pi r \sin \phi / \lambda) / \pi \sin^2 \phi$, where ϕ is the scattering angle illustrated in figure 4. Each of these particles will scatter $\pi r^2 I_h s^{-2}$ of light. The number of particles of mass m at solar radius s per unit length of a column of unit cross section aligned with the elongation is, by equation (1), $f_n f_s$. Thus, for small elongations the brightness of the zodiacal light observed from the Earth I_z is

$$I_z = \int_0^{1 \text{ AU}} \int_0^\infty \pi r^2 (I_h s^{-2}) [J_1^2(2\pi r \sin \phi / \lambda) / \pi \phi^2] (f_n f_s) dm ds \quad (36)$$

With equation (4) and the assumption that all particles are spheres, and noting that for small angles

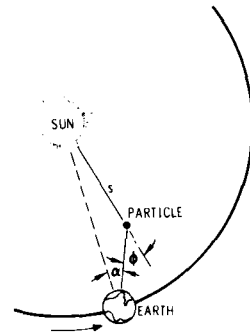


FIGURE 4. — Sun, particle, and Earth geometry for scattering of zodiacal light.

$$s\phi \simeq \alpha \quad (37)$$

equation (36) can be rewritten as

$$I_z = I_h B (4\pi\rho_p)^{1-\beta} 3\beta \alpha^{-2} \int_0^{1 \text{ AU}} f_s \left[\int_0^\infty r^{4-3\beta} J_1^2(2\pi r \alpha / \lambda s) dr \right] ds \quad (38)$$

Equation (38) can then be rewritten again as

$$I_z = I_h B (4\pi\rho_p)^{1-\beta} 3\beta \left(\frac{\lambda}{2\pi} \right)^{5-3\beta} \alpha^{-7+3\beta} \left[\int_0^\infty x^{4-3\beta} J_1^2(x) dx \right] \left[\int_0^{1 \text{ AU}} s^{5-3\beta} f_s ds \right] \quad (39)$$

The zodiacal-light data (Divari, 1965) shows that I_z varies approximately as $\alpha^{-2.4}$ for $1^\circ < \alpha < 10^\circ$. By equation (39), I_z varies as $\alpha^{-7+3\beta}$. Thus, from zodiacal-light data

$$\beta = 1.53 \quad (40)$$

It is interesting to note that β is independent of the form of the spatial distribution function.

Now, B can be determined by setting I_z determined by equation (39) equal to the observed values of I_z . This has been done assuming (van de Hulst, 1947) that $I_h = 51$, $I_z = 1.2(10)^{-7} \alpha^{-2.4}$, $\rho_p = 1.6 \text{ g/cm}^3$, $\beta = 1.53$, $\lambda = 4400 \text{ \AA}$, and f_s given by equation (11). The resulting value of B is

$$B = 10^{-14.1} \text{ particles-g}^\beta/\text{m}^3 \quad (41)$$

The value of the first integral in equation (39) does not change significantly when $x > 5$. Thus, the mass distribution function determined from the zodiacal-light data is valid for $10^{-10} < m < 10^{-8} \text{ g}$.

MICROPHONE DATA

Data on the near-Earth sporadic meteoroid flux have been obtained by acoustic detectors carried on rockets and spacecraft. A crystal microphone mounted against the rocket skin or a sounding board on the spacecraft measures the maximum pressure or pulse height p of the impact induced shock or sound wave. If p is above the detector threshold, an impact is recorded.

The peak pressure at the point of impact is $K_q \rho_q U_q v$, where K_q is a constant depending on the particle and detector material, ρ_q and U_q are the density and wave speed of the sounding board, and v is the particle impact speed. Since the wave transmitting the pressure pulse expands approximately spherically, the peak pressure at the crystal is approximately

$$p \simeq (K_q \rho_q U_q v) (r/y)^2 \quad (42)$$

where r is the radius or characteristic dimension of the particle and y is the distance between the impact point and the crystal. Assuming, again, that all particles are spherical, equation (42) can be rewritten as

$$p = \left(\frac{3K_q}{4\pi} \right) \left(\frac{\rho_q}{\rho_p} \right) \left(\frac{U_q}{y^2} \right) \left(\frac{1}{r} \right) m v \quad (43)$$

It is usually assumed that U_q is a constant and that for a large sample y^2 can be replaced by its average value. Thus, the pulse height at the detector is proportional to the particle impact momentum. However, in analysis of microphone data, the effect of the absolute size of the particle is usually overlooked. This effect has also been observed experimentally by Wlochowicz (1966).

Apparently, the threshold momentum of most microphone detectors used to date has been determined by dropping spheres weighing about a milligram from heights of a few centimeters onto the detector sounding boards. The momentum threshold measured by this means must, according to equation (43), be corrected for particle size. Thus, denoting the calibration particle by subscript r and the threshold meteoroid by subscript t , the true sensitivity threshold of these detectors, $m_t v_t$, is

$$m_t v_t = \left(\frac{r_t}{r_r} \right) (m_r v_r) \quad (44)$$

For spherical particles, equation (44) can be rewritten as

$$m_t = m_r (\rho_{pr}/\rho_p)^{1/2} (v_r/v_t)^{3/2} \quad (45)$$

The flux of particles counted by the microphone detectors F_Q is

$$F_Q = \int_{10.8}^{\infty} v_{\infty} f_{v_{\infty}} \left(\int_{m_t}^{\infty} f_m dm \right) dv_{\infty} \quad (46)$$

In equation (46) it has been assumed that the particle impact speed relative to the detector is v_{∞} , and that the maximum particle mass which will trigger the detector is much greater than m_t . With equations (4) and (45), equation (46) can be partially integrated to give

$$F_Q = \left(\frac{B}{\beta-1} \right) \left(\frac{\rho_p}{\rho_{pr}} \right)^{\frac{\beta-1}{2}} m_t^{1-\beta} v_r^{\frac{3(1-\beta)}{2}} \int_{10.8}^{\infty} v_{\infty}^{\frac{3\beta-1}{2}} f_{v_{\infty}} dv_{\infty} \quad (47)$$

Assuming that $\beta=1.9$, that the calibration particles weighed approximately a milligram and were made of glass, and that $f_{v_{\infty}}$ is given by equation (26), equation (47) has been solved for the various values of F_Q obtained from the rocket (McCracken and Alexander, 1963) and spacecraft (McCracken and Alexander, 1963; and Soberman and Lucca, 1963) microphone detector experiments to obtain B .

The results of this calculation are shown in table 1. The variation in B from these experiments is probably a reflection of the assumption that all detectors were calibrated with particles of the same size, rather than a true variation. These values of B may also be somewhat high due to errors in the evaluation of $f_{v_{\infty}}$ at $v_{\infty} \approx v_g$.

The flux of cosmic dust particles away from the influence of the Earth was measured by Mariner IV (Alexander et al., 1965). In this experiment the threshold sensitivity of the detectors was not obtained by dropping of spheres at low speeds, but rather by impact of smaller particles at speeds of approximately 3 km/sec. The value of B calculated in the same manner as above for $s \approx 1$ AU, but for the smaller calibration particles and for an impact speed distribution of the form of equation (25) with an average value of 3 km/sec, is also shown in table 1.

PENETRATION DETECTOR DATA

Pressurized cell penetration detectors were carried on the Explorer XVI (D'Aiutolo, 1964) and XXIII (O'Neal, 1965) spacecraft, and capacitor penetration detectors were carried on Pegasus I and II (Naumann, 1965). These detectors measured the flux of particles that had

TABLE 1.—Microphone Data

Spacecraft/rocket	Measured detector sensitivity, dyne-sec	Flux, particles/m ² -sec-2 π ster	B , particles-g ³ /m ³
Aerobee No. 80 ^a	10 ^{-3.22}	10 ^{0.99}	10 ^{-14.42}
	10 ^{-2.52}	10 ^{0.30}	10 ^{-14.80}
Aerobee No. 88 ^a	10 ^{-3.33}	10 ^{-0.24}	10 ^{-15.81}
Nike-Cajun AF-2 ^a	10 ^{-3.22}	10 ^{0.18}	10 ^{-15.24}
Nike-Cajun AA6.203 ^a	10 ^{-2.92}	10 ^{-0.32}	10 ^{-15.35}
	10 ^{-3.52}	10 ^{0.18}	10 ^{-15.65}
Nike-Cajun AA6.204 ^a	10 ^{-3.15}	10 ^{-0.01}	10 ^{-15.34}
Nike-Cajun AA6.206 ^a	10 ^{-3.82}	10 ^{-0.30}	10 ^{-16.52}
Spacerobee 10.01 ^a	10 ^{-3.31}	10 ^{0.40}	10 ^{-15.13}
Vanguard III ^a	10 ^{-2.0}	10 ^{-2.70}	10 ^{-16.51}
Explorer I ^a	10 ^{-2.6}	10 ^{-1.77}	10 ^{-16.37}
	10 ^{-2.6}	10 ^{-1.52}	10 ^{-16.12}
Explorer VIII ^a	10 ^{-1.6}	10 ^{-3.22}	10 ^{-16.50}
	10 ^{-0.6}	10 ⁻⁵	10 ^{-16.96}
Midas II ^b	10 ^{-3.52}	10 ^{-0.28}	10 ^{-16.10}
Mariner IV (1.0-1.2 AU) ^c	10 ^{-4.22}	10 ^{-4.13}	10 ^{-16.58}

^a Taken from McCracken and Alexander (1963).

^b Taken from Soberman and Lucca (1963).

^c Taken from Alexander et al. (1965).

sufficient energy or momentum to penetrate the detector panels.

The available experimental data on penetration threshold (Frost and Norem, 1966) for aluminum spheres impacting thin aluminum plates indicate that the thickness of material that will just be penetrated T varies linearly with impact speed v and particle radius r . This is illustrated by figure 5. Other studies (Hermann and Jones, 1961) have suggested that penetration varies with the square root of the projectile density; that is

$$T \approx K_p \rho_p^{1/2} v r \quad (48)$$

where K_p is a constant depending on the target material. From the data shown in figure 5, $K_p = 0.63$ for penetration of aluminum when ρ_p is in g/cm³ and v is in km/sec. Experimental studies (O'Neal, 1965) have shown that beryllium-copper and stainless steel are approximately equivalent in resistance to penetration and that both are about twice as resistant as aluminum. For these materials, it has been assumed that $K_p = 0.32$.

Assuming that the average projectile is a sphere, from equation (48) the threshold mass of the Explorer and Pegasus penetration detectors is

$$m_t = 4\pi T^3 / 3K_p^3 \rho_p^{1/2} v^3 \quad (49)$$

where T is in centimeters.

As in equation (46), the flux of particles counted by penetration detectors, F_p , is

$$F_p = \frac{B}{\beta - 1} \left(\frac{3K_p^3 \rho_p^{1/2}}{4\pi T^3} \right)^{\beta - 1} \int_{10.8}^{\infty} v_{\infty}^{3\beta - 2} f_{v_{\infty}} dv_{\infty} \quad (50)$$

Assuming that $\beta = 1.9$ and $\rho_p = 1.6$ g/cm³, B has been computed from the measured values of F_p . The results of this calculation are shown in table 2.

OPTICAL METEORS

The flux of optical meteors F_o is

$$F_o = \frac{B}{\beta - 1} \int_{10.8}^{\infty} v_{\infty} f_{v_{\infty}} m_t^{1 - \beta} dv_{\infty} \quad (51)$$

where m_t is the smallest meteor of speed v_{∞} that can be seen. From equations (19) and (32),

$$m_t = \left(\frac{H \cos \theta_r}{H_r \cos \theta} \right) \left(\frac{A}{A_r} \right)^{\frac{\epsilon - 1}{\epsilon}} \left(\frac{v_{\infty r}}{v_{\infty}} \right)^{\gamma/\epsilon} 10^{-0.4(M - M_r)/\epsilon} m_r \quad (52)$$

Again assuming that the average particle has a spherical shape, with equation (20) m_t becomes

$$m_t = \left[\left(\frac{4}{3\rho_p} \right)^{2(\epsilon - 1)/3} \left(\frac{H \cos \theta_r}{H_r \cos \theta} \right)^{\epsilon} \left(\frac{v_{\infty r}}{v_{\infty}} \right)^{\gamma} 10^{-0.4(M - M_r)/\epsilon} A_r^{1 - \epsilon} m_r^{\epsilon} \right]^{\frac{3}{2 + \epsilon}} \quad (53)$$

Hawkins (1959) found that the flux of meteors of visual magnitude less than -5 was $10^{-17.0}/\text{m}^2 \cdot \text{sec} \cdot 2\pi$ ster, and Hawkins and Upton (1958) found that the flux of photographic meteors of photographic magnitude less than zero to be $10^{-13.9}/\text{m}^2 \cdot \text{sec} \cdot 2\pi$ ster. Using the Trailblazer *Ig* (Jewell and Wineman, 1964) as the reference meteor, and assuming $\beta = 1.9$, average values for θ , H , and ρ_p , and a color index (Davis, 1963) of -1.8 , equations (24), (51), and (53) have been combined to determine B from the optical meteor flux data. Both flux measurements yield

$$B = 10^{-18.2} \text{ particles} \cdot \text{g}^{\beta} / \text{m}^3 \quad (54)$$

The distribution of meteors by visual magnitude, determined by naked-eye observations, has been reported by Hawkins (1959) (71 431 observations supplied by C. P. Olivier and approximately 1000 observations by the British Astronomical Association) and by Millman (1957) (10 287 meteors). Similar data have also

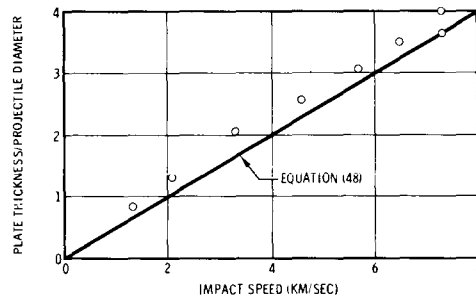


FIGURE 5.—Penetration threshold of aluminum projectiles fired into 2024 aluminum targets.

TABLE 2.—*Penetration Detector Data*

Spacecraft	Detector		Penetration rate, penetrations/m ² . sec-2 π ster	<i>B</i> , particles- g ³ /m ³
	Material	Thickness, cm		
Explorer XVI ^a	Be-Cu.....	0.0025	10 ^{-5.24}	10 ^{-18.0}
	Be-Cu.....	0.0051	10 ^{-5.46}	10 ^{-17.2}
Explorer XXIII ^b	Stainless steel.....	0.0025	10 ^{-5.21}	10 ^{-17.9}
	Stainless steel.....	0.0051	10 ^{-5.54}	10 ^{-17.3}
Pegasus I ^c	Al.....	0.0040	10 ^{-5.30}	10 ^{-18.1}
	Al.....	0.0200	10 ^{-6.22}	10 ^{-17.2}
Pegasus II ^c	Al.....	0.0040	10 ^{-5.32}	10 ^{-18.1}
	Al.....	0.0200	10 ^{-6.49}	10 ^{-17.6}
	Al.....	0.0400	10 ^{-7.24}	10 ^{-17.4}
	Al.....	0.0400	10 ^{-7.24}	10 ^{-17.4}

^a Taken from D'Aiutolo (1964).^b Taken from O'Neal (1965).^c Taken from Naumann (1965).

been obtained from 1842 telescopic visual observation (1961). Hawkins and Upton (1958) reported the distribution of the photographic magnitude of a random sample of 241 meteors.

The number of meteors brighter than a threshold magnitude, M_t , or correspondingly, larger than a threshold mass, m_t , is

$$N_0 = G_0 \int_{10.8}^{\infty} f_{v_{\infty}} \int_{m_t}^{\infty} f_m dm dv_{\infty} \quad (55)$$

where N_0 is the number of meteors brighter than M_t , G_0 is a normalizing constant, $f_{v_{\infty}}$ and f_m are given by equations (26) and (4), respectively, and m_t is given by equation (53) when $M = M_t$. By integration of equation (55)

$$N_0 \sim 10^{1.2M_t(\beta-1)/(2+\epsilon)} \quad (56)$$

The exponent β has been computed directly from the optical meteor data by comparing the observed variation of N_0 with M_t to that indicated by equation (56). The resulting values of β and their corresponding range of validity are shown in table 3.

RADIO METEORS

The flux of radio meteors with magnitudes less than 10.8 and the variation of the number distribution with magnitude have been reported by Kaiser (1961). If the variation of radio-meteor magnitude with air density, particle speed, and particle size is the same as for optical meteors,

then values of B and β can be determined from these data in the same manner as from the optical meteor data. For $\epsilon = 1/3$, this yields

$$B = 10^{-18.9} \text{ particles/m}^3 \quad (57)$$

for $M < 10.8$; and as shown in table 3, $\beta = 1.91$ for $8.3 < M < 10.8$.

METEORITES

The number distribution of meteorites N_M is

$$N_M = G_M \int_{10.8}^{\infty} f_{v_{\infty}} \int_{m_M/\zeta}^{\infty} f_m dm dv_{\infty} \quad (58)$$

where G_M is a normalizing constant, m_M is the mass in grams of the smallest meteorite considered in N_M , and ζ is the fraction of the original

TABLE 3.—*Meteor Data*

Data	Visual magnitude	β
Naked-eye visual ^a	$-10 < M < 2$	1.74
Naked-eye visual ^b	$-8 < M < -2$	2.10
Telescopic visual ^c	$-4 < M < 2$	1.72
Photographic ^d	$-0.7 < M < 2.8$	2.05
Radio ^e	$8.3 < M < 10.8$	1.91

^a Taken from Hawkins (1959).^b Taken from Millman (1957).^c Taken from McKinley (1961).^d Taken from Hawkins and Upton (1958).^e Taken from Kaiser (1961).

particle mass which survived passage through the atmosphere. Assuming that ζ is independent of the entry speed, with equation (4), equation (58) becomes

$$N_M = \frac{G_M B}{\beta - 1} \left(\frac{m_M}{\zeta} \right)^{1-\beta} \int_{10.8}^{\infty} f_{v_{\infty}} dv_1 \quad (59)$$

Brown (1960) found that for stony meteorites N_M varies as $m_M^{-0.77}$, and Hawkins (1960) found N_M varying as $m_M^{-1.0 \pm 0.3}$. By comparison with equation (59), values of $\beta = 1.77$ and 2.0 ± 0.3 are obtained from these data.

Similarly, the flux of meteorite particles, F_M , is

$$F_M = \frac{B}{\beta - 1} \left(\frac{m_M}{\zeta} \right)^{1-\beta} \langle v_{\infty} \rangle \quad (60)$$

Brown (1960) estimates that there are about 10^{-12} meteorite falls/m²-year. If it is assumed that the smallest meteorite included in this sample is 10^4 g, and from the Allen, Baldwin, and James (1965) analysis, that $\zeta = 10^{-2}$, then from equation (60)

$$B = 10^{-18.4} \text{ particles-g}^{\beta}/\text{m}^3 \quad (61)$$

Hawkins (1960) estimated a flux of $2.3(10)^{-16}$ meteorites larger than 10^4 g/m²-hour. This corresponds to

$$B = 10^{-18.1} \text{ particles-g}^{\beta}/\text{m}^3 \quad (62)$$

LUNAR CRATERS

The Ranger photographs have left little doubt that most of the lunar craters are the result of hypervelocity impacts. The cumulative number distribution of these craters, N_C , can be used to determine β .

The combination of particle speed and size required to form an impact crater of diameter D in rock can be estimated as follows. The initial pressure at the interface between the particle and the lunar surface just after impact is $\rho_C U_C w$, where ρ_C is the density of the lunar surface material, U_C is the speed of the impact-induced shock wave, and w is the speed of the interface material in the Moon-fixed coordinate system. This pressure is transmitted outward from the point of impact by an approximately hemispheri-

cal shock wave. Because the lunar surface is a free surface, the material behind the shock is thrown outward, thus forming the crater, until the shock is sufficiently weakened by its geometrical expansion that the peak stress behind it is less than the strength of the lunar surface material, η_C ; that is

$$\eta_C \approx (\rho_C U_C w) (2r/D)^2 \quad (63)$$

The shock speed can be approximated by

$$U_C = C_C + S w \quad (64)$$

where C_C and S are constants depending on the surface material. The initial interface speed w is

$$w = \xi v \quad (65)$$

where ξ is a constant depending on the particle and surface material, and v is the impact speed.

If it is assumed that the impacting particle and the surface material are of similar material,

$$\xi \approx 0.5 \quad (66)$$

By combining equations (63) to (66), D becomes

$$D = (2\rho_C C_C / \eta_C)^{1/2} [1 + (S/2C_C)v]^{1/2} v^{1/2} r \quad (67)$$

From the data of Maurer and Rinehart (1960), assuming that the lunar surface rock is similar to granite

$$(2\rho_C C_C / \eta_C) \approx 100 \text{ sec/km} \quad (68)$$

A typical value for $(2C_C/S)$ is

$$2C_C/S \approx 3 \text{ km/sec} \quad (69)$$

With equations (68) and (69) and the assumption that the average particle shape is spherical, the relationship between particle mass and speed and the crater diameter becomes

$$D = 10 v^{1/2} \left(1 + \frac{v}{3} \right)^{1/2} (3m/4\pi\rho_m)^{1/3} \quad (70)$$

where v is in km/sec, m is in grams, and D is in cm. Obviously, at high impact speeds, D varies linearly with v .

If the gravitational effect of the Earth and Moon are neglected, and it is assumed that the flux of particles is isotropic, the cumulative number distribution of the lunar craters Q_C is

$$Q_C = t \int_{-\infty}^{\infty} v_e f_{v_e} \int_{m(D, v_e)}^{\infty} f_m dm dv_e \quad (71)$$

where t is the time the lunar surface has been exposed to particle impacts. Combining equations (4), (70), and (71) and integrating yields

$$Q_C = \left(\frac{Bt}{\beta-1} \right) \left(\frac{4}{3} \pi \rho_p \right)^{1-\beta} \left(\frac{D}{10} \right)^{3(1-\beta)} \int_{-\infty}^{\infty} \left[v_e \left(1 + \frac{v_e}{3} \right) \right]^{3(\beta-1)/2} v_e f_{v_e} dv_e \quad (72)$$

From the Ranger VII data, Hartmann (1965) found that

$$Q_C = 10^{4.6} D^{-2.4} \quad (73)$$

By comparison with equation (72)

$$\beta = 1.8 \quad (74)$$

ASTEROIDS

At least 15 asteroids with perihelions less than 1 AU have been discovered (Shoemaker, 1966). The smallest of these bodies probably has a mass of at least 10^{15} grams. Since none of these asteroids has been rediscovered, using Whipple's (1966) argument, there is a 50 percent probability that 160 bodies of this size pass close enough to the Earth's orbit to be seen eventually. By comparison with Narin's (1966) data, approximately 20 of these asteroids should be concentrated within $\pm 1^\circ$ of the ecliptic. If these bodies have an average perihelion of about 0.9 AU, and have an average aphelion of about 2 AU, then on the average 14 percent, or 2.8, of them are at $s < 1$ AU and $-1^\circ < \delta < 1^\circ$ at any time, where δ is the heliocentric latitude.

The number of asteroids in this region, N_A , given by this model of the particle distribution is

$$N_A = 4\pi\delta \int_0^s f_s s^2 ds \int_{-\infty}^{\infty} f_v dv \int_m^{\infty} f_m dm \quad (75)$$

With equations (3), (4), and (10), equation (75) becomes

$$N_A = \frac{4\pi(10)^{33.5}\delta B s^7 m^{1-\beta}}{7(\beta-1)} \quad (76)$$

where B is in particles- g^β/m^3 , s is in AU, and m is in grams.

To obtain B from the asteroid data, equation (76) has been solved for $N_A = 2.8$, $\delta = 1^\circ$, $s = 1$ AU, $m = 10^{15}$ grams, and $\beta = 1.9$. It is found that

$$B = 10^{-18.4} \text{ particles-}g^\beta/m^3 \quad (77)$$

MASS DISTRIBUTION

Values of the mass distribution constants B and β have been computed from observational data on the zodiacal light, microphone and penetration-particle-detector measurements, optical and radio-meteor flux and magnitude distributions, the size distributions of meteorites and the lunar craters, and the number distribution of asteroids. These values are summarized on table 4.

TABLE 4.—Mass Distribution

Data source	Approximate mass range, g	B , particles- g^β/m^3	β
Zodiacal light.....	$10^{-10} < m < 10^{-8}$	$10^{-14.2}$	1.53
Microphone detectors.....	$10^{-14} < m < 10^{-9}$	^a $10^{-15.8}$	^b 1.9
Penetration detectors.....	$10^{-9} < m < 10^{-6}$	^a $10^{-17.6}$	^b 1.9
Radio meteors.....	$10^{-6} < m < 10^{-4}$	$10^{-18.9}$	1.91
Optical meteors.....	$10^{-1} < m < 10^5$	^b $10^{-18.2}$ ^b 10^{-18}	^b 1.9 ^a 1.90
Meteorites.....	$10^4 < m < 10^6$	$10^{-18.4}$ $10^{-18.1}$	1.76 2.0
Lunar craters.....	$10^6 < m < 10^{13}$	^b $10^{-18.6}$	1.8
Asteroids.....	$10^{15} < m$	$10^{-18.4}$	^b 1.9

^a Average values, see tables 1, 2, and 3.

^b Denotes values assumed in analysis.

To obtain the time-mass distribution, the various values of f_m obtained from these data have been plotted as a function of mass for the appropriate mass ranges in figure 6. Since only B can be determined from the microphone,

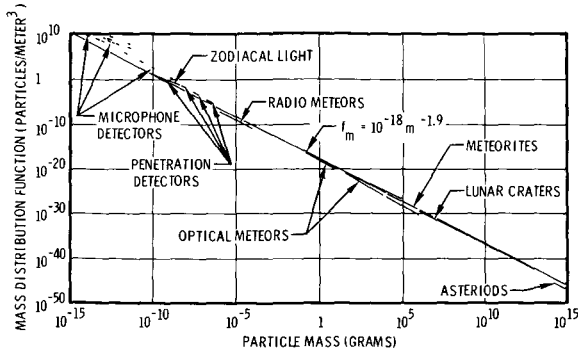


FIGURE 6.—Number-density distribution of particles with respect to mass.

penetration detector, and asteroid data, a value of $\beta = 1.9$ was assumed for these data. Similarly, since only β could be determined from the lunar-crater observations, the corresponding values of B have been chosen for the best match with the values of f_m determined from other observations.

As can be seen from figure 6, if the microphone data are excluded, a reasonable approximation for f_m is

$$f_m = 10^{-18} m^{-1.9} \text{ particles/m}^3 \quad (78)$$

The difference between the microphone data and the other observations is probably partially a consequence of the assumption made here that these detectors were all calibrated with milligram particles and partially a consequence of inaccuracy in the evaluation of f_{v_∞} near the singularity when $v_\infty = v_g$. Because of the regularity of the microphone data, this author does not believe they are invalid as has been argued by Nilsson (1966), although this possibility certainly cannot be disregarded.

METEOROID FLUX

The meteoroid environment is usually described in terms of a particle flux F . In the notation of this discussion, near the Earth

$$F_\infty = \frac{B}{\beta - 1} \langle v_\infty \rangle m^{1-\beta} \quad (79)$$

where the average particle speed $\langle v_\infty \rangle$ is

$$\langle v_\infty \rangle \equiv \int_{v_g}^{\infty} v_\infty f_{v_\infty} dv_\infty \quad (80)$$

With $B = 10^{-18}$ particles- g^β/m^3 and $\beta = 1.9$ and neglecting the concentration of low-speed particles at low altitudes, the flux is

$$F_\infty = 10^{-13.8} m^{-0.9} \text{ particles/m}^2\text{-sec-}2\pi \text{ ster} \quad (81)$$

Perhaps the most widely accepted previous estimate of the flux was made by Whipple (1963). He suggested that, for $\rho_p = 1.6 \text{ g/cm}^3$

$$F_\infty = 10^{-16.0} m^{-1.34} \text{ particles/m}^2\text{-sec} \quad (82)$$

The principal difference in these two estimates lies in the reinterpretation of the microphone detector and meteor data.

Whipple (1966) has informally suggested that the flux of particles smaller than about 10^{-6} g is lower than his earlier estimate (eq. (82)). Assuming the effect of particle density is the same as in his 1963 flux, Whipple's 1966 informal estimate of the flux can be approximated by

$$F_\infty = 10^{-14.5} m^{-1} \text{ particles/m}^2\text{-sec} \quad (83)$$

Both equations (81) and (83) are based on substantially the same data. The difference in these estimates is again a difference in the interpretation of the data for particles larger than 10^{-6} g . It does not appear that the use of a particle speed distribution in this analysis is a significant contributor to this difference.

DISCUSSION

Based on this analysis, the distribution of solid particles near the ecliptic can be described as follows: Nearly all particles are in direct orbits. They are distributed in a "doughnut" about the Sun, with the center of the doughnut tube at about 3 AU from the Sun.

The particle-number density near the center of the "doughnut" tube is probably nearly three orders of magnitude greater than that near the Earth. The average particle probably has a density of between 2 and 3 g/cm^3 , but due to its irregular shape it has aerodynamic characteristics as if it were a sphere having a density of

1.6 g/cm³. Near the Earth the average particle speed with respect to the Earth is quite low: about 11 km/sec. There may be a significant concentration of very low-speed particles at low altitudes due to the Earth's gravity.

This model differs significantly from others previously suggested, principally because the effect of nonequilibrium radiation has been included in the interpretation of the optical meteor data. As a consequence, it is found that the apparent speed distribution of meteor particles is biased with the 4.6 power of the entry speed. If this bias is removed, it is found that most particles are slow, and that the very fast ones are extremely rare.

This bias in velocity explains the apparent paradox that meteor data indicate that the particle flux may increase by several hundred percent during a shower, and yet no flux increase has been measured by the penetration-detector satellite experiments. The explanation is that the flux in the showers is relatively low compared with the background, but since the shower meteors are all moving quite fast relative to the Earth, an unusually large percentage of them are visible as meteors.

This model tends to support the observation of Ring et al. (1964) that most of the particles scattering the zodiacal light are in direct orbits. They found that, "If as many as 10 percent of the dust particles had been in contrarotation, the effect of a red shifted line would have been visible on our scans."

The present model indicates that there should be a concentration of low-speed particles near the Earth. The data presently available are not sufficient for an accurate determination of the magnitude of this concentration, but suggest that the number density at low altitudes is probably at least an order of magnitude greater than that far from the Earth.

Using this model, an estimate can be made of the age of the lunar and Martian surfaces. Equations (72) and (73) can be combined to yield t , the

age of the surface of the Moon. Using $\beta = 1.8$, $\rho_p = 1.6$ g/cm³, and $B = 10^{-18.6}$ particles-g ^{β} /m³, t is 10^{8.1} years for the maria. A similar calculation, using the Mariner IV Martian crater distribution data (Leighton et al., 1965), yields an age of approximately 10⁷ years for the present surface features of Mars.

In principle, this model could also be used to calculate the total mass of the particulate material in the solar system. However, if this is done, it is found that the total mass is approximately $10^{22} m^{2-\beta}$ g, where m is the mass in grams of the largest particle included in the total. Since $\beta \approx 1.9$ in this model, if m is greater than 10²⁵ g, then the integrated total mass would be less than the mass of the largest particle. The reason for this "failure" of the model is simply that the number density of bodies of this size is so low that they are improbable within the dimensions of the solar system. If $m = 10^{22}$ g, perhaps an upper limit on this model, then $m_t = 10^{24.6}$ g, corresponding to a body slightly smaller than the Moon.

NOTE ADDED IN PROOF

Subsequent to the presentation of this paper, several of the important results were reexamined. It was found that:

1. By comparison of equation (19) with the observational data reported by Jacchia, Verniani and Briggs (*An Analysis of the Atmospheric Trajectories of 413 Precisely Reduced Photographic Meteors*, Smithsonian Astroph. Obs. Special Report 175, 1965), a better choice for ϵ for the extremely important low-speed meteors would be $\epsilon = 0.6$.

2. If the Trailblazer and meteor data are corrected for differences in the efficiency of light production between iron and stoney particles, and $\epsilon = 0.6$, the average particle density is about 2 gm/cm³.

3. When the Mariner IV data are corrected for the effect on counting rate of spacecraft shielding, detector orientation, and spacecraft velocity, the peak in the observational data near 1.4 AU is suppressed. With this reanalysis, it was found that at $s = 1.5$ AU, $f_s = 3$. The values of f_s proposed in this paper are correspondingly high for all values of $s > 1$.

4. Although β can be treated as locally constant in the analysis of observational data, the use of a constant value of β over the entire mass range does not appear justified. A better fit to the data is given by letting β vary from 1.5 for $m = 10^{-15}$ g to 2.2 for $m = 1$ g to $\beta = 1.7$ for $m = 10^{15}$ g.

REFERENCES

- ALEXANDER, W. M., C. W. MCCrackEN, and J. L. BOHN, 1965, *Science*, **149**, 1240-1241.
- ALLEN, H. J., B. S. BALDWIN, and N. A. JAMES, 1965, NASA Tech. Note, D-2872.
- ARNOLD, J. O., V. H. REIS, and H. T. WOODWARD, 1965, *AIAA J.*, **3**, 2019-2025.
- BROWN, H., 1960, *J. Geophys. Res.*, **64**, 1679-1683.
- COOK, A. F., L. G. JACCHIA, and R. E. MCCROSKY, 1963, *Smithson. Contrib. Astrophys.*, **7**, 209-220.
- D'AIUTOLO, C. T., 1964, *Space Research IV* (Amsterdam: North Holland Publishing Co.), 858-874.
- DAVIS, J., 1963, *Smithson. Contrib. Astrophys.*, **7**, 233-236.
- DIVARI, N. B., 1965, *Soviet Physics Uspekhi*, **7**, 681-695.
- FROST, V. C., and A. G. NOREM, 1966, USAF-SSD TDR-669 (6730-01)-1.
- HARTMANN, W. K., 1965, *Icarus*, **4**, 207-213.
- HAWKINS, G. S., 1959, *Astron. J.*, **64**, 450-454.
- , 1960, *Astron. J.*, **65**, 318-322.
- HAWKINS, G. S., and R. B. SOUTHWORTH, 1958, *Smithson. Contrib. Astrophys.*, **2**, 349-361.
- HAWKINS, G. S., and E. K. L. UPTON, 1958, *Astrophys. J.*, **128**, 727-735.
- HERMANN, W., and A. H. JONES, 1961, MIT, ASRL 99-1.
- JEWELL, W. O., and A. R. WINEMAN, 1964, NASA Tech. Note No., D-2268.
- KAISER, T. R., 1961, *Mon. Not. Roy. Astron. Soc.*, **123**, 265-271.
- LEIGHTON, R. B., et al., 1965, *Science*, **149**, 627-630.
- MAURER, W. C., and J. C. RINEHART, 1960, *J. App. Phys.*, **31**, 1247-1252.
- MCCRACKEN, C. W., and W. M. ALEXANDER, 1963, *Smithson. Contrib. Astrophys.*, **7**, 71-83.
- MCCROSKY, R. E., and A. POSEN, 1961, *Smithson. Contrib. Astrophys.*, **4**, 15-84.
- MCKINLEY, D. W. R., 1961, in *Meteor Science and Engineering* (New York: McGraw-Hill Book Co., Inc.), 106.
- MILLMAN, P. M., 1957, *J. Roy. Astron. Soc. Can.*, **51**, 113-115.
- NARIN, F., 1966, *J. Spacecraft and Rockets*, **3**, 1438-1440.
- NAUMANN, R. J., 1965, NASA Tech. Memo., X-1192.
- NILSSON, C., 1966, *Science*, **153**, 1242-1246.
- O'NEAL, R. L., 1965, NASA Tech. Memo., X-1123.
- PAGE, W. A., and J. O. ARNOLD, 1964, NASA Tech. Rept., R-193.
- RING, J., J. F. JAMES, M. DAEHLER, and J. E. MACK, 1964, *Nature*, **202**, 167-168.
- SHOEMAKER, E. M., 1966, *Engineering and Science*, **29**, 11-15.
- SLOAN, R. K., 1966, *Sci. Amer.*, **214**, 5, 62-72.
- SOBERMAN, R. K., and L. D. LUCCA, 1963, *Smithson. Contrib. Astrophys.*, **7**, 85-88.
- VAN DE HULST, H. C., 1947, *Astrophys. J.*, **105**, 471-488.
- WHIPPLE, F. L., 1963, *J. Geophys. Res.*, **68**, 4929-4939.
- , 1966, "The Meteoritic Environment of the Moon," Informal notes, Highwater Laboratory Conference on Meteoroid Impact, McGill University.
- WLOCHOWICZ, R., 1966, *Canadian J. Phys.*, **44**, 1-25.

Page intentionally left blank

VI

SOLAR WIND

Page intentionally left blank

50. Interplanetary Electron Concentration and Variability Measurements With Pioneer VI and VII

H. T. HOWARD AND R. L. KOEHLER
*Stanford University
Stanford, California*

FROM THE LAUNCH OF PIONEER VI on December 16, 1965, and Pioneer VII on August 17, 1966, through February 1967, over 3000 hours of phase and group path data have been obtained from the radio propagation experiment. In this experiment, harmonically related phase-modulated signals near 50 and 425 MHz are transmitted from the 150-foot parabolic dish at Stanford and received by whip antennas on the spacecraft. These antennas are connected to a dual-frequency phase-locked receiver which compares the 50-MHz carrier with the 2/17th subharmonic of the 425-MHz carrier and counts the difference frequency to provide a differential phase path measurement. The sensitivity of the measurement is 1 cycle at 50 MHz, which is equivalent to 4×10^{14} electrons/m² for the columnar content between the Earth and the probe. This method is extremely sensitive to changes in electron content but does not provide an absolute number.

Total content is deduced from the comparison of modulation phase as transmitted from the ground and as received in space. The resolution of this measurement is 3° at the modulation frequency (7.692 or 8.692 kHz) which corresponds to approximately 2×10^{16} electrons/m². At a range of 0.5 AU (75×10^6 km), this resolution is equivalent to that in the average interplanetary concentration of 0.25 electron/cm³.

The two measurements thus complement each other, the modulation phase comparison providing a total columnar content between the Earth and the spacecraft, and the frequency difference counter giving a high resolution picture of the

variations in content with time. A complete discussion of the spacecraft receiver is given by Koehler (1965) and a more thorough treatment of the measurement, as well as a description of other experiments on board the probe, is given in the Symposium on Pioneer VI (1966).

Data from the experiments are telemetered at S band, received on Earth by the Deep Space Network, and recorded on magnetic tape. This tape is then processed by the Pioneer Project Office at NASA Ames Research Center to strip out scientific and engineering data, and a digital tape is generated for each experiment. Figure 1 is a typical data plot produced by the 7090 and plotter combination at Stanford. Phase path data have been superimposed by hand on group path results to show the behavior in detail. The gradual decline in content from 70×10^{16} to 20×10^{16} electrons/m² early in the pass is due primarily to the decreasing zenith angle of the spacecraft and, thus, the decreasing columnar content in the ionosphere.

Figure 2 depicts the first 6 months of the Pioneer VI and VII orbits. The plane of the paper is the plane of the ecliptic with a fixed Earth-Sun line. Several orbital parameters are tabulated on the figure where it can be seen that Pioneer VI was launched toward the Sun while Pioneer VII was placed in an orbit outside that of the Earth. Pioneer VI was tracked with the Stanford facilities to 10^8 km, and it is expected that Pioneer VII can still produce useful data at twice this range.

Since the first preliminary report of Pioneer VI results (Symposium on Pioneer VI, 1966), data collection and processing have proceeded at a

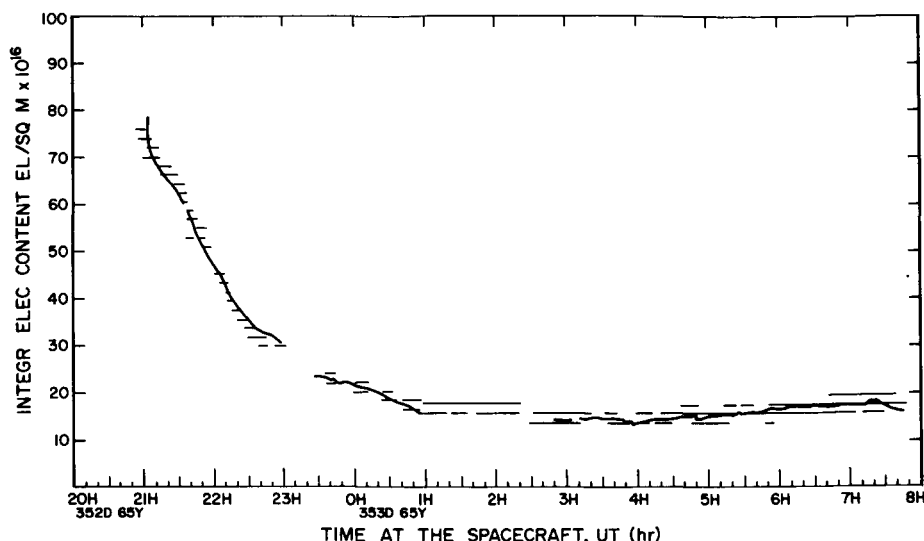


FIGURE 1.—Integrated electron content between Stanford and Pioneer VI obtained by group and phase-path measurements at 49.8 and 423.3 MHz.

	PN VI	PN VII
LAUNCH DATE	16 DEC '65	17 AUG '66
PERIOD	311.3 DAYS	402.9 DAYS
PERIHELION	0.81 AU	1.01 AU
APHELION	0.98 AU	1.125 AU

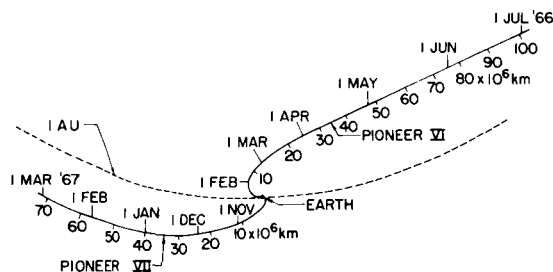


FIGURE 2.—Orbits of Pioneer VI and Pioneer VII.

steady rate. Although analysis of the Pioneer VI data is only partially complete and that on Pioneer VII has just begun, it is now possible to provide a number for the electron concentration in interplanetary space and to say something about the behavior of solar plasma disturbances propagating through space.

Figure 3 contains all the Pioneer VI integrated content data for which beacon satellite com-

parison data were available. In this plot, ionospheric electron content to 1000 kilometers (as calculated from beacon satellite differential Doppler measurements) has been subtracted from the Pioneer value. The remainder is then interplanetary content plus that of the Earth protonosphere, which is an ever decreasing percentage of the total as the spacecraft increases in range. The best-fit straight line plotted in the figure has a slope equivalent to an inter-

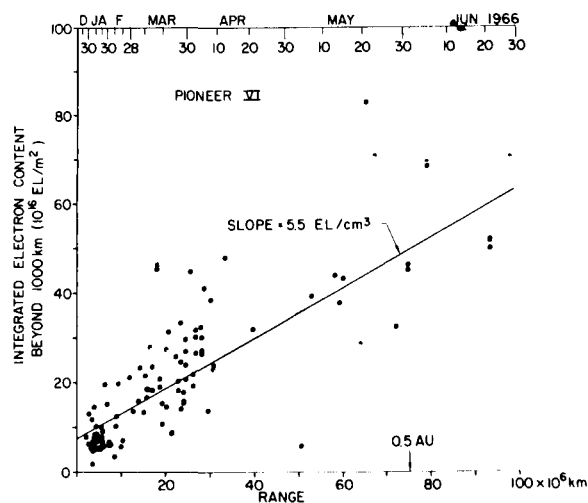


FIGURE 3.—Interplanetary plus protonosphere integrated electron content measured with Pioneer VI.

planetary concentration of 5.5 electrons/cm³. An indication of the contribution of the protonosphere to the path is given by the line intercept at 7.5×10^{16} electrons/m². It is interesting to note that, at the greater ranges, the near-Earth contribution is small enough that the effect of the protonosphere's either doubling in content or disappearing entirely would be to change the interplanetary number by only ± 0.75 electron/cm³.

Similarly, data from the first 3 months of Pioneer VII indicate an interplanetary concentration of 5.4 electrons/cm³ with about the same spread in data points. The very large number densities occasionally seen along the path for both Pioneer VI and VII are being investigated in comparison with other on-board experiments, notably the ARC plasma probe (Wolfe et al., 1966). For example, there have been several instances, at times of increasing solar activity, for which the integrated content has jumped to a value that would suggest a concentration of 30 to 40 electrons/cm³ for the entire propagation path.

An example of this is shown in figure 4 where the group path data for October 24, 1966, have been plotted along with data for several days, both before and after this date. In general, the group path plots are quite similar from day to day with only minor differences. These differences are usually small enough that the effect of the Earth ionosphere (included in this plot) could easily account for them. However, the difference between October 24 and, for example, the next data day (October 26) is many times larger than could be accounted for by the ionosphere.

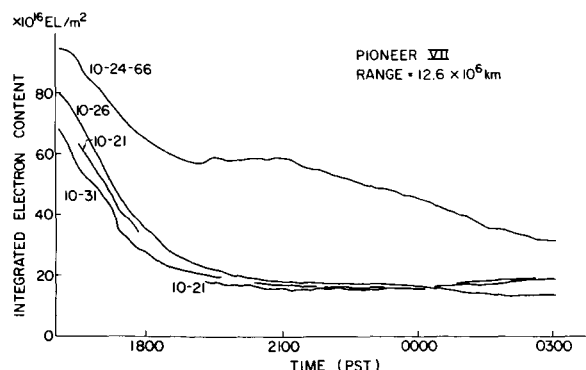


FIGURE 4.—Unusually high electron content on October 24, 1966, compared with that of several normal days.

sphere. This difference becomes more evident in figure 5 where the difference between the two days has been plotted. Figure 5 shows that the difference in the columnar content increased nearly linearly until approximately 2100 hours when it began a linear decrease. Points prior to approximately 1800 hours are of doubtful accuracy since, at that time, the path through the ionosphere was very long (spacecraft rise) and the ionosphere was changing fairly rapidly (sunset).

Straight lines have been drawn through the data points (neglecting those prior to 1800 hours) and dashed extensions have been added in an attempt to find the time at which interplanetary conditions were normal. The explanation of this event is that the propagation path was steadily filling with plasma until 2100 hours when the content began to decrease. Gee (1966) concluded that solar plasma bounded by collisionless shocks propagating through space could be detected by bistatic radar techniques. Several models were proposed and the data presented here very strongly suggest that just such an event has been observed.

The geometry of the situation on October 24 can be visualized with the aid of figure 2. At that time, the Sun-Earth probe angle was 150° and the probe was 12.6×10^6 kilometers from the Earth and 0.2×10^6 kilometers above the ecliptic. From figure 5 it is seen that the total difference between data of October 24 and the control days is 40×10^{16} electrons/m². This difference is equivalent to approximately 32 electrons/cm³ over the entire propagation path, an increase factor of 6

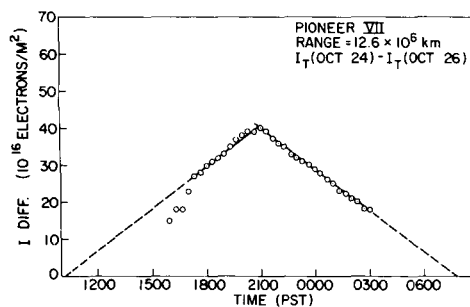


FIGURE 5.—Difference between the high electron content on October 24 and the normal electron content on October 26, 1966.

over quiet conditions. If it is assumed that a shock-bounded plasma stream equal in length to the distance from the Earth to the probe in the solar-wind direction (a longer or shorter stream would cause a flat top in fig. 5), it is possible to calculate a velocity for the stream. For example, the increase and decrease times are about equal, 11 hours, which gives a stream velocity of 290 km/sec.

At the time of this observation, the planetary magnetic index had been increasing for 48 hours and reached a peak of 19 on October 25.

Examination of preliminary "quick look" data available for the ARC plasma probe (J. H. Wolfe, private communication) shows that the solar-wind velocity on October 24 was 294 km/sec and

that, at some time around 1900 hours, the electron concentration at the spacecraft had increased by a factor of 5 or 6.

Thus, with this good first-order agreement between the two experiments, it can be concluded that a traveling stream of solar plasma with a number density 5 or 6 times that of the quiet interplanetary gas has been observed moving through space at near solar-wind velocities. Similar disturbances have now been found on numerous days in both Pioneer VI and VII data. From these data and the fact that the Sun-Earth probe angle changes greatly through each mission, it should be possible to learn a great deal about the extent, content, velocity, and direction of solar plasma propagating through space.

REFERENCES

- GEE, S., 1966, *J. Geophys. Res.*, **71**, 2729.
KOEHLER, R. L., 1965, NASA-CR-323.
Symposium on Pioneer VI, 1966, *J. Geophys. Res.*, **71**, 3287.
WOLFE, J. H., R. W. SILVA, D. D. MCKIBBIN, and R. H. MATSON, 1966, *J. Geophys. Res.*, **71**, 3329.

51. Satellite Observations of the General Characteristics and Filamentary Structure of the Solar Wind

I. B. STRONG, J. R. ASBRIDGE,
S. J. BAME, AND A. HUNDHAUSEN
*Los Alamos Scientific Laboratory
Los Alamos, New Mexico*

THE VELA SATELLITES AND ORBITS

THE SOLAR-WIND OBSERVATIONS REPORTED HEREIN were made by electrostatic analyzers on four separate Vela satellites, the Vela 2 satellites launched in July 1964 and the Vela 3 satellites in July 1965. Because of operational limitations data transmission was not continuous but each Vela 2 satellite covered approximately one-fourth of the time until the Vela 3 launch, after which point the bulk of the tracking time available was devoted to the new spacecraft.

The orbits of all these satellites are approximately circular with a radius of $17 R_E$ or $\sim 110\,000$ kilometers in a plane tilted $\sim 60^\circ$ to the ecliptic. The satellites therefore penetrate the bow shock on most orbits, about one-third of their time being spent in the unperturbed interplanetary solar-wind plasma. All the data in the following discussion were acquired on these excursions.

The spacecraft is spinning at ~ 2 rps about an axis nearly in the plane of the orbit. The Vela 2 spin axes are tilted $\sim 60^\circ$ to the ecliptic plane, while the Vela 3 axes, initially at $\sim 50^\circ$, were adjusted at a later date to $\sim 70^\circ$ to the ecliptic plane. Figure 1 shows that the orientation of a typical Vela orbit with the magnetosphere is such that the spacecraft penetrates the transition region or magnetosheath on each orbit and allows solar-wind measurements to be made on the sunward side of the Earth. For further details of the spacecraft and orbits, see Bame, Asbridge, Felt-hauser, Hones, and Strong (1967), Gosling, Asbridge, Bame, and Strong (1967), and Singer (1965).

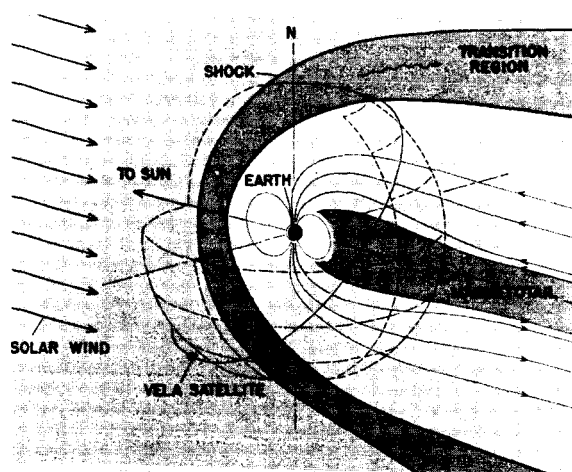


FIGURE 1.—Regions sampled by Vela satellites.

THE ELECTROSTATIC ANALYZERS

The Vela 2 type analyzer (fig. 2) rotates 5.8° during each counting period and consists of a pair of concentric hemispherical deflection plates with small entrance and exit apertures at opposite ends. For a given potential difference between the two plates, only ions with a narrow range of energy per unit charge are transmitted to the exit aperture. The emerging ions are counted with close to 100 percent efficiency by an electron multiplier. The voltage across the plates is programed to give 14 energy-per-unit-charge ranges on Vela 2. The Vela 3 analyzers are quite similar but have 64 such energy steps. By utilizing the spin of the satellite and a Sun trigger, the analyzer is able to make flux measurements in a number of directions at each energy

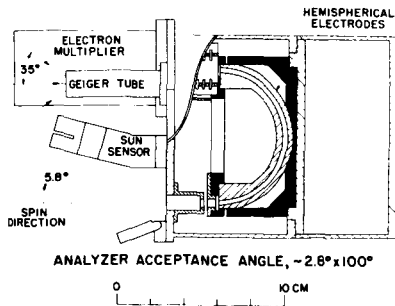


FIGURE 2.—Cross section of Vela 2 electrostatic analyzer.

step. From these sets of measurements of flux as a function of energy per unit charge and apparent direction, one may derive the basic parameters of the solar-wind bulk velocity, temperature, direction, alpha particle to proton ratio, and density. From the Vela 3 data certain more sophisticated parameters of the plasma velocity distribution function may also be found. A summary is given herein of some of the general results of the analysis of these solar-wind data. For more detailed discussions of much of the data, references are given at the end of this paper.

DIRECTIONAL PROPERTIES

The direction of flow of the solar wind has been shown to fluctuate considerably (Strong, Asbridge, Bame, Felthausen, and Olson, 1964). Examples of both slow and fast fluctuations are shown in figures 3 and 4, respectively. (The data are not corrected for aberration due to Earth rotation.) The direction can on occasion stay rather constant for periods up to an hour both

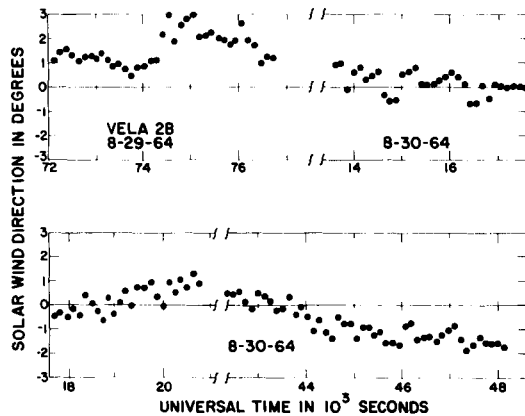


FIGURE 3.—Three examples from a period during which the solar-wind direction fluctuated slowly.

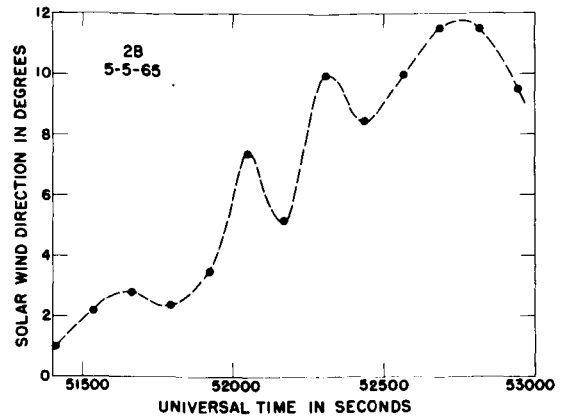


FIGURE 4.—An example of rapid changes in solar-wind direction (oscillations are real).

near radial and as much as 10° from radial (Strong, Asbridge, Bame, Heckman, and Hundhausen, 1966b). (The accuracy of determination of direction is demonstrated in the small amount of scatter in fig. 3.) On the other hand, quite sudden changes in direction, often accompanied by equally abrupt changes in other solar-wind parameters, are not uncommon and have been shown (Gosling, Asbridge, Bame, and Strong, 1967) to be associated with various types of magnetic disturbances recorded on ground-based magnetometers. The variability in direction of the solar-wind flow raises the question of whether the mean direction is radial. It has been shown (Strong, Asbridge, Bame, Heckman, and Hundhausen, 1966b) that over periods of several weeks the mean direction of flow can be consistently nonradial. The measurements of direction by the Vela spacecraft are made in the equatorial plane of the spacecraft which is tilted with respect to the ecliptic plane. Quoted directions east and west of the Sun are the components in the ecliptic plane, the accuracy of the transformation being fairly insensitive to this tilt provided the solar wind lies on the average near the ecliptic plane, as is demonstrated in Bame, Asbridge, Felthausen, Hones, and Strong (1967). Complete details will appear in Strong, Asbridge, Bame, and Hundhausen (unpublished report).

In figure 5 is plotted the mean measured direction of the solar wind, for each of the 15 successive solar rotations from July 1964 to July 1965. (All aberration and instrumental corrections have been applied.) In order to supply a visible sta-

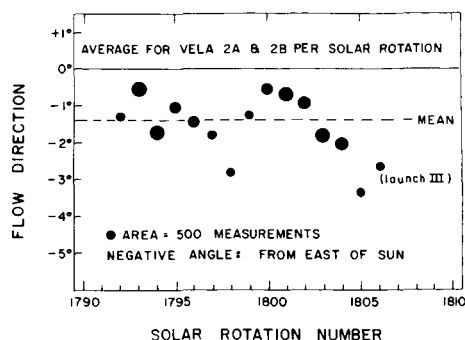


FIGURE 5.—Solar-wind directions from July 1964 to July 1965.

tistical weight, circles are drawn about the points whose areas are proportional to the number of measurements involved in determining each mean. The last point, for available Vela 3 launch data, is plotted at the center of the measurement period. It is clear that, at least during the period covered by the data, the solar wind flows, on the average, from east of the Sun. During none of the 15 solar rotations does it flow from the west of the Sun. The overall distribution of direction for the Vela 2A and Vela 2B data ($\sim 13\,000$ determinations) in figure 6 shows that the mean, median, and most probable values of the direction lie close together on a fairly symmetrical distribution curve. (Each measurement is corrected for aberration and all instrumental errors.) It should be reiterated here that the distribution is mostly due to real variations in direction since the probable error in any one measurement is $\pm 0.6^\circ$. The mean direction is from $\sim 1.4^\circ$ east of the Sun corresponding to a mean azimuthal velocity component of 10 ± 4 km/sec. This value is remarkably close in agreement to the value of 9 ± 3 km/sec found by Brandt (1966) in his analysis

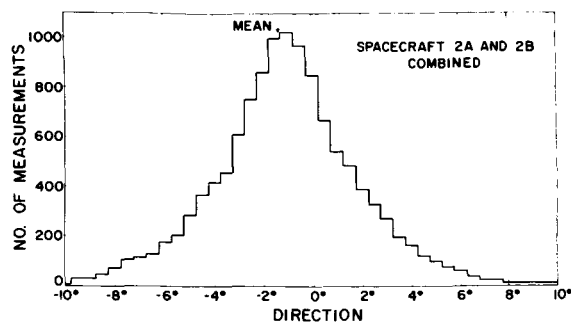


FIGURE 6.—Distribution of solar-wind directions from July 1964 to July 1965.

of approximately 600 measurements of the orientation of the Type I tails in 33 comets. The direction of the Earth's magnetotail should, on the average, parallel that of the average aberrated solar wind. The mean aberration angle during the period under consideration was 4.2° . Viewed from the Earth, therefore, the average direction of the magnetotail is not along the antisolar direction, but along a line $\sim 2.8^\circ$ west. Although no mechanism is suggested, it is interesting that the gegenschein also lies about 3° west of the anti-solar point, on the average.

SOLAR-WIND VELOCITY AND TEMPERATURE

During the period July 1964 to July 1965 the solar-wind bulk velocity varied from a low of ~ 265 km/sec to a high of ~ 730 km/sec, with a mean value of 420 km/sec (from $\sim 13\,000$ determinations). This value is distinctly lower than the 504 km/sec found by Neugebauer and Snyder (1966) on Mariner II. In figure 7 the distribution of velocities is plotted to show the number of cases in each of a number of velocity ranges. The positions and varying widths of the ranges were chosen because the energy steps of the electrostatic analyzer increase logarithmically with energy. For this reason the number of measurements in each range has been divided by the width of the range to get the height, the area of each block is then proportional to the number of measurements in the corresponding range. The distribution is quite smooth with the exception of the strong peak including measurements of ~ 325 km/sec. The presence of this peak reflects the existence of a base velocity toward which the solar-wind velocity tends when conditions are quiet. With the onset of a magnetically disturbed

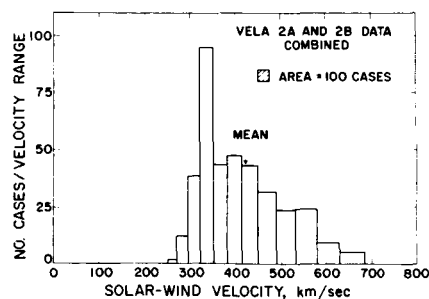


FIGURE 7.—Distribution of solar-wind velocity from July 1964 to July 1965.

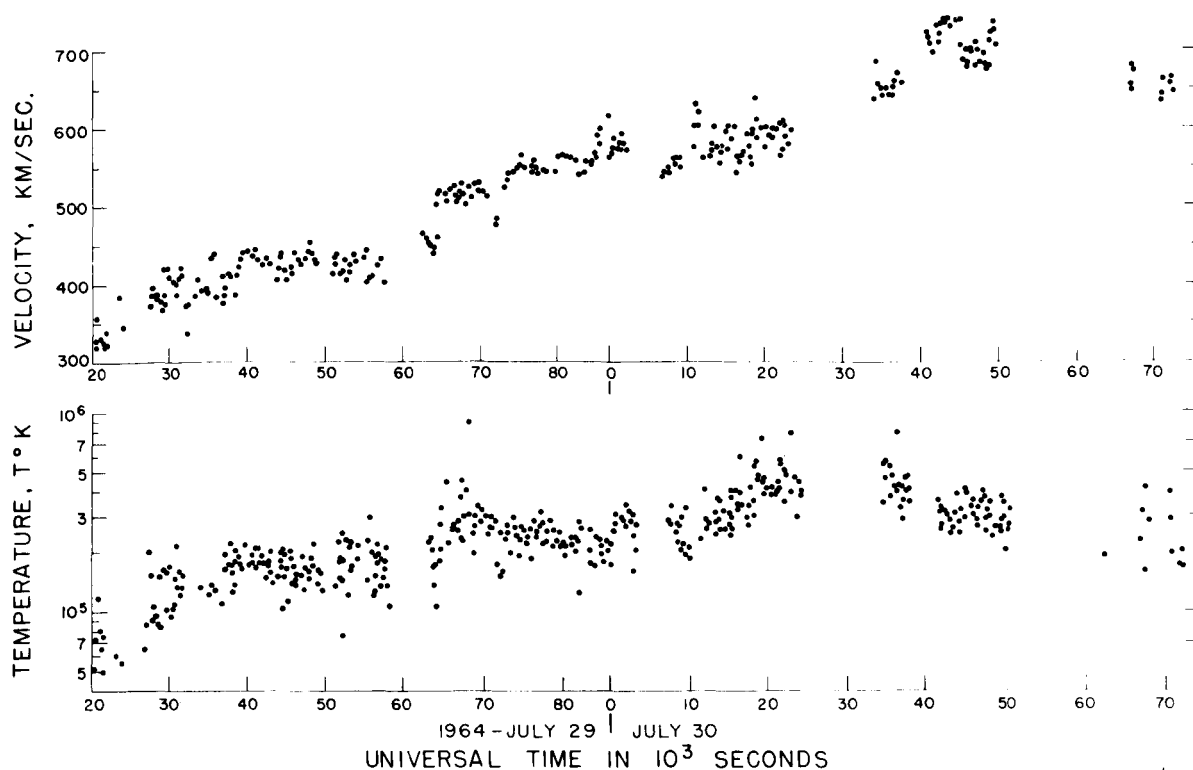


FIGURE 8.—Behavior of solar-wind temperature during a period of rising bulk velocity.

period on Earth, as recorded on ground-based magnetograms, the velocity usually rises rapidly to a much higher value, possibly accounting for the relative dearth of measurements around ~ 375 km/sec.

Since the behavior of the solar-wind temperature is closely linked with the velocity, it is of interest to examine a stretch of data for which both the temperature and the bulk velocity are plotted together. Figure 8 shows such a period during which the Kp index rose rapidly to a peak late on July 29 and then fell slowly throughout the next 2 days. The gaps in the plotted data are due to interruptions in real-time telemetry. The tendency for the temperature to follow the bulk velocity is quite obvious, although the inverse tendency does appear from ~ 65 000 seconds on July 29 through the remainder of the day. However, when the velocity and temperature data are averaged over complete solar rotations, the correlation is extremely good. Figure 9 shows the Vela 2A and 2B data. For the Vela 3 spacecraft the temperature is not available in the proper form. The temperatures measured by the analyzers

range from below 10^4 °K to nearly 10^6 °K. The very lowest temperatures occur only during long periods of geomagnetically quiet conditions and are associated typically with solar-wind velocities of about 320 km/sec and on rare occasions even lower velocities (Strong, Asbridge, Bame, Heckman, and Hundhausen, 1966a). Values much above 5×10^5 °K are also uncommon, occurring during geomagnetically disturbed periods when the

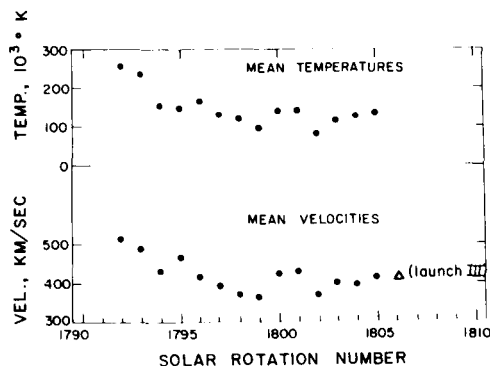
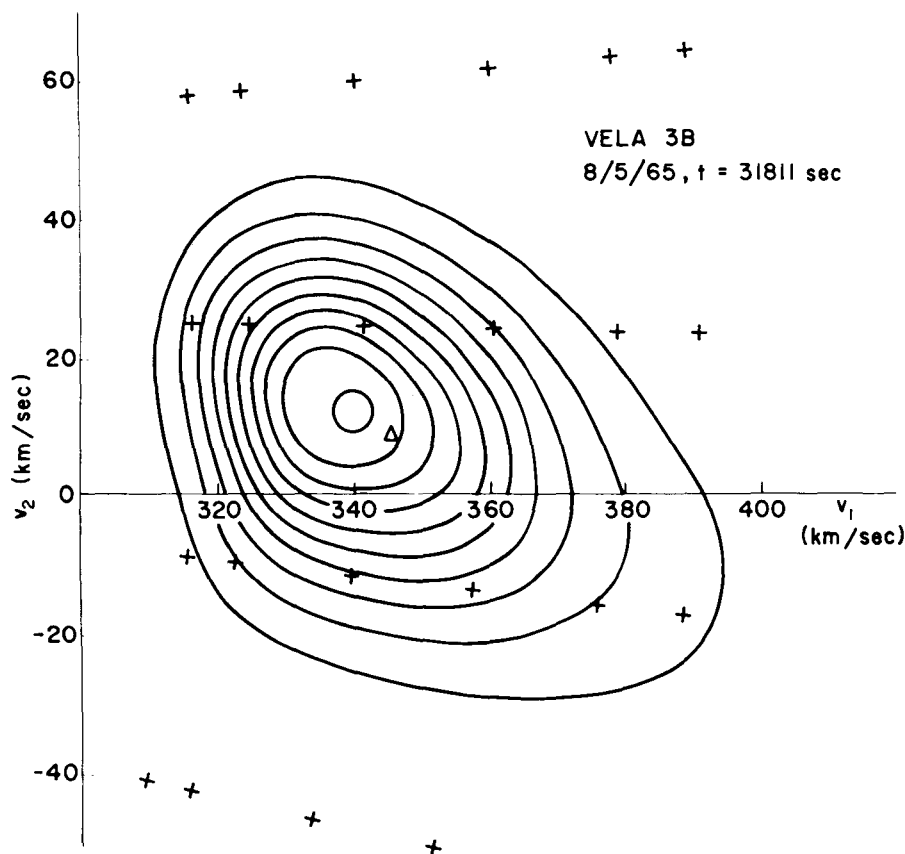


FIGURE 9.—Average values of solar-wind bulk velocity and temperature for 15 consecutive solar rotations.



CONTOUR MAP OF PROTON VELOCITY DISTRIBUTION FUNCTION

FIGURE 10. — Example of distribution of solar-wind proton density in velocity space.

solar-wind velocity is above 500 km/sec. The most probable temperature is $\sim 5 \times 10^4$ °K, and the average of all temperatures measured $\sim 1.4 \times 10^5$ °K.

The electrostatic analyzers on the Vela 3 satellites make flux determinations at many more energy steps than on the Vela 2 satellites. The spacing of the steps is such that it is useful to consider the flux as a function of radial and azimuthal velocity components and make a contour map as in figure 10 showing the lines of constant particle density in velocity space (Hundhausen, Asbridge, Bame, Gilbert, and Strong, 1966). In this display all the instrumental effects have been removed so that we have the velocity distribution function projected into the plane normal to the satellite spin axis. Details of this method of analysis have already been pub-

lished (Hundhausen, Asbridge, Bame, Gilbert, and Strong, 1967). Figure 10 illustrates an important feature of the solar-wind velocity distribution, namely that the random motions of the ions are not necessarily isotropically distributed. The random motions are commonly expressed in terms of a temperature and it is easily seen that the temperature is in this example not independent of the direction in velocity space. The anisotropy may be measured by the ratio of the maximum temperature to the mean. Figure 11 shows the distribution of the measured ratios of maximum to average temperature. The mean value of the anisotropy is ~ 1.4 . The direction of maximum anisotropy (of maximum temperature) is not distributed randomly but has a marked preference for a direction 45° from radial away from the Sun. The distribution of the directions

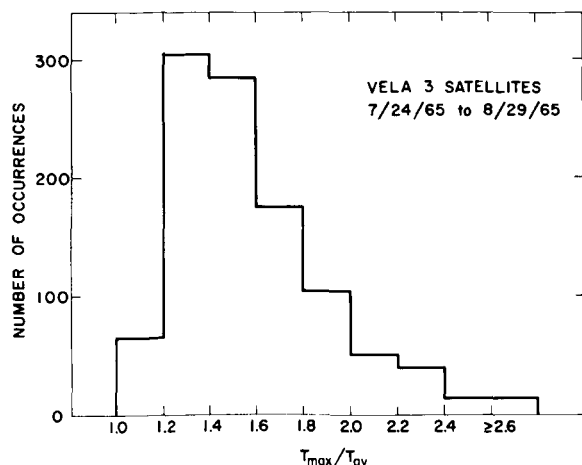


FIGURE 11.—Distribution of measured temperature ratios.

of the anisotropy, in a plane normal to the satellite spin axis, is shown in figure 12 where the area of each sector is proportional to the number of anisotropy measurements in that range. The distribution is remarkably similar to the distribution of measurements of the interplanetary magnetic field direction (Wilcox and Ness, 1965) and in fact the mean directions are almost the same. It remains to be shown that the instantaneous direction of the anisotropy follows that of the interplanetary magnetic field.¹

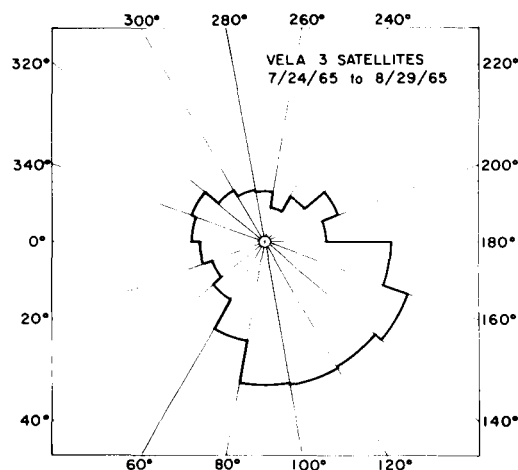


FIGURE 12.—Distribution of measured directions of maximum solar-wind temperature.

¹ This has been shown to be true since the presentation of this paper. See Hundhausen, Bame, and Ness, 1967.

The Vela 3 spacecraft have provided good measurements of the alpha-particle component of the solar-wind plasma. The bulk velocity is, naturally, the same as that for the accompanying proton component. So far no component of single-charged helium ions has been identified. Any such component must be at least one or two orders of magnitude below the alpha-particle component in density.

The alpha particles in the solar wind typically have temperatures four times that of the proton component. The random velocities are therefore approximately equal to those of the protons. The proportion of alpha particles to protons in the solar wind is distinctly variable. The Vela 2 data covering more than a year showed the alpha-particle component to range from more than 20 percent of the proton number density down to less than 1 percent (Coon, 1966). The Vela 3 data so far analyzed are shown in figure 13. The upper limit is not as high as that for the Vela 2 data, but the sample in time is much smaller and may not be typical of the conditions during which the Vela 2 data were collected. The mean value of the ratio of number densities of alpha particles to protons is 0.046; that is, the proportion of helium in the solar wind for this time sample appears to be only about half that generally accepted as being typical of the low corona. It is not yet clear whether this low measured proportion of helium is in disagreement with the approximately 10 percent figure or whether in some

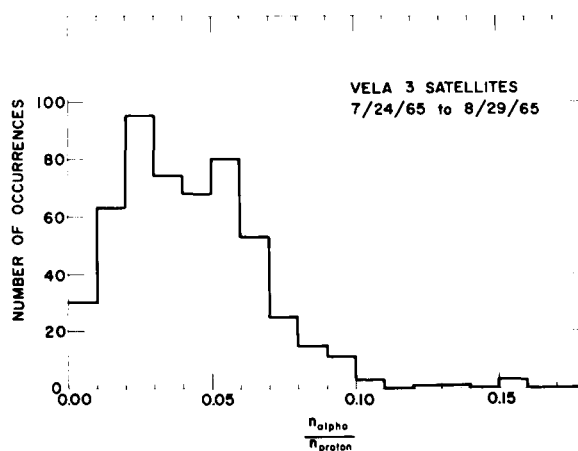


FIGURE 13.—Distribution of measured values of ratio of alpha-particle number density to proton number density in the solar wind.

way the composition of the solar wind itself is not representative of that of the lower corona. Some method of selectively emitting protons at the expense of alpha particles would be required, although the fact that the solar-wind composition is so variable indicates that such a mechanism is available and operating. On the other hand, lack of suitable lines in the solar spectrum makes the helium proportion very difficult to establish.

FILAMENTARY STRUCTURE IN THE SOLAR WIND

The fluctuations in the solar-wind parameters which give rise to the distributional properties previously described are of considerable interest. While these parameters may change slowly or remain steady for long periods of time, it is often possible to find a distinct structure to the solar wind, evidenced by abrupt changes in the value or slope of one or more of the solar parameters expressed as a function of time. The discontinuous transmission of data from the Vela satellites is less than ideal for displaying this structure; however, a particularly good example is shown in figure 14 where 12 hours of data were acquired over a period of 21 hours. The direction of flow, temperature, and bulk velocity are plotted separately against time. Times when one or more parameters change values or slopes are indicated by lettered arrows. For example, until ~ 0330 UT both the temperature and velocity were decreasing, after which they increased. The direction shows no such change. At ~ 0350 UT the direction and temperature reversed direction and decreased; the velocity abruptly leveled off. All such combinations of changes in parameters have been seen at one time or another. During quiet periods, with $V \sim 300$ km/sec, $T \sim$ few times 10^4 °K, and the direction from east of the Sun, there are few if any such events detectable in the Vela 2 data. Most of the data resemble the examples given here, in that any given trend lasts for a period ranging between ~ 20 and ~ 90 minutes. We thus have regions of solar wind with fairly constant or slowly changing properties separated by distinct boundaries, the regions presumably continuous back to the lower corona

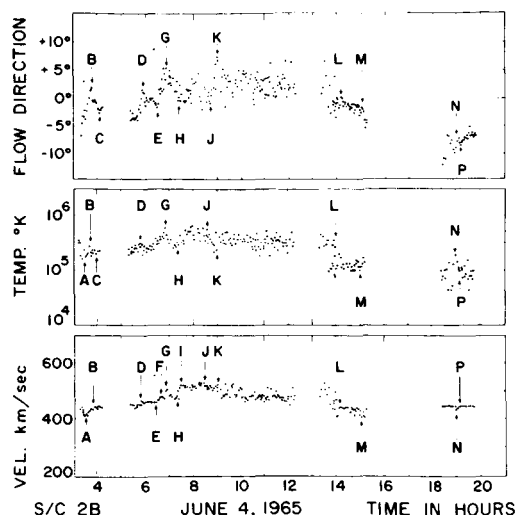


FIGURE 14.—Examples of solar-wind direction, temperature, and velocity as functions of time illustrating filamentary structure of the solar wind.

along a spiral and hence describable as filaments.

If we assume that a typical solar-wind filament passes the Earth in about an hour, at 400 km/sec, and that it is inclined to the Earth-Sun line at 45° , then its width is $(400 \times 3600)/\sqrt{2}$ km $\approx 10^6$ km. The width of the source area, assuming simple radial flow from near the Sun, should be the product of the equatorial surface velocity of the Sun and the transit time of the area or $2 \times 3600 = 7200$ km. It might be expected that the study of this solar-wind filamentary structure will lead to a better understanding of the regions of the Sun generating them.

ACKNOWLEDGMENTS

This paper is based on work performed as a part of the Vela Satellite Program for research and development on methods of detecting nuclear detonations in space. This is a joint program of the Advanced Research Projects Agency of the United States Department of Defense and the United States Atomic Energy Commission, under the administration of the Space Systems Division of the United States Air Force. The satellite instrumentation and logics are designed and built by two United States Atomic Energy Commission laboratories, Los Alamos Scientific Laboratory and Sandia Corporation. Data analysis is the responsibility of Los Alamos Scientific Laboratory.

REFERENCES

- BAME, S. J., J. R. ASBRIDGE, H. E. FELTHAUSER, E. W. HONES, and I. B. STRONG, 1967, *J. Geophys. Res.*, **72**, 113.
- BRANDT, J. C., 1966, *Astrophys. J.*, **144**, 1221.
- COON, J. H., 1966, Vela Satellite Measurements of Particles in the Solar Wind and the Distant Geomagnetosphere, in "Radiation Trapped in the Earth's Magnetic Field," ed. Billy M. McCormac, p. 231.
- GOSLING, J. T., J. R. ASBRIDGE, S. J. BAME, and I. B. STRONG, 1967, *J. Geophys. Res.*, **72**, 101.
- HUNDHAUSEN, A. J., J. R. ASBRIDGE, S. J. BAME, H. E. GILBERT, and I. B. STRONG, 1966, *Trans. Am. Geophys. Union*, **47**, 147.
- , 1967, *J. Geophys. Res.*, **72**, 87.
- HUNDHAUSEN, A. J., S. J. BAME, and N. F. NESS, 1967, *J. Geophys. Res.*, **72**, 5625.
- NEUGEBAUER, M., and C. W. SNYDER, 1966, *J. Geophys. Res.*, **71**, 4469.
- SINGER, S., 1965, *Proc. IEEE*, **53**, 1935.
- STRONG, I. B., J. R. ASBRIDGE, S. J. BAME, H. E. FELTHAUSER, and R. A. OLSON, 1964, *Trans. Am. Geophys. Union*, **45**, 624.
- STRONG, I. B., J. R. ASBRIDGE, S. J. BAME, H. H. HECKMAN, and A. J. HUNDHAUSEN, 1966a, *Phys. Rev. Letters*, **16**, 631.
- , 1966b, *Trans. Am. Geophys. Union*, **47**, 147.
- WILCOX, J. M., and N. F. NESS, 1965, *J. Geophys. Res.*, **70**, 5793.

52. Solar Wind Induced Torque on the Sun* (Abstract)

JERRY L. MODISETTE
Rice University
Houston, Texas

The torque on the Sun is determined by the solution of the equations of motion of the solar wind in which rotation and magnetic forces are considered. Through the solutions it is shown that the torque is the same as that calculated by assuming rigid body rotation of the corona out to the radius at which the solar wind velocity is equal to the Alfvén velocity, and flow with constant angular momentum thereafter. It is also shown that most of the torque is not the result of co-rotation, but it is primarily the product of electromagnetic radiation of angular momentum. The results are consistent with the torque calculated from comet tail deflections if it is assumed that comet tails are deflected by the total momentum flux in the solar wind rather than by the particle momentum flux alone.

*Published in *J. Geophys. Res.*, **72**, 1521–1526, 1967.

Page intentionally left blank

53. The Interplanetary Solar Wind Ion and Electron Characteristics (Abstract)

JOHN H. WOLFE, RICHARD W. SILVA, AND D. D. MCKIBBIN
Ames Research Center, NASA
Moffett Field, California

Recent data on the plasma characteristics in the interplanetary medium as observed by the Ames Research Center plasma probe on Pioneer VI show that the solar wind ions deviate at times from solar radial flow by as much as 5° . The observation of the plasma ions in a reference frame comoving with the solar wind convective velocity indicates that generally the ion temperature parallel to the local magnetic field exceeds the perpendicular temperature and that this thermal anisotropy is field aligned. Evidence supports the presence of a third ionic species in the solar wind. This species has been tentatively identified as singly charged helium.

Interplanetary solar wind ion and electron data for conditions of solar quiet have been compared with the plasma ion and electron characteristics noted by Pioneer VI during its traversal of the geomagnetosheath. The data reveal an interplanetary solar wind electron temperature on the order of 1 to 2×10^5 °K during quiet times when the solar wind velocity was approximately 290 km/sec with a maximum ion temperature on the order of 5×10^4 °K. The passage of Pioneer VI through the geomagnetosheath shows that the solar wind electrons are heated at the Earth bow shock to a temperature of approximately 5×10^5 °K and subsequently cool by about a factor of 2 as the flow proceeds downstream. The solar wind ions, on the other hand, although also heated at the shock front, do not appear to cool downstream and, in addition, reveal nonthermal characteristics. During quiet times the interplanetary data show that the electrons are somewhat hotter than the ions, whereas in the geomagnetosheath the ion and electron temperatures are more nearly equal. When the interplanetary medium becomes more disturbed, both ion and electron temperatures increase associatively with increases in the solar wind velocity and density. Plasma data obtained from Pioneer VI have been compared for various degrees of solar activity.

Page intentionally left blank

VII

ORIGIN AND EVOLUTION

Page intentionally left blank

54. Nature and Origin of Zodiacal Dust

S. FRED SINGER AND LOTHAR W. BANDERMANN

*University of Miami
Coral Gables, Florida*

A large number of hypotheses have been put forward to account for the existence of interplanetary dust and explain its origin. The source may be (a) dust injection from comets, (b) debris from asteroidal collision, (c) grains from condensation of gas on nucleation centers, (d) interplanetary dust which may be primeval in the sense that it may be the remains of an original dust cloud which was very much denser, or (e) an interstellar dust cloud through which the solar system may be passing. All of these possibilities are open, or any combination of these.

The purpose of this paper is not so much to discuss the origin as to try to define the present state of the zodiacal dust and to ascertain, in as much detail as possible, its physical parameters and its orbital parameters. Consideration is made of the possible modifications experienced by a dust particle through the various forces and other agents which act on it while it is in interplanetary space. For example, physical parameters of a dust particle are changed by sputtering and evaporation and radiation damage, whereas its orbital parameters are affected by solar electromagnetic and corpuscular radiation, by electromagnetic forces, and by planetary gravitational perturbations. Only after the present state of the dust has been described and the effects that modify this state are understood can meaningful arguments concerning the origin of particles be made.

This paper discusses dust measurements and interpretations (1) in ocean sediments, (2) near the Earth, (3) in the upper atmosphere, and (4) from the zodiacal light observations of dust in interplanetary space.

*By radiochemical measurements of radioactive Al^{26} in ocean sediments, the mass accretion to the Earth can be determined and, therefore, the mass concentration of dust in interplanetary space. At the same time, the mean size and size distribution is determined, and unreasonably low values of physical density (e.g., $\leq 1 \text{ g/cm}^3$) and exotic compositions such as carbon grains can be eliminated. The dust accretion is found to be $1250 \pm 1250 \text{ tons/day}$ ($1 \text{ ton/day} = 2.86 \text{ g/cm}^2\text{-sec}$).
— 1000*

Near the Earth, dust particles can be detected in satellite experiments. What is measured is never a concentration and usually not even a simple flux of particles, but rather a flux of particles having a momentum (or energy, etc.) greater than some minimum threshold which depends on the detector. This impact rate near the Earth should increase by a factor of about 10^3 compared with its value far away from the Earth. The penetration experiments are in good accord on an absolute basis, whereas the acoustic experiments give impact rates which are too high by a factor of about 100. A great deal can be deduced from any observed altitude dependence

or from any observed evening-to-morning asymmetry: the concentration of dust in interplanetary space, its size distribution, and the distribution of geocentric velocities which, in turn, allows the orbit distribution of dust to be determined.

Dust influx can also be measured in the upper atmosphere after the particles have slowed down. Their concentration can be determined by optical-laser light-scattering experiments. Again, the evening-to-morning asymmetry can be used to gain information on the distribution of geocentric velocities. Unfortunately, the atmospheric Rayleigh scattering overwhelms the dust scattering in the visible region. Any observations of dust layers must be interpreted as additional dust (aside from zodiacal dust), as due to vertical mass motions of the atmosphere which cause a compression and resulting increase in concentration of the dust particles, or as a spurious result.

In interplanetary space, the conventional analyses of the zodiacal light (following van de Hulst, 1947; Allen, 1946; Elsässer, 1955; Ingham, 1961; Giese, 1963; etc.) allow the determination of the size distribution and the albedo of the dust particles as well as their distribution of semimajor axes. Unfortunately, the interpretation is not unique. However, for this study the analysis has been extended to include the optical brightness data not only along the plane of the ecliptic but at higher ecliptic latitudes as well. Thus, the distribution of inclinations (to the plane of the ecliptic) of the dust particle orbits can be obtained; this result is of significance when the origin of dust is considered.

From a theoretical point of view, one can consider the various perturbing effects on dust particles. The solar radiation produces radiation pressure as well as the Poynting-Robertson drag which leads to a change in semimajor axis and eccentricity. New expressions have been derived which also include the effects of evaporation. The planetary perturbations produce both absorption of dust particles (those that are accreted to the planet) as well as a stirring of the orbital elements as dust particles are scattered by planetary gravitational fields.

The three major electromagnetic effects are (1) Lorentz force, (2) Coulomb drag, and (3) convective drag. It is shown that the latter is the most important and in many cases may overwhelm the Poynting-Robertson drag.

The importance of the various perturbation forces is shown in a parametric manner, and their influence is discussed in terms of various models for the origin of the zodiacal dust.

WHILE THE ORIGIN OF THE INTERPLANETARY DUST represents perhaps the most interesting problem and certainly the one of cosmogonic importance, it is necessary to concentrate on two steps before attempting to delimit the problem of the origin. The first step is a complete description of the interplanetary dust and especially of its physical parameters and orbital parameters. The second step is an understanding of the modifications which occur in these parameters because of various forces and agents which act on the dust particles in interplanetary space.

SYMBOLS

a semimajor axis

B shape parameter, defined by $B = (A/m) \delta s$,
where A is the surface area of the particle
 c speed of light
 e eccentricity
 i inclination
 m mass of dust particle
 N_{∞} particle concentration far from Earth, in
vicinity of Earth orbit
 n_e concentration of electrons in solar wind
 P period of orbit
 p exponent occurring in law for distribution
of dust particle radii
 Q particle equilibrium charge
 Q_s radiation pressure efficiency factor (referring
to a particle with radius s)

R_E radius of Earth

s radius of dust particle, defined by $m = \frac{4}{3} \pi \delta s^3$

T particle equilibrium temperature

v_E escape velocity from surface of Earth

V_0 dust particle equilibrium electrostatic potential

v_∞ geocentric speed of particles far from Earth

w solar-wind velocity

δ physical density of dust particle

ϵ elongation angle

ϑ scattering angle

μ the product of mass and universal gravitational constants

Ω longitude of right ascending node

ω argument of perihelion

This plan of work indicates the major sources of experimental evidence; that is, ocean sediments, near-Earth and upper atmosphere observations, and optical observations of the zodiacal light. From these, we can derive ideas about the orbital and physical parameters of the dust. The first step necessitates obtaining a distribution f of the dust parameters a , e , i , s , B , and δ which may be time dependent

$$f(a, e, i, s; B; \delta; t) = \frac{d^6 n(t)}{da de di ds dB d\delta} \quad (1)$$

where n for this instance refers to the total number of particles in interplanetary space. The assumption is sometimes made explicitly, but usually implicitly, that $B=3$ as in the case of a sphere, that the physical density is 3.5 g/cm^3 , and that the distribution does not change with time. It is also assumed that f is separable into a product of functions of each of the independent variables, so that

$$f(a, e, i, s) = f_1(a)f_2(e)f_3(i)f_4(s) \quad (B=3) \quad (2)$$

and that the interplanetary dust has a unique size distribution function (see fig. 1) given by $f_4(s) = Cs^{-p}$. Throughout it is assumed that ω and Ω are uniformly distributed over $[0, 2\pi]$. Several different values for p can be found in

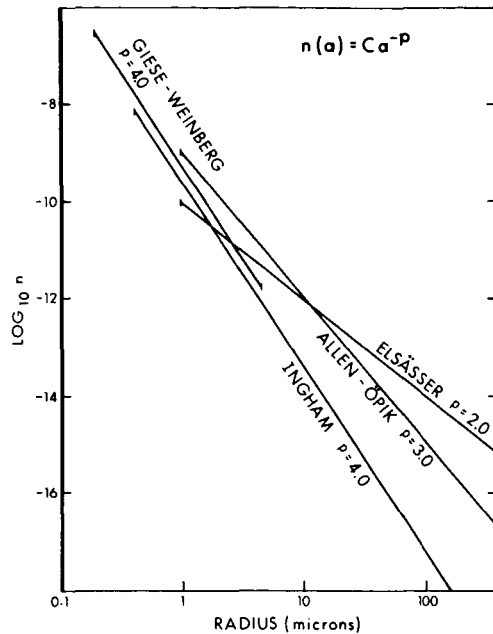


FIGURE 1.—Selected models of interplanetary dust medium.

literature. It is unnecessary, therefore, to introduce other distributions and we shall develop criteria which will eliminate some of the existing distributions and, if possible, provide new observational tests to verify any of those remaining.

The second step as shown involves the investigation of the various perturbations which affect the orbital and physical parameters. The modifications of the physical parameters of the particle are due to sputtering caused by the solar wind and evaporation caused by solar heating. The orbital parameters are modified by various forces, including solar radiation pressure, electromagnetic forces arising from the solar wind and interplanetary magnetic field, and by gravitational perturbations by the planets.

After having defined the properties of the present dust distribution, assumed to be in a steady state, and after having understood the time rate of change of the various parameters, a diffusion equation may be set up from whose solution we hope to recover the injection function; that is, distribution of the physical and orbital parameters of the dust particles as they are injected, which is required to maintain the present dust cloud properties at a steady state. By comparing the injection function with those which can be derived from various theories of

origin, we may be able to eliminate some and perhaps find the major source for the interplanetary dust.

PROPERTIES OF THE PRESENT INTERPLANETARY DUST CLOUD

Evidence From Ocean Sediments

Many properties of interplanetary dust can be gleaned from the study of ocean-bottom sediments. The Earth accretes dust particles at the rate

$$\pi R_E^2 N_\infty v_\infty (1 + v_E^2/v_\infty^2) = \pi R_E^2 N_\infty v_\infty (1 + u^{-2}) \quad (3)$$

The term $(1 + u^{-2})$ represents the effect of the Earth's gravitational field. For moderate values of u (between 0.1 and 0.5) it is responsible for most of the accretion. It becomes very large only for values of $u < 0.1$ which, however, are unreasonable.

It is difficult to identify zodiacal dust in deep-sea sediments. Various schemes have been suggested and used, including morphology (spherules) and chemical composition, for example, nickel content; also the osmium and the iridium content have been used at various times. The difficulty with these methods is that they are not specific, or they may be too exclusive. As a consequence, estimates of dust accretion to the Earth have varied from 10 tons/day up to 7 000 000 tons/day (Schmidt, 1965).

A method suggested by Wasson (1963) and experimentally established by Lal and Venkata-

varadan (1966) and Wasson is based on the presence of Al^{26} in deep-sea sediments. During the past year, two independent determinations have been made by Lal and Venkatavaradan (1966) and by Wasson, Alder, and Oeschger (1967) which indicate beyond doubt that Al^{26} is present in deep-sea sediments. It can be shown that the only source of this radioactive nuclide of half-life of 0.74 million years is interplanetary dust. Its presence is a more certain indicator of dust, therefore, than morphological or chemical evidence.

The method of determination is outlined in table 1. High energy protons (typically 10 MeV) produced in solar flares cause nuclear transformations in dust, leading to the production of Al^{26} . This value is based on an averaged proton intensity of $100/\text{cm}^2\text{-sec}$ and cross sections as given by Wasson (1963) and chondritic abundances (assumed). The saturation value of Al^{26} (i.e., if exposed for several half-lives) is 6.5×10^{11} atoms per gram of dust. From the measured activity and an estimate of the sedimentation rate (in Lal and Venkatavaradan's measurements, the sedimentation rate was obtained from simultaneous measurements of Be^{10}), an Al^{26} influx rate can be deduced and, in turn, from it, a mass accretion over the Earth amounting to 1100 tons/day. This accretion figure is uncertain by perhaps 2 orders of magnitude because of uncertainties in the solar proton flux, the reaction cross section, the sedimentation rate, the physical composition of the dust particle and, finally, the exposure time (Singer, 1967).

TABLE 1. — *Method of Determining Presence of Dust in Deep-Sea Sediments*

Solar protons ($100/\text{cm}^2\text{-sec}$)	$\xrightarrow{10 \text{ MeV}}$	$\left\{ \begin{array}{l} \text{Mg}^{26} (\text{p}, \text{n}) \\ \text{Al}^{27} (\text{p}, \text{pn}) \\ \text{Si}^{28} (\text{p}, 2\text{pn}) \end{array} \right\}$	$\xrightarrow{\text{Saturation if exposed for } 10^6 \text{ yr}}$	Al^{26} ($6.5 \times 10^{11} \text{ atoms/g}$)
Al^{26} influx rate ($5 \times 10^4 \text{ atoms/cm}^2\text{-yr}$ from measured activity)	\longrightarrow	Mass accretion ($2.5 \times 10^{-15} \text{ g/cm}^2\text{-sec}$)	\longrightarrow	Over the Earth $1.1 \times 10^3 \text{ tons/day}$
Flat size distribution (1 to 350μ)	$s^{-2.8} \text{ ds}$			$1250^{+1250}_{-1000} \text{ tons/day}$
Steep size distribution (0.17 to 4μ)	$s^{-4.0} \text{ ds}$			10^{-2} tons/day (Al^{26} equivalent)
				$\left\{ \begin{array}{l} \text{Undersaturation} \\ \text{Recoil loss} \\ \text{Sputtering} \end{array} \right\}$

On the other hand, a calculation of the accretion rate, based on various models which have been put forward to interpret the zodiacal light, can be obtained easily. Some of these models are shown in figure 1. For reasonable values of the geocentric velocity the "flat" size distribution gives an accretion rate of the order of 1250 tons/day, while the "steep" size distribution gives an accretion rate of approximately 1 ton/day which is clearly in disagreement with the Al^{26} measurements. The steep distribution is further made unlikely by the fact that small particles in the steep distribution will not be exposed for a time long enough to permit full saturation and because small particles lose much of the Al^{26} by recoil. In addition, sputtering takes its toll, decreasing their linear dimensions at the rate of approximately 5μ per million years (Wehner et al., 1963).¹ These effects combined result in an equivalent Al^{26} influx corresponding to 10^{-2} tons/day.

Therefore, from the existence of Al^{26} in deep-sea cores and from only an approximate value of its concentration, one can infer quite definitely that the flat distribution of large-sized particles (typically of the order of tens of microns) represents the distribution of interplanetary dust. In addition, the following conclusions can be drawn (Singer, 1967):

(1) The accretion rate to the Earth as well as the interplanetary mass concentration can be estimated within fairly narrow limits. A size distribution is suggested which corresponds most closely to those of van de Hulst, Allen, and Öpik; namely, $p = 2.8$ with maximum radius $s_{\max} = 350 \mu$ and minimum radius $s_{\min} = 1 \mu$, which leads to a median size of 2.4μ , a median for s^2 corresponding to 42μ , and a median for s^3 at 196μ .

(2) The physical density is consistent with 3.5 g/cm^3 and, in any case, cannot be much less than 1 g/cm^3 ; otherwise, the recoil losses become too large.

(3) The composition corresponds most closely to chondritic material. While moderate amounts of other material may be present, interplanetary dust cannot be composed predominantly of carbon, iron, or ice.

¹ The sputtering rate used in this paper is based on more recent work by Wehner, KenKnight, and Rosenberg (1967).

(4) Finally, the lifetime in the solar system for a typical dust particle cannot be much less than 1 million years, otherwise adequate saturation could not have been achieved.

Near-Earth and Upper-Atmosphere Measurements

Altitude Variation

Because of gravitation the concentration of dust particles increases near the Earth. The increase can be calculated with the help of Liouville's theorem. Because of the shielding effects of the Earth, a maximum in the concentration occurs somewhat below an altitude of 2000 kilometers. The results (Singer, 1961) are shown in figure 2, which gives the concentration (in units of its value at infinity) as a function of distance from the center of the Earth. The maxi-

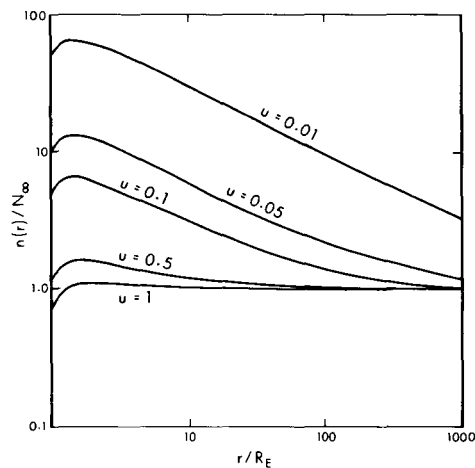


FIGURE 2.—Increase in dust concentration due to Earth's gravitational field.

imum referred to can be seen quite clearly. The analytic relationship is given by

$$n(r) = \frac{1}{2} N_\infty (1 + y/u^2)^{1/2} (1 + \cos \theta_c) \quad (4)$$

where $u = v_\infty/v_E$, and

$$\sin \theta_c = y \left(\frac{1 + u^2}{y + u^2} \right)^{1/2} \quad (5)$$

where r is the distance from the Earth's center, and $y = R_E/r$.

This result has been confirmed independently by Shelton, Stern, and Hale (1965) and by Colombo, Lautman, and Shapiro (1966), but not by others.

The concentration of dust is not measured directly by any of the present satellite experiments. However, we have calculated the flux of dust particles reaching a satellite in a circular orbit. The result is shown in figure 3. The flux to a satellite in a circular orbit is approximately

$$\frac{1}{2} N_x v_x (1 + \gamma/u^2) \left(\frac{1.5 + u^2}{\gamma + u^2} \right)^{\frac{1}{2}} (1 + \cos \theta_c) \quad (6)$$

The relative increase is about an order of magnitude greater than that of the concentration.

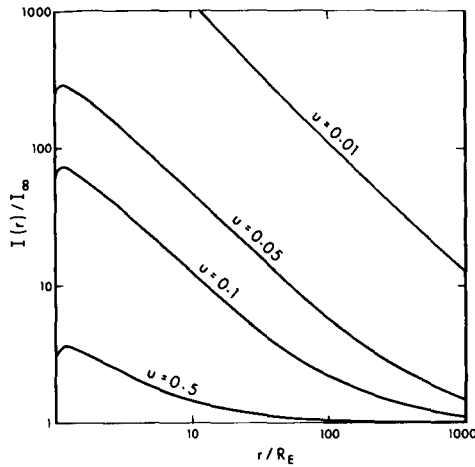


FIGURE 3. — Increase in total flux near Earth.

Now it needs to be pointed out that present satellite experiments do not measure a simple flux, but instead measure a flux of particles having a minimum momentum, or an energy, or some other kind of threshold. For a minimum momentum the dependence on distance from the Earth and on geocentric velocities is now approximately (see fig. 4)

$$\frac{1}{2} N_x v_x (1 + \gamma/u^2)^{\frac{(p+5)}{6}} \left(\frac{1.5\gamma + u^2}{\gamma + u^2} \right)^{\frac{(p+2)}{6}} (1 + \cos \theta_c) \quad (7)$$

For $p=2.8$, $\frac{p+5}{6}=1.3$ and substantial increases

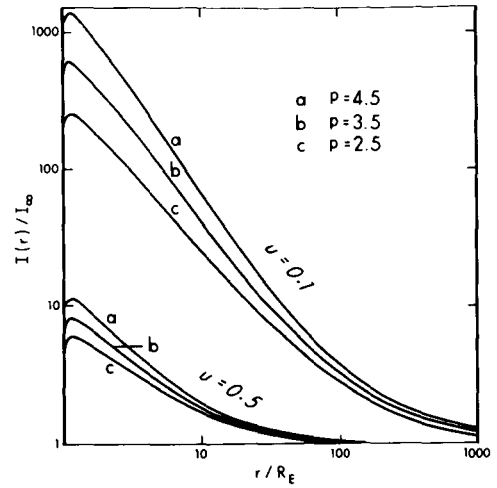


FIGURE 4. — Increase in counting rate of detector with momentum threshold on satellite in circular orbit.

in impact rate will occur for low values of geocentric velocities (Singer, 1961).

In general we can show that, if a detector is sensitive to the dust-particle mass and velocity according to relation $m^\alpha v^\beta$, then its counting rate is proportional to

$$(1 + \gamma/u^2)^{\left(1 + (\beta/\alpha) \frac{p-1}{6}\right)} \quad (8)$$

and the sensitivity on a threshold K varies as

$$K^{\left(\frac{1-p}{3\alpha}\right)} \quad (9)$$

For the case of a momentum detector, a penetration detector, and an energy detector, the relationships are shown in table 2.

One interesting result is the expected large variation in penetration rate with distance. According to table 2, and for $p=2.8$, the penetration rate should vary as with exponent 1.6 as for an energy sensitive detector. The graphs are shown in figure 4. It is seen that, even for moderately large geocentric velocities, the variation can be 3 orders of magnitude between a value near the Earth and one far from the Earth. On the basis of this result, we can use the penetration experiments to exclude the existence of a sizable component with small geocentric velocities, that is, less than 100 m/sec.

TABLE 2.—Relationships for Flux of Particles for Particular Thresholds

Type of detector	Type of threshold	Altitude variation	Sensitivity to threshold
	$m^{\alpha}v^{\beta}$	$(1+y/u^2)^{\left(1+(\beta/\alpha)\frac{p-1}{6}\right)}$	$K^{\frac{1-p}{3\alpha}}$
Momentum.....	mv	$(1+y/u^2)^{\frac{p+5}{6}}$	$p_{\min}^{\frac{1-p}{3}}$
Penetration.....	$m^{1/3}v^{2/3}$	$(1+y/u^2)^{\frac{p+2}{3}}$	D_{\min}^{1-p}
Energy.....	mv^2	$(1+y/u^2)^{\frac{p+2}{3}}$	$E_{\min}^{\frac{1-p}{3}}$

Interpretation of Satellite Data

If we assume that the dust far from the Earth has an isotropic velocity distribution, then the impact rate at a distance r from the Earth's center onto a satellite which faces randomly in all directions will be proportional to

$$\int_{s_{\min}(r)}^{s_{\max}} s^{-p} ds \int_v \int_{\theta=0}^{\theta=\theta_c} \int_{\phi=0}^{2\pi} v^2 w f_r(v) dv \sin \theta d\theta d\phi \quad (10)$$

where $f_r(v)$ is the distribution of speeds, w is the speed of a particle relative to the satellite, $s_{\min}(r)$ is the radius of the smallest particle triggering the counting mechanism, and

$$v(r) = v_{\infty}(1+y/u^2)^{1/2} \quad (11)$$

For momentum sensitive detectors (e.g., acoustic detectors) exhibiting a threshold momentum p_{\min} , the satellite counting rate is approximately

$$\frac{1}{2} N_{\infty} v_{\infty} \left(\frac{s_{\min}}{s_{\min}(y=0)} \right)^{(p-1)} (1+y/u^2)^{\left(\frac{p+5}{6}\right)} \left(1 + \frac{V^2}{v^2} \right)^{\left(\frac{p+2}{6}\right)} (1 + \cos \theta_c) \quad (12)$$

where V is the satellite speed and $\frac{4}{3} \pi \delta s_{\min}^3 v = p_{\min}$.

The last bracket contains the expansion of an angular integral, and dominant terms are shown. Note that the counting rate is proportional to $(p_{\min})^{\frac{1-p}{3}}$ and that the altitude dependence over

large distances is predominantly determined by

the factor $(1+y/u^2)^{\frac{p+5}{6}}$. As in the case of concentration, because of the shielding of the solid Earth, a maximum is attained whose location depends on u and the index p , and usually is below an altitude of 2000 kilometers. If $p_{\min} = 2.5 \times 10^{-3}$ dyne-sec and $v_{\infty} = 5$ km/sec, the smallest particle counted near the Earth ($y=1$) has a radius of approximately 4.4μ (assuming $\delta = 3.5$ g/cm³). The van de Hulst model ($s_{\min} = 1 \mu$; $N_{\infty} = 5.5 \times 10^{-14}$ cm⁻³; $p = 2.6$) predicts an impact rate of about 8×10^{-9} per cm² per second. This value is more than 2 orders of magnitude removed from the Explorer VIII data (1.47×10^{-6} /cm²/sec). The situation improves somewhat for zodiacal models with larger average particle size and for larger values of v_{∞} , but the discrepancy remains at least an order of magnitude.

For an estimate of the satellite penetration rates, we have assumed that the threshold is given by the requirement (Naumann, 1966)

$$D_0 < 0.56 m^{0.352} \delta^{0.147} (w \cos \Theta)^{0.667} \quad (13)$$

where D_0 is the foil thickness and Θ the angle of incidence (equal to zero for vertical incidence). For $p = 2.6$, the penetration rate is equal to

$$I = 7.02 \times 10^{-6} I_0 (1.5y + u^2)^{0.5} D_0^{-1.512} \quad (14)$$

I_0 would be the penetration rate with no threshold requirement. The expression is valid only if the factor multiplying I_0 is smaller than unity. Note that the rate strongly depends on D_0 . For $v_{\infty} = 5$ km/sec, we obtain the rate shown in table 3.

TABLE 3.—Impact Rates

$$[v_{\infty} = 5 \text{ km/sec}; N_{\infty} = 5.5 \times 10^{-14} \text{ cm}^{-3}; s_{\min} = 1\mu]$$

Satellite	Type of detection	Threshold	Predicted rate, $\text{cm}^{-2}\text{-sec}^{-1}$	Observed rate, $\text{cm}^{-2}\text{-sec}^{-1}$
Explorer VIII.....	Acoustic.....	2.5×10^{-3} dyne-sec	8×10^{-9}	1.47×10^{-6}
Explorer XVI.....	Penetration.....	$D_0 = 0.005 \text{ cm}...$	1.1×10^{-10}	1.99×10^{-10}
		$D_0 = 0.0025 \text{ cm}...$	3.1×10^{-10}	3.85×10^{-10}
Explorer XXIII.....	Penetration.....	$D_0 = 0.005 \text{ cm}...$	1.1×10^{-10}	2.37×10^{-10}
		$D_0 = 0.0025 \text{ cm}...$	3.1×10^{-10}	3.99×10^{-10}

We thus find that the penetration rates as predicted by the van de Hulst model (which is perhaps typical of a flat large-particle model) do agree very well with the observed rates, whereas the impact rates predicted by any reasonable zodiacal light model disagree with the acoustic rates.

Morning-Evening Asymmetry

A unique method of deriving information about the properties of interplanetary dust is through the observations of asymmetries. A morning-to-evening asymmetry is predicted because of an expected anisotropy of the geocentric velocities. There are two separate causes for this anisotropy: (1) the eccentricity of the Earth's orbit which leads to a seasonal variation; and (2) the radiation pressure effects which are especially pronounced for the smallest particles and which lead to a nonseasonal effect.

This nonseasonal symmetry situation is illustrated in figure 5 which indicates the Earth in its orbit around the Sun with velocity V_E and a dust particle having a slightly different velocity V_D .

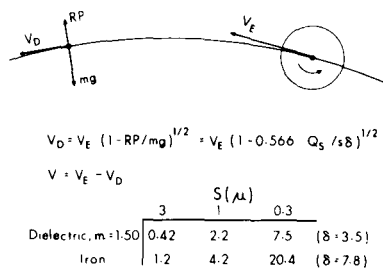


FIGURE 5.—Nonseasonal symmetry due to eccentricity of Earth's orbit and radiation pressure.

The streaming velocity V is given by $(V_E - V_D)$. The relevant relations can be obtained from figure 5, which also derives the appropriate values of V for particles of different composition and size. A typical streaming velocity is 3 km/sec. due to radiation pressure effects on a $1\text{-}\mu$ particle. A typical streaming velocity due to the orbital eccentricity of the Earth is 1 km/sec on particles of all sizes.

Under certain circumstances, the evening-to-morning asymmetry may be strong enough to be observable. A typical set of results is shown in figure 6 for a positive streaming velocity, where V is the speed of the Earth relative to the dust medium and v_{∞} is the speed of dust in the dust medium (equal to geocentric speed for $V=0$). (For a negative streaming velocity, the ratio is changed to a morning-to-evening ratio.) Ratios as large as a factor of 5 or more may be obtained for a streaming velocity of 3 km/sec if the geocentric velocity is very low, of the order of 1 km/sec, and if the measurement is performed at about 1.25 Earth radii. Usually, however, the asymmetries are very much smaller. Note that the impact rate is usually greater on the evening side for a positive streaming velocity.

For the same positive streaming velocity, the rate of influx will be greater on the morning side than on the evening side. Rate of influx is usually measured in atmospheric collection experiments and is shown in figure 7 for two different geocentric velocities (isotropic). The ratio refers to the respective points on the symmetry axis rather than to the total flux over the respective hemispheres. On the basis of these calculations, we would predict that asymmetries should be ob-

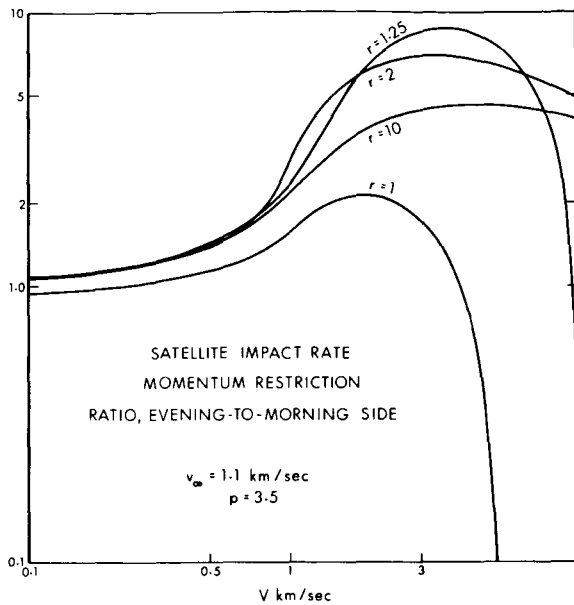
(a) $v_{\infty} = 1.1$ km/sec.

FIGURE 6.—Ratio of counting rate (evening-to-morning side) of detector with momentum threshold on satellite in circular orbit.

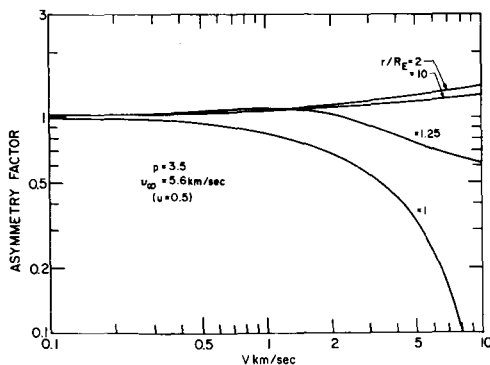
(b) $v_{\infty} = 5.6$ km/sec.

FIGURE 6.—Concluded.

servable. From such asymmetries, one can obtain unique information concerning the geocentric velocities of the particle.

Since the rate of influx is usually not measured at the top of the atmosphere, but only after the particles have had a chance to slow down, in the high atmosphere at about 100 kilometers, it is more convenient to list the altitude to which a particle of a given size ($\delta = 1$ g/cm³) falls in a 3-hour interval. (See the following table.)

Size of particle	Altitude reached
1 μ	75 km
10 μ	60 km
100 μ	40 km

The influx of dust is measured not only in collection experiments but can also be measured by optical scattering experiments (laser pulse sent from the ground into the upper atmosphere). The amounts of scattering to be expected from various dust models and from the atmosphere itself are shown in figure 8 in which the specific scattering coefficient in units of cm²/cm³ is plotted against altitude. The flatter distribution ($p = 3.0$) gives a cumulative cross section which is by 5 orders of magnitude smaller than atmospheric Rayleigh scattering at a wavelength of 7000 Å (corresponding to a ruby laser). Although a steeper distribution like that of Giese (1963) and Weinberg (1964) ($p = 4$) would give a much larger cumulative cross section, it is still smaller than the atmospheric Rayleigh cross section. We conclude, therefore, that interplanetary dust coming to a terminal velocity and then falling in a quiescent atmosphere should not be detectable by backscattering experiments in the visible region. It may be detectable by backscattering experiments in the infrared region, however.

If the atmosphere undergoes vertical motions, however, there can be a great enhancement in the dust particle density; that is, formation of dust layers, at least for periods of time in re-

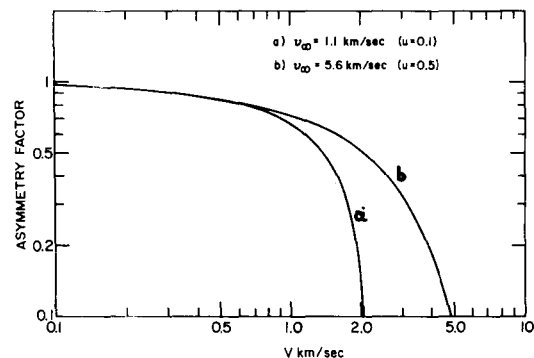


FIGURE 7.—Ratio, evening-to-morning side, of influx of dust into the Earth's atmosphere.

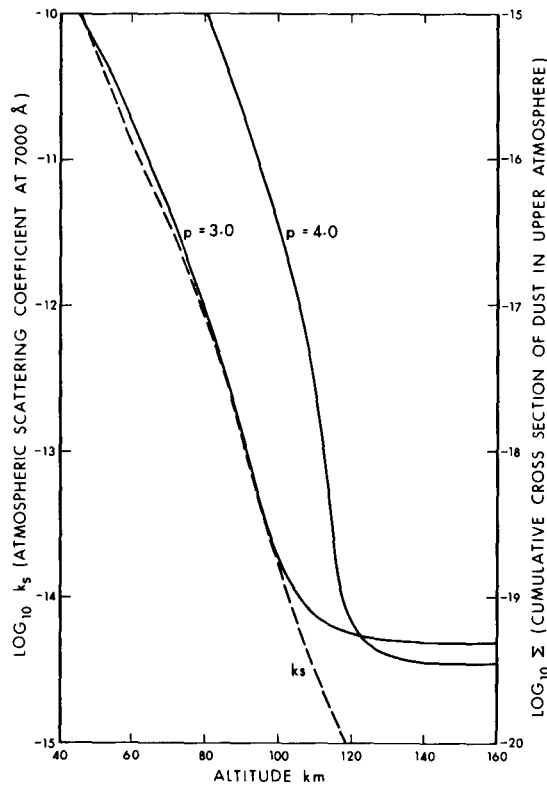


FIGURE 8.—Comparison between cumulative dust cross section in upper atmosphere (cm^2/cm^3) and atmospheric scattering coefficient (cm^{-1}) at 7000 \AA .

stricted regions. We believe that it may be possible to explain the observed dust layers in terms of vertical atmospheric motions. The presence of noctilucent clouds also argues for the existence of (upward) vertical motions at high latitudes.

Clearly, more careful studies must be made at various latitudes and various times in order to establish the dynamic regime of the upper mesosphere.

Analysis of the Zodiacal Light Isophots

Analyses of the brightness of the zodiacal light have been carried out since 1946, beginning with the pioneering work of Allen (1946) and van de Hulst (1947). It was hoped to derive the size distribution, shape parameter, albedo, and spatial distribution of dust. This is an inversion problem since the brightness is a quantity resulting from the integration over all these parameters. It can be solved uniquely only if there are a sufficient number of observational parameters by which

assumed model distributions can be tested. Most of the analyses were confined to data taken in the ecliptic plane, and one can easily convince oneself that in such a case there are not enough observational parameters available to test a given model. Indeed, many different models have been proposed, all of which successfully described the variation of brightness in the ecliptic plane. Some of these are shown in table 4. Now, during the last few years, a body of data has become available concerning the brightness of the zodiacal light away from the ecliptic plane. The inversion problem still can-

TABLE 4.—*Zodiacal Dust Models*

Distribution model	$\langle s \rangle$	$\{\langle s^2 \rangle\}^{1/2}$	$T \equiv \frac{\lambda \langle s \rangle}{\langle s^2 \rangle}$
$p = 2.0$ (Elsässer).....	5.9	19.	0.009
$p = 2.6$ (van de Hulst).....	2.7	6.1	.03
$p = 3.0$ (Allen).....	2.0	3.4	.09
$p = 4.0$ (Ingham).....	.60	.69	.7
$p = 4.0$ (Giese and Weinberg).....	.26	.29	1.5

not be solved uniquely, but because of the increased number of observational parameters, the choice of model distributions will be much narrower. In particular, one may hope to eliminate some of the zodiacal models that have been put forward to describe the zodiacal light in the ecliptic plane only. We have analyzed the isophote data, therefore, as summarized by Smith, Roach, and Owen (1965) with the intention of extracting from the analysis some information about the size distribution of dust, the spatial concentration, and, from the latter, the distribution of the orbital parameters a , e , and i , or at least some average values. For instance, we found that the isophotes seem to support a flat (rather than steep) size distribution, with micron-sized (rather than submicron-sized) particles. Furthermore, from the radial dependence of the concentration (with certain assumptions), we could determine the distribution of semimajor axes of the particle orbits, but not the distribution

$$f(i) \propto (\sin i) \exp(-bi) \quad (19b)$$

where b is positive, as suggested by Briggs (1962). (With $b=6$, the orbits of 359 photographic meteors with aphelion distance smaller than 6.7 AU are described.)

Now it can be shown that if $\xi(a, e) = g(a) \cdot h(e)$, and if $g(a)$ is given by a power law ($\propto a^\alpha$), then the radial distribution is

$$n(r, \theta) \propto r^{-2+\alpha} = r^{-\beta} \quad (20)$$

We took this form for $n(r, \theta)$ with $\alpha=0, 0.5, 1, 1.5$, and 2.

The results are shown in figures 10 to 15 in which only the results corresponding to functions $f(i) \propto \exp(-bi) \sin i$ are shown. The main defect of functions of the other type was the indication of a slow decrease of brightness above the ecliptic plane as compared with the experimental data. The models shown here are a small sample only from the many we have computed. Of these, model A gives the best fit and has these properties:

1. Flat size spectrum (large particles)

$$\left(T \equiv \lambda \frac{\langle s \rangle}{\langle s^2 \rangle} \approx 0.1 \right) \quad (\text{fig. 11})$$

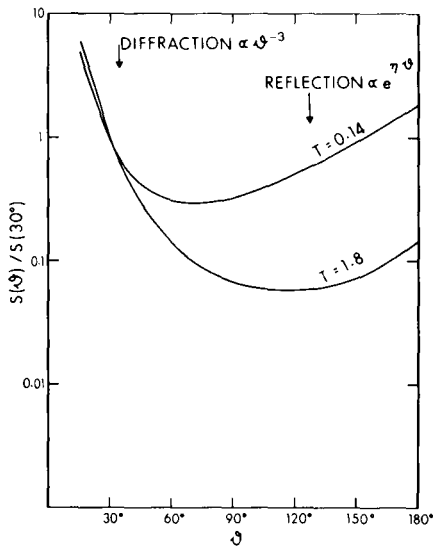


FIGURE 11.—Scattering functions used in zodiacal light analysis (normalized at 30°).

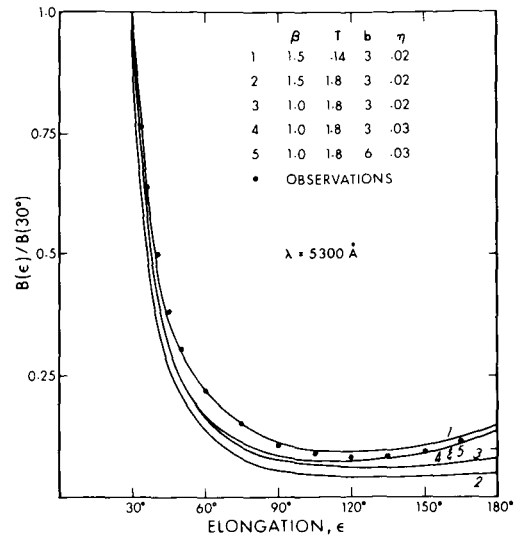


FIGURE 12.—Zodiacal light brightness in ecliptic plane (normalized at 30°).

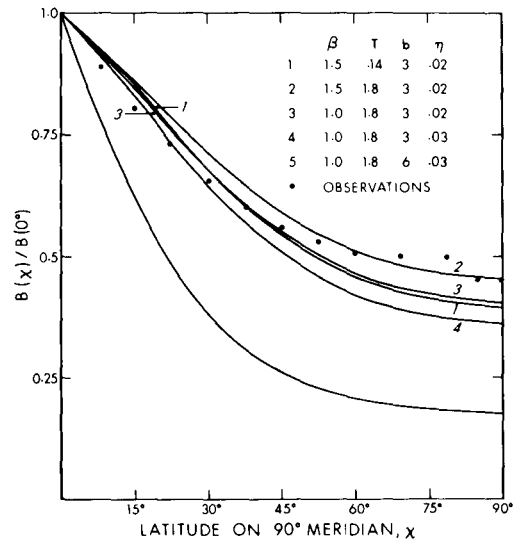


FIGURE 13.—Ratio of zodiacal light brightness as function of latitude on 90° meridian to brightness at elongation 90° in ecliptic plane.

2. Large average orbital inclinations ($i \approx 30^\circ$) (fig. 10)

3. Strong radial dependence of concentration ($\sim r^{-1.5}$) (the number of particles weakly increasing with semimajor axis; $\alpha=0.5$)

Essentially, from figure 12 one finds the value of η , from figure 13, the value of b , and from figure 14, the value of T . The value of β is not uniquely fixed by any of these, but $\beta = 1.5$ seems

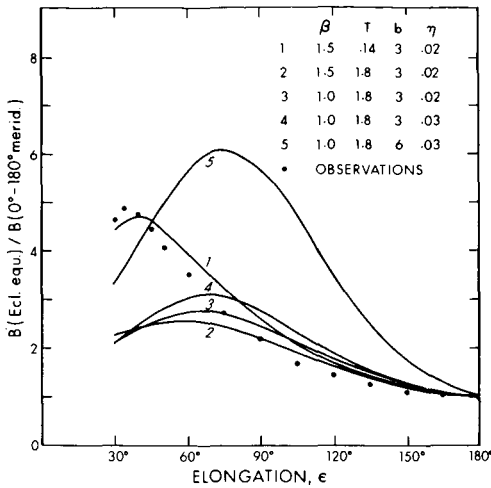


FIGURE 14.—Ratio of zodiacal light brightness in ecliptic plane (i.e., on ecliptic equator) to brightness on the 0° to 180° meridian.

a satisfactory fit to all. Note how weakly the computed brightness in the ecliptic plane discriminates between the models shown and how sensitive the ratio

$$\frac{B(\text{ecliptic equator})}{B(0^\circ \text{ to } 180^\circ \text{ meridian})}$$

is to the values of b and T (fig. 14). Note that model A does not fully account for the observed brightness at the ecliptic poles; we would suggest that the residual brightness possibly is not due to the main zodiacal cloud.

In all models we assumed a particle albedo of 10^{-1} . The choice of $\eta = 0.02$ (magnitude per

degree) successfully accounts for the increase in brightness in the counter glow region, as was already found by Briggs (1962).

In figure 15 the lines of constant particle concentration in a plane perpendicular to the ecliptic are shown. For figure 15, the dependence on distance from the Sun is related to $r^{-1.5}$ and the distribution of inclination of dust orbits is given by $f(i) = \exp(-3i) \sin i$. The blackened region is probably dust free due to evaporation near the Sun. The vertical and horizontal scales are in AU. The large average inclination (about 30°) as found in this analysis may be compared with the data shown in table 5 (Allen, 1955). Obviously, an efficient scattering mechanism for inclination seems suggested for dust particles if their sources are short-period comets or asteroids.

TABLE 5.—Average Inclination for Cometary and Asteroidal Particles

	Average a , AU	Average e	Average i , degrees
Short-period comets ($P < 100$ yr).....	3.6	0.56	15
Long-period comets ($P > 100$ yr).....			(Random)
1560 asteroids.....	2.9	.15	9.7

Physical Effects and Dynamical Perturbations

The present state of interplanetary dust can be altered in essentially two ways: by altering the

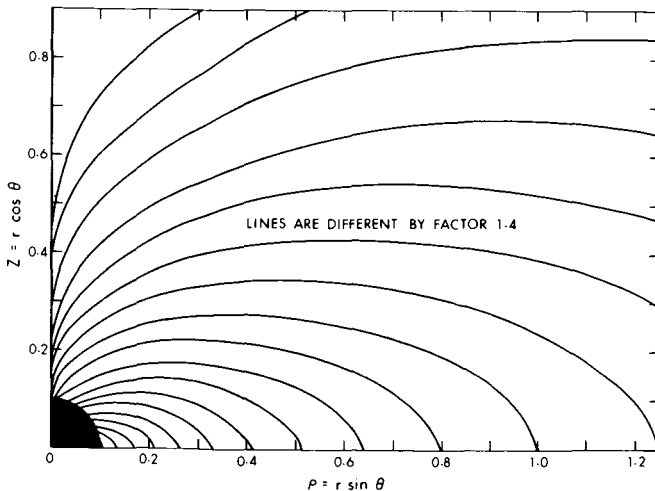


FIGURE 15.—Lines of constant concentration of dust in a plane perpendicular to ecliptic plane.

physical parameters of particles (sputtering, evaporation, radiation damage) and by perturbing the particle orbits. There are two types of orbit perturbations: random (planetary perturbations, scattering by fluctuating magnetic field) and steady (Poynting-Robertson drag).

Ejection by Radiation Pressure

Steady perturbations are caused by radiation pressure and radiation drag. Since radiation pressure varies as the inverse square of distance, it effectively reduces solar gravity and is conveniently expressed as a fraction of solar gravity. This fraction is given by

$$\frac{F_{RP}}{F_G} = 2.26 Q_p \frac{I}{cs\delta} \quad (21)$$

where I here is the solar constant at 1 AU ($=1.4 \times 10^6$ ergs/cm²-sec). Furthermore,

$$Q_p = \frac{\text{Energy rescattered in forward direction}}{\text{Total incident energy } (= \pi s^2 I)} \quad (22)$$

where Q_p can be greater than unity. In equation (21), Q_p has been integrated over the solar spectrum. At a particular wavelength λ , Q_p depends on the parameter $\frac{2\pi s}{\lambda}$. Figure 16 shows Q_p as a function of this parameter for materials with various refractive indices (data taken from Irvine, 1965). We have integrated some of these over the

solar spectrum and computed the ratios (F_{RP}/F_G) which are shown in figures 17 to 20. The integrations were done graphically, and the ratios are probably accurate to no better than 10 percent. The ratio is inversely proportional to the physical density of the particle. If one assumes ordinary densities—as seems more reasonable on account of the Al²⁶ analysis—purely dielectric particles (no imaginary part to the refractive index) will be retained by the solar system. However, because of surface deterioration (sputtering, radiation damage) the particles may absorb appreciably, and the ratio (F_{RP}/F_G) may in some cases exceed unity. Ferritic particles with radii smaller than about 0.3μ will be expelled from the solar system because of radiation pressure since the ratio (F_{RP}/F_G) exceeds unity even for very small ferritic particles. However, a comparison of F_{RP} and F_G on a static basis for a given particle will not tell whether such a particle may be present in the system in a stable orbit. Although the net force may be attractive, a particle may escape to infinity if the particle has enough angular momentum derived from its source of injection. Thus, most of the material injected by comets at their perihelia may, in fact, escape on hyperbolic orbits because of their initial high angular momenta (Harwit, 1963).

Orbit Modification by Radiation Effects

The Poynting-Robertson drag has often been misinterpreted by saying that it reduces the eccentricity so that dust particles are in nearly

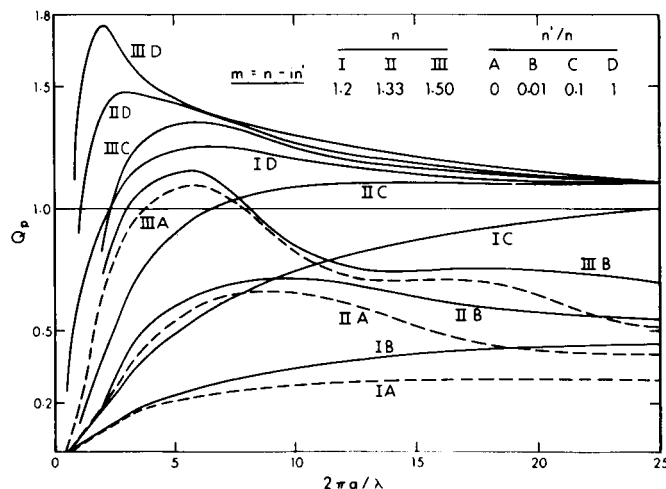


FIGURE 16.—Radiation pressure efficiency for spherical particles with complex index of refraction (Irvine, 1965).

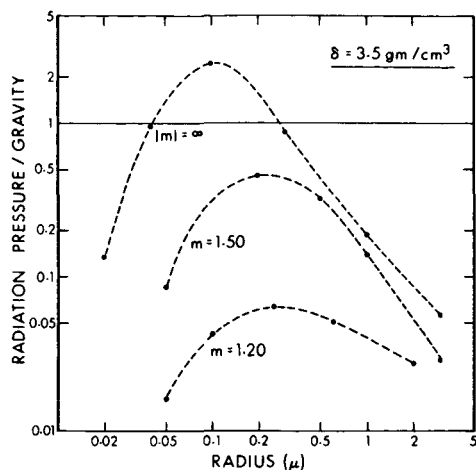
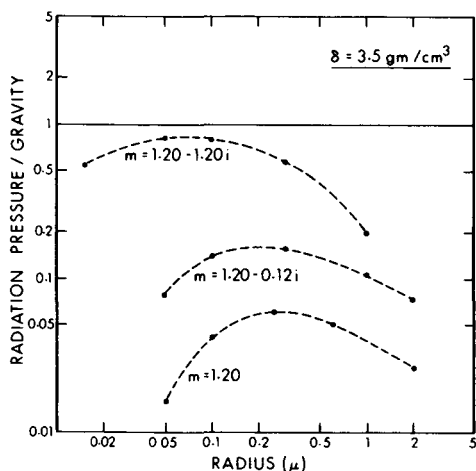


FIGURE 17.—(Radiation pressure/solar gravity) for dielectric particles.

FIGURE 18.—(Radiation pressure/solar gravity) for spherical particles with $n = 1.20$.

circular orbits in the vicinity of the Earth's orbit. If we take the ratio da/de from Wyatt and Whipple (1950)

$$\frac{da}{de} = \frac{2}{5} \frac{a}{e} \frac{2 + 3e^2}{1 - e^2} \quad (23)$$

we find that in case of a highly eccentric orbit, the Poynting-Robertson drag, roughly speaking, first reduces the semimajor axis; that is, the orbit shrinks and only then becomes more nearly circular. Since the average eccentricity of short-period comets is 0.56, such will be the case for most grains injected from comets (see fig. 21). For low-eccentricity orbits, the eccentricity is reduced further, and only then will the semimajor

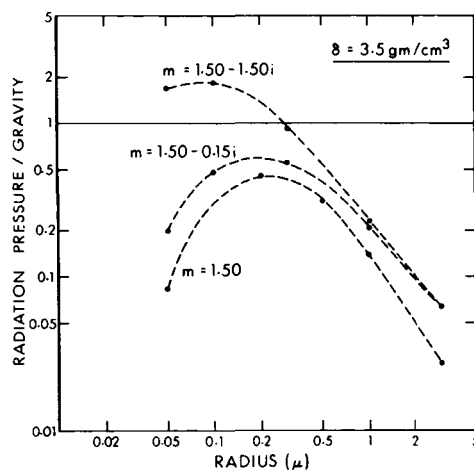
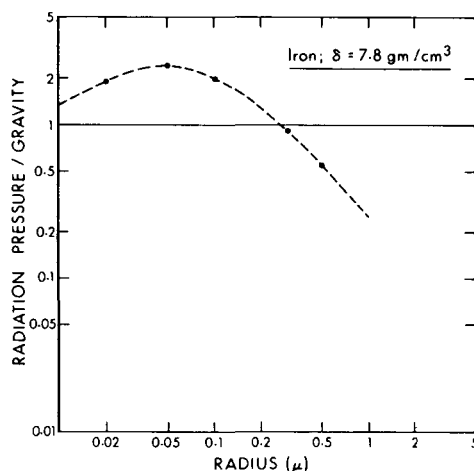
FIGURE 19.—(Radiation pressure/solar gravity) for spherical particles with $n = 1.50$.

FIGURE 20.—(Radiation pressure/solar gravity) for spherical iron particles.

axis shrink. Thus, depending on how the particles were injected into their orbits, they may still be in highly eccentric orbits at a time when, because of the Poynting-Robertson drag, they drift past the Earth's orbit.

We have investigated what would be the effect of surface evaporation (due to solar heating) on the evolution of the particle orbit. Since the rate of surface evaporation depends on temperature exponentially (Öpik, 1958) one finds that for interplanetary dust particles drifting toward the Sun under the Poynting-Robertson effect, the onset of mass loss is very sudden. Within 0.1 AU from the Sun, mass loss by sputtering is negligible. At 0.1 AU, the decrease in particle radius

due to evaporation can be as high as 10μ per year. Thus, the dust-free region of the Sun can be set at about 20 solar radii. Since the radius decreases, the effective solar gravity also decreases; this will tend to increase the semimajor axis and the eccentricity. Usually, however, such effects will not be critical since the particle evaporates rapidly. The minimum distance of approach to the Sun (for particles spiraling in on circular orbits), as set by the dynamical effects of evaporation, is given by relation (24).

$$r^2 |ds/dt| > 0.00125s \quad (24)$$

where r is in AU and t is in years.

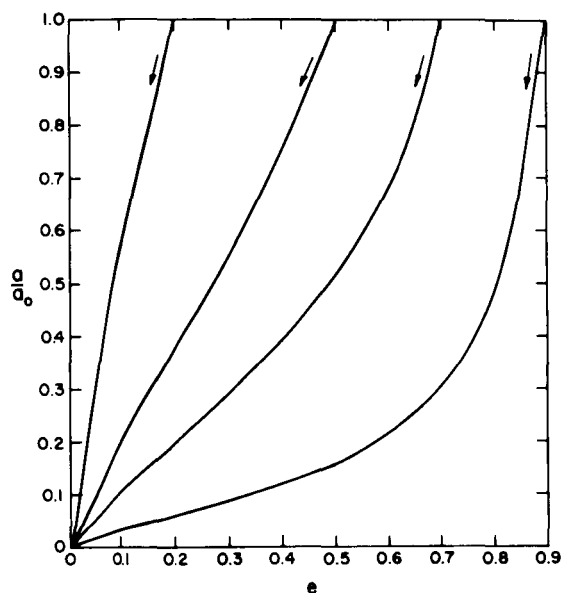


FIGURE 21.—Relation between semimajor axis and eccentricity for particles under influence of Poynting-Robertson drag.

Sputtering

In table 6, the rate of shrinkage due to sputtering is compared with that due to evaporation. The sputtering rate is taken to be 0.5 \AA/yr at 1 AU. Table 6 illustrates the sudden onset of evaporation and it is suggested that a zone of about 0.1 AU in radius about the Sun is essentially dust free.

Electromagnetic Effects

Dust particles are most certainly charged and, if particles are spheres, the relation between charge Q and electrostatic potential V_0 is

$$Q = V_0 s \quad (25)$$

(cgs units). The charge Q is determined largely by the competition between ejection of photoelectrons by solar ultraviolet and the preferential accretion of electrons from the surrounding plasma. Under steady-state conditions, the net current to the particle is zero. It is now generally accepted that V_0 is only a few volts rather than about 100 volts as had earlier been assumed on the basis of unrealistic values of the quantum yield and the solar ultraviolet flux. The accelerations due to three main electromagnetic forces acting on the particle depend on the ratio of charge to mass, and if V_0 is independent of s , the acceleration depends on s^{-2} . They become important, therefore, for small particles in interplanetary space. A Coulomb drag or plasma drag arises from the electrostatic interaction between the charge of the dust particle and the plasma ions and electrons. The integrated effect of momentum exchange results in the force

TABLE 6.—Comparison of Effects of Sputtering and Evaporation on Rate of Shrinkage

Distance from Sun, AU	Evaporation rate for stone, \AA/yr	Evaporation rate for iron, \AA/yr	Sputtering rate for iron or stone, \AA/yr
0.1	1.5×10^5	7.3×10^1	5.0
.15	5.7×10^1	5.9×10^{-3}	2.2
.2	7.4×10^{-2}	(2.1×10^{-6})	1.3
.25	2.1×10^{-4}		.80
.3	(1.0×10^{-6})		.56

$$F_c = 10^{-23} n_e Z^2 \frac{\lambda}{A w^2} \quad (26)$$

where Z is the number of elementary charges on the dust grain, A is the atomic weight of the plasma ions, w is the plasma velocity (really the relative velocity), λ is a number depending on the charge and equal to about 9 for conditions applying to interplanetary space. The Lorentz force

$$\mathbf{F}_L = \frac{Q}{c} \mathbf{v} \times \mathbf{B} \quad (27)$$

is due to the interaction with the interplanetary magnetic field alone, whereas the convective force

$$\mathbf{F}_{\text{conv}} = \frac{Q}{c} \mathbf{w} \times \mathbf{B} \quad (28)$$

depends on the fact that the solar wind carries the magnetic field along at a high speed w (high as compared with v). It can be viewed as due to the electric polarization field set up in a moving plasma pervaded by a magnetic field (Singer, 1956).

The various forces have been evaluated numerically for typical interplanetary conditions and are shown in table 7 as functions of s , δ , V , and distance r from the Sun. The Coulomb drag is several orders of magnitude less than the convective drag and is in contradiction to earlier results (Singer, 1956) which because of insufficient available data were based on an unrealistic value of the potential V_0 and too high a value of the plasma density. As can be seen, both Coulomb drag and Lorentz force can usually be neglected when compared to Poynting-Robertson and convective drag; the latter becomes more important for particles smaller than 1 mm in radius. In order to understand the effect of convective drag, we have investigated the effects of a steady B -field such as proposed by Parker (1958) and reviewed by Coleman (1966). We averaged the effect of the convective drag over an orbital period and found the long-term variations of the orbital elements. The variation of inclination and semimajor axis with eccentricity is shown in figures 22 and 23. For figure 22, we assumed the interplanetary magnetic field

possesses a nonzero average component normal to the ecliptic, as suggested by some satellite data. Contrary to the Poynting-Robertson drag,

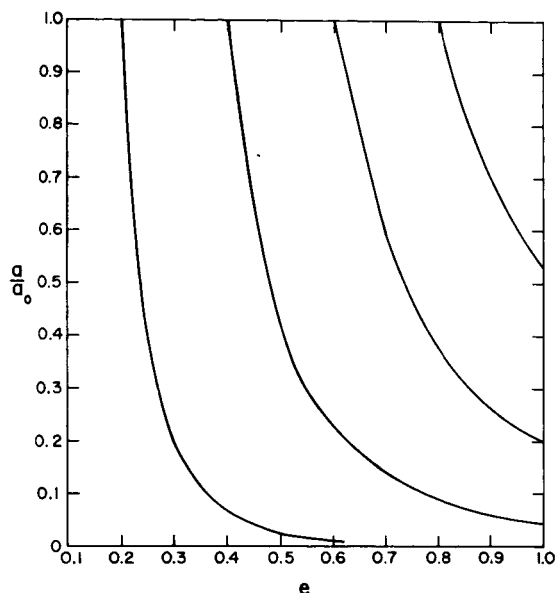


FIGURE 22.—Relation between semimajor axis and eccentricity for particles under influence of steady convective drag due to a component of the interplanetary magnetic field normal to the ecliptic plane.

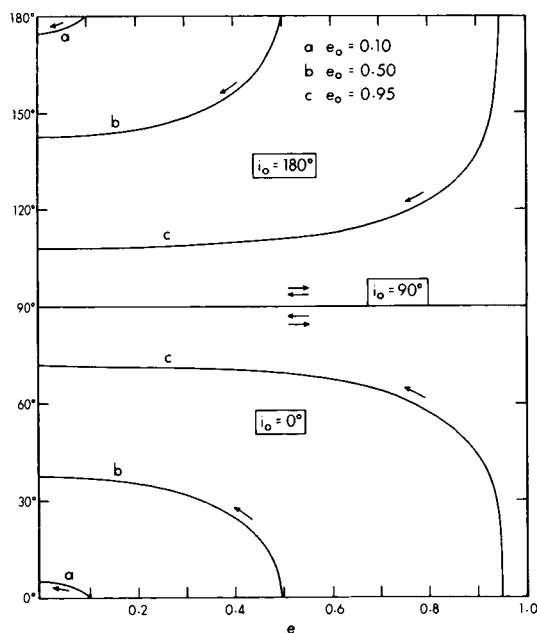


FIGURE 23.—Relation between inclination and eccentricity for particles under influence of steady convective drag.

TABLE 7.—Comparison of Various Forces for Typical Interplanetary Conditions

[$s = 1 \mu$; $\delta = 3.5 \text{ g/cm}^3$; $r = 1 \text{ AU}$; $V_0 = 3.3 \text{ volts}$; $B = 10^{-4} \text{ gauss}$; $w = 330 \text{ km/sec}$; $n_e = 1 \text{ cm}^{-3}$]

Particle radius, μ	Gravity, $2.58s^3r^{-2}$	Radiation pressure, $1.5 \times 10^{-4} Q_s s^2 r^{-2}$	Poynting-Robertson drag, $1.5 \times 10^{-8} Q_s s^2 r^{-5/2}$	Coulomb drag, $3.5 \times 10^{-9} s^2 V_0^2 w^{-2} n_e$	Lorentz force, $3.0 \times 10^{-11} s V_0 B r^{-1/2}$	Convective drag, $10^{-12} s V_0 w B r^{-1}$
10^3	-8.7×10^{-3}	1.5×10^{-6}	1.5×10^{-10}	3.5×10^{-15}	10^{-11}	10^{-10}
10^2	-8.7×10^{-6}	1.5×10^{-8}	1.5×10^{-12}	3.5×10^{-17}	10^{-12}	10^{-11}
10	-8.7×10^{-9}	1.5×10^{-10}	1.5×10^{-14}	3.5×10^{-19}	10^{-13}	10^{-12}
1	-8.7×10^{-12}	1.5×10^{-12}	1.5×10^{-16}	3.5×10^{-21}	10^{-14}	10^{-13}

the semimajor axis increases with decreasing eccentricity and vice versa. Whereas the Poynting-Robertson drag does not change either inclination, longitude of node, or argument of perihelion, all of these may change under convective drag. However, a polar orbit remains polar. As the inclination increases from a zero value (or decreases from 180°), the eccentricity decreases. Also, the argument of perihelion tends to migrate toward the line of nodes, as we would expect for reasons of symmetry. These are some preliminary results on the effects of convective drag based on a steady magnetic field. However, we know from recent satellite observations that the field has a sector structure, adjoining sectors having opposite signs. Scattering effects due to the sector structure, and irregularities, are the subject of our continuing studies. Some of the intricacies can be gleaned from the report by Coleman (1966), especially from his figure 3 which shows the angles of the magnetic field, and figures 4, 5, and 6 which show joint distributions of the radial, tangential, and normal components of the field.

Planetary Perturbations

The effects of planetary close encounters and planetary perturbations seem to be most difficult to treat in a formal way. The pioneering work in statistics of close planetary encounters was done by Öpik (1951, 1961, 1963). His work has recently been extended by Wetherill (1967). One of the main results of Öpik's work concerning zodiacal

dust was to show that particles above millimeter size, because of their slow drift past the planetary orbits, under Poynting-Robertson drag repeatedly encounter the planet and eventually are eliminated by direct collisions with the planets. Schmidt also, via sample orbit calculations, has shown (see paper No. 47) that close encounters not leading to direct collisions also prevent such particles from penetrating into the inner regions of the solar system. Essentially, close encounters present a loss mechanism depleting the dust medium of large particles. Distant encounters result in a scattering among the orbital elements for particles which are able to penetrate the inner parts of the solar system. Of greatest interest to us, for instance, is the significance of the resulting increase in average inclination. Work in this field is in progress.

NOTES ADDED IN PROOF

1. A more complete and updated treatment of the topics discussed in this paper as well as work referred to as being "in progress" (but since then completed) will be found in *Physical Properties and Dynamics of Interplanetary Dust* by L. W. Bandermann [Univ. of Maryland, Dept. of Physics and Astronomy, Technical Report No. 771, Dec. 1967].

2. The degree of Al^{26} saturation of dust particles accreted by the Earth was determined on the basis of the Poynting-Robertson lifetimes. This may in many individual cases be unrealistic: A small particle (expected to be undersaturated because of its short *PR* lifetime) may originally have been part of the skin of a larger body (say in the asteroid belt) or be a fragment of a large, entirely saturated particle, and therefore be itself saturated in spite of its short *PR* lifetime. Also, the *PR* lifetime depends on eccentricity, whereas here only circular orbits were assumed.

REFERENCES

- ALLEN, C. W., 1946, *Mon. Not. Roy. Astron. Soc.*, **106**, 137.
 —, 1955, *Astrophysical Quantities*, 163f (London: Athlone Press).
 BRIGGS, R. E., 1962, *Astron. J.*, **67**, 710.
 COLEMAN, P. J., 1966, *J. Geophys. Res.*, **71**, 5509.
 COLOMBO, G., D. A. LAUTMAN, and I. I. SHAPIRO, 1966, *J. Geophys. Res.*, **71**, 5707.
 ELSÄSSER, H., 1955, *Zeits. f. Astrophys.*, **37**, 114.
 GIESE, R. H., 1963, *Space Science Reviews*, **1**, 589.
 HARWIT, M., 1963, *J. Geophys. Res.*, **68**, 2171.
 INGHAM, M. F., 1961, *Mon. Not. Roy. Astron. Soc.*, **122**, 157.
 IRVINE, W. M., 1965, *J. Opt. Soc. Am.*, **55**, 16.
 LAL, D., and V. S. VENKATAVARADAN, 1966, *Science*, **151**, 1381.
 NAUMANN, R. J., 1966, NASA Tech. Note D-3717.
 ÖPIK, E. J., 1951, *Proc. R.I.A.*, **54**, 165.
 —, 1958, *Physics of Meteor Flight in the Atmosphere* (New York: Interscience Publishers, Inc.).
 —, 1961, *Ann. Acad. Sci. Fenn.* (Series A, III Geologica-Geographica), 185.
 —, 1963, *Advances in Astronomy and Astrophysics*, **2** (Z. Kopal, ed.), 219–262 (New York: Academic Press).
 PARKER, E. N., 1958, *Astrophys. J.*, **128**, 664.
 SCHMIDT, R. A., 1965, NASA Tech. Note No., D-2719.
 SHELTON, R. D., H. E. STERN, and D. P. HALE, 1965, NASA Tech. Note D-2575.
 SINGER, S. F., 1956, *Scientific Uses of Earth Satellites* (J. A. Van Allen, ed.) (Univ. of Michigan Press).
 —, 1961, *Nature*, **192**, 321.
 —, 1967, *Science*, **156**, 1080.
 SMITH, L. L., F. E. ROACH, and R. W. OWEN, 1965, *Planetary Space Sci.*, **13**, 207.
 VAN DE HULST, H. C., 1947, *Astrophys. J.*, **105**, 471.
 WASSON, J. T., 1963, *Icarus*, **2**, 54.
 WASSON, J. T., B. ALDER, and H. OESCHGER, 1967, *Science*, **155**, 446.
 WEHNER, G. K., C. KENKNIGHT, and D. L. ROSENBERG, 1963, *Planetary Space Sci.*, **11**, 885.
 —, 1967, *Investigations of Sputtering Effects on the Moon's Surface*. Final Report, Litton Systems, Inc.
 WEINBERG, J. L., 1964, *Ann. d'Astrophys.*, **27**, 718.
 WETHERILL, G. W., 1967, *J. Geophys. Res.*, **72**, 2429.
 WYATT, S. P., and F. L. WHIPPLE, 1950, *Astrophys. J.*, **111**, 134.

Page intentionally left blank

55. Observational Evidence of the Meteoritic Complex

PETER M. MILLMAN
*National Research Council
Ottawa, Ontario*

IN THIS PAPER the term "meteoritic complex" will be used to include the small solid particles in interplanetary space, ranging in size from dust grains bigger than the largest molecules up to objects of the smallest asteroid class, appreciable fractions of a kilometer in diameter.

For this complex we can list the major groups of physical parameters of interest in discussing its present character, together with its past and future development. Descriptive of the basic character of the complex we have

density D —the number of particles occupying a unit volume of space,

velocity V —the functions describing the nature of the motions of the particles, and

size distribution S — the relative numbers of particles in different size, or mass, categories.

A given combination of D and V will result in an impact rate N on a unit surface area, counted down to a minimum particle size and integrated over one hemisphere (2π steradians). Observationally, S usually appears as N , given as a function of minimum particle mass, or some other quantity related directly to particle size.

Variations in the basic background complex can be grouped under three main headings:

distance from the Sun R —since the Sun is the gravitational center of the solar system it is logical to expect the complex to exhibit its major variation relative to distance from this center,

time T —variation with time is synonymous with the past and future history of the complex, and

unevenness or clumping O —a property of

prime importance in defining the small-scale structure of the complex.

Finally, the nature of the particles themselves is of considerable interest. Under

material M —we can include all items such as composition, density, structure, hardness, strength, etc.

There are eight major observational areas which provide us with data related to the groups of parameters noted: impact craters, meteorites, meteor photography, radio meteor studies, penetration and cratering records, interplanetary dust collecting, acoustic and photometric impact counting, and zodiacal light observations.

IMPACT CRATERS

Impact craters are being identified in increasing numbers on the Earth, Moon, and Mars, the three planetary bodies whose surfaces are most easily available for study. Craters help us estimate N for the larger particle sizes and, in particular, give us information under T for the past (Krinov, 1963; Beals, Innes, and Rottenberg, 1963).

METEORITES

The study of meteorites from interplanetary space is our chief source of information under M . Meteorites also provide numerous clues relating to the history of the complex T . The subject is very broad. It is sufficient to note here that the bulk of the solid material found in meteorites is either a nickel-iron alloy of a mean density about 8 g/cm³, or silicates, bulk density 3 to 5 g/cm³ with inclusions of nickel-iron and small near-spherical units called chondrules. Many meteorites have a complicated internal structure,

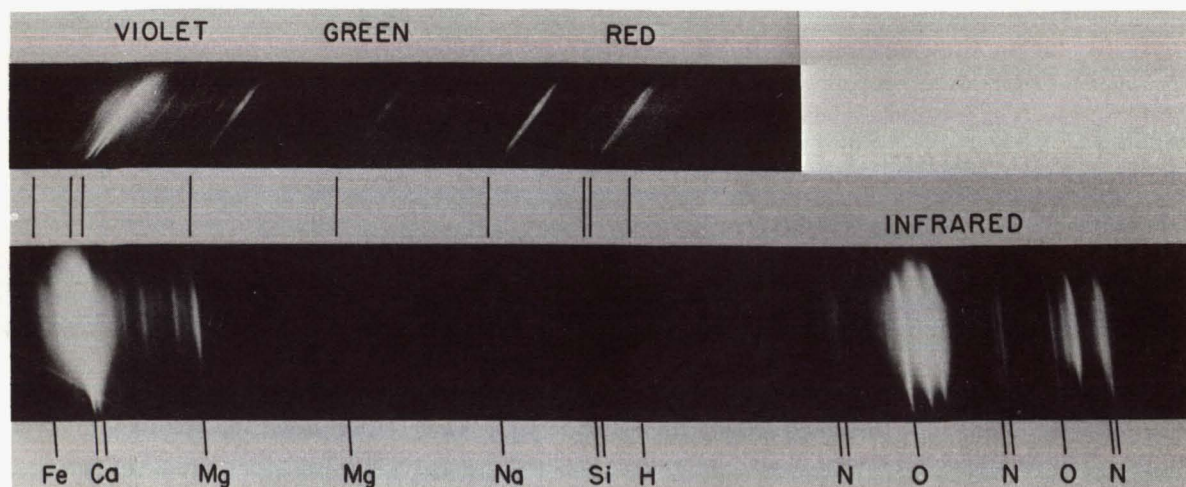


FIGURE 1.—Two Perseid meteor spectra, typical of the light from fast cometary meteors.

suggesting a past history that is far from simple. The crystal structure of the nickel-iron indicates parent bodies up to diameters of 300 kilometers. Radioactive studies of meteorite ages show that, in general, meteoritic material solidified more than 4×10^9 years ago, but that it broke up into the small pieces, which the Earth now encounters at various times, less than 10^9 years ago (Wood, 1963; Anders, 1963).

METEOR PHOTOGRAPHY

Meteor photography, supplemented by visual and photoelectric records, gives us our best quantitative information regarding the central portion of the particle size range. These are the objects small enough that their encounters with the Earth are frequent, yet large enough to produce visible radiant energy on collision with the Earth's atmosphere. Data, such as those resulting from the Super-Schmidt programs, contain information on hourly flux N and size distribution S , as well as on definitive orbits for individual particles which help in the study of R and O . The orbital characteristics of this part of the complex are very similar to, and in some cases identical with, the values for short-period comets. Data of a completely different class are provided by meteor spectrography (fig. 1). Since no cometary particle of any appreciable size has been identified on the surface of the Earth, the elements found in meteor spectra give us the only direct information on M for particles in this

size range. The almost universal appearance of iron in meteor spectra, and the normal occurrence of the elements sodium, magnesium, silicon, calcium, chromium, and manganese, point to a general similarity in composition between the cometary meteoroids and the silicate meteorites. The frequent presence of hydrogen in meteor spectra supports Whipple's comet model and suggests that cometary debris of any appreciable size may contain ices of the lighter elements (Millman, 1963).

RADIO METEOR STUDIES

The radar recording of ionization produced by meteors duplicates some of the rate values N and the orbital data O available from meteor photography, but extends the survey down to considerably smaller particle sizes. Because of its greater sensitivity and the capability of operating in daylight and through cloudy periods, a radio meteor program generally records a far greater number of meteors than a photographic program and thus gives us statistics with a higher number value. Smaller particles tend to have orbits with lower values for the semimajor axes and smaller inclinations to the ecliptic. Several papers surveying work on radio meteor orbits have already been presented at these sessions.

PENETRATION AND CRATERING RECORDS

Various new observational techniques, which involve a study of penetration and crater-

ing, have become available in connection with the flights of spacecraft, artificial satellites, and upper air rockets. One of the most reliable and unambiguous sets of data comes from Explorers XVI and XXIII and the three Pegasus satellites. The penetration rates for metal sheets of various thicknesses were recorded by the shorting of a capacitor, or equivalent methods. Naumann (1966) has recently summarized the impact rate N resulting from all data recorded by these vehicles to the end of 1965, and Dozier and Naumann have included additional data from 1966 in paper No. 27. It is worth noting that the penetration records from these five satellites now total 1862 individual hits, an impressive number value. The study of cratering and erosion on polished surfaces exposed to the space environment should also be included in this section, though here it is more difficult to convert the observational material into meaningful quantitative information on the complex.

INTERPLANETARY-DUST COLLECTING

Interplanetary-dust collecting is the counterpart of the laboratory study of meteorites, and should give us material M information for particles in the small size ranges. The chief difference is that in the case of meteorites there is rarely any doubt concerning their interplanetary origin; whereas in the case of cosmic dust studies it has been very difficult, up to the present, to be absolutely certain about the interplanetary origin of any specified particle. Collecting methods have included recovery from old arctic snows and glaciers, and from deep-sea sediments and sedimentary deposits on land; the use of collecting plates at isolated locations on Earth, and on high-flying aircraft and balloons; and the extension of these techniques to rockets and satellites, including some of the manned satellite flights. The problem of terrestrial contamination is a serious one. Although industrial contamination has only become heavy in recent centuries, volcanic dust has been spread widely throughout the Earth's history. Even in satellites outside the Earth's atmosphere we are troubled by the possibility of contamination from the vehicle itself. Tousey and Koomen's pictures (paper No. 19) of particles orbiting near his rockets highlight

this problem. It is anticipated that continuing work in this field will eventually resolve some of the difficulties. Considerable evidence seems to have appeared already for a marked variety in types of small particles. At one end of the spectrum we find fairly dense hard compact objects and at the other fragile so-called fluffy particles that fragment easily.

For collections made within or below our atmosphere there is one type of contaminant which, though originating in space, is not true interplanetary dust. This is the residue of larger meteoroids which have fragmented in the upper air.

ACOUSTIC AND PHOTOMETRIC IMPACT COUNTING

Included under acoustic and photometric impact counting are a great variety of experiments that have been mounted on upper-air rockets, Earth-girdling satellites, and interplanetary spacecraft. As distinguished from the penetration experiments, these record impulses that register on various types of acoustic crystal detectors or count light flashes caused by minute impacts on a sensitized surface. In general these systems give considerably higher rates N than do the penetration experiments. This discrepancy, which may amount to as much as four orders of magnitude, was very evident at the Cambridge symposium in 1965 (D'Aiutolo, Kinard, and Naumann, 1967; McCracken, Alexander, and Dubin, 1967; Berg and Secretan, 1967) and still exists unresolved, judging from the papers presented in this volume. Estimates of N made from dust collecting tend to agree with the higher values of the acoustic detectors; extrapolations from meteor counts and the theoretical densities derived from zodiacal light studies tend to fit the lower values of the penetration records.

To summarize the discussions at this symposium the suggested explanations of this discrepancy can be grouped under three headings:

(a) Instrumental and calibration effects—Fictitious impacts might be recorded as a result of temperature cycling or other physical effects. The calibration of both acoustic and penetration detectors may not be correct in relation to the particle mass scale. Nilsson (1966) has noted some of these problems in a recent paper.

(b) Vehicle atmosphere—It is possible that contaminants from the vehicle, combined with other particles, are maintained as a semipermanent “atmosphere” around the rocket or satellite. The presence of such particles has been observed and photographed in a number of cases. These might be recorded by acoustic detectors but not by the penetration detectors.

(c) Variation in particle types—There may be such variations in the physical nature of the particles themselves that some types could be recorded by acoustic detectors while being too fragile to affect a penetration detector. Naumann (1966) has already suggested this possibility. Perhaps all three of these explanations are needed to resolve the difficulty.

Zodiacal light as a source of observational data relating to the meteoritic complex gives us

information on D , N , and R and makes possible indirect conclusions bearing on M . Since the zodiacal light has already been fully discussed in other papers, it will not be treated further here.

Information on variations from the basic background of the meteoritic complex can be obtained from a summary of some recent analyses of records made with the Ottawa meteor patrol radar.

Variations in the daily mean for N throughout the year were published by Millman and McIntosh (1964, 1966). The annually recurring major meteor showers appear as prominent peaks, especially for the longer duration echoes representing the larger meteoroids. A detailed analysis of N for the nine most prominent annual showers in the northern hemisphere has just been completed and will be published

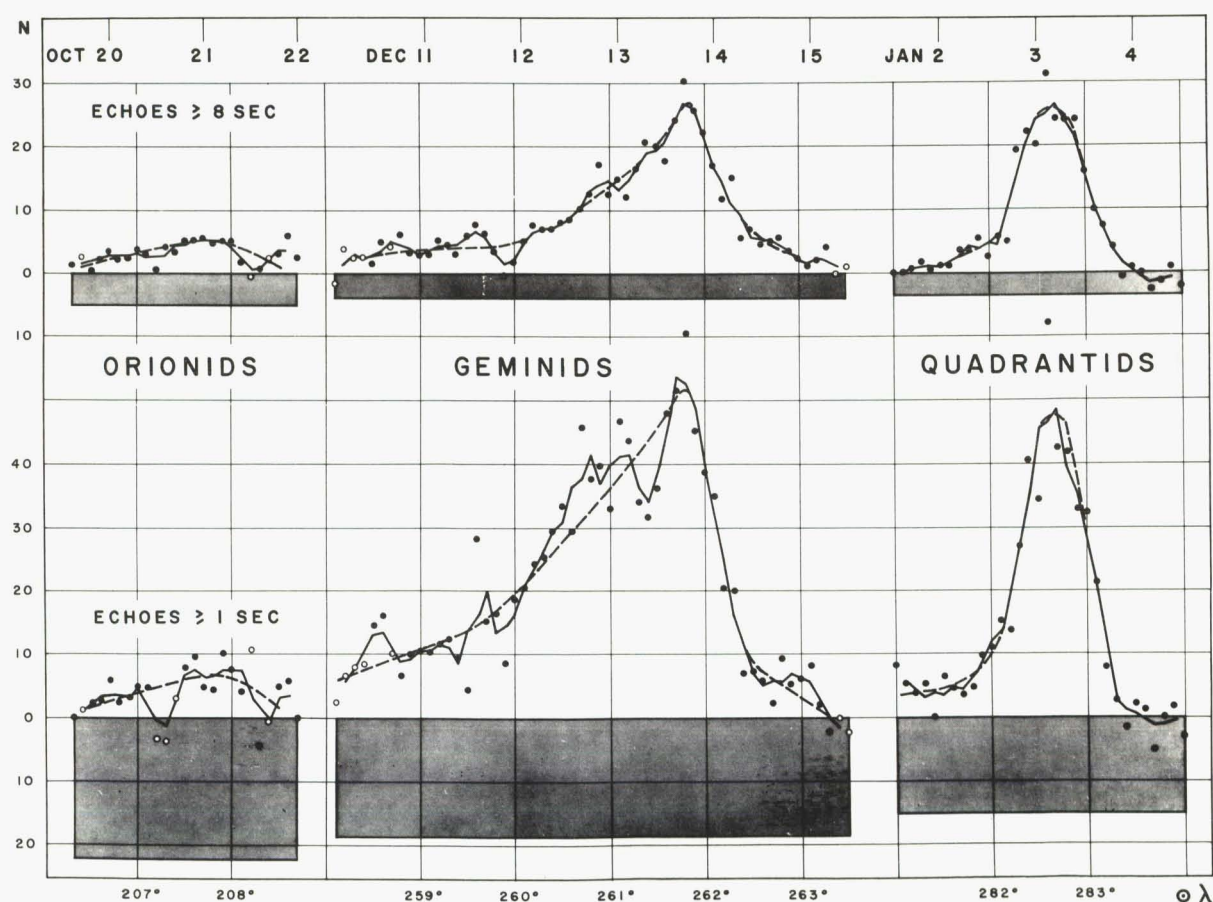


FIGURE 2.—Radar-echo hourly rates recorded at Ottawa for three of the regular annual meteor showers.

shortly by Millman and McIntosh. Figure 2 is taken from this paper and illustrates the mean hourly rates (averaged over period from 1959 to 1962) of three showers in relation to solar longitude and the average background rate from which the shower meteors were extracted. The shaded areas are background rates, averaged for the hours when each shower radiant was above the horizon. The dates at the top of the figure are the mean positions of 12 hours UT for the date given. All shower rates (dots) have been reduced to values corresponding to a radiant elevation of 30° , in other words, to conditions where the shower meteors enter the atmosphere at an angle of 30° to the horizontal. Echoes equal to or greater than 8 seconds correspond very roughly to counts down to 0.5-gram meteoroids, and echoes equal to or greater than 1 second to counts down to 0.1-gram meteoroids.

The duration of a shower and its peak rate can be given in various ways. In the present context it seems logical to list quantities relative to the mean background rate for 24 hours. In table 1 shower durations are listed between points where the shower rate reaches a value equal to the background rate (signal-to-noise ratio=1), and peak shower rates are given in units of the mean background rate. Enhancements over the background range up to 10 for the long-duration

TABLE 1.—*Annual Meteor Shower Characteristics*

Shower	Echoes ≥ 1 sec		Echoes ≥ 8 sec	
	Shower duration (days)	Peak rate (in units of background)	Shower duration (days)	Peak rate (in units of background)
Lyrids.....		0.9	1.1	1.8
η Aquarids.....		0.9	2.7	2.8
Arietids- ζ Perseids.....	(26)	2.0	(16)	2.8
δ Aquarids.....		0.8		0.8
Perseids.....	0.9	1.1	4.2	2.8
Orionids.....		0.4	1.0	1.4
Geminids.....	2.6	3.2	4.1	7.8
Quadrantids ...	1.1	3.8	1.6	10.2

Parentheses indicate approximate or doubtful values.

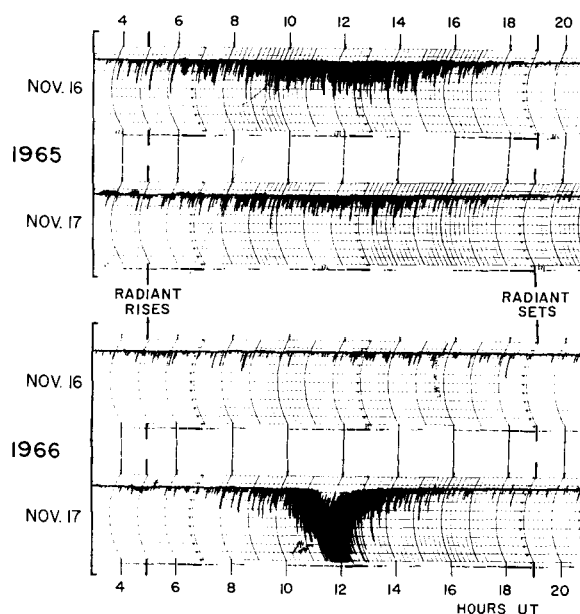


FIGURE 3.—A qualitative chart record of the integrated amplitude of Leonid meteor echoes.

Geminid echoes. Apart from the daytime summer shower complex, the durations listed correspond to distances traveled by the Earth up to 11 000 000 kilometers. This gives us some concept of the nature of the regular meteor streams which intersect the Earth's orbit. These streams may be taken as typical of many others that exist in interplanetary space.

In November of 1965 and 1966 we had good examples of the return of a shower that is not regular on an annual basis. This is the Leonid shower and it was surprisingly different on its last two appearances. Since records were made with the same radar equipment used to derive the results just discussed, the Leonid echo counts are strictly comparable with those for the regular annual showers.

Figure 3 reproduces sections of a paper chart record used to monitor the auroral radar equipment operated near Ottawa at a frequency of 48 MHz. It records integrated echo amplitude in a qualitative form. Since no aurora was present on the nights in question, the echoes recorded were primarily from meteors. The slower buildup and longer duration of the Leonid shower in 1965, as compared with that in 1966, is marked. The 1966 Leonid maximum was outstanding

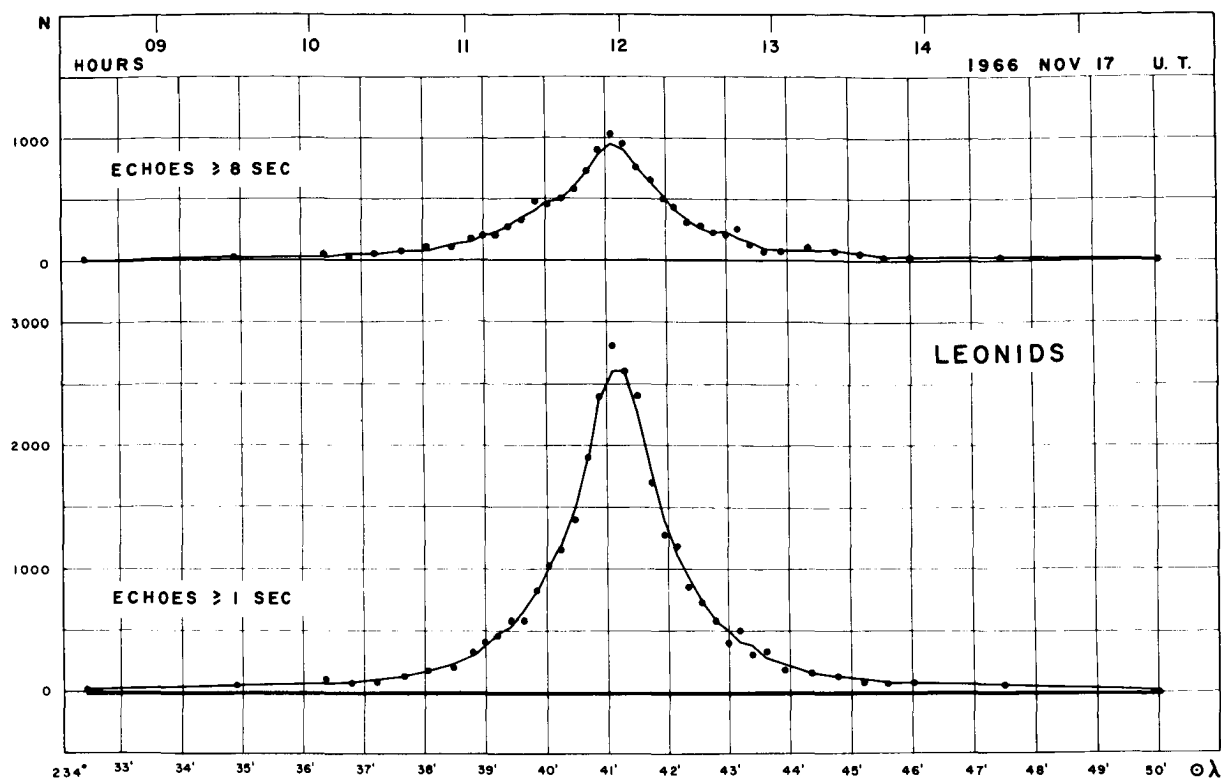


FIGURE 4. — Radar-echo hourly rates recorded at Ottawa for the Leonids on November 17, 1966 (McIntosh and McMillman, unpublished paper).

and was probably the most concentrated stream of meteoroids that the Earth has encountered in this century. Echo counts from the Ottawa meteor patrol radar are plotted in figure 4 in the same form as was used in figure 2. The thickness of the line at zero rate indicates approximately the mean background for the hours the radiant was above the horizon, 22 for the ≥ 1 second echoes

TABLE 2. — *Leonid Meteor Shower Characteristics*

Shower	Echoes ≥ 1 sec		Echoes ≥ 8 sec	
	Shower duration (days)	Peak rate (in units of back-ground)	Shower duration (days)	Peak rate (in units of back-ground)
Leonids (1965)	1.7	(4)	2.4	(16)
Leonids (1966)	0.3	150	0.4	260

Parentheses indicate approximate or doubtful values.

and 5.3 for the ≥ 8 second echoes. Here also all rates have been reduced to a Leonid radiant elevation of 30° . Values for the Leonid shower of duration and peak rate are listed in table 2, these being defined in the same way as were those in table 1. Since the 1965 peak occurred when the radiant was below the horizon in Ottawa, the values for peak rate in this year are not very certain.

For a shower as dense as the Leonids in 1966 it is useful to consider the width out to points where the particle density is one-quarter that of the peak. For the ≥ 1 -second echoes, the duration between quarter-strength points was 1.15 hours and for the ≥ 8 -second echoes 1.30 hours. Since the Earth crosses the Leonid orbit at an angle just over 15° , this gives a perpendicular width of the Leonid stream between quarter-strength points of about 35 000 kilometers for the point where the Earth passed through it in 1966. The geometry of the situation is illustrated in figure 5.

Unfortunately the 1966 Leonid maximum was

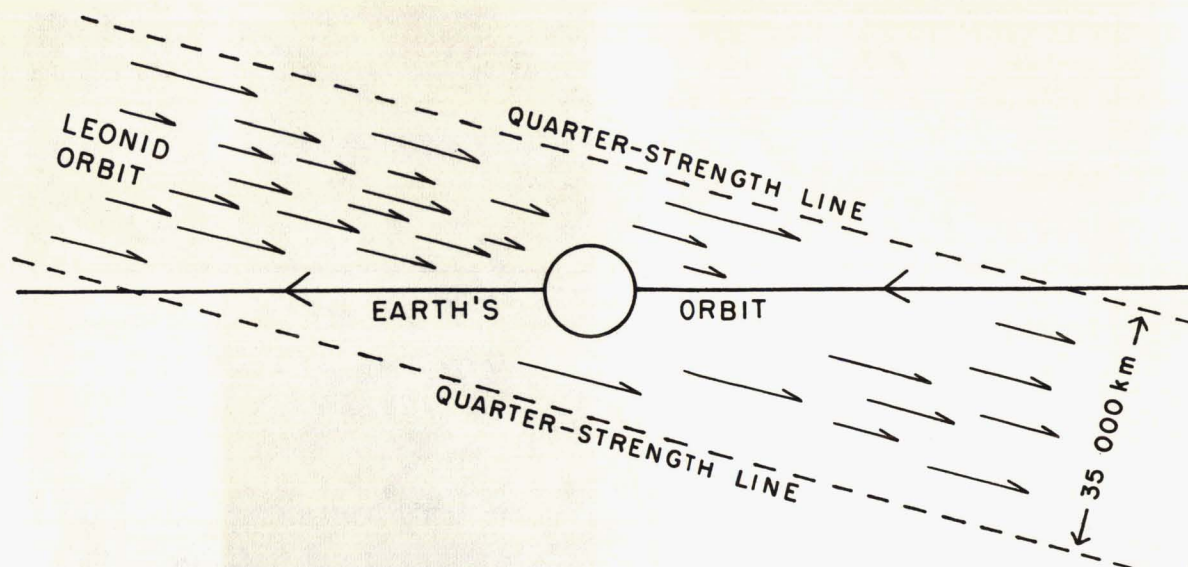


FIGURE 5.—Path of Earth through denser portion of Leonid stream on November 17, 1966.

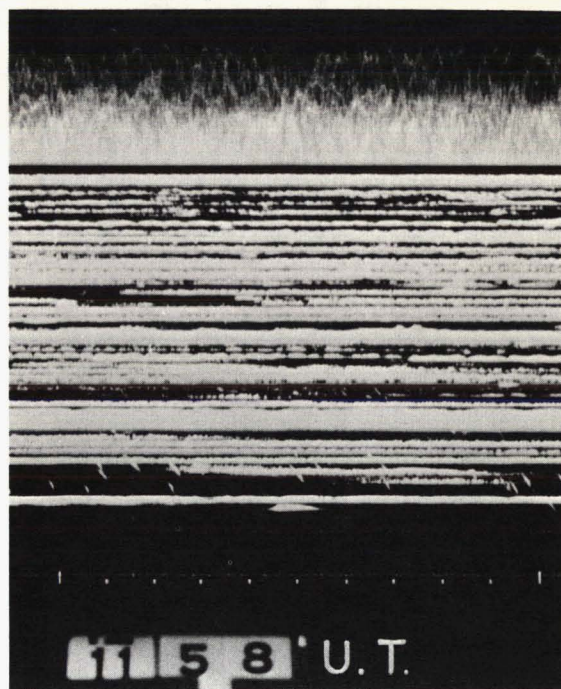
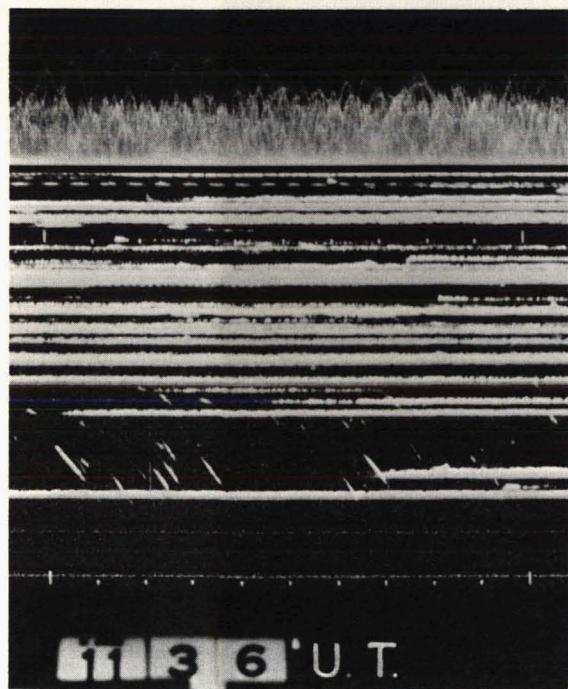


FIGURE 6.—Two sections from the high-power meteor radar record at Ottawa made during the Leonid shower on November 17, 1966.

completely clouded out in Ottawa; therefore, no visual or photographic observations were possible. However, records were obtained from the high-power meteor radar at Ottawa (3- to 4-MW peak power, 32-MHz frequency) for this shower. Figure 6 shows the amplitude-time record at the

top and the range-time record below going to 380 kilometers. Second markers appear at the bottom. The short slanting lines are head echoes of Leonid meteors. The 22-minute interval shows a marked buildup of long enduring echoes.

A party of 13 visual observers led by Dennis

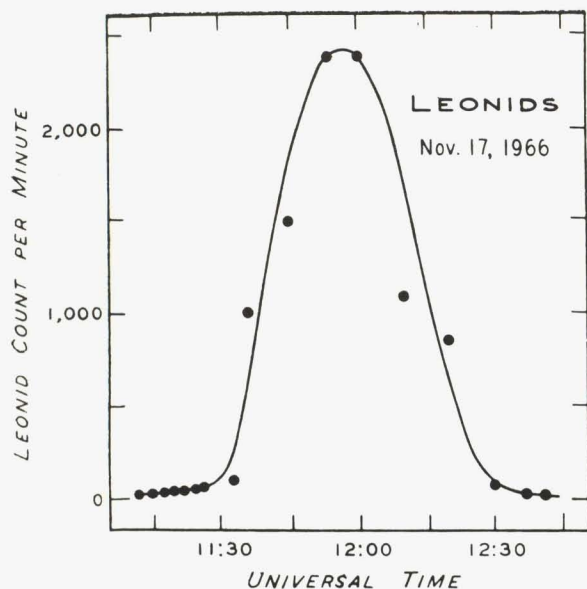


FIGURE 7.—Visual Leonid rates for a single observer (Kitt Peak, Ariz., November 17, 1966).

Milon secured excellent visual and photographic records of the Leonid shower on Kitt Peak, Arizona, at an elevation of 6850 feet. Milon is a regular contributor to the Ottawa visual meteor program, and his own reduction of the visual counts sent to the Meteor Centre at Ottawa is reproduced in figure 7. The enhancement of the visual rates over the background was somewhere in the range 10^3 to 10^4 , much higher than that recorded for the radar echoes. The reason for this discrepancy is not entirely clear. For these data the width between quarter-strength points is about 45 minutes, considerably narrower than for the radar records. The times for the peak of the shower as determined from the two sets of observations agree very well. Milon estimates 11^h55^m UT from his visual counts and the Ottawa radar gives 11^h58^m UT. Figure 8 is a photograph exposed by Milon for 210 seconds at the shower maximum (lens Voigtlander, f.l. 105 mm, F/3.5,



FIGURE 8.—Photograph by Milon of Leonid shower at maximum at approximately 12 hours UT, exposed for 210 seconds (Kitt Peak, Ariz., November 17, 1966).

Tri-X film). The Sickle of Leo appears at the center, and an overexposed image of Jupiter near Praesepe at the upper right. On the original negative over 60 Leonid trails are visible.

The 1966 Leonid shower may be regarded as typical of localized high concentrations of meteoroids that can be encountered in interplanetary space.

REFERENCES

- ANDERS, E., 1963, in *The Solar System*, 4 (Middlehurst and Kuiper, eds.), 402 (Univ. of Chicago Press).
 BEALS, C. S., M. J. S. INNES, and J. A. ROTTENBERG, 1963, in *The Solar System*, 4 (Middlehurst and Kuiper, eds.), 235 (Univ. of Chicago Press).
 BERG, O. E., and L. SECRETAN, 1967, *Smithson. Contrib. Astrophys.*, 11, 271.
 D'AIUTOLO, C. T., W. H. KINARD, and R. J. NAUMANN, 1967, *Smithson. Contrib. Astrophys.*, 11, 239.
 KRINOV, E. L., 1963, in *The Solar System*, 4 (Middlehurst and Kuiper, eds.), 183 (Univ. of Chicago Press).

- MCCRACKEN, C. W., W. M. ALEXANDER, and M. DUBIN, 1967, *Smithson. Contrib. Astrophys.*, **11**, 259.
- MILLMAN, P. M., 1963, *Smithson. Contrib. Astrophys.*, **7**, 119.
- MILLMAN, P. M., and B. A. MCINTOSH, 1964, *Canadian J. Physics*, **42**, 1730.
- , 1966, *Canadian J. Physics*, **44**, 1593.
- NAUMANN, R. J., 1966, NASA Tech. Note D-3717.
- NILSSON, C., 1966, *Science*, **153**, 1242.
- WOOD, J. A., 1963, in *The Solar System*, **4** (Middlehurst and Kuiper, eds.), 337 (Univ. of Chicago Press).

Page intentionally left blank

56. On Maintaining the Meteoritic Complex*

FRED L. WHIPPLE

Smithsonian Astrophysical Observatory
Cambridge, Massachusetts

The meteoritic influx on the Earth is derived from measurements of penetration of space vehicles, radio and photographic meteors, meteorite falls, Apollo asteroids, lunar craters, and comets. The total flux is about 2×10^{-16} g/cm²-sec on the surface of a corresponding nongravitating sphere. Such a cloud is self-destructive by collisions. It requires some 10 times the continuous contribution that the Poynting-Robertson effect alone would demand to maintain the zodiacal light and cloud, that is, some 10 tons per second for quasi-equilibrium.

This observational model is consistent with the etching rates observed on stone and iron meteorites and on photographic meteoroids. Various observational and theoretical facts indicate that the cloud up to masses of about 10^5 grams is maintained by "live" comets. "Half-baked" asteroids, however, may compete with comets in contributing to the brightest fireballs. The stony meteorites may be maintained by collisional spallation from Earth-crossing asteroids induced by smaller bodies, the Apollo asteroids being derived from the asteroid belt by the gravitational effects of Mars.

The cometary meteoritic complex of smaller particles, carrying most of the mass, has a mean lifetime of some 1.7×10^5 years. Certain puzzles remain in the orbital properties of the Apollo asteroids and of iron and stone meteorites.

THIS PAPER concerns the "ecology" of the meteoritic material in the solar system and involves its immediate origin from larger bodies and some details of its dissipation. To date there is no evidence for any meteoritic matter with an immediate origin beyond the gravitational field of the Sun, nor is there an indication of any accumulative processes on smaller bodies. The meteoritic complex is self-destructive.

Comets provide a large known source of this small material. We shall accept the icy comet model (Whipple, 1950), in which the comets produce meteoritic material intrinsically by

solar radiation, which, via sublimation, releases gas, dust, and finite-size low-density meteoritic material into the planetary region of the solar system. Undoubtedly, comets can produce material extrinsically by collisional spallation. It is not yet clear whether larger comets that have somehow attained an aphelion distance within the orbit of Jupiter can, indeed, leave finite inactive nuclei indistinguishable from the smaller asteroids. Öpik (1963, 1966) has strongly supported this suggestion. The possibility is so extremely important from an evolutionary point of view that it needs to be demonstrated as true or false, not lightly accepted as probable. It specifies important factors and processes involved in the original development of the cometary nuclei themselves, presumably in the very early stages of solar system development. In

*This research has been supported in part by grants NSR-09-015-033 from the National Aeronautics and Space Administration, AF 19(628)3248 from the U.S. Air Force Cambridge Research Laboratories, and NAS 9-4873 from the NASA Manned Space Flight Center, Houston, Texas.

other words, we should make a special effort to demonstrate either the existence or the absence of many persistent, inert cometary nuclei.

The asteroids as well as comets are important in the meteoritic complex, acting as a source of smaller bodies, presumably the meteorites, by means of collisional spallation. We have no direct knowledge that the larger satellites or Mercury may not make intrinsic contributions to the meteoritic complex by means of volcanic-type eruptions. Their contributions by collisional spallation are neglected in this discussion, although the Moon may be a minor contributor.

Among the outer satellites without atmospheres, the asteroids and the comets, all significant physical processes known to date are dissipative. We are concerned with activities within the orbit of Saturn, and our attention is concentrated mainly within that of Jupiter. Besides the intrinsic ejection processes and collisional spallation just mentioned, other dissipative processes include the elimination from the system by gravitation, the capture by bodies with atmospheres, and the reduction to gas by various processes, including close approaches to the Sun. There is every reason to believe that the solar wind eliminates gases almost immediately from any part of the inner solar system, while solar light pressure removes most particles smaller than a certain size.

This paper first treats in some detail the numerous dissipative processes. Then follow a quick summary of the factual knowledge concerning the distribution of the meteoritic complex and a detailed discussion of the process rates as far as they can be ascertained at the present time.

DISSIPATIVE PROCESSES OF THE INNER SOLAR SYSTEM

Solar Radiation

Direct Light Pressure

Light pressure in the Sun on a spherical particle of radius s and density ρ exceeds the solar gravitational attraction when

$$\rho s < 5.8 \times 10^{-5} \theta \quad \text{cgs} \quad (1)$$

where θ is the fraction of the incident solar radiation effective in transferring momentum to the particle.

Although equation (1) is satisfied only for submicron-sized particles of reasonable density and the value of θ is highly dependent upon their electrical characteristics, the process is responsible for eliminating considerably larger particles when they are injected into fairly eccentric orbits, for example, comet orbits. A slight reduction in the effective gravity because of light pressure throws them into hyperbolic orbits. This matter has been discussed by Harwit (1963), who shows that the smallest particles remaining in the solar system after ejection at low velocities from Comet Encke would have radii of the order of a few microns, and for Comet Halley a few tens of microns. Thus, we should expect contributions from comets to be confined to those in short-period orbits and for particles greater than a few microns. The comets of longer period, for other reasons (Whipple, 1955), should not be able to contribute significantly to the zodiacal light. Because of the effect of light pressure, it is not surprising that the zodiacal light and the influx rate of particles on the Earth become less significant at low masses of the order of 10^{-10} to 10^{-12} gram, as is shown, for example, in figure 1 and discussed by Southworth (1964) and Biermann (paper No. 39).

The Poynting-Robertson Effect

Because of the momentum of light, its reradiation or general reflection from a particle in orbit about the Sun produces a retarding force on the motion, as described by Robertson (1937) in relativistic terms, based upon an earlier suggestion by Poynting. Thus, the Poynting-Robertson effect (P-R effect) causes a general reduction in the eccentricity and major axes of small bodies in orbit about the Sun until, other circumstances permitting, they spiral near the Sun to sublimate. The time of spiraling into the Sun for a black, or perfectly reflecting, spherical particle of radius s and density ρ in an orbit of perihelion distance q (in AU) is given by the following equation:

$$\text{spiral time} = C(e) \rho s q^2 \times 10^7 \text{ yr} \quad (2)$$

where the factor $C(e)$ depends solely upon the orbital eccentricity e . This coefficient is 0.70 for a circular orbit, 1.9 for $e = 0.5$, 7.3 for $e = 0.9$, and

28.9 for $e=0.99$ (see Wyatt and Whipple, 1950). Öpik (1963) has shown that for Earth-crossing orbits the mean lifetime by gravitational perturbations is of the order of 10^8 years, and for Jupiter it is 10^6 years. Hence, the P-R effect can be significant only for particles of dimension ≤ 10 centimeters for Earth-crossing orbits, and $< 10^{-1}$ centimeter for Jupiter-crossing orbits.

Charge on Particles

Solar radiation on an isolated particle can, by the photoelectric effect, impart a positive charge of a few electron volts (see papers of Belton, No. 43; Rhee, No. 41; and Singer and Bander-mann, No. 54). A charged particle then becomes susceptible to other physical forces that may interact with its electrical charge.

Direct Material Sublimation

Near the Sun, sublimation of meteoritic material becomes significant. (See Kaiser and Newkirk, paper No. 42.) Particles less than a few hundredths AU from the Sun are soon eliminated.

The Solar Wind

Sputtering

Wehner, Kenknight, and Rosenberg (1963) show that a solar wind flux of 2×10^8 protons/cm²-sec, moving with a velocity of 600 km/sec with a normal solar component of heavier ions, will produce a radial sputtering erosion of 0.4 Å/yr for iron or stony meteorite surfaces, a smaller effect than earlier estimates (Whipple, 1955). We can evaluate the significance of sputtering by comparing its erosion rate to the P-R spiraling rate. Let us adopt the Allen (1963) approximation for the P-R effect ($C(e)q^2=0.7aq$ in eq. (2)) with q taken as constant. We then derive for a sputtering rate of 0.4 Å/yr in s the relation:

$$\frac{ds}{s} \cong \frac{da}{a} 0.10 \frac{(1-e)}{(1-e^2)^{1/2}} \quad (3)$$

For $e=0$ the sputtering rate of loss in radius is 0.10 the rate of loss in the semimajor axis, while for $e=0.5$, 0.99, and $(1-\delta)$ the factor is reduced to 0.06, 0.007, and $0.07 \delta^{1/2}$, respectively ($\delta \ll 1$). Hence, sputtering is not relatively important in small-particle ecology.

An Injection Process

The solar wind makes a minor contribution of a nondissipative character by injecting heavier atoms into the matrices of solids in space. Because of the relative dearth of heavier atoms as compared with hydrogen, this contribution is small compared with the loss produced at the surface through sputtering. Laboratory experiments of such trapping have been conducted by Bühler, Geiss, Meister, Eberhardt, Huneke, and Signer (1966).

Pressure on Ions in Space

The solar wind by direct interaction and charge exchange with atoms or molecules in space, coupled with the collisionless shock wave of magnetohydrodynamic origin, can help produce and can force back ions in cometary Type-I tails. Since no free atom or molecule within planetary distances can escape eventual ionization by solar radiation, the solar wind acts as a cleaning agent to eliminate all free gas from within the inner solar system.

Pressure on Meteoritic Particles

The solar wind, because of its relatively low velocity with respect to light, carries a small radial pressure, about 10^{-3} of that due to solar radiation. The pressure effect of the solar wind can be neglected.

Pseudo-Poynting-Robertson Effect

For a proton flux of 2×10^8 protons/cm²-sec at 1 AU radially from the Sun, the mass encountering a surface is 0.22 of that contributed by solar radiation. For total bulk interception and isotropic reradiation or ejection, the pseudo-P-R effect by the average solar wind is then 0.22 of that induced by solar radiation. Hence, the solar wind increases the normal P-R effect by 22 percent, or possibly more for charged particles or those for which diffraction reduces the effective area for radiation. (See Whipple, 1955, and Biermann, paper No. 39.)

Magnetic-Field Effects

The existence of appreciable magnetic fields carried by the solar wind and solar storms may produce significant forces on small isolated parti-

cles positively charged by solar photoionization. Parker (1964) has made this suggestion, and predictions of such effects on the motions of small particles have been made by Belton (paper No. 43) and by Singer and Bandermann (paper No. 54). For extremely small particles ($\leq 1 \mu$), there are a number of dissipative effects involving electric charge and electromagnetic effects. We shall not consider them in this discussion because the predictions remain difficult and uncertain.

MISCELLANEOUS EFFECTS

Öpik (1951, 1956) has discussed a number of dissipative effects on small particles in space, including some depending upon rotation. Rotation can be set up by particle collisions and by solar radiation for asymmetrical bodies. In turn, the rotation can make possible forces normal to the radius vector by interaction with particles and radiation. The latter is called by Öpik the Yarkovsky effect. Also, Öpik shows that a rapid rotation rate, like too great an electrical charge, may explosively destroy a small particle, especially if the particle is of low density and of weak structural strength.

Since no detailed theories suitable for direct application are available for these various processes, they will be ignored in this paper, although it is not impossible that they may be significant in space.

Collisional Effects

Meteoritic Erosion in Space

Direct evidence for erosion of stony meteorites in space can be deduced from the low exposure ages, less than approximately 5×10^7 years, obtained by measurements of short-lived radioactive elements produced by cosmic-ray spallation. The concept was first presented by Whipple and Fireman (1959) for an iron meteorite. Cosmic-ray spallation can produce stable isotopes such as Ar^{38} and radioactive isotopes such as Ar^{39} (half-life order of ~ 300 yr) from heavier atoms in meteorites; the radioactive isotopes measure the current spallation rate due to cosmic rays, and the stable isotopes the total accumulation. Combined, the rate and the accumulation lead to a calculated exposure age. At first such an exposure age was interpreted as the interval

since the meteorite broke off from a much larger body in which it had been protected from cosmic rays. On the erosion hypothesis the earlier greater size of the meteorite reduced the accumulation rate of the stable isotope in the earlier stages and led to a shorter measured exposure age. An alternative explanation can be made by assuming that the cosmic-ray intensity increases with time.

Fireman and DeFelice (1961) suggested that stones exhibit much shorter exposure ages ($< 5 \times 10^7$ yr) than do irons because of their greater friability and brittleness; stones are thus eroded more rapidly than irons by collisions with interstellar dust. This thesis has been supported strongly by Fisher (1966). Whipple (1963) noted that erosion is a likely cause of the relatively short lives deduced for bright photographic meteors. Nearly half of these bodies move in identifiable streams, and those with aphelia within the orbit of Jupiter show no alinement of their lines of apsides with that of Jupiter, as is observed for the asteroids and might be expected for bodies with lifetimes greater than 10^4 to 10^5 years. Perturbations should also cause these orbits to lose their identification with streams over periods of the order of 10^4 years. Hence, it appears that cometary meteoroids are eroded at a rate of the order of a micron per year in radius.

These conclusions are summarized in table 1. I assume that the encountering small mass knocks out 200 times its mass in iron, 1000 times in stone, and 3200 times in cometary meteoroids. We can fairly assume that the erosion is caused by impacts with dust particles within Jupiter's orbit moving at an inclination of some 20° to the plane of the ecliptic. (See, e.g., Southworth, paper No. 31.) At a mean collisional speed of some 10 km/sec for average encounters in this region, the mean density of small particles ($< 10^2$ g) is of the order of 2×10^{-22} g/cm³ and provides an influx rate of some 1.0×10^{-16} g/cm²-sec on the surface of a nongravitating sphere. At the Earth the space density and influx rates should exceed the average by a small factor. Presumably this dust is the material that produces the scattering and diffraction of sunlight observed in the zodiacal light and the Fraunhofer corona.

TABLE 1.—*Erosion in Space*

Particles	Exposure age, yr	Etching rate, cm/yr	Etching rate, g/cm ² -sec	Impact rate, g/cm ² -sec
Irons.....	$\sim 5 \times 10^8$	5×10^{-8}	1.3×10^{-14}	6×10^{-17}
Stones.....	$< 5 \times 10^7$	5×10^{-7}	5.0×10^{-14}	5×10^{-17}
Cometary meteors...	$\sim 10^4$ *	$\frac{2.3}{\rho} \times 10^{-5}$ †	7.0×10^{-13}	20×10^{-17}

* Average lifetime.

† ρ = density.

It must be noted that the calculated and critical erosion rate for stones is proved unless one of two assumptions is made: (1) that no stony meteorites were broken to cross the Earth's orbit prior to 50 million years ago, or (2) that cosmic radiation has increased markedly in this period of time.

Larger Body Collision

Grinding effects due to collisional spallation must occur among the larger bodies of the asteroid belt, including the Mars-crossing and the Earth-crossing asteroids. Piotrowski (1953) has shown that within the asteroid belt the continuous grinding should lead to a distribution of particle size giving a population index of $S=2$.

The population index S applies to a distribution of particle sizes following an inverse power law of the dimension, where the cumulative number larger than a given radius S , area A , or mass m is given in the forms s^{-S} , $A^{-S/2}$, or $m^{-S/3}$. The distribution of the observable asteroids (Kuiper, Fujita, Gehrels, Groeneveld, Kent, van Biesbroeck, and van Houten, 1958) indicates that Piotrowski's law, although not completely proved theoretically, is not far from observation. For a population index $S=2$, the integrated area of bodies in any logarithmic step in dimension is constant, so that integration to diffraction-limited small-particle sizes does not lead to excessive surface area. Hawkins (1960) shows that this comminution law in ball mills for rock crushing begins at first breakage with $S=2$ and proceeds to approximately $S=3$ for continued crushing.

In hypervelocity-impact breakage, Gault, Shoemaker, and Moore (1963) measure the dis-

tribution of particle sizes resulting for a basalt target. They find that the ratio of the total mass of the crater material to that of the projectile at 14.1 km/sec is $\phi \approx 10^3$; the inverse ratio of the largest fragment to the total mass ejected is approximately $\zeta=27$ and a population index $S \approx 2.4$ for the broken fragments. They find that various losses amount to about 30 percent, due mostly to evaporation. Since these are the only measures available to the writer, they will be adopted as applicable to collisional spallation by hypervelocity impact on stony meteoritic bodies in space. Since it appears quite possible that the meteorites falling on the Earth have been dislodged from Earth-crossing asteroids by hypervelocity impacts, this possibility will be considered in subsequent discussions.

That the Moon contributes appreciably to the meteoritic complex in space is doubtful. We (Jacchia and Whipple, 1961) find no significant evidence for a direct lunar contribution to the photographic meteors. On the other hand, Arnold's (1965a, b) discussion of orbital changes produced for such particles by Earth perturbations makes a definitive answer somewhat less clear-cut until more precise orbits have been determined for meteorites. Unless more convincing evidence is accumulated, I prefer to ignore this probably small source of material.

Gravitational Effects

Öpik (1963) has developed a theory showing the gravitational effects that a planet exerts on the orbits of bodies crossing the orbit of the planet in question. Close approaches produce large changes in the orbital elements, which can result in ejection or the shifting of the orbits

to cross those of other planets. Captures by the planets or by the Sun are other possible endings to this stochastic process. For objects in orbits crossing those of the Earth or Venus, Öpik finds a mean life of the order of 1.0×10^8 years, which usually results in capture. For Mars, the corresponding mean life is considerably larger, some 6×10^9 years, again usually resulting in capture; this means that objects in Mars-crossing orbits have not been drastically reduced in number by Mars since the formation of the solar system, some 4.7×10^9 years ago. For Earth-crossing orbits, Arnold (1965a, b) has demonstrated by Monte Carlo calculations the validity of Öpik's theory. For Jupiter, the mean life is of the order of 10^6 years and is quite likely to result in elimination from the system.

Öpik further shows that objects in purely Mars-crossing orbits have a finite probability of being moved into orbits crossing that of the Earth. To maintain a population in Earth-crossing orbits with a mean life of 10^8 years, Öpik finds that about 300 times that many objects must continuously exist in orbits that cross only the orbit of Mars.

It is generally recognized that the comets of short periods (less than 100 yr) are captured from highly eccentric, randomly inclined orbits by planetary perturbations, primarily by Jupiter. These perturbations lead to direct-moving orbits with mean inclinations of the order of 30° to Jupiter's plane of motion; the aphelia tend to be concentrated near and beyond Jupiter's orbit.

THE APOLLO ASTEROIDS, COMETS, AND LUNAR CRATERS

The Apollo Asteroids

To form any judgment as to the asteroidal or cometary origin of the Earth-crossing or Apollo asteroids, we must first estimate their numbers. Öpik (1963), on the basis of observational circumstances, estimates the number to be 39 exceeding a diameter of 1.0 kilometer. Whipple (1966a) notes that none of the eight discovered Apollo asteroids has been rediscovered by chance. This leads to the probability of 0.50 that the total number does not exceed 43, and 0.75 that there are fewer than 100 in all. Here I shall assume that there are 50 Apollo asteroids of absolute magnitude < 18.2 (apparent magni-

tude at the hypothetical distances of 1 AU from both Sun and Earth).

The masses of small asteroids can be estimated only from their magnitudes by assuming both albedos and mean specific densities. I adopt with Kuiper, Fujita, Gehrels, Groeneveld, Kent, van Biesbroeck, and van Houten (1958) the lunar Bond albedo of 0.07 and a density of 3.5 g/cm^3 , which lead to a radius of 10 kilometers for an absolute magnitude of 12.0, and to a radius of 0.58 kilometer and mass of $10^{15.45}$ grams for the lower mass limit of the 50 assumed Apollo asteroids. Enormous uncertainty lies in these values because there are no measures whatsoever for the albedos of small asteroids or the nuclei of small comets. The albedo might lie in the range from 0.03 to 0.30, producing a possible uncertainty in radius by a factor of 3, or in mass by a factor of 30. Possibly the albedo is underestimated because darkening of the surface must occur by solar wind ions. No darkened particles knocked off a small asteroid by collision can be recovered, as is usually the case for the Moon. Hence, the darkening process for the asteroids may be less pronounced than for the Moon.

Figure 1 depicts the influx rate on the surface of a gravitationless sphere in an Earth-like orbit for the assumed 50 Apollo asteroids of mass $> 10^{15.45}$ grams with an assumed mean life for Earth crossing of 10^8 years and a mean

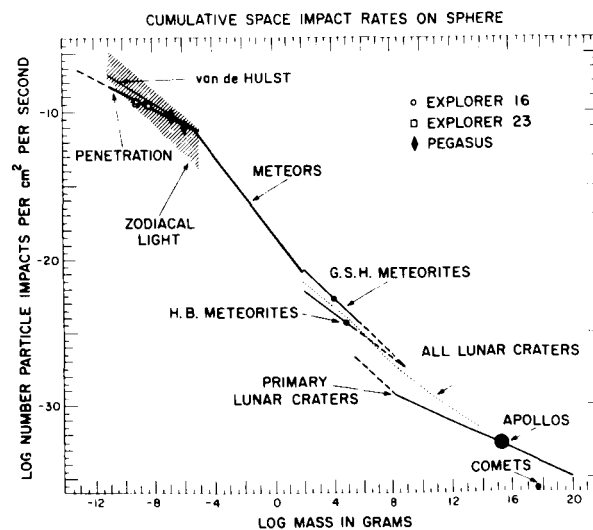


FIGURE 1.—Cumulative impact rates of meteoritic material on a sphere near Earth orbit.

encounter velocity of 15 km/sec (19 km/sec on the Earth). The cumulative influx rate for masses exceeding $10^{15.45}$ grams is $10^{-32.7}/\text{cm}^2\text{-sec}$. The population index is not well enough known for these objects to provide a flux-mass curve, although Öpik (1963) estimates $S=2.7$.

To conclude that the Mars perturbations on Mars-crossing asteroids cannot produce enough Apollo asteroids to maintain the quasi-equilibrium numbers, Öpik extrapolates the observed number of much larger Mars-crossing asteroids to the smaller asteroids. At Mars, the observations are probably complete to a diameter of 10 to 30 kilometers. Öpik assumes $S=1.6$ ($m^{-0.53}$ law) to give the extrapolation in the third column of table 2. At minimum diameter 1.05 kilometers, some $300 \times 50 = 15\,000$ Mars-crossing asteroids are required. Table 2 shows the extrapolation for $S=2.0$ ($m^{-2/3}$ law in column 4) and for $S=2.4$ ($m^{-0.8}$ law in column 5). Kuiper, Fujita, Gehrels, Groeneveld, Kent, van Biesbroeck, and van Houten (1958) find $1.6 < S < 3.0$ for larger asteroids. At $S=2.7$, as assumed by Öpik for the Apollo asteroids, a more than adequate number would be provided. At $S=2$, perhaps the best present estimate available, the observed and calculated numbers are in fair agreement.

TABLE 2.—*Distribution of Mars Asteroids*

Minimum diameter, km	Observed number	$m^{-0.53}$ law	$m^{-2/3}$ law	$m^{-0.8}$ law
68	1	1	1	1
34	5	5	4	5
17	11	15	16	28
8.5	22	45	64	147
4.2	31	135	256	776
2.1	32	405	1 024	4 100
1.05	33	1 215	4 096	20 000
.52	34	3 645	16 400	100 000

On the basis of these considerations alone I do not feel that it is necessary to assume that old inactive cometary nuclei must be postulated to supply the observed Apollo asteroids. Other aspects of the problem are taken up in later sections.

Cometary Nuclei

The basis for the point comets in figure 1, the cumulative flux rate for cometary nuclei, has been presented previously (Whipple, 1966a). The evaluation is highly uncertain. I adopt a total rate of $1/3$ comet/yr for apparitions of comets with perihelion distance ≤ 1 AU and an absolute magnitude $H \leq 6.0$ (H =apparent magnitude at 1 AU from Earth and Sun on the basis of an inverse-square law of brightness variation from the Earth and an inverse-fourth law from the Sun). The corresponding mass is calculated by the relation

$$\log \text{mass} = 21.34 - 0.6 H \quad \text{cgs} \quad (4)$$

based on Öpik's (1963) relation for a specific density of 1.3 g/cm^3 . The rate of influx is based on two crossings per apparition of a comet on a sphere of area $2\pi(\text{AU})^2$.

Lunar Craters

The Moon is a proving ground for natural interplanetary missiles. The distribution of primary lunar craters (fig. 1) has become available from the remarkable Ranger photographs made by the National Aeronautics and Space Administration and the Jet Propulsion Laboratory. The measures and calculations by Kuiper, Strom, and LePoole (1966) lead to the cumulative number N , corresponding to impacting masses exceeding m grams and given by

$$\log N = \sim 25.14 - 0.49 \log m \quad \text{cgs} \quad (5)$$

on the lunar maria for $m > 10^{8.3}$ grams (fig. 1). Here I assume an age of 4×10^9 years for the impacting interval. Kuiper, Fujita, Gehrels, Groeneveld, Kent, van Biesbroeck, and van Houten (1958) find a curve for $m < 10^{8.3}$ grams with about twice the aforementioned slope. Below what mass or crater size overlapping and destructive crater effects predominate is a matter of opinion, although $m = 10^{8.3}$ grams is suggested by the data. A much larger limiting mass is possible.

The dotted curve labeled "All lunar craters" in figure 1 is based on Shoemaker's (1965) crater counts on Ranger VII photographs of Mare Cognitum and on Shoemaker, Hackman, and Eggleton's (1961) observations that for high-energy

terrestrial explosion craters, the crater diameter and explosive energy are fairly well connected by the relation

$$\text{Crater diameter} = 0.00230 W^{1/3} \quad \text{cgs} \quad (6)$$

where W is the kinetic energy at a velocity of 15 km/sec. The resultant cumulative frequency distribution for all craters is

$$\log N = -23.3 - 0.6 \log m \quad \text{cgs} \quad (7)$$

The apparently perfect agreement in figure 1 between the calculated impact rates for lunar craters and the Apollo asteroids is, of course, fortuitous. Uncertainties of more than an order of magnitude exist in the calculated masses, not to mention uncertainties concerning the ages of the lunar maria. Even greater uncertainties apply to the data point for comets in figure 1. One may conclude tentatively that "live" comets do not contribute much to the formation of lunar craters, although this conclusion is by no means definitive. Figure 1 tells us nothing about the frequency of "old" comet nuclei, but does suggest that the supply of Apollo asteroids has been fairly stable for a significant astronomical interval. This gives us some confidence that we may be dealing with a quasi-stable distribution of larger bodies in the meteoritic complex.

THE METEORITIC POPULATION OF SMALL BODIES

This section has been intentionally curtailed because of the comprehensive coverage of the subject by Millman (paper No. 55).

In figure 1, the impact rates for meteorites of mass $> 10^2$ grams are based on estimates by G. S. Hawkins (1960) (GSH) and by Harrison Brown (1960) (HB), both estimates being corrected from terrestrial falls to outside the Earth's atmosphere by an ablation correction of five times. The cumulative impact rates become

$$\text{(GSH)} \log N = -18.67 - \log m \quad \text{cgs} \quad (8)$$

$$\text{(HB)} \log N = -20.54 - 0.77 \log m \quad \text{cgs} \quad (9)$$

For the meteors in the mass range from 10^{-5} to 10^{+2} grams, the cumulative influx rate is taken as

$$\log N = -18.30 - 1.34 \log m \quad \text{cgs} \quad (10)$$

This equation is taken from a recent compilation (Whipple, 1965) with a correction of a factor of 2 in number to allow for Earth shadowing in the original equation and a factor of 1/1.3 to allow for the effect of the gravitational attraction of the Moon as compared with that of the Earth (velocity at Earth = 22 km/sec). The coefficient of 1.34 ($S=4$) for $\log m$ is based upon the photographic meteor studies of Hawkins and Upton (1958), consistent with determinations for visual meteors by Millman and Burland (1957). The luminous efficiency factor for photographic meteors has been determined from artificial meteors and recognized asteroidal meteors by Cook, Jacchia, and McCrosky (1963), and leads to a cometary meteoroid density of 0.44 g/cm³. The mass determination is in fair agreement with more recent determinations by Verniani and Hawkins (1964) based upon radio-meteor observations in the Harvard Meteor Program and from calculations of ionizing efficiency.

Undoubtedly the meteor influx curve is not a straight line in the $\log N - \log m$ plane, and radar-meteor data generally give a smaller value by about a factor of 10 than that of equation (10) for masses below 10^{-3} to 10^{-2} gram. The calibration of the radio-meteor mass scale is particularly difficult, as is the correction at small velocities for the electron-production function and at high velocities for the electron spreading in the high atmosphere. Until the radio-meteor data are well calibrated at faint optical magnitudes, I will have little confidence in the absolute values of the mass flux deduced from radio data. Orbital data are similarly prejudiced by this observational optimization in the middle-velocity range. Temporal and spatial variations over the Earth, on the other hand, can generally be well determined from radio data.

In the mass range from 10^{-6} to 10^{-10} gram, the penetration data in space from the NASA Explorer and Pegasus probes are remarkably consistent and apparently more precisely calibrated than any other data used for figure 1. I have

adopted the directly reduced data by Naumann (1966), from the penetration experiments, as the most complete and satisfactory. These data are corrected to deep space near the Earth's orbit by a factor of $1/1.3$ in N for Earth attraction, and by a factor of π to correspond to 2π ster of exposure on an open sphere. The Explorer and Pegasus data are fitted by least squares to

$$\log N = -13.85 - 0.51 \log m \quad (11)$$

and labeled "Penetration" in figure 1 in the range $10^{-11} < m < 10^{-5.36}$ gram.

For comparison, van de Hulst's (1947) original estimate based on his theory of the zodiacal cloud is plotted from the equation

$$\log N = -14.50 - 0.66 \log m \quad \text{cgs} \quad (12)$$

The agreement between the "Penetration" and the "van de Hulst" lines is rather striking, if fortuitous. For the much wider range in particle flux from theories of the zodiacal cloud, note figure 1 and refer to several papers in this symposium, especially paper No. 55 by Millman.

I have left out of consideration the near-Earth acoustic measures of impacts by rockets and satellites and the collection data, since they are orders of magnitudes greater than the apparently reliable penetration data. The latter and the meteor data lead to a total influx rate of small particles amounting to 1.6×10^{-16} g/cm² (2π ster)-sec. At an impact velocity of 15 km/sec, this corresponds to a space density $\rho = 4 \times 10^{-22}$ g/cm³ near the Earth's orbit. This influx and space density are consistent with the erosion rates observed for irons, stones, and cometary meteoroids as indicated previously in the section "Meteoritic Erosion in Space."

For future discussions I shall adopt the "Penetration" and "Meteors" curves (eqs. (10) and (11)) in figure 1 for other basic calculations without a specific lower cutoff in mass. Most of the mass is contributed by particle masses in the neighborhood of 10^{-6} to 10^{-3} gram, less than 0.1 centimeter in radius. The discontinuity at $m = 10^{-5.6}$ gram cannot be physically significant. The use of straight lines in the $\log N - \log m$ plane sim-

plifies calculation, and we have inadequate data to produce a proper curve. The flattening of the observed curve near 10^{-10} gram suggests a curvature that in Naumann's (1966) solution leads to an absence of particles much smaller in mass, consistent with the solar-light pressure theory for the partially opaque dielectric particles that we might expect.

MASS INPUT REQUIRED TO MAINTAIN THE ZODIACAL CLOUD

Classical Viewpoint

We must assume that only very small particles are significant in producing the diffraction, scattering, and reflection of sunlight that provides the zodiacal light, and we have seen that the mass influx to the Earth is carried primarily by particles less than 0.1 centimeter in radius. If all the small particles were undisturbed by sputtering or mutual collisions, they could spiral toward the Sun by the P-R effect. This I have shown (Whipple, 1955) requires a continuous contribution of only about 1 ton/sec, regardless of particle size or density if the necessary particles are somewhat larger than the wavelength of light. In fact, however, collisions and particle breakup will increase the quasi-equilibrium input rate (Whipple, 1955), while the problem is quite complicated by the possible need for submicron particles, which appear to be eliminated rapidly by both light pressure and solar wind.

Total Mass of the Zodiacal Cloud

Once we have determined the total mass of the zodiacal particulate cloud, we can determine the needed input rate by calculations of the particle lifetimes. If we assume a mean space density of 2×10^{-22} g/cm³ over a volume of 3.5 AU radius about the Sun within $i < 20^\circ$ of the ecliptic, the total mass of the zodiacal cloud becomes 4.5×10^{19} grams.

We may make another estimate for those particles with perihelion distance of < 1 AU. For a mean orbital period of 3 years, the Earth of radius R will intercept a fraction $1.3R^2/1.5(2 \sin i)$ (AU)²/yr, or 7.2×10^{-17} /sec. At an influx rate of 1.6×10^{-16} g/cm²-sec, this leads to a total mass of 1.1×10^{19} grams for the zodiacal cloud ($q < 1$).

Since the first estimate of 4.5×10^{19} grams is probably too high, the outer region probably being less dense, and since the latter estimate of 1.1×10^{19} grams is too low since $q > 1$ AU for perhaps half the mass, a reasonable estimate is perhaps 2.5×10^{19} grams for the entire cloud.

For a mean life of 10^5 years, this mass corresponds to a total influx rate of 8 tons/sec for the entire cloud. By the pure P-R effect a particle of density 1 g/cm^3 in an orbit of $q=1$ AU and $e=0.5$ ($C(e)=1.92$) with a life of 10^5 years would have a radius of some 52μ . These calculations, based on the measured influx rates of particles on the Earth, are encouragingly close to the classical calculation of 1 ton/sec total input to the zodiacal cloud.

We have noted that for particles micron sized or greater in dimension the solar wind increases the pure P-R effect by some 22 percent, and solar wind sputtering reduces the radius at a rate 10 percent or less of the rate of decay in perihelion distance. Other dissipative effects except collisions do not appear to be significant. Let us then adopt the P-R effect increased by 30 percent and compare collisional lifetimes with the P-R lifetimes for small particles. In this manner we can estimate the input mass rate to maintain the zodiacal cloud. Later we can consider likely sources of material and the actual production of the zodiacal light.

Collisional Loss Rates for Small Particles

When the observed flux of particles at the Earth is known, the calculation of the rate of collisional destruction as a function of particle size is relatively straightforward. This calculation combined with the P-R effect provides a mean life for average particles that can be used to calculate the required input rate for the zodiacal cloud.

The collisional loss rate for small particles must be considered as made up of two parts, erosion and collisional destruction. For bright photographic meteoroids, in the mass range 10 to 0.1 grams, the erosion constitutes essentially the total effect, as we assumed earlier, because most of the mass is concentrated in much smaller particles, at least if $S > 3$, as we have assumed ($S=4$). Thus, as we go to smaller

particle radii, destructive collisions with particles of mass $> m/\phi$ must be considered separately from the erosion by particles of mass $< m/\phi$. The collisional destruction effect is now considered. Let the cumulative flux rate for mass $> m$ be $N/\text{cm}^2\text{-sec}\cdot(2\pi \text{ ster})$, where

$$N = \frac{K}{m^\beta} \quad \text{cgs} \quad (13)$$

and $\beta = S/3$.

The collisional area of a spherical particle of density ρ is $Am^{2/3}$, where $A = (3\sqrt{\pi}/4\rho)^{2/3}$. I adopt the cross section of the larger particle for completely destructive collision when the mass ratio of the two particles is less than ϕ . For destructive collisions of a particle of mass m , with smaller particles to a lower limit m_0 , the integrated flux in cross-sectional area is then

$$\begin{aligned} \text{Flux area} &= Am^{2/3} \int_{m_0}^m \frac{\beta K}{m^{\beta+1}} dm \\ &= AKm^{2/3} (m_0^{-\beta} - m^{-\beta}) \end{aligned} \quad (14)$$

For destructive collisions of larger particles up to mass $= m_l$ (area $= Am_l^{2/3}$) with mass m , the flux area is similarly

$$\text{Flux area} = \frac{\beta AK}{(2/3 - \beta)} \left(m_l^{2/3-\beta} - m^{2/3-\beta} \right) \quad (15)$$

so long as $\beta \neq 2/3$.

In the mass range $m < 10^{-5.36}$ g, from figure 1 and equation (11), I adopt $\beta=0.51$ and $K_{\text{obs}} = 10^{-13.85} \text{ g}^{0.51}/\text{cm}^2\text{-sec}\cdot(2\pi \text{ ster})$. However, K_{obs} must be corrected by a factor of 1/1.5 from a velocity of 15 km/sec near the Earth's orbit to the adopted mean collisional value of 10 km/sec, and by a factor of 4 to include 4π ster of flux. For a sphere of radius s , the total 2π ster of flux falls on an area of $4\pi s^2$, but $Am^{2/3}$ corresponds only to πs^2 . Also, I correct K by a factor of 1/2 to allow for a lower average space density than that near the Earth's orbit. Hence, for $m < 10^{-5.36}$ g, $K = 10^{-13.73} \text{ g}^{0.51}/\text{cm}^2\text{-sec}\cdot(8\pi \text{ ster})$ and $\rho = 1 \text{ g/cm}^3$.

For $m > 10^{-5.36}$ g, I adopt $\beta=1.34$, $\rho=0.44 \text{ g/cm}^3$, and $\log K = -18.18 \text{ m}^{1.34}/\text{cm}^2\text{-sec}\cdot(8\pi \text{ ster})$. For all values of m for these low-density particles I adopt $\phi=3200$, corresponding to

destruction by collision with a particle of mass $> m/3200$ at a velocity of 10 km/sec. Limiting the encounter area only to the cross section of the larger particle is a compromise, since the area for comparable particles is less than 4 times the adopted value, and the area is overestimated when the radii are highly different. Unfortunately, I have not had sufficient time to include the contribution to the zodiacal cloud of the smaller fragments introduced by collisions. This effect is doubtless significant.

For colliding particles of mass $< m/3200$, simple erosion is assumed at a rate of 3200 times the integrated mass of the small particles.

Calculation of Particle Lifetimes

Three different kinds of lifetime are now involved in our calculation:

(1) τ_{PR} = Poynting-Robertson spiraling lifetime (reduced by 30 percent from eq. (2)), where

$$\tau_{PR} = 1.16 m^{1/3} \times 10^7 \text{ yr} \quad \text{for } m < 10^{-5.36} \text{ g} \quad (16a)$$

$$\tau_{PR} = 1.52 m^{1/3} \times 10^7 \text{ yr} \quad \text{for } m > 10^{-5.36} \text{ g} \quad (16b)$$

(2) τ_e = erosional lifetime, where the total mass encountered at individual masses $< m/3200$ is assumed to erode 3200 times its mass from the larger particle.

(3) τ_c = collisional mean life equal to the time required for the flux area (eqs. (14) and (15)) to equal unity. Hence, $e^{-\tau_c}$ of the particles should survive if $\tau_{PR} = \tau_c = \infty$.

In combining these three types of lifetime, I have first calculated an intermediary lifetime τ_i from τ_{PR} and τ_e , corresponding to the reduction of τ_{PR} by erosion, where

$$\tau_i = \frac{\tau_{PR}\tau_e}{\tau_{PR} + \tau_e} \quad (17)$$

Finally, the destructive probability given by τ_c is combined with τ_i to give the final mean lifetime τ in the form

$$\tau = \tau_c(1 - e^{-\tau_i/\tau_c}) \quad (18)$$

The average lifetime T of the entire zodiacal

cloud is then the complete integral ratio

$$T = \frac{\int \tau(m) dm}{\int dm} \quad (19)$$

The results of the calculations are shown in table 3.

An interesting observation from table 3 is the relatively slow change in the mean lifetimes of the particles, which is considerably slower than the change in radius for the larger particles and only 5 times over the mass range 1.0 to 10^{-8} gram. At the largest particle sizes erosion is the limiting factor. This will hold up to masses of the order of 10^6 grams, where Earth perturbations begin to limit the mean life. Destructive collisions control in the middle range 10^{-2} to 10^{-5} gram, and finally, the corrected P-R effect controls for the smaller particles. Table 4 omits an important column, namely, the calculated input from breakup of larger particles. A rough calculation leads to a somewhat greater yearly input than output for particles in the mass range 10^{-7} to 10^{-12} gram by a factor of 2 to 3. The law for breakup of such low-density particles is not known, however, and the use of the relation found by Gault, Shoemaker, and Moore (1963) (Sec. II.C.2) for stones may not be applicable. A tendency for cometary material to be grainy at masses of $\sim 10^{-5}$ gram could greatly affect the distribution.

Even though table 3 will be considerably modified by a more accurate distribution law of particle flux with mass, particularly by the reduction in concentration near 10^{-5} gram, it explains a surprising characteristic of the mass distribution curve, namely, the large value of S or the rapid increase in numbers with decreasing mass. At intermediate and large masses in table 3, the self-destructive character of the zodiacal cloud controls the lifetimes and, by spallation, undoubtedly causes a large concentration of smaller masses. Finally, the P-R effect controls the loss of very small particles because collisions become less important, and so the distribution curve flattens out (S falls).

The present analysis is too crude (omitting the input factor by collisions) to predict the

TABLE 3. — *Distribution of Masses and Lifetimes*[Weighted mean life of all particles, $T = 8.3 \times 10^4$ yr]

Particle mass, g, log m	Particle radius, cm, log s	Percent mass, $10^{-0.5} m$ to $10^{+0.5} m$	Poynting-Robertson, ^a log τ_{PR}	Lifetimes, yr		Mean, ^b log τ
				Erosion, log τ_e	Collision mean, log τ_c	
-12.0	-4.21	0.02	3.06?	6.70	5.92	3.06?
-11.0	-3.87	.04	3.40?	6.54	5.84	3.40?
-10.0	-3.54	.14	3.73	6.39	5.76	3.73
-9.0	-3.21	.44	4.06	6.23	5.65	4.05
-8.0	-2.87	1.4	4.40	6.07	5.53	4.37
-7.0	-2.54	4.2	4.73	5.92	5.41	4.66
-6.0	-2.21	12.9	5.06	5.76	5.28	4.88
-5.0	-1.76	40.9	5.51	5.61	5.13	5.00
-4.0	-1.42	21.5	5.85	5.45	4.96	4.91
-3.0	-1.09	10.0	6.18	5.29	4.77	4.75
-2.0	-.76	4.6	6.51	5.14	4.40	4.40
-1.0	-.42	2.2	6.85	4.97	5.02	4.79
.0	-.09	1.0	7.18	5.17	5.69	5.10
1.0	.24	.5	7.51	5.45	6.36	5.42
2.0	.58	.2	7.85	5.76	7.02	5.75
> 2.0	.58	.2				

^a From eqs. (16a, b).^b From eqs. (17), (18), (19).

number of extremely fine particles ($s < 1 \mu$). If larger particles ($s \geq 2 \mu$) can indeed produce the polarization as well as the brightness of the zodiacal light, then the present solution is consistent. If submicron particles are the major contributors, as suggested by Powell, Woodson, Alexander, Circle, Konheim, Vogel, and McElfresh (paper No. 35), then the present solution is not very specific and gives too few very small particles. A more complete theory will be needed.

As noted in table 3, the mean lifetime of the entire small-particle population is calculated to be $T \sim 8.3 \times 10^4$ years. However, the contributions from the breakup of larger particles may be taken as one-half the losses, assuming a 30 percent loss to evaporation and submicron particles. This effectively doubles the mean life of the entire cloud to 1.7×10^5 years. Hence, the required total influx rate, previously found to be 8 tons/sec for $T = 10^5$ years, becomes some 4 tons/sec. With the observed distribution of masses we have failed by a factor of 3,

however, to destroy the brighter photographic meteors in 10^4 years. Similarly, for the stony meteorites our solution is inadequate by a factor of 2. Hence, we apparently need 10 to 20 tons/sec continuous input to maintain the zodiacal cloud in quasi-stable equilibrium, an estimate very close to the original 1955 estimate. Let us now look to the sources of this material.

ON THE SOURCE OF THE ZODIACAL CLOUD

Orbital Considerations

The general story of the photographic and radio meteors need not be repeated here. The mass range involved is from a few grams down to the order of 10^{-4} to 10^{-6} gram. The orbits are indicative of the short-period comets with a large fraction of streams among the brighter photographic meteors, and a lesser stream contribution among the radio meteors. The evidence is conclusive that the particles involved are in large measure highly fragile low-density objects, $\rho \sim 0.44 \text{ g/cm}^3$, as adopted earlier in this paper for the brighter meteors. From the physical

characteristics, less than 1 percent suggest a meteorite type of body of stone or iron. Orbitally, figure 2 illustrates the distribution of aphelion distances from the precision photographic meteors (Jacchia and Whipple, 1961) and a random sample (Hawkins and Southworth, 1961). The aphelion distances show no strong indication of any concentration near the asteroid belt at ~ 3 AU, the distribution filling in to Jupiter's orbit near 5 AU and falling away at greater aphelion distances in the manner of comets. The Mars asteroids, on the other hand, show the normal asteroid distribution with a maximum of aphelion distances just above 3 AU. From orbital considerations alone and the inclinations, one would deduce that more than 90 percent of the photographic meteors have cometary origin and, as noted above, the physical circumstances suggest an even higher percentage.

Among the radio meteors, the aphelion distances are somewhat more concentrated within the orbit of Jupiter than among the brighter photographic meteors, but there is no indication of an asteroidal origin. The orbits are suggestive of very short-period comets (see, for example, Millman, paper No. 55). We now have information concerning the much brighter fireballs up to masses of perhaps 10^6 grams or more, as presented by McCrosky (1966) from the Prairie

Network of observing stations covering more than 10^6 km² in the Midwest. The aphelion distances of some 3 dozen of these orbits reduced by McCrosky are presented in figure 3. Here we note a striking difference in the distribution of aphelia, a high concentration just within Jupiter's orbit and another concentration between 1 and 2.5 AU, a surprising gap occurring in the region 2.5 to 3.0 AU. The aphelia of the six photographic meteors that are known to be of meteorite physical structure show this same gap. Correspondingly, the eight Apollo asteroids have orbital aphelia distributed similarly. Before the Prairie Network bright fireball program was started, the author had expected the meteorite type of body to match the cometary meteoroid in frequency at apparent magnitudes of the order of -6 to -10 visual. McCrosky's result, which comprises much brighter and more massive objects than these, shows a very small percentage of nonfragmenting, apparently solid stones or iron bodies. Thus the evidence is strong that, among the bright fireballs, we are dealing with incoming bodies of weak physical structure, unless it is indeed possible that the "frothing process" found for melting stones (Allen and Baldwin, unpublished report) may cause a misinterpretation of meteoritic densities. For bodies with masses of many kilograms, however, this

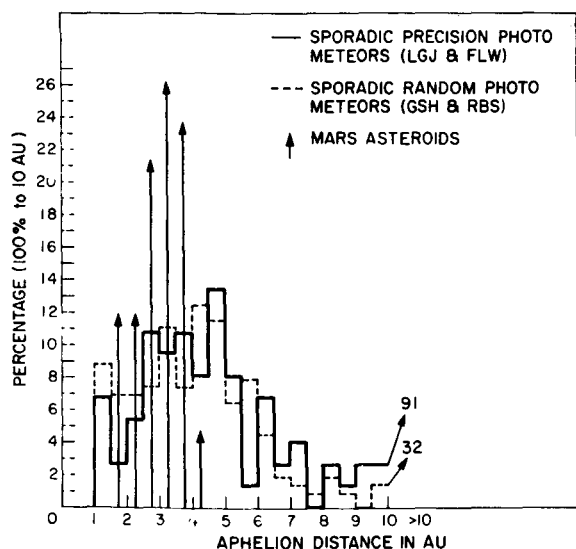


FIGURE 2.—Aphelion distances of precision photographic meteors and of Mars asteroids.

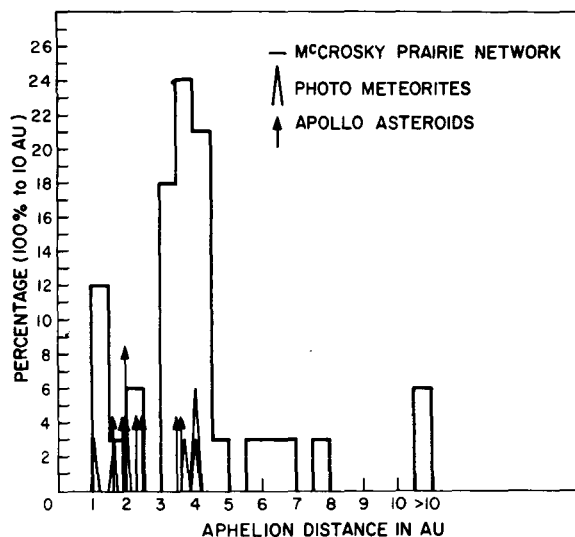


FIGURE 3.—Aphelion distances of fireballs (McCrosky Prairie Network), photographic meteorites, and Apollo asteroids.

effect should not be important. As an example of extraordinary friability in a very large body, McCrosky (private communication) reports a fireball of an approximate magnitude of -18 lasting for only 1 second and disappearing at an altitude of 70 kilometers. There is no question that a large fraction of bright as well as faint meteoroids are extremely friable and of low density.

I have no explanation for the minimum in the aphelion distribution centered at the middle of the asteroid belt as observed in common by bright fireballs, the photographic meteorites, and the Apollo asteroids. Quite possibly they are closely connected in origin, or perhaps the statistics are inadequate to make the conclusion incontestable. I have suggested (Whipple, 1966b) a further possibility, namely, that these friable bodies may include a considerable membership from the extreme limit of carbonaceous chondrites. If the asteroid belt has suffered only a minor fragmentation by collisions, it is possible that we are dealing with "half-baked" asteroids of small dimension, less than 30 kilometers in diameter, which are similar to the extremely friable and rather low-density carbonaceous chondrites. Hence, they could have a structure so weak that we find no examples on the Earth because of destruction in atmospheric passage, as is the case for cometary meteoroids.

Anders (private communication) suggests that the bodies with aphelia near Mars represent an origin as Mars-crossing asteroids, whereas those with aphelia within the outer limits of the asteroid belt to Jupiter represent old cometary nuclei. This assumption, as mentioned earlier in this paper, is quite possible, but it is one that I prefer not to make until direct proof is available.

In view of the high abundance of highly friable material in the mass ranges from 10^{-5} gram to 10^6 grams, the smaller particles being quite clearly of cometary origin, it would be quite surprising if among the still finer material the source should be other than cometary. The mean inclinations of the radio and photographic meteors, the bright fireballs, the Apollo asteroids, and the Mars-crossing asteroids all lie in the range from 11° to 20° as indicated in table 4, which summarizes the distribution of the aphelion distances. We should note that in all cases except for the Mars-crossing asteroids there is considerable selection toward small inclinations by the higher probability of encounter with the Earth. This is true also to some extent for the Apollo asteroids, since their chance of discovery is generally small; hence, those with higher inclinations may tend to be missed because of the still smaller chance of their having a close approach to the Earth.

TABLE 4.—*Distribution of Aphelia: Sporadic Meteoroids and Asteroids*

Category	Number of meteoroids and asteroids for aphelia of—			Mean inclination to the ecliptic for aphelia of < 5.2 AU
	< 2.5 AU	2.5 to 5.2 AU	> 5.2 AU	
Photographic meteors ¹	49	115	121
Photographic meteors ²	11	42	88	18°
(By cosmic weights).....	10	57	74	20°
Asteroidal meteors.....	3	3	0	15°
Fireballs ³	7	24	6	12°
Apollo asteroids.....	5	3	0	11°
Mars asteroids (mean $q = 2.85$ AU)....	4	30	0	15°

¹ Hawkins and Southworth (1961).

² Jacchia and Whipple (1961).

³ McCrosky (1966).

It is interesting to note from table 4 and figure 2 that the bright fireballs show a rather small percentage with aphelia beyond Jupiter's orbit. However, I note that, among this group of larger bodies, the etching rate gives them lifetimes of the order of 10^6 years, which in Jupiter-crossing orbits produces selective elimination by Jupiter perturbations. This, again, allows the possibility that most of the bright fireballs arise from a cometary origin, although some may be of the "half-baked" asteroid type.

In view of a cometary origin for the radio and photographic meteors, it is of considerable interest to see whether the expected input rate can indeed match the necessary 10 to 20 tons/sec required to maintain the zodiacal cloud in quasi-equilibrium. The next two sections of this paper consider this question.

Physical Characteristics of Comets

In estimates of the meteoritic contribution of cometary nuclei, it is important to have an estimate of the ratio of gas to dust in these bodies. We have little direct evidence as to the numerical value of this ratio. The observations of comets themselves give quite imprecise values since we see neither the parent molecules of the gases nor the meteoroids above micron dimensions. There is no check on the validity of the assumption that the original composition of material that freezes at temperature $\sim 30^\circ$ K approximates that of the present solar atmosphere. This assumption leads to a ratio ice/meteoritic (I/met) of about 8 (Whipple and Stefanik, 1966), representing a near maximum value, although a high concentration of hydrates (Delsemme, 1966) might give a higher ratio.

It is argued (e.g., Harwit, 1963) that the lack of an observable dust continuum in the spectra of "old" comets, such as P/Encke, as compared with relatively weak-band spectra in some "new" comets, means that old comets contain a smaller proportion of meteoritic material than new comets. I believe that the strong meteor contribution by P/Encke indicates possibly even the reverse. The basic idea is that in old large comets, the cores, either by heat or by compression, contain meteoritic material that is more consolidated than the fine dust in the

outer regions of "new" comets. There is evidence that the meteoroids from some comets, particularly when observed fairly soon after ejection, are of extremely low density. The best example is the striking Draconid meteor shower from Comet Giacobini-Zinner of 1946. The low-velocity (~ 21 km/sec) meteors disappeared nearly 20 kilometers higher in the atmosphere than average meteors of the same velocity (Jacchia, Kopal, and Millman, 1950). Few deceleration measures could be made, but the mean meteoroid density must have been 0.1 g/cm³ or possibly much less. Thus, it seems likely that the outer volumes of new comets may contain very friable or even "fluffy" meteoritic material that readily breaks into the fine dust often observed.

Our most direct evidence comes from cometary meteoroids themselves. Suppose the observed density is ρ , for which the compact solid density would be ρ_M . Suppose further that the icy fraction by mass was originally I , the solid density ρ_I , the fractional volume of void λ , and that no losses of earthy material occurred; then the total unit volume was originally made up as follows:

$$\frac{\rho}{\rho_M} + \frac{I}{\rho_I} + \lambda = 1 \quad (20)$$

Our desired icy mass fraction then becomes

$$I = \rho_I(1 - \lambda - \rho/\rho_M) \quad (21)$$

We may reasonably adopt $\rho_I = 0.9$ g/cm³, $\rho_M = 3.4$ g/cm³, and $\lambda = 0.1$, or 10 percent void volume. The solution is not very sensitive to λ for small values, so that table 5 may be indicative of I and $I/\rho = I/\text{met}$ as a function of the observed meteoroid density ρ .

Although the observed meteoroid density may represent a region of abnormally high concentration of meteoritic material in the comet because the meteoroid has, in fact, stuck together, we see that a typical value, adopted here, of $\rho = 0.44$ g/cm³ leads to $I/\text{met} = 1.58$. We may thus be justified in assuming that ices simultaneously eject with them one-half their mass in meteoritic material. I feel that the presence in a comet of highly volatile materials can lead to cracking, breakage, and ejection of con-

TABLE 5.—*The Icy Component and the Ice/Meteoritic Ratio*

ρ , g/cm ³	I	I/met
0.005	0.81	162
.05	.80	16
.10	.78	7.8
.20	.76	3.8
.30	.73	2.4
.40	.70	1.7
.44	.69	1.58
.60	.66	1.10
.80	.60	.75
1.00	.56	.56
1.50	.41	.27

siderable water ice, hydrates, and meteoritic material. Generally, this assumption leads to smaller icy nuclei and relatively more rapid disintegration than would occur if solar heat had to sublimate all the icy mass before it could be released from the nucleus.

Mass Contributions by Comets

To calculate the meteoritic contributions to the zodiacal cloud by actual comets, let us assume that the solar radiation is 0.9 effective in providing heat for sublimation of ices at a mean value of 450 cal/g, and that the comet in one perihelion passage receives effectively f years of radiation at 1 AU (see Whipple, 1955). Then for a comet density of 1.3 g/cm³, a ratio I/met of 2, and the mass-luminosity relation of equation (4), we find that the meteoritic loss per revolution about the Sun M_{rev} is

$$M_{\text{rev}} = f \times 10^{17.61-0.4H} \text{ g} \quad (22)$$

where H is the absolute magnitude of the comet.

For Halley's comet, $H=4.6$ magnitude, $f=1.5$, and period=76 years, the meteoritic mass loss becomes 5 tons/sec; and for Comet Encke with its average $H=9.0$ magnitude for the early 19th century and $f=3.5$, the mass loss is 3.5 tons/sec. The corresponding diameter for Comet Encke is 3.4 kilometers, whereas Roemer (1966) measures 1.2 kilometers for an albedo of 0.7, and 7.0 kilometers for an albedo of 0.02 from the brightness at large solar distances. We have meteor-stream evidence (Hamid and Whipple, 1951) that Comet Encke has been

in existence for several thousand years. Both from the basic principle of the icy comet model and from brightness observations of Comet Encke since 1786, we expect the brightness and rate of mass loss to be greater in the past, the rate of the change with time being quite uncertain (see, e.g., Krésak, 1965; Whipple and Douglas-Hamilton, 1966).

The orbit of Comet Encke is nearly unique, since its aphelion distance is well within Jupiter's orbit (4.10 AU). Hence, it is an ideal source for zodiacal cloud material. Only the very faint Comet Wilson-Harrington (1949 III) (aphelion 2.47 AU) and the extinct source of the Geminid meteor shower qualify as astronomically currently active sources. Material injected in Jupiter-crossing orbits is rapidly lost by Jupiter perturbations and by orbital velocity effects for very small particles.

Quite probably, then, Comet Encke over the past several thousand years has been the major support for maintaining the quasi-equilibrium of the zodiacal cloud. Our evidence is lacking for as much as the mean life of the zodiacal cloud, 1.7×10^5 years, but the 50×10^6 year maximum exposure ages for the stony meteorites indicate that erosion, averaged over this longer interval, has been as rapid as or more so than at present. Enormous comets have been observed in the past 300 years; Comet 1729 was a naked-eye object at 4.1 AU from the Sun. Thus, over 10^5 years one need not be surprised if the short-period comet supply does not average as well as or, indeed, better than our present sample. Note that a collision-controlled mean life leads to a zodiacal cloud density varying as the square root of the influx rate. Hence, rather large fluctuations of influx rate do not strikingly change the cloud mean density.

Thus, the consensus suggests that comets are an adequate source. A primarily asteroidal source would probably produce too high a concentration toward the fundamental plan of the solar system. Comets clearly contribute most of the material in the mass range 10^{-2} to 10^5 grams, and collisions are clearly a dominating destructive factor. The steepness of the particle population curve in this mass range and the concentration of mass in the 10^{-5} -gram range suggest, not simple col-

lisional spallation, but a tendency for some fundamental grain mass to lie in this region, not characteristic of meteorites but quite possibly of friable cometary material.

If a massive population of short-lived sub-micron particles is finally shown to be necessary

in producing polarization, or possibly color, in the zodiacal light, then the present data and this model will require adjustment in the submicron range. Otherwise, the model based directly on meteoritic observations appears to be a fair approximation.

REFERENCES

- ALLEN, C. W., 1963, *Astrophysical Quantities* (2d ed., London: Athlone Press).
- ARNOLD, J. R., 1965a, *Astrophys. J.*, **141**, 1536.
- , 1965b, *Astrophys. J.*, **141**, 1548.
- BROWN, H., 1960, *J. Geophys. Res.*, **65**, 1679.
- BÜHLER, F., J. GEISS, J. MEISTER, P. EBERHARDT, J. C. HUNEKE, and P. SIGNER, 1966, *Earth Planet. Sci. Letters*, **1**, 249.
- COOK, A. F., L. G. JACCHIA, and R. E. MCCROSKY, 1963, *Smithson. Contrib. Astrophys.*, **7**, 209.
- DELSEMMÉ, A. H., 1966, *Univ. Liège Inst. Astrophys. Coll. 8°*, **21**, No. 510, 69.
- FIREMAN, E. L., and J. DEFELICE, 1961, *J. Geophys. Res.*, **66**, 3547.
- FISHER, D. E., 1966, *J. Geophys. Res.*, **71**, 3251.
- GAULT, D. E., E. M. SHOEMAKER, and H. J. MOORE, 1963, *NASA Technical Note No. D-1767*.
- HAMID, S., and WHIPPLE, F. L., 1951, *Helwan Obs. Bull.*, **41**, 1.
- HARWIT, M., 1963, *J. Geophys. Res.*, **68**, 2171.
- HAWKINS, G. S., 1960, *Astron. J.*, **65**, 318.
- HAWKINS, G. S., and R. B. SOUTHWORTH, 1961, *Smithson. Contrib. Astrophys.*, **4**, 85.
- HAWKINS, G. S., and E. K. L. UPTON, 1958, *Astrophys. J.*, **128**, 727.
- JACCHIA, L. G., Z. KOPAL, and P. M. MILLMAN, 1950, *Astrophys. J.*, **111**, 104.
- JACCHIA, L. G., and F. L. WHIPPLE, 1961, *Smithson. Contrib. Astrophys.*, **4**, 97.
- KŘESAK, L., 1965, *Bull. Astr. Inst. Czech.*, **16**, 348.
- KUIPER, G. P., Y. FUJITA, T. GEHRELS, L. GROENEVELD, J. KENT, G. VAN BIESBROECK, and C. J. VAN HOUTEN, 1958, *Astrophys. J. Suppl.*, **3**, 289.
- KUIPER, G. P., R. G. STROM, and R. S. LEPOOLE, 1966, *JPL Tech. Rept. 32-800*, 35.
- MCCROSKY, R. E., 1966, *Meteorite Photography and Recovery Network*, NASA Contract NsG 291-62 Prog. Rept. No. 8.
- MILLMAN, P. M., and M. S. BURLAND, 1957, *Sky and Telescope*, **16**, 222.
- NAUMANN, R. J., 1966, *NASA Technical Note No. D-3717*.
- ÖPIK, E. J., 1951, *Proc. Roy. Irish Acad.*, **54A**, 165.
- , 1956, *Irish Astron. J.*, **4**, 84.
- , 1963, in *Advances in Astronomy and Astrophysics*, **2** (Z. Kopal, ed.), 219 (New York: Academic Press).
- , 1966, in *Advances in Astronomy and Astrophysics*, **4** (Z. Kopal, ed.), 301 (New York: Academic Press).
- PARKER, E. N., 1964, *Astrophys. J.*, **139**, 951.
- PIOTROWSKI, S. L., 1953, *Acta. Astron.*, **5A**, 115.
- ROBERTSON, H. P., 1937, *Mon. Not. Roy. Astron. Soc.*, **97**, 423.
- ROEMER, E., 1966, *Univ. Liège Inst. Astrophys. Coll. 8°*, **21**, No. 510, 23.
- SHOEMAKER, E. M., 1965, *JPL Tech. Rept. 32-700*, 75.
- SHOEMAKER, E. M., R. J. HACKMAN, and R. E. EGGLETON, 1961, in *Advances in Astronautical Sciences*, **8** (New York: Plenum Press), 70.
- SOUTHWORTH, R. B., 1964, *Ann. N.Y. Acad. Sci.*, **119**, 54.
- VAN DE HULST, H. C., 1947, *Astrophys. J.*, **105**, 471.
- VERNIANI, F., and G. S. HAWKINS, 1964, *Harvard Radio Meteor Proj. Res.*, Rept. No. 5.
- WEHNER, G. K., G. KENKNIGHT, and D. L. ROSENBERG, 1963, *Planetary Space Sci.*, **11**, 885.
- WHIPPLE, F. L., 1950, *Astrophys. J.*, **111**, 375.
- , 1955, *Astrophys. J.*, **121**, 750.
- , 1963, *Smithson. Contrib. Astrophys.*, **7**, 239.
- , 1965, Proceedings of the Third International Symposium, Bioastronautics and Exploration of Space (T. C. Bedwell, Jr., and H. Strughold, eds.), 7.

- WHIPPLE, F. L., 1966a, paper presented at Met. Soc. Meeting, Washington, D.C., November.
—, 1966b, *Proc. Roy. Soc. (London)*, **A296**, 304.
WHIPPLE, F. L., and D. H. DOUGLAS-HAMILTON, 1966, *Mém. Roy. Soc. Liège*, **12**, 469.
WHIPPLE, F. L., and E. L. FIREMAN, 1959, *Nature*, **183**, 1315.
WHIPPLE, F. L., and R. P. STEFANIK, 1966, *Univ. Liège Inst. Astrophys. Coll. 8°*, **21**, 33.
WYATT, S. P., and F. L. WHIPPLE, 1950, *Astrophys. J.*, **111**, 134.

List of Participants

- ALLEN, W. H., NASA, Ames Research Center
ALLER, L. H., University of California, Los Angeles
ALVAREZ, J. M., NASA, Langley Research Center
BANDERMANN, L., University of Miami
BELTON, M. J. S., Kitt Peak National Observatory
BERG, O. E., NASA, Goddard Space Flight Center
BIERMANN, L., Max-Planck-Institut für Physik und Astrophysik, Munich
BLACKWELL, D. E., University of Oxford
BOGGESE, R. L., Haleakala Observatory, University of Michigan
BRANDT, J. C., NASA, Institute for Space Studies
BUNTON, G. W., Bishop Museum and Planetarium, Honolulu
CAGLE, B., Office of Naval Research, Pasadena
CARR, M. H., Geological Survey, Menlo Park
DEIRMENDJIAN, D., Rand Corporation, Santa Monica
DOHNANYI, J. S., Bellcomm, Washington
DOZIER, J. B., NASA, Marshall Space Flight Center
DRYER, M., Environmental Science Services Administration, Boulder
DUBIN, M., NASA, Washington
DUMONT, R., Observatoire de Bordeaux
ESHLEMAN, V. R., Stanford University
FARLOW, N. H., NASA, Ames Research Center
FIOCCO, G., Massachusetts Institute of Technology
FOGLE, B., University of Alaska
FREDRIKSSON, K., Smithsonian Institution, Washington
GALLAGHER, J. F., Jet Propulsion Laboratory
GIESE, R. H., Max-Planck-Institut für Physik und Astrophysik, Munich
GILL, JOCELYN R., NASA, Washington
GILLET, F. C., University of California, San Diego
GREENBERG, J. M., Rensselaer Polytechnic Institute
GREENMAN, N. N., Douglas Aircraft, Santa Monica
HALLIDAY, I., Dominion Observatory
HARWIT, M., Cornell University
HAUGHNEY, L. C., NASA, Ames Research Center
HEMENWAY, C. L., Dudley Observatory
HODGE, P. W., University of Washington
HOWARD, H. T., Stanford University
HURUHATA, M., Tokyo Astronomical Observatory
JAMES, J. F., University of Manchester
KAISER, C. B., High Altitude Observatory
KOOMEN, M. J., Naval Research Laboratory
KULKARNI, P. V., Physics Research Laboratory, Ahmedabad
MANN, H. M., Haleakala Observatory, University of Hawaii
MATTHEWS, R. O., NASA, Washington
MCCOY, J. G., Ball Brothers Research Corporation, Boulder
MILLMAN, P. M., National Research Council, Ottawa
MODISETTE, J. L., NASA, Manned Spacecraft Center
MORRIS, E. C., Geological Survey, Flagstaff
NILSSON, C. S., Smithsonian Astrophysical Observatory
PEALE, S. J., University of California, Los Angeles
PETERSON, A. W., University of Missouri
POWELL, R. S., Melpar, Falls Church, Virginia
REGENER, V. H., University of New Mexico
RHEE, J. W., Rose Polytechnic Institute
ROACH, F. E., Hawaii Institute of Geophysics
ROOSEN, R. G., University of Texas
SANCHEZ MARTINEZ, F., Observatorio del Teide, Tenerife
SCHMIDT, T., Landessternwarte, Heidelberg-Königstuhl
SHAFRIR, U., Tel-Aviv University
SILVA, R. W., NASA, Ames Research Center
SIMPSON, J. W., Lockheed, Sunnyvale
SINGER, S. F., University of Miami

SKRIVANEK, R. A., Air Force Cambridge Research Laboratories

SMITH, L. L., Environmental Science Services Administration, Boulder

SOBERMAN, R. K., General Electric, Philadelphia

SOUTHWORTH, R. B., Smithsonian Astrophysical Observatory

STRONG, I. B., Los Alamos Scientific Laboratory

TANABE, H., Tokyo Astronomical Observatory

TAYLOR, J. H., University of California, San Diego

TOUSEY, R., Naval Research Laboratory

VANDE NOORD, E. L., University of New Mexico

WALL, J. K., Douglas Aircraft, Huntington Beach

WEINBERG, J. L., Haleakala Observatory, University of Hawaii

WHIPPLE, F. L., Smithsonian Astrophysical Observatory

WOLSTENCROFT, R. D., Royal Observatory, Edinburgh

WRIGHT, FRANCES W., Smithsonian Astrophysical Observatory

Author Index*

Alexander, M. A.	35 (225)	Kashcheyev, B. L.	32 (189)
Allen, W. H.	17 (91)	Kerridge, J. F.	24 (147)
Aller, L. H.	36 (243)	Kilston, S.	36 (243)
Alvarez, J. M.	22 (123)	Koehler, R. L.	50 (361)
Asbridge, J. R.	51 (365)	Komissarov, G. D.	29 (171)
Asunmaa, S. K.	23 (131)	Konheim, A. G.	35 (225)
Bame, S. J.	51 (365)	Koomen, M. J.	14, 19 (79, 109)
Bandermann, L. W.	54 (379)	Krumm, W. J.	17 (91)
Belton, M. J. S.	43 (301)	Lebedinets, V. N.	32 (189)
Berg, O. E.	26 (161)	Leckrone, D.	36 (243)
Biermann, L.	39 (279)	MacQueen, R. M.	16 (89)
Blackwell, D. E.	3 (17)	McElfresh, T. W.	35 (225)
Brandt, J. C.	10 (57)	McKibbin, D. D.	53 (375)
Circle, R. R.	35 (225)	Mann, H. M.	1 (3)
Divari, N. B.	5, 46 (33, 321)	Millman, P. M.	55 (399)
Dohnanyi, J. S.	45 (315)	Modisette, J. L.	52 (373)
Dozier, J. B.	27 (165)	Montgomery, J.	36 (243)
Dubin, M.	21 (121)	Naumann, R. J.	27 (165)
Duffner, G.	36 (243)	Nazarova, T. N.	29 (171)
Dumont, R.	11 (63)	Newkirk, G.	42 (299)
Dworetsky, M.	36 (243)	Nilsson, C. S.	33 (201)
Dziembowski, C. v.	38 (271)	Oliver, J.	36 (243)
Elsässer, H.	40 (287)	Peale, S. J.	48 (337)
Fiocco, G.	20 (115)	Peterson, A. W.	4, 16 (23, 89)
Giese, R. H.	38 (271)	Powell, R. S.	35 (225)
Gillett, F. C.	2 (9)	Randle, R. J.	17 (91)
Gilpin, C. B.	23 (131)	Regener, V. H.	8 (45)
Greenberg, J. M.	34 (215)	Rhee, J. W.	41 (291)
Greenman, N. N.	23 (131)	Rose, L. J.	9 (49)
Gudehus, D.	36 (243)	Rybakov, A. K.	29 (171)
Hallgren, D. S.	24 (147)	Sanchez Martinez, F.	12 (71)
Harwit, M.	44 (307)	Saito, K.	7 (41)
Hemenway, C. L.	21, 24 (121, 147)	Schmidt, T.	40, 47 (287, 333)
Hodge, P. W.	30 (173)	Secretan, L.	26 (161)
Hoffmeister, C.†	15 (87)	Shafrir, U.	25 (155)
Howard, H. T.	50 (361)	Silva, R. W.	53 (375)
Hundhausen, A.	51 (365)	Simpson, J. W.	18 (97)
Huruhata, M.	6, 7 (37, 41)	Singer, S. F.	54 (379)
Ingersoll, R. G.	23 (131)	Skrivanek, R. A.	28 (167)
Ingham, M. F.	3 (17)	Southworth, R. B.	31, 37 (179, 257)
James, J. F.	13 (75)	Strong, I. B.	51 (365)
Kaiser, C.	42 (299)	Tanabe, H.	6 (37)

*First number indicates paper number; number in parentheses indicates page number.

Tousey, R.	14, 19 (79, 109)	Wolfe, J. H.	53 (375)
Vande Noord, E. L.	8 (45)	Wolstencroft, R. D.	9, 10 (49, 57)
Vogel, D. C.	35 (225)	Woodson, P. E., III	35 (225)
Wall, J. K.	49 (343)	Wright, F. W.	30 (173)
Weinberg, J. L.	1 (3)	Yaniv, A.	25 (155)
Whipple, F. L.	56 (409)	Zimmerman, E.	36 (243)

National Aeronautics and Space Administration

WASHINGTON, D. C. 20546

OFFICIAL BUSINESS

POSTAGE AND FEES PAID
NATIONAL AERONAUTICS AND
SPACE ADMINISTRATION

070 001 55 51 3DS 68168 00903
AIR FORCE WEAPONS LABORATORY/AFWL/
KIRTLAND AIR FORCE BASE, NEW MEXICO 87117

NAS.

ONS

ATT MISS MADELINE F. CANOVA, CHIEF TECHNICAL
LIBRARY /WLIL/

important, complete, and a lasting contribution to existing knowledge.

TECHNICAL NOTES: Information less broad in scope but nevertheless of importance as a contribution to existing knowledge.

TECHNICAL MEMORANDUMS: Information receiving limited distribution because of preliminary data, security classification, or other reasons.

CONTRACTOR REPORTS: Scientific and technical information generated under a NASA contract or grant and considered an important contribution to existing knowledge.

TECHNICAL TRANSLATIONS: Information published in a foreign language considered to merit NASA distribution in English.

SPECIAL PUBLICATIONS: Information derived from or of value to NASA activities. Publications include conference proceedings, monographs, data compilations, handbooks, sourcebooks, and special bibliographies.

TECHNOLOGY UTILIZATION PUBLICATIONS: Information on technology used by NASA that may be of particular interest in commercial and other non-aerospace applications. Publications include Tech Briefs, Technology Utilization Reports and Notes, and Technology Surveys.

Details on the availability of these publications may be obtained from:

SCIENTIFIC AND TECHNICAL INFORMATION DIVISION
NATIONAL AERONAUTICS AND SPACE ADMINISTRATION

Washington, D.C. 20546